DEVELOPMENT OF MAGNETOTELLURIC PROCESSING AND MODELLING PROCEDURES - APPLICATION TO NORTHERN ENGLAND

RONALD S. PARR

Ph. D. Thesis

University of Edinburgh

1991

DECLARATION

This thesis has been composed by me and has not been submitted for any other degree. This work is original, except where acknowledgement has been made.

Ronald S. Parr

ABSTRACT

The magnetotelluric (MT) method is a geophysical technique which uses observations of the naturally occurring electromagnetic (EM) field variations to determine the electrical impedance as a function of frequency. Owing to the variable signal and often high level of noise contamination, it is usual to collect large numbers of observations and perform parameter regression in order to gain reliable estimates of this Earth response function. It is then transformed into more interpretable, albeit non-unique, resistivity versus depth models.

In the course of this study, the processing, modelling and interpretation of MT observations from Northern England are considered. This includes previously unpublished data as well as a re-examination of spatially more extensive measurements which were acquired during earlier investigations. Existing MT field equipment has been adapted to allow local and remote reference observations to be collected and the results show that the amplitude of the impedance is contaminated by a lower level of noise induced bias. In addition, the resolution of the resulting model of the near structure can be enhanced by supplementary D.C. resistivity measurements.

Considerable attention is focused on the development of new methods for processing and modelling MT observations. In particular, the background theory and implementation of a robust and constrained method for the estimation of the impedance is described in some detail. This method is demonstrated on real and synthetic unreferenced observations and shown to improve the consistency and the reliability of the resulting response function by reducing the level of noise contamination.

One dimensional models are obtained for 42 MT response functions from Northern England. These are computed using a new 'exploratory' parametric technique which not only aims to find the best fitting model, but also to investigate its range of uniqueness. Additional, more interpretative modelling methods are also developed to improve the consistency of the models from adjacent sites. An experimental procedure which uses the constraining information provided by 2-D gravity model sections is also considered. At a subset of the sites over the Alston Block and the southern margin of the

Northumberland Trough a strictly 2-D MT model is derived.

Finally the structure within and beneath the Alston Block and Northumberland Trough is investigated using a data set consisting of previously published seismic, gravitational and electrical studies integrated with the results derived from this study. After presenting a detailed review of some of the existing Earth science observations and inferences, the models from this study are interpreted. The presence of a lower crustal electrically conductive zone is believed to have significant implications for the closure of the Iapetus ocean during the Ordovician and Silurian eras and subsequently the initiation and evolution of the Alston Block and Northumberland Trough. The location, extent and possible origin of other significant intra-basement and intra-basinal layers are also considered.

ACKNOWLEDGEMENTS

I would like to gratefully acknowledge the help and support of everybody who either directly or indirectly contributed to this study.

First and foremost my sincere thanks go to Rosemary Hutton for introducing me to the magnetotelluric method, suggesting this study and most importantly for continued guidance, friendship and help during my subsequent years as a research student. I wish to extend my appreciation to all the other staff at the geophysics department at Edinburgh University and my fellow contemporary students. I would like to especially thank Maxwell Meju and Roger Hill for many useful discussions and practical help with mastering the magnetotelluric (MT) method and inversion theory. Further help and advice was provided by T. 'Hari' Harinarayana, Sergio Fontes, Bruce Hobbs, Dimitrious Galanopolous and Phil Jones on various MT matters, whilst Turgul Genc and Roger Hipkin gave advice on gravity modelling. My two other supervisors, Alan Reid and Roger Scrutton provided many useful comments and constructive criticisms on a number of aspects of this study.

I gratefully acknowledge the N.E.R.C. and Robertson Research International for providing finance for this study and funding the fieldwork. I wish to also thank Tom Breheney for help and advice in the final preparation of many of the diagrams and the support of the staff of B.P. Exploration in Glasgow, during the final closing stages of this study. I also greatly appreciate the love and support of my wife Vivien and her tireless efforts in producing the diagrams and checking of this 'monster'. Finally I want to thank my son Andrew for his pleasant, albeit noisy, distractions.

TABLE OF CONTENTS

LIST OF FIGURES

CHAPTER 1

INTRODUCTION

For words like Nature half reveal

And half conceal the soul within

Lord Tennyson 1809-1892

1.1. GEOPHYSICAL EXPLORATION

The rock structure within the Earth is not well understood. Traditionally, geological inferences were based upon surface rock exposures and a small number of relatively shallow boreholes. Earth science investigations acquired a new dimension with the advent of surface geophysical techniques which could 'remotely sense' gross changes in the rock properties. It is likely that the miners who used magnets to identify ore prospects were the first to undertake 'exploration geophysics'. Now the subject is more sophisticated and diverse and includes measurements of the density, resistivity and acoustic properties of rock to complement the purely geological observations.

The rapid and low cost surveys supplied by the potential methods (gravity and magnetics) mean that they are ideal regional reconnaissance tools. However, they can not provide the same level of detail as the seismic reflection technique which is currently demanded in the commercial search for hydrocarbons. In general, measurements of the electrical resistivity of rocks within the Earth tend to fall between both of these extremes in terms of cost, survey speed and resolution.

The electrical resistivity, which is of primary interest to this study, is a measure of the ability of rocks to impede the passage of electrical currents. It can vary over several orders of magnitude and is sensitive to a very broad range of rock properties. It can therefore be used to gain a better understanding of the subsurface lithology.

Major changes in the resistivity of rocks can be measured at the Earth's

surface by a number of different methods. Direct Current (D.C.) resistivity sounding is the most intuitively obvious method which, at it simplest, requires that a known current be injected into the ground and measurements then made of the resulting potential difference. Ohm's Law is then applied to help determine the resistivity of the rocks. Very deep D.C. resistivity surveys have been performed (e.g. Blohm *et al.* 1977), but they suffer severe logistical difficulties. Other methods which require an artificial electromagnetic (EM) source field include Induced Polarization (I.P.; Parasnis 1982) and Controlled Source Audio MagnetoTellurics (CSAMT: Hughes and Carlson 1987). These methods are becoming increasingly widely used in exploration owing to the pre-determined nature of the source fields. However, like D.C. resistivity the artificially induced fields require large power sources and these methods usually only have a limited depth of penetration. Furthermore, there can be a number of modelling and interpretative problems associated with the results.

There are some EM methods which use only naturally occurring field variations to acquire resistivity information with depth. Measurements of the 3 orthogonal components of the natural transient magnetic fields allows the Geomagnetic Depth Sounding (G.D.S.; e.g. Banks and Beamish 1984) method to determine the extent of low resistivity zones by identifying the likely presence of induced current concentrations. However this method cannot, in itself, give unambiguous resistivity information.

This particular study is mainly concerned with another of these natural source techniques, known as the MagnetoTelluric (MT) method.

1.1.1. The Magnetotelluric Method as an Exploration Tool

Magnetotellurics developed in the 1950's after the influential papers by Tikhonov (reprinted in 1986) and Cagniard (1953). As its concatenated name suggests, this method requires measurements of the time varying amplitudes of both the horizontal magnetic and orthogonal electric fields. The latter are also known as Earth or telluric currents.

Land MT observations are usually collected from a site on the Earth's surface. These are used to determine the complex valued electrical impedance, or its associated scalar quantities, as a function of frequency of the EM field. This 'response function' can then be modelled to give a

quantitative measure of the resistivity of the subsurface rocks with depth within the Earth. Under ideal conditions this transformation can be performed without recourse to any other information.

The major advantage of the MT method is that its depth range of investigation is not restricted by the length of the measuring cables or the size of the power source. Magnetometers and a relatively short electrode array (usually less than 100 m.) can be used to find the electrical resistivity variation at any desired depth by simply collecting measurements of the EM field at lower frequencies. For deeper targets, MT is very cost effective because it does not need any large power source.

The MT method cannot compete in terms of resolution with seismic reflection, but it is known to be better at imaging steeply dipping structures and in the vicinity of some other difficult seismic targets. For example, the presence of lavas interbedded within a sedimentary sequence (Prieto *et al.* 1985) will strongly attenuate seismic energy, but present little problem to the transmission of EM fields.

There are a number of case studies which describe the application of the MT method for the exploration of different geological targets (see for example the reviews by Hermance 1983 and Chave and Booker 1987). Since magnetotellurics can readily acquire information about the Earth's deep interior, a number of global induction studies have been undertaken (reviewed by Parkinson and Hutton 1989). On a more regional scale, there have been MT lithospheric examinations of subduction zones (e.g. Kurtz *et al.* 1986, Ingham 1988b) and shield regions (Jones 1982, Strangway *et al.* 1986). More localised studies have been performed on granite intrusions (Beamish 1990, P. Jones, person commn.), major thrust and fault zones (Hill 1987, Meju 1988) and sedimentary basins (Vozoff 1972, Christopherson 1991). The strong dependence of resistivity on both temperature and the presence of water has meant that MT has frequently been used for geothermal exploration (Hoover *et al.* 1978, Devlin 1984, Galanopolous 1989). With the advent of broad band MT recording systems, particularly at higher frequencies, increasingly more studies have been concerned with investigations of the shallower structure of the Earth.

The MT method, like all geophysical techniques, does have its problems and limitations. To summarize, some of the more important ones are as follows:

1. Its resolving power is inherently limited by the attenuation of high frequency components of the EM field by the presence of overlying rocks.

2. The MT results are often degraded because the method relies upon the nature and vagaries of natural EM source fields. These are often either not strong enough, or do not conform to a number of assumptions in order to acquire accurate estimates of the electrical impedance. Densely populated and industrialised countries are particularly difficult survey locations owing to the additional problem of cultural noise.

3. Models based on the estimated impedance as a function of frequency invariably produce non-unique information on the resistivity variation with depth. Modelling is further hindered by the presence of anisotropy, near surface distortions and topography.

4. The minimum and maximum depths of investigation are variable as they depend upon the frequency range of the observations collected and the geoelectric structure of the site.

5. The resistivity cannot be used to give an unambiguous identification of lithology as it depends upon too many different rock properties.

Some of these problems will be addressed in this study.

1.2. Research Aims of this Study

The primary objectives of the research work undertaken in this study were: 1) the acquisition of accurate and unbiased MT response functions, 2) the determination of the optimum Earth model for the response functions, and 3) the analysis and interpretation of the results of a detailed geophysical study of both the near surface and deeper crustal structure of Northern England.

1.3. Outline of this Thesis

This thesis starts by deriving some of the fundamental MT relationships from basic EM wave theory. Other related topics, including the source of the EM field variations and the inter-relationship between the observed resistivity and other rock properties, are also reviewed. Since previous investigations in Northumberland had demonstrated that MT was unable to resolve the top 100

m. alone (Novak 1981, Harinarayana 1987), supplementary D.C. resistivity observations were also collected. Some of the fundamental applied theory for this technique is therefore developed.

The field methods and strategy employed for the acquisition of MT and D.C. resistivity data are given in chapter 3. This includes a discussion of MT field techniques site selection criteria and a brief discussion of the sites which were occupied in Northumberland.

Over the last decade, the reference field technique has been introduced at other centres of MT research, worldwide, to reduce noise contamination of the impedance estimates. In the course of this study, pre-existing MT data acquisition equipment was adapted to perform local (< 500m.) and remote (1-10km.) reference. Chapter 3 therefore also includes a description of these modifications and the manner in which the equipment was deployed.

Since large numbers of observations are often manipulated during the processing and modelling of MT data, considerable use of parameter regression has been made. Consequently, chapters 4 and 5 provide an extensive review of the least squares method of parameter estimation and useful adaptations to it. Its advantages and shortcomings are described in the general context, before highlighting a number of problems from MT impedance estimation. This includes a derivation of the relevant equations and a description of their inadequacy in the presence of the typical assortment of EM noise sources which are often encountered.

Chapter 5 is concerned with some of the more sophisticated adaptations or alternatives to basic least squares. Like chapter 4, the emphasis is directed towards presenting mathematical regression theory which is relevant to the different stages of processing from the conversion of MT time series observations into the final interpretable Earth models. The topics covered include impedance estimation using the reference and Singular Value Decomposition (SVD) methods, robust statistics and the estimation of parameters by constrained and non-linear techniques.

Accurate MT response functions are essential to provide good Earth models. Frequently the MT source field is too contaminated by noise or too unreliable to achieve this. As many unreferenced observations have been

collected by this and previous authors, a large proportion of the research effort was directed towards the development of post field computer software for the estimation of MT response functions from such data. This technique uses a modified SVD method to compute initial impedance estimates before imposing certain physical conditions upon the form of the response function. This 'idealized response function' is then used to constrain a re-evaluation of the initial impedance estimates. The method is fully described in a companion paper (' Constrained Estimation of the Magnetotelluric Impedance Tensor') which has been submitted to the Geophysical Journal International. It is reproduced here as Appendix - A. The computer programs written or adapted for this type of processing, together with other algorithms developed to undertake response function modelling, are described in Appendix - B.

The above robust and constrained impedance estimation method was routinely applied to process all of the field observations acquired by this author. To provide more extensive coverage, the EM time series data from a further 11 MT sites (collected by Harinarayana 1987) were reprocessed using the new programs. The detailed results are given in Appendix - C, whilst a comparison between a few different impedance estimation procedures (including local and remote reference and robust estimation methods) is given at the end of chapter 5.

Chapter 6 commences with a review of different 1-D MT response function modelling methods, their limitations and some multi-dimensional alternatives which are available. The remainder of this chapter is concerned with a description of the particular methods which were applied to the response functions from Northern England. These are based upon: 1) simple contoured sections from 1-D Bostick transformed values, 2) more detailed 'exploratory' 1-D models, 3) constrained 1-D ('pseudo 2-D') models and for a small sub-set of the sites, 4) a strictly 2-D MT model. For the purposes of the modelling study, the response functions from the new reprocessed observations were augmented by a further 21 which had been published following previous investigations.

The pseudo 2-D modelling computer program was also adapted to generate simple models from 2-D gravity anomaly observations, with the ultimate goal of performing joint and constrained modelling of coincident MT

and gravity boundaries. The theory and implementation of these methods are discussed and demonstrated.

Chapter 7 presents a wide ranging and relatively comprehensive review of the Earth science literature from previous studies of Northern England. It draws on both geological and geophysical observations to provide some background information concerning the known evolution and structure of the region. It also tries to lend additional support to the interpretation placed on the geophysical models from this study, which are discussed in chapter 8. The nature of the lower crust, 'basement' rock and sedimentary layer are discussed at some length with a strong emphasis on integrated interpretations drawing on other sources of geophysical data. Finally, a personal and speculative scenario for the geological evolution of Northern England is presented.

Chapter 9 summarizes some of the more significant conclusions and results of this study before providing some recommendations for further research work.

CHAPTER 2

THE MAGNETOTELLURIC AND D.C. RESISTIVITY METHODS

2.1. INTRODUCTION

Two geophysical measuring tools were used in this study to observe the gross electrical resistivity (or conversely the conductivity) changes with depth in the Earth. This chapter reviews some of the theoretical and practical background to the magnetotelluric and D.C. resistivity methods.

Maxwell's equations (section 2.2) provide the starting point for the derivation of some of the key equations for both methods. The MT method is then described in some detail (sections 2.3–2.7). This discussion covers several aspects of the technique ranging from the solution of the induction problem in one and more dimensions, properties of its estimated impedance tensor and the origin of the naturally occurring EM source field. A brief discussion of the relevant D.C. resistivity theory is then presented (section 2.8) and this chapter concludes with a description of the likely causes of observed shallow and deep resistivity structure (section 2.9).

The following account draws heavily from a number of EM and MT references, but most notably, Patra and Mallick (1980), Kaufman and Keller (1981), Grant and Phillips (1980), Keller and Frischknecht (1970), Porstendorfer (1975), Novak (1981), Fontes (1988), Meju (1988) and Parkinson and Hutton (1989). Whilst only a limited discussion of the D.C. resistivity method is presented here, more thorough reviews are given by Telford *et al.* (1976), Koefoed (1980), Parasnis (1982), Bhattacharya and Patra (1968).

2.2. MAXWELL'S EQUATIONS

All EM problems must satisfy the inter-related Maxwell's equations:

$$\nabla \times E = -\delta B/\delta t \qquad (2.2.1a)$$
$$\nabla \times H = J + \delta D/\delta t \qquad (2.2.1b)$$
$$\nabla \cdot B = 0 \qquad (2.2.1c)$$
$$\nabla \cdot D = \rho^* \qquad (2.2.1d)$$

where **E** is the electric field intensity (in $V.m^{-1}$), **B** is the magnetic induction field (in Wbm^{-2} or T), **H** is the magnetic field intensity ($A.m^{-1}$), **J** is the current density ($A.m^{-2}$), **D** is the electric induction field ($C.m^{-2}$) and ρ^* is the charge density ($C.m^{-3}$).

Faraday's law of induction (eqn. 2.2.1a) shows that the presence of a time varying magnetic field will induce a corresponding change in the electric field. Within a conducting medium, currents can then flow around any closed loop whose axis is coincident with the direction of **B**.

In contrast, if an electrical current is already flowing around a closed loop, Ampere's law (eqn. 2.2.1b) shows that a magnetic field will be associated with it, with a magnitude proportional to the total current flowing. There are two currents described by equation 2.2.1b: a steady conduction current **J** and a time dependent displacement current. The latter are transient currents which are produced when fluctuations in the **D** field affect the polarisation of the dielectric material within the conductor. These decay very rapidly in free space for low frequency EM fields (<100 kHz.) and in most realistic geoelectric environments they have a negligible effect at typical MT frequencies (e.g. Oristaglio and Worthington 1980). Therefore it is usual to assume a quasi-static field situation in which $\delta D/\delta t$ is zero and only the conduction currents are significant.

Equation 2.2.1c states the well known experimental result that no free magnetic charges or monopoles exist.

Since any charge distribution decays very rapidly within a conductive material, it can be assumed that no charges accumulate and consequently eqn. 2.2.1d can be simplified by setting ρ^* to be zero. This particular equation is solved when there are static electric currents present, as for example, during D.C. resistivity surveying (section 2.8).

To derive relationships between Maxwell's equations, the experimentally

determined constitutive equations must be used:

$$\mathbf{D} = \varepsilon \, . \, \mathbf{E} \qquad (2.2.2a)$$

$$\mathbf{B} = \mu \, . \, \mathbf{H} \qquad (2.2.2b)$$

$$\mathbf{J} = \sigma \, . \, \mathbf{E} \qquad (2.2.2c)$$

$$\sigma = 1 \, / \, \rho \qquad (2.2.2d)$$

where ε is the electrical permittivity (ε_0=8.9 10^{-12}F.m^{-1} in free space), μ is the magnetic permeability (μ_o= 4.π.10^{-7}H.m^{-1} in free space), σ and ρ are the electrical conductivity and resistivity of the medium in mhos.m^{-1} and ohm.m^{-1} respectively. For most heterogeneous and anisotropic rocks, ε and μ will change with position and direction. However the variation in these parameters is small when compared with the vast range of resistivities within the Earth. Therefore by assuming that the Earth is homogeneous, isotropic and time invariant in these parameters ($\varepsilon=\varepsilon_0$ and $\mu=\mu_0$), the constitutive equations allow a simplification of Maxwell's equations by eliminating the B, J and D terms.

2.2.1. The Magnetotelluric Diffusion Equation

Taking the curl of equation 2.2.1a and then substituting equation 2.2.2b into the right hand side:

$$\nabla \times (\nabla \times \mathbf{E}) = -\delta/\delta t(\nabla \times \mathbf{B}) = -\mu_0 \, . \, \delta/\delta t(\nabla \times \mathbf{H}) \qquad (2.2.3)$$

Expanding the left hand side of equation 2.2.3 and then substituting equation 2.2.1b and using equation 2.2.2c to eliminate H:

$$\nabla \; (\nabla \, . \, \mathbf{E}) - \nabla^2 \mathbf{E} = -\mu_0 \; \sigma \; \frac{\delta \mathbf{E}}{\delta t} \qquad (2.2.4)$$

Since eqn. 2.2.1d states that $\nabla \, . \, \mathbf{E} = (\nabla . \mathbf{D}/\varepsilon_0) = 0$, then the first term in eqn. 2.2.4 disappears.

Although the actual field variations may be very erratic, the solution of eqn. 2.2.4 becomes tractable if it can be assumed that the frequency range has quasi-periodic variations. As MT measurements consist of time domain observations of the EM field variations (E(t) and H(t)) a Fourier transformation is performed to determine their amplitude as a function of angular frequency ($\omega = 2\pi.f$). The linearity of eqn. 2.2.4 allows its solution for one such frequency (i.e. a monochromatic wave $E(t) = E_0.e^{-i.\omega.t}$) and then the superposition of sine waves of other frequencies. Acquisition of a frequency

domain solution has a number of advantages over its time domain equivalent. Most notably, the time invariance of the results and the ease with which the phase difference between the EM fields can be estimated.

Taking the derivative of E(t) in eqn. 2.2.4 gives:

$$\nabla^2 E = -i \cdot \omega \cdot \mu_0 \cdot \sigma \cdot E \qquad (2.2.5)$$

A similar equation can also be derived from equation 2.2.1b, for the propagation of the magnetic field in a homogeneous medium:

$$\nabla^2 H = -i \cdot \omega \cdot \mu_0 \cdot \sigma \cdot H \qquad (2.2.6)$$

In free space (e.g. air or very poorly conducting rocks with $\sigma = 0$ approx.), eqn. 2.2.5 (Laplace's equation) shows that the EM field propagates without attenuation. In more geophysically interesting situations, induced electric currents within the conductive rocks will dissipate the field energy according to these diffusion equations.

2.2.2. Further Assumptions

The solution of the diffusion equation can be very difficult unless the following additional simplifying assumptions are made:

1. The Earth is a passive system which cannot produce EM field energy and only dissipates or absorbs it.

2. The Earth is a causal system in which there is no response prior to excitation from the magnetic field (c.f. Egbert 1990, Yee and Paulson 1990); but it responds immediately afterwards (i.e. minimum phase in seismic reflection terminology).

3. The source of the magnetic field is external to the Earth and the resultant is a vertically incident ('plane') wave whose horizontal variations in amplitude are negligible compared with its vertical ones. In practical terms, the source should be located sufficiently far away that the horizontal extent of the resulting EM fields is much greater than its penetration depth at the measuring site.

4. The Earth is a linear system in which a change in the 'input' magnetic field directly induces an 'output' electric field variation.

5. For the relatively high frequency work ($> 10^{-4}$Hz.) of interest to this study, the influence of the curvature of the Earth can be neglected, as planar structures are simpler to solve.

The solution of the diffusion equations (eqns. 2.2.5 and 2.2.6) within homogeneous regions are now considered. The EM field boundary equations, which can be derived from equations 2.2.1 and 2.2.2 and which are relevant to conductivity discontinuities are also discussed.

2.3. ONE DIMENSIONAL MAGNETOTELLURIC INDUCTION

In a Cartesian coordinate system (x: north, y: east, z: vertically downward), the simplest model structure consists of a homogeneous and isotropic half space of uniform conductivity, σ below the surface and the non-conductive air or 'free space' (σ=0) above it ($z < 0$). In this environment, a polarised magnetic field (e.g. in the east direction; H_y) will induce a perpendicular electric field (E_x). As a plane wave will not then induce variations in any of the other components of the electric field ($E_y = E_z = 0$), eqn. 2.2.5 simplifies to:

$$\delta^2 E_x/\delta z^2 = -i.\omega.\mu_0.\sigma.E_x \qquad (2.3.1)$$

The solution of this differential equation is given by the superposition of plane waves diffusing upwards and downwards as:

$$E_x = C_1.e^{kz} + C_2.e^{-kz} \qquad (2.3.2)$$

where C_1 and C_2 are constants and k is known as the wavenumber ($k=(i.\mu_0.\omega.\sigma)^{1/2}$). Because the Earth is a passive system (section 2.2.2), the electric field cannot take arbitrarily large values. Therefore to avoid such unphysical singularities it is necessary to impose the boundary condition that C_1=0. Taking the derivative of eqn. 2.3.2 with respect to z ($\delta E_x/\delta z = -k.C_2.e^{-kz}$) and equating this with eqn. 2.2.1a ($\delta E_x/\delta z = -i.\omega.\mu_0.H_y$), at the Earth's surface (z=0), gives:

$$C_2 = (i.\mu_0.\omega/\sigma)^{1/2}.H_y \qquad (2.3.3)$$

This coefficient contains information about the conductivity distribution as well as the primary (inducing) and secondary (induced) parts of the EM fields. Although the amplitude of these fields is time variant and unknown, this is unimportant to the MT method which uses the ratio:

$$E_x/H_y = Z = (i.\mu_0.\omega/\sigma)^{1/2} \qquad (2.3.4)$$

Assuming that μ_0 and σ are constants, eqn. 2.3.4 can be explicitly written as:

$$Ex(\omega) = Z(\omega) \cdot Hy(\omega) \qquad (2.3.5a)$$

or equivalently

$$Ex(f) = Z(f) \cdot Hy(f) \qquad (2.3.5b)$$

The complex valued impedance has 2 degrees of freedom so that 2 scalar quantities, which are also functionally dependent on the frequency, can be obtained. The first of these, sometimes referred to as the Cagniard resistivity (Cagniard 1953) can be computed from the amplitude of the impedance:

$$\rho(f) = | Z(f) |^2/(\mu_0 \cdot \omega) \qquad (2.3.6)$$

If the EM fields have been measured in the practical units of $mV.km^{-1}$ (E) and γT (B) then eqn. 2.3.6 simplifies to:

$$\rho(f) = 0.2 \cdot | Z(f) |^2/f \qquad (2.3.7)$$

The second scalar quantity is the phase difference between the E and H fields: of Z:

$$\phi(f) = \tan^{-1}(Im(Z(f)) / Re(Z(f))) \qquad (2.3.8)$$

where ϕ is 45^O in a homogeneous medium.

As a result of the directional generality of the 1-D model, the Cagniard impedance can be evaluated from any other orthogonal pair of horizontal electric and magnetic field observations, (e.g. $Z(f) = -E_y(f)/H_x(f)$).

2.3.1. Skin Depth

Equation 2.3.2 shows that upon entering the conductive Earth, there is an exponential decay in the amplitude of the EM field owing to the generation of electrical currents. The expansion of the wavenumber, k, allows the "skin depth" of a monochromatic wave to be determined in a uniform environment of resistivity ρ:

$$k = (1+i).(\mu_0.\omega.\sigma/2)^{1/2}$$

$$\delta = 1/Re(k) = (2.\rho/\mu_0.\omega)^{1/2} \qquad (2.3.9)$$

Therefore at the depth δ within a conductive medium, the amplitude of the incident wave is damped by a factor of 1/e of its initial, surface value.

For this trivial Earth model it is apparent that the impedance is related to

the subsurface conductivity structure and can be evaluated from Fourier transformed EM field observations collected at the Earth's surface (eqn. 2.3.4). Furthermore equation 2.3.9 shows that the depth of penetration of an electromagnetic wave, and hence the depth from which information can be gleaned, is increased within resistive environments and by measuring lower frequency field variations. The Earth thus acts like a low pass filter, selectively attenuating the higher frequency EM field oscillations. Therefore, the MT impedance is estimated at a broad range of frequencies in order to obtain a response function which can provide information concerning the conductivity distribution over a range of depths.

2.3.2. Multilayered 1-Dimensional Electromagnetic Induction

In realistic situations, a homogeneous 1/2-space Earth model is never encountered. A very common practice in the interpretation of MT response functions requires the assumption that the changes in resistivity only occur in the vertical (z) plane. The Earth model then consists of a stack (N) of horizontal layers, each with a uniform conductivity (σ_j; j=1,N-1) or resistivity (ρ_j) at a depth h_j, terminated by a homogeneous 1/2 space model of resistivity ρ_{N_i}. The MT impedance which would be observed above such a model can be evaluated by first computing the Cagniard impedance for each individual layer in the stack. As before, this can be accomplished by solving the diffusion equation (eqn. 2.3.1) for each individual layer in the stack and imposing continuity conditions for the EM fields (E_x and H_y) across the boundaries. After elimination of the constants C_1 and C_2, the following recurrence relation can be obtained (e.g. Kaufman and Keller 1981):

$$Z_N(0) = \omega\mu/k_1.\coth\{-ik_1h_1 + \coth^{-1}[(k_1/k_2).\coth(-ik_2h_2+\coth^{-1}\{(k_2/k_3).\coth[-ik_3h_3+ +....+\coth^{-1}((k_{N-2}/k_{N-1}).\coth\{-ik_{N-2}h_{N-1}+\coth^{-1}(k_{N-1}/k_N)\})...]\})]\} \quad (2.3.10)$$

It is not readily possible to invert this equation to recover conductivity as a function of depth, but during 1-D MT modelling (section 6.2), eqn. 2.3.10 is routinely used to calculate the impedance at the Earth's surface for a given multi-layered model ('forward modelling').

The resistivity (eqn. 2.3.6 or 2.3.7) corresponding to the impedance over a multi-layered model is only the true resistivity of an equivalent homogeneous

and isotropic 1/2 space. The quantity calculated using equation 2.3.6 varies with frequency and is known as the apparent resistivity (ρ_a). In an analogous fashion to D.C. resistivity depth profiling (section 2.8), it gives a qualitative indication of the resistivity variation with depth and can be loosely regarded as a type of weighted average of the individual 1-D layer resistivities. The behaviour of the MT phase cannot be so readily interpreted (c.f. Fischer 1985) although in theory, it should provide almost the same information as contained in the apparent resistivity response function (section 2.6). As a rough guide, the phase is a constant (45^{O}) in a homogeneous environment and decreases in a more resistive layer. Conversely it increases when the EM fields enter a more conductive zone. The phase is properly specified in one quadrant, usually between $0^{O} <= \phi(f) <= 90^{O}$ (Loewenthal 1979). The apparent resistivity and phase have more direct intuitive significance than the impedance and so are widely quoted in this and other MT research work.

2.4. TWO DIMENSIONAL INDUCTION

1-D models are very useful interpretative tools in simple environments, but are only an approximation to the real heterogeneous Earth. A strictly 2-D geoelectric structure displays conductivity variations in both the vertical (z) and one horizontal (say y) directions (i.e. $\sigma = \sigma(y,z)$). Ideally, such a structure should extend uniformly to infinity in the x (strike) direction. In practice, a 3-D feature needs only to be uniform over a distance of a few skin depths in the strike direction to be reasonably well approximated by a 2-D model. As Patra and Mallick (1980) have pointed out, such 2-D features (e.g. rift valleys, faults, dykes etc.) are at least as common as layered (1-D) structures.

To solve this problem it is necessary to make the same basic assumptions as for the 1-D case, but assuming further that there is no conductivity variations in the x direction ($\delta/\delta x = 0$). Expanding Maxwell's equations (eqns. 2.2.1a and 2.2.1b) into Cartesian component form will give rise to 6 equations. When the geoelectric structure is truly two dimensional, the EM fields de-couple into 2 distinct polarizations. The first of these, the 'E polarization' (or TE mode), is a function of (Hy,Hz,Ex) only, whilst the second, the 'H polarization' (or TM mode) is dependent upon (Hx,Ey,Ez):

$$\frac{\delta Hz}{\delta y} - \frac{\delta Hy}{\delta z} = \sigma.Ex \qquad \frac{\delta Ex}{\delta z} = -i\omega.\mu_0.Hy \qquad \frac{\delta Ex}{\delta y} = i.\omega.\mu_0.Hz \qquad (2.4.1a)$$

$$\frac{\delta Ez}{\delta y} - \frac{\delta Ey}{\delta z} = -i.\omega.\mu_0.Hx \quad \frac{\delta Hx}{\delta z} = \sigma.Ey \qquad \frac{\delta Hx}{\delta y} = \sigma.Ez \qquad (2.4.1b)$$

Each of these modes corresponds with the electric and magnetic fields being respectively polarized parallel to the strike of the structure. In the latter case, electric currents flow perpendicular to the strike creating a charge accumulation at the conductivity discontinuity (section 6.3). The observed impedances for the two polarizations are not the same but vary according to the distance of the MT site from the discontinuity and to the frequency under investigation.

Two non-linear differential equations result from the elimination of Hy and Hz from equation 2.4.1a and Ex and Ey from equation 2.4.1b. They can only be solved analytically for a few simple structures because of the difficulty in imposing boundary conditions.

2.5. THE IMPEDANCE TENSOR

2.5.1. Formulation

The scalar Cagniard impedance cannot satisfactorily account for the conductivity variations in an anisotropic Earth. Cantwell (1960) therefore proposed the use of the rank 2 impedance tensor:

$$E(f) = Z(f) \cdot H(f) \qquad (2.5.1a)$$

$$\begin{vmatrix} Ex(f) \\ Ey(f) \end{vmatrix} = \begin{vmatrix} Zxx(f) & Zxy(f) \\ Zyx(f) & Zyy(f) \end{vmatrix} \cdot \begin{vmatrix} Hx(f) \\ Hy(f) \end{vmatrix} \qquad (2.5.1b)$$

In filter terminology, eqn. 2.5.1 suggests that the two 'output' electric field components are linearly related to the complex multiplication of the two 'input' magnetic field components and the impedance tensor. Such a coupling has not been proven, but has been widely adopted and appears to hold within the accuracy of the measuring equipment (Vozoff 1972, Yee and Paulson 1988a, Rokityansky 1982).

A similar relationship is also assumed to exist between the horizontal and

vertical components of the magnetic field:

$$Hz(f) = (Tx(f)\ Ty(f)) . \begin{vmatrix} Hx(f) \\ Hy(f) \end{vmatrix} \qquad (2.5.2)$$

where Tx(f) and Ty(f) are known as the tipper elements because they transform, or tip, the observed horizontal magnetic field into the vertical plane.

Owing to the presence of noise in EM field measurements, a large number of observations are usually performed in order that reliable estimates of the impedance and/or tipper parameters may be obtained. This is a least squares regression problem which is discussed further in section 4.7.

In simple geoelectric environments, the response functions derived from the off-diagonal impedance elements have the greatest significance. These elements relate the orthogonal components of the EM fields and their corresponding apparent resistivity and phase estimates are given by (c.f. eqns. 2.3.7 and 2.3.8):

$$\rho_{axy} = 0.2 . |Zxy|^2/f \qquad \phi_{xy} = \tan^{-1}(Im(Zxy)/Re(Zxy)) \qquad (2.5.3a)$$

$$\rho_{ayx} = 0.2 . |Zyx|^2/f \qquad \phi_{yx} = \tan^{-1}(Im(Zyx)/Re(Zyx)) \qquad (2.5.3b)$$

2.5.2. Rotation of the Impedance Tensor

In the presence of 1-D geoelectric structures, equation 2.5.1 reduces to the Cagniard impedance when the diagonal elements are zero (Zxx = Zyy = 0) and the off-diagonal elements are equal in magnitude but opposite in sign (Z = Zxy = -Zyx). In general, none of the 4 elements is zero and their magnitudes depend upon the orientation of the measuring frame of reference. Consequently, Ex(f) and Ey(f) are induced not only by the corresponding orthogonal magnetic field, but also by the parallel field to some extent.

For strictly 2-D structures a direction can be found in which the rotated impedance elements Zxx' = Zyy' = 0. This direction corresponds to the geoelectric strike and consequently Zxy' and Zyx' are the impedances parallel and perpendicular to strike (the E and H polarization modes respectively).

The impedance is usually measured in an arbitrary orientation around the vertical axis (e.g. magnetic north) with respect to the largely unknown strike

('azimuth') of the structure. The impedance tensor can be numerically rotated to any direction via:

$$Z' = R \,.\, Z \,.\, R^T, \qquad (2.5.4)$$

where R is the rotation tensor = $\begin{vmatrix} \cos\theta & \sin\theta \\ -\sin\theta & \cos\theta \end{vmatrix}$

As the diagonal elements of the rotated impedance tensor rarely reach zero, several different ways of identifying the strike direction (θ) have been proposed. For example, the angle which maximises $Z'_{xy}(\theta)$ and minimises $Z'_{yx}(\theta)$, or the angle which minimizes $|Z'_{xx}(\theta)|^2 + |Z'_{yy}(\theta)|^2$. Alternatively, Swift (1986) has proposed an analytical method which maximises $|Z'_{xy}(\theta)|^2 + |Z'_{yx}(\theta)|^2$. When $Z'_{xy}(\theta)$ is maximised and $Z'_{yx}(\theta)$ minimised, the 'principal directions' are determined. Correspondingly, the 'major' and 'minor' apparent resistivity and phase can be computed (c.f. eqn. 2.5.3).

There is an ambiguity in the determination of the strike direction as both θ and $\theta + \pi/2$ produce the same result in the rotation equations. This cannot be overcome without additional vertical magnetic field observations (Vozoff 1972).

2.5.3. Dimensionality

It is clear from the discussion in the previous section, that a negligible value for Zxx and Zyy with respect to the magnitude of Zxy and Zyx suggests the presence of a low dimensional structure. Therefore a quantitative measure of the dimensionality of the geoelectric structure (the 'skew') is defined as (Vozoff 1972, Swift 1986):

$$\text{Skew} = \left| \frac{Zxx + Zyy}{Zxy - Zyx} \right| \qquad (2.5.5)$$

where Zxx + Zyy and Zxy - Zyx are rotationally invariant quantities (i.e. they are approximately constants with respect to θ). Although it is obvious that a higher value of skew indicates a more complex geoelectric environment, the threshold skew value between 2 and 3-D structures is not clear. In this study, it was taken to be at 0.3 (see Appendix - C).

It has been recognized by a number of other authors that the skew is not

always a good dimensionality indicator. For example, this particular author has noted that the presence of high skews can also be attributed to the presence certain types of EM field noise (section 5.9.4). A number of alternative dimensionality tests, including the eccentricity, ellipticity and the Kao and Orr (1982) dimensionality weights have therefore been proposed. The benefits of each have been reviewed by Beamish (1986a).

2.5.4. Coherence

The coherence (e.g. Swift 1986, Travassos and Beamish 1988) is a frequently used MT data quality test statistic calculated for 2 components (e.g. **A** and **B**) of the Fourier transformed EM fields:

$$\mathrm{Coh}(A,B) = \frac{[A^H B]}{([A^H A].[B^H B])^{1/2}} \qquad (2.5.6)$$

where $[A^H B]$ is the cross spectral power averaged over a range of frequencies and/or time series sections (c.f. section 4.7). If for example **A** = **Hx** and **B** = **Hy**, then eqn 2.5.6 gives an estimate of the similarity between the 2 'input' EM fields. The coherence is real valued and lies between 0 to 1; the lower bound implying that the 2 signals are completely uncorrelated and the upper bound that they are perfectly linearly related.

It is very common for MT data processors to compute a 'predicted coherence' between the observed electric field and its predicted counterpart computed from the product of the observed magnetic fields and the estimated impedance. It is often assumed that a high coherence implies that the signals are predictable and have a low level of random noise. Consequently, it is widely used as a criterion for the selection of time series segments. This procedure cannot be justified in the presence of coherent noise between the EM fields.

2.6. DISPERSION RELATIONS

The form of the MT response function can be constrained because it characterizes the Earth's conductivity distribution, which is a real physical and linear system (Yee and Paulson 1988a). In particular, the principle of causality (section 2.2.2) imposes the constraint that the response is an analytic function,

so that the real and imaginary parts of the complex response function (or equivalently the apparent resistivity and phase) are not independent. They are 'conjugate functions' which are related by integral relationships known as 'Hilbert transforms' or 'dispersion relations'. They have been described by Bode (1949), Weidelt (1972), Kaufman and Keller (1981), Patra and Mallick (1980), Fischer and Schnegg (1980), Rokityansky (1982), Kanasewich (1981) and Yee and Paulson (1988a). In this study, as in a number of applications (e.g. tippers, seismics and optics), dispersion relations are used in the determination of the value of one of the conjugate pair, given the other.

In the time domain, the linear relationship between the magnetic (H(t)) and electric (E(t)) fields can be described by a convolution:

$$E(t) = \int_{-\infty}^{\infty} Z(\tau) \, . \, H(t-\tau) \, \delta\tau \qquad (2.6.1)$$

where $Z(\tau)$ is the impulse response function. Since causality implies that the response cannot occur before the input (magnetic field) is applied (i.e. $Z(\tau) = 0$, for $\tau < 0$), then the lower limit of integration in eqn. 2.6.1 must be zero. Fourier transformation of equation 2.6.1 into the frequency domain gives:

$$E(\Omega) = Z(\Omega) \, . \, H(\Omega) \qquad (2.6.2)$$

$$\text{where } Z(\Omega) = \int_0^{\infty} Z(t) \, . \, e^{-i.\Omega.t} \, \delta t$$

Equation 2.6.2 is identical to equation 2.5.1a if Ω is real valued and positive, but for the derivation of the dispersion relationships it is necessary to consider the entire complex valued frequency domain ($\Omega = \omega + i\omega'$). Assuming that Z(t) is finite for all $t>0$, the integral in eqn. 2.6.2 is convergent because $e^{-i.\Omega.t}$ is finite for frequencies in the half-region below the real axis. Therefore $Z(\Omega)$ must be free of singularities (poles) for $Im(\Omega) <= 0$ and fully differentiable in the region. The MT response is therefore an analytic function and Cauchy's integral formula can be used to calculate the impedance at any point on or inside a closed contour within this region. This analytic function is therefore, in principle, completely specified over any arbitrarily small frequency range (e.g. Weidelt 1985).

Consider a semi-circular contour which resides along the real frequency axis and whose radius extends a long way down into the negative imaginary region. In the limit, only the contribution from real frequencies is significant ($\Omega=\omega$), as points on the circle, in the imaginary plane, do not contribute to the Cauchy integral (Weidelt 1972). The dispersion relations between the real and imaginary parts of the impedance can then be derived for those frequencies which are actually observed, on the positive real axis ($0 < \omega_0 < \infty$). For points on this part of the contour, the Cauchy integral is given by:

$$i.\pi.Z(\omega_0) = PV \int_{-\infty}^{\infty} \frac{Z(\omega)}{\omega_0 - \omega} \delta\omega \qquad (2.6.3)$$

It is fortunate that this integral depends primarily on the principal part (PV) of the frequency range, as observations are necessarily limited to a finite bandwidth. By separating equation 2.6.2 into its real and imaginary parts ($Z = Re[Z] + i.Im[Z]$) and using the symmetry properties of the response function ($Z(\Omega) = Z^H(-\Omega)$; Yee and Paulson 1988a) the two dispersion relations can be obtained:

$$Re[Z(\omega_0)] = 1/\pi \; . \; PV \int_{-\infty}^{\infty} \frac{Im[Z(\omega_0]}{\omega_0 - \omega} \delta\omega \qquad (2.6.4a)$$

$$Im[Z(\omega_0)] = -1/\pi \; . \; PV \int_{-\infty}^{\infty} \frac{Re[Z(\omega_0)]}{\omega_0 - \omega} \delta\omega \qquad (2.6.4b)$$

Equations 2.6.4 can therefore be used to acquire the real part of the impedance from the imaginary, or vice versa. They may also be written in a variety of equivalent forms (see Bode 1949). Probably of more interest to MT is the acquisition of the apparent resistivity from the phase, or vice versa. Describing the complex impedance as ($Z(\omega_0) = |Z(\omega_0)|.e^{i\phi(\omega_0)}$) and taking the logarithm results in a separation as follows:

$$ln[Z(\omega_0)] = ln[|Z(\omega_0|] + i.\phi(\omega_0) \qquad (2.6.5)$$

Consequently the dispersion relations for the apparent resistivity ($\rho_a \; \alpha \; |Z(\omega_0)|^2$) and phase ($\phi$) can be developed in a similar manner and are given in Appendix - A. A much more complete derivation is given by Fischer and Schnegg (1980) and details of its practical implementation are described in Appendix - B (**FISCHZ**).

Weidelt (1972) presented the following approximate expression for calculating the phase from the apparent resistivity at individual periods, without recourse to integration:

$$\phi(T) \sim \pi/4.(1+ \delta \ln \rho_a(T)/\delta \ln T) \qquad (2.6.6)$$

If $0 <= \phi <= \pi/2$ radians (section 2.3.2), then the theoretical maximum absolute gradient of log ρ_a plotted against log T, is 1. As ρ_a and T are usually plotted on log-log scales, this expression provides a useful visual test of the consistency of the acquired response functions.

Parker (1983) pointed out that such dispersion relations are only weak constraints on the permitted form of the response function as the exact distribution of poles and zeros in the upper half of the complex frequency plane places further restrictions on it (i.e. $\mathrm{Im}(\Omega>0)$.

2.7. SOURCE OF MT SIGNALS

The greatest contribution to the observed magnetic field on the Earth is caused by motions in the Earth's core. This 'main' field is virtually time invariant for most purposes and so MT investigations are primarily interested in the much shorter period and lower amplitude changes superimposed upon it.

Magnetotelluric signals must be generated at a sufficient distance from the survey location that they can be considered as being virtually vertically incident 'plane waves' (section 2.2.2). The sources of most MT signals are therefore external to the Earth. In contrast, MT noise is that part of the observed field which is either not induced or has been locally induced (section 4.7.2).

There exists a broad spectrum of MT signals which can be used for geophysical exploration. At the high frequency limit (e.g. 15 kHz.) military transmitters provide the source of signals for shallow penetration VLF surveys (e.g. for mineral prospecting: Telford *et al* 1976). Lower frequency variations, with periods of the order of a day, or longer are used for probing the deep interior of the Earth (reviewed by Parkinson and Hutton 1989).

This particular study is mainly concerned with U.L.F. (Ultra Low Frequency)

field variations with frequencies in the range from 200 to 0.01 Hz. At these frequencies, fig. 2.1 demonstrates the large variation in the magnetic field power spectrum as determined by 3 investigators, including this author. Any difference between these curves reflects the the prevailing induction properties of the measuring site and time dependent noise. The presence of a prominent minimum is apparent at frequencies around 1 Hz in all of these experimental studies. Within this so called 'dead band' it is notoriously difficult to acquire good quality MT data because of the persistently low level of the signals and the normally high level of noise (Boehl *et al.* 1977). In this study, this was also one of the more critical frequency bands which typically coincided with observations from the base of the Northumberland sedimentary basin.

The frequency of 1 Hz. roughly marks the watershed between 2 different sources of EM waves (e.g. Kaufman and Keller 1981, Rokityansky 1982 and particularly detailed reviews of EM source fields are provided by Orr 1973 and Parkinson 1983).

Above 1 Hz. (the 'audio' frequency range), EM field variations are generated primarily in the atmosphere. There are numerous thunderstorms each day, particularly during the summer months in the humid climatic zones of Brazil, Malaysia and parts of Africa. Statistically, there should be at least one thunderstorm in progress, somewhere in the world, at any given instant of time. Lightning discharges produce large amplitude, broad frequency band EM waves. If these occur close to the measuring site these impulses can saturate the recording equipments amplifiers and will seldom directly meet the criterion for good MT signals. However, the EM waves become trapped and reflect off the sides of a waveguide between the conductive Earth and the ionosphere, 60-90 km. above the Earth. The waves can then propagate around the Earth from the more distant thunderstorms. The waveguide absorbs energy at certain frequencies (e.g. > 1kHz.) and at others - the Schumann cavity resonance frequencies (8,14,20,25 and 32 Hz.)- the field strength is enhanced. These are very useful for MT exploration and the author has found consistently high quality measurements can be collected over the range of Schumann frequencies (e.g. the response functions from MWD displayed in fig. 5.7).

There is still some controversy as to the mechanism for the generation of

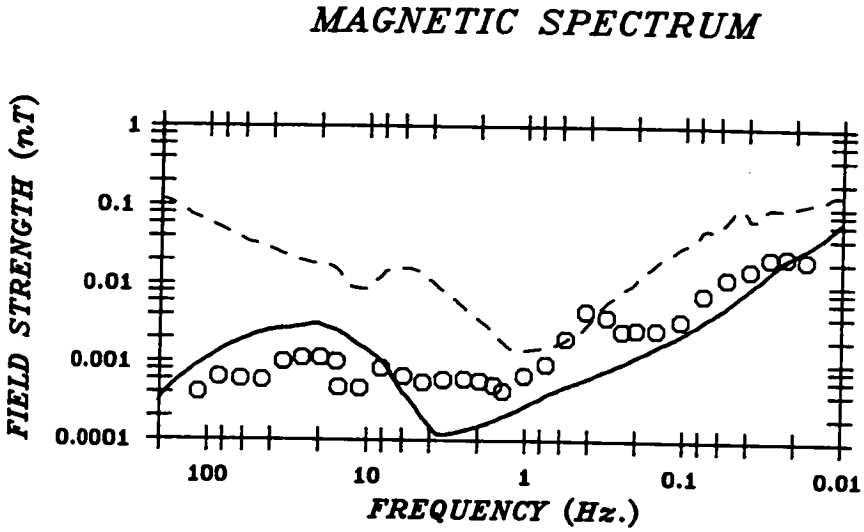

Figure 2.1: The magnitude of the magnetic field spectrum from the results of experimental studies published by Bleil (1964) (dashed line), Keller and Frischknecht (1970) (solid line) and this author (at site DBK; denoted by circles). There are clearly differences between these curves reflecting the time of observation, latitude and possibly the prevailing induction properties of the particular measuring site. All of them show that the maximum magnetic field power is attained at the lowest frequencies (0.01 Hz.) within this range and there is also a pronounced minima in the spectrum around 1 Hz.. This is often reflected in the quality of the MT results.

the EM signals below 1Hz. It is generally believed that they are produced by the interaction between a stream of charged particles from the sun (the 'solar wind') and the Earth's own main geomagnetic field and ionosphere. The charged particles are deflected and set up current systems with their own secondary magnetic field which cancels the effect of the main field at a boundary known as the 'magnetopause'. This boundary is not symmetrical but is more compressed in the direction of the solar wind and moves erratically with variations in the solar wind.

The Earth's main geomagnetic field controls the motions of any charged particles which pass through the magnetopause and into the magnetosphere. The presence and amplitude of the resulting time varying EM fields is strongly correlated with magnetic storms and polar auroral activity. The quasi-continuous set of EM field pulsations produce pronounced peaks in the magnetic field spectrum at discrete frequencies (e.g. Pc1: f = 5-0.2 Hz, Pc2: f = 0.2-0.1 Hz., Pc3: f = 0.1-0.2 Hz. etc.). The amplitude of the Pc is dependent upon the time of day but they tend to diminish during the night when Pi (irregular pulsations) become more dominant.

2.8. D.C. RESISTIVITY METHOD

The D.C. resistivity method requires an artificial, direct current to be injected into the Earth via 2 'current' probes. The resulting potential difference is then measured using a pair of electrodes (section 3.3). The absence of any time varying EM fields ($\delta B/\delta t = 0$) simplifies the induction problem because the static electric fields are conservative (eqn. 2.2.1a; $\nabla \times E = 0$). This is a necessary pre-requisite for using the scalar potential ($E = -\nabla V$) to transform eqn. 2.2.1d:

$$\nabla \cdot (-\nabla V) = -\nabla^2 V = 0 \qquad (2.8.1)$$

Laplace's equation (eqn. 2.8.1) has been solved for a variety of different electrode configurations. Here, the 'single electrode' scenario is used to help derive an expression for resistivity for the case of a symmetrical Schlumberger spread.

Assume that the return current electrode is located far from the point of current injection (A: fig. 2.2). If the Earth is homogeneous and isotropic of resistivity ρ, then the current (I) will then spread out radially in the

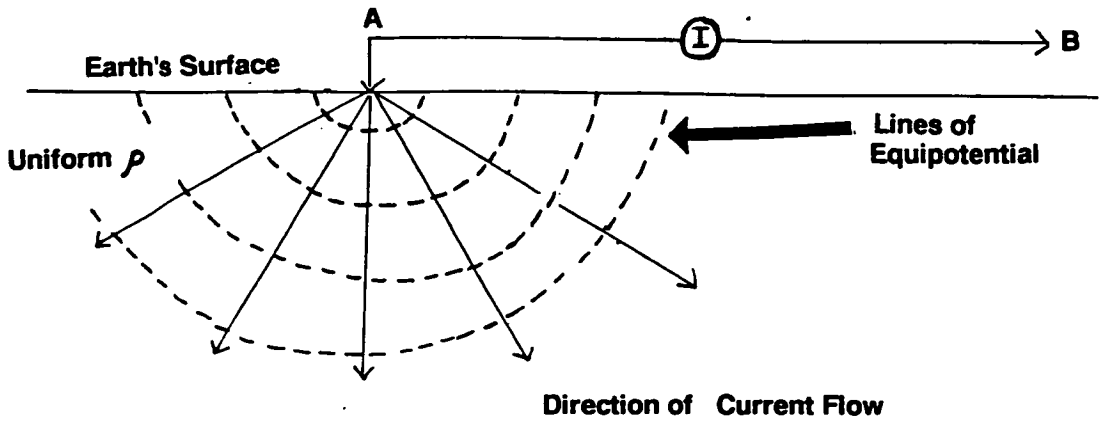

Figure 2.2: A current is injected into the homogeneous Earth (at point A) in the artificial situation of a single electrode D.C. resistivity measurement. It spreads out radially (solid lines) if the return electrode (B) is located far enough away.

The electric potential (dashed line), at right angles to the direction of current flow has complete spherical symmetry which simplifies the solution of Laplaces' equation.

subsurface. The resulting electric potential can be readily computed for any desired point by solving equation 2.8.1, in spherical polar coordinates (r,θ,ϕ). If there is only a single source of current, there is complete symmetry with respect to θ and ϕ and thus the derivatives in these directions can be eliminated from Laplace's equation:

$$\delta^2V/\delta r^2 + 2/r \,.\, \delta V/\delta r = 0 \qquad (2.8.2)$$

After integrating eqn. 2.8.2 and imposing the boundary condition that $V \rightarrow 0$ as $r \rightarrow \infty$ the general solution is attained:

$$V = C/r \qquad (2.8.3)$$

Equation 2.8.3 shows that the equipotential surfaces are hemispherical (fig. 2.2). The constant C can then be evaluated by comparing the current injected into the electrode with the integrated current density in a hemisphere around it. The resulting expression for the potential at a radial distance r, from the single point source is given by:

$$V = \left| \frac{I \,.\, \rho}{2 \,.\, \pi} \right| \,.\, \frac{1}{r} \qquad (2.8.4)$$

In real situations the separation between the 2 current electrodes (the "source" and the "sink") is finite and the measured potential will be influenced by both of them. Expression 2.8.4, can be generalised because the potentials measured from different current sources are additive. In the particular situation of a Schlumberger spread (fig. 2.3), which is symmetrically located about an origin on the Earth's surface, the observed potential at point M is given by:

$$V_M = \underbrace{\frac{I.\rho}{2.\pi(L-l)}}_{\text{from A}} - \underbrace{\frac{I.\rho}{2.\pi(L+l)}}_{\text{from B}} \qquad (2.8.5)$$

An expression for the observed potential difference between the two electrodes can be obtained after a little manipulation as:

$$\Delta V = V_M - V_N = \frac{2.I.\rho.l}{\pi.(L-l).(L+l)} \qquad (2.8.6)$$

If $L >> l$ (in practice $L > 5.l$, is satisfactory), then equation 2.8.6 becomes:

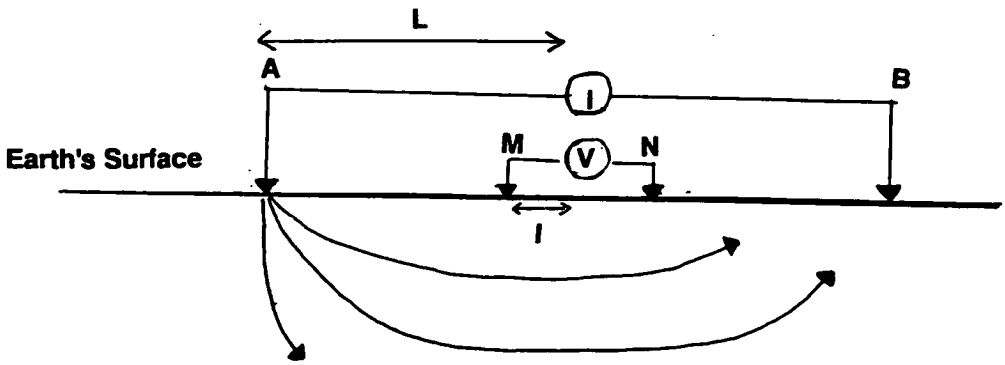

Figure 2.3: A more realistic representation of a D.C. resistivity depth sounding (c.f. fig. 2.2) uses the symmetrical Schlumberger spread, which assumes that there is a finite separation between the injection and return current electrodes (2.L). A relatively simple expression for the apparent resistivity can be derived if the length of the collinear potential spread (2.l) is small.

$$\rho = \frac{\pi.L^2}{2.l} \cdot \frac{\Delta V}{I} \qquad (2.8.7)$$

This relatively simple expression shows that the measured resistivity is a function of the spread length and potential difference, and is inversely proportional to the current injected. Within the inhomogeneous Earth, the observed resistivity is the apparent resistivity (ρ_a), whose variation with depth can be determined by changing the half-spread length (L; c.f. section 2.3.2). In a similar fashion to MT, D.C. resistivity strictly requires orthogonal line measurements to be undertaken to detect any anisotropy.

In this study the V.E.S (vertical electrical sounding) method was used to gain information about the geoelectric structure with increasing depth (section 3.3).

2.9. ELECTRICAL RESISTIVITY AS A GEOPHYSICAL PARAMETER

The resistivity, or its inverse, the conductivity (eqn. 2.2.2d), is a measure of the ease with which electrical current can pass through a medium. The electrical resistivity of rocks has been observed to vary over many orders of magnitude from about 0.3 to 10^7 Ω.m (fig. 2.4). As Olhoeft (1980) has pointed out, this level of sensitivity is useful for identifying variations but will not give unambiguous information about the rock on its own.

Significant changes in resistivity can occur over a large range of length scales from the microscopic (<1 cm.) to greater than the Earth's crustal thickness (> 50 km.). Since the present work is concerned mainly with identifying the subsurface resistivity from coarse surface geophysical measurements (MT and D.C. resistivity), the lower depth bound tends to be more appropriate.

Electrical currents can flow by three conduction mechanisms: a) metallic, b) semiconductor or c) electrolytic. Free electrons enable metals to be very conductive ($\rho < 10^{-2}$ Ω.m). While metals are economically important, they are relatively rare in the Earth. The conduction of electrons in rocks is therefore primarily achieved by the few free carriers in semiconductor material, or by ion movement within an electrolyte. In turn these 2 mechanisms are affected by a large range of rock properties including the pressure, temperature, degree

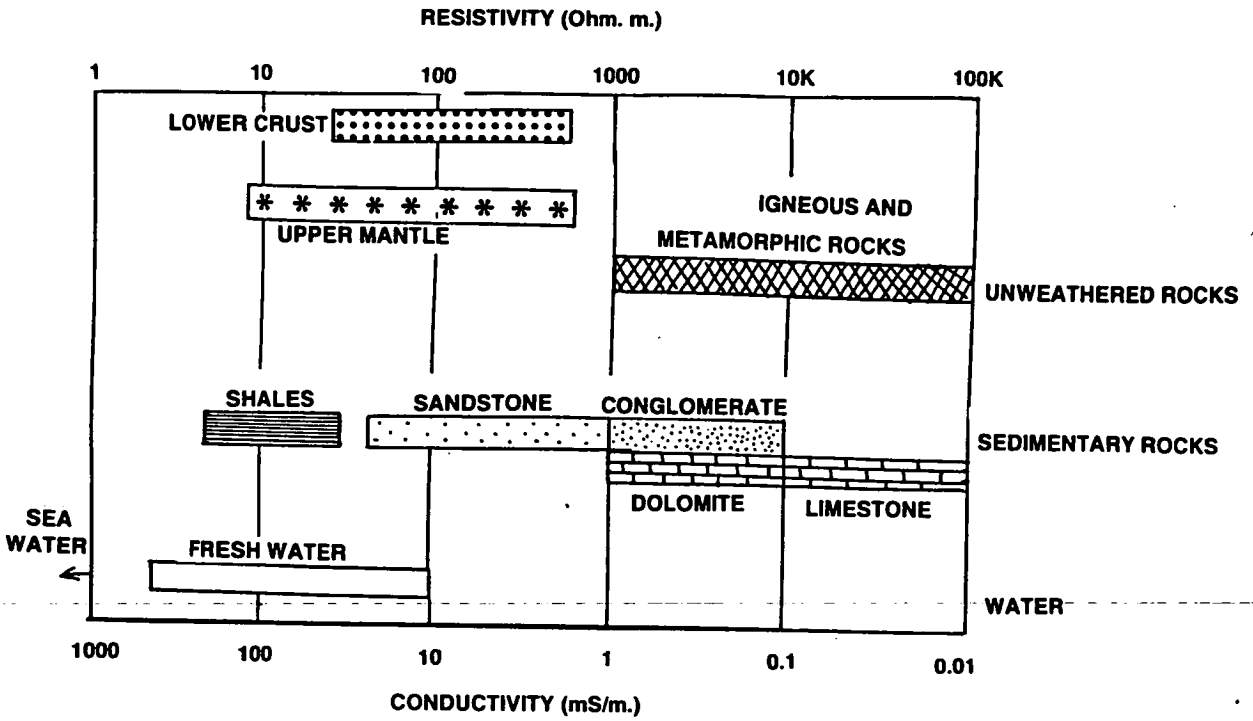

Figure 2.4: The range of electrical resistivities (and conductivities) found for some commonly occurring rock types within the Earth (based on Haak and Hutton 1986 and Keller 1987).

of melting, mineral composition and its purity, permeability, porosity and the nature and salinity of any pore filling.

Laboratory measurements have long attempted to re-create Earth conditions on small rock samples so that a correspondence between various rock properties and resistivity can be established. These experiments have been hindered by the difficulty in maintaining the in situ conditions and the very significant changes in resistivity which corresponds to only a slight change in the physical properties of the rocks. Consequently, their results provide a useful, albeit crude guide to the cause of resistivity values.

The following brief review is drawn primarily from Keller (1971), Shankland and Ander (1983), Haak and Hutton (1986), Hall (1986), Kay and Kay (1986) and Hyndman and Shearer (1989).

2.9.1. Deep (Mid-Lower Crustal) Electrical Resistivity

The lower crust is thought to comprise igneous and metamorphic rocks such as granites, andesites, gabbro, gneiss, amphiboles and slates. Most of the rock forming minerals are electrical semiconductors with few free electrons, so 'dry' lower crustal rock is thought to be resistive. As the presence of heat helps to increase electron mobility, the resistivity of such rocks exhibits a very strong, inverse temperature relationship as given by the semiconduction equation.

The semiconductor equation cannot however explain the widespread occurrence of low resistivity zones at lower crustal levels (section 8.2.1). The inaccessibility of these depths to drilling has led to a plethora of speculative suggestions for the source of the electrical conductor. Composite models have therefore been suggested in which the resistivity of the bulk mineralogy is altered by the presence of metallic oxides, hydrated minerals (e.g. serpentinite, clay, amphibole), sulphur, partial melts, carbon or fluids. The latter three are probably the most favoured explanations.

Partial melting is likely to be a strong contributory factor in reducing the resistivity (electrolytic conduction) in tectonically active regions (temperature $> 700\ ^{o}C.$), but is unlikely to be significant within the stable British crust.

Free carbon, in the form of graphite is very conductive (metallic conduction) and thin films of this material have been found in some rock samples (e.g. black shale; Stanley 1989). Although it may be the source of some lower crustal anomalies, carbon does not appear to be found as widely as the conductive zones and cannot be readily envisaged as forming an inter-connected film, over dimensions of many kilometres.

It is widely recognised that, a very small quantity of free fluids can have a very significant effect in reducing the bulk rock resistivity by several orders of magnitude, particularly if there are dissolved minerals present (electrolytic conduction). This phenomenon has been used to explain the order-of-magnitude discrepancy between resistivity observations on 'dry' laboratory specimens and surface measurements on 'wet' in situ rocks.

Methane, carbon dioxide and brine have all been proposed as possible fluids for filling the likely pore space. Some authors (e.g. Hyndman and Shearer 1989) have shown that only 0.5-3% of the rock's volume needs to be fluid filled pores to account for the low conductivity zone. Since brine (sodium chloride rich water) is an excellent electrolytic conductor it has a particularly low resistivity. This property and its abundance within inclusions in mineral grains makes it the most favoured candidate.

2.9.2. Shallow (Upper Crustal) Resistivity

There is considerably less doubt that electrolytes provide the main mechanism for electron transportation in the Upper Crust as the rocks (sandstones, limestones, clays and exposed igneous and metamorphic rocks) all show some degree of porosity. Unconsolidated sedimentary rocks can comprise up to 40% of their volume of pore space, although more typically, such rocks tend to have porosities in the range of 5 to 25 %. The lower bound is generally found in older and more deeply buried rocks where pressure has reduced the pore space and closed fractures by compaction. In metamorphic and many igneous rocks the porosity tends to be lower than sedimentary rocks (< 4%), whilst weathering tends to reduce their resistivity from about 10 KΩ.m to between 10-1000 Ω.m. Granites, which are of particular interest to this study, are believed to have in situ resistivities of about 4 KΩ.m (Palacky 1987).

The abundance of water beneath the water table and its strong solvent properties make it the most obvious fluid to fill any pores or fractures in the rock. In sedimentary rocks, the water is often trapped from the original deposition (connate water). Although water itself is a good insulator, the constituent ions of any salt present separate when dissolved in water and the bulk electrical resistivity of the rock is then greatly reduced reflecting the increased ion mobility. Ion mobility is further enhanced in more concentrated saline solutions and at higher temperatures, but the exact chemical composition of the salt is usually only of secondary importance.

The strong inter-dependence of resistivity and porosity can be observed in an example which was taken from a borehole log in the Worcester sedimentary basin (fig. 2.5). Small variations in the resistivity within the sedimentary section cannot be correlated directly with the changes in the porosity, which was derived empirically from the acoustic wave velocity (Telford *et al.* 1976). However the increase in resistivity at the unconformity with the Pre-Cambrian igneous basement is directly attributable to the decrease in porosity.

The raw Stonehaugh resistivity and lithological log (B.G.S. 1976) shows a correspondence between resistivity and rock type (fig. 2.6). In this cyclic sedimentation sequence, the limestone and sandstone beds are demonstrably more resistive than the shales, as the latter are rich in clay with a higher ion mobility.

Archie's Law (e.g. Archie 1942, Telford *et al.* 1976, Keller 1987, Parkinson and Hutton 1989) has been the most successful empirical attempt to relate the bulk resistivity (ρ) of a rock to its porosity (ϕ) and the resistivity of the pore filling fluid (ρ_f) for both near surface and deeper rocks:

$$\rho = a \, . \, \rho_f \, . \, \phi^{-m} \qquad (2.9.1)$$

where a and m are specified constants which attempt to characterize the interconnection of the pores and the cementation of the rock. Typical values for these parameters are a=0.62 , m=1.95 for well cemented sedimentary rocks and a=1.4 , m=1.58 for most igneous and metamorphic rocks with little pore space. Typical fluid resistivities tend to be in the range from 1 to 10 Ω.m (Keller 1971).

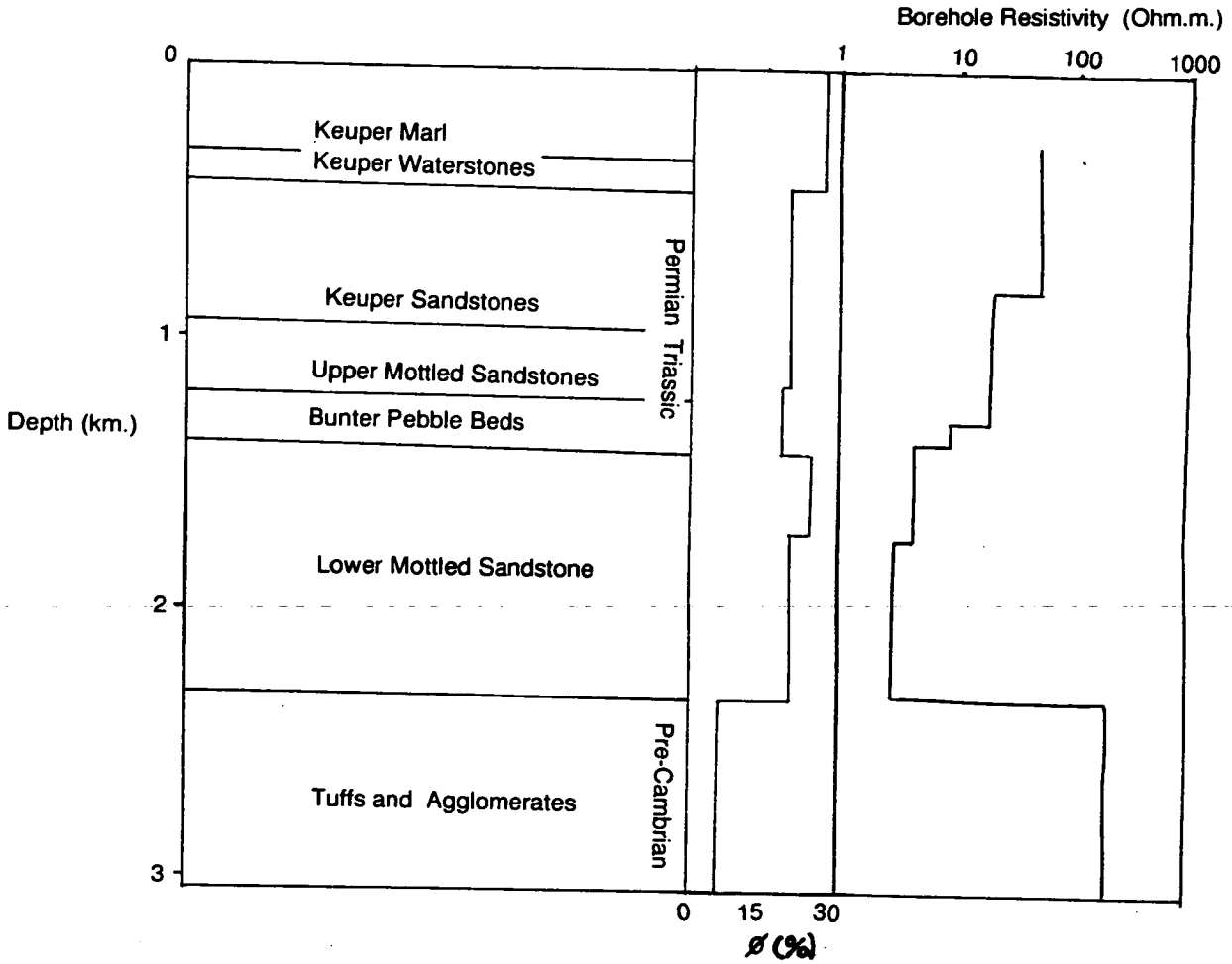

Figure 2.5: The gross electrical resistivity variation determined within a borehole near to Worcester, with the geological log and calculated porosity (ϕ). Local variations within the porosity and bulk lithology of the Permo-Triassic sedimentary rocks cannot be readily compared to changes in the bulk resistivity, but the increase at the unconformity with the igneous basement rock is directly attributable to the decrease in porosity in this layer.

Detailed inferences concerning rock properties from surface observations alone are strongly hampered by the underdetermined nature of equation 2.9.1. Only with detailed borehole information or strict assumptions about the subsurface rock type can bulk resistivities be transformed into either porosity or fluid resistivity information. The majority of geoelectric interpretations can thus seldom proceed to a more quantitative examination of the likely causes of the resistivity values themselves. Instead it is common practice to use a qualitative assessment of the likely correspondence between the geological structural units and bulk resistivity and also to interpret the presence of structural boundaries from the resistivity contrasts.

CHAPTER 3

FIELD MEASUREMENTS AND METHODS

It is a capital mistake to theorize before one has data.

Sir Arthur Conan Doyle 1859-1930.

3.1. INTRODUCTION

This chapter contains a description of the equipment and methods used in the acquisition of the geoelectric field observations from the Northumberland sedimentary basin.

The MT field technique as previously used by the University of Edinburgh group (e.g. Meju 1988, Whelan 1989) was modified in two ways to help improve the resolution of the acquired model Earth sections:

1. Electromagnetic noise levels were reduced by recording extra a) local or b) remote reference observations.

2. D.C. resistivity measurements provided extra controlling information concerning the near surface structure.

Additionally, as in recent Edinburgh University MT studies elsewhere, a relatively high density of sites was used to obtain some consistency between the models which were obtained for adjacent sites (c.f. section 6.4.6).

Section 3.2 provides an introductory review of the magnetotelluric equipment used for a) single site (SS), b) locally referenced (LR) and c) remotely referenced (RR) MT field data acquisition. The latter two are described in some detail because the particular field methods used were devised jointly by the author and Dr. E. R. G. Hill.

This is followed by a brief description of the D.C. resistivity equipment and the methods employed in the acquisition of shallower geoelectric information (section 3.3).

The general strategy used for site selection in both basins is discussed in

section 3.4 and the locations of the soundings undertaken by the author and other geoelectric measurements relevant to this study are reviewed in section 3.5

3.2. MAGNETOTELLURIC FIELD DATA ACQUISITION

Previous shallow MT investigations across the Northumberland Trough (Novak 1981, Harinarayana 1987) demonstrated that the base of the sedimentary sequence (about 2-3 km.) could be resolved by collecting electromagnetic (EM) observations at frequencies greater than 1 Hz. This was also consistent with the theoretical depth of penetration of EM fields calculated from the skin depth equation (eqn. 2.3.9; average ρ = 40 Ω.m., f = 0.6 Hz., gives δ = 4 km.). Resolution of intra-basement structures required lower frequencies. The longer period measurements undertaken by Jones and Hutton (1979a,b), Novak (1981) and Beamish (1986a) showed that in some of the more conductive regions, it would be necessary to acquire frequencies below 0.01 Hz. to properly identify some lower crustal/upper mantle features.

There were thus several advantages, for the present study, in using an MT system which operated in the frequency range from 200 to 0.01 Hz.:

1. A reasonable depth of penetration (10-40 km.) could be achieved at most locations. Additional "long period" equipment was thus unnecessary.

2. The presence of coherent noise at frequencies above 50 Hz. often hampers MT exploration in the U.K. (section 4.7.2). These frequencies were largely avoided.

3. Supplementary geoelectric information about structures above the minimum depth of MT investigation (50-100 m.), could be readily gained by D.C. resistivity measurements.

4. Two, almost identical MT acquisition systems (SPAM) were available to allow remotely referenced observations to be performed.

The basic N.E.R.C. (Natural Environment Research Council) SPAM (Short Period Automatic Magnetotelluric) field equipment is summarized in fig. 3.1.

This system can simultaneously record up to a maximum of seven different sets of EM field observations. To allow the full tensor impedance to be

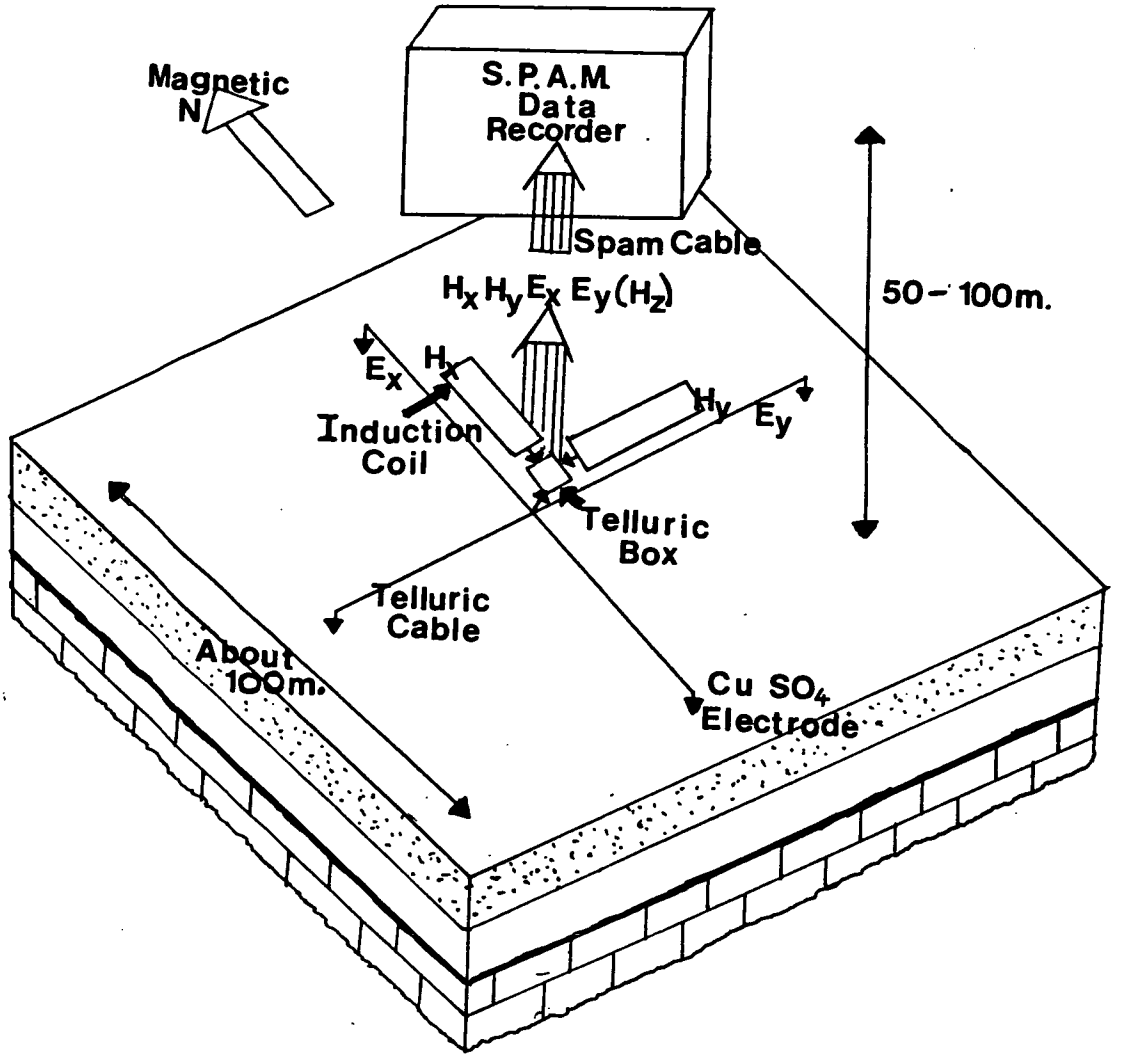

Figure 3.1: A schematic drawing depicting the N.E.R.C. SPAM magnetotelluric field equipment deployment in the field. The electric field sensors comprise 2 grounded electrodes separated over a distance of 100m., in orthogonal directions. The potential differences induced in the telluric cables (Ex and Ey) are amplified in the telluric box before being passed to the SPAM data recorder situated 50–100m away. In a similar fashion, the horizontal coil sensors (Hx and Hy) are orientated parallel and perpendicular to the Earth's main magnetic field direction.

evaluated (section 2.5), 2 orthogonal components of both the horizontal magnetic and electric fields need to be recorded. Optionally, variations in the vertical magnetic field amplitude can be collected on a fifth channel, whilst the remaining two channels are available for locally referenced (electric and/or magnetic) measurements.

Vertical magnetic field information is most useful in areas where it is anticipated that there will be a significant three dimensional geoelectric structure. It was not routinely used during either of the author's fieldwork campaigns owing to the need to bury the vertical magnetic field sensor to avoid wind noise. Local reference observations (section 3.2.3) were recorded on a single SPAM system, but remote reference measurements were collected on a second, identical SPAM, a short distance away (section 3.2.4).

3.2.1. Field Sensors

Magnetic field variations are measured by induction coils which consist of a large number of turns of copper wire which are wound around a high permeability (mumetal) core. Time variations induce small potential differences in the coils with an amplitude proportional to the rate of change of the magnetic field (c.f. eqn. 2.2.1a). The coils used in this study (Societe E.C.A. CM 11E) had low electronic noise, relatively high sensitivity within the same frequency range as the SPAM, and incorporated built-in amplifiers to minimise signal losses prior to recording.

Two such coils were used in the field to measure the magnetic north (Hx) and east (Hy) components of the horizontal magnetic field. They were usually placed in shallow trenches to protect them from wind vibration. Their orientation was measured exactly (to within 1 ^{O}: Nichols *et al.* 1988), so that the measured signals did not include a significant component of the magnetic field from the other direction. For the same reason, a spirit level was used to ensure that the horizontal coils did not measure a component of the vertical magnetic field (Hz).

The electric ('telluric') field variations were detected by measuring the potential differences induced between two grounded electrodes positioned approximately 100 m. apart. Like the coils, two telluric systems were deployed in orthogonal directions to measure the Ex and Ey field components.

Since the investigation of Petiau and Dupis (1980), it has been recognized that erratic electrochemical noise is generated when metal electrodes are placed directly into the ground. Low frequency MT (< 10 Hz.), D.C. resistivity and self potential (Telford *et al.* 1976) measurements, therefore require the use of more stable and lower noise non-polarizable electrodes. These generally consist of metal rods (e.g. Copper, Zinc or Lead) which are immersed in a porous pot containing a saturated solution of their own salt. When the electrode is put into the ground, the slow diffusion of the salt removes any sharp electrical contacts. To avoid spurious potential differences between the electrodes, they should be as nearly identical as possible.

The author always used electrodes which consisted of copper rods immersed in a concentrated copper sulphate and gelatin suspension contained in a porous pot (see Devlin 1984 for details). These electrodes had to be kept moist at all times. When required, they were buried in a shallow hole and connected up to the 100m. long 'telluric cable'. To minimize the effects of wind induced disturbances, these cables were kept flush against the ground particularly if the cable traversed a bush or wall. A continuity test was then performed on the electrode circuit by measuring the resistance of the wires (less than about 5 KΩ.).

The centre of the sensor array was usually placed 50-100m. away from the metallic recording vehicle, to reduce EM noise induced by its vibration in the Earth's main magnetic field. All the observed signals had therefore to be amplified to prevent their attenuation within the connecting cables. A wide frequency band amplifier (the 'telluric box') was therefore placed close to the centre of the field sensor array. This performed the role of a junction box; supplying power from the SPAM to the coils' amplifiers, directly amplifying the electric field signals and also passing all the information back along the screened 'SPAM cable' for recording.

3.2.2. Data Recording

A detailed description of the use of the vehicle based parts of the SPAM system is omitted here, since it is more substantially described by Hutton *et al.* (1984), Meju (1988) and Whelan (1989).

The apparent complexity of MT recording instruments often seems to baffle

the casual observer, but any MT instrument basically attempts to record the amplitude and phase difference between the various components of the EM field. The particular SPAM recording system which was used in this study (fig. 3.2) consisted of an amplifier/filter box which received the electrical signals, an LSI computer for in-field processing, two cartridge drives for program loading and data storage and some peripherals (i.e. terminal and printer) for communication between the computer and the operator. Most of this equipment was powered by three 12 V. rechargeable batteries.

The acquired signals were initially amplified by the same fixed gain for all of the channels. It was common practice to use the optional 50 and 150 Hz. notch filters to selectively reduce the high amplitude, coherent noise from power lines.

The amplitudes of the EM fields vary substantially with direction, time and especially frequency. Furthermore, as high frequency EM data can be recorded much more quickly than low frequency data, the signals were not recorded simultaneously over the entire frequency band, but were instead measured in one of four overlapping sub-bands (Band '0': 180-8 Hz., Band '1': 24-1 Hz., Band '2': 3-0.125 Hz., Band '3': 0.35-0.01 Hz.). Amplification was then applied to optimize the corresponding signal strength in each recording band and to each of the EM field components separately. Filters were also applied to remove frequencies outwith the chosen band.

The signals were then digitized by means of an analogue-to-digital converter at a sampling rate related to the frequency sub-band chosen (Band '0': 512 Hz., '1': 64 Hz., '2': 8 Hz. and '3': 1 Hz.). Upon an instruction from the computer, 256 samples were collected, simultaneously from all of the EM channels. This data 'window' was passed across into the computer's memory for subsequent processing and handling. Like many contemporary MT field systems measuring at these frequencies (Pedersen person. commn.), the remaining data handling and storage procedures were controlled by a computer. The author considers that it would have been desirable to have a back-up facility to allow the digitized observations to be directly dumped onto cartridge should the computer fail to function properly. A sample of the resulting EM time series measurements taken from each of the 4 recording bands, is shown in fig. 3.3.

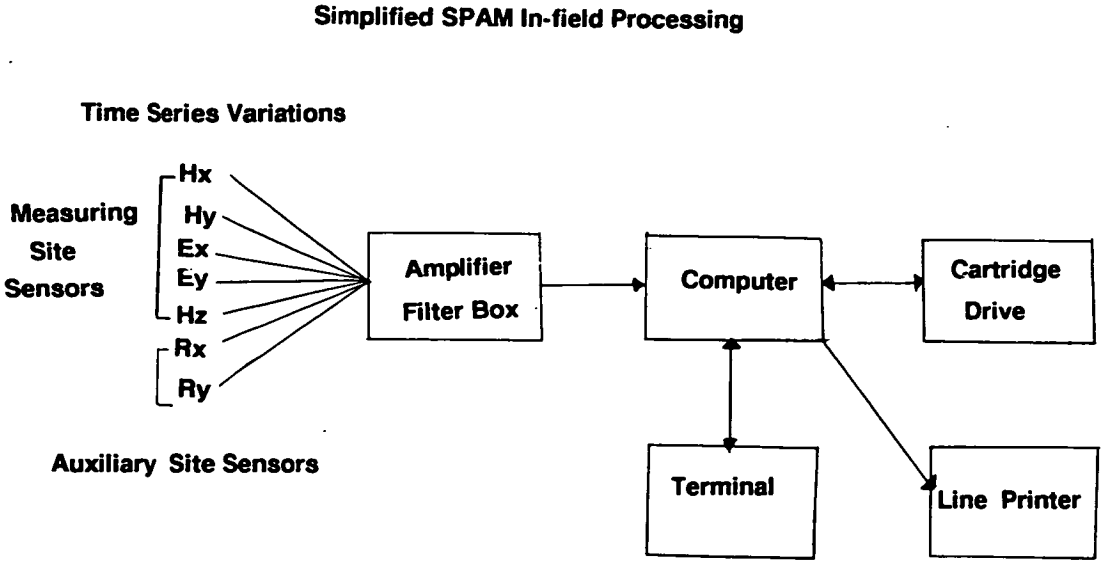

Figure 3.2: The SPAM 'hardware' for processing EM time series variations from the 4 basic sensors (Hx,Hy,Ex and Ey) and the optional and auxiliary sensors (Hz, Rx and Ry).

Figure 3.3: Examples of time series data recorded in the 4 SPAM frequency bands at the MT site DBK. The magnetic (continuous line) and electric (dashed line) fields show a high degree of correlation across most of the frequency range. In band 0, the observations are dominated by sinusoidal residual mains power line noise. At this site, like many others, band 1 produced the best quality results due to the strong signals and occasional natural impulses (e.g. at 1.8s). Band 2 is usually noisier which is witnessed by the lower level of correlation between Ex and Hy, whilst band 3 is dominated by low frequency signals (c.f. fig. 2.1).

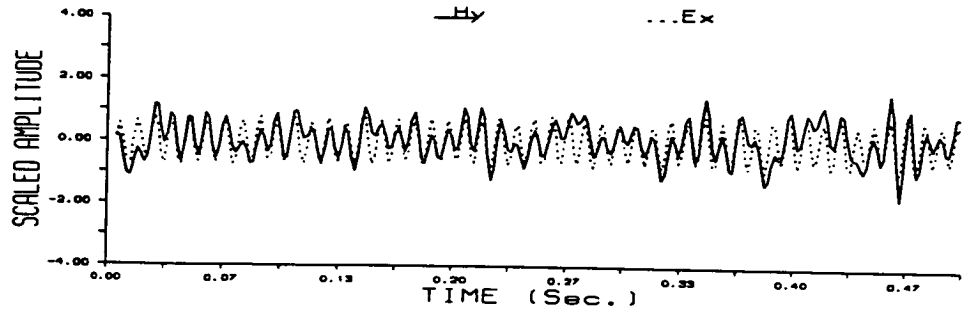
DBK: BAND 0 FILE D WINDOW 3
Hy
...Ex
SCALED AMPLITUDE
4.00
2.00
0.00
-2.00
-4.00
0.00
0.07
0.13
0.20
0.27
0.33
0.40
0.47
TIME (Sec.)

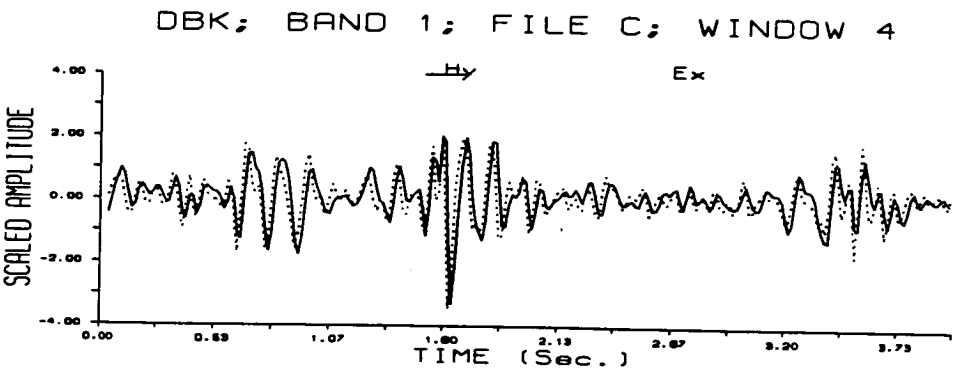
DBK; BAND 1; FILE C; WINDOW 4
Hy
Ex
SCALED AMPLITUDE
4.00
2.00
0.00
-2.00
-4.00
0.00
0.53
1.07
1.60
2.13
2.67
3.20
3.73
TIME (Sec.)

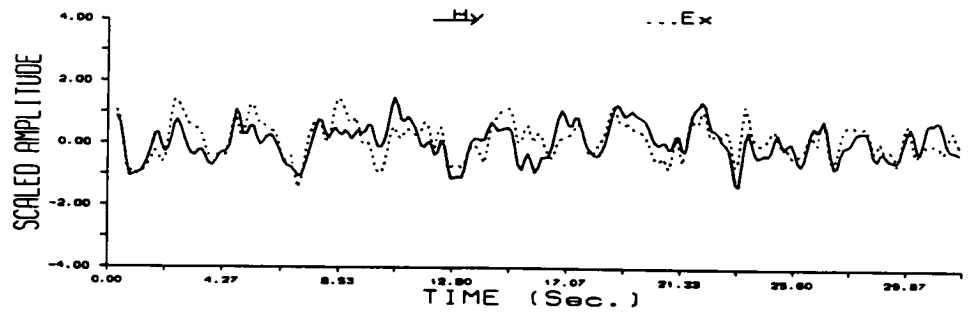
DBK; BAND 2; FILE D; WINDOW 2
Hy
...Ex
SCALED AMPLITUDE
4.00
2.00
0.00
-2.00
-4.00
0.00
4.27
8.53
12.80
17.07
21.33
25.60
29.87
TIME (Sec.)

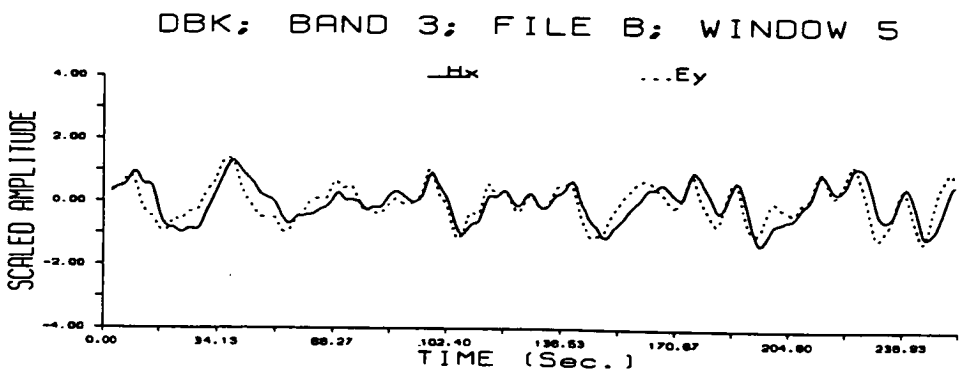
DBK; BAND 3; FILE B; WINDOW 5
Hx
...Ey
SCALED AMPLITUDE
4.00
2.00
0.00
-2.00
-4.00
0.00
34.13
68.27
102.40
136.53
170.67
204.80
238.93
TIME (Sec.)

The preliminary in-field time series analysis was automatically performed by the SPAM on each data window. Initially the samples from each channel were Fourier transformed into 128 frequency spectral estimates. These were then corrected for the sensors response, frequency band averaged and the apparent resistivity, phase and coherence computed from the impedance tensor. If required, these could be listed out on the line printer for quality control purposes.

Several optional acceptance criteria were sometimes set to ensure that only those windows which surpass some user specified thresholds were retained. Except in the presence of coherent noise, a low EM predicted coherence (eqn. 2.5.6) was found to be the most useful criterion for rejecting poor quality data windows. However, at many locations the noise level was either too high, or the signal strength was too low to allow rigid acceptance criteria to be set (e.g. coherence $>$ 0.9). This was particularly serious for measurements in the 'dead frequency band' around 1Hz (see Appendix - C for numerous examples). It was therefore decided to accept many more poor quality observations in order to keep costly field time to a minimum. In such cases, the post-field data re-processing methods discussed in Appendix - A were essential for acquiring low noise response functions.

All the selected time series windows were transferred to data cartridges. Each of these could store 30 windows of the 4 component EM field data on each one of four tracks. Storage of the time series data then allowed fuller re-processing using both window and frequency spectral band averaging to estimate the impedance.

The standard SPAM computer programs could accept and record locally referenced observations but could not process them in the field. Since the in-field programs were not available for adaptation, all the EM noise reduction programs written by this author were mounted on the E.M.A.S. (Edinburgh Multi-Access System) mainframe computer. For the majority of these programs, their objectives are such that they could now be more appropriately adapted to a faster, field base computer with larger memory capacity, rather than to the SPAM itself.

3.2.3. Local Reference (LR)

A local EM field reference provided extra, field observations which were recorded simultaneously a short distance away from the primary 'measuring' site. The aim of this technique was to reduce uncorrelated noise between the two sets of sensors. A fuller discussion of the background theory is given in section 5.3.

In this study, the extra local reference information usually came from telluric sensors, owing to the high cost of induction coils. These sensors were located up to 500m. away from the measuring site (fig. 3.4a) and the signals sent via a second SPAM cable directly into two of the spare SPAM recording channels.

A 500m. length of standard multicore SPAM cable would have been unnecessarily heavy and expensive. A new cable, with fewer cores was thus devised. Power was supplied directly to the reference telluric box amplifier from two adjacent 12 Volt batteries to save 2 cores. Since only two reference sensors were in use at any given time (either Ex and Ey, or Hx and Hy), further reductions were possible by manually switching the chosen sensor's output into the two signal cores which were then required in the second SPAM cable.

An example of the LR impedance results are given later (fig. 5.7d).

3.2.4. Remote Reference (RR)

In principle, increasing the separation between the measuring and reference sites should decrease the level of correlateable noise which can be detected at both sites (section 5.3). For a separation beyond about 500m, signal attenuation within the second SPAM cable and survey logistics limit the usefulness of the LR technique. The RR technique used in this study could, in principle, be used with any desired separation, although in view of local induction effects, the 2 sites should ideally be located over similar geoelectric structures.

Two virtually identical SPAM systems were used in Northumberland (a Mk. II and a computationally faster Mk. IIa) to record simultaneously the EM field variations across separations of between 1 and 10 Km. (fig. 3.4b). Since, the

Figure 3.4 These diagrams summarize the 'local reference' (fig. 3.4a) and 'remote reference' (fig. 3.4b) methods of MT data collection which were used by this author. The former of these techniques involved 'hardwiring' either the magnetic (Hx or Hy) or electric (Ex or Ey) observations to the SPAM from an auxiliary site located up to 500m. away. The latter technique used 2 SPAM systems which were separated between 1 and 10 km..

Remote reference data synchronization was achieved by an automatic timekeeping device at each site. It is schematically depicted by fig. 3.4c. F.M. timing signals were detected by an Omega radio receiver which was connected to a digital clock (the Omega Face). This gave out pulses every 10s which were counted by a triggering device, developed by the author. Once a pre-set number of pulses had elapsed (i.e. MAXCOUNT), the trigger would allow the EM time series window to be initiated.

LOCAL REFERENCE

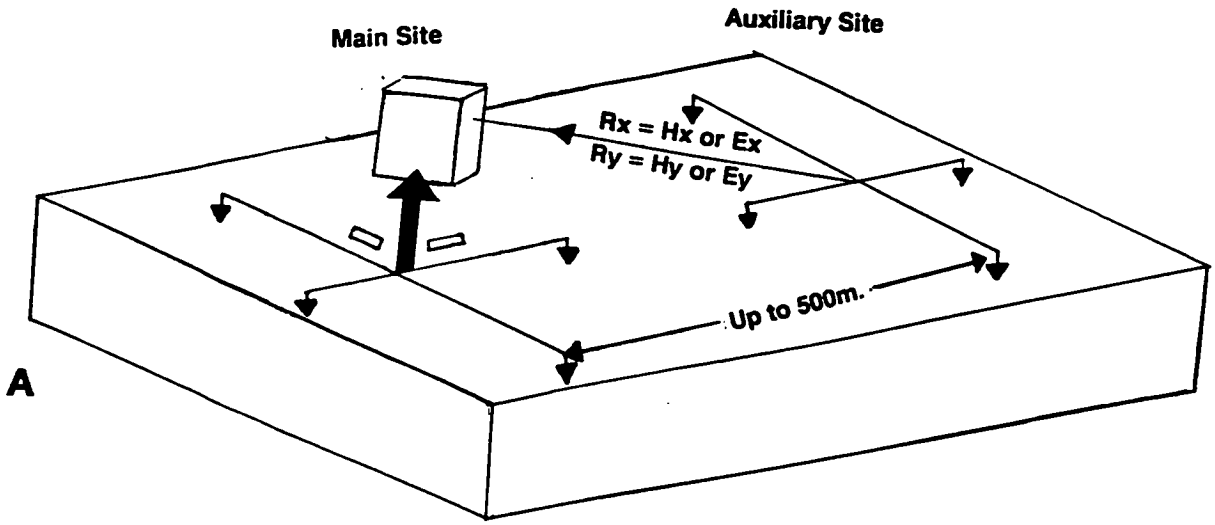

REMOTE REFERENCE

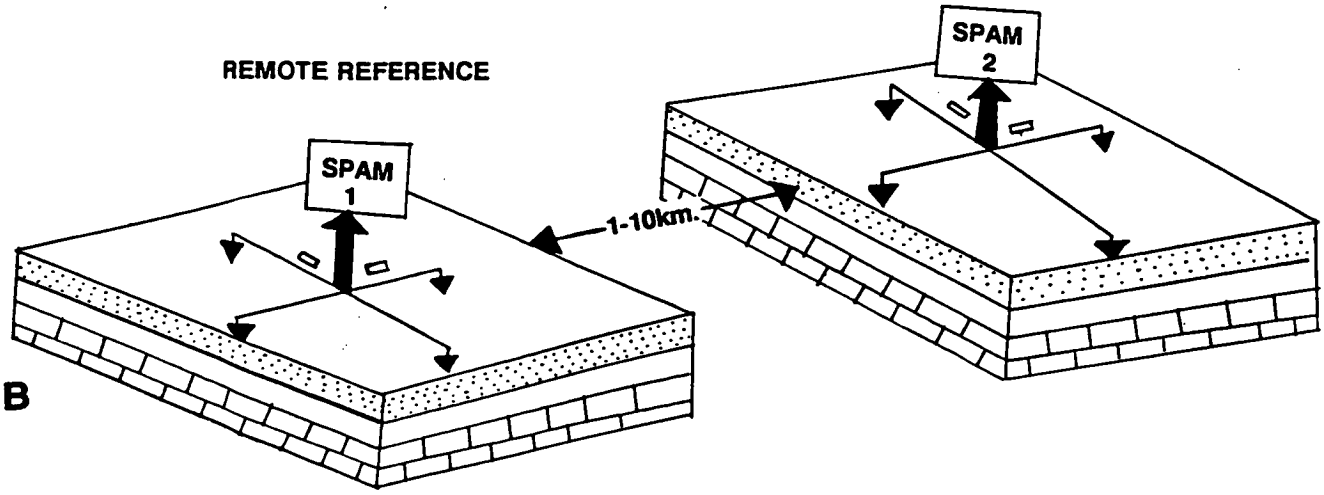

REMOTE REFERENCE TIMEKEEPING

C

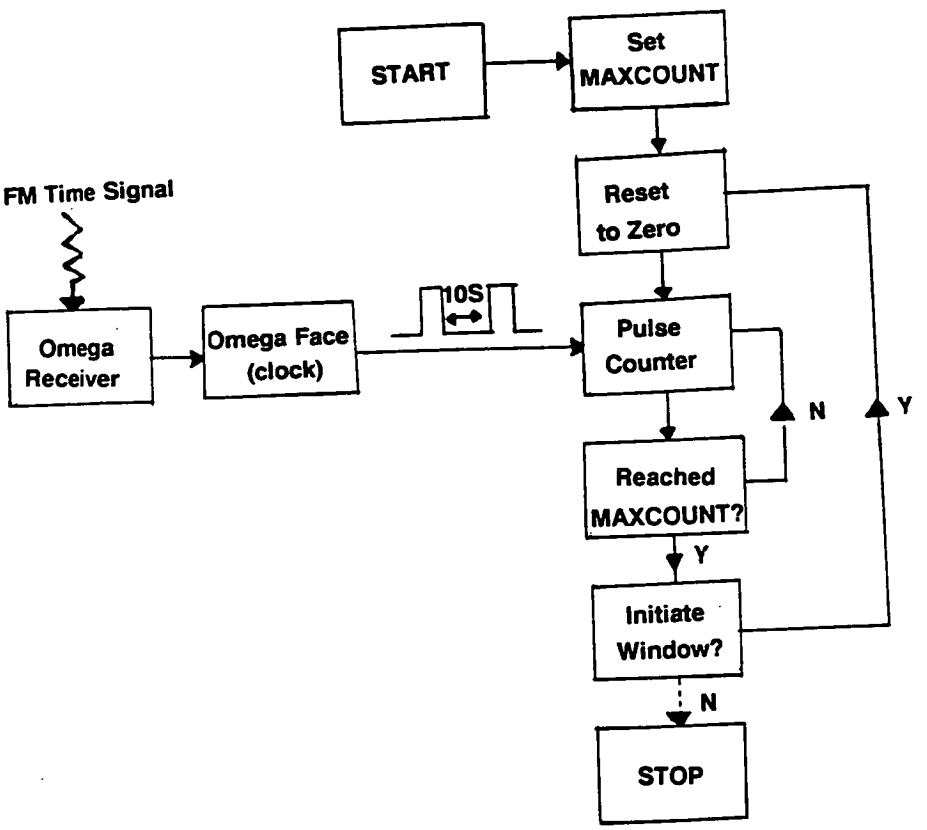

SPAM samples once every 2 milleseconds and the entire data window takes only 0.5 seconds to collect at the highest frequency band, an automatic synchronization procedure was essential (see fig. 3.4c).

An OMEGA (NERC) clock provided high accuracy time-keeping at both the measuring and reference sites. These clocks received F.M. radio time pulses from Norway (OMEGAREC) to maintain the accuracy of a quartz digital clock (OMEGAFACE) to within 1/100th of a second. In turn, the OMEGAFACE provided a usable pulse every 10 seconds which could be used to initiate the synchronized data window collection. Electronic noise from the SPAM systems occasionally affected the F.M. timing signals but this did not appear to affect the overall accuracy of the clocks unduly.

The measuring frequency band and the recording start time were agreed in advance by the field operators at each site. The two SPAM systems had to be ready to accept the first sample of a data window at the agreed time. The precise acquisition time of the window was then controlled by a triggering device. The first sample was only collected after a fixed time interval had elapsed which corresponded to the trigger counting a preset number of timing pulses. Immediately after the initiation of the data window, the counter was reset to zero. The trigger would then only allow the next window to commence after the fixed time interval had elapsed again. By fixing this time interval to be greater than the total window collection, processing and storage time, the window was synchronized at both sites. This window collection time was found to be dependent upon not only the frequency band, but also the particular SPAM used. The triggering time was therefore set to be the smallest multiple of 10 seconds, which was greater than the experimentally determined window collection time. For example: frequency band '0': collection time = 0.5 seconds + processing and storage time (approx.) = 11 seconds (Mk. II) or 8 seconds (Mk. IIa). The trigger time was therefore set to count 2, 10 second pulses before allowing the next data window to be collected.

This procedure significantly increased the data acquisition time for the highest frequencies but had little detrimental effect at the other recording bands. The operators of each SPAM had to be ready to initiate the recording with an accuracy of 10 seconds between two successive pulses. The

electronics then achieved simultaneous recordings to within 1/100th of a second. At the highest frequency band, this resulted in the recorded windows being started within 5 samples of each other.

In RR mode, it was necessary to suppress the SPAM's own data window acceptance criteria (section 3.2.2), to prevent synchronization being lost if windows were selectively rejected by only one system. Consequently, many more observations were collected compared with the conventional single site MT acquisition.

The author often found that one of the systems was unready for data acquisition or was an integer number of windows out of step. These incidents were mainly due to relatively minor equipment problems (e.g. sensors disrupted by animals), or failure of the operators to initiate recording within the required 10 second time interval. Such disruptions slowed down the rate of data collection and increased the complexity of post-field processing.

Prior to a later fieldwork campaign, the electronics were adapted to allow the time at which each data window was collected to be transcribed onto the cartridge along with the measured variations in the EM fields. If this technique had been fully implemented in the field, it would have allowed those windows which had recorded in synchronization to be readily identified. This would have enabled the SPAM operators to impose low threshold acceptance criteria and reject some of the poorer quality windows in the field.

The author considers that a future and simpler RR method could perhaps dispense with the clocks and triggering device completely, for the lower frequency measurements. At the great majority of sites occupied for this study, the MT observations were relatively unaffected by uncorrelated noise at the highest NERC SPAM frequency ranges (bands 0 and 1), and remote reference could do little to improve the results. This method was found to be most beneficial across the 'dead frequency band' (Band 2). As adept field workers should be able to achieve synchronization to within about 6-10 samples in band 2 or 1-2 samples in band 3, this is probably sufficiently accurate to permit manual RR acquisition in these bands.

If the sychronisation equipment could be dispensed with, then remote referencing would become quicker and much easier to implement.

Alternatively, a more sophisticated system would filter, amplify and digitize the EM signals from 1 or more 'slave' reference sites and use FM telemetry systems to relay the signals. A similar technique is currently used for seismic reflection work and has been successfully used for MT by Gamble *et al.* (1979a). However, this would require major changes to current versions of the SPAM and would be logistically more difficult owing to the presence of extra field equipment. Ultimately, its application in Britain would be hindered by the lack of radio transmission frequencies available for such work.

3.2.5. Magnetotelluric Field Procedures

Once the equipment was deployed and connected several tests were performed to check the correct functioning of the equipment. This usually consisted of inspecting the degree of correlation between the observed orthogonal components of the electric and magnetic fields, looking for any high amplitude spikes and then collecting a few test time series windows. The magnitude and consistency of the calculated apparent resistivities illuminated any sensor problems and rapidly gave an assessment of the noise level at the site.

As the electromagnetic signal and noise strengths over the frequency spectrum can be strongly dependent upon the time of day, it was common practice to alternate the frequency bands in which measurements were made. Occasionally data collection was terminated prior to filling all of the available space on a cartridge track, if for example, there were little usable signals being recorded.

The majority of the sites in Northumberland were occupied for 2 to 3 days to gain the best quality data possible. The author occupied some sites, in a latter study, for as little as 24 hours, to collect only the higher frequency (bands 0 to 2) data. Two field workers with one vehicle were required for SS or LR operation, whist three field workers were needed for D.C. resistivity soundings or RR. The latter technique also required 2 vehicles. The author found that more data could be collected if, during MT recording at the current location, he used a bicycle to identify and gain permission for potential future sites.

During LR operation, the author found the most efficient use of field time

was achieved by setting up and testing the main site first. Lower frequency measurements could then be obtained whilst deploying equipment at the reference site, for later use.

Remote reference was much more logistically complex since more equipment, vehicles, personnel and sites had to be arranged. The referencing system used was experimental and therefore measurements were disrupted by minor problems. During the early stages, the author found that radio contact between the two sites was very useful. However, the Citizen's Band (C.B.), F.M. radio transmitter/receivers which were used during this study had little more than 'line-of-sight' range (variable between 500 - 5000 m.) even on 'high power' operation. The operating SPAM, particularly the older Mk. II, produced considerable noise at both the C.B. and OMEGA receiver radio frequencies. Conversely the transmitting radios generated data windows which were contaminated by highly coherent 'pick-up' noise. To alleviate these difficulties, the radio transmitters were located 20 to 30 m. away from the instruments. Disruption of communications by other radio users was virtually negligible during the fieldwork.

Initially, the radios were used to enable the selected frequency band and time of data recording to be agreed at the sites. This allowed any problems to be identified and corrected prior to recording. Later a more efficient 'silent running' method was devised whereby the schedule was agreed in advance of the fieldwork. The onus was then placed upon the field workers to note down which measurements had actually been achieved. Post-field processing (**RRMERGE** in Appendix - B) was used to edit and join those data windows that had been acquired simultaneously into a common data file for analysis.

3.3. D.C. RESISTIVITY PROFILING

A Schlumberger resistivity spread configuration (Telford *et al.* 1976, section 2.8) was adopted because of its logistical simplicity. The basic equipment used was a portable D.C. Terrameter which allowed resistivity measurements to be made up to a maximum electrode half spread length (AB/2) of 1 km. The author assumed, for simplicity, that the subsurface was isotropic and that there were few near surface distortions along the length of the cables.

Current drawn from a rechargeable 12 Volt battery was passed from a T

(transmitter) box at the centre of the spread, through long cables mounted on winding drums and into the ground through a pair of steel electrodes (A and B in fig. 2.3). The resulting change in the potential difference was measured by an R (receiver) box which was connected to 2 non-polarizing copper sulphate electrodes (section 3.2.1). These electrodes (M and N in fig. 2.3) were placed symmetrically and collinear to the current probes. A Wheatstone Bridge arrangement in the R box removed the effects of static self potentials in the potential electrodes prior to switching on the current from the T box. The author found that some of the more spurious self potential variations could be reduced by periodically 'shorting' the two potential electrodes and reversing their polarity.

To obtain the apparent resistivity, equation 2.8.7, requires only a knowledge of the electrical current (I) injected into the ground, the half spread length between the current electrodes (L = AB/2), and the resulting potential difference (ΔV) measured across the potential electrodes of known half spread separation (l = MN/2). Taking measurements of the apparent resistivity at increasing AB/2, on a logarithmic scale from 10 to 1000 m., enabled the geoelectric structure to be determined in the depth range from about 1 to 150 m.

As the current electrode separation was increased, the power output from the T box had to be occasionally adjusted. A larger power source would have been desirable as the observed potential difference, resulting from the injection of the current, was of the same order as the spurious self potentials (about 0.1–0.5 mV) at the longest spread lengths. After a few measurements, the potential electrode separation (MN/2) had to be increased to ensure an adequate signal deflection was received on the R box's galvanometer. The potential electrode separation was usually kept less than AB/5, as required by the simplifying assumption for the Schlumberger spread (section 2.8). The author found that it was useful to take measurements at the same current electrode separation before and after increasing MN/2 so that any discrepancies could be identified.

Communication with field helpers was maintained at the wider separations by using the C.B. radios. Three radios were used: a portable radio was carried by each of the field helpers at the current electrodes and a more powerful

base station transmitter was located at the centre of the spread. The reliability of the two portable transmitters diminished rapidly after 3 to 4 hours as the power in the rechargeable batteries became exhausted. This time was usually just about sufficient to complete the full D.C. resistivity sounding.

To increase efficiency, these observations were usually performed simultaneously with the low frequency MT measurements (band 2 or 3). The short duration of the artificial D.C. resistivity currents meant that the author considered it unlikely that the nearby MT measurements would be adversely affected.

The D.C. resistivity measurements were usually made on a long, straight and quiet road close to the SPAM carrying vehicle. This could be readily achieved in Northumberland because of the geological strike and the subsequent Roman legacy. The author recognizes that roads do not provide typical geoelectric environments, however, they facilitated a rapid near surface geoelectric survey to be performed.

The biggest drawbacks to the D.C. resistivity method identified by this author were 1) the lack of ideal locations, 2) the effort and size of power sources required to obtain relatively shallow information and 3) the frequency with which the thin cables broke whilst increasing the spread separation. However, the deeper information (AB/2 > 100 m.) supplied by the technique was found particularly valuable if combined with the much more deeply probing MT measurements.

3.4. MAGNETOTELLURIC SITE SELECTION

A profile of geoelectric soundings across the strike of a structure of interest generally provides considerably more information than a more random scattering of sites. For this study, the linearity of such a profile, a fixed desired density of soundings and the accessibility of many areas for the semi-portable SPAM, provided the most significant regional constraints on the location of the sites.

It was desirable that each chosen site should be close to a road or track, away from strong topographic features and as far away from cultural noise sources as possible (e.g. houses, factories, radio transmitters, electrified

railways, heavy microseismic activity, power lines, etc.). Some contamination from the all pervasive 50 Hz. power lines is inevitable everywhere in Britain, but this was only found to be a particularly damaging source if it saturated the SPAM's amplifiers and consequently led to poor resolution of the lower amplitude natural signals superimposed upon it. The ideal site was a flat field of minimum dimensions of 80 by 80 metres. The sensors themselves were placed away from trees, metallic fences and telephone wires.

Electric fences are becoming an increasing menace for MT fieldwork because the currents they carry often leak into the ground and demonstrate a much larger, impulsive amplitude than that of the naturally induced currents. It can be a very time consuming task to locate all the offending electric fences, but it is important, whenever possible, for an MT field worker to try and persuade the farmers responsible, to switch off the currents in those fences in the immediate vicinity of the site.

Crop damage during the fieldwork is minimized if grass covered fields are used, but these often contain farm animals such as horses, sheep and cattle. In the authors experience, sheep and horses produce little interference with the field equipment. Occasionally an animal may 'trip' over the telluric cables and thereby induce an observational spike. On the other hand, cattle have a prediliction for any type of cable and show considerable interest in the telluric boxes and induction coils. MT field measurements are likely to be prone to severe disruption if such animals are present.

In summary, rough moorland locations were found to be the best in terms of ability to gain permission and were generally located away from strong cultural noise sources. Boggy regions should be avoided because of the risk of progressive mis-alignment of the coils and also water penetration into the sensors. More cultivated farmland was usually found to be more accessible for vehicles but also more difficult to acquire the necessary permission to use it. This author would suggest that any future MT field leader would stress the environmentally friendly nature of the method to any wary farmer.

The presence of a LR requires a very much larger field or access to another field, a distance away from the measuring site. The reference site should ideally be as free from animal interference as possible, otherwise there

will be considerable disruption to data acquisition from the main site, whilst damaged equipment is being repaired a few hundred metres away.

Remote reference requires little more than 2 standard MT sites. Ideally the reference site should be located in a quieter region than the measuring sites (c.f. Kröger *et al.* 1983) and it may be helpful if they are within C.B. range of each other.

3.5. FIELDWORK CAMPAIGNS

3.5.1. New Measurements

A total of eight MT soundings were performed by this author during 3 weeks in July 1987, along a roughly north-south traverse across the Stublick Fault in Northumberland (fig. 3.5). Most of these soundings had some referenced (local or remote) observations for at least part of the time and, at 5 of the MT locations, D.C. resistivity measurements were also acquired.

This particular area was chosen for 3 main reasons:

1. Previous magnetotelluric measurements had identified one particular area around Whitfield (WHI: Harinarayana 1987) which was deemed to be a suitably quiet location for the deployment of a static remote reference SPAM. It was assumed that a series of measuring sites to the north would encounter higher noise levels whilst crossing the east-west axis of human activity between Carlisle and Newcastle.

2. Measurements made in this region could be used to give more information about the Stublick Fault zone when augmented into a larger study of the geoelectric structure of the Alston Block and Northumberland Troughs.

3. The presence of thin resistive layers at shallow depths within the sedimentary basin (mainly the Whin Sill and the Great Limestone) would provide a useful test for the resolution of the joint MT and D.C. resistivity models.

A number of fieldworkers were involved at various times (the author, Catherine Johnson, Phil Jones and Bernhard Steinberger). Initially one SPAM carrying vehicle performed 3 SS, LR and DC soundings on the northern margin of the Alston Block (HGN, DBK and CHM), to familiarise the fieldworkers with the use of the equipment. MT data was collected from RDY (SS/LR/RR/DC) for

Figure 3.5: The MT site locations in Northern England at which the author acquired new data (underlined) or reprocessed/remodelled pre-existing observations. More precise site locations and the full station names are given in Appendix - C.

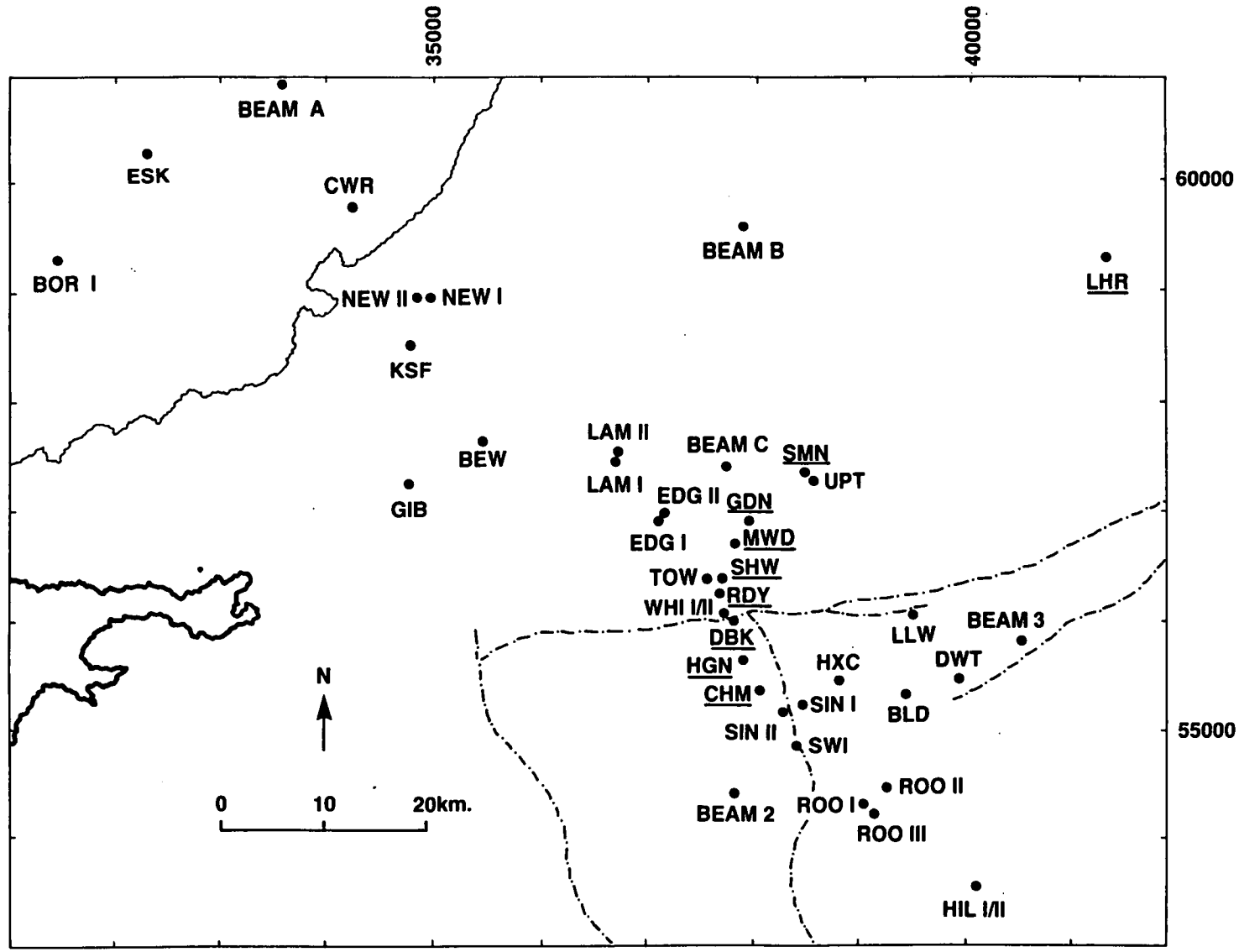
35000
40000
60000
55000
BEAM A
ESK
CWR
BOR I
NEW II
NEW I
KSF
BEAM B
LHR
BEW
GIB
LAM II
LAM I
BEAM C
SMN
UPT
EDG II
GDN
EDG I
MWD
SHW
TOW
RDY
WHI I/II
DBK
LLW
BEAM 3
HGN
HXC
DWT
CHM
SIN I
BLD
SIN II
SWI
N
0
10
20km.
BEAM 2
ROO I
ROO II
ROO III
HIL I/II

60

11 days, whilst the observations were used to remotely reference the 4 soundings to the north within the Northumberland Trough (SHW, MWD, GDN and SMN). SHW was located close to RDY so that any preliminary problems with the referencing equipment or SPAM's could be more rapidly solved. The author would have preferred the next sounding to have been closer to SHW, but there were no suitable sites north of MWD (SS/LR/RR/DC). The author could not gain vehicular access to a wide region enclosed by the National Park which includes all the land to the north of Hadrian's Wall. Instead of setting up a site close to the electric fences near EDG (which had already been occupied by both Novak (1981) and Harinarayana (1987)) the remaining two sites were situated to the NE. SMN (SS/RR) in particular was much further away than had been originally intended.

The quality of the acquired response functions were variable (see diagrams in Appendix - C). To summarize, CHM and HGN were both fairly noisy, but like WHI, DBK, RDY and SHW were very good sites. MWD was found to be rather noisy, whilst the equipment problems at GDN gave rise to almost valueless scalar observations. SMN gave very good results, but only after manual and automatic (c.f. Appendix-B; **ROBANAL**) window editing removed those which were clearly affected by electric fence 'spike' noise.

A second fieldwork season (April 1988) started with a 2 day, SPAM SS/LR/DC recording at LHR, adjacent to a borehole in Northumberland. The Landrover, equipment and personnel (the author and Ai Jun Zhang) then moved to Worcestershire to make further measurements. Apart from fig. 6.6, the results from this latter study are not discussed further here.

3.5.2. Incorporation of Previous Geoelectric Measurements

A large number of other geoelectric measurements have been performed in and around Northumberland. To provide a spatially more comprehensive survey, a number of these were re-investigated using some of the (MT) processing and (MT and D.C. resistivity) modelling programs described in Appendix - B.

A number of low frequency response functions were gleaned and re-modelled from the published apparent resistivity and phase estimates given by Jones and Hutton (1979a,b), Novak (1981) and Beamish (1986b). These

observations must be interpreted warily as manual transcription of the response functions inevitably introduced extra errors which were not in the original data. More recent measurements by Harinarayana (1987) were available for complete re-processing and subsequent re-modelling using the programs developed for this study. More details of each of the sites is given in Appendix - C.

In addition to the D.C. resistivity measurements acquired by this author, a number of other deep D.C. resistivity measurements were made in this region by Leeds University students and then compiled by Roxis (1984). The average of these 2-D measurements were used for the sites near to ROO II and LAM II and subsequently used for joint MT/DC resistivity modelling.

CHAPTER 4

LEAST SQUARES PARAMETER ESTIMATION TECHNIQUES

Where is the wisdom we have lost in knowledge?

Where is the knowledge we have lost in information?

T.S. Elliot (1888-1965)

4.1. OVERVIEW

Parameter estimation is a very important step in many sciences in which experimental observations are used to estimate some characteristic quantities which aim to model the system under investigation. Practical problems range from an estimate of the central tendency (location) or spread (scale) of a (univariate) single set of observations to large multiparameter or non-linear regression problems. The standard procedures for solving these problems fail when the specified model is inadequate or the observations do not conform to a number of assumptions.

Usually in the physical sciences, an experiment can be repeated many times. On each occasion the observations will be subjected to some variable and unknown errors. The resulting overdetermined problem will have more observations than the number of parameters sought. This chapter and the next one are mainly concerned with obtaining the "best" solution to this type of problem.

The least squares method has historically played a prominent role in overdetermined parameter regression. In sections 4.2 and 4.3, the basic, linear least squares theory is developed for both the parameters and their associated error estimates. Various properties of the least squares estimates are then discussed. Section 4.5 describes in detail a number of assumptions associated with and limitations to, the use of this technique. Various statistical regression tests for checking some features of the observations and the model's parameters are then discussed in section 4.6. Finally, section 4.7 is

concerned with a description of the estimation of the magnetotelluric impedance. This is a particularly interesting application of the least squares method on a large, and usually far from perfect, set of observations.

This chapter thus aims to describe the basic least squares parameter estimation technique and to lay the foundations for the more elaborate regression methods used in various stages of MT and other geophysical data processing (chapter 5).

The contents of this chapter are mainly drawn from Daniel and Wood (1971), Claerbout (1976), Twomey (1977), Gunst and Mason (1980), Weisberg (1980), Huber (1981), Draper and Smith (1981), Menke (1984), Lines and Treitel (1984), Press *et al.* (1986) and Rousseeuw and Leroy (1987).

4.2. BASIC LINEAR LEAST SQUARES THEORY

The least squares method assumes that a set of N dependent (response) observations **y** can be partly explained in terms of a linear combination **F(b)** of M independent (explanatory or carrier) measurements **X** and the model parameters **b**, which are to be estimated. Additionally, some fraction of the observed values of **y** must be explained in terms of observational errors which are lumped together into a residual error matrix **r**. This can be written in matrix notation as:

$$\begin{aligned} \mathbf{y} &= \mathbf{F(b)} + \mathbf{r} \\ &= \mathbf{X} \,.\, \mathbf{b} + \mathbf{r} \end{aligned} \qquad (4.2.1)$$

or in terms of individual observations:

$$y_i = \sum_{j=1}^{M} x_{i,j} \,.\, b_j + r_i \qquad (4.2.2)$$

for i=1,2,...,N observations, where, in the overdetermined situation N is much greater than M.

Realistically it will be impossible to satisfy every set of observations exactly, because each set will contain some variable and unknown errors. The best solution that can be obtained by any regression method will

approximately fit the majority of the observations and not be severely influenced by an excessively noisy minority.

The aim of the least squares method is to minimise some measure of the vector length (norm) between the observations **y** and their associated predicted observations which are derived from the linear combination **X . b**. In fact, as the method's full name ("least *sum of* squares") suggests, it minimises the sum of the square of the residuals:

$$Q = \sum_{i=1}^{N} |r_i|^2 = \mathbf{r}^T . \mathbf{r} \qquad (4.2.3)$$

where, $\mathbf{r}^T$ is the transpose of the matrix **r**. This method is also called the minimisation of the Euclidean or L2 norm whilst the scalar function Q is known by a variety of names including the misfit, cost, least squares, penalty or chi-squared (χ^2) function.

In order to find the parameter values which minimize Q, the quadratic function (eqn. 4.2.3) is first expanded.

$$\begin{aligned} Q &= (\mathbf{y} - \mathbf{X.b})^T . (\mathbf{y} - \mathbf{X.b}) \\ &= \mathbf{y}^T.\mathbf{y} - (\mathbf{X.b})^T.\mathbf{y} - \mathbf{y}^T.\mathbf{X.b} + (\mathbf{X.b})^T.\mathbf{X.b} \end{aligned} \qquad (4.2.4)$$

Since, $(\mathbf{X.b})^T.\mathbf{y} = \mathbf{b}^T.\mathbf{X}^T.\mathbf{y}$ is a scalar quantity, its transpose, $\mathbf{y}^T.\mathbf{X.b}$, must have the same value. Thus

$$Q = \mathbf{y}^T.\mathbf{y} - 2.\mathbf{b}^T.\mathbf{X}^T.\mathbf{y} + (\mathbf{X.b})^T.\mathbf{X.b} \qquad (4.2.5)$$

Taking the derivative of Q with respect to the vector **b** is equivalent to differentiating Q with respect to each element of **b** in turn and writing the resulting derivatives one below the next in matrix form:

$$\frac{\partial Q}{\partial \mathbf{b}} = -2.\mathbf{X}^T.\mathbf{y} + 2.\mathbf{X}^T.\mathbf{X.b} = \mathbf{O}$$

$$\text{or} \quad (\mathbf{X}^T.\mathbf{X}).\mathbf{b} = \mathbf{X}^T.\mathbf{y} \qquad (4.2.6)$$

Equation 4.2.6 represents M simultaneous equations which must be solved to obtain estimates for the parameters'. These are known as the normal equations because the residual error vector is normal to the columns of the

independent measurements (Claerbout 1976). From equation 4.2.6 the Gauss-Newton equation for the parameter estimates is obtained as follows:

$$\mathbf{b} = (\mathbf{X}^T.\mathbf{X})^{-1}.\mathbf{X}^T.\mathbf{y} \qquad (4.2.7)$$

The square matrix $(\mathbf{X}^T.\mathbf{X})$ can be inverted by Gaussian elimination or LU decomposition (Press *et al.* 1986), but these methods can only work when the inverse actually exists. The effects of inverting a singular or near singular matrix are discussed in section 4.5, whilst a number of possible alternatives to the solution of the Gauss-Newton equation are considered in Chapter 5

Equation 4.2.7 is applicable for real arithmetic data. Least squares parameter estimation from complex valued data, which often occurs in spectral applications, requires only slight modifications to the methods described (Claerbout 1976, Menke 1984). In particular, the positive real valued quadratic function to be minimised is:

$$Q = \mathbf{r}^H . \mathbf{r} \qquad (4.2.8)$$

where $\mathbf{r}^H$ is the Hermitian conjugate (complex conjugate transpose) of r. The normal equations thus become:

$$(\mathbf{X}^H.\mathbf{X}) . \mathbf{b} = \mathbf{X}^H.\mathbf{y} \qquad (4.2.9)$$

and the corresponding Gauss-Newton equation:

$$\mathbf{b} = (\mathbf{X}^H . \mathbf{X})^{-1} . \mathbf{X}^H.\mathbf{y} \qquad (4.2.10)$$

4.3. PARAMETER ERROR ESTIMATES AND CONFIDENCE BOUNDS

This section describes three methods for estimating the standard errors of the acquired parameter values. The discussion which then follows is concerned with the conversion of these into regions of confidence constructed in parameter space. Within these regions it is anticipated the true result will lie, to some specified probability level.

4.3.1. Variance–Covariance Matrix

The Gauss–Newton equation (eqn. 4.2.7) can be written as a linear mapping between the observations **y** and the estimated parameters **b**:

$$\mathbf{b} = \mathbf{M} \,.\, \mathbf{y} \qquad (4.3.1)$$

where $\mathbf{M} = (\mathbf{X}^T.\mathbf{X})^{-1}.\mathbf{X}^T$

Correspondingly, the estimated observational error variance–covariance matrix Cov(**y**) can be mapped into the estimated parameter error matrix Cov(**b**) by:

$$\text{Cov}(\mathbf{b}) = \mathbf{M} \,.\, \text{Cov}(\mathbf{y}) \,.\, \mathbf{M}^T \,. \qquad (4.3.2)$$

Under the assumption that the observational errors are random, independent and drawn from a Gaussian distribution with a constant variance σ^2 (the problem variance; section 4.6), then Cov(**y**) = σ^2.**I**, where **I** is the identity matrix.

$$\text{Cov}(\mathbf{b}) = (\mathbf{X}^T.\mathbf{X})^{-1}.\mathbf{X}^T \,.\, \sigma^2.\mathbf{I} \,.\, [(\mathbf{X}^T.\mathbf{X})^{-1}.\mathbf{X}^T]^T \qquad (4.3.3)$$

Since $(\mathbf{X}^T.\mathbf{X})^{-1}$ is a symmetric matrix and identical to its transpose, then:

$$\begin{aligned} \text{Cov}(\mathbf{b}) &= \sigma^2\mathbf{I} \,.\, (\mathbf{X}^T.\mathbf{X})^{-1}.\mathbf{X}^T \,.\, [\mathbf{X}. (\mathbf{X}^T.\mathbf{X})^{-1}] \\ &= \sigma^2\mathbf{I} \,.\, (\mathbf{X}^T.\mathbf{X})^{-1} \qquad (4.3.4) \end{aligned}$$

The diagonal elements are usually used as estimates of the variance for the corresponding parameters. The standard error (deviation) on the jth parameter is then given by:

$$\sigma_j = \sqrt{(\, [\, \text{Cov}(\mathbf{b}) \,]_{jj} \,)} \qquad (4.3.5)$$

These errors may not reflect the true parameter uncertainties if inter-relationships exist between parameters (section 4.6.2) or the observational errors are correlated (section 4.5.1).

4.3.2. Most Squares Error Estimates

An alternative to the covariance-matrix-based error estimates has been proposed by Jackson (1976). The objective of his method is to find an

extreme value for individual, or a linear combination of, parameters which is still consistent with the observations and their error estimates. As the parameters are perturbed away from their "optimum" least squares values ($\mathbf{b}_{L.S.}$; eqn. 4.2.7), the residual sum of squares Q (eqn. 4.2.3) correspondingly increases from its minimum $Q_{L.S.}$, to some threshold Q_T.

The mathematical problem is to find the extreme value of $\mathbf{b}^T.\mathbf{d}$ (where e.g. $\mathbf{d} = [1,0,0....,0]^T$, picks out the first parameter to be optimized) subject to the constraint that the residual sum of squares $|\mathbf{y} - \mathbf{X} . \mathbf{b}|^2 = Q_T$. The most squares parameter estimates ($\mathbf{b}_{M.S.}$) can then be found by solving by the method of the Lagrange undetermined multiplier (Hill 1987, Meju 1988):

$$\mathbf{b}_{M.S.} = \mathbf{b}_{L.S.} \pm \beta.(\mathbf{X}.\mathbf{X}^T)^{-1}. \mathbf{d} \qquad (4.3.6)$$

Q_T can be chosen so that the estimated parameter errors correspond to a desired number of standard deviations. If $Q_T > Q_{L.S.}$, then β is the scalar Lagrange multiplier whose value can be calculated.

The most squares parameter estimates allows the maximal range of parameter values to be explored. Upon repeating this procedure for all individual members or combinations of the poorly resolved parameters (i.e. those which have little influence on the residual sum of squares), unphysical features within the model can be readily identified. Jackson (1976) has recognised that the resulting range of parameter values can be much larger than their covariance based error counterparts.

Meju (1988) has recently developed an iterative version of this technique for use in the non-linear modelling of magnetotelluric response function data. This variant has also been adapted by this author for gravity modelling (section 6.4.8).

4.3.3. Jacknife (non-parametric) Error Estimates

Both methods of error estimation previously described are parametric estimators (e.g. Hampel *et al.* 1986) because they require specific model distributional assumptions to be made in advance. In particular, the pre-requisite of a Gaussian error distribution is essential to the interpretation

of standard errors from the covariance matrix. The jacknife requires no such assumptions and furthermore, it does not require an accurate estimate of the number of observational degrees of freedom to estimate the problem variance.

Efron (1982), Rousseeuw and Leroy (1987) and Thomson and Chave (1990) describe the jacknife estimator and Chave and Thomson (1989) further discuss the adaptations required for its implementation in the complex valued MT impedance estimation problem. Only a very brief review of the method is given here.

A jacknife error estimate is just the standard variance estimate of a set of substitute observations, which are known as pseudo-values. These pseudo-values are formed not only from an estimate of the model parameters from the entire set of original observations, but also by deleting the corresponding observation and evaluating the parameter values from this subset.

The computational load for jacknife errors is high, but they are straightforward to compute, even when there are complicated error distributions present. The resultant errors estimates are generally believed to be more realistic, particularly if there is a breakdown in the observational error assumptions.

4.3.4. Confidence Bounds

The standard error (eqn. 4.3.5) is a weak statistical parameter (Gunst and Mason 1980, Jones *et al.* 1983). It is more informative to be able to describe a region of parameter space around the least squares estimates, in which the true parameter values are likely to be found. The breadth of this region then provides a measure of the accuracy of these estimates to some desired probability level.

A confidence interval for individual parameters can be computed from the product of the standard error and a multiplier factor. When the observational errors have a Gaussian distribution, the estimated parameters, predicted values, etc. will also have Gaussian distributions because they are all linear combinations of the observations and therefore the errors. Confidence

intervals are then based on the Students t - distribution. A $(1-\alpha).100\%$ confidence interval around the true value b_j is given by:

$$\hat{b}_j - t(\nu,1-\alpha/2).\sigma_j < b_j < \hat{b}_j + t(\nu,1-\alpha/2).\sigma_j \qquad (4.3.7)$$

Where ν is the number of degrees of freedom (approximately N-M: see section 4.6.1). As $\nu \rightarrow \infty$, equation 4.3.7 gives the well known expressions for an e.g. 68% confidence interval: $b_j-\sigma_j < b_j < b_j+\sigma_j$ or 94%: $b_j-2.\sigma_j < b_j < b_j+2.\sigma_j$, etc. (Press *et al.* 1986).

These limits are constructed around individual parameters and cannot be used to specify a joint multi-parameter confidence region. The resulting rectangularly shaped region will be seriously misleading if a high degree of correlation exists between any of the parameters. The confidence region is then properly specified by an ellipse (2 parameters) or ellipsoid (>2 parameters) and the appropriate multipliers (eqn. 4.3.7) is derived from an F distribution (Weisberg 1980, Draper and Smith 1981).

The multiplier factor in both the individual and joint confidence regions are derived from the same probability distributions used to perform tests upon the relevance of estimated parameter values (i.e. the t and F - tests : Daniel and Wood 1971). Both the confidence regions and these parameter tests provide the same type of statistical information concerning the significance of the estimated parameter values (Gunst and Mason 1980).

4.4. LEAST SQUARES PROPERTIES

The least squares method has a number of useful properties which help to account for its widespread popularity.

Firstly for linear relationships it is very straightforward to compute the parameters (eqn. 4.2.7), their associated errors (eqn. 4.3.4) and a variety of regression statistics (section 4.6). The inversion of the square matrix $(X^T.X)$ (eqns. 4.2.7 and 4.3.4) may be difficult in certain situations (section 4.5.2), but is a trivial calculation for small M.

Its second property requires that the errors are uncorrelated and drawn from a probability density function with a constant variance. Under these

circumstances, the Gauss-Markov theorem states that least squares gives the most precise and unbiased parameter estimates (e.g. Daniel and Wood 1971, Meyer 1975, Constable 1988).

This property can be explained by visualising a situation in which numerous sets of observations are made on a system and the parameters (**b**) are estimated from each set. Any one set of observations will contain some random noise. Since the estimated parameters are linear combinations of random variables (the observations), they themselves will be random variables (Jackson 1972). The estimated parameter values will therefore take different values when compared with estimates acquired from any other set of observations. If a sufficient number of sets of observations are obtained, the distribution of the estimated parameters can be assessed. An unbiased parameter estimator is one whose mean (or expectation) value of this distribution coincides with the true parameter value. i.e.:

$$E(\hat{\mathbf{b}}) = \mathbf{b} \qquad (4.4.1)$$

Biased estimators are usually avoided because they are statistically more likely to give an incorrect solution. The degree of bias introduced is usually unknown and cannot be reduced by increasing the number of observations.

It is very desirable to use a minimum variance parameter estimator (Var(**b**) -> minimum, for large sample sizes) because on average, **b** will deviate less from the true value than an estimator with a larger variance. Least squares estimates possess this property regardless of the form of the probability density function (Tarantola 1987); this helps to explain the methods wide usage even when a non-Gaussian distribution is assumed. Such a "most precise" estimator is termed efficient.

Parameter estimates may be biased if (a) they are non-linear combinations of other parameters (c.f. section 5.8), (b) they are estimated by "non" least squares methods (e.g. ridge regression: section 5.7.3, Marquardt 1970), (c) the specified model is incorrect (Draper and Smith 1981) or (d) the independent measurements are subject to errors (section 4.5.2). Furthermore, lower variances than the least squares "minimum" can be attained by non-linear models (Daniel and Wood 1971). The main advantage in solving the linear

problem is its relative ease.

The final least squares property additionally assumes that the errors are drawn from a Gaussian distribution. In this case, least squares is the maximum likelihood (M. L.) technique for the estimated parameters. It is then "optimum" in that it will have the minimum variance of any of the others from *any* unbiased estimation techniques. The M.L. estimates will maximise the probability (likelihood) that the observations y, were actually observed (Meyer 1975, Press *et al.* 1986). This slightly strange assertion can be clarified by considering the derivation of the sample mean (i.e. the least squares univariate estimator) from the maximum likelihood viewpoint:

If there is a set of random observations, x_i, drawn from a Gaussian distribution with mean $\langle x \rangle$ and variance σ^2, the probability that one of the observations will take a particular value is given by a Gaussian probability density function:

$$P(x_i) = \frac{1}{\sqrt{(2\pi)}\sigma} \exp - \left| \frac{(x_i - \langle x \rangle)^2}{2\sigma^2} \right| \qquad (4.4.2)$$

The joint probability function for all N observations is the product of these individual distributions:

$$P(\mathbf{x}) = \prod_{i=1}^{N} \frac{1}{\sqrt{(2\pi)}\sigma} \exp - \left| \frac{(x_i - \langle x \rangle)^2}{2\sigma^2} \right|$$

$$= \sigma^{-N} . (2\pi)^{N/2} . \exp[-1/(2\sigma^2) . \sum_{i=1}^{N} (x_i - \langle x \rangle)^2] \qquad (4.4.3)$$

This function is further complicated if the variance is not constant or the errors are not independent. In this case, σ^2 is replaced by the observational covariance matrix, Cov(x) (section 5.5).

The maximum likelihood technique maximises this probability density function or equivalently its logarithm, for the parameters $\langle x \rangle$ and σ^2.

$$L(<x>,\sigma^2) = \ln P(x) = - N.\ln \sigma - 1/(2.\sigma^2) \cdot \sum_{i=1}^{N} (x_i - <x>)^2$$

$$= - N.\ln \sigma - 1/(2.\sigma^2) \cdot \sum (x_i - <x>)^2 \qquad (4.4.4)$$

If the derivative of L is taken with respect to these two parameters in turn and the resulting equations are set equal to zero, their simultaneous solution gives the usual definitions for the sample mean and variance (Menke 1984) which can be obtained by minimizing the sum of squares residuals (L2 norm) in equation 4.2.7.

In the more general situation, the maximum of the likelihood function L(**b**) is found by obtaining the minimum of an objective function ρ:

$$\max [L(\mathbf{b})] = \min \sum_{i=1}^{N} \rho(r_i) \qquad (4.4.5)$$

where r_i is the residual error corresponding to the i th observation. This equation underlies the robust M- regression estimates described in section 5.6.5.

The appropriate maximum likelihood estimator for an error distribution implies that it is the high efficiency, minimum variance, unbiased estimator which will provide the "optimum" parameter estimates in large sample situations. In practice, sufficiently large sample sizes are rarely available for an accurate assessment of the underlying error distribution.

The particular need for an estimator based on a Gaussian error distribution is emphasised by the Central Limit Theorem (Winsor's principle) (e.g Claerbout 1976, Draper and Smith 1981). In many situations when the observational errors are drawn from a number of different sources of comparable size this theorem states that their sum will tend towards a Gaussian distribution. This holds regardless of the individual probability distributions and is increasingly valid for a larger number of observations. Thus, frequently in experimental observation regression, the judicious use of least squares can be justified.

4.5. ASSUMPTIONS AND LIMITATIONS OF THE LEAST SQUARES METHOD

Throughout the preceding sections three assumptions concerning the statistics of the residual errors have been mentioned. Likewise, a number of limitations upon the ability of least squares to estimate the parameters correctly have been implicit. In this section both these assumptions and limitations are described in some detail.

4.5.1. Assumptions

The first assumption requires that the residual errors r_i on the dependent observations have been drawn randomly from a probability density distribution with a) a mean (expectation) value of zero ($E(r_i) = 0$) and b) a constant, but possibly unknown, variance ($Var(r_i) = \sigma^2$). To fulfill the first part of this assumption the model needs to have either an intercept term, or any systematic errors removed. A constant variance is generally regarded as being one of the less important assumptions. In fact, if the variance of the individual observations can be quantified prior to regression, the problem can be readily transformed to a common variance by weighted least squares (section 5.5).

The second assumption is rather more critical for the estimation of both parameters and errors. In least squares regression, any pair of residual errors r_i and r_j are uncorrelated (i.e. $E(r_i,r_j) = 0$, for i not equal to j). This assumption can be violated if the collected observations are ordered in time or space (Weisberg 1980) but often appears to be violated even for observations which are expected to be completely independent but have some unsuspected long range inter-correlations (Hampel *et al.* 1986).

Thirdly, although a strictly Gaussian error distribution is not absolutely necessary for parameter estimation, it is clearly desirable for the estimates to be "optimum" with minimum variance (section 4.4). In contrast, the standard parameter errors estimated from the covariance matrix (eqn. 4.3.5) requires strict adherence to this assumption.

Considerable attention has been paid recently to the very considerable

influence of just a small fraction of "outliers" or "mavericks" on both parameter and their error estimates (section 5.6.2). These observations are grossly in error and cannot be explained within the framework of a single Gaussian error distribution.

4.5.2. Limitations

Least squares can only give an accurate solution if the model parameters are truly constants. An inappropriate model parameterization (e.g. poor discretization of the MT response function; section 4.7) or observations performed upon a non-stationary process will result in the incorrect estimation of both parameters and errors.

A second limitation is that the observations should be a representative sample drawn from the entire population of possible samples (Daniel and Wood 1971). A characteristic set of model parameters cannot be expected to be obtained from an unusual set of observations.

Thirdly, least squares can only be used when a linear model functional relation (F(b) in eqn. 4.2.1) is known to hold exactly from theory or a reasonably good approximation can be assumed. In geophysical applications, model over-specification is especially common because of the over-zealous nature of most interpreters to 'resolve' the maximum amount of information in their observations. Equivalently, a set of inadequate observations may not be able to support all of the expected or desired model details. This may result from:

1. Poor experimental design whereby a) not all or b) non-independent observables are measured (e.g. for some graphic examples see Menke 1984, p46-51). In the MT data acquisition context, performing a) only scalar measurements or b) non-orthogonal tensor measurements will not be particularly useful at unravelling a complex geoelectric structure.

2. Excessive observational noise.

Such problems suggest there will be some duplication of information provided within or between the sets of explanatory observables. This phenomenon is known as collinearity and manifests itself as linear

relationships between the columns of **X**. Numerically ($\mathbf{X}\mathbf{X}^T$) (in eqns. 4.2.7 and 4.3.4) is then singular and cannot be inverted and the parameters cannot be independently determined (for a lucid example; see Golub 1969). Exact singularity is rare, but near singularity (or ill conditioning) when approximate linear relations are present is also potentially dangerous. In this case, the parameter variance will become inflated (section 4.6.2), and on average the parameter estimates will fall further from their true values than a properly conditioned matrix (Hoerl and Kennard 1970a). In practice, small changes in the observations may result in parameter values having much larger values than may have been otherwise expected or even taking the wrong sign. Upon substitution of these estimates back into the functional relation F(**b**), to obtain the predicted observations, detection of this problem should become obvious.

In general such model over-parameterization can only be justified if it is used in an exploratory fashion to identify the important model features (Jackson 1972), or the model is constrained using some "a priori" information (section 5.7.4).

In contrast to the above, deliberate model under-parameterization was previously a common procedure because it avoided the numerical difficulties encountered with ill-conditioned matrices. Jackson (1979) has pointed out that by limiting the number of parameters places an unjustified, a priori, assumption upon the model functional form. Consequently, the estimated parameters will be biased, leading to inaccurate predicted observations and an unnecessarily inflated residual sum of squares. This may not be particularly easy to detect.

The inability of least squares to accommodate noise on **X**, the independent measurements is a potentially serious limitation. Not all authors discuss this explicitly and consequently few practitioners of the method realise the damaging effects.

Initially, the researcher using least squares must choose which of the observable quantities will be the dependent responses (whose errors will be minimised) and which are the independent observables (whose errors will result in introduction of a bias in the estimated parameters). The implicit assumption is thus made that any random variation of the independent

observations is small compared to the likely range of errors in the dependent ones (Draper and Smith 1981). In a controlled experiment the choice of independent quantities is often apparent and this limitation is not a serious problem. If however all the measurable quantities are actually all observed and thus random variables (Gunst and Mason 1980), the influence of all observational errors must then be considered. The likely severity of this noise influence upon parameter estimates can be tested by using an index proposed by Weisberg (1980). Draper and Smith (1981) have demonstrated the likely biasing that will occur in simple regression, whilst a similar example is given in the more specific example of magnetotelluric impedance estimation in section 4.7.2.

Apart from biasing associated with noise in the independent observables, any unusual values can have a very large effect upon the regression solution (Weisberg 1980). In fact, the parameter values can be essentially determined by only a few "outliers in factor (X) space", regardless of whether the corresponding dependent observations are accurate or otherwise.

4.6. REGRESSION TEST STATISTICS

Frequently, users of the least squares method seem to be interested only in the acquisition of some values for the parameters and errors. There exists however, an enormous range of statistical tests which can be used to assess various facets of the observations, parameters and the model. To completely ignore some of these tools in practical situations is at best naive, as many can be used to alert the researcher to the inherent defects in the regression technique. This section aims to discuss a number of tests of relevance to this study and some which are increasingly used in related work.

4.6.1. Goodness of Fit

This is a commonly used statistic which attempts to quantify in a single number, a measure of how well the parameter estimates obtained fit the observations.

On the assumption that the parameter estimates (eqn. 4.2.7) are close to their true values they can be used to represent them for this statistic. The

residual misfit after least squares minimisation can then be readily calculated by summing the squares of the residual errors (c.f. eqn 4.2.3):

$$\hat{Q} = \hat{r}^T . \hat{r} = (y - X . \hat{b})^T . (y - X . \hat{b}) \qquad (4.6.1)$$

Under the usual statistical assumptions of a Gaussian distribution of random errors with constant variance of σ^2; Q will be a random variable drawn from a χ^2 distribution with ν degrees of freedom. The number of degrees of freedom (or redundancy) is usually taken to be the number of observations, N, reduced by p, the number of parameters resolved (the rank: see section 5.4.2):

$$\nu = N - p \qquad (4.6.2)$$

Sometimes ν is replaced by a lower value, the effective number of degrees of freedom, as a result of a lack of observational independence or re-weighting (Chave *et al.* 1987, Appendix A).

The expected value of this χ^2 distribution is $\nu . \sigma^2$ for large ν. If this value is approximately attained, the model is deemed to fit the observations well. For example, Parker's magnetotelluric response inversion procedure (section 6.2.5) usually accepts a model around $\nu + 2.\sqrt{(2.\nu)}$ (Parker 1983).

Frequently, the misfit is different from its expected value. If $Q << \nu.\sigma^2$, their exists over-fitting of the observations by the estimated parameters (Jackson 1976, Pedersen 1979). A simpler model may remedy this and ensure that the parameter estimates are properly supported by the given observations. Conversely, if $Q >> \nu.\sigma^2$, either the parameters are inadequate to model the assumed relationship or the observations are grossly in error. Unless the goodness-of-fit is credible, the whole estimation of the parameters is suspect (Press *et al.* 1986).

The above procedure assumes that the problem variance σ^2, is known accurately in advance. In theory this is true only if each dependent observation, y_i, can be repeated several times for fixed independent measurements, x_{ij} (e.g. the MT impedance estimated several times at each frequency) or if other a priori information is available (Weisberg 1980). When the problem variance is unknown, an unbiased model dependent estimate of it can be obtained from:

$$\hat{\sigma}^2 = \hat{\Omega} / \nu$$
$$= \sum_{i=1}^{N} r_i^2 / (N-p) \qquad (4.6.3)$$

Equation 4.6.3 precludes the use of the goodness-of-fit test, but permits the parameter covariance matrix (eqn. 4.3.4) to be evaluated.

4.6.2. Parameter Correlation

Linear dependencies between the carrier observables (columns of **X**) can severely affect the solution and the estimated errors. Collinearity (section 4.5.2) can be detected for pairs of variates by measuring the strength of the relationship by correlation coefficients.

A correlation matrix **C** can be computed for pairs of pre-scaled (Hoerl and Kennard 1970a,b) explanatory variables by:

$$\mathbf{C} = \mathbf{X}\mathbf{X}^T \qquad (4.6.4)$$

where ideally, $\mathbf{C} = \mathbf{I}$, the variates are non-collinear and $\mathbf{X}\mathbf{X}^T$ is termed orthogonal. Equivalently the Pearson correlation coefficient (c_{ij}) can be defined using the parameter covariance matrix (eqn. 4.3.4):

$$c_{ij} = \frac{[\ \mathrm{Cov}(\mathbf{b})\ ]_{ij}}{\sigma_i \cdot \sigma_j} \qquad (4.6.5)$$

(e.g. Meyer 1975) where σ_i is the standard error for the ith parameter and c_{ij} takes values in the range from −1 to +1, both extreme values representing a strong correlation between the corresponding parameters. A large absolute value of c_{ij} will have a significant effect upon the parameter values obtained. The parameter variance will be increased (Daniel and Wood 1971, Belsley *et al.* 1980) by a factor of $1/(1-c_{ij}^2)$; the variance inflation factor (VIF). As c_{ij}^2 approaches 1, the variance will become arbitrarily large and the corresponding estimated parameter value can be strongly in error.

As a means of detecting collinearity, a low value of c_{ij} does not imply the absence of multiple collinearity between several variates. A multiple correlation coefficient R_j^2 can be used to measure the strength of one variate

against all the remainder, although this statistic can be numerically unstable if collinearity exists. In principle, correlation coefficients need to be calculated for all possible combinations of variates to detect collinearity. A number of SVD (section 5.4.2) based alternatives are described in Belsley *et al.* (1980).

During the modelling of resistivity response data (both magnetotelluric and D.C.) the correlation coefficients can provide valuable information as to which model layer resistivities and thicknesses can be individually resolved (c.f. section 6.2.4; Hoverstein *et al.* 1982). A value close to −1 suggests that only the product of the two parameters can be resolved from the observations, whilst conversely, a value near to +1 indicates that only their ratio is known.

4.6.3. Information Density ("Hat") Matrix

This diagnostic tool allows a measure of how well individual observations are predicted by the parameters. Equivalently, it allows the information content of the observations to be assessed retrospectively.

Assuming that the parameters **b**, solve the linear problem $\mathbf{y} = \mathbf{X}.\mathbf{b}$, then we can rewrite this as a mapping (c.f. eqn. 4.3.1):

$$\mathbf{b} = \mathbf{M}.\mathbf{y} \tag{4.6.6}$$

where $\mathbf{M} = (\mathbf{X}^T.\mathbf{X})^{-1}.\mathbf{X}^T$, for a least squares solution.

The predicted values of the observations based on these parameter estimates can then be given by (Menke 1984):

$$\begin{aligned} \mathbf{y}^{PRED.} &= \mathbf{X}.\ \mathbf{M}.\mathbf{y} \\ &= \mathbf{X}.\ (\mathbf{X}^T.\mathbf{X})^{-1}.\mathbf{X}^T\ .\ \mathbf{y} \\ &= \mathbf{H}\ .\ \mathbf{y} \end{aligned} \tag{4.6.7}$$

H is an N by N projection or 'hat' matrix which transforms the observations **y** into their predicted values $\mathbf{y}^{PRED.}$. Its useful diagnostic properties are fully discussed by a number of authors (Gunst and Mason 1980, Weisberg 1980, Rousseeuw and Leroy 1984) and it has applications to MT impedance estimation (Chave and Thomson 1989) and other geophysical inverse problems (Wiggins 1972, Pedersen 1977 and Crossley and Reid 1982).

The diagonal elements of **H** (h_{ii}) are often scrutinized because they directly measure the effect of the i th observation on its own predicted value. The range of possible values for the elements are $0 <= h_{ii} <= 1$, the lower bound implying that the observation has no influence upon the solution and the upper bound indicating that it contributes completely independent information and is therefore crucial to the estimated parameters (section 4.5). Although they have a small residual error [$r_i = y_i - y_i \sim y_i.(1-h_{ii}) \sim 0$], these leverage points are potentially very dangerous to the solution of the regression equations. They have an over-riding influence on the estimated parameter values, regardless of the accuracy of the corresponding independent observation y_i.

Traditional residual based diagnostic tests (section 5.6.4) will fail to detect this problem because the leverage effect is a consequence only of the independent (**X**) measurements. Discarding observations whose hat matrix value is above some threshold is probably the most widely used solution to this problem [e.g. $h_{ii} > (2.p)/N$, where p is the rank of **H**]. A number of other techniques are discussed by Rousseeuw and Leroy (1987).

4.6.4. Resolution Matrix

The resolution matrix measures the degree of proximity of individual estimated parameters **b** to the true, but unknown solution $\mathbf{b}^{TRUE}$ (Wiggins 1972, Jackson 1972,1979 Menke 1984). Its role can be readily compared to that of the information density matrix upon the observations.

If $\mathbf{y} = \mathbf{X}.\mathbf{b}^{TRUE} + \mathbf{r}$ and $\mathbf{b} = \mathbf{M}.\mathbf{y}$ as before, then:

$$\begin{aligned} \mathbf{b} &= \mathbf{M}.\mathbf{X}.\mathbf{b}^{TRUE} + \mathbf{M}.\mathbf{r} \\ &= \mathbf{R}.\mathbf{b}^{TRUE} + \mathbf{M}.\mathbf{r} \end{aligned} \qquad (4.6.8)$$

where **R** is the model resolution matrix. The rows of the resolution matrix can be viewed as a set of filters such that the true solution will be filtered by the corresponding row of the resolution matrix **R** and the acquired solution will be further distorted by a hopefully small random error. Like the information density matrix, the greater the rows of **R** are smeared out from the identity matrix, the less the corresponding parameters are resolved or can be independently predicted.

Fully overdetermined least squares estimates [$\mathbf{M} = (\mathbf{X}^T.\mathbf{X})^{-1}.\mathbf{X}^T$] should give $\mathbf{R} = \mathbf{I}$, the identity matrix. Mixed determined problems (section 4.5.2) will not and the resolution matrix can give an assessment of the parameters resolution.

4.7. MAGNETOTELLURIC RESPONSE ESTIMATION: AN EXAMPLE OF LINEAR LEAST SQUARES

4.7.1. Impedance Estimation

The acquisition of EM field observations has already been discussed in section 3.2. An impulse response function can be computed in the time domain (c.f. eqn. 2.6.2, Kunetz 1972), but the advent of the Fast Fourier Transform has resulted in the widespread computation of the frequency domain equivalent.

Given a large set of spectral estimates of both orthogonal magnetic (**Hx** - north, **Hy** - east) and the electric field (**Ex**, **Ey**), subject to some unknown level of noise, then the estimation of the tensor impedance (**Z**) can be formulated as an overdetermined complex valued least squares problems through (c.f. eqn. 2.5.1):

$$\mathbf{Ex(f)} = \mathbf{Hx(f)}.Zxx(f) + \mathbf{Hy(f)}.Zxy(f) \qquad (4.7.1a)$$
$$\mathbf{Ey(f)} = \mathbf{Hx(f)}.Zyx(f) + \mathbf{Hy(f)}.Zyy(f) \qquad (4.7.1b)$$

If the vertical magnetic field (Hz) has also been measured, least squares regression is usually performed on a third linear equation (eqn. 2.5.2) to obtain the tippers. As noted in section 2.5, these relationships cannot be directly proved but given the usual source field assumptions (section 2.2.2) then the parameters are independent. As will be demonstrated later, the presence of noise may induce collinearity (section 4.5), or inter-relationships between these parameters. Furthermore, if only a subset of the variables can be measured (e.g. Lanzerotti *et al.* 1986) then other linear equations may be solved:

$$\mathbf{E(f)} = \mathbf{Hx(f)}.Ax(f) + \mathbf{Hy(f)}.Ay(f) + \mathbf{Hz(f)}.Az(f) \qquad (4.7.2)$$

In the presence of a complex geoelectric environment beneath the site, a linear relationship will exist between the observed magnetic field components

which will lead to ill-conditioning.

Consider finding the least squares solution of equation 4.7.1a. In the notation of section 4.2, $\mathbf{y} = \mathbf{Ex}$, $\mathbf{X} = (\mathbf{Hx}, \mathbf{Hy})$, and the parameters $\mathbf{b} = (Zxx, Zxy)^T$. The two normal equations (eqn. 4.2.9; Sims *et al.* 1971 eqns. 8 and 9) are:

$$\begin{vmatrix} (Hx^H.Hx) & (Hx^H.Hy) \\ (Hy^H.Hx) & (Hy^H.Hy) \end{vmatrix} . \mathbf{b} = \begin{vmatrix} Hx^H \\ Hy^H \end{vmatrix} . (Ex) \qquad (4.7.3)$$

Simultaneous solution of these equations will give (eqn. 4.2.10; Sims *et al.* 1971 eqn. 15):

$$\begin{vmatrix} Zxx \\ Zxy \end{vmatrix} = \frac{1}{(Hx^H Hx)(Hy^H Hy) - (Hy^H Hx)(Hx^H Hy)} \begin{vmatrix} (Hy^H.Hy) & -(Hx^H.Hy) \\ -(Hy^H.Hx) & (Hx^H.Hx) \end{vmatrix} \cdot \begin{vmatrix} Hx^H \\ Hy^H \end{vmatrix} . (Ex) \qquad (4.7.4)$$

Similarly, (Zyx , Zyy) and the tippers can be evaluated from auto and cross spectral 'windowed' (section 3.2.2) observations of the EM field variations at one frequency and/or over a narrow frequency sub-band. Especially in the latter case, it must be recognised that the parameter values obtained are only approximately constant. Within this frequency sub-band, some, hopefully small and gradual, variation in their values must be anticipated (Jupp 1978). For the complete frequency range, the response function obtained comprises a set of discrete impedance estimates which only approximate the continuously varying function (Larsen 1989).

Compared to expressions like 4.7.4, the full impedance relations can be more succinctly written as:

$$Z = [\, H^H . E \,] . [\, H^H . H \,]^{-1} \qquad (4.7.5)$$

where $E = (Ex\ Ey)^T$
$H = (Hx\ Hy)^T$ and $Z = \begin{vmatrix} Zxx & Zxy \\ Zyx & Zyy \end{vmatrix}$

4.7.2. Magnetotelluric Noise Contamination

There is an enormous range of potential sources of phenomena, which can be regarded as being noise and error, in the acquisition and processing of EM

observations. In this section, different noise sources are placed into one of three groups according to their likely electromagnetic coherence characteristics (Kröger *et al.* 1983). It must be stressed that the least squares assumptions/limitations *may* be valid for a *subset* of noise sources within the first group, whilst, noise sources from any of the other two groups strictly violate at least one of the assumptions or limitations.

The most common and most desirable group of noise sources (if any source of noise can be described as desirable) does not correlate with the natural EM field signals or any of the observed EM field components (incoherent). The most common causes are sensor noise, the electronic circuitry or recording errors. Magnetic coil sensors generate relatively little noise but are susceptible to wind or microseismic vibration. Vibrations of the coils in the Earth's main magnetic field will induce noise. Magnetic field noise can also be generated by the motion of nearby magnetized objects (e.g. vehicles) whilst some types of sensors are prone to thermal variations.

The electric sensors are usually regarded as being even noisier than the magnetic. Wind vibration of the cables and electrochemical changes within the electrodes are both major contributors. Furthermore, the electric field measurements are sensitive to any leakage currents that might be present. Streaming potentials, D.C. electric railways, local lightning discharges and electric fences will produce noise over a broad frequency spectrum. The latter are becoming an increasing hazard at the present time. The impulsive nature of some of these sources may also saturate the equipment's amplifiers and make recording of the lower amplitude signals very difficult. Some of these sources can be detected simultaneously over large spatial areas and will therefore remove the effectiveness of remote referencing (section 3.2.4). Electronic circuitry noise is usually random and independent of the signals. Any filter noise and "cross-talk" between the different electromagnetic observables can usually be kept to a minimum by good equipment design. Data recording can sometimes be subject to timing errors (Jones *et al.* 1983), dropped bits of digital information or data transcription errors. Finally, errors may be incorporated by preliminary data processing (e.g. digital filtering) or because of the finite length of any data series (Clay and Hinich 1981).

Even if these sources of error can be regarded as random, they can still

violate some of the other least squares pre-requisite assumptions. For example, if the equipment is not properly calibrated, the sensors not exactly aligned (Nichols *et al.* 1988) or the telluric line length has been measured incorrectly, systematic errors will be incorporated into the regression equations. Correlated errors may occur when transient geomagnetic phenomena are observed (Chave and Thomson 1989) or the estimation of the impedance tensor is made from overlapping time or frequency data sets. Finally, the uniform error variance assumption may well be invalid. Egbert and Booker (1986) have shown that a breakdown in the uniform source field assumptions can create noise whose variance is dependent upon the strength of the signals. More generally, it is very difficult to envisage that the large number of different noise sources will all have an identical error distribution and variance.

Precisely because of the diversity of the noise sources, the central limit theorem (section 4.4) would suggest that for the very large numbers of electromagnetic observations which are usually acquired, the overall distribution will approximate to a single Gaussian. However, outlying observations can still be present (Egbert and Booker 1986, Chave *et al.* 1987). In this author's own experience, animal interference of either the electric or magnetic field sensors, electric fences and equipment malfunctions have all, at some time, sporadically corrupted the data recorded.

When the orthogonal components of the magnetic field are coherent, this generates a second, distinct group of effects upon the calculated magnetotelluric impedance. This may be caused by "input-coherent noise" (Kröger *et al.* 1983) or by a polarized signal (Pedersen 1982, Sims *et al.* 1971). Physical motion of the magnetic sensors, as discussed earlier, may actually induce input-coherent noise whilst source field polarisation can be a problem at higher frequencies (>1 Hz.) during local lightning discharges when there is a lack of distributed uniform fields (Boehl *et al.* 1977). Swift (1986) has also noted the absence of adequate unpolarised random signal at the lower frequencies which are dominated by the diurnal variation

The effect of input coherent noise can be visualised by considering fig. 4.1. This shows a strongly polarised magnetic field Hr at an angle α to magnetic north. Since they are not independent, any number of observations of Hr will

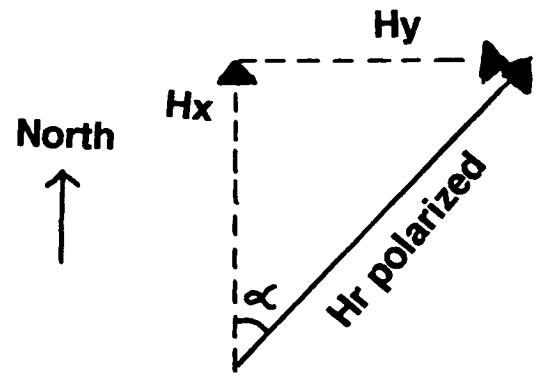

Figure 4.1: A schematic drawing to highlight the problems of input coherent noise. If the magnetic field (Hr) is entirely polarized at an angle α to magnetic north (e.g. due to a strong noise source), then the 2 orthogonal components (Hx and Hy) are not independent observations. In the notation of section 4.7.1, $\mathbf{X} = (Hx,Hy) = (Hx,Hx \tan \alpha)$ and the inverse of $\mathbf{X}^H.\mathbf{X}$ (c.f. eqn. 4.7.3) will be indeterminant. In practice such perfect correlations will never occur, but a high degree of coherence between Hx and Hy can lead to numerical instability.

not resolve the 2 impedance parameters in eqn. 4.7.1a separately (Sims *et al.* 1971).

For any angle α, the matrix $(\mathbf{X}\mathbf{X}^H)$ in equation 4.7.1 is singular and the inverse (eqn. 4.7.3) ceases to exist. This is a collinear system, where *only* a linear combination of the two original parameters ($Zxx.Cos(\alpha) + Zxy.Sin(\alpha)$) can be resolved from these observations. Therefore an infinite number of different solutions exist for Zxx and Zxy separately. In reality, perfect correlation between the two orthogonal magnetic field observations will never completely occur but a high degree of coherence will still cause the matrix $\mathbf{X}\mathbf{X}^H$ to be ill-conditioned (section 4.5).

The third and final type of noise can be described as being "multiple-coherent": i.e. coherent between any of the electric and magnetic fields. The proximity of the source of this noise to the measuring site (less than about 4 skin depths; Hughes and Carlson 1987) induces non-uniform electromagnetic radiation. The most common and readily identified source at higher frequencies are mains power lines. At most sites within Great Britain, the fundamental frequency (50 Hz.) and a number of the harmonics (100, 150 Hz. etc.) can be clearly observed to produce large amplitude sinusoidal noise. The inhomogeneous and complex pattern of the inducing fields make these frequencies useless to MT impedance estimation. Fortunately, this type of noise is stationary and usually to be found at narrow, readily identified frequencies thus allowing notch or delay line filtering of them (**ROBANAL** in Appendix-B). Other frequencies have been known to be contaminated by coherent EM noise as a result of the operation of motors (Meju 1988) and mains power switching equipment.

Coherent noise can also be generated naturally. Chave *et al.* (1987) cite the example of a magnetic storm which generated high power observations contaminated by coherent noise. These could have a strong influence on the estimation of the magnetotelluric impedance.

Any type of coherent noise from the latter two groups must at least violate the least squares restriction of noise free independent observables and almost certainly the assumption of correlated errors. Furthermore, the regression model is mis-specified because a noise source dependent term is not included

(c.f. Kröger *et al.* 1983).

4.7.3. Calculation of the Signal and Noise Powers

On the assumption that the signal and noise is uncorrelated, then it has been shown (Gamble *et al.* 1979b, Clarke *et al.* 1984) that an estimate of the "signal" can be computed from the predicted electric ($E_P = Z \cdot H$) and magnetic ($H_P = A \cdot E$: $A = Z^{-1}$) field observations:

$$[E_S{}^H \cdot E_S] = ([E^H.E_P] + [E^H{}_P.E]/2) \qquad (4.7.6a)$$

$$[H_S{}^H \cdot H_S] = ([H^H.H_P] + [H^H{}_P.H]/2) \qquad (4.7.6b)$$

Consequently, the noise power can be estimated by subtracting the calculated signal power from the total observed power:

$$[E_N{}^H \cdot E_N] = [E^H.E] - [E_S{}^H.E_S] \qquad (4.7.7a)$$

$$[H_N{}^H \cdot H_N] = [H^H.H] - [H_S{}^H.H_S] \qquad (4.7.7b)$$

4.7.4. Magnetotelluric Impedance Bias

The choice of EM independent and dependent observables is a final and widely explored problem in the application of least squares to MT impedance estimation. As already noted, the electric field is often regarded as being noisier than the magnetic. The former is therefore the obvious choice for the dependent observables and consequently any noise on the telluric signals is minimised (as for example given by equations 4.7.1 to 4.7.5).

The presence of noise in the independent observations has a biasing effect upon the impedance amplitude estimates (Sims *et al.* 1971, Swift 1986, Boehl *et al.* 1977, Clay and Hinich 1981). If for example, the measurements have been made over a 1-D geoelectric structure (Zxx=0) and the magnetic fields are unpolarised (i.e. $(Hy^H.Hx) = (Hx^H.Hy) = 0$), equation 4.7.4 simplifies to:

$$Zxy = \frac{(Hy^H.\ Ex)}{(Hy^H.\ Hy)} \qquad (4.7.8)$$

If the sources of signal and noise are different, then the resulting errors are additive (e.g. $Ex = Ex_S + Ex_N$; where Ex_S and Ex_N are the signal and noise

components of Ex). For large numbers of observations with random and incoherent noise, the cross spectral products such as ($Hy_S^H.Ex_N$) and ($Hy_N^H.Ex_S$) are negligible. Therefore:

$$\hat{Z}xy = \frac{(Hy_S^H.Ex_S)}{(Hy_S^H.Hy_S) + (Hy_N^H.Hy_N)}$$

$$= \frac{Zxy^{TRUE}}{(1 + (NSR_{Hy}))} \qquad (4.7.9)$$

where NSR_{Hy} is the magnetic field noise to signal ratio >= 0. Equation 4.7.9, shows that the impedance estimates of Zxy will be unaffected by any random noise on the electric field, whilst the amplitude will be biased down by random noise on the magnetic field observations. This is also valid for the other off-diagonal impedance tensor element Zyx. Kao and Rankin (1977) therefore proposed an iterative procedure for reducing noise in these autopowers, but it was found to do little to reduce cross powers of noise. Meanwhile, diagonal elements can suffer from "bias coupling". Pedersen (1982) and Pedersen and Svennekjaer (1984) have shown that in the one dimensional situation, diagonal elements such as Zxx can be biased away from zero, by an amount proportional to the off-diagonal element Zxy. The apparent resistivity, which is proportional to the square of the impedance amplitude must therefore be biased to a greater degree. It must be stressed that the traditional regression approach of collecting more observations to reduce the effects of random error will *not* result in the autospectra within equation 4.7.9 converging to their noise free values (Boehl *et al.* 1977). A reduction in the bias error cannot thus be achieved. For the large numbers of observations typically collected during high frequency magnetotelluric soundings, bias errors eventually dominate random errors as in the extreme example given in fig. 5.7a.

In contrast, the phase is determined from the ratio of the imaginary and real parts of the impedance element. Since the denominator of equation 4.7.9 is the sum of 2 real valued autospectra, the phase is determined only by the complex valued numerator. This is unaffected by the simple noise model given and therefore the phase is an unbiased estimate of the response function. As a consequence of this, Boehl *et al.* (1977) suggested that low pass filtering of the phase response will remove the high spectral content

resulting from noise.

These relatively straightforward bias properties will only hold under the assumptions described earlier. A two dimensional structure (Boehl *et al.* 1977), polarised magnetic fields (Swift 1986) or multiple coherent noise may distort *both* the apparent resistivity and phase estimates because of the presence of noise in cross spectral terms.

Other least squares estimates of the impedance can be obtained by reversing the roles of dependent and independent observations. For example, by reformulating equation 4.7.1a: $\mathbf{Hx} = \mathbf{Ex}.Yxx + \mathbf{Ey}.Yxy$, then a least squares solution could be found for the elements of the admittance tensor Y_{ij}. The resulting off-diagonal impedance elements ($Z = Y^{-1}$) will be biased upwards by any random noise on the electric fields. Like eqn 4.7.4, the solution is unstable when there is a high degree of correlation between the two independent observables (Swift 1986, Jones *et al.* 1983). In the two dimensional geoelectric situation, the correlation is greater between the two orthogonal electric fields than the magnetic ones. These admittance based estimates tend therefore to be more unstable. However, the envelope formed between the up and downward biased estimates is usually thought to contain the true solution (e.g. Travassos and Beamish 1988, Jones *et al.* 1989).

There are in fact a total of 6 possible independent estimates of each impedance element resulting from the simultaneous solution of pairs of the four normal equations (c.f. eqn 4.7.3):

$$(\mathbf{A}^H.\mathbf{Hx}).Zxx + (\mathbf{A}^H.\mathbf{Hy}).Zxy = (\mathbf{A}^H.\mathbf{Ex}) \qquad (4.7.10)$$

for $\mathbf{A} = \mathbf{Hx}$, $\mathbf{Hy}$, $\mathbf{Ex}$ and $\mathbf{Ey}$ (Sims et al 1971: eqns. 6–9). All six estimates contain autopowers of spectra and therefore will be biased. Of these estimates, 2 are shown to result in the apparent resistivity being biased down by random magnetic field noise, the solution of 2 of them is unstable and the remaining 2 are biased upwards by electric field noise (Sims *et al.* 1971, Boehl *et al.* 1977). There has therefore been a suggestion to take an arithmetic or geometric average of the stable but biased estimates (Sims *et al.* 1971, Jones *et al.* 1983, Tzanis and Beamish 1989). This is known to have little theoretical basis, but gives more appealing results than either extreme cases (e.g. fig. 5.7b). Travassos and Beamish (1988) have however found that this procedure

has not provided the same results as remote reference. They therefore do not recommend its use as it can produce a false, bias dependent gradient within the response function. Its use must also be clearly questionable when coherent noise is present. The subject of unbiased MT impedance estimation is discussed again in sections 5.3 and 5.4

CHAPTER 5

MORE SOPHISTICATED PARAMETER ESTIMATION TECHNIQUES

5.1. OVERVIEW

This chapter aims to describe a number of adaptations or alternatives which can help to alleviate some of the shortcomings of the parameter regression methods, which were discussed in the previous chapter. These are described with specific regard to four main applications which were encountered, by this author, during the various stages of the conversion of time varying electromagnetic (EM) field observations:

- Spike detection in the EM field time series variations (**ROBANAL** in Appendix - B).
- Estimation of the magnetotelluric (MT) impedance (section 4.7, Appendix - A)
- Fitting polynomial approximations to the acquired Earth response function (Appendix - A)
- Calculation of a parametric geoelectric model which could approximately reproduce the response function (chapter 6).

A fuller description of each of these applications is given in section 5.2. There then follows a detailed account of the variants on the least squares method which were applied in the different situations (sections 5.3-5.8). Finally, an experimental comparison of different impedance estimation methods is presented (section 5.9). This helps to review and clarify some of the points raised in chapters 4 and 5.

5.2. LEAST SQUARES APPLICATIONS

5.2.1. Observational Spike Detection

Natural time variations of the EM fields (both magnetic and electric) can be affected by high amplitude, short duration impulsive noise. In order to automatically identify these spikes, an estimate of the scale of the typical natural variations needs to be computed. A traditional non-robust least

squares estimate of scale (e.g. the standard deviation eqn. 4.3.5) will be misleading in the presence of such grossly non-Gaussian and erroneous data. To alleviate this problem it is necessary to use robust univariate estimators (section 5.6.4) which are more insensitive to such observations.

5.2.2. Magnetotelluric Impedance Estimation

The problems encountered within this application have already been discussed in considerable detail (section 4.7), so that further description here is unnecessary. The following adaptations were used in this study to enhance the least squares parameter estimates.

A reduction in the level of noise induced bias in the apparent resistivity was the aim of the first of these adaptations. Two alternative methods were applied. The first of these (section 5.3) was the reference technique in which the offending noise autopowers (eqn. 4.7.9) were removed from the impedance calculations by the inclusion of extra EM observations from a second site. Section 5.4 presents the mathematical details concerning the second of these impedance estimation methods which was based upon a Singular Value Decomposition (SVD) of a single site's observational data matrix. The aim of this technique was the simultaneous minimization of noise sources from all the observable quantities.

Robust statistical procedures provided the next adaptation which was applied to both reference and SVD impedance estimation. Multivariate robust regression is therefore described (section 5.6) with particular regard to the useful M-parameter estimation method.

Coherent or excessive levels of random EM noise were thought to introduce collinearity (sections 4.5.2 and 5.9.4) and resulted in erroneous impedance estimates. This author found that the application of prior knowledge concerning the impedance values could significantly improve the results. In mathematical terms, constraining information was imposed on the regression equations (section 5.7.4).

Although, in this chapter, these three adaptations are described individually their joint application is discussed in the companion paper ('Constrained Estimation of the Magnetotelluric Impedance') which is reproduced in this

thesis as Appendix - A.

5.2.3. Polynomial Fitting to the Response Function

This application arose twice (see Appendix - A) because of the need 1) to obtain a smooth response function (**ZFIT** in Appendix - B) and 2) to interpolate and differentiate the response function at a large number of intervening frequencies for evaluation of the dispersion relationships (**FISCHZ** in Appendix - B).

The aim of this application was to acquire M coefficients (the parameters) of a polynomial which would locally model the functional relationship between the frequency (f) and each of the four complex impedance elements (Z_{kl}) (or the corresponding scalar apparent resistivity and phase), in turn. Here, the N estimates of Z_{kl} form the set of dependent observations (y_i in the least squares notation of section 4.2), to be explained in terms of a linear combination of the coefficients (b_j) and some functions of the frequency, $u_j(f_i)$ (= x_{ij}) i.e.:

$$Z_{kl}(f_i) = \sum_{j=1}^{M} u_j(f_i) \cdot b_j \qquad i=1,2,...N \qquad (5.2.1)$$

where u_j could be a power series expansion or, to avoid numerical problems, the orthogonal Chebychev polynomial expansion (Twomey 1977, Rikitake *et al.* 1987):

$$u_1 = 1, \quad u_2 = f_i, \quad u_j = 2 \cdot f_i \cdot u_{j-1} - u_{j-2} \qquad (5.2.2)$$

Since N > M, eqn. 5.2.1 was solved by a modified linear least squares method:

1. To compensate for the lack of error uniformity (section 4.5.1), the estimated impedance errors were used to weight their corresponding dependent observations (section 5.5).

2. As the procedure was exploratory (c.f. section 4.5.2: i.e. the most appropriate number of parameters (M) was not known in advance), the regression model was initially over-specified (i.e. an excessively large number of parameters were used to model the Z_{kl}'s). To avoid collinearity problems, the surplus parameters had then to be identified and removed by the formation of the Lanczos inverse (section 5.7.2).

3. The Lanczos inverse also helped to alleviate numerical round-off which would have resulted from the direct solution of the

normal equations.

4. After the acquisition of a well resolved model, robust M-regressive techniques were iteratively applied to reduce the influence of any outlying impedance observations (section 5.6.4 to 5.6.6).

5.2.4. Modelling ('Inversion') of Magnetotelluric Response Functions

Least squares is widely used in the acquisition of a geophysically useful Earth model from a collection of observations. In the specific examples given in section 6.4, the dependent observations (e.g. the apparent resistivities) were sampled over a range of frequencies / dipole lengths from one or more MT and/or D.C. resistivity sites. Alternatively, these observations comprised a linear set of gravity anomaly values sampled across the Earth's surface.

The non-linear relationship between the model parameters was an additional problem for this least squares application. Section 5.8 therefore describes a method which was used to approximate ("linearize") the non-linear regression problem iteratively, from an assumed starting model, via the solution of a succession of linear ones. Computationally, the solution of this problem was then broadly similar to the steps already described (section 5.2.3). In this instance, the influence of extraneous parameters (stage 2) was damped by the less severe ridge regression method (section 5.7.3.). In order that gravity and pseudo 2-D MT models could be computed, additional constraining information was applied during the parameter estimation process (section 5.7.4).

5.3. UNBIASED MAGNETOTELLURIC IMPEDANCE ESTIMATION I:

THE REFERENCE METHOD

In the magnetotelluric context, this method was originally proposed by Goubau *et al.* (1978). As Jones *et al.* (1989) have pointed out, a similar principle was originally applied much earlier in the field of econometrics in 1941. Its success in reducing much of the biasing of the impedance amplitudes is evident from its widespread adoption and the considerable body of literature on the subject (e.g. Gamble *et al.* 1979a,b, Pedersen 1982, Fischer 1982, Kröger *et al.* 1983, Clarke *et al.* 1983, Goubau *et al.* 1984).

The uniform source field assumption (section 2.2.2) requires that magnetotelluric signals should be detectable simultaneously over considerable spatial distances. Although there may be some local differences in the induced components of the EM field, reflecting a complex geoelectric environment, most MT researchers consider that the field variations should still demonstrate some degree of correlation over tens of kilometres. In contrast, as this author has also observed from the Northumberland field data, most noise is random and incoherent and shows little correlation even over a few hundred metres (sections 4.7.2 and 5.9.2). With the exception of power line noise, coherent noise usually has only a fairly localized influence which diminishes with increasing distance from its source. The reference technique requires extra, simultaneously recorded, electromagnetic observations acquired at a second "reference" site. This is located at a sufficient distance from the "measuring" site of interest, for the noise in the observed EM fields at the two sites to be incoherent.

Figure 5.1 shows the time varying amplitude of the EM field recorded at 2 MT sites (MWD and RDY) a distance of 4km. apart. They are not identical, but the measuring and reference sites magnetic field impulses are strongly correlated.

It is possible to use the reference observations to remove noise by time domain data adaptive filtering (Hattingh 1988). More often referenced impedance estimation is performed in the frequency domain, using a variant of least squares regression. The derivation of the referenced impedance estimation equations described below broadly follows that given by Pedersen (1982).

Since the part of the observed magnetic field deemed to be signal should be almost identical between both the measuring (H) and reference (R) sites, a transfer function (f_{HR}) between them can be given by (frequency dependence implicit):

$$\mathbf{H} = \mathbf{R} \cdot \mathbf{f}_{HR} + \mathbf{r}_H \qquad (5.3.1)$$

H, E and Z are defined in section 4.7.1 and the magnetic reference field $\mathbf{R} = (Hx^R, Hy^R)^T$, and r_H , r_E' and r_E'' are the residual error matrices. The least squares solution of equation 5.3.1 gives (c.f. eqn. 4.2.10):

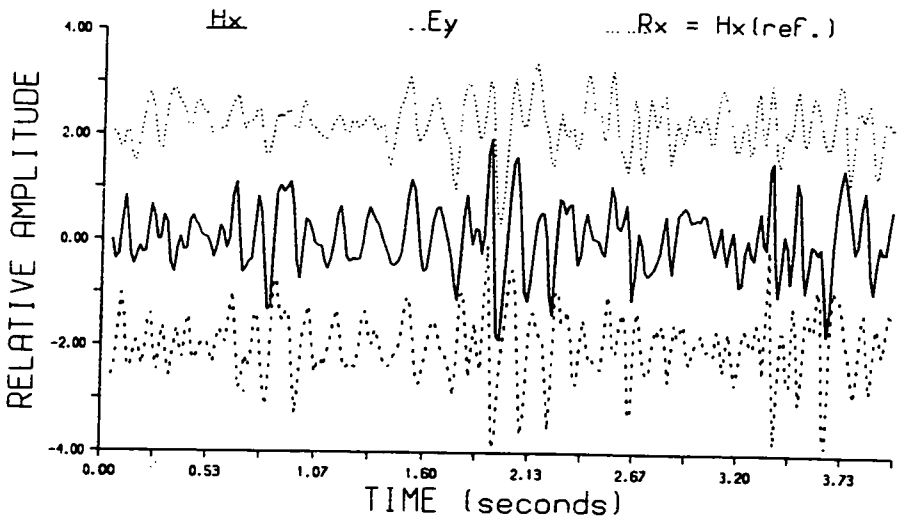

Figure 5.1: "Band 1" (section 3.2.2) time variations of the EM field from the MT site MWD (fig. 3.5). The magnetic (Hx) and orthogonal electric (Ey) fields are shown in the middle and bottom portions of this graph. At the top, the simultaneously recorded magnetic reference (Rx) from the MT site RDY (4km. away) is not identical to Hx, but there is some correlation between them (e.g. at 2s).

$$f_{HR} = R^H.H \; . \; (R^H.R)^{-1} \qquad (5.3.2)$$

Inserting eqn. 5.3.2 into the usual, single site regression equation ($E = H.Z + r_E'$):

$$E = (f_{HR}.R) \; . \; Z + r_E''$$

$$= R.Z' + r_E'' \qquad (5.3.3)$$

A least squares solution for the "modified impedance" ($Z' = f_{HR} \; . \; Z$) in eqn. 5.3.3 is then given by :

$$Z' = R^H.E \; . \; (R^H.R)^{-1} \qquad (5.3.4)$$

By inserting eqn. 5.3.4 into $Z = f^{-1}{}_{HR} \; . \; Z'$ and then using eqn. 5.3.2:

$$Z = (R^H.E) \; . \; (R^H.H)^{-1} \qquad (5.3.5)$$

As might be expected, eqn. 5.3.5 gives the single site estimate of the impedance (eqn. 4.7.5), when the reference field is identical to its locally measured counterpart (i.e. R = H). Consider again the effects of noise upon the off diagonal impedance tensor elements (Z_{XY}, Z_{YX}), in a 1-D geoelectric environment (c.f. section 4.7.4). The bias generating auto spectra are now replaced by cross spectra:

$$Zxy = \frac{Ry_S{}^H.Ex_S + Ry_N{}^H.Ex_N}{Ry_S{}^H.Hy_S + Ry_N{}^H.Hy_N} \qquad (5.3.6)$$

If the noise at the reference site does not correlate with the noise at the measuring site, the cross spectral estimates of noise will average to zero ($Ry_N{}^H.Ex_N = Ry_N{}^H.Hy_N = 0$). Zxy will therefore contain no noise powers and is asymptotically (with an increasing number of observations) unbiased in both the amplitude and phase. However if the noise does correlate between the 2 sites, the acquired response functions will still display up or downwards bias according to whether an electric or magnetic reference is used.

Using this method, a field investigation by Gamble *et al.* (1979a) produced results which were spectacularly successful. They obtained a smoothly varying response function from some seemingly corrupted observations with coherences as low as 0.1. Subsequently, Nichols *et al.* (1988) expressed the view that impedances of arbitrary accuracy can be obtained by sufficient

spectral stacking of referenced magnetotelluric data. This Utopian view is typical of many who have used the technique.

The crucial and largely unanswerable question is how "remote" the reference site should be from the measuring site in order that noise sources will not correlate. Goubau *et al.* (1984) tried to determine this distance experimentally and concluded that much of the noise at higher frequencies (> 1Hz.) resulted from the measuring equipment, and so a separation of as little as 2m. would have a significant bias reducing effect. At lower frequencies, a greater separation (200m.) was necessary. It can be argued that this was a unique situation. The ideal separation distance is probably a function of frequency, local resistivity structure, signal and noise characteristics and even the equipment and the competence of its operators. These variables cannot readily be quantified. In general, typical separations of a few kilometres are the norm, although this may well be increased at lower frequencies or in resistive environments (c.f. section 2.3.1). In practice logistical constraints tend to limit very large separations.

There is no major impediment to reformulating eqn. 5.3.6 for the use with an electric field reference. The field procedure is then similar to the telluric-magnetotelluric method described by Thayer *et al.* (1981). Lower field equipment cost is the prime benefit of this approach, but as the measured electric fields tend to be noisier and more dependent upon the geoelectric structure, this reference method is of questionable value. The field experiment by Travassos and Beamish (1988) showed that consistent results could be obtained using electric and magnetic field reference results, but the presence of uncorrelated level shifts within all the electric field measurements degraded the accuracy of their results.

A number of failings of the entire reference technique have become apparent in recent years. For example, the presence of source field polarisation, coherent noise or even the absence of coherent signal between the measuring and reference sites will cause this method to fail (e.g. if $\mathbf{Hy} = \mathbf{Hy_S}$ only, $\mathbf{Ry} = \mathbf{Ry_N}$ only, then eqn. 5.3.6 will be unstable; Larsen 1989). Kröger *et al.* (1983) have suggested that the noise amplitude in Western Europe is often greater than the signal at audio MT frequencies, so that a reference is of little use and may even degrade the estimated impedance. Ideally, the

reference site location should therefore be chosen to be as free from noise as possible. Chave and Thomson (1989) recognised that referencing does not preclude the presence of outliers or leverage points. Finally reference data processing is more inefficient than its single site equivalent because additional observations, themselves contaminated by noise, are incorporated into the impedance estimation. Consequently, the variance of referenced estimates is increased or more observations must be acquired to reduce the excess random error generated.

5.4. UNBIASED MAGNETOTELLURIC IMPEDANCE ESTIMATION II:

THE SINGULAR VALUE DECOMPOSITION (SVD) METHOD

5.4.1. Overview

A reduction in the bias present in the magnetotelluric impedance amplitude may be achieved by simultaneously minimizing noise sources from all of the observations. Unlike conventional least squares, this method requires no choice of independent, noise free EM field quantity and consequently the results may be unbiased in certain situations. This process was first proposed for the magnetotelluric impedance estimation context by Jupp (1978), although this type of "multivariate errors-in-all-variables" problem has already been tackled in a number of other research fields (c.f. Egbert and Booker 1989).

This particular section will discuss the relevant SVD mathematical theory which is not only required for a description of this technique, but is also widely used in more traditional least squares regression (section 5.7.2). It is then shown that the MT impedance can be estimated after a complex valued SVD has been performed upon the observational data matrix from a single site. Further discussion of this method is given in Appendix A.

5.4.2. Properties of the Singular Value Decomposition

For a rectangular N by M real valued matrix $\mathbf{X}$, this factorization into the product of three matrices can always be performed:

$$\underset{NxM}{X} = \underset{NxN}{U} \cdot \underset{NxM}{\Lambda} \cdot \underset{MxM}{V^T} \qquad (5.4.1)$$

(Description by Golub 1969, Wiggins 1972, Lawson and Hanson 1974, Golub and Saunders 1970, Lanczos 1961, Lines and Treitel 1984, Menke 1984 : Algorithms by: Dongarra *et al.* 1979, Businger and Golub 1969, Press *et al.* 1986)

U and V are orthogonal eigenvector matrices (i.e. $X \cdot X^T = U \cdot \Lambda^2 \cdot U^T$ and $X^T \cdot X = V \cdot \Lambda^2 \cdot V^T$). Λ is a diagonal matrix of elements called singular values; the positive square roots of the eigenvalues which are usually ordered in decreasing size: $\lambda_1 >= \lambda_2 >= ..... \lambda_M >= 0$.

In a genuinely overdetermined least squares problem, the number of resolvable parameters (the rank), p = M, is the same as the number of parameters present. However, in a mixed determined problem (section 4.5.2), M-p linear relationships will exist between the columns of X and cause this matrix to be rank deficient (p < M). Since U and V are each orthogonal and therefore of full rank, Λ must reflect the deficiency in X. Consequently, the last M-p singular values of Λ are all zero:

$$\lambda_{p+1} = \lambda_{p+2} = ... = \lambda_M = 0 \qquad (5.4.2)$$

Equation 5.4.1 can thus be partitioned as:

$$X = [\, U_p \mid U_0 \,] \cdot \begin{vmatrix} \Lambda_p & 0 \\ 0 & 0 \end{vmatrix} \cdot \begin{vmatrix} V_p \\ \hline V_0 \end{vmatrix} \qquad (5.4.3)$$

where Λ_p is the matrix of the first p non-zero singular values and U_p and V_p are the first p columns of U and V, the other parts are cancelled by the zeros in Λ. Whilst V_p provides information about linear combinations of the parameters which are uniquely resolved by the data, V_0 gives M-p combinations of parameters which are not. The U_p and U_0 eigenvectors can be used to find corresponding information concerning the resolution of the observations (section 4.6.3).

The eigenvectors are orthogonal and normalized so that:

$$V_p^T \cdot V_p = U_p^T \cdot U_p = V_0^T \cdot V_0 = U_0^T \cdot U_0 = I, \qquad (5.4.4)$$

but e.g. $V_p^T \cdot V_0 = 0$.

Post multiplication of eqn. 5.4.3 by **V** gives two independent sets of equations:

$$X \cdot V_p = U_p \cdot \Lambda_p \qquad (5.4.5a)$$

$$X \cdot V_0 = 0 \qquad (5.4.5b)$$

The former equation (5.4.5a) suggests that **X** and a so-called 'pseudo inverse' X^+ (section 5.7.2), can be constructed from only the p eigenvectors which correspond with the non-zero eigenvalues. In fact, more generally, the Eckart-Young theorem (Press *et al.* 1986, Golub 1969, Jupp 1978) is sometimes used to construct a lower rank approximation to **X** from only the first q (<=p) significant singular values. If many of the singular values are small and can be neglected, then an approximation to **X** and its inverse can be rapidly computed.

Corresponding to the null eigenvalues, the latter equation (5.4.5b) can be used to find the coefficients of the linear combinations of the parameters (the "nullity") which are not illuminated by the data set (Belsley *et al.* 1980).

5.4.3. SVD Impedance Estimation

A complex valued variant of the SVD technique [$X = U \cdot \Lambda \cdot V^H$] can be used to compute the coefficients of the two linear relations which should exist between the columns of the data matrix **X** = [Hx(f) , Hy(f) , Ex(f) , Ey(f)].

Using the Lanczos (1961) definition (the rank is the maximum number of elements in a linear combination of the observables), eqn. 4.7.1 suggests that the theoretical rank of **X** should be 2 (i.e. $\lambda_3 = \lambda_4 = 0$). Therefore:

$$X = U.\Lambda.V^H = U. \begin{vmatrix} \lambda_1 & & 0 \\ & \lambda_2 & \\ & 0 & \\ 0 & & 0 \end{vmatrix} . \begin{vmatrix} v_{11}^* & v_{21}^* & v_{31}^* & v_{41}^* \\ v_{12}^* & v_{22}^* & v_{32}^* & v_{42}^* \\ v_{13}^* & v_{23}^* & v_{33}^* & v_{43}^* \\ v_{14}^* & v_{24}^* & v_{34}^* & v_{44}^* \end{vmatrix} \qquad (5.4.6)$$

Where e.g. v_{11}^* is the complex conjugate of v_{11}. Equation 5.4.5b then permits the direct evaluation of the impedance coefficients from the V_0 sub-matrix.

$$| Hx\ Hy\ Ex\ Ey | \cdot \begin{vmatrix} v_{13} & v_{23} & v_{33} & v_{43} \\ v_{14} & v_{24} & v_{34} & v_{44} \end{vmatrix}^{T} = 0 \qquad (5.4.7)$$

Simultaneous solution of the 2 equations in equation 5.4.7 allows the elimination of the Ey term and after some rearrangement into the form of equation 4.7.1a, the two impedance coefficients are given by:

$$Zxx = \frac{v_{14}.v_{43} - v_{13}.v_{44}}{v_{33}.v_{44} - v_{34}.v_{43}} \qquad Zxy = \frac{v_{24}.v_{43} - v_{23}.v_{44}}{v_{33}.v_{44} - v_{34}.v_{43}} \qquad (5.4.8a)$$

Similarly, by elimination of Ex:

$$Zyx = \frac{v_{13}.v_{34} - v_{14}.v_{33}}{v_{33}.v_{44} - v_{34}.v_{43}} \qquad Zyy = \frac{v_{23}.v_{34} - v_{24}.v_{33}}{v_{33}.v_{44} - v_{34}.v_{43}} \qquad (5.4.8b)$$

Since the U matrix is not required in these equations, the author has found that it was more efficient computationally to form and factorize the 4 by 4 matrix product $X^H.X$ (section 5.4.2) to obtain the necessary V matrix.

In practice the "null" singular values are never completely zero because of the presence of observational noise, a breakdown in the plane or unpolarized electromagnetic wave assumptions or inexact computer arithmetic. In the extreme situation, the difference between the "zero" and "non-zero" singular values will be so small that the apparent rank of X cannot be regarded as being 2 (fig. 5.11b). The elements of V_O will thus become poorly distinguished (Park and Chave 1984) from V_p and the impedance estimated will be strongly in error. The condition number was found in some cases, to be a useful diagnostic check for identifying some noise problems and could be simply calculated from the ratio of the largest to the smallest singular values λ_M/λ_1.

If the vertical magnetic field observations are also included in X, the rank of this matrix is then also reliant upon the complexity of the geoelectric environment and the presence, or otherwise, of an additional linear relationship between the magnetic field observations (Jupp 1978, Chave *et al.* 1981).

Both these authors have proposed diagnostic tests for assessing the apparent rank of X based upon an examination of the singular values or other derived statistics (e.g. the estimated signal to noise ratio). After obtaining the

optimal value for p, they then suggest using equation 5.4.5a to form a "signal" matrix with all the small singular values set to zero (i.e. $\lambda_{p+1}=...\lambda_M=0$). From this matrix the unbiased impedance estimates can then be evaluated.

In the application of the SVD technique described in Appendix A, the author preferred to set the rank at 2, irrespective of the noise level of the observations. Following a direct evaluation of the impedance from equation 5.4.8, robust regressive methods then permit the enhancement of the noisiest observations to conform with this assumed and desirable model. Iterative robust re-weighting and the imposition of a geophysically realistic constraining model was found to result in an improved separation between the null and non-null singular values (c.f. section 5.7.1).

Further details concerning this method are given in Appendix - A, whilst Appendix - B (ROBEST) summarizes its implementation.

SVD analysis can be readily adapted to the estimation of any other combination of the MT parameters. For example, this author has acquired scalar impedances [X = [Hx,Ey], X = [Hy,Ex]], tippers [X = [Hx,Hy,Hz]] and full tensorial impedances with tippers [X = [Hx,Hy,Hz,Ex,Ey]] using the same type of technique. In fact the method described could be adapted to help solve other "errors-in-all-variables" problems.

5.5. WEIGHTED LEAST SQUARES

Observational errors will seldom be drawn from a distribution with a constant variance (c.f. section 4.5.1). If the errors can be quantified as ($Var(\mathbf{r}) = \sigma^2.\mathbf{V}$: where, in this section $\mathbf{V}$ represents a diagonal N by N matrix with non-negative elements), the observations can be transformed to meet this assumption.

There exists a weighting matrix $\mathbf{W}$ (where $\mathbf{V}^{-1} = \mathbf{W}.\mathbf{W}^T = \mathbf{W}^T.\mathbf{W}$), which transforms the observational errors ($\mathbf{r}'$) to have a constant variance:

$$\begin{aligned} Var(\mathbf{r}') &= Var(\mathbf{W}.\mathbf{r}) = \mathbf{W}.Var(\mathbf{r}).\mathbf{W}^T = \sigma^2.\mathbf{W}.\mathbf{V}.\mathbf{W}^T \\ &= \sigma^2.\mathbf{I} \end{aligned} \qquad (5.5.1)$$

Here the weights are inversely proportional to the assumed standard error (eqn. 4.3.5) on each corresponding observation. Similarly by transforming the

whole regression equation (eqn. 4.2.1; $\mathbf{W} \cdot \mathbf{y} = \mathbf{W} \cdot \mathbf{X} \cdot \mathbf{b} + \mathbf{W} \cdot \mathbf{r}$), the weighted least squares parameter estimates can then be obtained:

$$\mathbf{b} = (\mathbf{X}^T.\mathbf{V}^{-1}.\mathbf{X})^{-1} \cdot (\mathbf{X}^T.\mathbf{V}^{-1}.\mathbf{y}) \qquad (5.5.2)$$

In some applications the entire covariance matrix may be known so that the above procedure can be repeated to remove any correlation existing between the errors.

In the third MT application (described in section 5.2.3) each impedance 'observation' was weighted by its estimated error prior to fitting polynomials to the response function. A similar 'row scaling' procedure was also used to reduce the effect of influential observations prior to SVD estimation of the impedance (Appendix-A).

5.6. ROBUST ESTIMATION

5.6.1. Introduction

Robust methods broadly encompass any technique which is insensitive to slight departures from any of the model assumptions (Huber 1981, Rousseeuw and Leroy 1987; section 4.5.1). Whilst relatively little is known about the effects of a breakdown of the first two regression assumptions, considerable attention has been focused upon the problem of estimating model parameters in the presence of non-Gaussian errors. The following section will therefore discuss the presence of these outliers and review the remedial action which is available.

The author believes that the subject of robust parameter estimation is shrouded in excessive statistical theory and terminology. This should not deter any experimenter from using these techniques as the actual implementation involved is often very straightforward. The following review is quite detailed but in view of the growing importance of the subject it is considered worthy of such attention.

This section draws from Claerbout (1976), Mosteller and Tukey (1977), Thomson (1977a,b), Kleiner *et al.* (1979), Kleiner and Graedel (1980), Huber (1981), Draper and Smith (1981), Hoaglin *et al.* (1983), Rousseeuw (1984), Menke

(1984), Hampel *et al.* (1986), Chave *et al.* (1987), Rousseeuw and Leroy (1987) and Silva and Cutrim (1989).

5.6.2. Observational Outliers

The most common and influential 'slight departure' from the Gaussian model assumption involves the presence of a small fraction of grossly outlying errors in a data set. Observations with an absolute deviation greater than about 3 standard deviations from the mean may be regarded as such outliers. Their occurrence is highly improbable in terms of a single Gaussian distribution. In fact Press *et al.* (1986) have noted, an error drawn from a Gaussian distribution has a probability of being deviant at 20 standard errors once in every 10^{88} observations. In practice outliers of this size are far more common.

Outliers can occur as the result of transient observational phenomena, blunders due to manual data punching or computations on the data. If observational errors are drawn from only a *finite number* of different distributions (c.f. central limit theorem; section 4.4), the resultant joint distribution will approximate to a Gaussian at its centre, but the presence of outliers will produce a 'thickening of the tails'. This phenomenon is widely observed in many different types of data sets.

The automatic rejection of such outliers as errors must be carefully considered. When parameter regression is used in an exploratory fashion (absence of a well pre-defined model), outliers may provide useful information about an unusual set of circumstances and warrant a separate analysis (Draper and Smith 1981). Since in the applications discussed here, robust methods were only usually employed once an accurate model had been obtained, the outliers were assumed to be erroneous and their influence was thus either 'constrained' or they were rejected outright.

5.6.3. The Need For Robust Methods

The low theoretical probability of outliers means that a non-robust parameter estimation method must distort the results seriously to include them. The influence of outliers on various estimators is discussed later but can be demonstrated by considering a very simple, artificial univariate example

(fig. 5.2a).

The mean and standard deviation are poor estimators of the location and scale of these 'observations' because, unlike their robust counterparts, a single gross outlier has a strongly detrimental effect on their values. Although the outlier is obvious in this example, their presence is often more insiduous.

Several other authors have given examples demonstrating the superiority of robust multivariate regression over least squares in reducing the influence of outliers in the response observables, y_i (e.g. Kleiner and Graedel 1980, Press *et al.* 1986, Rousseeuw and Leroy 1987). The particular example in fig 5.2b demonstrates the ability of robust methods to find parameters which will fit the majority of the observations, whilst largely ignoring the outliers. Chave *et al.* (1987) have further pointed out that the estimation of the MT response functions and coherence are particularly sensitive to outliers as multiple EM field time series regression and ratios of spectra are involved.

5.6.4. Robust Methods

There are two broad classes of methods for the identification and removal of outliers:

Diagnostic methods aim to identify and remove influential observations prior to standard least squares regression. Such diagnostic tools include Q-Q plotting to identify non-Gaussian outliers, or other ad hoc methods which involve some preliminary data screening for obvious discordant values (e.g. visual rejection of an MT time series window). These manual processes are time consuming and prone to unavoidable human bias. Furthermore they may leave the masked or less obvious maverick points unaffected.

Robust regression, in this context, tries to accommodate departures from the Gaussian model directly during the calculation of parameter values. Such methods are more flexible and more appropriate for the automatic processing of the large quantity of observations frequently manipulated during MT data analysis.

Most robust techniques fall into one of three classes: 1) R (Rank tests), 2) L (Linear combinations of order statistics) and 3) M (Maximum likelihood)

Figure 5.2: Simple, artificial examples highlighting the difficulties encountered in univariate (fig. 5.2a) and multivariate (fig. 5.2b) regression, in the presence of observational outliers.

If 8 (e.g. temperature) measurements are performed (fig. 5.2a), and one is written down incorrectly, then the arithmetic mean (the L2 norm) and standard deviation are badly biased towards this outlier. The more robust median (the L1 norm) and interquartile range (eqn. 5.6.1) are not at all affected by this observation and so are more accurate representations of the majority of observations.

In a similar fashion, fig. 5.2b (from Menke 1984) shows that least squares (L2) estimation of the coefficients of the best fitting straight line unduly weights the single outlier. L1 regression gives a solution which is more in keeping with the random scatter of the rest of the observations.

A

EXAMPLE OF OUTLIER CONTAMINATION

Simulated temperatures:

20.3^{O}, 16.0^{O}, 17.4^{O}, 173.2^{O}, 12.8^{O}, 19.7^{O}, 18.5^{O}, 20.7^{O}.

Mean: $37.3^{O}C$. Standard Error: $51.4^{O}C$.

Median: $19.1^{O}C$. Interquartile Range: $4.3^{O}C$.

B

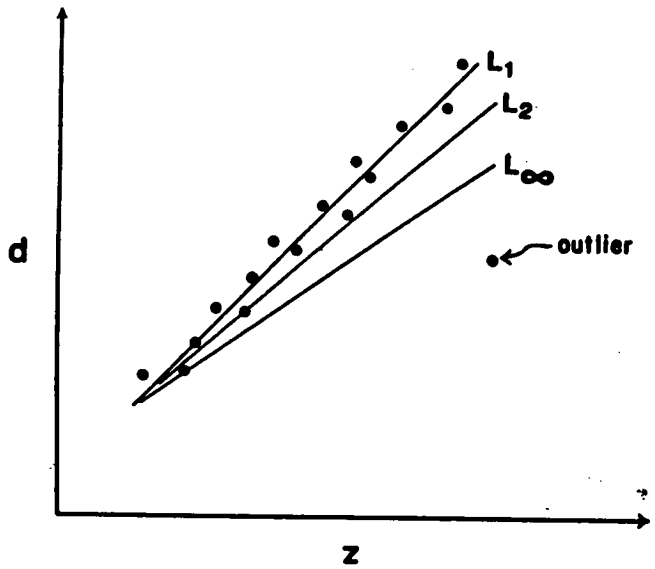

estimators (e.g. Andrews 1974, Hogg 1979, etc.).

The ranking of a univariate set of observations x_i, is simply the set of integer values (i=1,2,.....N) which corresponds to the ordered observation values (Press *et al.* 1986). R-estimators are derived from tests on these values. Unfortunately, the resulting location estimates do not tend to be as good as the M-regression estimates for small to moderate sample sizes and therefore will not be discussed further.

L-estimators are very important univariate estimators of both location and scale. Implementation of the α-trimmed mean location estimator can be achieved very easily by 1) ordering the observations by size, 2) removing the fraction of the total number of observations (α) which resides at the extremes of the ordered sample and then 3) finding the mean of the remaining subset. After ordering, the outlying observations will be relegated to the extreme portion of the sample where they will have no influence on the resultant parameter estimates. The two end members of this class are the non-robust mean (α = 0) and the robust median (α = 0.5), but for a broad class of probability distributions α=0.25 is thought to give a good location estimate.

Robust L-estimators of scale include α-trimmed variances and the interquartile distance (also known as the fourth spread). This is the range between the upper quarter and lower quarter of the ordered observations.

$$S_{IQ} = X_{(3N/4)} - X_{(N/4)} \qquad (5.6.1)$$

The primary drawback of L univariate estimators is the preset level of trimming so that it cannot respond to the level of outlier contamination present. This inability to be 'data adaptive' may result in insufficient or excessive outlier rejection. In the present study, both the median and the interquartile range were used during EM time series spike detection and in the evaluation of the robust M estimates.

M estimators are usually more straightforward and flexible to implement than either L or R estimators, particularly in multivariate situations and they increasingly constitute the most widely used class of robust parameter estimators.

5.6.5. Theory of M Robust Regression

M-estimators are generalizations of maximum likelihood methods and as suggested in section 4.4, they are formed by the minimization of a general objective function ρ, with respect to the model parameters b_j:

$$\min_{b_j} \sum_{i=1}^{N} \rho(y_i , y_i^{PRED.}) = \min_{b_j} \sum_{i=1}^{N} \rho(r_i) \qquad (5.6.2)$$

In this application ρ is only a function of the difference between each observation (y) and its predicted value ($y^{PRED.} = F(b) = X . b$). M estimates of location are not scale equivariant (e.g Rousseeuw and Leroy 1987), which implies that a multiplication of the observations by a constant factor will not result in a similar change in the parameter estimates. The residuals are therefore standardized by an estimate of their scale S, whilst a fixed constant (c) tunes the M-estimator to have a maximum efficiency at a particular error distribution:

$$r_i = [y_i - y_i^{PRED.}]/[c . S] \qquad (5.6.3)$$

The properties of individual members of the M-estimator class are usually described in terms of an influence function $\psi(r_i) = \partial \rho(r_i)/\partial b_j$: Differentiating eqn. 5.6.2, with respect to the parameters b gives:

$$\sum_{i=1}^{N} \psi(r_i) . x_i = 0 \qquad (5.6.4)$$

where $x_i = (x_{i1}, x_{i2}, \ldots\ldots x_{iM})^T$. Equation 5.6.4 is a generalization of the least squares normal equations (eqn. 4.2.6). Unlike standard least squares, the solution of these equations is usually non-linear and needs to be performed simultaneously for both the parameters and the scale estimate. The solution is not trivial unless a fixed auxiliary scale estimate is set, so that eqn. 5.6.4 can be re-written as:

$$\sum_{i=1}^{N} \frac{\psi(r_i)}{r_i} . r_i . x_i = \sum_{i=1}^{N} w(r_i).r_i.x_i = 0 \qquad (5.6.5)$$

The solution of this 'W-estimator' problem is identical to the weighted least squares one discussed earlier (section 5.5) where the weighting function has

been defined to be $w(r_i) = \psi(r_i)/r_i$.

Good initial parameter estimates are required to initiate robust re-weighting. In the course of this study, the far from satisfactory results of ordinary non-robust least squares were used to fulfill this role. A residual error was then calculated for each set of observations and a robust auxiliary scale estimate, S determined from the interquartile range (eqn. 5.6.1). In the EM application, the estimator was tuned to have maximum efficiency in the presence of a Rayleigh distribution (i.e. the square root of the sum of squares of the real and imaginary (Gaussian) parts of the EM field residuals). The constant (c) was taken to be 0.90658 (Chave *et al.* 1987). The scaled residuals were then used to evaluate weights which were subsequently applied to their corresponding observations (Andrews 1974). Finally the parameters were re-evaluated with those observations having demonstrated large residual errors were given weights less than 1.

Typically, iterative re-weighting had to be performed several times to linearize the problem (c.f. section 5.8). This was a data adaptive procedure which allowed outliers, masked by the presence of others, to be identified on subsequent iterations. It was anticipated that upon convergence, the fully iterated 'W-estimator' would give results which were identical to the M-estimator. Andrews (1974) has noted that a fully iterated solution may not necessarily be better than parameter estimates acquired from only a fixed number of iterations. The author's own experience also suggests that a reasonable solution was usually gained within 4 iterations. If excessive number of iterations needed to be applied then often the starting parameter values were badly in error. An example of the type of problems that can be encountered is given in section 5.9.4.

5.6.6. Some Examples of M-estimators

In view of the discussion in section 4.4, it is not surprising that the most familiar member of this class is formed by the minimization of the sum of squares (or the L2 norm) of the residuals, i.e. the non-robust least squares method:

$$\rho(r_i) = r^2_i/2 \qquad \psi(r_i) = r_i \tag{5.6.6}$$

The ψ function for the univariate least squares estimator (the mean) is shown in fig. 5.3a. Since ψ increases in an unbounded manner, the more deviant the observation, the greater is the emphasis placed upon it. An alternative, but equivalent viewpoint is that least squares weights all the observations to the same extent (in equation 5.5.2, **W** =**I**) thereby over stressing the deviant ones.

The least squares' assumed Gaussian error distribution (section 4.5.1) is often too short tailed to represent a real distribution. An asymptotically longer tailed and, some authors believe, more realistic distribution is the Laplacian (also known as a double exponential). The corresponding objective and influence functions are:

$$\rho(r_i) = |r_i| \qquad \psi(r_i) = \text{sgn}(r_i)$$

$$\text{where } \text{sgn}(r_i) = \begin{cases} 1 & r_i > 0 \\ 0 \text{ if} & r_i = 0 \\ -1 & r_i < 0 \end{cases} \tag{5.6.7}$$

Minimization of eqn. 5.6.7 gives the least absolute residual (or L1) estimator. In the univariate case this is just the median whose resistance to outliers corresponds to its bounded influence function (fig. 5.3b). A low order norm of this type is useful when the data are widely scattered and no significance can be placed on outliers.

An estimator's resistance to outliers can be quantified by the breakdown bound ε^*. This is the smallest fraction of contaminated data that will cause the estimator to take on arbitrarily large values. The median attains the maximum value of $\varepsilon^* = 0.5$, beyond which good and bad observations become indistinguishable. In contrast the mean can be corrupted by a single outlier ($\varepsilon^* = 0$). The median is however, vulnerable to rounding errors as it is determined by, at most, only 2 observations.

Some authors have cautioned against a corresponding conversion from multivariate minimization of the L2 norm to the L1 norm (e.g. Chave *et al.* 1987, Rousseeuw and Leroy 1987). Their arguments are primarily based on the high efficiency properties of least squares in the Gaussian error framework (section 4.4) and inference problems based on the Laplacian distribution.

Figure 5.3: The variation in the influence function (ψ as a function of the residual error (r) for a) the least squares estimator (e.g. the mean), b) the least absolute residual estimator (e.g. the median) and c) the Huber M-regression estimator (based on Rousseeuw and Leroy 1987).

The least squares estimator function is unbounded and weights ($w = \psi/r$) all the observations equally and therefore over-emphasises the more deviant ones. The least absolute residual estimator is bounded and down-weights outliers but the median value is only computed from one or two observations, at most. The Huber weighting function is a compromise, behaving like a Gaussian least squares estimator for small residuals ($|r| <= k$), but limiting the influence of the observations with higher absolute residual errors.

A

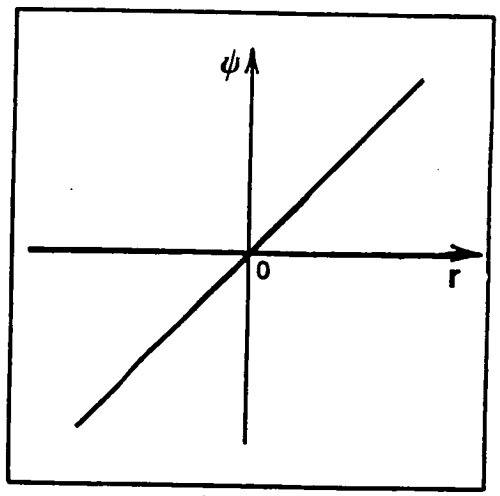

B

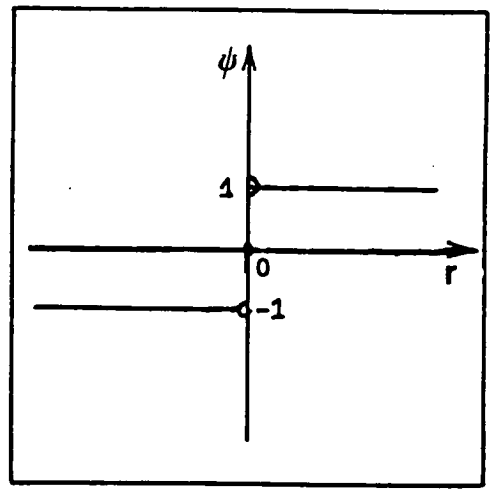

C

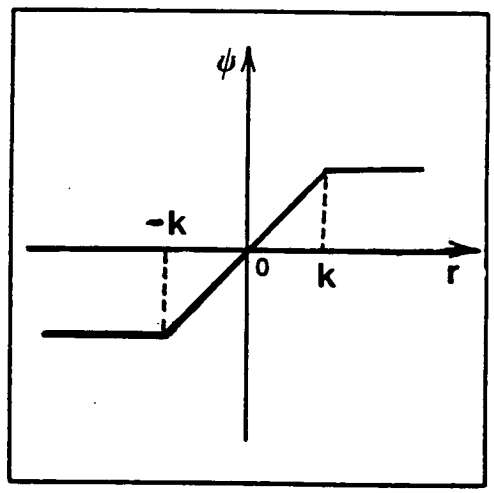

Furthermore, the presence of leverage points (section 4.5.2) in a general multivariate regression problem means that the breakdown point of the L1 estimator is as poor as its L2 counterpart (i.e. $\varepsilon^* = 0$).

The aim of much recent research has gone into designing the M estimator to have some specific and desirable range of features for a wide range of different distributions (usually Gaussian based). Constable (1988) has even suggested determining the error distribution present in a data set in order that the most appropriate estimator can be applied. One of the earliest and probably most widely used estimators was developed by Huber (1964) and is given by:

$$\begin{aligned} \rho(r_i) &= r^2_i/2 & \psi(r_i) &= r_i & \text{for } |r_i| <= k \\ &= k.|r_i| - k^2/2 & &= k.\mathrm{sgn}(r_i) & \text{for } |r_i| > k \end{aligned} \qquad (5.6.8)$$

Like many M-estimators, it includes a user specified tuning constant k, which is usually chosen to be 1.5. This is a compromise (fig. 5.3c). In the small residual limit, it has the same properties as the least squares method so that it can accommodate a Gaussian error distribution at its centre, but the inclusion of Laplacian tails reduces the influence of outliers with large residual errors. The main disadvantage of using the Huber function is the influence of outliers may not decrease rapidly enough. To remove severe outliers completely, M-estimators with redescending influence functions ($\psi(r_i) \rightarrow 0$, as $|r_i| \rightarrow$ large) have been developed. For example the Thomson weight (Thomson 1977a, Chave *et al.* 1987):

$$w(r) = \exp\left(-e^{\beta(|r_i|-\beta)}\right) \qquad (5.6.9)$$

where $\beta = 2\log(2N)$.

Since this "non-redescending" M-estimator does not necessarily converge to a global minimum misfit solution, it should only be applied for a limited number of iterations (usually 2) and only then after convergence has been attained using a less severe influence function.

These multivariate methods are only resistant to outliers in the observations. Leverage points will produce different results and correlation between outliers in both variables will yield well fitting, yet erroneous

parameter estimates (c.f. coherent noise; section 4.7.2).

A number of methods exist for removing leverage points which include GM (Generalized M) and Least Median of Squares (L.M.S.) estimators. These may provide useful techniques for future consideration, but the authors own preliminary attempts to use the latter method (**PROGRESS**; Rousseeuw 1984, Rousseeuw and Leroy 1987) on MT impedance estimation problems was hindered by the high computational cost.

5.7. PRACTICAL EVALUATION OF UNDERDETERMINED PARAMETERS

5.7.1. Introduction

It has become increasingly less common for researchers to evaluate the Gauss-Newton equation directly (eqn. 4.2.7) in order to estimate parameter values because 1) the formation of the matrix products ($\mathbf{X}^T \cdot \mathbf{X}$) and ($\mathbf{X}^T \cdot \mathbf{y}$) will rapidly accumulate round-off errors in the presence of large numbers of observations (N) and/or parameters (M) and 2) underdetermined parameters will result in ill conditioned matrices which may be difficult or impossible to invert (section 4.5.2).

The Singular Value Decomposition (SVD; section 5.4.2) circumvents the numerical problem of matrix multiplications and also underdetermined problems can be solved by either discarding, damping or constraining the influence of the unresolved parts of the model. Matrix manipulation is often performed by constructing either the 'Lanczos inverse' from only the largest and most significant singular values or by 'ridge regression' which damps the influence of the troublesome smaller ones. Depending upon the form of the 'a priori' information available, constrained regression will either reduce the number of free variables present (c.f. Lanczos inverse) or reduce the influence of the ill-determined parts of the model (c.f. ridge regression).

5.7.2. Lanzcos Inverse

Numerous authors have expounded the benefits of forming the "Lanczos" ("pseudo" or "generalized") inverse $\mathbf{X}^+$. This can be readily computed after an SVD of **X** and then the parameters can be computed from:

$$\mathbf{b} = \mathbf{X}^{+}.\mathbf{y} \qquad (5.7.1)$$

This will always give a numerically robust solution irrespective of the conditioning of **X** and the SVD can be more accurately computed for **X** than the formation of the matrix product $\mathbf{X}^{T}.\mathbf{X}$. However, this method may be computationally slower and require extra computer memory storage capability than by solving the normal equations. The results can also be strongly dependent on the magnitude of the elements in **X** and **y** (Wiggins 1972) so some form of normalization (section 5.5) should be performed prior to calculation of the SVD.

Inserting eqn. 5.4.5a into eqn. 5.7.1 gives (Jackson 1972, Lines and Treitel 1984, Belsley *et al.* 1980):

$$\mathbf{b} = [\, \mathbf{U}_p \,.\, \mathbf{\Lambda} \,.\, \mathbf{V}_p^{T} \,]^{-1} \,.\, \mathbf{y} \quad = [\, \mathbf{V}_p \,.\, \mathbf{\Lambda}^{-1} \,.\, \mathbf{U}_p^{T} \,] \,.\, \mathbf{y} \qquad (5.7.2)$$

$\mathbf{X}^{+}$ does not share the same properties as the more usual inverse of a square matrix. Although equation 5.7.2 provides the least squares solution (eqn. 4.2.7) in a purely over determined situation, the exclusion of the zero singular values means that, even in the presence of collinearity, a solution will always be found. In fact, the particular solution obtained will have a minimum length ($|\mathbf{b}|^2$ = min.); a very useful property when using this procedure to find the "simplest" parametric MT model (section 6.2.4).

Complicated inter-relationships between the parameters can be simplified by performing a model re-parameterization. If eqn. 5.7.2 is pre-multiplied by $\mathbf{V}_p^{T}$ then:

$$\mathbf{V}_p^{T} \,.\, \mathbf{b} = \mathbf{\Lambda}_p^{-1} \,.\, \mathbf{U}_p^{T} \,.\, \mathbf{y} \qquad (5.7.3)$$

$$\mathbf{b}' = \mathbf{\Lambda}_p^{-1} \,.\, \mathbf{y}'$$

b' are generalized parameters (eigenparameters) each of which are uniquely coupled to a generalized observation (eigendatum) and weighted by the corresponding singular value (Pedersen 1977, Jones 1982, Ilkisik and Jones 1984, Gomez-Trevino and Edwards 1983). The smallest singular values corresponding to collinear observables have questionable accuracy and so their reciprocal has a dominant effect upon the eigenparameters and the corresponding linear combination of **b**.

Jones and Foster (1984) have suggested using eqn. 5.7.3 to analyse the resolution of the eigenparameters during MT field data acquisition. They propose that the worst resolved eigenparameters and consequently the real Earth model parameters could be enhanced by concentrating subsequent data collection on the corresponding eigendata. This is an interesting procedure, although the author knows of no other researchers who have tried to use it.

Small eigenvalues can also create havoc on the estimated variance (eqn. 4.3.4):

$$\mathrm{Cov}(\mathbf{b}) = \sigma^2 \cdot \mathbf{V}_p \cdot \mathbf{\Lambda}^{-2}{}_p \cdot \mathbf{V}^T{}_p \qquad (5.7.4)$$

A very large proportion of the parameters' variance will result from the smaller singular values (c.f. variance inflation; section 4.6.2).

The identification of the small singular values is not necessarily trivial. A plot of the size of each singular value λ_j against its index j (Menke 1984) may show an obvious cliff separating the so-called important from the unimportant values, but in general the transition will be smooth (fig. 5.11b) so that a variety of techniques for estimating the effective rank, q, of **X** has been proposed. The particular method adopted by this author for the third application (section 5.2.3) followed Jackson (1972). He suggested the use of the maximum number of singular values in the construction of the inverse, for which the resulting parameter variance (eqn. 5.7.4) was below some reasonable threshold.

5.7.3. Ridge Regression

The ridge regression (damped least squares or Marquardt-Levenberg) method does not discard the poorly resolved parameters but rather damps them to control the numerical instability and variance inflation. It is therefore more applicable in situations where the range of possible models must not be restricted. This technique has been detailed by numerous authors including Hoerl and Kennard (1970a,b), Marquardt (1963,1970), Lines and Treitel (1984), and discussed in the geophysical context by Inman (1975), Oristaglio and Worthington (1980), Hoverstein *et al.* (1982), Jupp and Vozoff (1975), Meju (1988), Hill (1987), Hatton *et al.* (1986), Constable *et al.* (1987), amongst others.

From the discussion in the previous section it is apparent that small, ill-determined singular values have an inordinately large effect on the

estimated parameters and their errors. To damp their influence a bias is introduced into the solution. In ridge regression the standard least squares normal equations (eqn. 4.2.7) are modified by adding a small positive constant (β) to the diagonal of ($\mathbf{X}^T.\mathbf{X}$):

$$(\mathbf{X}^T.\mathbf{X} + \beta.\mathbf{I}) \,.\, \mathbf{b} = \mathbf{X}^T \,.\, \mathbf{y} \qquad (5.7.5)$$

Expanding the left hand side of eqn. 5.7.5 in terms of the SVD:

$$(\mathbf{X}^T.\mathbf{X} + \beta.\mathbf{I})^{-1} \,.\, \mathbf{b} = \mathbf{V}.(\Lambda^2 + \beta.\mathbf{I})^{-1}.\mathbf{V}^T \,.\, \mathbf{b} \qquad (5.7.6)$$

Where $(\Lambda^2 + \beta.\mathbf{I})^{-1} = (\lambda_j^2 + \beta)^{-1}$ j=1,2..,M; all of the eigenvalues have been incremented by β. This has little effect on the important singular values ($\lambda_j >> \beta^{1/2}$), but the smaller ones are increased so removing the possibility of a singular ($\lambda_j = 0$), or ill conditioned ($\lambda_j <= \beta^{1/2}$) matrix.

The ridge solution is therefore given by:

$$\mathbf{b} = (\mathbf{X}^T.\mathbf{X} + \beta.\mathbf{I})^{-1} \,.\, \mathbf{X}^T.\mathbf{y} \qquad (5.7.7)$$

A value of $\beta = 0$ will give the least squares solution and its associated problems. On the other hand, a large β value leads to a very biased solution. If the bias is carefully chosen at a trade off point between these two extremes, the resulting ridge parameter estimates is more accurate than their least squares counterparts. Often the most appropriate method for calculating the damping factor involves the automatic evaluation of the parameters' values over a range of β values followed by the selection of the largest which will still produce a stable solution.

5.7.4. Constrained Regression

Since many geophysical regression problems lead to a non-unique solution, it is desirable to improve data conditioning by collecting more, or more independent, observations. Frequently this is impossible experimentally, so constrained regression is sometimes used to add *independent* 'a priori' information (literally *in advance*). This imposes limits on the values which one or more of the parameters are allowed to take (Golub and Saunders 1970, Lawson and Hanson 1974, Twomey 1977, Crossley and Reid 1982, Menke 1984, Meju 1988). Once the regression equations are solved, the constraints will, hopefully, improve the accuracy of the results by decreasing the number of parameters which need to be determined and reduce the range of solutions

open to the others.

The general principle underlying this method can be visualised by considering a few examples.

In section 4.7 it was suggested that the presence of perfectly polarized EM signals will mean that only a linear combination of the MT impedance tensor elements can be resolved (i.e. $Zxx.Cos(\alpha) + Zxy.Sin(\alpha)$). Assuming that the value of one of the parameters is known (for example in a one dimensional geoelectric environment $Zxx = 0$), then by restricting its value during parameter estimation, the range for other parameters in the linear combination is simultaneously limited. In this trivial case, Zxy can be immediately and unambiguously evaluated subject to any random error. Imposing these fixed (or 'strong') constraints is exactly equivalent to reducing the complexity of the model.

In more general geophysical data modelling (chapter 6), surface geology, well logs or other geophysical surveys may provide quantifiable estimates of some of the model parameters. Usually of most interest is the depth to an interface which can be identified from more than one survey method. By fixing this value during regression, the remaining model parameters should become better resolved. Smoothness (i.e. consistency between adjacent parameters) is another constraint which is increasingly being used to prevent over-parameterization (section 6.2.4).

Alternatively, some of the model parameter values may be known within some error bound. The effect of such 'weak constraints' may be visualised by considering the schematic example shown in fig. 5.4. The underdetermined situation has no clearly defined maximum probability distribution (c.f. section 4.4). A weak constraint (e.g. a Gaussian distribution of the likely parameter values) imposed on the original observations helps the regression process to identify the most likely solution. This principle was used by this author (Appendix - A) to weakly constrain a re-evaluation of the MT impedance.

Although not used in this study, a third type of constraint involves assigning maximum and minimum thresholds for the parameter values. The author believes that these 'inequality constraints' hold some potential for both constrained impedance estimation and MT response function modelling

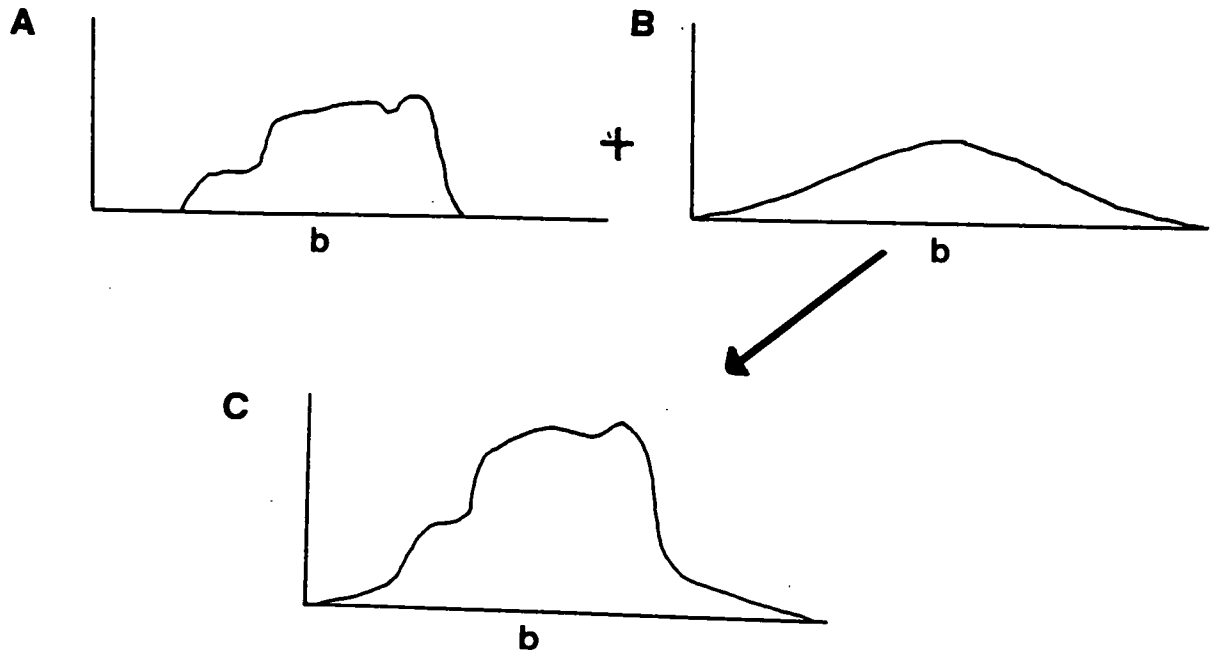

Figure 5.4: An illustration of the effect of weak constraints on a distribution of univariate observations (loosely based on Menke 1984).

Figure 5.4a depicts the occurrence of a range of parameter values (b). As there is no clearly defined maximum, least squares (Gaussian maximum likelihood; section 4.4) may fail to determine the correct solution. If the parameter value can be assumed from 'a priori' information to lie within some specified bounds, this can be represented by a Gaussian distribution of synthetic observations (fig. 5.4b). Constrained regression, as implied by eqn. 5.7.12, can be identified with finding the maximum likelihood of the resulting joint distribution (fig. 5.4c).

procedures by imposing geophysical bounds on their respective models.

5.7.5. Linear Equality Constraints

Least squares regression can be adapted to include information in the form of linear equality constraints on the parameter values. For example:

$$b_j = h_j \qquad (5.7.8a)$$

or

$$b_j - b_{j+1} = 0 \qquad (5.7.8b)$$

where eqn. 5.7.8a suggests that the jth parameter has a constant value (h_j) and eqn. 5.7.8b emphasises the presence of a linear relationship existing between 2 of the parameters.

These constraints can be specified in matrix notation by:

$$\mathbf{D} \,.\, \mathbf{b} = \mathbf{h} \qquad (5.7.9)$$

where $\mathbf{D} = [0,...,0,1,0,...0]$ and $\mathbf{h} = [h_j]$ for eqn. 5.7.8a and $\mathbf{D} = [0,...0,1,-1,0,...0]$ and $\mathbf{h} = [0]$ for eqn. 5.7.8b. In general there will be NC (>1) such constraints placed on a multivariate regression problem. D is then an NC by M matrix and h has NC column elements.

The regression equations can be solved by the method of Lagrange multipliers (i.e. minimize $\mathbf{r}^T.\mathbf{r}$ subject to the constraint that $\mathbf{D.b-h=0}$):

$$\Omega = (\mathbf{y}-\mathbf{X.b})^T.(\mathbf{y}-\mathbf{X.b}) + \beta.(\mathbf{D.b}-\mathbf{h})^T.(\mathbf{D.b}-\mathbf{h}) \qquad (5.7.10)$$

Following the same minimization procedure described in section 4.2, the parameters are given by:

$$\mathbf{b} = (\mathbf{X}^T.\mathbf{X} + \beta.\mathbf{D}^T.\mathbf{D})^{-1}.(\mathbf{X}^T.\mathbf{y} + \beta.\mathbf{h}) \qquad (5.7.11)$$

In the special case in which $\mathbf{D} = \mathbf{I}$ and $\mathbf{h} = [0,....,0]^T$, eqn. 5.7.11 is identical to the eqn. 5.7.7. Thus the aim of both the constrained and ridge regression methods is to increase the magnitude of the small eigenvalues of $\mathbf{X}^T.\mathbf{X}$.

An alternative, but equivalent treatment of constraints is to view the information contained in eqn. 5.7.11 like a set of observations and then augment them directly onto the real data matrices (e.g. Chyba 1983). Subsequently the joint problem is solved by standard least squares:

$$\left|\begin{array}{c} \mathbf{y} \\ \hline \beta.\mathbf{h} \end{array}\right| = \left|\begin{array}{c} \mathbf{X} \\ \hline \beta.\mathbf{D} \end{array}\right| . \mathbf{b} \qquad (5.7.12)$$

$$\mathbf{y}' = \mathbf{X}' . \mathbf{b}$$

β is again the Lagrange multiplier, but in eqn. 5.7.12 its role can be more readily visualised to be a relative scaling factor between the real and constraint observations. If β is set to be 0, eqn. 5.7.12 simply gives the unconstrained least squares solution, whilst if β is set to be a large number, the constraint equations will be satisfied exactly. A compromise β is usually carefully selected depending on the level of bias which is to be introduced.

5.8. NON-LINEAR LEAST SQUARES REGRESSION

It is often necessary in geophysical applications to estimate parameters which have a non-linear functional relationship ($F(\mathbf{b})$) with the observed quantities. The difficulty with this type of problem is the resulting non-linear normal equations cannot be readily solved (Draper and Smith 1981). Sometimes $F(\mathbf{b})$ can be transformed into a linear equation (Menke 1984) but as the error distribution is usually distorted some of the usual regression assumptions are then invalidated. The resulting parameter estimates will be biased.

Instead, a more general and common procedure involves successively approximating the non-linear problem around an initial set of parameter estimates $\mathbf{b}^0$. This model is then improved by computing corrections for these trial estimates (c.f. section 5.6.5) (Marquardt 1963,1970, Jackson 1972, Wiggins 1972, Meyer 1975, Chyba 1983, Lines and Treitel 1984, Van Heeswijk and Fox 1988). This is known as the linearized, Taylor series or Gauss-Newton method.

Given a non-linear relationship ($F(\mathbf{b})$), a first order Taylor series expansion can be performed around a starting model $\mathbf{b}^0$:

$$F(\mathbf{b}) = F(\mathbf{b}^0) + \sum_{j=1}^{M} \frac{\partial F(b_j^0)}{\partial b_j} . (b_j - b_j^0) \qquad (5.9.1)$$

Inserting equation 5.9.1 into the regression equation 4.2.2 and then

re-arranging gives:

$$\mathbf{y} - F(\mathbf{b}^0) = \sum_{j=1}^{M} \frac{\partial F(b_j^0))}{\partial b_j} \cdot (b_j - b_j^0) \qquad (5.9.2a)$$

Or

$$\Delta \mathbf{y} = \mathbf{J}^0 \cdot \Delta \mathbf{b} + \mathbf{r} \qquad (5.9.2b)$$

where $\Delta \mathbf{y}$ is the difference between the actual ($\mathbf{y}$) and predicted response observations ($F(\mathbf{b}^0)$), $\mathbf{J}$ is the Jacobian (design, sensitivity or system) matrix of partial derivatives and $\Delta \mathbf{b}$ is the vector of parameter corrections which are to be determined. If $F(\mathbf{b})$ is a linear function of the parameters then $\mathbf{J} = \mathbf{X}$ and eqn. 5.9.2b is identical to equation 4.2.1. In the more general non-linear situation the Jacobian is often computed numerically by perturbing each of the parameters in turn by a small amount $\partial \mathbf{b} = (0,..0,\partial b_j,0,...0)$ (e.g. ∂b_j = 3% of $|b_j|$). Forward modelling can be used to compute:

$$\mathbf{J}_{\partial \mathbf{b} \to 0} = \frac{F(\mathbf{b}+\partial \mathbf{b}) - F(\mathbf{b})}{\delta \mathbf{b}} \qquad (5.9.3)$$

As eqn 5.9.2b is linear it can be solved by the methods described in section 4.2.

The addition of these computed parameter corrections to the initial estimates ($\mathbf{b}^0$) gives parameter values which locally minimize the sum of squares residual error and are therefore hopefully closer to the true solution. Normally a number of iterations must be performed with both $\mathbf{b}$ and $\mathbf{J}$ being updated prior to linear least squares solution of equation 5.9.2b.

Ill conditioning of $\mathbf{J}$ is a major problem which results in the parameter values either oscillating wildly on each successive iteration or even diverging completely. Consequently, it is common to use ridge regression (section 5.7.3) to acquire a more stable solution. Limiting the magnitude of the parameter correction or imposing physical (e.g positivity) constraints on the parameter values may also help prevent overshooting the correct solution. For the particular problem of MT response function modelling, the parameter values (the depths and resistivities) are constrained to be physically realistic (i.e.

greater than zero) by finding the logarithm of the value rather than the parameter value itself.

However fully iterating until either the minimum misfit (Q; eqn. 4.2.3) or negligible parameter corrections are attained, is wasteful in computational time. Furthermore, as the non-linear problem does not possess the unique ellipsoidal shaped minimum misfit found in the linear situation, convergence to the correct solution cannot be guaranteed in either case. The contours of constant misfit can be distorted and may have a number of local minima and maxima and even a few global minima values over the range of possible parameter values (fig. 5.5).

Linearization of such a problem can thus only work effectively if the Q contours are typically elliptical in shape in the immediate vicinity of the solution. Rapid convergence to a global solution is therefore strongly dependent upon the accuracy of the $\mathbf{b}^0$. If $\mathbf{b}_0$ is specified far from the correct solution, linearized methods will, at best, converge only slowly or will not converge at all. At worst convergence may occur to one of these local minima and subsequently give an erroneous model.

Unfortunately no "golden" rule exists for the estimation of $\mathbf{b}_0$ and so they must therefore be obtained in any ad hoc fashion (e.g. by using a priori information or by guessing).

Once a solution has been obtained it is clear from fig. 5.5, that it is crucial to test its uniqueness. The only accurate method requires that the whole non-linear procedure be repeated from a very large variety of different starting values and the range of resulting solutions be considered. If the minima obtained is unique, the separate linearized solutions should all be identical and will be equivalent to the solution to the non-linear problem. This is the basis of the exploratory MT data modelling technique described in section 6.4.3.

As suggested at the beginning of this section, non-linear regression has a number of applications throughout most branches of geophysics. For example, in 1-D MT response modelling (see section 6.2.3 for further discussion), observations of the apparent resistivity and/or phase (y_i) over a range of frequencies (x_i) are inverted to an Earth model parameterized ($\mathbf{b}^0$) in terms of depth (or thickness) and resistivity (b_j). The functional relation $F(\mathbf{b})$ can then

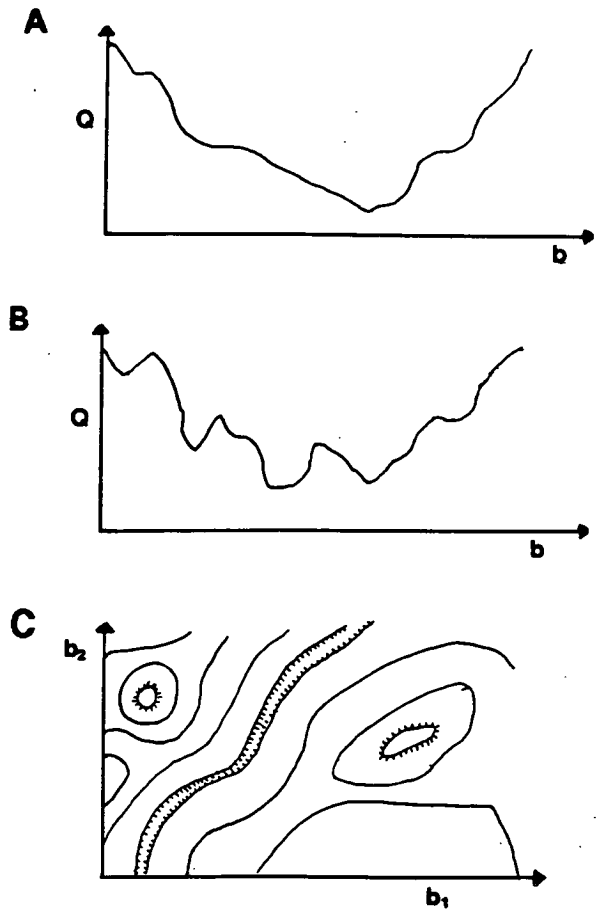

Figure 5.5: These 3 diagrams (based on Menke 1984) schematically depict the misfit (Q) as a function of parameter values (b). In the ideal linear least squares situation (fig. 5.5a), there is usually only one global minimum misfit value which corresponds with the desired solution. In non-linear least squares regression (fig. 5.5b), there can be local maxima and minima, and even a few global minima over the range of possible parameter values. In the multivariate situation (fig. 5.5c) contours of constant Q map out 'valleys' which correspond to the range of equally acceptable model parameter values. It is therefore important to test the uniqueness of the solution or attempt to reduce it by the application of constraining information.

be computed by "forward modelling" (section 2.3.2) over the frequency range of interest. Similar problems have been described in the context of 2-D MT (Weidelt 1986), 1-D D.C. resistivity (Hoverstein *et al.* 1982), joint MT and D.C. resistivity (Vozoff and Jupp 1975), EM (Oristaglio and Worthington 1980), gravity and magnetic (Pedersen 1977), gravity and seismic (Lines *et al.* 1988) response modelling, amongst many others. Using similar principles, this author has also performed linearized modelling on 1-D D.C. resistivity and 2-D gravity observations.

5.9. IMPEDANCE ESTIMATION METHODS: A CASE STUDY

The last 2 chapters have provided a general description of the least squares parameter estimation method in the MT data processing and modelling context. This section aims to demonstrate some aspects of this theory by showing the results of different least squares estimation procedures on the data set for the MT site MWD, in Northumberland. While there is necessarily some overlap with the examples from site HGN (given in Appendix-A), the following examples attempt to demonstrate and explain the results acquired from a range of different methods rather than the particular mechanics of the constrained method.

5.9.1. The Observations

MWD is located on the southern margin of the Northumberland Trough (fig. 3.5). At this site observations were collected as follows: a) a large quantity of single site data, b) a moderate amount of remotely referenced data (both electric and magnetic field reference from RDY) and c) a small quantity of locally referenced data (magnetic). For the purposes of this comparison data set (b) were processed by all of the methods, while fig. 5.7d shows the results from the processing of data set (c). The reader should note that in the interests of clarity, the apparent resistivity response function is plotted on an expanded scale compared with other similar diagrams (e.g. in Appendix - C).

In general the data were of below average quality at most frequencies. It is highly unlikely that the signal and noise power decomposition (eqns. 4.7.6 and 4.7.7) assumptions will be completely valid for these observations, but estimating the signal and noise power allows a number of interesting points to be demonstrated. Figure 5.6a shows the estimated magnetic signal (crosses)

and noise (circles) power from a high quality MT site (DBK), whose observations were collected about a week before those at MWD. Over much of the frequency range and in both directions there is a separation of between 1 and 2 orders of magnitude between the signal and noise (see also fig. 3.3 for the time series variations). At the 'dead frequency band' (around 0.5 Hz.), these curves approach each other, but there remains a sufficient separation between them to obtain reliable impedance estimates (see the response function presented in Appendix - C). Note also, that the SPAM's cut-off filters produce an apparently low spectral estimate at the edge of each recording frequency band.

In contrast, the estimated signal only exceeds the noise power at MWD, at the extremes of the frequency range (fig. 5.6b; > 20 Hz. and < 0.05 Hz.). The noise contamination is worst around 1 Hz. and in the Hy (approximately corresponding to Zxy) direction.

The remainder of this section shows that most impedance estimation programs fail to produce a satisfactory set of results for these observations.

5.9.2. "Conventional" Edinburgh University Programs

The suite of programs currently routinely utilized at Edinburgh University has been discussed by a number of authors. The most recent review (Whelan 1989) gives a full account of the methods employed. A large number of variants of the basic program exist, but only one is discussed here (known as **RRPROG**: Appendix - B) and was applied in 3 different ways (Versions A, B and A'). Note that the impedance error estimates have been suppressed in figs. 5.7a-d because, at the time of processing, a program fault gave unrealistically large values.

This program was first used (Version A) to calculate the impedance using a basic single site least squares method with no rejection of 'bad' data. Incoherent noise was thought to be the primary source of contamination since the phase estimates for the up and down biased estimates were very similar (fig. 5.7a). The author thus considers that the phase information would give a good Earth model, if the near surface resistivity could be accurately determined. Noise present in the independent variables resulted in badly biased apparent resistivity estimates (up and down pointing triangles),

Figure 5.6: The estimated magnetic signal (crosses) and noise power (circles) as determined at the DBK (fig. 5.6a) and MWD (fig. 5.6b,c) MT sites. The former site gave high quality results. This is reflected in the 1 to 2 orders of magnitude between the signal and noise in both the Hy and Hx directions. The data quality is poorer at the 'dead frequency band' (about 0.5 Hz.) but the separation is still adequate to gain acceptable results.

The MWD site demonstrated much poorer quality results, particularly in the Hy direction and in the middle frequency bands. In fact, the estimated signal power only exceeds the noise power at the extremes of the frequency range ($>$ 20Hz. and $<$ 0.05Hz.). Finally, fig. 5.6c shows the estimated signal and noise power after robust and constrained impedance estimation (section 5.9.4). Both these procedures have artificially increased the separation between signal and noise. This stabilizes the regression procedure and may lead to more accurate results.

DBK Signal/Noise Power

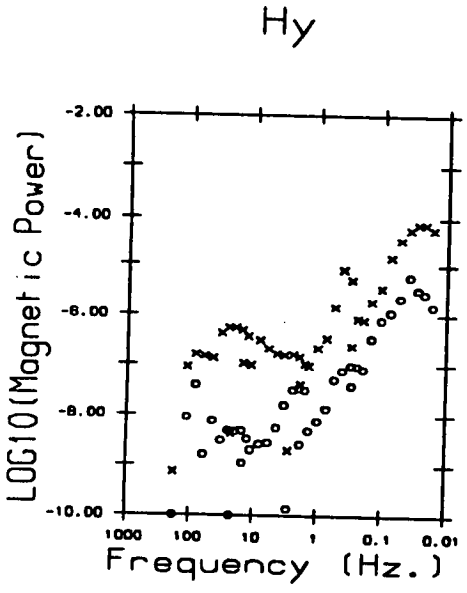

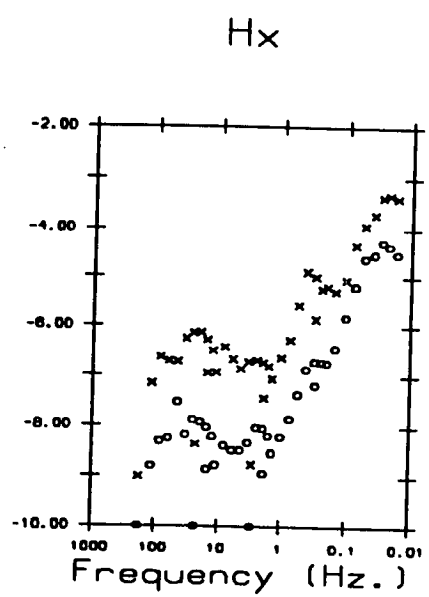

MWD Row Signal/Noise Power

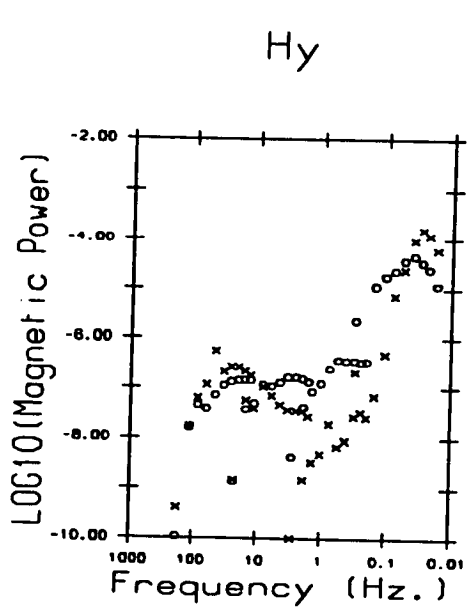

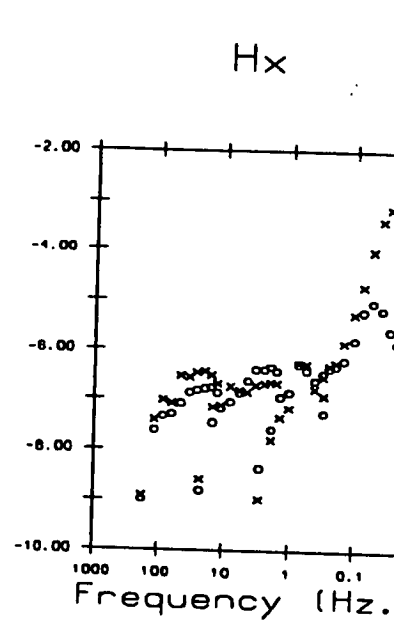

MWD: Constrained + Iterated Signal/Noise Power

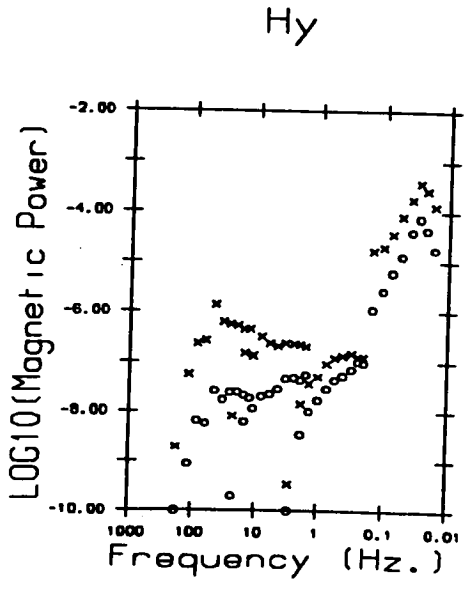

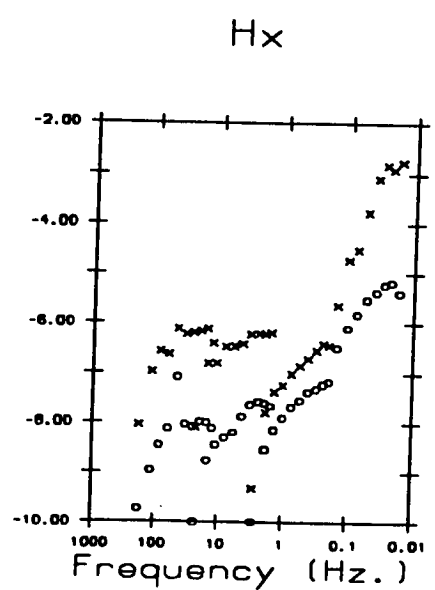

Figure 5.7: The apparent resistivity (ρ_a) and phase (ϕ) response functions estimated from MWD MT data using a variant of the "conventional" Edinburgh University processing programs. The apparent resistivity information has been plotted on an enlarged scale for clarity.

The up and downwards pointing triangles in fig. 5.7a show the large bias introduced into the apparent resistivity estimates if no data selection criterion is used. The phase results are very similar, implying that incoherent noise is primarily responsible. Figure 5.7b shows the type of results more often obtained with Edinburgh University programs which perform preliminary data selection and subsequently average the up and down biased results.

The results obtained using a remote electric and magnetic reference (up and down pointing triangles) on the same data set are shown in fig. 5.7c. The relatively narrow bias range and the isotropy in the response functions permits some confidence in these results, but there is a sharp and unphysical drop in the XY apparent resistivity estimates. Finally, fig. 5.7d presents the results of a local magnetic reference on a non-simultaneous subset of the remotely referenced data.

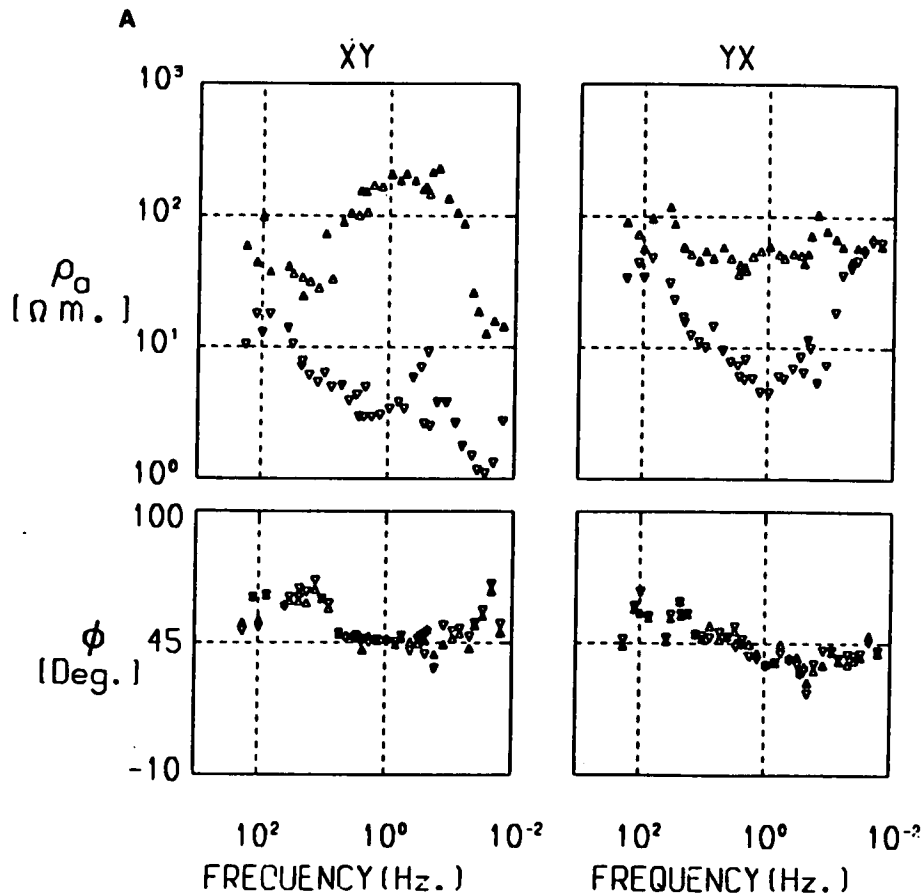
A
XY
YX
10^3
10^2
10^1
10^0
ρ_a
[Ω m.]
100
45
-10
ϕ
[Deg.]
10^2
10^0
10^{-2}
FRECUENCY(Hz.)
FREQUENCY(Hz.)

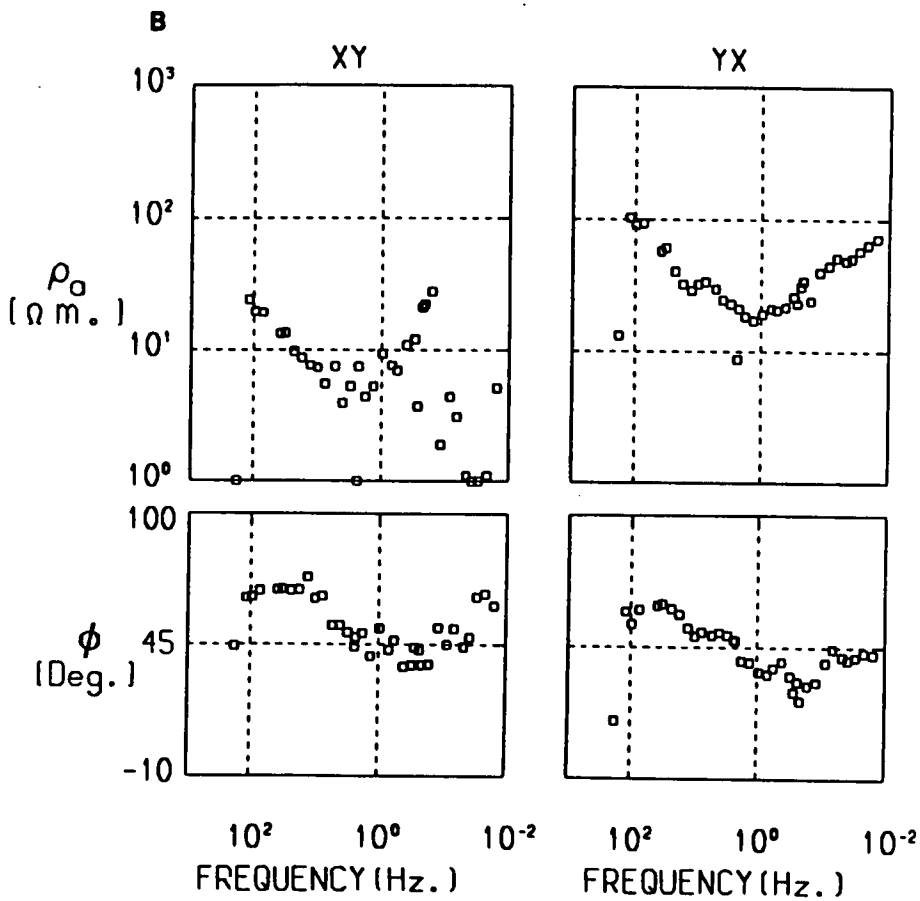
B
XY
YX
10^3
10^2
10^1
10^0
ρ_a
[Ω m.]
100
45
-10
ϕ
[Deg.]
10^2
10^0
10^{-2}
FREQUENCY(Hz.)
FREQUENCY(Hz.)

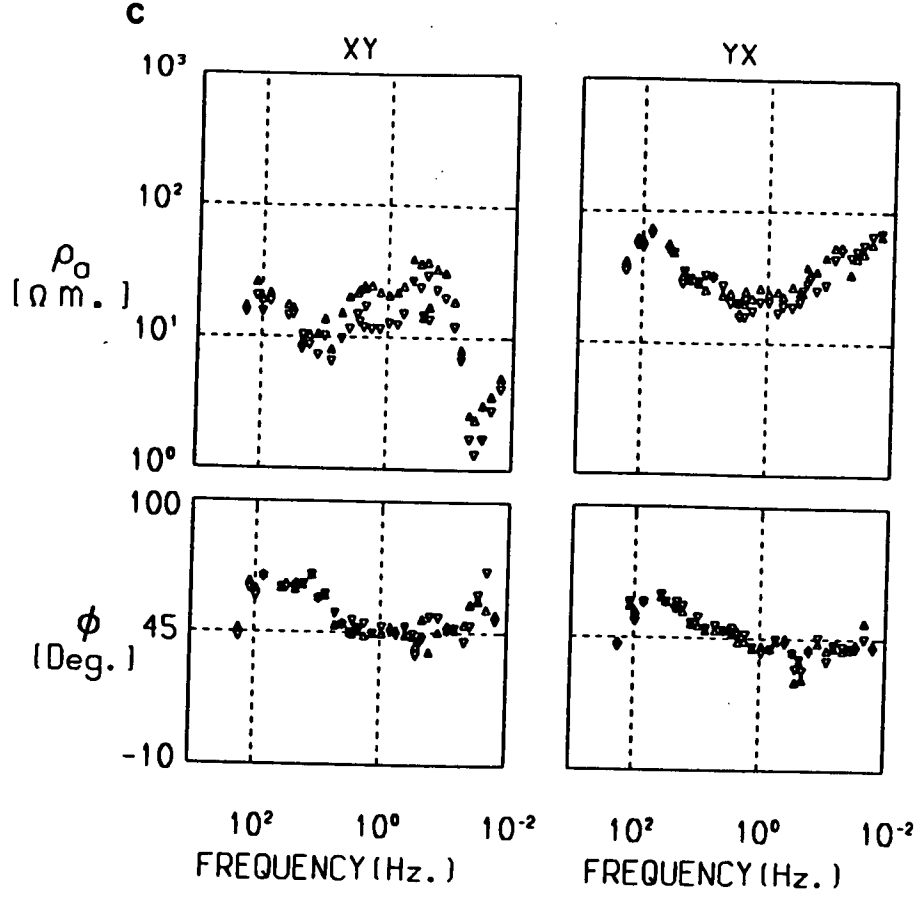
C
XY
YX
10^3
10^2
ρ_a
[Ω m.]
10^1
10^0
100
ϕ
[Deg.]
45
-10
10^2
10^0
10^{-2}
FREQUENCY (Hz.)

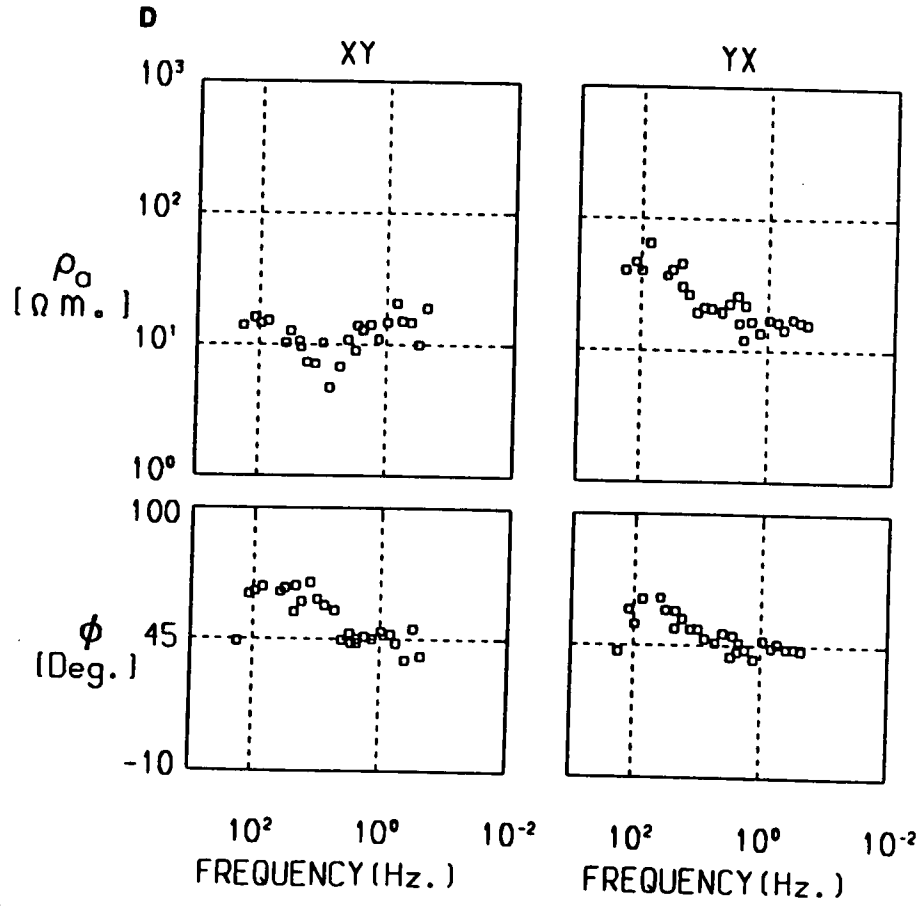
D
XY
YX
10^3
10^2
ρ_a
[Ω m.]
10^1
10^0
100
ϕ
[Deg.]
45
-10
10^2
10^0
10^{-2}
FREQUENCY (Hz.)

particularly at the centre of the frequency range.

Figure 5.7b shows the results obtained from the type of processing now most frequently performed at Edinburgh (Version B). Spectral observations are frequency band averaged to give preliminary impedance estimates. The derived coherence and other criteria are then used to select the 'better' data windows. The impedance is re-evaluated by both up and downwards biasing methods and then their average (Jones *et al.* 1983) is calculated in the anticipation that the intermediate results will lie closer to the 'true' response function.

The YX amplitude appears to be well determined and realistically situated between the 2 extremes given in fig. 5.7a. In the XY direction, the low frequency apparent resistivity estimates are wildly scattered and some are below the physically realistic limit of 1 Ω.m. The author considers that at these frequencies the adopted selection procedure has rejected too many observations and so leads to statistically unstable parameter estimates. Indeed, it will later become evident that no raw impedance estimation procedure has given an entirely satisfactory solution for this portion of this response function.

Version A' (figs. 5.7c and 5.7d) is the author's own adaptation of version A which allows local and remote referenced observations to be processed. Figure 5.7c shows the results obtained using extra remote electric and magnetic field (up and downwards pointing triangles) observations on the same single site data shown earlier. The YX amplitude is almost identical to that obtained using version B (fig. 5.7b), but the XY amplitude is much higher for frequencies below 10 Hz. Since MWD is located in the Northumberland sedimentary trough, it is reasonable to expect that the two response functions will be approximately isotropic. Figure 5.7c is therefore probably a more realistic representation.

There remains a small, but persistent bias between the electric and magnetic referenced results. The author tentatively attributes this to the presence of coherent noise between the measuring and reference sites. However, the source of this noise is not immediately obvious, particularly in view of its presence over a wide frequency spectrum and the separation

between the 2 sites. Another worrying feature of these results, is the sharp decrease in the XY apparent resistivity curve at the lowest frequencies. Even allowing for the expanded log-log scale, this slope is greater than 45^{o} (the maximum allowable; section 2.6). In summary, the referenced measurements show a distinct improvement over the earlier methods, but the resulting response function cannot be regarded as being accurate over the entire frequency range.

Figure 5.7d shows the results obtained with the use of a local magnetic reference (100 m. away from the main site). As these observations were only a non-simultaneous subset of the others presented here, over-comparison between results is considered unwise. The lower number of observations would probably account for the greater scatter in the impedance estimates, but the results still show a considerably lower bias than those acquired by single site impedance estimation (fig. 5.7a,b). This implies that much of the noise cannot be correlated very far (c.f. Goubau *et al.* 1984). In view of the relative ease of acquisition of these locally referenced observations (section 3.2.3), the author considers that a much more complete investigation of this method should be undertaken.

5.9.3. The Chave and Thomson Program

Figures 5.8a and 5.8b show the response functions as calculated by the Chave and Thomson (1989) method (computer program **CHAVE2**; Appendix - B) of non-robust and robust remote (magnetic) reference impedance estimation respectively. Considering both diagrams display results which have used the additional reference information, neither appears to give a particularly accurate XY apparent resistivity response function, for frequencies less than 1Hz.. The robust M-regression method has removed some of the more extreme impedance estimates and reduced the scatter but, in this author's opinion, the results of the application of this program are poorer than the non-robust reference results given in fig. 5.7c. The cause of this is unclear and requires further investigation, although the author suspects that **CHAVE2** may not be numerically stable in the presence of certain types of noise.

The jacknife error estimates (section 4.3.3) which were used in **CHAVE2** appear to give larger and in this case more realistic errors than their

Figure 5.8: The response functions obtained by the Chave and Thomson (1989) program for non-robust (fig. 5.8a) and robust (fig. 5.8b) impedance estimation using the remote (magnetic) referenced data from MWD.

Robust down-weighting has led to a clear decrease in the scatter of both the apparent resistivity and phase estimates, but the overall response functions do not appear to be particularly well determined. The jacknife method (section 4.3.3) has yielded larger and more realistic error estimates than more conventional methods.

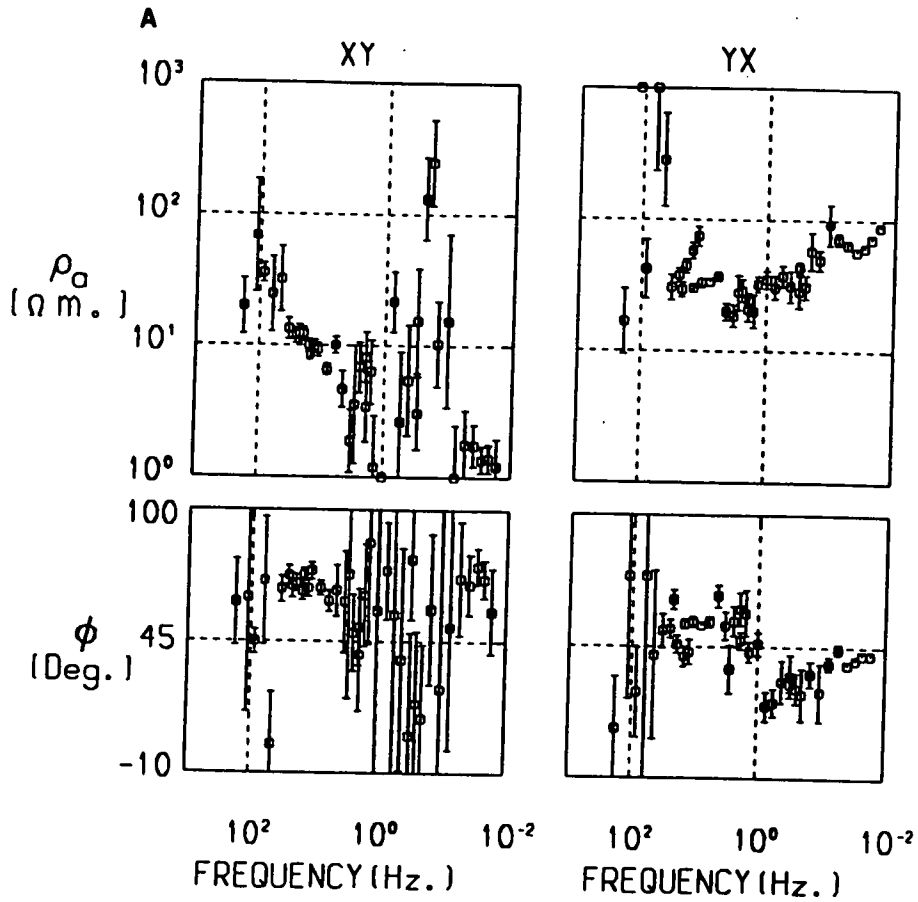
A
XY
YX
10^3
10^2
10^1
10^0
ρ_a
[Ω m.]
100
45
-10
ϕ
[Deg.]
10^2
10^0
10^{-2}
FREQUENCY (Hz.)
FREQUENCY (Hz.)

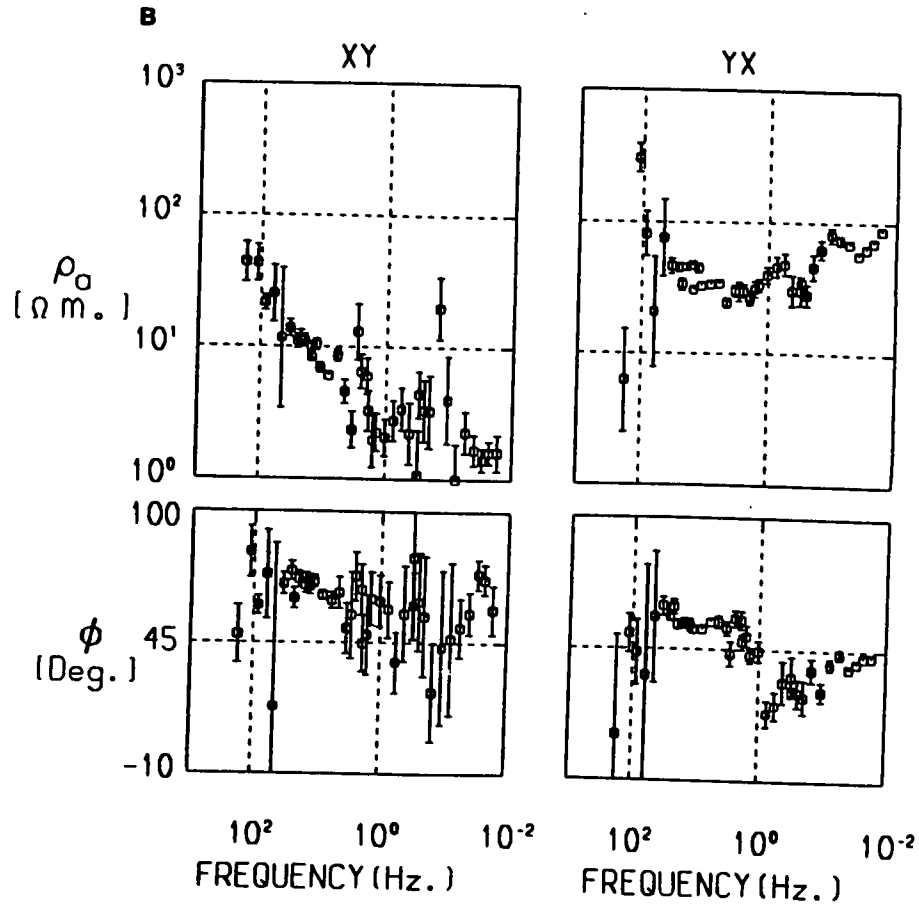
B
XY
YX
10^3
10^2
10^1
10^0
ρ_a
[Ω m.]
100
45
-10
ϕ
[Deg.]
10^2
10^0
10^{-2}
FREQUENCY (Hz.)
FREQUENCY (Hz.)

covariance matrix counterparts (section 4.3.1) which were computed for figs. 5.9.

5.9.4. The Constrained Method

This single site impedance estimation method is fully described in Appendix - A and a number of other facets are demonstrated here. Figure 5.9a shows the raw results computed from eqns. 5.4.8a and 5.4.8b after performing a SVD on the observational data matrix. The response function in the YX, and at high frequencies in the XY directions are consistent with those acquired by other methods, but at lower frequencies the apparent resistivity is completely erroneous. In fact, at some frequencies the bias is *greater* than the up and down biased "limits" (fig. 5.7a).

The author found that the SVD method when used alone, gave very unstable results. Pre-scaling the data matrix, to equalize the error variance (c.f. section 5.5) was particularly crucial as the high power observations could dominate the final results. Frequently these were the observations most afflicted by electric fences, power lines, etc. Routinely, both high and low (broken connections, low signal etc.) power observations were therefore deleted. Figure 5.9b shows the SVD derived response functions after a fraction of the observations had been trimmed (c.f. section 5.6.4) prior to application of the SVD based impedance computations. The apparent resistivities now show little obvious sign of bias, except at the troublesome lowest frequencies in the XY direction.

A second observational selection procedure was based upon the level of predicted coherence estimated from data 'windows'. The method used was adapted from the conventional Edinburgh University programs (section 5.9.2; Version B). Observations could either be rejected by setting a minimum acceptable coherence threshold, or by rejecting a fixed percentage of the lowest coherence observations. The author found that the latter method was often more applicable as it preserved the number, albeit of poor quality, observations at the noisiest frequencies.

Figure 5.9c shows the SVD results after data had been rejected based on both the power level and on low coherence (50% observations rejected in the second stage). Although there is a slight improvement at the low frequencies

Figure 5.9: Some properties of the programs for the constrained method of impedance estimation using the unreferenced MWD data.

Raw SVD determined response functions (fig. 5.9a) are very susceptible to noise contamination. In this figure the apparent resistivity and phase are particularly badly contaminated in the XY direction. If the extreme power observations are removed prior to regression the response functions are much more smoothly varying and realistic (fig. 5.9b). Further data enhancement is possible by rejecting observations which give rise to a low predicted coherence (fig. 5.9c) and then iteratively downweighting the influence of statistically outlying data (fig. 5.9d).

An idealized response function is derived from these results and used to constrain a re-evaluation of the impedance. Figure 5.9e shows a marked reduction in the scatter of the results, but the persistent problem in the XY direction has been enhanced by this process. If instead, the magnitude of the diagonal elements of the idealized impedance tensor are constrained to be small, then the more realistic response functions shown in fig. 5.9f are obtained.

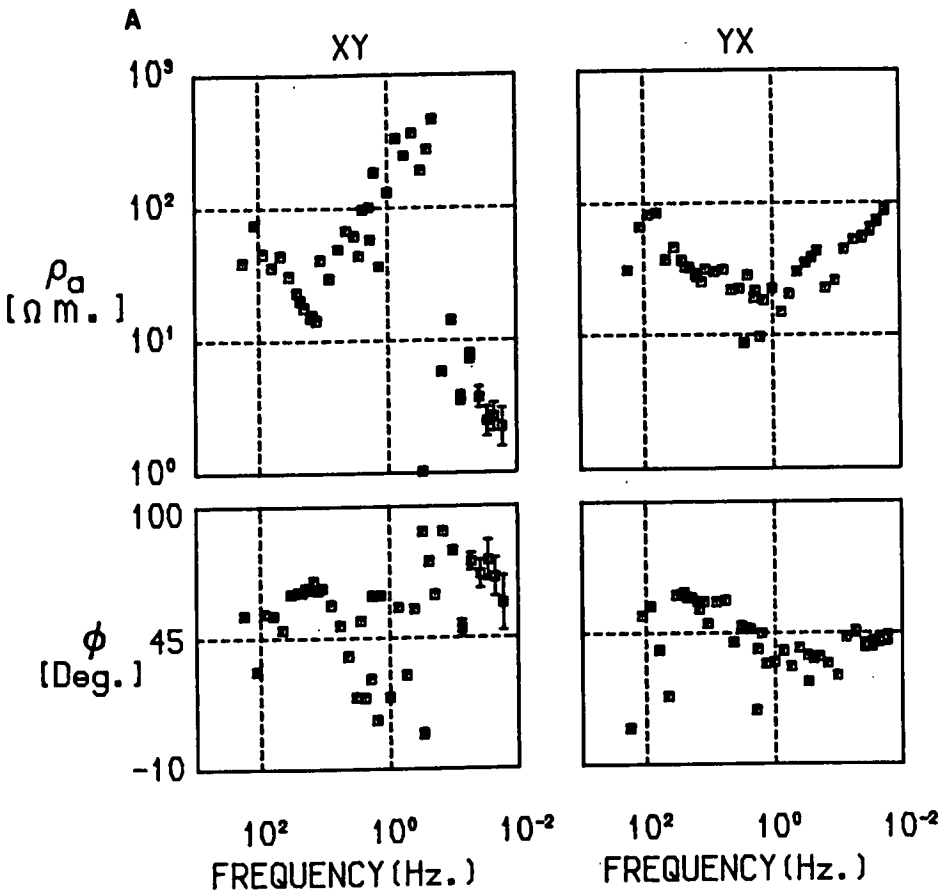
A
XY
YX
10^3
10^2
10^1
10^0
ρ_a
[Ω m.]
100
45
-10
ϕ
[Deg.]
10^2
10^0
10^{-2}
FREQUENCY (Hz.)

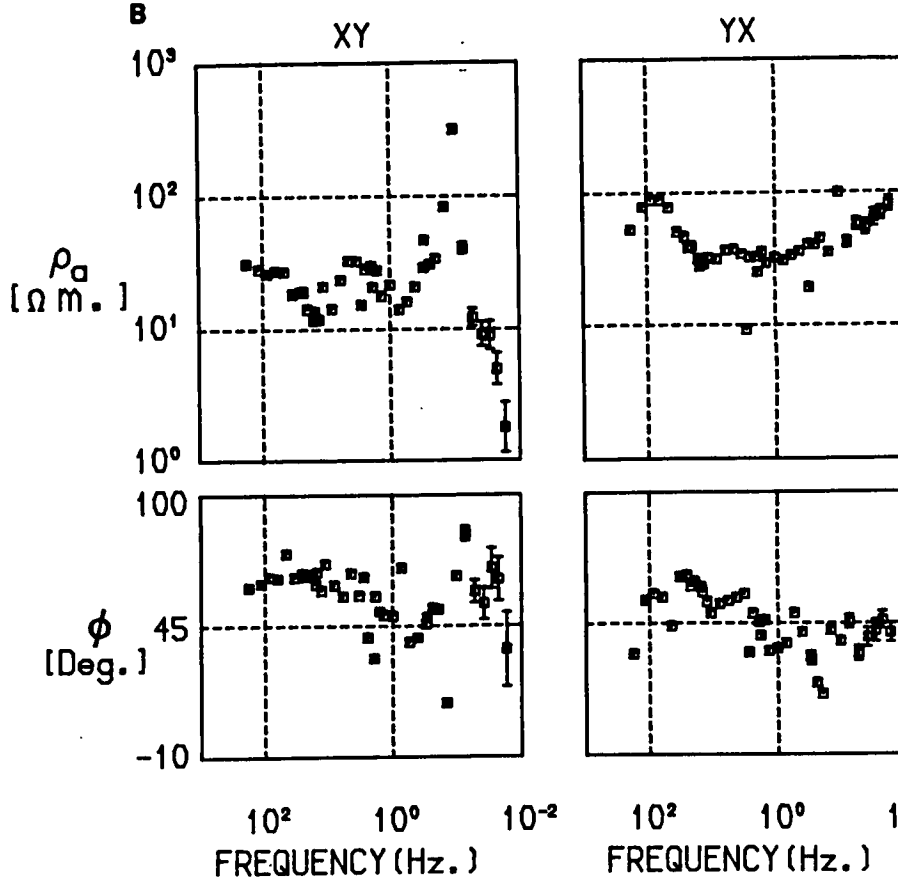
B
XY
YX
10^3
10^2
10^1
10^0
ρ_a
[Ω m.]
100
45
-10
ϕ
[Deg.]
10^2
10^0
10^{-2}
FREQUENCY (Hz.)

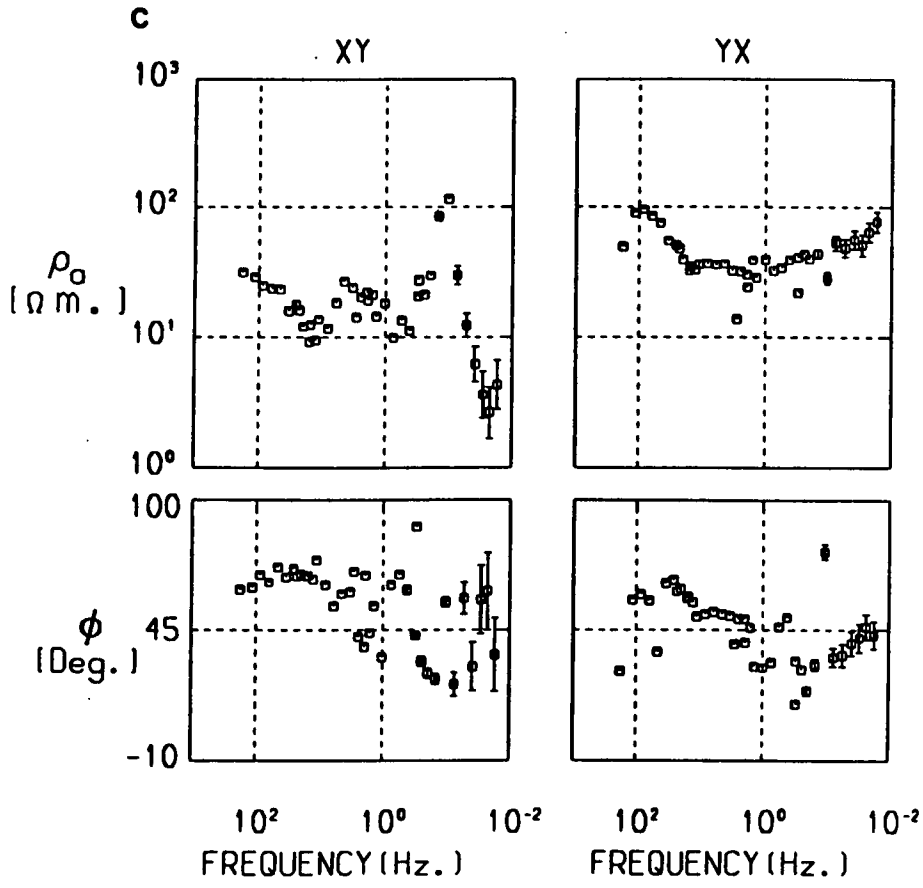
C
XY
YX
10^3
10^2
10^1
10^0
ρ_a [Ω m.]
100
45
-10
ϕ [Deg.]
10^2
10^0
10^{-2}
FREQUENCY [Hz.]

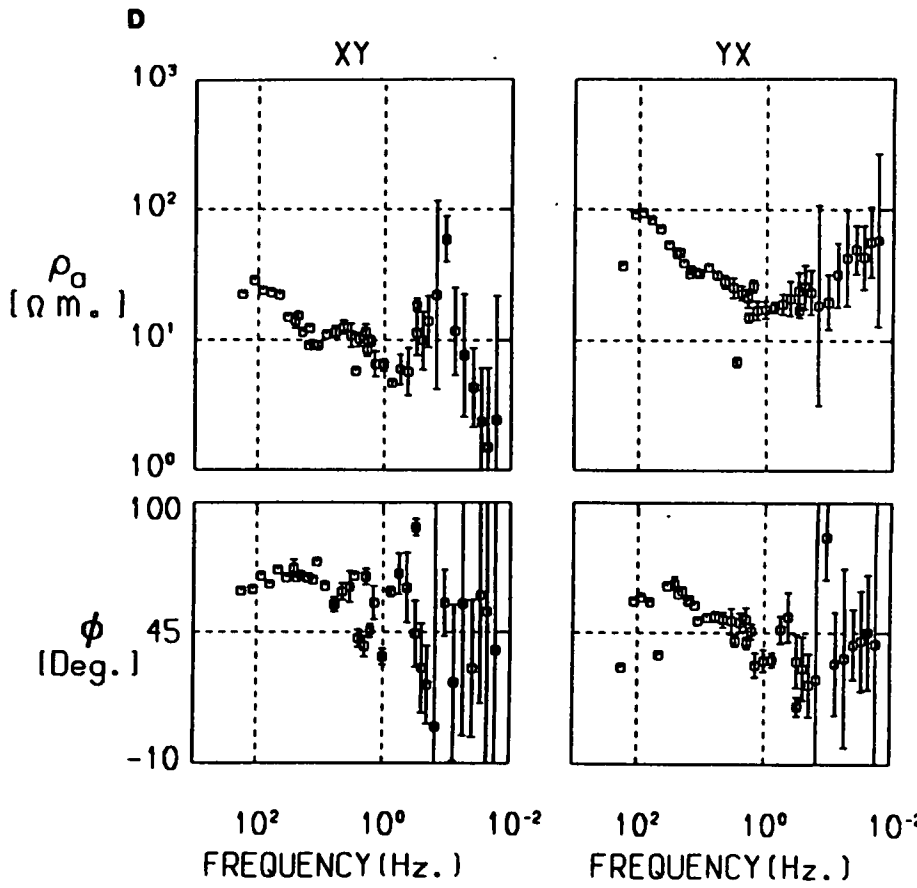
D
XY
YX
10^3
10^2
10^1
10^0
ρ_a [Ω m.]
100
45
-10
ϕ [Deg.]
10^2
10^0
10^{-2}
FREQUENCY [Hz.]

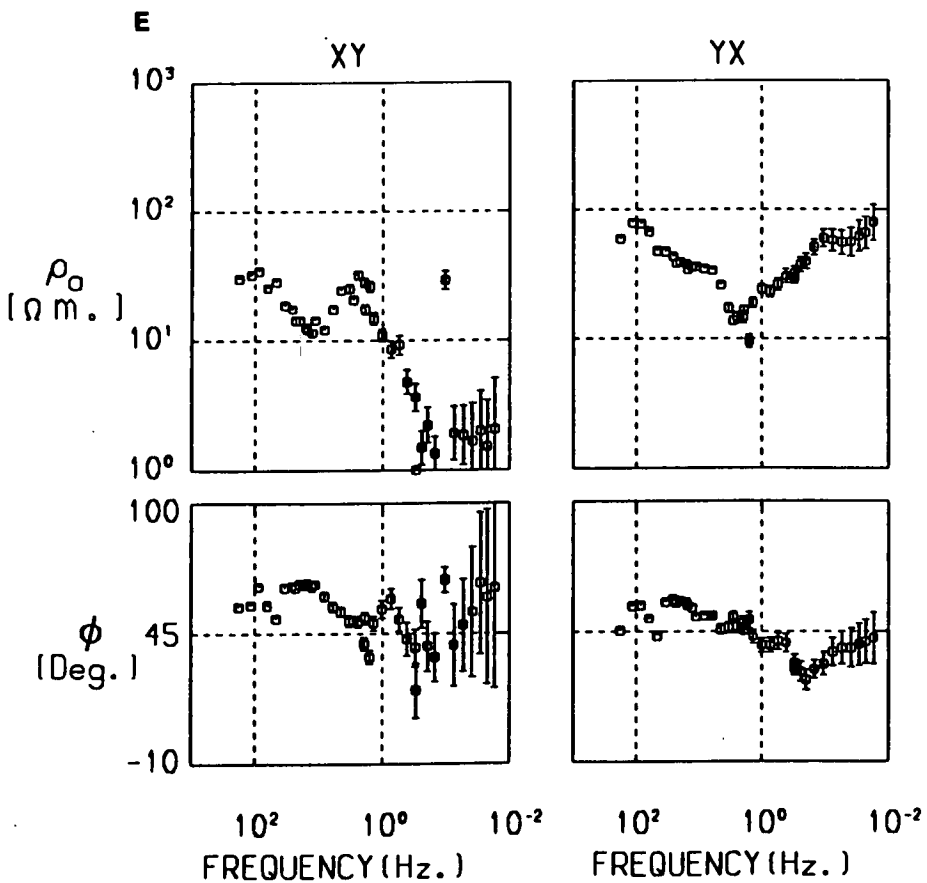
E
XY
YX
10^3
10^2
ρ_a
[Ω m.]
10^1
10^0
100
ϕ
45
[Deg.]
-10
10^2
10^0
10^{-2}
FREQUENCY(Hz.)

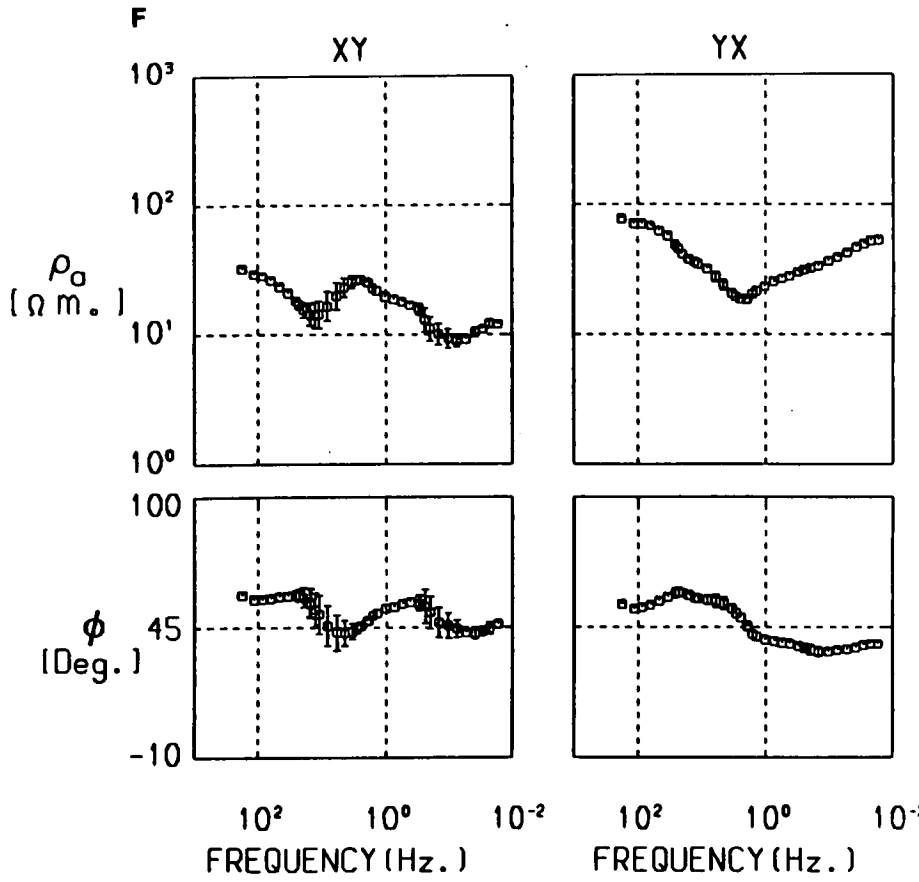
F
XY
YX
10^3
10^2
ρ_a
[Ω m.]
10^1
10^0
100
ϕ
45
[Deg.]
-10
10^2
10^0
10^{-2}
FREQUENCY(Hz.)

in the XY direction, coherence based rejection did not substantially change the results when compared with anomalous power rejection.

The final "unconstrained" SVD response function (fig. 5.9d) was calculated from these selected observations, but with outliers robustly downweighted (section 5.6.5 and Appendix - A). The results are unquestionably more self consistent (e.g. around 5Hz. in the XY direction). The instability of the parameter estimation method and the number of robust iterations has however, badly degraded the apparent number of degrees of freedom (fig. 5.10a) and produced an unrepresentative estimate of the coherence. Another symptom of an underlying problem is the unrealistically high skew values computed at this stage.

The scatter of the individual impedance estimates was often found to be higher after robust S.V.D. impedance estimation than by other methods, but in general they were not deemed to be as badly biased. Thus the original aim of the constrained impedance estimation was to minimize this variability between adjacent impedance estimates in the frequency domain. The formation of an idealized response function is described in Appendix - A and the subsequent constrained re-evaluation of the impedance tensor from the unconstrained results shown in fig. 5.9d. Completing this process gives rise to the response functions shown in fig. 5.9e. These are the more self-consistent than the unconstrained one from which they were derived, but the unphysical drop in the XY direction persists and has even been enhanced by this process. After such constrained regression, the apparent number of estimates has been increased to a more realistic level and produced more representative coherence estimates (fig. 5.10b). Both robust and constrained regression gives an apparent improvement in the signal to noise ratio (fig. 5.6c), but the skew still demonstrates abnormally high values in an area which isotropy had been expected. In fact, the author considers that this is a manifestation of collinearity (section 4.7.2) caused by overwhelming random noise or strong coherent noise. The virtual absence of suitable signals in the Hy direction may also be responsible.

This data deficiency can be explored via the magnitude of the singular values which were computed during parameter regression. Ideally, the 2 significant singular values should be approximately the same size and

A

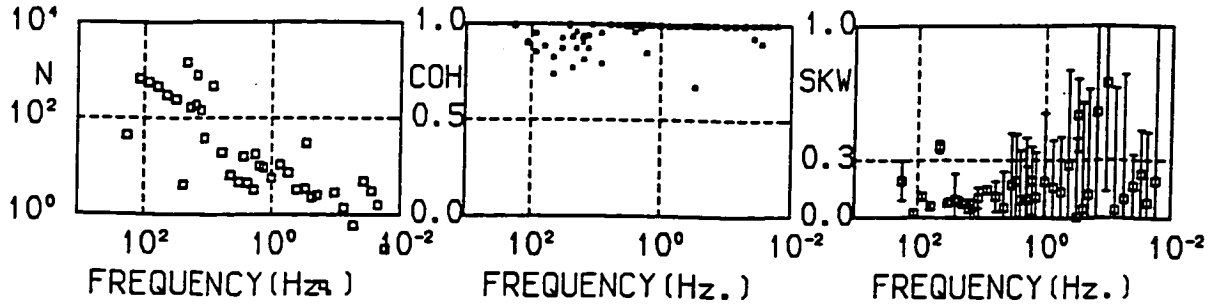

B

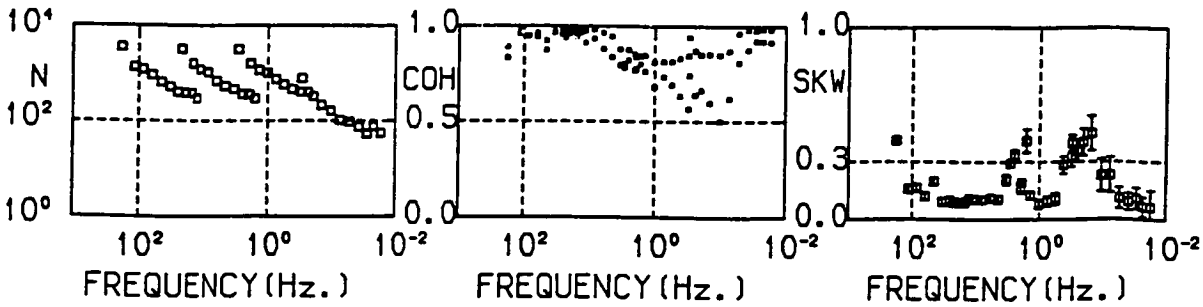

C

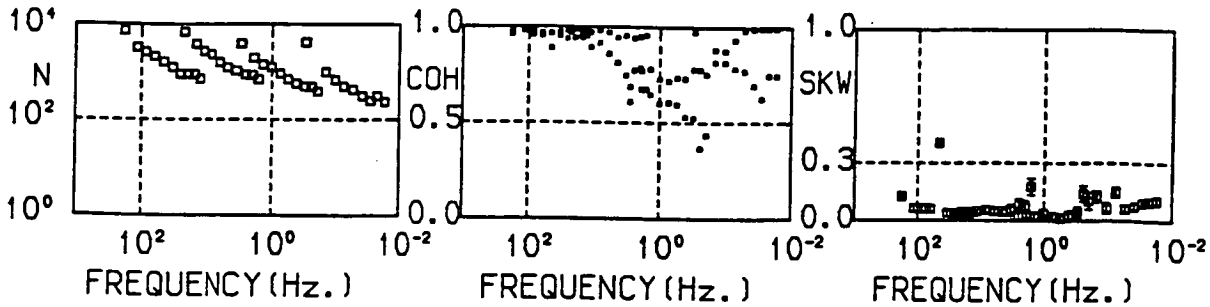

Figure 5.10: The apparent number of degrees of freedom (N), the predicted coherence (COH) and the skew (SKW) in the XY and YX directions as a function of frequency.

Figure 5.10a demonstrates that the preliminary data selection and robust down-weighting has eroded the number of degrees of freedom and produced an unrealistic estimate of the coherence. Applying a constraint model reduces the need for radical robust weighting and consequently gives a more representative estimate of the coherence (fig. 5.10b), but the scatter and unacceptably high skews imply that observational collinearity may be present. Figure 5.10c shows that the skew can be reduced by performing constrained regression using a model in which the overall magnitudes of the diagonal impedance elements are small.

considerably larger than the 2 "null" values (sections 5.4.2 and 5.4.3). Figure 5.11a shows a singular value plot for the impedance parameters for a relatively well-conditioned part of the frequency spectrum (11.2Hz.). Robust and constrained methods can do little to enhance the "cliff" between the 2 significant and null singular values. In contrast, the raw singular value plot for 0.25 Hz (dashed line in fig. 5.11b) does not show the same cliff between λ_2 and $[\lambda_3,\lambda_4]$. In this instance the apparent rank of the data matrix is probably only 1. The full impedance tensor cannot then be properly evaluated since relations of the form $Hx = C_1.Ex$, $Hx = C_2.Ey$ and $Hx = C_3.Hy$ will exist between the observables. The last of these inter-relationships shows that this scenario will arise in the presence of strong input coherent noise.

As the skew is sensitive to changes in the magnitude of the impedance tensor elements, any ill determined values will correspondingly affect it. In fact, the magnitude of the diagonal tensor elements often seem to be increased which leads to the high skew values shown in fig. 5.10a. If this assumption is correct, then for sites which are expected to show low dimensional characteristics an idealized response function can be constructed in which the magnitudes of Zxx and Zyy are constrained to be small. It is anticipated that by further inhibiting the number of free parameters to be resolved, their values will be more accurately determined.

If the impedance is re-evaluated for MWD using such a model then the characteristic separation is found to exist between the 2 pairs of singular values (solid line in fig. 5.11b). Correspondingly, the final response function (fig. 5.9f) is more isotropic and does not exhibit the same worrying tendencies at low frequencies. The accuracy of the skew does however suffer following the application of such harsh constraints (fig. 5.10c).

Figure 5.11: The magnitude of the 4 singular values (λ_1 to λ_4) at 11.2Hz (fig. 5.11a) and 0.25Hz (fig. 5.11b).

The dashed line in the former diagram shows the ideal situation in which the 2 significant singular values are approximately the same magnitude and are much larger than the 2 "null" ones. The application of robust (line marked by squares) and constraints (line marked by crosses) can do little to improve or change the results.

The raw data in the latter example (dashed line in fig. 5.11b) are very noisy and poorly conditioned (i.e. λ_3 and λ_4 have non-zero values and λ_2 is not significantly larger than λ_3). Robust re-weighting has forced the observations to conform to a model in which there are 2 null singular values but has done little to alleviate the collinearity. The conventional constraint model (i.e. all the $Z_{i,j}$'s are non-zero) reduces the need for robust downweighting, but the magnitude of λ_2 is still not substantially increased (line marked by crosses). If a constraint model is applied in which the diagonal elements of the impedance tensor are small, then the reduction in the number of parameters leads to a better eigenvalue separation (solid line).

A FREQUENCY 11.20HZ

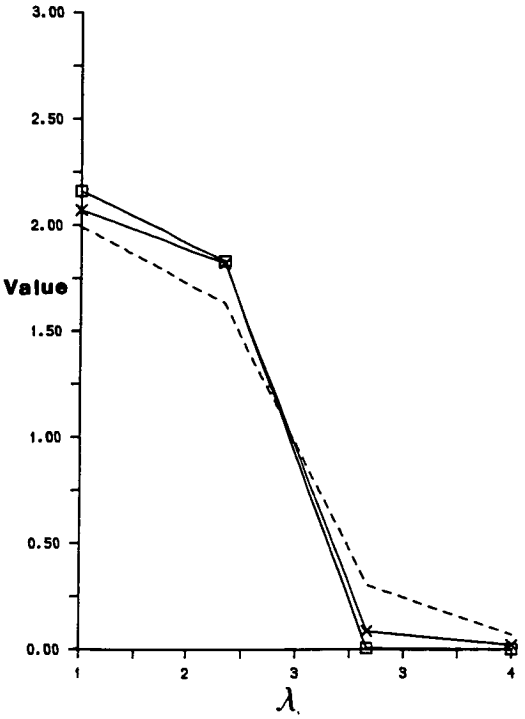

B FREQUENCY 0.246HZ

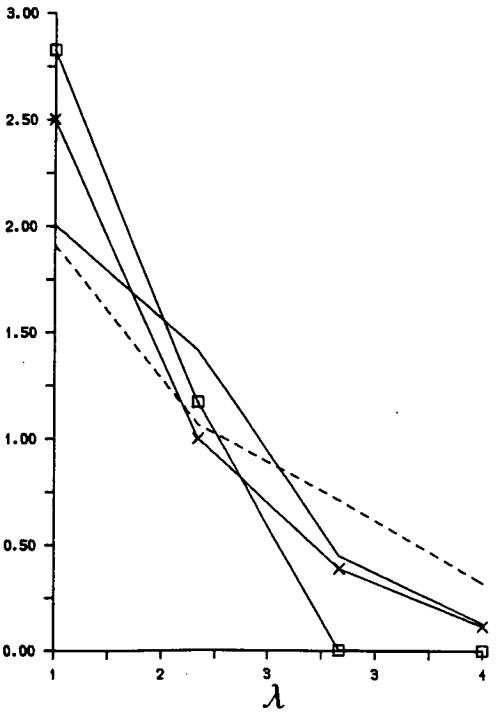

CHAPTER 6

MODELLING OF GEOELECTRIC DATA

6.1. INTRODUCTION

The response functions acquired by magnetotelluric (MT) sounding usually consist of estimates of the apparent resistivity and/or phase over a range of frequencies. For the major part, this chapter is concerned with the transformation of such response functions into depth sections.

The surface rocks in Northern England are relatively uniform, correlateable and isotropic so the acquired response functions usually demonstrated low dimensionality characteristics (e.g. skew < 0.3). Consequently, considerable use of 1-D modelling procedures was made in the interpretation of the observations from this study. Several of these procedures are described in section 6.2. The real Earth is, unfortunately, more complex and heterogeneous than can be properly simulated in one dimension and a few of the response functions showed the presence of distortions or anisotropy. The latter was especially obvious in the vicinity of the large resistivity contrast between the Alston Block granite and its surrounding rock. Therefore, in section 6.3, the problems that can be encountered in multi-dimensional environments and some of the more sophisticated modelling procedures now available, are discussed. Finally this chapter concludes (section 6.4) with a detailed description of the modelling procedures which were actually applied to the MT, D.C. resistivity and gravity observations.

6.2. REVIEW OF ONE DIMENSIONAL GEOELECTRIC MODELLING

This is the simplest and most widely used class of MT modelling methods which transform the acquired frequency domain response function at one site to a model Earth in which the resistivity is only a function of depth. Strictly, it can only be applied in regions which have no lateral variation in resistivity, but in practice it is frequently used even in complex geoelectric environments to obtain starting models for more sophisticated, higher dimensional procedures.

The transformation of response functions into model resistivity and depth

sections is non-linear and in the presence of real, noisy observations, it is also non-unique. In fact, an infinite number of different models produces a statistical fit to the observed response function. Normally for interpretation purposes, it is desirable to find a single model to reproduce the observations reasonably well. Any good MT modelling technique should also explore the resolution of each of its parameters. It then usually becomes apparent that additional independent geophysical or geological information concerning one or more of the parameters should be incorporated into the procedure to reduce the range of non-uniqueness. Parker's (1983) review of magnetotelluric modelling techniques and section 6.2.3 enlarge on a number of aspects of the inverse problem. Particular emphasis is placed here on describing those modelling methods which were employed in this study.

6.2.1. The 1-D Response Function

MT response functions usually consist of 4 complex valued elements of the impedance tensor acquired over a range of EM field frequencies. From the discussion in section 2.5, the 1-D impedance is given by:

$$Z = Z_{XY} = -Z_{YX} \qquad (6.2.1)$$

In real soundings, the magnitude of these off-diagonal elements is never exactly the same so the 1-D model may then be based on any one of a number of response functions. Berdichevsky and Dimitriev (1976) have suggested as a reasonable approximation the use of the average of the two principal elements:

$$Z = (Z_{XY} - Z_{YX})/2 \qquad (6.2.2)$$

1-D models have also been determined from other combinations of the impedance tensor elements (e.g. the rotated major - Jones and Hutton 1979b; the minor - Adam *et al.* 1982 and the rotationally "invariant" impedance Berdichevsky *et al.* 1980, Ranganayaki 1984, Ingham 1988, Jones 1988). The latter, which is also referred to as the "effective" or "determinant" impedance has been found to give a better average in three dimensional situations and is given by:

$$Z = \sqrt{(Z_{XX}.Z_{YY} - Z_{XY}.Z_{YX})} \qquad (6.2.3)$$

Any of the above impedances and their associated error estimates can be

transformed to apparent resistivity, phase (eqn. 2.5.3), or the Schmucker impedance C (e.g. Larsen 1975, Parker 1983) and then modelled by a variety of different algorithms. In this study, the "effective" and an average of the major and minor impedances (section 2.5.2) $Z = (Z^{MAJ.} + Z^{MIN.})/2$, were used to determine the 1-D models presented in Appendix - C.

6.2.2. Approximate Models

There are two widely used schemes which give an approximate model from smoothly varying estimates of the apparent resistivity (ρ_a). The Schmucker and Niblett-Bostick transformations (e.g Goldberg and Rostein 1982, Jones 1983b, Jones *et al.* 1983, Parkinson and Hutton 1989) cannot be proved mathematically but both give a continuously varying resistivity - depth profile. They are ideal for use in the field owing to their very small computational cost (e.g. Jones and Foster 1986), or as in this study, the Niblett-Bostick transformation (section 6.4.2) was used as the basis for further modelling and preliminary interpretation (section 6.4.5).

The Niblett-Bostick transformation originally used the apparent resistivity (ρ_a) alone to find model resistivities (ρ) and depths (d):

$$\rho(d) = \rho_a(T).\ \frac{1+m(T)}{1-m(T)} \quad , \qquad d = \left|\frac{\rho_a(T).T}{2.\pi.\mu_0}\right|^{1/2} \tag{6.2.4}$$

where $m(T) = (\delta \log(\rho_a(T))/\delta \log T)$ is the gradient of the apparent resistivity curve on a log-log scale, at the period T.

A modified Niblett-Bostick resistivity transformation has been proposed which uses Weidelt's (1972) approximate expression for one of the dispersion relations (eqn. 2.6.6) to give:

$$\rho(d) = \rho_a(T)\ .\ [(\pi/(2.\phi(T)) - 1] \tag{6.2.5}$$

This equation is computationally simpler to implement, but in view of the discrepancy inherent in utilizing Weidelt's approximation (c.f. Fischer and Schnegg 1980), this author believes that the results of this modelling technique are correspondingly degraded.

6.2.3. Parametric (Discontinuous) Methods

This is the commonest type of modelling method in which the model Earth is parameterized in terms of a small number of layers (less than the number of observations). Each layer has a homogeneous resistivity within a specified depth range and the model is terminated at its base by a resistivity half space (e.g. Larsen 1975, Fischer and Le Quang 1982, Meju 1988).

Traditionally, simple models were obtained by manually matching the observed response function to sets of theoretical master curves, computed from the solution of the 1-D recurrence relation (eqn. 2.3.10: Cagniard 1953). The introduction of high speed digital computers now allows the MT response function to be found more quickly by direct solution of the recurrence relation for any specified multi-parameter model.

Most modern parametric modelling techniques (1) take a starting model, (2) calculate its response function, (3) compare this with the observed response function and its associated errors and then (4) iteratively adjust the model's parameter values to reduce the discrepancy (or misfit) between them. A qualitative assessment of the fit can be made by visual inspection, although more frequently a quantitative statistic (e.g. χ^2; section 4.6.1, Fischer *et al.* 1981) is considered.

Automatic model adjustments can be carried out by random search (Monte Carlo) or by non-linear inversion techniques as follows:

1. The Monte Carlo method (Jones and Hutton 1979b, Rokityansky 1982, Fontes 1988) generates a large number of random models around an initial set of specified parameter values. It then evaluates the forward model response for each and retains those which most closely fit the observations. Subsequently, the starting model is revised on the basis of these best fitting models and the whole procedure repeated. This scheme, if used properly, will fully explore the range of uniqueness of the solutions. In practice, the high computational costs involved tend to restrict such a search.

2. Linearized inversion methods are widely used to compute for a starting model, parameter correction values which aim to reduce the misfit. A review of some of the relevant theory for the solution of these non-linear least squares problems has already been given in section 5.8. The uniqueness of the final solution can be investigated by computing the resolution matrix (Ilkisik

and Jones 1984, section 4.6.2), or by finding the most extreme parameter values which will produce a response function which is consistent with that observed (c.f. section 4.3.2).

6.2.4. Limitations of MT models

The resulting best fitting parametric models from both the linearized and restricted search Monte Carlo methods are strongly dependent upon the starting models (c.f. section 5.8). The inherent dangers of model mis-specification (under or over parameterization) have already been discussed for general least squares problems (section 4.5.1). MT model specification is often a trade-off between a desire to obtain the most accurate representation of the Earth and the increased complexity and computational load in solving a large multi-parameter problem. Furthermore, extraneous thin layers are particularly dangerous as they can be readily added to a model with little significant change in the misfit, but with the possibility of a greatly altered interpretation of the geoelectric structure (c.f. Fischer and Schnegg 1980). Since there are seldom real situations in which the misfit will have a pronounced minimum (Fischer *et al* 1981), the MT modeller must ultimately choose one of the equally good models. As a rule, members of the MT community prefer to use the model with the 'minimum structure' (Smith and Booker 1988).

MT models are also very sensitive to the shape of the response functions. It only takes a very small change (e.g. due to observational noise) to result in a very large effect on the estimated model parameter values (e.g. fig. 6.7a).

On a more positive note, Oldenburg (1988) has pointed out that if the starting model is correctly specified, the non-uniqueness of the inverse problem is greatly reduced and so the final model may be a good representation of the Earth's conductivity distribution.

A hidden danger in the interpretation of geoelectric models results from the principle of thin layer equivalence (e.g. Patra and Mallick 1980, Tripp *et al.* 1976, Raiche *et al.* 1985). This suggests that, in certain situations, the MT response functions cannot be used to determine the model layer thickness and resistivity separately. The only parameter that can be resolved is either the layer conductance (conductivity-thickness product) or resistance

(thickness-resistivity quotient). To distinguish properly between a thin conductive layer and a thicker, more resistive layer (see e.g. BEAM-C at 10 km. depth, in Appendix -C), constraining information concerning the layer thickness or resistivity must be applied. Jones (1987) pointed out that thin conductive layers seem to be detected more often and suggested that this was possibly as a result of the minimum misfit modelling procedures (section 6.2.3) now widely used. In addition, this author considers this phenomenon may be a more fundamental limitation of the resolution of resistive layers by the MT method (section 6.2.6).

Acquired geoelectric models are often presented on a logarithmic resistivity and depth scale. This tacitly accepts that there will be order-of-magnitude variations in both these parameters and their values need to change by at least a third to a half a decade before they can be deemed to be significant. In addition, this also implies that the resolvability of thin layers diminishes rapidly with increasing depth. For example, although MT measurements might be able to resolve a layer 100 m. thick at a depth of 300 m., the attenuation of high frequency EM fields means that a layer 5 km. thick may be undetectable at a depth of 50 km. These are important points which are frequently not recognized by geophysicists in other fields.

6.2.5. Other Modelling Techniques

It is highly improbable that any model will exactly fit the acquired response functions. In fact, the model corresponding to the global minimum misfit is not necessarily geophysically desirable because it comprises a set of conductivity delta functions (the D^+ model: Parker 1980,1983, Parker and Whaler 1981). A sequence of thin, highly conducting layers separated by insulators is not normally a realistic geoelectric model. It is therefore common practice to obtain a smoother and more interpretable model by relaxing this misfit criterion.

Testing the existence of a 1-D model within the acquired response function is one of the more practical applications of the D^+ modelling method. Alternatively, in this study, D^+ models were constructed in order to identify impedance estimates which were inconsistent with the best fitting 1-D model (Appendix - A).

Several schemes have been proposed for generating models whose resistivities are continuously varying functions of depth (e.g. Hobbs 1982, the Bostick transformation; section 6.2.2). Recognizing the limitations of discontinuous model parameterizations, "Occam" type modelling schemes have recently been proposed (Constable *et al.* 1987, Meju 1988). The aim of these methods is to derive the smoothest possible resistivity-depth profile by numerically constraining (section 5.7.4) an over-parameterized starting model. The depths to each layer are kept constant and the misfit is decreased by calculating correction values to the layer resistivities by linearized methods (section 5.8). Upon convergence any departures from the starting model will directly reflect changes in the observations rather than result from the addition of unnecessary layers. This principle was also applied, by this author, to the analogous problem of gravity modelling (section 6.4.8).

6.2.6. Joint Modelling of Geoelectric Observations

There are a number of different geophysical techniques which aim to determine the resistivity structure with depth (e.g. MT, D.C. resistivity and controlled source EM). None of these methods, applied separately, can unambiguously resolve the underlying structure throughout the entire depth range because of survey limitations (e.g. the frequency range/spread length), noise, or the equivalence principle (section 6.2.4). Several researchers have therefore recognized the potential benefits in resolution afforded by joint modelling of any two of these methods (Vozoff and Jupp 1975, Tripp *et al.* 1978, Petrick *et al.* 1977, Raiche *et al.* 1985, Harinarayana 1987, Fontes 1988).

Assuming that the observed resistivities are not strongly dependent upon the frequency of the electromagnetic field (c.f. Keller 1971), D.C. resistivity can help to overcome the insensitivity of the MT method to resistive layers. Conversely, as MT is highly responsive to the presence of even thin conductive layers, this may help to reduce the ambiguity present in thin layer D.C. resistivity models. Moreover, MT is not as limited by logistics in its useful depth of penetration as the D.C. resistivity method (c.f. chapter 1).

For an identical model Earth, joint MT and D.C. resistivity 1-D modelling is facilitated by the same asymptotic properties of the apparent resistivity response function, at the extremes of their frequency and half-spread range

respectively (Kaufman and Keller 1981). It was therefore relatively straightforward for this author to adapt a standard MT parametric computer modelling program (**MTINV**: Meju 1988) to take account of the additional D.C. resistivity observations and then compute their response (**MAXMUL** in Appendix - B).

6.2.7. Footnote to 1-D MT Modelling

In Hermance's review (1983), he suggested that most of the effort exerted in developing new 1-D modelling algorithms was academic because, for well conditioned observations, it made little difference which of the many modelling algorithms was used. In the subsequent seven years, an ever-increasing array of such methods has still been forthcoming.

This author feels that the time is approaching when the efforts of some MT researchers should be directed away from designing new algorithms and towards a new COPROD (Jones 1980b) type of comparative modelling study. This should be performed on both synthetic and real, ill-conditioned response functions with a view to finding not only the most appropriate model but also to testing its resolution. This review would help to clarify the potential benefits of the various current modelling procedures, not only for active MT practitioners, but also, more importantly, for other interested members of the geophysical community.

6.3. DISTORTION AND MORE SOPHISTICATED MODELLING

The real Earth is complex and so MT response functions can be affected by channelled currents, near surface conductivity variations (section 6.3.1), topography (Harinarayana 1987, Fischer 1989), and the coast effect (e.g. Patra and Mallick 1980) as well as higher dimensional structures.

6.3.1. Electromagnetic Field Distortion

A plane EM wave interacting with a laterally inhomogeneous, 3-D Earth induces anomalous excess currents and charge concentrations (Berdichevsky and Dimitriev 1976, Rokityansky 1982, Jones 1983a,1988, Berdichevsky *et al.* 1989). These produce respectively, inductive and galvanic distortion of the electric field measurements and consequently the impedance estimates.

Inductive distortion results from currents flowing preferentially in the more conductive region producing a frequency dependent distortion of both the apparent resistivity and phase response functions. At the highest frequencies and in strictly 2-D situations this will not be a problem. Galvanic distortion has been the subject of much recent interest, particularly with regard to near surface inhomogenities. Erroneous observations of the electric field occur when charge concentrations around local, surficial inhomogenities generate potential differences between the measuring electrodes. Galvanic distortions do not change the phase observations, but result in the apparent resistivity response function being 'statically' shifted by a frequency independent multiplicative factor. The resulting 1-D model has the correct structural shape but the layer parameters are in error.

This phenomenon can be identified manually or automatically (Whelan 1989) by comparing the response functions in the two orthogonal directions and/or from adjacent soundings. The effects of static shift can be alleviated by a number of methods including separation of the impedance tensor (Larsen 1975,1977, Zhang *et al* 1987), the EMAP array profiling method (Oldenburg 1988) or by 2-D finite element modelling (Poll *et al.* 1989). If the true surficial model resistivity value is known, the phase response function can be modelled directly as it should, theoretically contain the same information as that in the unshifted apparent resistivity curve (section 2.6).

Distortion effects have been demonstrated in a number of field (e.g. Berdichevsky *et al.* 1980, Kurtz *et al.* 1986, Beamish 1990, Adam and Varga 1990) and numerical studies (Park *et al.* 1983, Wannamaker *et al.* 1984).

6.3.2. Distortion of the Northumberland Field Observations

The relatively low density of stations in Northumberland precluded a detailed investigation of distortion effects, but comparison of the acquired response functions revealed a few soundings which demonstrated static shift.

Site SHW (Appendix-C) had the most significant shift and its close proximity to RDY (about 1 km.) facilitated a comparison between the response functions from these 2 sites. Figure 6.1, shows the apparent resistivity (top) and phase (bottom) response for RDY (vertical lines) and SHW (horizontal lines) superimposed for both orthogonal directions. As the 4 phase response

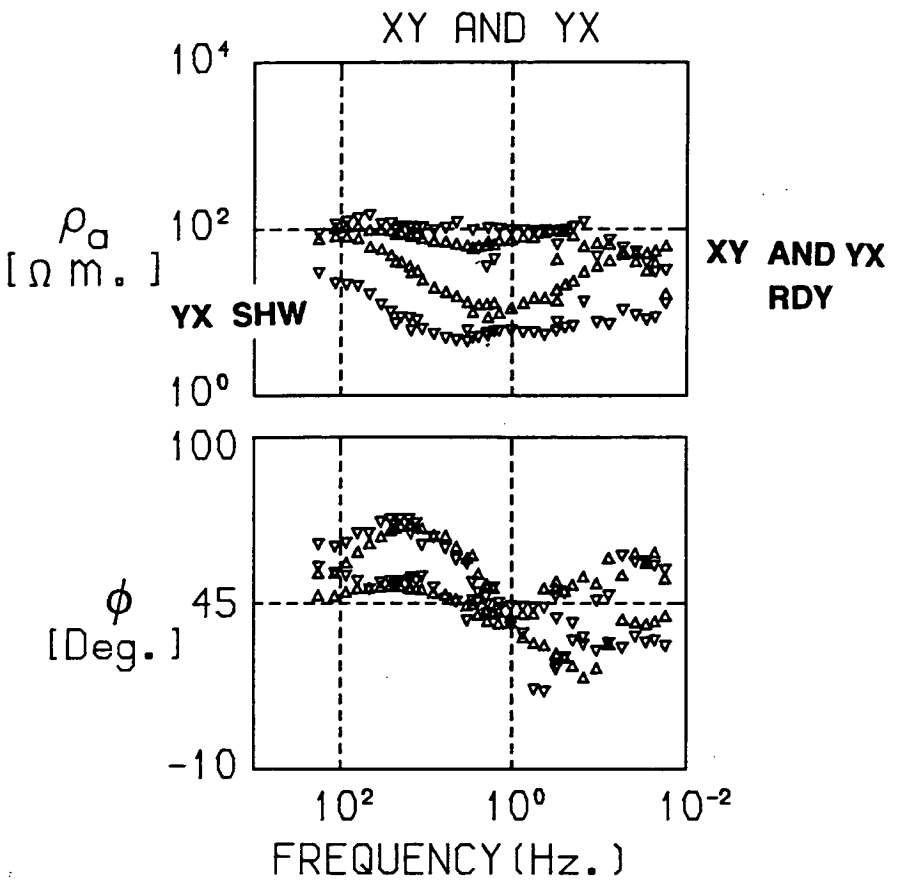

Figure 6.1: The apparent resistivity (ρ_a) and phase (ϕ) response functions for 2 orthogonal directions (XY and YX) at sites RDY (triangles) and SHW (deltas), located about 1 km. apart.

The phase curves from both sites and directions are very similar and all 4 such curves show the same asymptotic high frequency characteristics. Correspondingly, 3 of the apparent resistivity response functions are broadly similar, but the fourth one (YX at SHW) is shifted down by a frequency independent factor. This is thought to be the result of static shift.

functions are very similar this indicates that the structure is relatively uniform between both sites. Correspondingly, 3 of the apparent resistivity curves demonstrate the same high frequency asymptotic properties. The fourth one, the XY curve for SHW, shows the same general shape but is clearly shifted down by half a decade.

Geological mapping of this area (BGS 1975) tentatively suggested that there was an igneous dyke situated close to SHW. As this was more accurately identified by its aeromagnetic signature (fig. 6.2), the author considers that the presence of a resistive and magnetic intrusion is the most obvious explanation for the observed static shift.

Since the invariant impedance (eqn. 6.2.3) at SHW did not appear to be strongly affected by the static shift, no correction was made prior to 1-D modelling. However, to achieve an optimal fit during 2-D modelling, the phase response function alone was used.

6.3.3. Multi - Dimensional Magnetotelluric Modelling

Various 2-D modelling procedures can be applied to MT observations. They assume that the response function can be rotated to a strike direction in which the geoelectric model cross-section is constant for large distances (section 2.4). Several analytical solutions have been obtained for simple structures (e.g. across a fault; d'Erceville and Kunetz 1962, a vertical dyke; Rankin 1962 and a catalogue of early models has been given by Porstendorfer 1975). In more complex situations, Maxwell's equations and the appropriate boundary conditions are usually discretized prior to a numerical solution. There are 4 basic methods for the subsequent calculation of the 2-D forward model response, as reviewed by Patra and Mallick (1980). These are the finite difference (e.g. Brewitt-Taylor and Weaver 1976, Hill 1987, Harinarayana 1987), finite element (Wannamaker *et al.* 1986), integral equation (Hohmann 1983) and transmission line analogy (Brewitt-Taylor and Johns 1980) methods.

Some of these forward modelling methods have been incorporated into linearized 2-D inversion schemes (Jupp and Vozoff 1975, Oristaglio and Worthington 1980), which allow the model resistivity values to be automatically adjusted to minimize the difference between the observed and calculated response functions. The computational load for linearized schemes

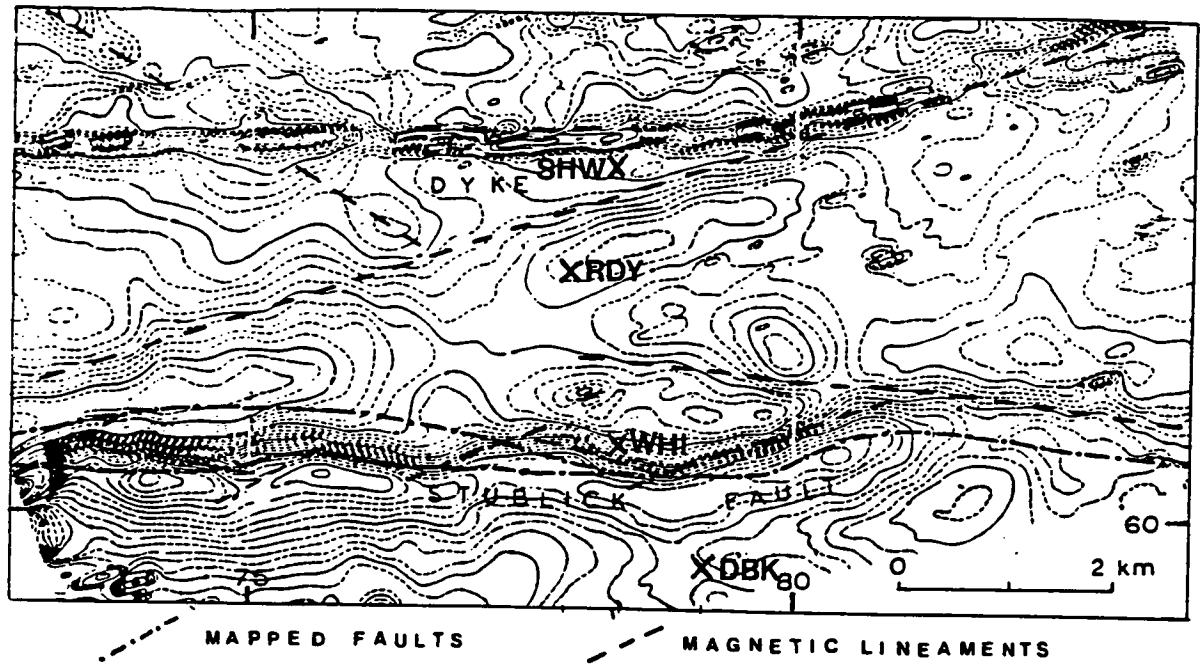

Figure 6.2: A map showing the results of a detailed aeromagnetic anomaly study published by Cornwell and Evans (1986) across part of the Stublick Fault in Northern England. The location of 4 of the MT sites (DBK, WHI, RDY and SHW) have also been superimposed.

Note in particular the presence of a strong linear magnetic anomaly close to SHW which has been interpreted as being due to an igneous dyke intrusion. The author considers that this is a likely source of telluric field distortion and static shift on the MT response functions from this site.

is heavy in 2-D and prohibitive for automated inversion of 3-D models. If 3-D modelling is attempted, the problems are usually solved either numerically by trial and error forward modelling (e.g. several papers in Vozoff 1986) or by using analogue scale models of the region. These methods have been applied to the study of EM induction in Britain by Dosso *et al.* (1980) and the methods more recently described by Dosso *et al.* (1989).

6.4. MODELLING PROCEDURES FOR NORTHUMBRIAN OBSERVATIONS

This author performed modelling of the Northumbrian geophysical data set in the following stages, prior to interpretation (chapter 8):

1. The Bostick transformation was used to produce a resistivity contour plot on an MT traverse-depth section (section 6.4.2).

2. An exploratory modelling procedure generated detailed 1-D parametric M.T. and/or D.C. resistivity models for all of the soundings (section 6.4.3).

3. A pseudo 2-D geoelectric section was computed by undertaking successive 1-D constrained inversions on the response functions for several (<= 5) adjacent response functions along a traverse (section 6.4.6).

4. Gravity models were obtained along 4 north-south trending profiles by using a semi-automatic inversion procedure (sections 6.4.7 and 6.4.8).

5. An experimental joint, constrained gravity and MT model was evaluated over part of the MT traverse (sections 6.4.9 and 6.4.10).

6. A 2-D MT model was computed for the soundings around the Stublick Fault (section 6.4.11).

The first 2 of these modelling methods require little background geological or geophysical understanding of the area, but after a brief explanation of their results (section 6.4.5), the remaining more interpretative procedures are described. For a number of the above stages, the methodology employed is discussed in some detail and special attention is paid to the ideas and computer programs which are unique to this study.

6.4.1. Northern England Geoelectric Profile

The distribution of soundings made by this and other researchers have already been discussed (section 3.5). Many of the sites lie along a 110 km. SSE–NNW trending profile (the 'long traverse') from the granite intruded Alston Block in Northern England, across the strike of the Northumberland sediment filled trough and over the southern margin of the Lower Palaeozoic rock outcrop in the Southern Uplands of Scotland (fig. 6.3). In some areas, particularly in Northern Northumberland, the density of geoelectric soundings is sparse and so the response functions from some more distant soundings were projected onto the 'long traverse' (e.g. GIB and KSF). A more detailed study (e.g. gravity and 2–D MT modelling) was also undertaken for a number of the MT sites around the Stublick Fault on the northern edge of the Alston Block.

6.4.2. Bostick Contour Section

The Niblett–Bostick transformation (eqns. 6.2.4 and 6.2.5) was used to compute estimates of the resistivity/depth variation for sites along the 'long traverse'. If two or more soundings were less than 0.5 km. apart, then a smoothed composite response function (using ZFIT; Appendix – B) was processed (e.g. HIL). The transformed values were then contoured to obtain a pseudosection (e.g. Ranganayaki 1984).

Static shift and noisy observations produced short wavelength variations in the response functions and scattered their transformed values. Computer packages were initially used to contour the resistivity data in the 2–D traverse/depth plane. These attempts were unsuccessful because of the very high density, and unequal spacing of the data in the vertical direction, compared with the lateral separation between sites. These problems were alleviated by preliminary, robust numerical smoothing of neighbouring resistivity estimates in both directions. This then facilitated hand contouring by reducing the presence of spurious features. The resulting semi–quantitative geoelectric sections are shown in fig. 6.4; the upper showing the near surface structure (to 3 km. below sea level), whilst the lower diagram displays the total crustal structure. On the whole, inferences were more confidently drawn from the shallow section because of the higher density of measurements.

Figure 6.3: The location of some of the most relevant geophysical studies and their relationship to the Solway Firth coastline (bold), the Southern Uplands (medium line) and the major faults around and within the Alston Block (dashed and dotted lines).

The locations of the MT sites have been reproduced here (large dots; c.f. fig. 3.5). The thin line drawn diagonally across the map represents the 'long profile' upon which many of the 2-D cross sections (e.g. figs. 8.9a and 8.19a) are based.

The location of the 4 (north-south) gravity profiles (thick dashed lines) are shown extending from 60000N to 50000N. The light dashed lines represent the position of the seismic profiles whose results have been published by K (Kimbell *et al.* 1989), E3,E4 and E5 (Evans *et al.* 1988), CH (Chadwick and Holliday 1991) and CSSP (Bott *et al.* 1985).

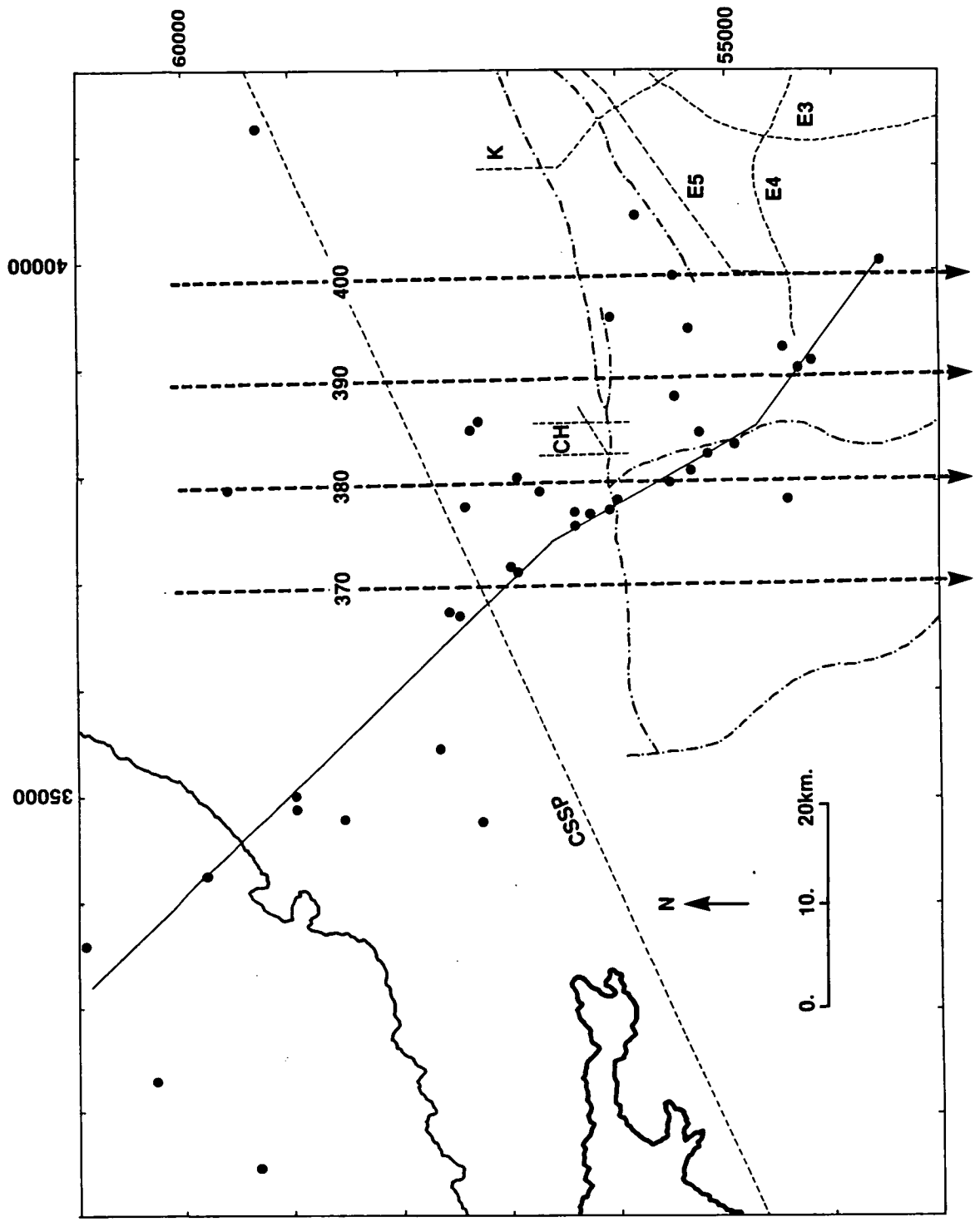
60000
55000
40000
35000
K
E5
E4
E3
400
390
380
370
CH
CSSP
N
0.
10.
20km.

Figure 6.4: The variation in the Bostick determined resistivity with depth along the line of the 'long profile'. The resistivity values have been smoothed and contoured on a logarithmic (base 10) scale. Figure 6.4a shows the shallow (< 3.5 km.) structure whilst fig. 6.4b gives the observed deeper variation (< 30 km.) at the corresponding MT site locations annotated at the top.

The near surface sedimentary rocks usually have a lower resistivity (less than 1.6 $\log_{10}$ resistivity; 40 Ω.m.), than the more deeply buried ones. A high resistivity basement (up to 3.0 $\log_{10}$ resistivity; 1000 Ω.m.) is found in the vicinity of ROO/HIL corresponding to the Weardale granite batholith. Elsewhere, the sedimentary rocks are underlain by more moderately resistive basement rock (about 2.0 $\log_{10}$ resistivity; 100 Ω.m.). Some of the smaller scale structures in this model are not dissimilar to some of the more 'sophisticated' ones which are presented later.

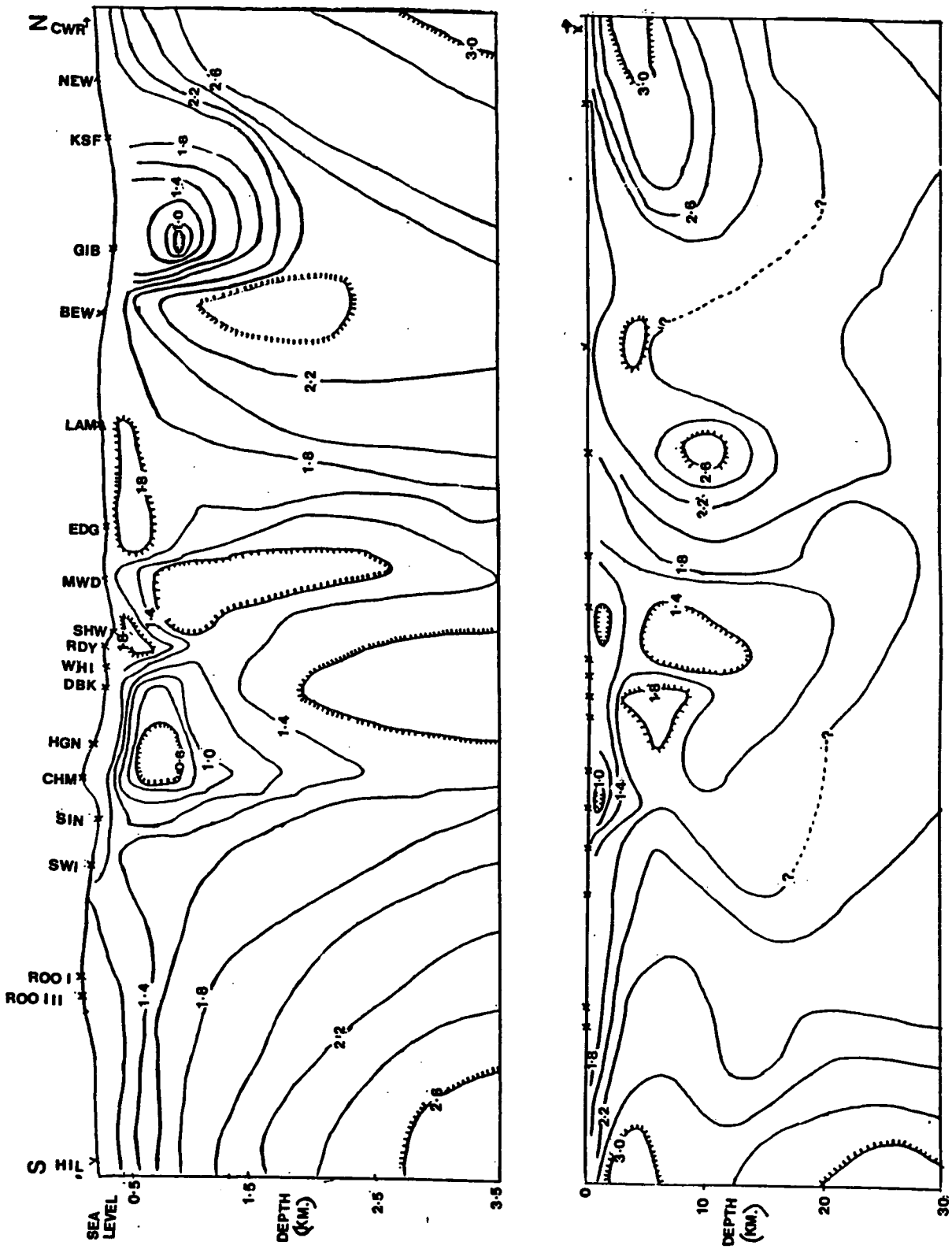
N
CWR
NEW
KSF
GIB
BEW
LAM
EDG
MWD
SHW
RDY
WHI
DBK
HGN
CHM
SIN
SWI
ROO I
ROO III
S
HIL
SEA LEVEL
0·5
1·5
2·5
3·5
DEPTH (KM.)
0
10
20
30
DEPTH (KM.)

6.4.3. Exploratory Geoelectric Modelling

The aim of this modelling stage was the acquisition of a well fitting, yet interpretable, parametric 1-D MT and/or D.C. resistivity model and then the consideration of its uniqueness.

The adopted method used a linearized 1-D inversion scheme to test a number of starting models in turn. The aim was to identify the resulting models for which the corrected parameter values produced the best fit. The retention of those models which produced similarly small misfits helped to show the range of equally-acceptable-models and the joint parameter resolution. From the resulting display the author was able to identify the "simplest model" (i.e. the one with the fewest layers; section 6.2.4) which was consistent with the acquired observations and assess its overall uniqueness. Since the relevant computer program has been described elsewhere (Appendix - B: **MAXMUL**) no further description of the method is required here.

It was found that the basic modelling method was very sensitive to grossly erroneous observations. Occasionally, an excessively influential outlier had to be removed manually and the modelling procedure repeated to improve the fit to the majority of the observations. Manually transcribed response functions (section 3.5.3) were especially prone to such errors. In a future adaptation of **MAXMUL** it is recommended that the iterative procedure on the acquired suite of best fitting models is repeated with the outliers downweighted (c.f. sections 6.4.6 and 6.4.8).

This exploratory modelling method was routinely used on all of the MT and D.C. resistivity response functions within the study area (fig. 3.5) and the complete results are given in Appendix - C. Four examples, taken from sites spread along the 'long traverse' (ROO I, RDY, MWD and CWR) are reproduced in fig. 6.5.

The range of models from RDY and CWR indicates that the near surface (< 100m.) and deeper structure (> 50 km.) cannot, in general, be resolved by the frequency band limited MT response functions. The lower frequency observations collected at ROO I allows lower crustal and upper mantle resistivities to be estimated, but as observations were not acquired in the middle frequency bands at this site (between about 0.1-10 Hz.; Novak 1981),

Figure 6.5: Examples of the exploratory models computed from 4 sites along the length of the 'long traverse' (reproduced from Appendix - C). The best fitting (minimum misfit) model is usually displayed as a continuous line and the 5-10 almost equally acceptable models shown with dashed lines.

The range of models from ROO I is much greater than those from the other sites, reflecting the larger range of error in the impedance estimates (i.e. they had been manually transcribed; section 3.5.2). Conversely, MWD shows more detailed near surface geoelectric structure because of the additional D.C. resistivity observations used to produce this joint model.

The annotation gives a crude interpretation of these models. The relatively conductive Carboniferous age Cover of sedimentary rocks (CC) extends from ROO I to beyond MWD but locally can show variable resistivities (e.g. the postulated Whin Sill: WS). There is little evidence of such a layer at CWR where the near surface layer is interpreted to be a 'Basement Rock' (BR). The sub-sedimentary resistivity at ROO I is relatively high and reveals the presence of the concealed Weardale granite (G). Underlying the entire region, a High Conductivity Layer (HCL) extends from near the mantle (M) at ROO I, to close to the surface at RDY and MWD before descending further beneath the Northumberland Trough.

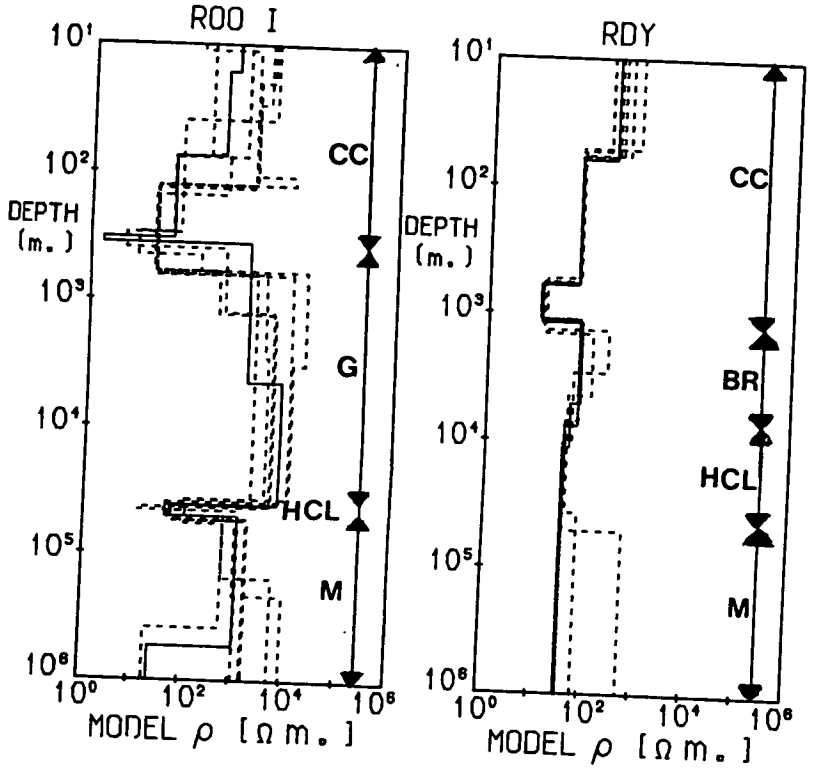
ROO I
RDY
DEPTH (m.)
CC
G
HCL
M
BR
MODEL ρ [Ω m.]

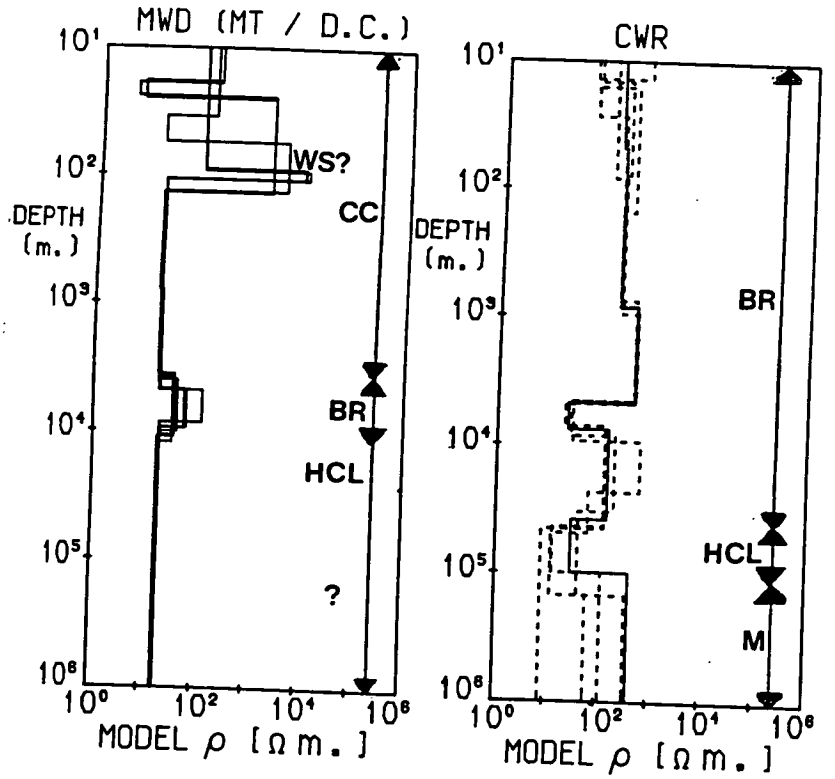
MWD (MT / D.C.)
CWR
DEPTH (m.)
WS?
CC
BR
HCL
?
M
MODEL ρ [Ω m.]

then the models are not as well determined overall than those from neighbouring sites. The wider range of parameter values for the resistive layers reflects MT's ability to detect preferentially more conductive sequences of rock (section 6.2.6).

The range of models for MWD was derived jointly from MT and D.C. resistivity observations. In general, the author found that this method could provide more information concerning thin, near surface resistive features than the modelling of the MT response function alone (more examples can be found in Appendix - C). However, if the response functions were incompatible (e.g. due to noise or lateral variations in resistivity structure between the electrodes) a joint model was not readily attained. Furthermore, the joint method was unable to resolve the deeper structure as well as the MT models (e.g. ROO II in Appendix - C). This was thought to be the result of a deficiency in the computer program rather than in the method itself.

These exploratory models were found to be particularly useful for determining the 'least information' (minimum number of layers) which can be gleaned from the response functions and estimating the range of possible parameter values. For example most of the models between 600m. and 35km. depth at ROO I suggest the presence of 2 layers. However, the distribution of equally-acceptable models implies that they cannot be independently resolved from this response function. Constraining information is needed if further clarification of the structure is required.

This author considers that in future, larger and more realistic parameter bounds would be obtained from the exploratory MT modelling method if the most extreme response functions at each site were modelled separately. This suggestion is supported by a comparison of borehole data and MT model results. Figure 6.6 shows the results of an MT sounding, acquired by this author, in the Worcester sedimentary basin with those from a smoothed resistivity log from a nearby borehole. The invariant impedance has resulted in a very narrow range of 1-D MT models, which are broadly similar in shape to the resistivity log, but the resistivities are overestimated, particularly at the bottom of the basin. In contrast, the most extreme models obtained from independently analysing the major and minor impedances show much broader ranges of resistivities which more accurately encompass the borehole values.

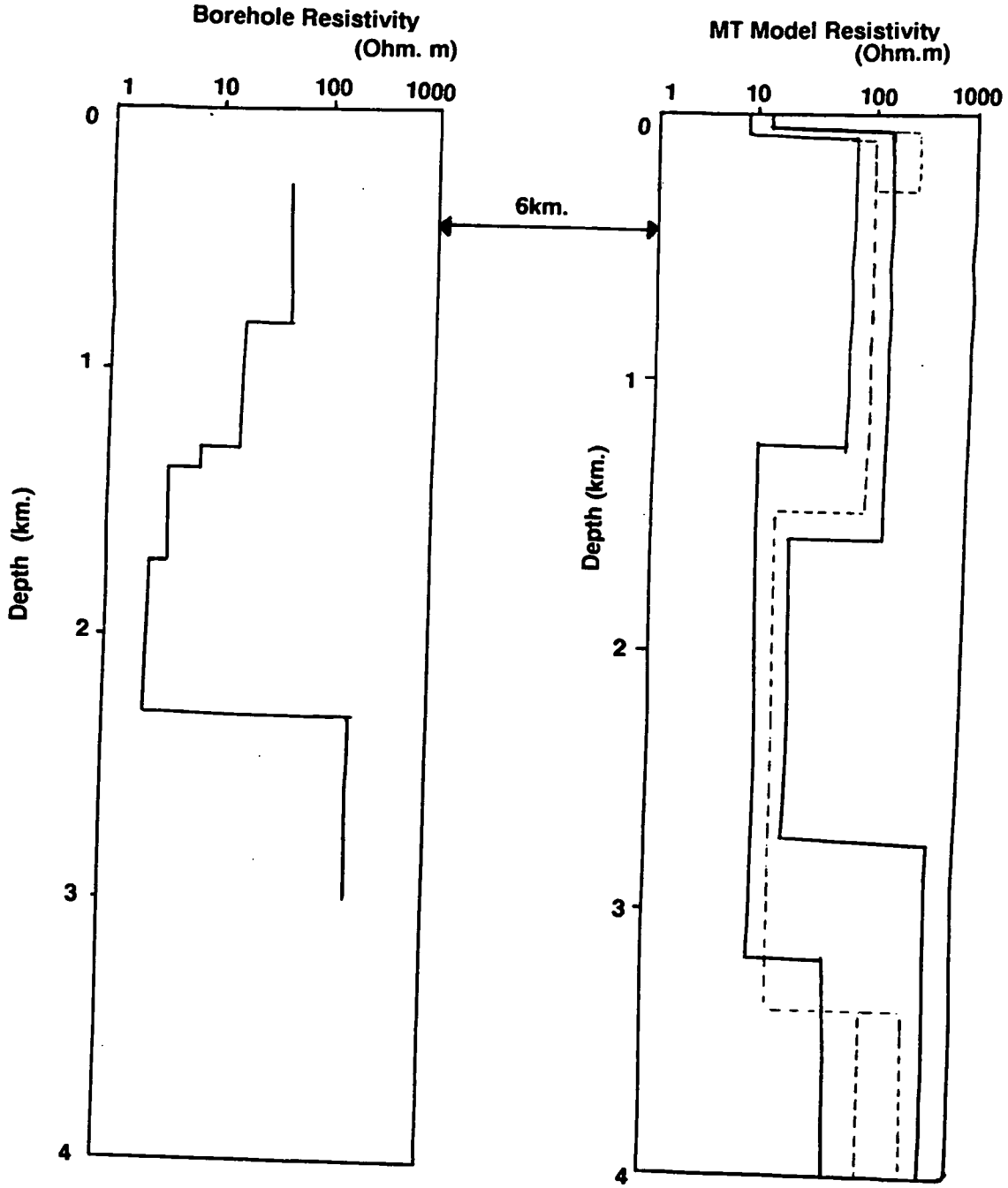

Figure 6.6: A comparison of the resistivities determined from a borehole in the Worcester sedimentary basin with models from a nearby MT site. Exploratory modelling of the 'effective' invariant response function (dashed line) has produced an unrealistically narrow range of models. They are unquestionably similar to the borehole log, but a better comparison can be drawn with the extremal models acquired from modelling the major and minor impedances separately (solid lines).

Figures 6.6 and 8.20 (later) also underline the widely experienced problem with comparing surface and downhole geophysical measurements.

As the author has developed the exploratory modelling method into a technique for routine use, future work should concentrate on determining its merits relative to the other parametric techniques discussed in section 6.2.3.

6.4.4. Comparison with the Models obtained from Previous Studies

In order to assess the results of re-processing and re-modelling data during this study, some of the invariant response functions and exploratory 1-D models have been compared with the results published from the earlier study (Harinarayana 1987). Figure 6.7 (a-d) compares the results of the earlier Monte-Carlo modelling (left hand side) with the exploratory modelling (right hand side) from this study for the MT sites ROO III, SIN II, LAM II and CWR.

Re-processing using the constrained impedance procedure, has produced a much smoother response function at all 4 of the sites. The greatest differences are to be found at the lower frequencies. For example, both ROO III and SIN II show that the apparent resistivity is higher (> 100 Ω.m.) for the new results, at frequencies below 0.1 Hz.. This is reflected in the 1-D model for SIN II, which shows a much higher and more realistic resistivity for the Alston Block granite, below 2km. depth. The new model results for ROO III show an apparently low granite resistivity at depths from 1km.. It is, as yet, unclear if a geophysical or processing explanation is required for the corresponding change in shape of the response function at 0.5 Hz..

The low frequency portion of both the apparent resistivity and phase response functions at LAM II are now markedly different. As a result, a thin highly conducting layer (the 'H.C.L.') has been resolved by all of the best fitting exploratory models, beneath a more resistive basement. In a similar fashion, the response function from CWR had previously demonstrated an unrealistic change in the apparent resistivity curve, near to the 'dead frequency band'. This author now considers that this was the result of noise induced bias (section 4.7.4). Quite justifiably, the original models were primarily based on the phase response function, but now constrained impedance estimation has ensured consistency between the apparent resistivity and phase response functions. The resulting models imply a relatively complex structure exists

Figure 6.7: A comparison of the response functions and models published following the original investigation (left hand side; from Harinarayana 1987), with those obtained after reprocessing/remodelling in this study (right hand side).

The reprocessing has generated a smoother response function and at the well determined parts of the original response functions (usually > 1Hz.), the results are very similar. At the lower frequencies there are significant differences which are reflected in the 1-D models. For example, the original response function acquired at SIN II shows a considerable scatter in both the apparent resistivity and phase estimates at the low frequencies. The reprocessed results are significantly smoother and different at these frequencies. The exploratory model also shows a resistive layer from a depth of 2 km. (the Weardale granite) overlying a more conductive zone. Neither of these layers were evident in the original results. Reprocessing the data from LAM and CWR also shows a similar enhancement of the lower crustal layers. Inconsistencies which were present between the observed and computed response functions have been removed by applying the dispersion relations during constrained impedance estimation.

The modelled results from ROO III are possibly less satisfactory. The 2 sets of models show similar sedimentary layers but reprocessing has introduced a small inflection in the response function at 0.5 Hz.. As a result, there is now less clear evidence of the granite layer.

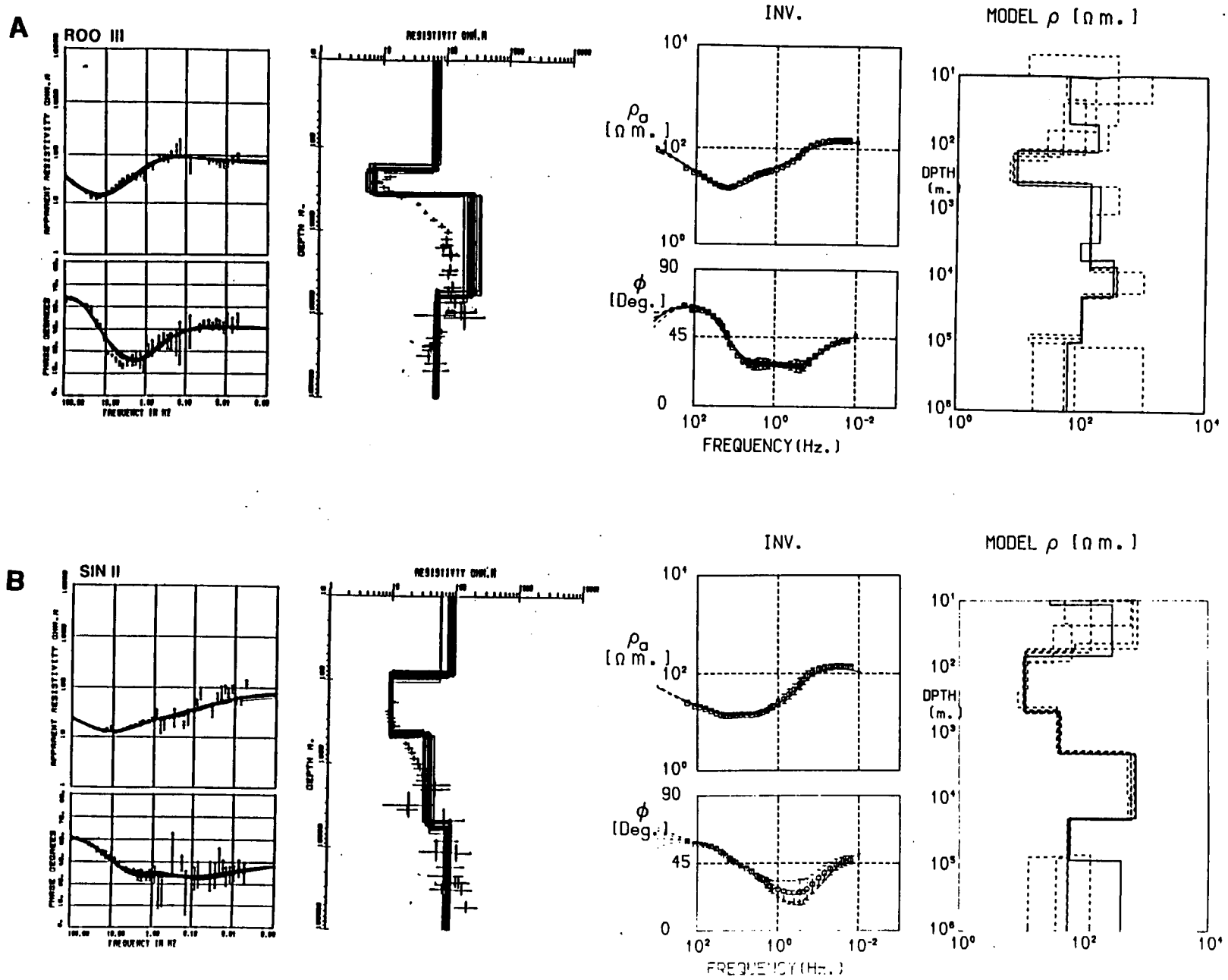
A
ROO III
INV.
MODEL ρ [Ω m.]
ρa [Ω m.]
φ [Deg.]
DPTH (m.)
FREQUENCY (Hz.)
B
SIN II
INV.
MODEL ρ [Ω m.]
ρa [Ω m.]
φ [Deg.]
DPTH (m.)

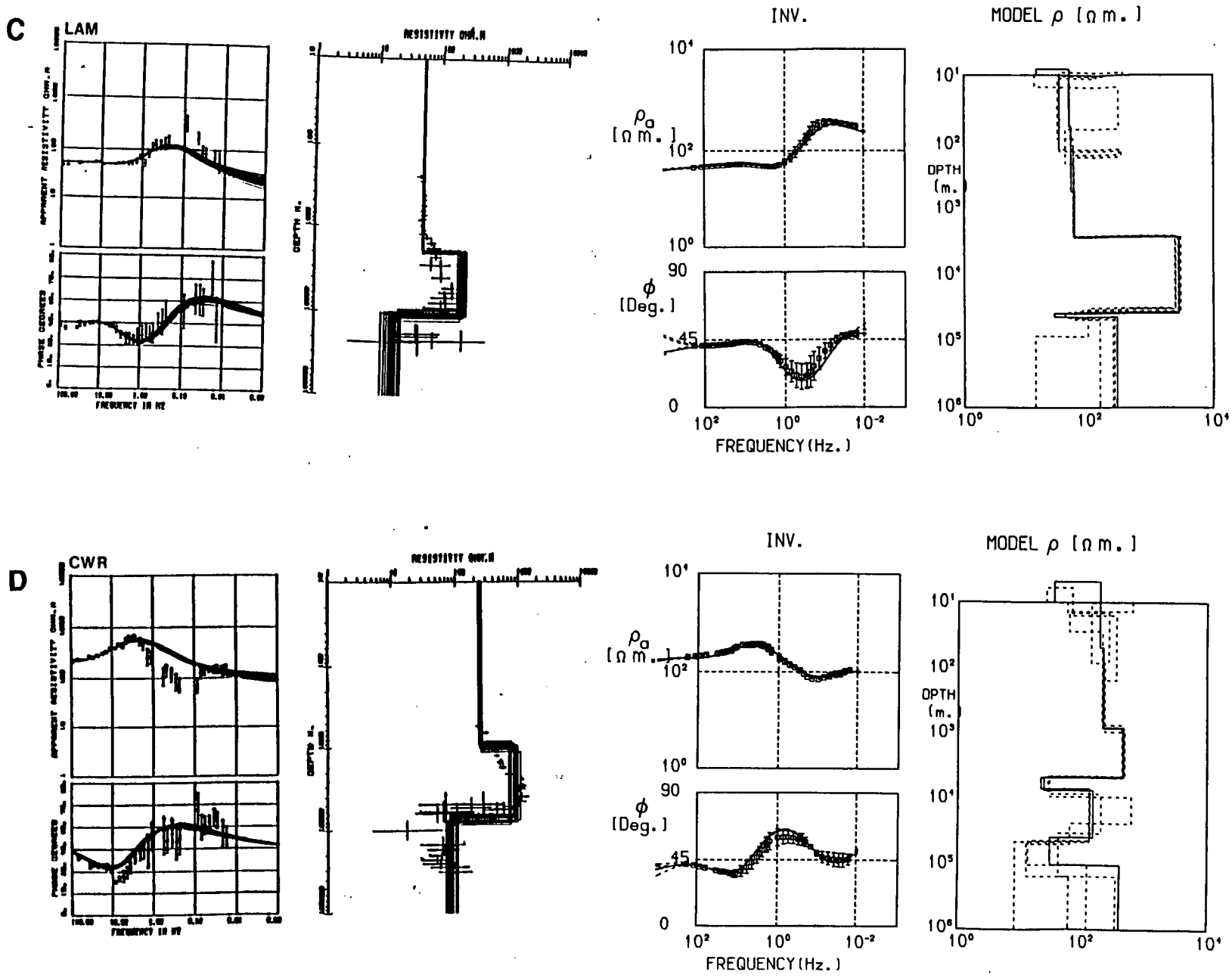
C
LAM
INV.
MODEL ρ [Ω m.]
ρ_a [Ω m.]
ϕ [Deg.]
FREQUENCY (Hz.)
DPTH (m.)
D
CWR
INV.
MODEL ρ [Ω m.]
ρ_a [Ω m.]
ϕ [Deg.]
FREQUENCY (Hz.)
DPTH (m.)

below 1km. depth.

As the high frequency response functions were virtually unchanged, the sedimentary layer has been modelled in a similar fashion in both the current and the earlier studies. The models however imply that a much wider range of structures may be present in the top 200m.. For example, there may be some thin, ill resolved resistive beds within this rock layer at LAM II.

6.4.5. Preliminary Interpretation of the Results

A much more complete review of the known geology of Northern England is given in the next chapter, but in order to undertake constrained MT and gravity modelling it is necessary to perform a preliminary interpretation of the models presented so far.

The most conspicuous feature of the Bostick geoelectric profiles (fig. 6.4) is the presence of low resistivities close to the surface (typically 4 - 60 Ω.m.: $\log_{10}$ resistivity 0.6 - 1.8) and a higher resistivity basement (80 to 8000 Ω.m). Geological mapping has identified a widespread covering of Carboniferous age sedimentary rocks (C.C.) which are known to extend to depths which are comparable to this geoelectric boundary. It is very likely that some or all of the more conductive regime is related to this rock type.

This view is further supported by consideration of the resistivity structure as determined from the limited number of boreholes (located later in fig. 7.1) in Northumberland. The electrical resistivity logs show locally very variable resistivities (e.g fig. 2.6: Stonehaugh and Rookhope; Dunham *et al.* 1965) but after using a Walsh transformation to perform a low pass filter (Gubbins *et al.* 1971, Lanning and Johnson 1983) the smoothed bulk resistivities are usually found to be of the same order as those determined from surface MT observations (fig. 6.5) and in the range from 10 to 80 Ω.m. Although MT cannot possibly resolve the same level of detail as observed in the borehole, some structure is discernable within the sedimentary sequence at most of the sites.

The level of porosity (13% in the Stonehaugh borehole; Scott and Colter 1987) and resultant water saturation seem to be the primary cause of such

low resistivities (section 2.9.2) in these rocks. In contrast, it is anticipated that the underlying igneous or metamorphic 'Basement Rock' (B.R.) has a lower porosity and consequently higher electrical resistivity. The Bostick resistivity contour section (fig. 6.4) correspondingly shows such a resistivity increase and the 1.8 $\log_{10}$ (= 63 Ω.m) resistivity contour is considered to separate the 2 rock units approximately, along the length of the 'long traverse'. The majority of the exploratory MT models (fig. 6.5 and Appendix - C) also show a rise in the resistivity to about 100 Ω.m at depths, typically, of between 0.5 and 3.5 km. Site CWR, situated on the Lower Palaeozoic outcrop in the Southern Uplands, provides further confirmation of these higher resistivities for the concealed B.R. as the model demonstrates significantly higher surficial resistivities than elsewhere (200 Ω.m).

The electrical basement shows considerable lateral variations in resistivity. In particular, the resistivity in the vicinity of the Alston Block (e.g. ROO I in fig. 6.5) is markedly higher than elsewhere (up to 8kΩ.m.). As discussed more fully later, these resistivities are attained at depths comparable to the known granitic intrusion in the Rookhope borehole (Dunham *et al.* 1965). Many of the exploratory models suggest that a more conductive layer (the 'High Conductivity Layer'; H.C.L.) exists within the more resistive mid and lower crustal rocks.

6.4.6. Pseudo Two Dimensional Modelling

The exploratory method described in section 6.4.3 provides models which are ideal for those who are wary of over-interpretation of the response functions. This author considers that the 'fuzziness' of these individual 1-D models can be reduced by the imposition of constraining information from surrounding sites. This method assumes that a sufficiently high density of soundings has been performed for the exploratory models to show gross geoelectric structures (' structural marker beds'), which can be traced from site to site. In such a situation, the model parameters (either the resistivity or depth) should, in general, change imperceptably from one site to the next. By quantifying this geophysical argument within the mathematical concept of constrained regression (section 5.7.5), it was anticipated that the remaining free parameter values would be better determined and site to site variability

would be reduced. Such a procedure can be regarded as interpretative modelling; because the user has to identify marker beds by using his structural knowledge, but a numerical procedure is subsequently used to derive the best fitting model subject to the applied constraints.

An interactive modelling program (**MAXMAY** in Appendix - B) allowed this author to assign individual model layers, observed at a particular MT site, to a laterally more extensive structural unit. Constraints were then applied to the regression equations which minimized the difference between the chosen layer thicknesses or resistivities at these sites. Thus the validity of an identified structural unit could be substantiated by considering the change in the misfit. Finally, once a minimum misfit model had been attained, any observational outliers could, optionally, be downweighted. Further iterations were then performed to revise the parameter values. The result was a composite pseudo 2-D geoelectric section with site-to-site correlation and structural units mapped out between them.

The method used must still be regarded as being experimental, but an example of it is given here. Figure 6.8a shows a simplified monochrome reproduction of a colour display which was generated by the computer program on the display terminal. At the top of this figure, 4 MT apparent resistivity response functions (ρ) are shown from SWI I, HGN, DBK and MWD (denoted by stars). The first 2 of these sites also display their MT phase response functions (ϕ), whilst the latter 2 show the D.C. resistivity observations (ρ_{DC}) as a function of half-spread length (AB/2) instead. In the lower portion of this figure, the initial pseudo 2-D model section, for the relevant sites on the traverse (line 380E), has been redrawn. This is based on the individual best fitting exploratory 1-D models. Finally, the forward model responses have been evaluated and superimposed on the observed (continuous line) ones.

The 'least information' exploratory models (section 6.4.3) presented in Appendix - C demonstrated a persistent and well resolved conductive marker bed, near to the presumed base of the Carboniferous age strata at 3 sites (CHM, HGN and DBK). It was anticipated that changes in the thickness of this layer had greatest significance, so that the difference between the resistivity at these sites (HGN and DBK) was numerically constrained (eqn. 5.7.8b) to be as

Figure 6.8: An illustration of the pseudo 2-D geoelectric modelling approach discussed in section 6.4.6.

In the top part of this diagram, the observed apparent resistivity (ρ in Ω.m.) and phase (ϕ in degrees) (denoted by small stars) have been plotted as a function of frequency (F in Hz.) for 4 MT sites (SWI, HGN, DBK and MWD) along part of the 'long profile'. At the latter 2 of these sites, the phase observations have been replaced by the D.C. resistivity observations (ρ_{DC}) up to a half-spread length (AB/2) of 1km. Beneath these response functions a selected 1-D exploratory resistivity-depth model has been drawn for each of these sites. The relative spatial separation between the models has been preserved.

A number of these distinct layers were deemed to be part of a single more extensive structural unit ('marker beds'), so the pseudo 2-D modelling technique was used to reduce their site-to-site differences. Constraints were applied to minimize the difference between the layer resistivities which have been indicated by a dashed line. Figure 6.8b shows that after the application of constrained regression, the discrepancy in the resistivity of the granite layer at SWI I and HGN has been removed and some of the model depths have been slightly altered. This was achieved without appreciably changing the misfit between the observed and computed (continuous line) response functions.

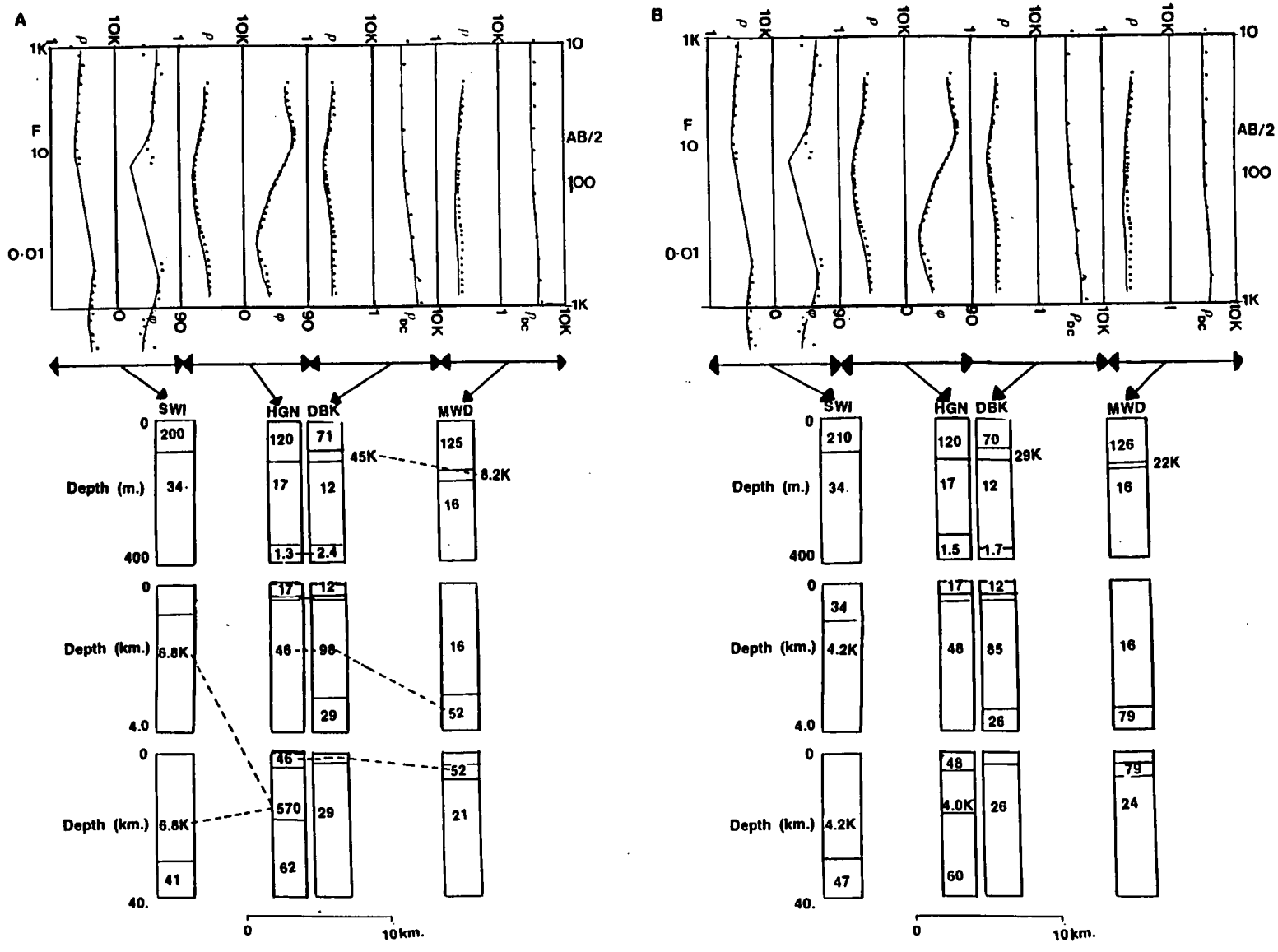
A
B
1K
F
10
0·01
AB/2
100
10
1K
10K
1
ρ
0
90
φ
ρ_ac
SWI
HGN
DBK
MWD
Depth (m.)
Depth (km.)
0
400
4.0
40.
200
34
120
17
1.3
71
12
2.4
125
16
45K
8.2K
6.8K
41
46
570
62
98
29
52
21
210
4.2K
47
48
4.0K
60
70
29K
1.5
1.7
85
26
126
22K
79
24
0
10km.

small as possible. Constraints were similarly applied to the other structural marker layers indicated in fig. 6.8a (e.g. the granite: 6.8 KΩm at SWI I and 570 Ωm at HGN). Figure 6.8b was attained after iterating to obtain the best fitting model subject to these constraints. In this example, the depth to the layer boundaries demonstrated modest changes (e.g. 15% increase in the depth to layer boundary at 3km. below DBK). More importantly, the ambiguity in the resistivity of the granite has been removed without appreciably changing the fit.

This method was repeated for sets of 4-5 sites along the main traverse. Whenever possible, the response functions from MT or D.C. resistivity sites which were slightly off this traverse (e.g. ROO I) were also used to constrain the models for those sites which lay directly on it. The final models were then collated and transcribed into a readily interpretable format (figs. 8.2a, 8.9a, 8.17a and 8.19a).

This method could, in the future, be adapted to allow the imposition of strong constraints (eqn. 5.7.8a). If for example, a bulk resistivity has been determined from a borehole, then by fixing the value of the corresponding MT model parameter, the range of possible values open to the remaining parameters is immediately reduced. This could help to alleviate the problem of equivalently resolved layers.

Instead of performing pseudo 2-D modelling upon the minimum misfit model, the above constraining procedure could perhaps be further enhanced if the starting model is chosen from the acceptable exploratory range on the basis that it demonstrated the characteristics most consistent with models computed from adjacent sites. This would require an automatic selection procedure to identify the common layers.

6.4.7. Gravity Anomaly Observations

The next section describes an automatic method for calculating a simple 2-D gravity model for a collection of Bouguer anomaly observations. The particular observations used in this study were obtained from a gravity data base (R. Hipkin; person. commn.) along 4, 100km. long north-south trending profiles (fig. 6.3) which cross from the Alston Block into the southern part of the Northumberland Trough.

Prior to modelling, a regional trend was removed by calculating the coefficients of a least squares fitting line across each profile. The resultant anomalies (shown later with the models in figs. 8.11a–d) are dominated by the presence of a large negative anomaly (about −20 mgal) which is primarily attributed to the concealed low density Weardale granite batholith (section 7.4.1), embedded in the higher density Lower Palaeozoic basement. At the surface, a layer of low density Carboniferous sediments of variable thickness is assumed to have produced a second overlapping gravity anomaly

6.4.8. Two Dimensional Gravity Modelling

Two dimensional gravity models of Northumberland were computed, by this author, using a combined interactive and automatic modelling technique. Although the methods described below were devised to find a gravity model across this particular region, the ideas developed could be more generally applied to other problems in the future.

In an ideal sedimentary basin, gravity anomalies would only arise from spatial variations in the thickness of two homogeneous rock units with different densities (i.e. a low density, but homogeneous sedimentary sequence of variable thickness and extent overlying a metamorphosed, denser basement rock). If rock density data were known for both rock types, then the depth to the base of the sedimentary covering rock could be determined. In the real Earth, neither rock unit is homogeneous due to the presence of near surface variations, igneous intrusions, differential metamorphism etc.. As a result, the observed gravitational anomaly is the complex superposition of the signatures of various constituent structural units whose densities, geometries and even exact presence are largely unclear. In these situations, little unique quantitative information can thus be gleaned from gravity anomalies *alone*. The nature of the gravity problem is such that the incorporation of constraints is not just desirable, but essential to the acquisition of a useful set of model parameters.

Borehole information is sparse in Northern England and although Kimbell *et al.* (1989) attempted to account for vertical density variations within the sedimentary layer using seismic information (fig. 7.10), most models including those presented in this study, cannot accommodate any variations at all within

the main structural units.

Traditionally, much interpretation has been based upon trial-and-error forward gravity models. These models can be easily adapted to enable the incorporation of any constraining information (e.g. surface geological observations, seismically determined boundaries or frequently ad hoc educated guesses). A number of least squares based modelling procedures (e.g. Tanner 1967, Pedersen 1979, Silva and Cutrim 1989) have been developed to model either the surface variation of a sedimentary type layer or a body within the basement but they cannot readily model multi causative body problems.

In the author's opinion, most gravity modelling is biased towards the interpreters initial prejudice. Moverover, the uniqueness of the resulting solution has seldom been explored. To alleviate some of these deficiencies, the author chose to undertake 2-D gravity modelling from a perspective which was broadly similar to that already described for the MT response functions. The 2 aims were thus to a) find a gravity model which produced a small misfit but which was not influenced by excessive interpreter bias and b) explore the model uniqueness and/or improve parameter resolution by the incorporation of additional constraining information. The details of the relevant computer program are given in Appendix - B (**MAXMAY**) and an illustration of the full method as it was applied for a profile along line 380E is presented here in figs. 6.9a-d and described below.

The initial specification of any starting model inevitably biases the final solution, so for this study, the model was chosen to be relatively simple and account only for the known gross structural features. As sedimentary rocks are known to cover this region to variable depths (section 6.4.5), then fig. 6.9a shows that the initial model for this layer was assigned a thickness of 1 km. and extended beyond the edges of this profile to avoid edge effects. The position of the initial granite intrusion matched the limits of the main anomaly. Like previous investigations (section 7.5.1), the base of this intrusion was assigned to be at a depth of 10 km. and its upper surface was placed 5 km. from the surface.

Rock samples (Yassi 1983, Lee 1986, Evans *et al.* 1988, Kimbell *et al.* 1989) have estimated the density of the granitic rocks to be in the range from 2.6 to

Figure 6.9: A demonstration of the capability of the program **MAXMAY** to find a well fitting 2-D gravity model and explore its range of uniqueness.

An initial model (lower portion of fig. 6.9a) consisting of a granite intrusion and sedimentary layer (of density contrast RHO1 and RHO2 respectively, compared to the basement) was specified to emulate the observations (upper portion). These layers were then subdivided into a series of blocks (labelled 1 to 12 for the granite and 13 to 28 for the sedimentary layer) whose thicknesses/depths and density contrasts were parameters during subsequent regression. The response for this model was then computed and the misfit statistics gave an indication of model acceptability.

Shorter wavelength changes were automatically modelled by the inversion algorithm (fig. 6.9b) and this substantially reduced the absolute residual misfit (statistic II). The number of parameters was increased but smoothness constraints were imposed to avoid collinearity (fig. 6.9c). Finally robust procedures were applied to downweight observational outliers and after further iterations the model and response shown by dotted lines (in fig. 6.9c) was obtained. The range of uniqueness was then tested for a subset of the observations using this best fitting model (fig. 6.9d). Figure 6.9d illustrates that many of the parameters could not be uniquely resolved from the observations and were thus subject to considerable uncertainty.

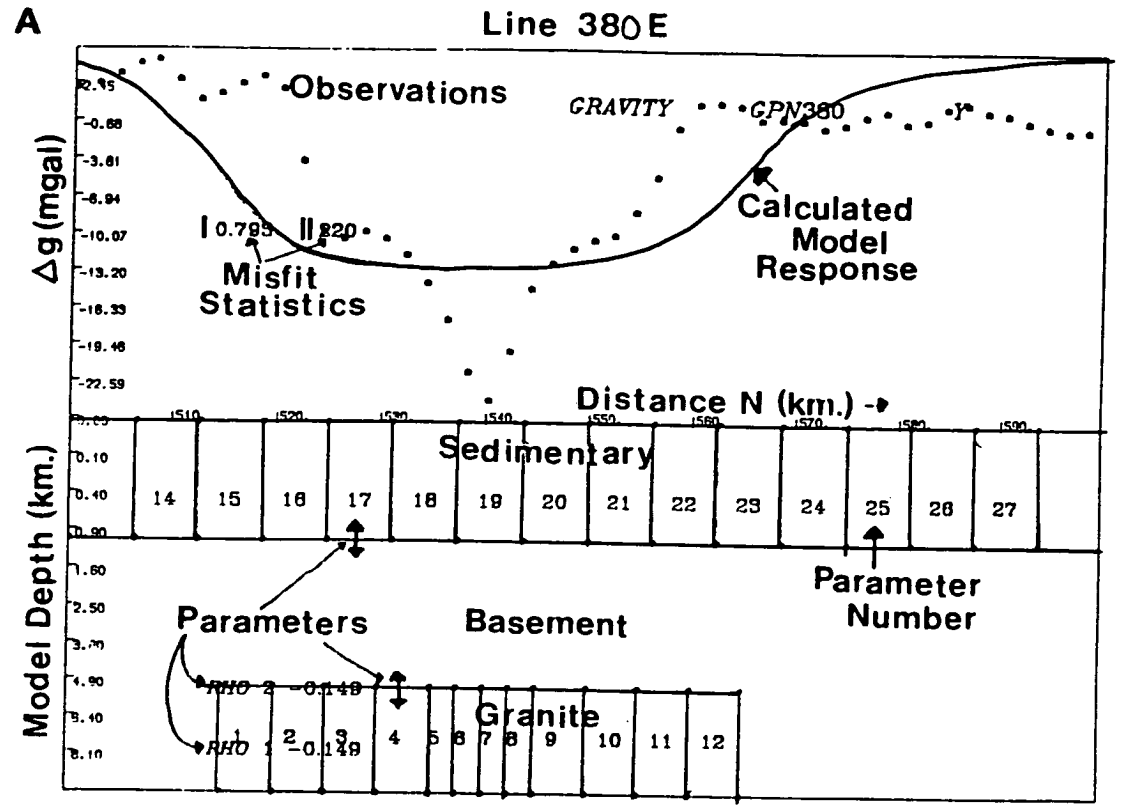
A
Line 380E
Observations
GRAVITY
GPN380
Δg (mgal)
Calculated
Model
Response
I 0.795
II 820
Misfit
Statistics
Distance N (km.) →
Sedimentary
Model Depth (km.)
14
15
16
17
18
19
20
21
22
23
24
25
26
27
Parameter
Number
Parameters
Basement
RHO 2 -0.149
Granite
RHO 1 -0.149
1
2
3
4
5
6
7
8
9
10
11
12

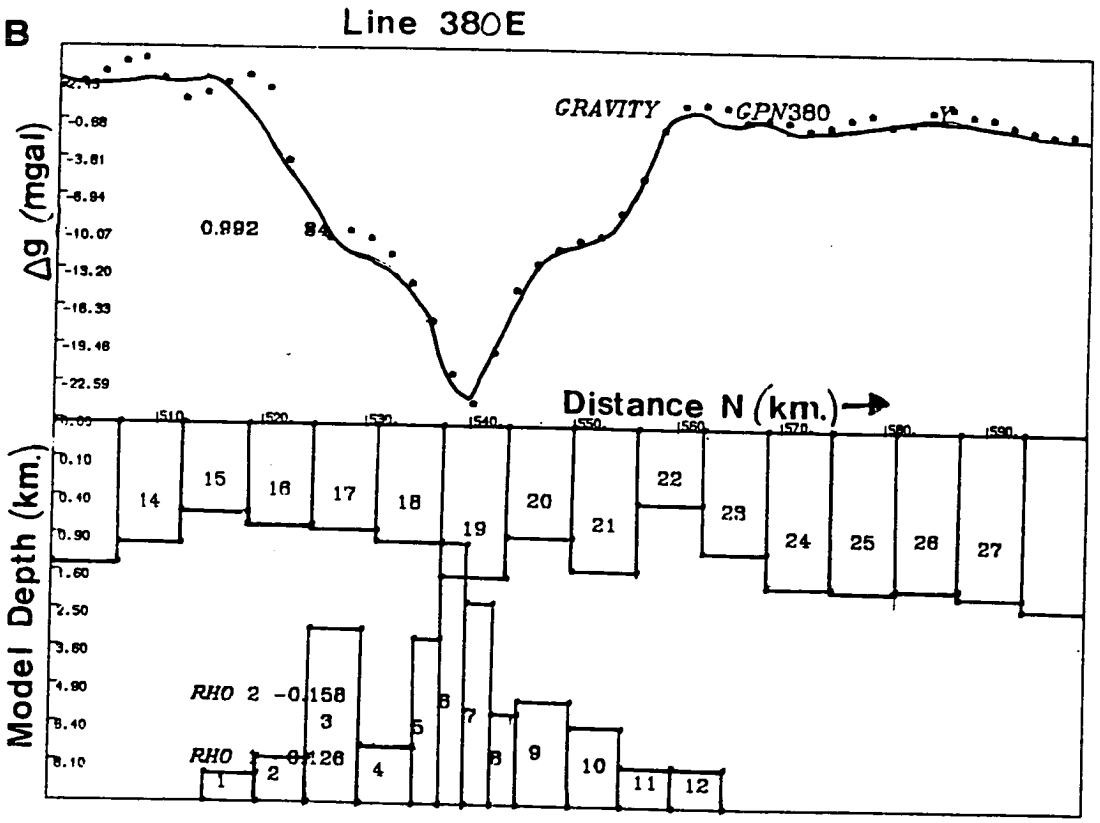
B
Line 380E
GRAVITY
GPN380
Δg (mgal)
0.992
Distance N (km.)→
Model Depth (km.)
14
15
16
17
18
19
20
21
22
23
24
25
26
27
RHO 2 -0.158
RHO 1 -0.126
1
2
3
4
5
6
7
8
9
10
11
12

C

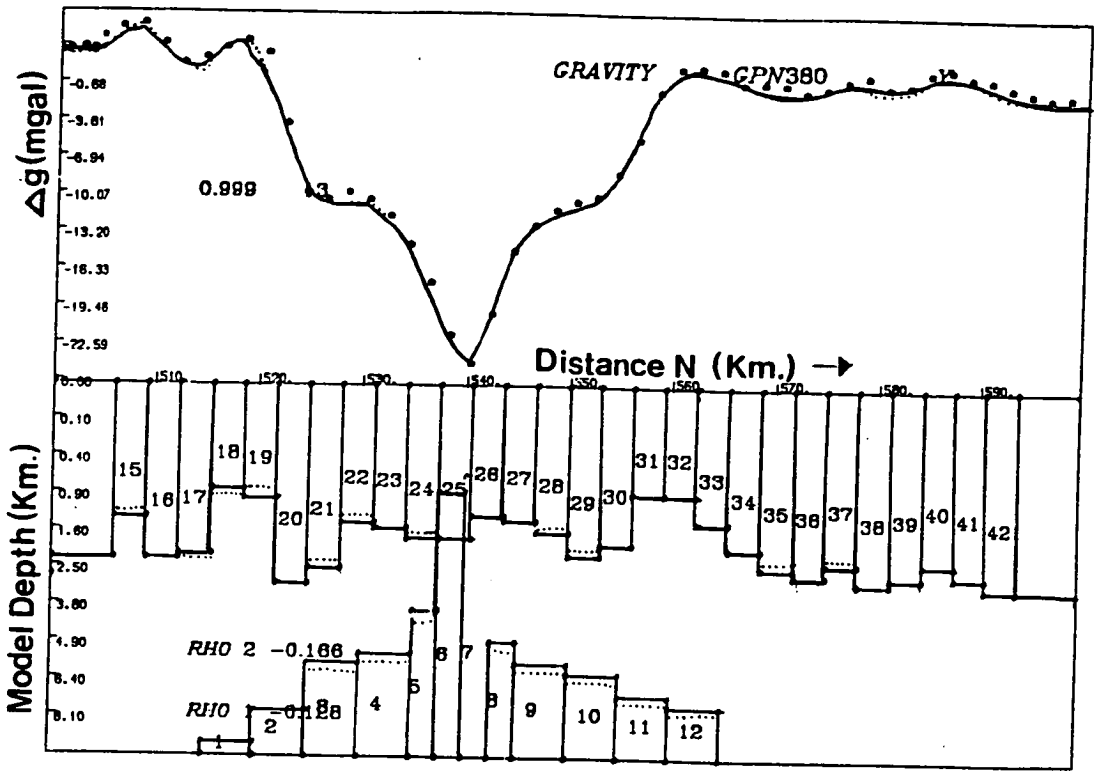
Line 380E
GRAVITY
GPN380
Δg(mgal)
0.999
Distance N (Km.)
Model Depth (Km.)
RHO 2 -0.166
RHO 1 -0.128

D

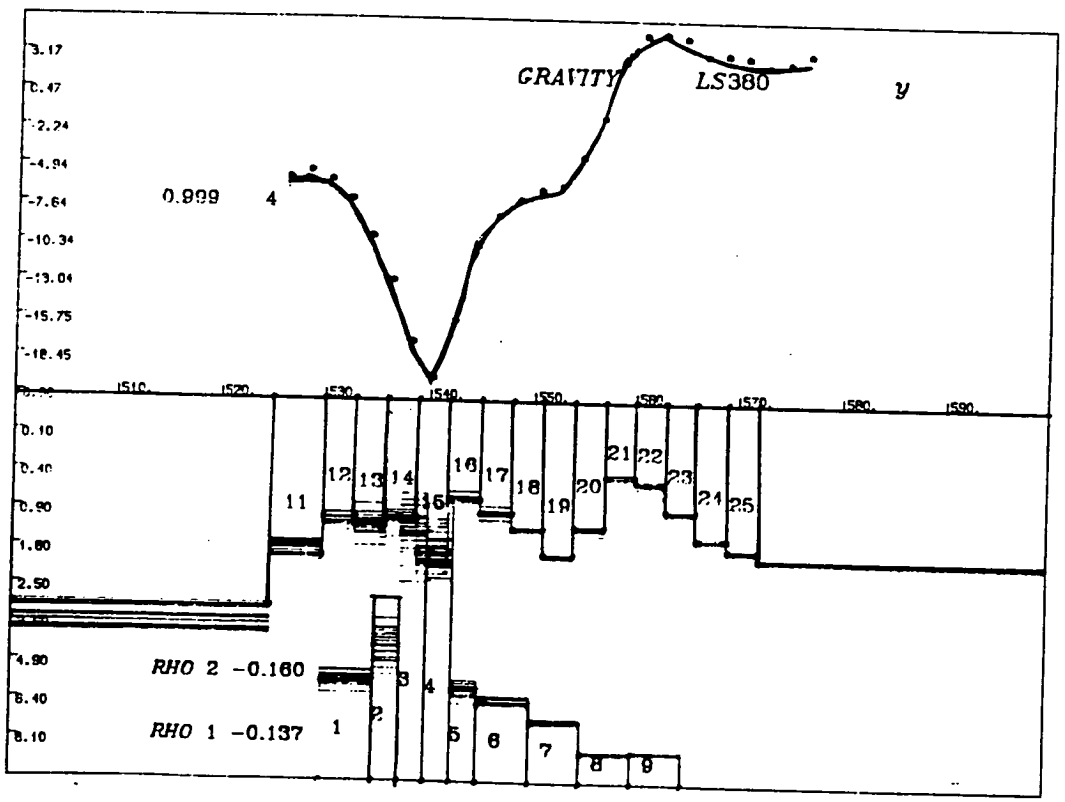
GRAVITY
LS380
0.999
RHO 2 -0.160
RHO 1 -0.137

2.66 g.cm^{-3} intruded into the denser Silo-Ordovician age basement (2.72 to 2.78 g.cm^{-3}). Covering both, the Carboniferous age sediments have variable densities from 2.5 to 2.7 g.cm^{-3}. Consequently the model granite was assigned a preliminary model density contrast ("RHO1") of -0.15 g.cm^{-3} with respect to the basement rock and the sedimentary layer was also assigned a density contrast ("RHO2") of -0.15 g.cm^{-3}. The calculated response of this model was found to match the observed anomaly crudely (fig. 6.9a).

Shorter wavelength features were then automatically modelled by subdividing the granite and sedimentary layer into a number of smaller blocks. Using linearized inversion techniques (section 5.8) correction values for the 30 parameters (2 density contrasts, 12 granite and 16 sedimentary layer model thicknesses) were calculated. Although **MAXMAY** was written to allow interactive modelling, no further user intervention or other constraints were found to be necessary to obtain the model shown in fig. 6.9b. The author believes that incorporation of other constraining information (e.g. the depth to the granite from the Rookhope borehole) would have further enhanced the accuracy of this model.

To emulate the fine structure in the gravitational anomaly, significant changes occurred in the values of many of the parameters. The results show a reasonably well fitting model (cross correlation factor 0.992). However, there remained a number of sharp discontinuities between adjacent blocks (e.g. blocks 21 and 22) and some fine anomaly structure did not appear to be properly reproduced (e.g. at position 515 km.). It was thought that by increasing the number of free parameters these discrepancies could be removed, but as 30 parameters were being used to model 50 observations, ill conditioning (section 4.5.2) was perceived to be a potential problem.

The next stage of modelling thus involved doubling the number of sedimentary layer parameters present, whilst imposing the constraint that the difference between adjacent block thicknesses was to be as small as possible (eqn. 5.7.8b). This smoothness constraint removed the possibility that discontinuities were generated as artefacts of the inversion procedure (c.f. Tanner 1967, section 6.2.4) and the resulting model (fig. 6.9c) was better resolved overall. Finally, once the iterative modelling procedure approached convergence, user intervention downweighted those observations whose

residual misfits suggested that they were outliers (section 5.6.2). In this data set, such outliers may have resulted from the smoothing/contouring packages used, or very short wavelength features at the limit of model resolution. Downweighting of these outliers and subsequent modelling iterations reduced the misfit, as well as the effective number of observations present. The changes in both the model and the response function from the application of robust re-weighting are superimposed upon fig. 6.9c (dotted lines). This final model shows both the gross structure and a number of finer details can be considered to genuinely reflect changes in the gravity anomaly owing to the imposition of constraints.

It must be stressed that the model shown in fig. 6.9c remains ambiguous because, for example, changes in the thickness of the sedimentary layer and its density contrast can lead to an equally acceptable model, in terms of its misfit. In the terminology of section 5.8, there is very likely to be more than one misfit minima. The author thus adapted the most squares method (section 4.3.2) to find the most extreme model parameter values, which remain consistent with the assumed observational errors (0.2 mgal). This allows the determination of a quantitative measure of the uniqueness of the best fitting solution to be gained. Figure 6.9d demonstrates the results obtained by application of this method to a subset of the observations and the models generated for line 380E. As might have been expected, at those locations where the granite and sedimentary rock signatures overlap (e.g. 540N), there is considerable scope for acquisition of different models. Conversely, where the model granite is thin or absent (e.g. 560N), the sedimentary cover is better resolved. Furthermore, fig. 6.9d shows that although a large number of parameters were used to model these observations, they are not all necessarily resolvable independently (e.g. blocks 12, 13 and 14).

6.4.9. Modelling of Different Types of Geophysical Data

Most MT field researchers use geophysical information for their area of interest either only as a guide to locate their soundings or later to draw comparisons with their 'best fitting' geoelectric models. This author considers that in the interests of model resolution and interpretability, it is desirable not only to integrate other relevant geophysical observations at an early stage of an MT study (c.f. Eliason *et al.* 1983, Prieto *et al.* 1985, Jones and Craven 1990),

but it may, in some instances, be preferable to model them jointly (c.f. section 6.2.6, Johansen 1977, Bahr 1983, Prieto *et al.* 1985, Lines *et al.* 1988). Model resolution can then be enhanced by reducing the ambiguities present in any one data set. In theory, the greater the extent that information can be introduced from other sources, the more accurate will be the subsequent geophysical interpretation.

Joint modelling does not preclude the possibility that one geophysical technique will detect different structures from another, but it does imply that all observations should relate to the same Earth. If it can be assumed that more than one rock property appreciably changes across a major structural boundary, then the depth to this interface can be constrained by jointly modelling different geophysical observations. As the individual model results can be afflicted by the presence of noise or ill determined parameters, then the ability to constrain common model parameters should lead to an improvement in the overall model reliability and interpretability.

6.4.10. Joint Modelling of Geoelectric and Gravity Data

In sections 6.4.6 and 6.4.8, modelling of geoelectric and gravity observations along a coincident profile were described. It became apparent to this author, that the depth to the interpreted base of the low resistivity Carboniferous age sedimentary sequence was broadly coincident with the depth to the top of the higher density basement rock. The author therefore undertook joint and constrained modelling of the depth to this unconformity from both gravitational and magnetotelluric observations. The density contrasts and layer resistivities remained free parameters.

This method has not yet been fully implemented or tested and a number of program problems remain. The simplified example given here shows the observations from the 4 MT sites discussed in section 6.4.6 projected onto the gravity profile 380E. From these, the numerical regression procedure was found to work most efficiently if only a representative subset of the observations and models were processed. The starting models corresponded to the best fitting constrained geoelectric and gravity methods. The numerical algorithms used were similar to those previously described. In this context, the difference between the thickness of the gravitationally determined low density

layer and the *cumulative* thicknesses of the corresponding geoelectric layers, were minimized.

At 2 of the MT sites (SWI and DBK), the electrical and gravitational depth to basements are virtually coincident (fig. 6.10a). At MWD, there is other evidence which suggests that the gravity model has underestimated the depth to this boundary (section 8.4.2). Following joint modelling, the MT observations have in fact pulled this interface down (fig. 6.10b). The gravity misfit is consequently increased but remains at a tolerable level. The electrical model shows little change.

Joint modelling at HGN could not immediately reconcile the difference between the 2 depth to basement estimates. The earlier pseudo 2-D model (fig. 6.8b) had shown that the presumed Lower Palaeozoic basement resistivity at this site (48 Ω.m.) remained virtually unchanged and lower than its neighbours (i.e. DBK 85 Ω.m. and MWD 79 Ω.m.). The presence of a significant gravity contrast within a layer of anomalously low resistivity suggested that the 48 Ω.m. electrical layer should be properly subdivided into a lower basement type (about 80 Ω.m.) and an upper sedimentary type (between about 20 to 30 Ω.m.). This is depicted in the joint model in fig. 6.10b and was further substantiated following more detailed pseudo 2-D modelling.

By adapting this method, it should be possible to constrain the depth to the top of the low density and high resistivity granite. The method would significantly improve the resolution of the intermediate high density and moderately resistive basement. This is not currently well resolved from MT observations alone.

6.4.11. Two Dimensional Magnetotelluric Modelling

Strictly 2-D MT modelling was undertaken to test the validity of the pseudo 2-D model section for the part of the 'long' traverse which showed the most anisotropy. As such modelling used more of the acquired response function information (i.e. E and H polarizations separately), then it was further anticipated that 2-D modelling would produce a more accurate, albeit discretized Earth representation. Finally, some tests were then performed on the resolution of the more significant parameters.

Figure 6.10: A simplified example of the computer terminal display generated by the experimental gravity and MT modelling program.

This shows the basic 3 layer gravity model which resulted from earlier modelling (fig. 6.9), but in this case, the location of some of the influential electrical boundaries have been overlain at their appropriate locations (short horizontal lines).

The thickness of the electrically determined sedimentary layer (marked with an 'S') is comparable with the gravitationally determined boundary at SWI and DBK. Whereas at HGN and MWD the depth to the presumed electrical basement ('B') is different from the gravity model. Joint and constrained regression was performed to minimize the difference between the cumulative thicknesses of the electrical low resistivity layers and the gravitational depth to basement. At HGN the models could not be reconciled without separating the 48 Ω.m. 'B' layer into a more conductive sedimentary type overlying a more resistive basement type. This altered interpretation is depicted in fig. 6.10b. At MWD, the gravity model was considerably altered following constrained modelling. There still is a discrepancy between the 2 basement depths, but the new model shown in fig. 6.10b is thought to be more realistic.

The presumed granitic layer (G) and high conductivity layer (H) are also marked.

A

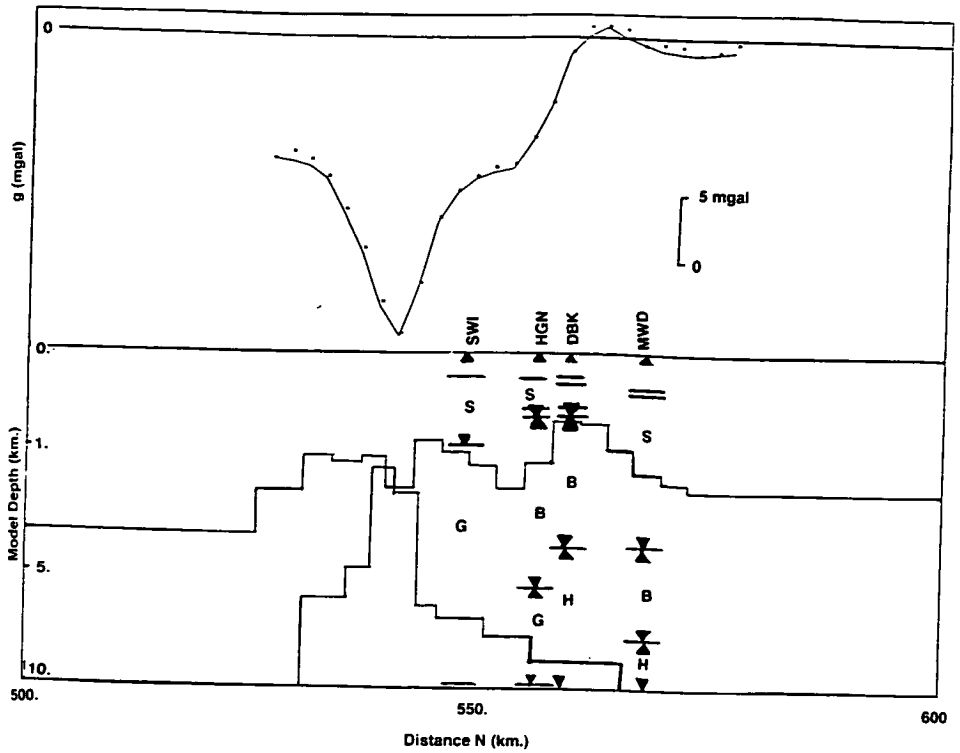
0
g (mgal)
5 mgal
0
SWI
HGN
DBK
MWD
0.
1.
5.
10.
Model Depth (km.)
S
B
G
H
500.
550.
600
Distance N (km.)

B

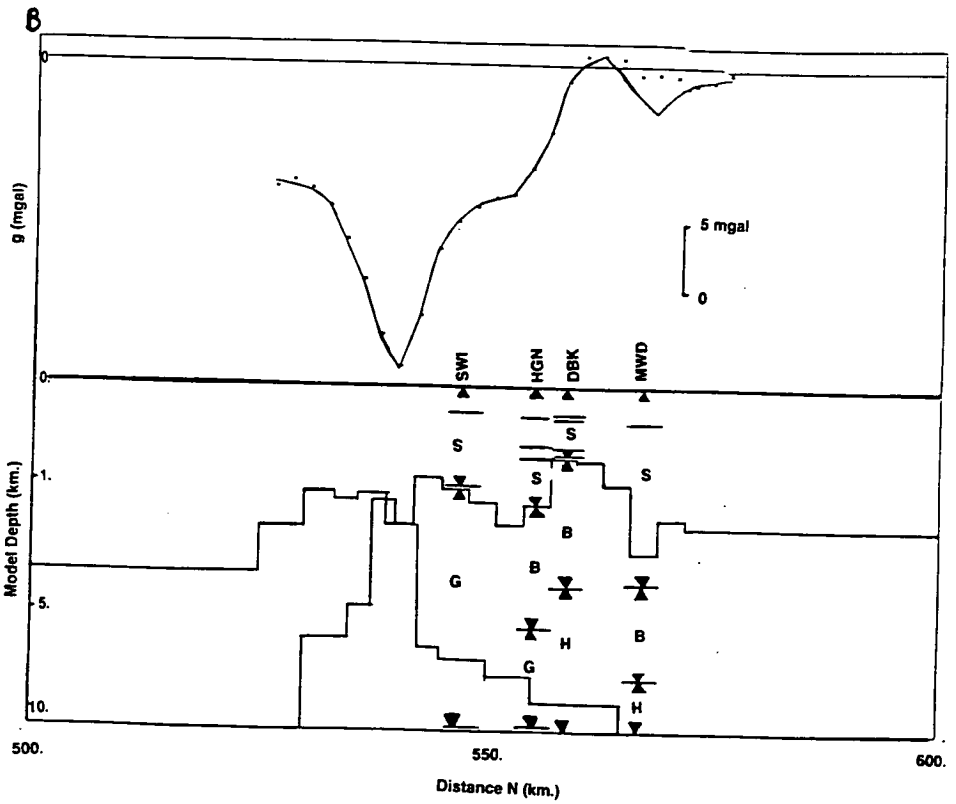
0
g (mgal)
5 mgal
0
SWI
HGN
DBK
MWD
0.
1.
5.
10.
Model Depth (km.)
S
B
G
H
500.
550.
600.
Distance N (km.)

The approach used for this study took a discretized model comprising resistivity values specified on a rectangular mesh, across the simulated MT profile. The mesh was designed (e.g. Wannamaker *et al.* 1985) to allow the individual structural units to be properly resolved and this involved specifying a greater concentration of nodes at the centre of the mesh. In order to limit the computational effort, little emphasis was placed upon finding an accurate model for the presumed 1-D sedimentary structure, although it was necessary to derive a reasonable approximation prior to modelling the lower structures. The forward problem was then solved by reducing the differential equations (eqn. 2.4.1) by the computationally efficient method of integral equations (Madden 1972) within the specified inhomogenities. The relevant boundary conditions were then imposed for each of the 2 modes.

A short section (30 km.) of the main profile was chosen because of the high density of good quality soundings (9 used), the relatively high skew values and the presence of strong lateral resistivity contrasts in the composite 1-D section. The observations from all 9 sites were rotated to a common azimuth (eqn. 2.5.4 : 90 ^{O}) This was assumed to correspond with the regional geological (ENE; section 7.3.2 including 11^{O} to change geographical north to magnetic north) and often electrical (see azimuths in Appendix - C) strike direction. The full impedance tensor information was unavailable from a number of older soundings across this area (c.f. section 3.5.2), so the absence of these extra and lower frequency response functions limited the resolving power of the 2-D model compared with the pseudo 2-D section.

The starting 2-D model was based upon a simplified version of the corresponding pseudo 2-D section (fig. 8.9a and 8.17a) and comprised a mesh of approximately 25 by 25 nodes. This included 12 vertical nodes for the air above the model and 4 horizontal nodes for lateral extensions of the model outwith the region of interest. After the forward model response was evaluated and then compared with the observed, the resistivity values and mesh positions were manually changed to try to improve the fit on a trial-and-error iterative basis. The final model had a finer grid mesh of 35 by 31 points.

Preliminary attempts to obtain a crude fit were based on visual inspection of the calculated response compared to that which was observed. The author

rapidly recognised that 2 misfit statistics could be more readily used to fit the finer detail. These simply summed the absolute residual difference between the calculated and observed (log) apparent resistivity and phase for both E and H polarization directions at all the sites. No preferential weighting was given to any particular observation, site or polarization except that the apparent resistivity response data were not used at SHW owing to the obvious static shift present (section 6.3.2). These 2 statistics gave a quantitative measure of the relative model improvement.

More than 60 different models were tested. The improvement from initial to final model was approximately 35% in both of these statistics. The greatest change was achieved within 10–15 models as these concentrated on acquiring a reasonable approximation to the influential surficial structure. The remaining models were used in a systematic search pattern with the primary aim of investigating the relationship between the lower crustal conductor and the granite. The best fitting model at each stage was always retained and used for subsequent iterations. Several selected model parameters were also varied in order to determine their resolution.

The final best fitting models were redrawn with linear depth scales to show the deep (figs. 8.2b and 8.9b) and shallow (figs. 8.17b and 8.19b) structure. The corresponding apparent resistivity (ρ_a) and phase (ϕ) response functions for the E and H polarizations are superimposed on the observed in figs. 6.11a–c, for each of the 9 sites. To give an estimate of the fit, the value of the appropriate apparent resistivity or phase test statistic is given at the right hand edge of each of these curves.

The fit is very good for almost all of the sites and becomes progressively better towards the 2 least noisy sites near the Stublick Fault (DBK and WHI). The static shift present at SHW can be clearly seen between the observed and computed apparent resistivity response functions.

Figure 6.11: The observed $\log_{10}$ apparent resistivity (ρ_a) and phase (ϕ in degrees) E and H polarization estimates as a function of $\log_{10}$ frequency for the 9 sites used to derive the 2-D model shown in figs. 8.9b and 8.19b. The computed response functions from this model is overlain (shown by the continuous line). An apparent resistivity and phase misfit statistic is given on the right hand side of each computed curve.

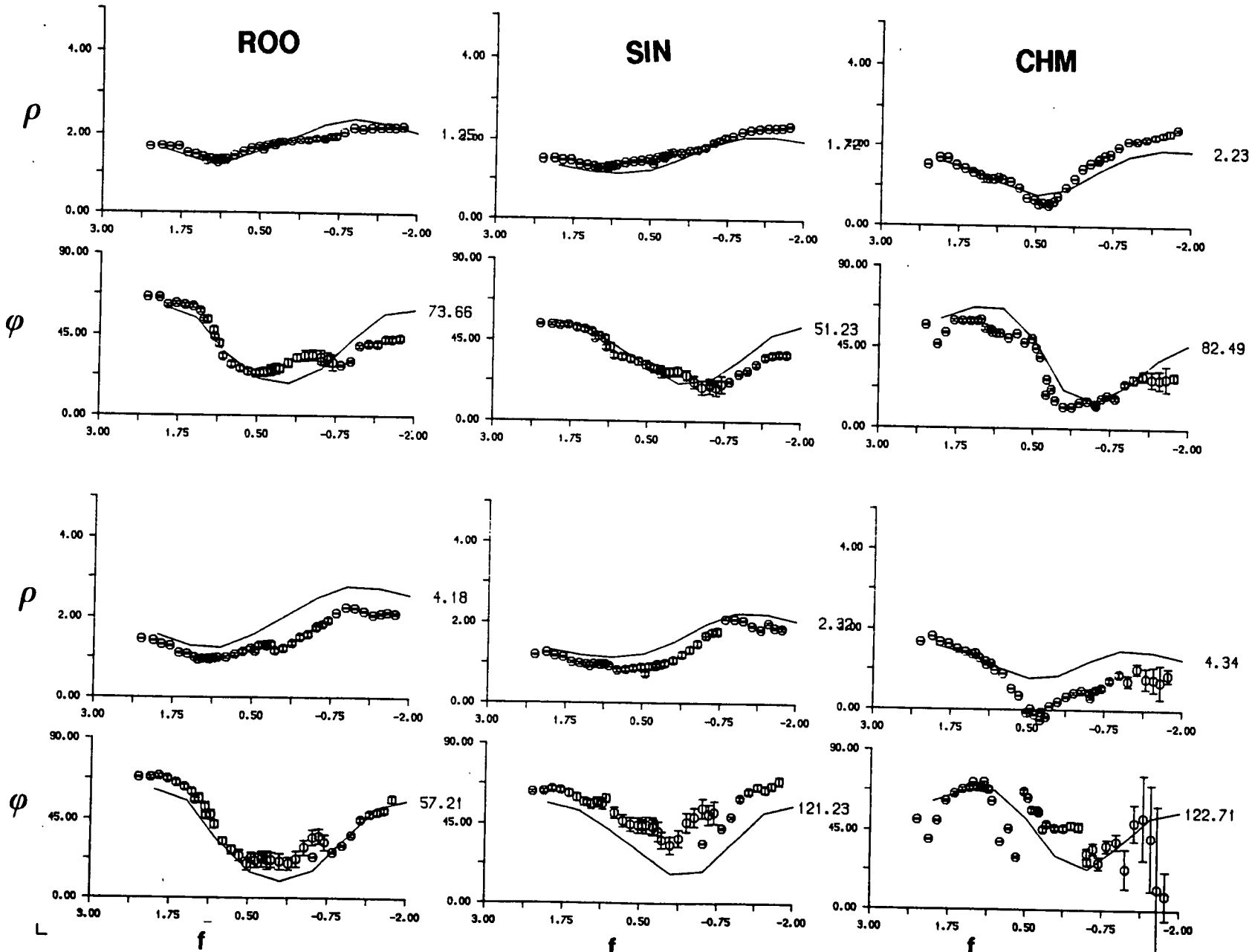
ROO
SIN
CHM
ρ
φ
f
73.66
51.23
82.49
4.18
2.32
4.34
57.21
121.23
122.71
2.23

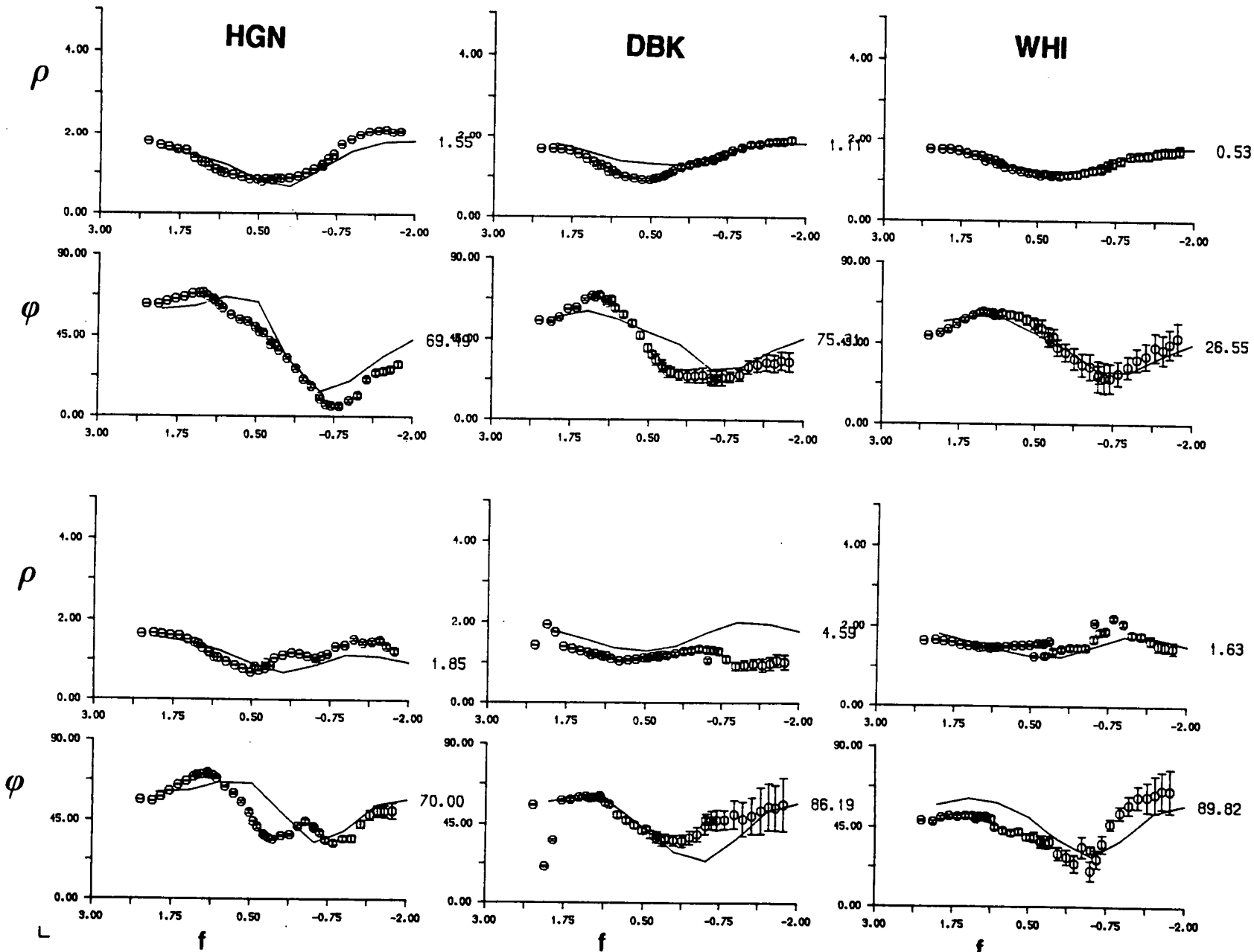
HGN
DBK
WHI
ρ
φ
4.00
2.00
0.00
90.00
45.00
3.00
1.75
0.50
-0.75
-2.00
1.55
1.71
0.53
69.49
75.43
26.55
1.85
4.59
1.63
70.00
86.19
89.82
f

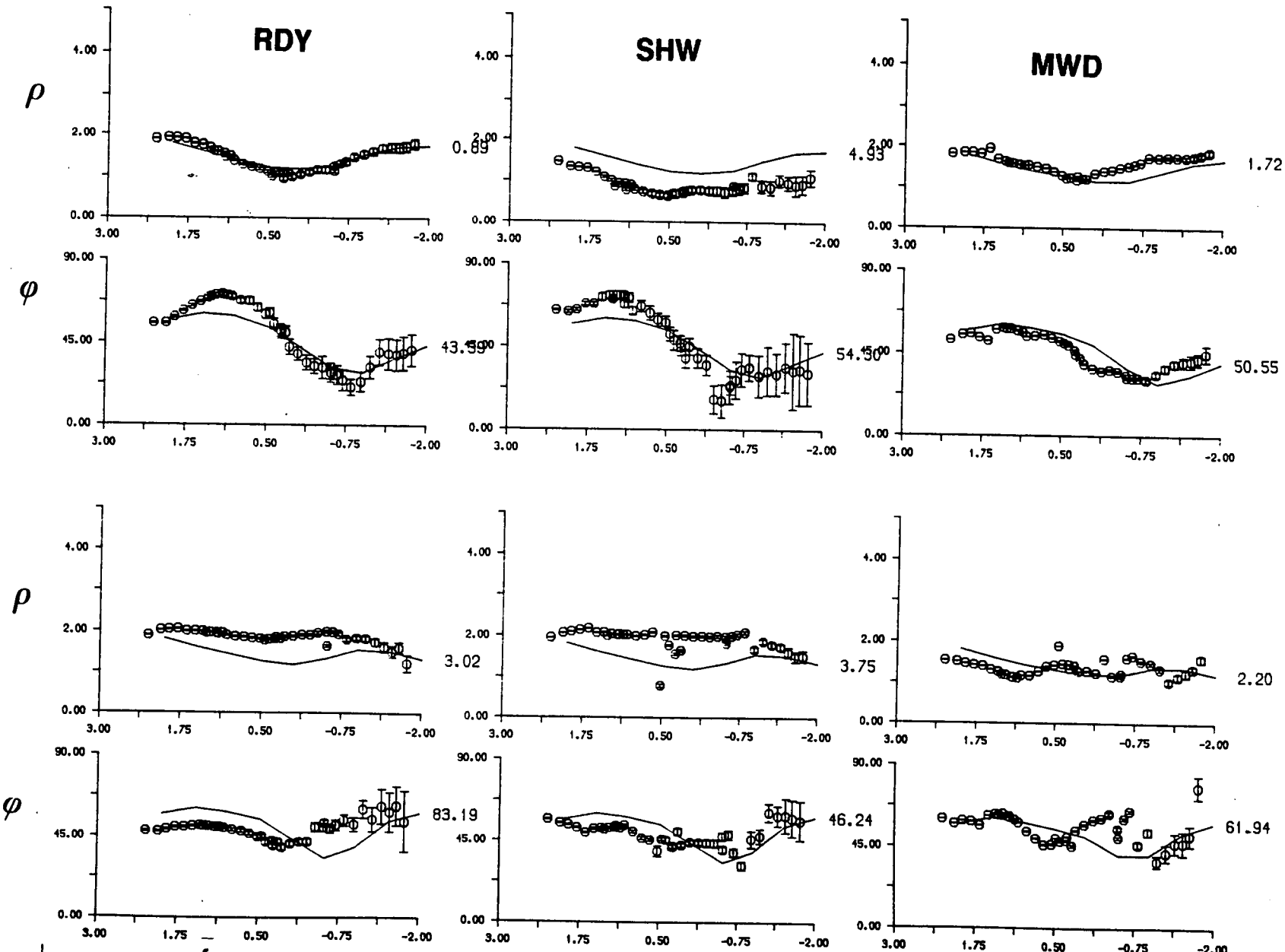
RDY
SHW
MWD
ρ
φ
0.89
4.93
1.72
43.99
54.30
50.55
3.02
3.75
2.20
83.19
46.24
61.94
4.00
2.00
0.00
90.00
45.00
3.00
1.75
0.50
-0.75
-2.00

CHAPTER 7

REVIEW OF THE GEOLOGICAL HISTORY

OF NORTHERN ENGLAND

7.1. BACKGROUND AND GEOLOGICAL OVERVIEW

For the last century, Northern England has been the subject of considerable scrutiny by the Earth science community. This level of interest is probably explained by the economic value of the region (e.g. coal and mineral mining and more recently hydrocarbon and geothermal exploration) and the number of targets for research projects (e.g. evidence for the closure of the Iapetus ocean, concealed granites and the development of the sedimentary basins). In addition, the proximity of the region to a number of centres of research (e.g. Leeds, Lancaster, Durham, Newcastle and Edinburgh) must also be a factor in its apparent popularity. However, even in one of the best investigated regions of Britain, further Earth science investigations are required to fully unravel the geological history of the area.

The difficulty and high cost of collecting detailed information from deep within the Earth have necessarily limited progress in understanding the nature of the continental collision which is thought to have occurred here late in the Silurian era. A review of the currently available information on the "basement" (sub-sedimentary) and deep crustal rocks is given in section 7.2. This draws mainly upon geological evidence but also introduces some of the results from previous geophysical studies. Section 7.3 then contains a brief review of the speculative tectonic models which are thought responsible for the formation of the deep structure.

Within the rocks in the lower parts of the crust, a number of granite batholiths (section 7.4) were intruded during the Lower Devonian era (415-390 Ma.). These intrusions provided buoyancy to surrounding blocks of crustal material, whilst adjacent unsupported troughs subsided in response to crustal extension (sections 7.5 and 7.6). Subsequent Lower Carboniferous sedimentation patterns were controlled by differential subsidence across hinge

lines separating the blocks and sedimentary basins. Later, more regional subsidence permitted sedimentary rocks to be deposited widely during an era of hot, marginal marine conditions (section 7.7). Finally, the presence of later intrusives and mineralization are discussed, with regard to the thermal history of the region (section 7.8).

Two very useful reviews on the geological history of the region have been edited by Hickling (1972) and Robson (1980). The breadth and quantity of published geological and geophysical literature has long prevented authors from reviewing the entire subject (c.f. Robson 1980). By necessity, a similar constraint is placed upon this chapter. The author thus provides a relatively short synthesis of the broad spectrum of currently available background Earth science information, whilst concentrating on those parts which he believes are most relevant to his particular study. Finally in the subsequent chapter, an interpretation of the geophysical models generated in the course of this study, is presented.

7.2. PRE-DEVONIAN BASEMENT STRUCTURE

7.2.1. Basement Geology

Within Northumberland, geological evidence concerning the rocks beneath the thick sedimentary sequence is sparse (Robson 1980). Two inliers (at Cross Fell and Teesdale; see fig. 7.1) and a small number of boreholes [e.g Crook on the Alston Block (Woolacott 1923) and Beckermonds on the Askrigg Block (England *et al.* 1980)] have proved the existence of metamorphosed rocks of Ordovician and Silurian age (515-415 Ma.). These rocks broadly compare with extensive Lower Palaeozoic outcrops in the Southern Uplands of Scotland and within the eroded Lake District block of Northern England. There are also similar rocks found across the Irish Sea in the Isle of Man and NW Ireland.

The Northumberland basement is therefore assumed to be composed of rocks similar to the metamorphosed mudstones (e.g. Skiddaw Slate Group), volcanic (e.g. Eycott or Borrowdale) or sedimentary rocks (e.g. the Coniston Limestone Group) which are found in the Lake District. The subsurface lithology of Northern Northumberland may alternatively relate to the oceanic derived greywackes and shales which outcrop in the Southern Uplands.

Figure 7.1: A simplified surface geological map of Northern England and Southern Scotland (based primarily on Johnson 1984 and Robson 1980). This diagram shows the major Lower Palaeozoic outcrops of rock (the hatched area) in the Southern Uplands of Scotland and the Lake District of England. The 2 exposed granitic batholiths at Criffel and Cheviot are shaded by stars. On the margins of the latter locality, Devonian age igneous and sedimentary rocks (large dots) are exposed at the surface. The remainder of the area of this map is covered by either Carboniferous age (unshaded) or younger Permian (small dots) age sedimentary rocks.

There are 2 Lower Palaeozoic inliers in the sedimentary rock at Cross Fell (CF) and Teesdale (TD). Some of the major boreholes in the region are also marked at Rookhope (RO), Crook (CK), Harton (HT), Stonehaugh (SH), Ferney Rigg (FR) and Longhorsley (LR). The 2 main centres of population are at Carlisle (C) and Newcastle-upon-Tyne (N). Some of the major faults which delineate the Alston Block are also shown.

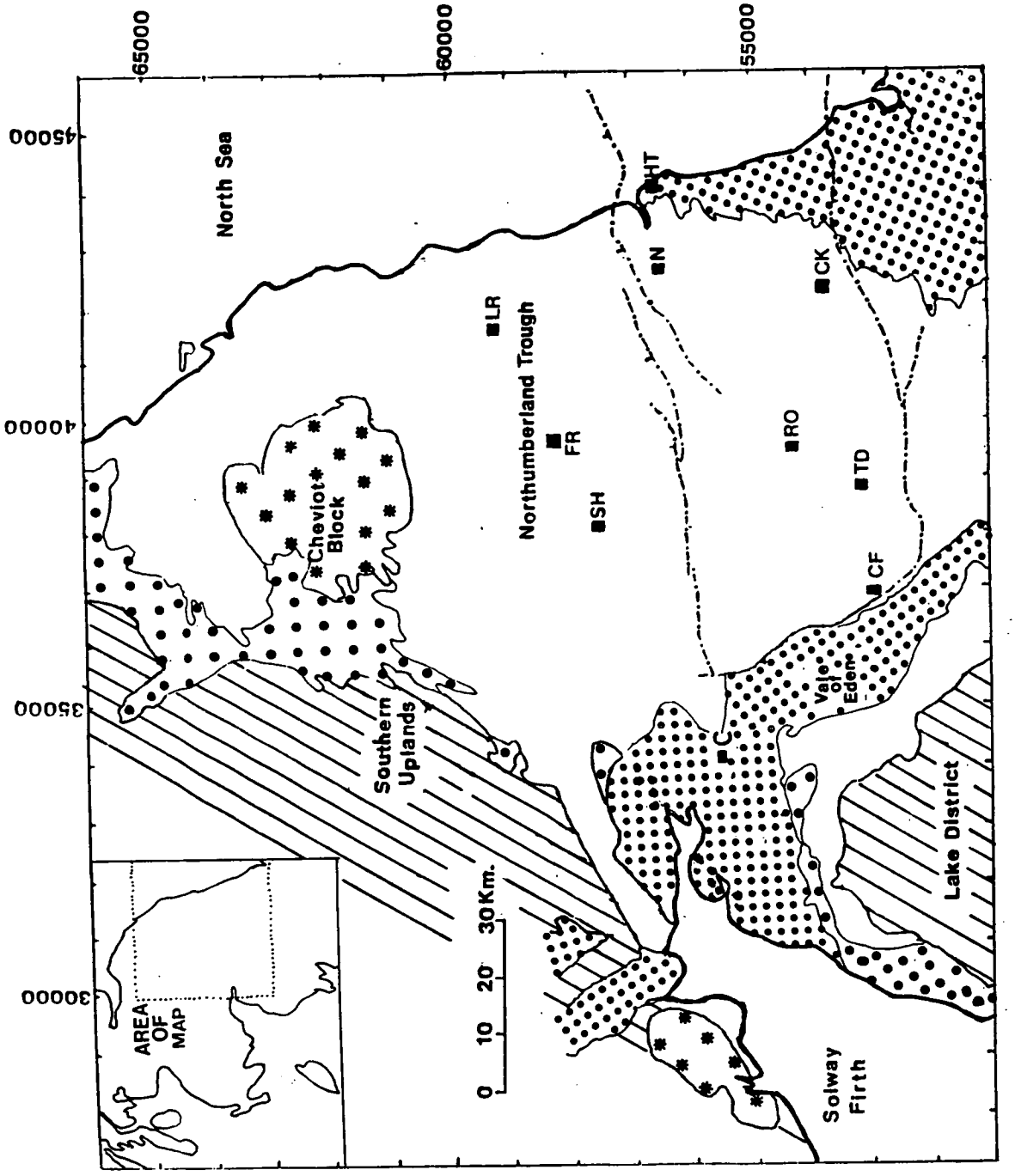
65000
60000
55000
45000
40000
35000
30000
North Sea
HT
N
CK
LR
Northumberland Trough
FR
SH
RO
TD
CF
Cheviot Block
Southern Uplands
Vale of Eden
Lake District
Solway Firth
AREA OF MAP
0 10 20 30Km.

7.2.2. Geological Evidence for the Iapetus Suture

Various structural, palaeomagnetic and palaeontological observations on the Lower Palaeozoic rocks in Britain and the Canadian Appalachians (Haworth 1986) have shown that, until the Silurian, they originally existed on different continental terranes which were separated by the Iapetus ocean. The suture, or line of final closure of this ocean, was originally identified on the basis of markedly different fauna in the basement rocks of Southern Scotland and Northern England. In general, wide oceans (greater than about 1000 km.) provide natural barriers to the migration of continental based aquatic organisms. Their evolution is therefore distinct until the respective continents come close to convergence when faunal mixing is allowed to occur. Fossil dating thus permits the palaeo-ocean width to be estimated and palaeo-continental margins delineated at different epochs during continental collision.

The fauna in the Lower Palaeozoic rocks of Southern Scotland have been found to be more akin to those of North America, whilst in Northern England, the fauna have a closer affinity to the rest of England and Wales (Fortey *et al.* 1989). Most authors (e.g. Soper *et al.* 1987), with only a few exceptions (Allen 1987) have ascribed the Iapetus Suture to lie along the "Solway Line" which extends NE from the western end of the Northumberland Trough towards the Cheviot Block (fig. 7.2). There is little geological evidence to define its position more exactly within Britain because of the thick cover of post-Devonian rocks overstepping the suture. In fact, numerous authors have confidently placed its location near the Cheviot Block. As far as this author is aware, there are no deep boreholes or rock exposures which have proved the presence of basement rock in the NE corner of the Northumberland Trough. As a consequence, there appears to be little evidence to support such an extrapolation.

The suture's presence has been more directly associated further westwards with the Navan-Silvermines Fault in Ireland. This fault separates the Longford-Down massif to the north (the SW continuation of the Southern Uplands) and the Leinster-Wexford terrane to the south (the SW extension of the English Lake District). Additional circumstantial evidence for this line has been based on the aeromagnetic anomaly pattern and the distribution of lead

Figure 7.2: The presumed location of the faunally determined Iapetus Suture in Britain and Ireland. On the east coast of Ireland, the Iapetus Suture has been associated with the Navan-Silvermines Fault (NSF) which separates the Longford-Down and Leinster-Wexford terranes. Elsewhere, the Iapetus Suture cannot be directly observed at the surface owing to the presence of a thick sequence of Carboniferous age sediments which have overstepped it. On the basis of fossil evidence, the trace of the Iapetus Suture has been constrained to lie along the Solway Line, between the Southern Uplands of Scotland and the Lake District of England.

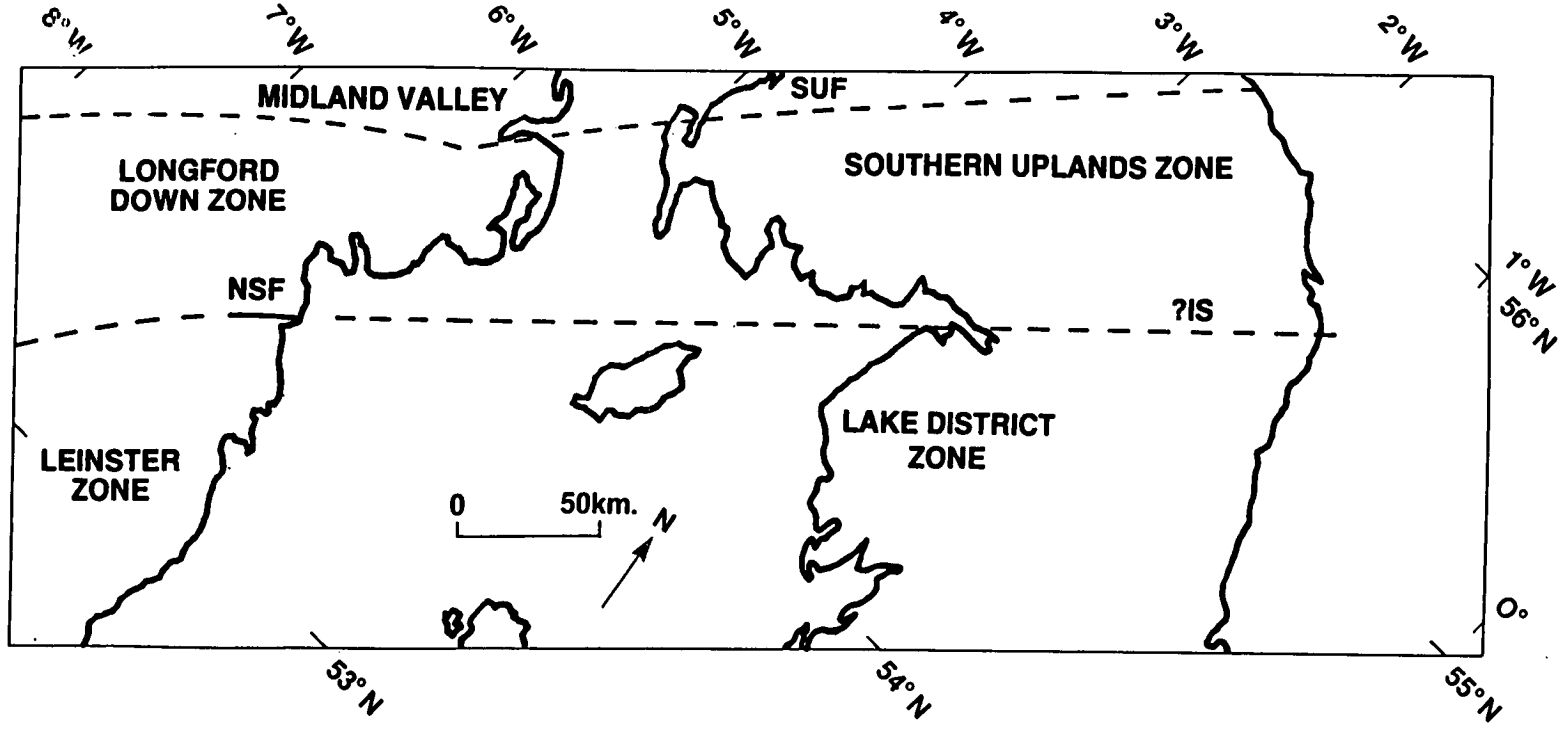
8°W
7°W
6°W
5°W
4°W
3°W
2°W
1°W
56°N
0°
53°N
54°N
55°N
MIDLAND VALLEY
SUF
LONGFORD
DOWN ZONE
SOUTHERN UPLANDS ZONE
NSF
?IS
LAKE DISTRICT
ZONE
LEINSTER
ZONE
0
50km.
N

isotopes (Kennan *et al.* 1979). This author also considers that the regional gravitational change within the basement rock of Northumberland (Kimbell *et al.* 1989) may be another manifestation of a major lithological change (c.f. section 8.3.1).

As the faunally determined Iapetus Suture does not give any indication of its subsurface geometry, geophysical techniques have been used to image the postulated "Iapetus Convergence Zone" (c.f. Soper *et al.* 1987) at depth.

7.2.3. Deep Seismic Observations

Three deep seismic refraction surveys have been carried out across Northern England. Two of these are approximately perpendicular [the NERL (Swinburn 1975, Bott *et al.* 1984) and LISPB lines (Bamford *et al.* 1978)] and the other parallel (CSSP: Bott *et al.* 1985) to the proposed strike of the Iapetus Suture (fig. 7.3).

LISPB identified a refractor of velocity 5.8 $km.s^{-1}$ at a depth of about 2 km. beneath the Carboniferous age sedimentary cover. This layer has been interpreted as Lower Palaeozoic basement and is thought to overlay a continental (Pre-Cambrian metamorphic crystalline) basement of velocity 6.25 $km.s^{-1}$ at depths of between 10 and 15 km. Although LISPB observations suggested that there was a lateral transition to a higher velocity continental basement near the Southern Uplands Fault, the Solway Line could not be assigned any special importance, nor was there any significant remnant of oceanic crust observed. These measurements were broadly supported by the shorter NERL survey.

Across most of the profile, CSSP unexpectedly detected continental basement (6.15 $km.s^{-1}$) at shallow depths (4 km.) beneath a thin Lower Palaeozoic basement (see fig. 7.4). This feature has not been substantiated by later surveys (e.g. Kimbell *et al.* 1989) and so Beamish and Smythe (1986) have suggested that these anomalous results were due to an underestimation of the thickness of the sediments in the Solway Basin (c.f. section 8.4.2). Many of these seismic studies have identified a relatively flat Moho at a depth of between 28-30 km., where the seismic velocity increases to 8 km. s^{-1}.

These seismic refraction surveys have been unable to give detailed

Figure 7.3: The location of some of the regional geophysical studies which have been undertaken in Northern England, Southern Scotland and parts of Ireland (the small dots delineate the region which is of primary interest to this study).

Key:

- Seismic refraction studies:

  * NERL: Northern England Refraction Line (Swinburn 1975, Bott *et al.* 1985).

  * LISPB: Lithospheric profile of Britain (Bamford *et al.* 1976).

  * CSSP: Crustal Seismic Suture Profile (Bott *et al.* 1984).

Seismic reflection studies:

  * WINCH 2E/3/4 lines: Western Isles North Channel (Brewer *et al.* 1983, Hall *et al.* 1984, Beamish and Smythe 1986)

  * NEC: North East Coast line (Freeman *et al* 1988, Klemperer and Matthews 1989, Chadwick and Holliday 1991)

  * BS: Commercial data published by Beamish and Smythe (1986)

  * CH: Commercial data published by Chadwick and Holliday (1991)

  * E: B.G.S. data published by Evans *et al* (1988)

  * K: B.G.S. data published by Kimbell *et al.* (1989)

Magnetotelluric profiles:

  * S: Sule (1985)

  * SIMP: Southern Ireland MT profile (Whelan 1989)

  * IMP: Irish MT profile (Meju 1989)

Other Deep magnetotelluric site locations (large dots):

  * Jones and Hutton (1979b), Ingham and Hutton (1982), Harinarayana (1987), P. Jones (person. commn.)

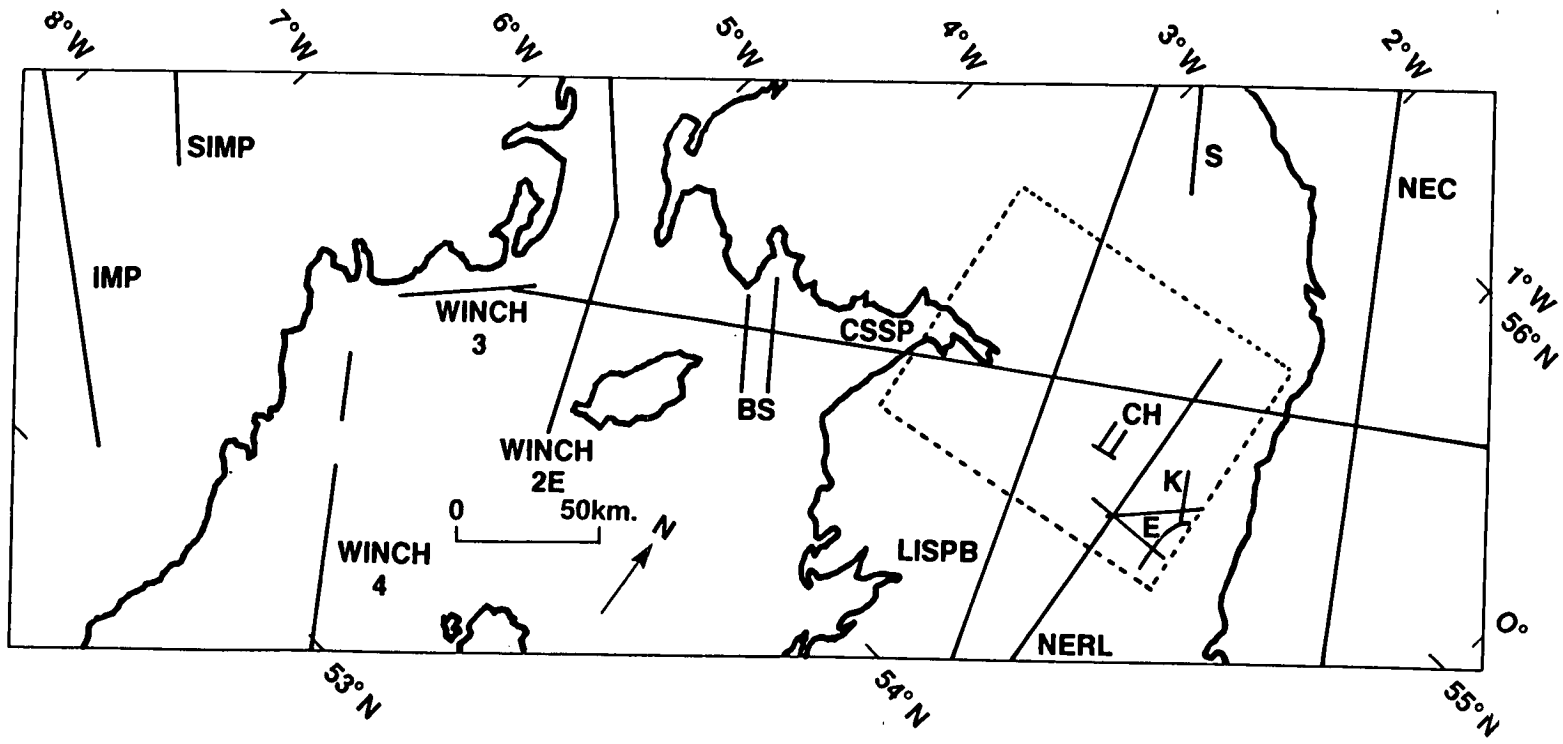
8°W
7°W
6°W
5°W
4°W
3°W
2°W
1°W
0°
56°N
55°N
54°N
53°N
SIMP
IMP
WINCH 3
WINCH 2E
WINCH 4
BS
CSSP
S
NEC
CH
K
E
LISPB
NERL
0 50km.
N

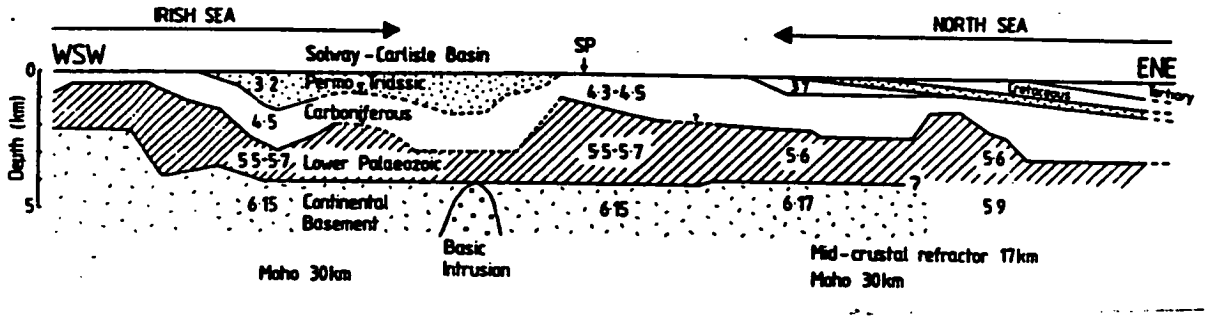

Figure 7.4: A cross section through Northern England derived from the results of the CSSP seismic refraction study (Bott *et al.* 1985). The seismic velocity for each of the structural units (i.e. Permo-Triassic and Carboniferous sedimentary rocks and Lower Palaeozoic and continental basement) is given in $km.s^{-1}$.

Note in particular the anomalously shallow depth to the continental basement (< 5km.) across the section and the thinning of the sediments at SP (Spadedam) in Northumberland. This latter structure is identified with the Bewcastle anticline in chapter 8.

information concerning the geometry of the Iapetus Convergence Zone. A large number of offshore seismic reflection profiles have therefore been undertaken [North Sea: NSDP85 and NEC (Freeman *et al.* 1988, Chadwick and Holliday 1991), Irish Sea: WINCH and commercial seismics (Brewer *et al* 1983, Hall *et al.* 1984, Beamish and Smythe 1986, Freeman *et al.* 1988) and the West coast of Ireland: WIRE (Klemperer 1989)]. These studies proved relatively uninformative concerning the Lower Palaeozoic basement because of the lack of coherent reflections. Inferences on continental collision have thus been based largely on the more distinct reflectors persisting in the lower crust and sometimes extending below the Moho.

Since most of these reflection studies identified either a northerly dipping band of reflectors or change in the reflectivity characteristics of the rock, an initial interpretation of these results seemed to have confirmed the hypothesised northward subduction of the Iapetus ocean (section 7.3.2). These reflectors are usually observed at depths of between 10 and 25 km.. The corresponding reflector detected from the WINCH line (fig. 7.5) is at its shallowest close to the faunal suture and the Navan - Silvermines Fault. According to Klemperer (1989) this seismic reflector now appears to have been traced for some 900 km along the strike of the Iapetus Suture.

However, if this reflector is extrapolated towards the surface, it emerges south of the Isle of Man (Beamish and Smythe 1986) and within the Lake District (McKerrow and Soper 1989). As both these localities are within the southern faunal province, the feature identified on the WINCH line, is now being interpreted as a fault or a thrust/shear zone rather than the suture itself. Freeman *et al.* (1988) have identified a second band of northward dipping reflectors which they attribute to the "Iapetus Suture". However, this latter feature lies even further south of the Solway Line. In the most recent study, Chadwick and Holliday (1991) propose that the shear zone lies south of the faunal suture at the upper and middle crustal levels, but may lie close to it in the lower crust.

Different views also appear to be held by members of the seismic reflection community as to the surface manifestations of the deep reflectors. If they mark continental collision, Beamish and Smythe (1986) consider it unlikely that any geophysically resolvable signature would exist within the

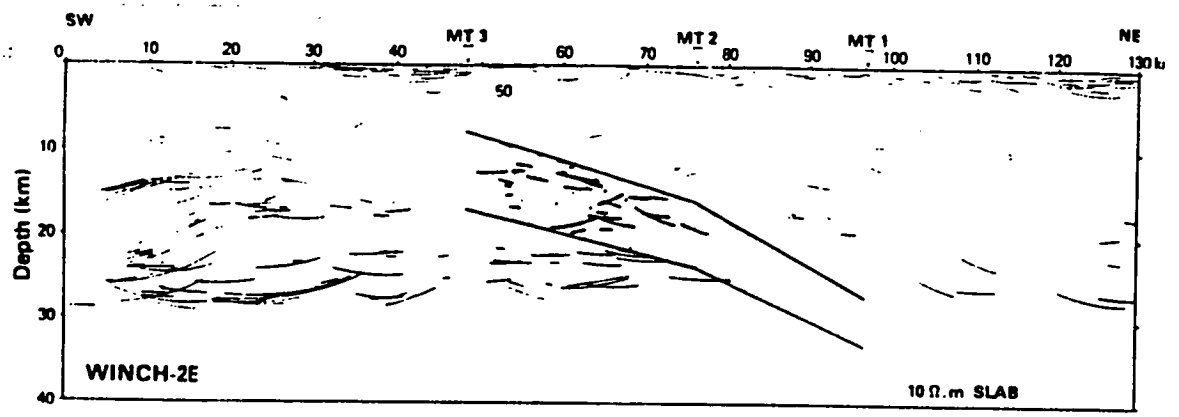

Figure 7.5: A northward dipping band of seismic reflectors from the WINCH (2E) line (from Beamish and Smythe 1986). These are relatively near to the surface (10km.) close to the Navan-Silvermines Fault but dip down to a depth of about 25 km. further north.

This diagram also shows an apparent correlation between the depth to this band of reflectors and an electrically conductive zone (10 Ω.m.) in the lower crust. This relationship is more fully discussed in section 8.2.3.

remnants of the two overlying Lower Palaeozoic rock packets. However, Chadwick and Holliday (1991) have recently identified a narrow band of reflectors at shallow depths (about 5 km.; fig. 7.6). They believe these reflectors are consistent with the up-dip extrapolation from the feature which was observed at greater depths. They further propose that these reflectors will sub-crop the Carboniferous age rock, possibly along the strike of the Causey Pike thrust near Keswick in the Lake District.

This author considers that although these seismic reflection studies show significant events, their interpretation is weakened by the absence of 'tie-lines' between them. The CSSP line (Bott *et al.* 1985) could provide such information but because of the different physical properties being measured, the results of seismic reflection and refraction cannot be readily compared (c.f. McGeary *et al.* 1987).

7.3. EARLY TECTONIC EVOLUTION OF NORTHERN ENGLAND

The structure of the deeper parts of the crust in Britain has been governed by continental movements and collisions. Primarily, the events culminating in the Caledonian orogeny are of particular interest. Over the last two decades, there has been and still is, considerable speculation as to the geometry, timing and even the number of lithospheric plates involved. However, in section 7.2 it has already suggested that there is now a considerable level of opinion favouring at least one major tectonic event in Northern England.

Most early models for the Silurian continental convergence were based upon the faunal identification of two distinct continental margins (e.g. Phillips *et al.* 1976, Dewey 1982), but these models were unable to explain many of the observations. More sophisticated models have since been proposed which suggest that the formation of much of Britain was the result of a long period of microcontinental accretion onto the major continental blocks. The formation of pre-Devonian Northern England is now thought to have been most influenced by the collision of the 3 major continental plates (Cocks and Fortey 1982, McKerrow and Cocks 1986, Hutton 1987, McKerrow and Soper 1989, Trench and Torsvick 1991) of Laurentia (including present day Scotland, N Ireland, Greenland and parts of North America), Baltica (Scandinavia) and the microcontinent of Avalonia (possibly in 2 parts: Cadomia [England, Wales,

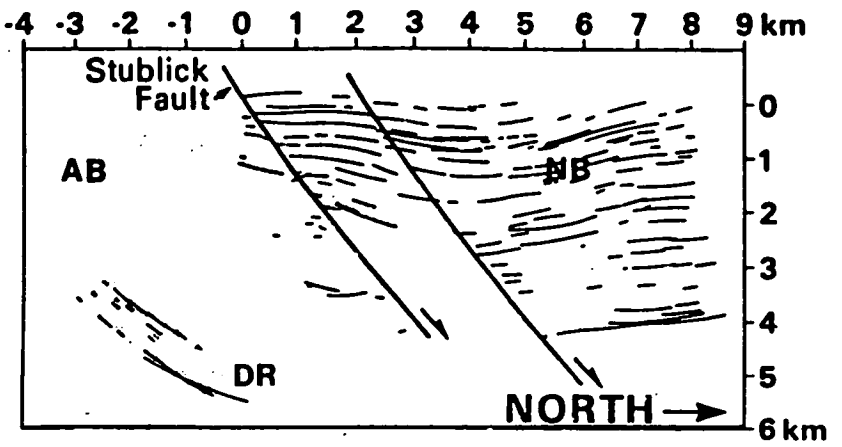

Figure 7.6: Some of the seismic reflection results presented by Chadwick and Holliday (1991).

The Northumberland Basin (NB) is dominated by a thick sequence of strong, near horizontal reflections from the sedimentary rocks. As discussed in section 7.5.2, there is only a thin sequence of such rocks over the Alston Block (AB). This block and basin structure is separated by a narrow hinge belt of northward throwing faults in the Stublick Fault complex.

Apart from a band a northerly dipping band of deep reflections (DR) at the northern edge of the Alston Block, the sub-sedimentary rock has few strong reflections. Chadwick and Holliday (1991) believe that these reflections are consistent with the up-dip extrapolation from the deeper seismic reflections observed offshore (e.g. fig. 7.5).

France] and Western Avalonia [Newfoundland]) (see fig. 7.7).

Prior to collision (the Cambrian and early Ordovician eras), Avalonia was probably related to Gondwanaland (including Europe south of the Ardennes and Poland), south of the equator. Between the Cambrian (e.g. McKerrow and Cocks 1986) and the middle of the Silurian (Cocks and Fortey 1982), Avalonia drifted northwards away from Gondwanaland and did not reconverge with Southern Europe until the Hercynian orogeny (section 7.6.1). By the late Ordovician faunal differences between Avalonia and Baltica had disappeared with the closure of the Tournquist sea. The Baltican and Laurentian margins then converged along a north-south trending subduction trench until the end of the Silurian.

Numerous models for the closure of the Iapetus ocean have been proposed (Holland *et al.* 1979, have collated some of the earlier ones). The subduction trench is thought to have had an ENE trend, although the specific direction in which subduction occurred has been the subject of some speculation (sections 7.3.1 and 7.3.2) and is also of some interest to the present study (section 8.2). Final collision of Laurentia and Avalonia is thought to have been completed by strike-slip motion in the Early Devonian. This type of convergence particularly confuses the overall picture by displacing previously adjacent terranes.

From the foregoing discussion, it is highly unlikely that continental convergence produced a single suture. The recent emergence of a complex geophysical picture in Britain and Ireland (sections 7.2 and 8.2.3) seems to confirm this. The remainder of this section consists of a discussion of some of the geological implications of the closure of the Iapetus ocean for Northern England.

7.3.1. Southward Subduction of the Iapetus Ocean

Several authors have ascribed early convergence between Avalonia and Laurentia to southward subduction of the Iapetus oceanic crust beneath present day England, Wales and Southern Ireland (Fitton and Hughes 1970, Phillips *et al.* 1976, Johnson *et al.* 1979, Brown *et al.* 1979, Leggett *et al.* 1983, Stillman 1986, Hutton 1987).

The earliest evidence for subduction related plutonism was observed in the

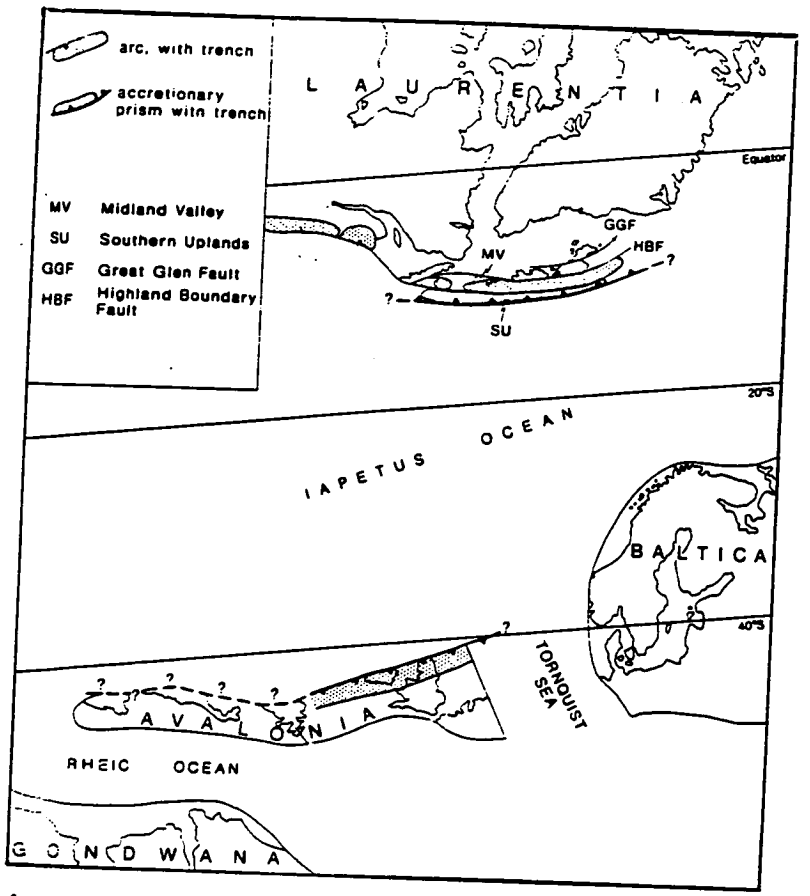

Figure 7.7: The likely positions of the palaeo-continents of Gondwana, Baltica, Avalonia and Laurentia during the Ordovician (from McKerrow and Cocks 1986). The closure of the Iapetus ocean may have been accomplished by southward subduction of oceanic crust beneath Avalonia (present day England) and almost certainly northwards beneath Laurentia (present day Scotland and parts of Ireland). The remnants of the latter of these accretionary prisms is now to be found in the Southern Uplands of Scotland.

progressive change in age and chemical composition of Ordovician age volcanic rocks from the Lake District to Wales. The former locality is thought to have endured a very long period of igneous intrusions (Firman and Lee 1987). Similar changes have also been noted along the strike of the Iapetus Suture in E and SE Ireland. The chemistry of the Borrowdale Volcanic Group in the Lake District also supports its eruption above continental crust, possibly within a magmatic island arc above the downgoing oceanic slab.

Volcanic activity climaxed in the middle of the Ordovician and then waned suggesting that southward subduction had diminished. Some later minor volcanism in Southern England and Wales (Leggett *et al.* 1983) has also been attributed to some subduction continuing in this direction until the Early Silurian. Final closure of the Iapetus ocean was almost certainly accomplished by northward subduction of the quiescent Northern England margin for another 30 Ma., prior to final continental docking.

Some problems have arisen with this model.

Firstly, the close proximity of the Lake District to the Solway Line (about 40 km.) is not compatible with the larger separations between present day trenches and their associated magmatic arcs (greater than 150 km.). It has therefore been suggested that the missing forearc and accretionary prism which presumably developed against the northern margin of Avalonia, was underthrust beneath Laurentia (e.g. Leggett *et al.* 1983). This is consistent with the LISPB refraction observations which show a low velocity, Northern England type of crust, beneath the Southern Uplands (section 7.2.3).

Secondly, a recent reinterpretation of the Ordovician geology of the Lake District (Branney and Soper 1988) has thrown some doubt upon the volcanic evidence for southward directed subduction.

Thirdly, no substantial geophysical evidence has previously been presented to support this hypothesis. Nevertheless, some of the models produced from the present study (fig. 8.2a) do show a significant southward dipping structure beneath the Alston Block.

7.3.2. Northward Subduction of the Iapetus Ocean

There is considerably less doubt regarding the evidence for subduction north of the Solway Line. The model of Leggett *et al.* (1983) has been widely adopted although some details are still in dispute (Haworth 1986). This model has 2 phases of subduction from the Cambrian until the Lower Devonian eras. Both phases produced a great volume of calc-alkali volcanic material in the Midland Valley and the Grampians of Scotland.

The first phase of subduction generated an accretionary prism in the Southern Uplands of Scotland and the Longford-Down massif in Ireland (e.g. Dewey 1982, McKerrow 1986, Soper *et al.* 1987). Turbidites were originally deposited at or near the Iapetus subduction trench. These low density sediments were scraped off the oceanic plate as it descended and were then thrust upwards and imbricated on the southern margin of Laurentia. The accretionary prism developed steadily between the Caradoc (455 Ma) and the Wenlock (420 Ma) eras, in a SE direction from the Southern Uplands Fault. The Southern Uplands now consists of chronologically ordered, accreted packets of rock which are separated by major faults. This subduction-accretion phase terminated as Avalonia impinged on Laurentia.

The second phase of subduction commenced as a thinned ('telescoped') Avalonian crust was underthrust northwards beneath Laurentia. As far as this author is aware, such continental subduction has no obvious modern analogues which can aid its interpretation. However, he does find it difficult to imagine that large quantities of continental crust could be subducted in this manner.

The Southern Uplands were uplifted during this second phase, causing an influx of turbidites to cross the Solway Line into the subsiding Lake District. The Iapetus Suture was subsequently overstepped by the Cheviot lavas and by early Carboniferous sedimentary deposition. As discussed earlier (section 7.2.3), geophysical observations have identified a northward dipping feature within the mid and lower crust, close to the Solway Line.

Folding of the Lower Palaeozoic rock was widespread throughout the Ordovician and a very pronounced metamorphic and folding event is thought to have occurred during the Late Silurian or Early Devonian. The "slate beds"

were thus formed during the Caledonian orogeny, within the "non-metamorphic Caledonides", south of the Scottish Highland Boundary Fault. Final continental docking may have occurred as the Avalonian crust impinged on the Midland Valley. This event was approximately contemporaneous with the widespread emplacement of granitic intrusions (section 7.4). The resulting Lower Palaeozoic basement rock shows a characteristic Caledonian (ENE) trend (Dunham 1948) observed not only in the small scale rock folds, but also in the larger scale structural features (i.e. the granites and the sedimentary basins; Soper *et al.* 1987). These latter features thus presumably follow the pre-existing lines of weakness in the basement rocks.

7.4. DEVONIAN GRANITE INTRUSIONS

A major phase of widespread Lower Devonian plutonism has been identified in Britain [e.g. the Shap, Skiddaw, Doon, Criffel, Weardale and Wensleydale granites together with those concealed in Eastern England (Allsop 1987) and the North Sea (Donato *et al.* 1983) and Ireland (Leinster)]. The exposed granites and a suite of associated lamprophyre dykes (McKerrow and Soper 1989) have all been dated radiometrically and found to have similar ages (390-410 Ma.).

These igneous intrusions are found on both sides of the Solway Line and so must either post date, or be contemporaneous with, the final closure of Iapetus Ocean (Brown 1979). Their existence cannot be directly reconciled with the the closure of Iapetus ocean if compared with contemporary subduction tectonic models.

Possible mechanisms (Stillman and Francis 1979, Leeder 1982, McKerrow and Soper 1989) have included a) continued subduction, b) subduction occurring elsewhere in Britain, c) magma generation during a post-Iapetus relaxation phase, or d) a reactivation of the suture and its related fractures. In fact, "rigorous theories for the origin of this magmatic province are non-existent" (Leeder 1982) and so no one explanation has been widely accepted.

On the southern margin of the area of primary interest to this study lies the Alston Block which is underlain by the Weardale granite. The

identification, structure and emplacement of this intrusion is now described in some detail.

7.4.1. Identification of the Weardale granite

The presence of a batholith was first postulated to explain the zones of mineralization (Dunham 1934) in the Carboniferous strata covering the Alston Block (section 7.8.2). These zones compared with similar features found around the exposed Cornish granites in SW England.

Other indirect evidence (summarized by Bott and Masson-Smith 1957a) included the presence of thermally metamorphosed Lower Palaeozoic rock in the Teesdale inlier and at the Crook borehole (Woolacott 1923), a broad negative vertical magnetic field anomaly (Bott and Masson-Smith 1957b) and a distinctive gravity anomaly (observed during several surveys: Bott 1967). This large negative anomaly (up to -37 mgal) could not be interpreted as anything but a low density granite intruded into a higher density rock.

The presence of the Weardale granite was subsequently proved after drilling through 390m of Carboniferous age strata at Rookhope (Dunham *et al.* 1965).

7.4.2. Emplacement of the Weardale Granite

The Weardale granite was probably emplaced during several distinct intrusive phases over a long period of time. This is supported by a significant geochemical change within the relatively short penetration of granite in the Rookhope borehole and the absence, in the surrounding rock, of much folding which can be attributed to its intrusion. One proposal was that magma was intruded over a span which lasted hundreds of millions of years (Robson 1980). This would involve older, cooled granite being exposed at the surface whilst molten rock was still being underplated.

There are geochemical and isotopic similarities between the Weardale granite and the Lake District batholith (Holland and Lambert 1972). The presence of a gravity anomaly ridge has led to some speculation that there exists some sub-surface connection between them and that they are part of a single, extensive batholith with a Caledonian trend (Bott *et al.* 1984). However,

some more recent gravity models attribute the anomaly ridge to low density rocks in the Vale of Eden (Lee 1986).

7.5. STRUCTURE OF THE ALSTON BLOCK AND THE NORTHUMBERLAND TROUGH

In the Lower Carboniferous, a number of block and basin structures formed over a wide shelf stretching from the Caledonian highland land mass (now the Scottish Highlands) to St. Georges Land (Wales and the English Midlands) in the south. Throughout a long period of lithospheric tensional stress blocks of upper crustal rock, often underlain by Devonian granite plutons, remained uplifted. Deep sedimentary basins formed in the unsupported regions between or beyond these blocks.

From Southern Scotland southwards, the following block and basin structures were formed: the Tweed basin, the Cheviot Block, the Northumberland Trough (Solway and Northumberland Basins), the Alston/Lake District Block, the Stainmore Trough, the Askrigg Block, the Craven Basin, the Rossendale Block, the Pennine Basin, the Derbyshire Massif and the Staffordshire Basin.

The structure of both the Alston Block and Northumberland Trough (fig. 7.8) are of most interest to the present study. This section therefore consists of a review of some of the geophysical studies undertaken while the more detailed results from this study are discussed later (chapter 8).

7.5.1. Review of Geophysical Structural Investigations

The characteristic block and basin structure was first identified by geological mapping (Trotter and Hollingworth 1928). Amongst the various subsequent geophysical studies, gravity anomaly observations played an important part in detailed investigations and still provide the most spatially extensive information.

The size and shape of the main Alston Block gravitational anomaly (fig. 7.9) is broadly consistent with corresponding signatures found around other, exposed granites. Five shorter wavelength minima are superimposed on this

Figure 7.8: The main structural regions in Northern England and Southern Scotland. The block and basin structures are usually delineated by major fault systems (dot and dash lines). In particular the Alston Block is surrounded by the Butterknowle (B.F.), Pennine (P.F.), Stublick (S.F.) and Ninety Fathom faults (N.F.F). The Northumberland Trough has a number of major intra-basinal faults with similar trends. These are the Harretts Linn (H.L.F), Antonstown (A.F.) and Sweethope Faults (S.H.F.). The Ridlees Fault (R.F.) is thought to mark the northern limit of the trough. Later Hercynian tectonic movements produced the more northerly trending Burtreeford Disturbance (B.D.) on the Alston Block and the Bewcastle Anticline complex (B.A.) which separates the Northumberland Basin in the east, from the Solway Basin in the west.

This map also shows a) the presumed extent of the concealed Weardale granite (dotted line), b) its 5 cupolas (shown by closed circles) within the Alston Block, the largest being centred on Rookhope (R) and c) other igneous rock which is now exposed at the surface (shaded). The extent of the Birrenswark (B.L.) and Kelso Lavas (K.L.) are shown on the northern edge of this region. On the southern margin of the Northumberland Trough, the Cockermouth Lavas (C.L.) are located adjacent to the Lake District Block. Other igneous rock is thought to have been extruded up to the surface via the Burtreeford Disturbance, on the Alston Block. The Late Carboniferous Whin Sill (W.S.) is concordant with the sedimentary sequence over a wide portion of the SE corner of this map. It outcrops in a quasi-continuous manner from the Pennine Faults in the SW to the North Sea in the NE.

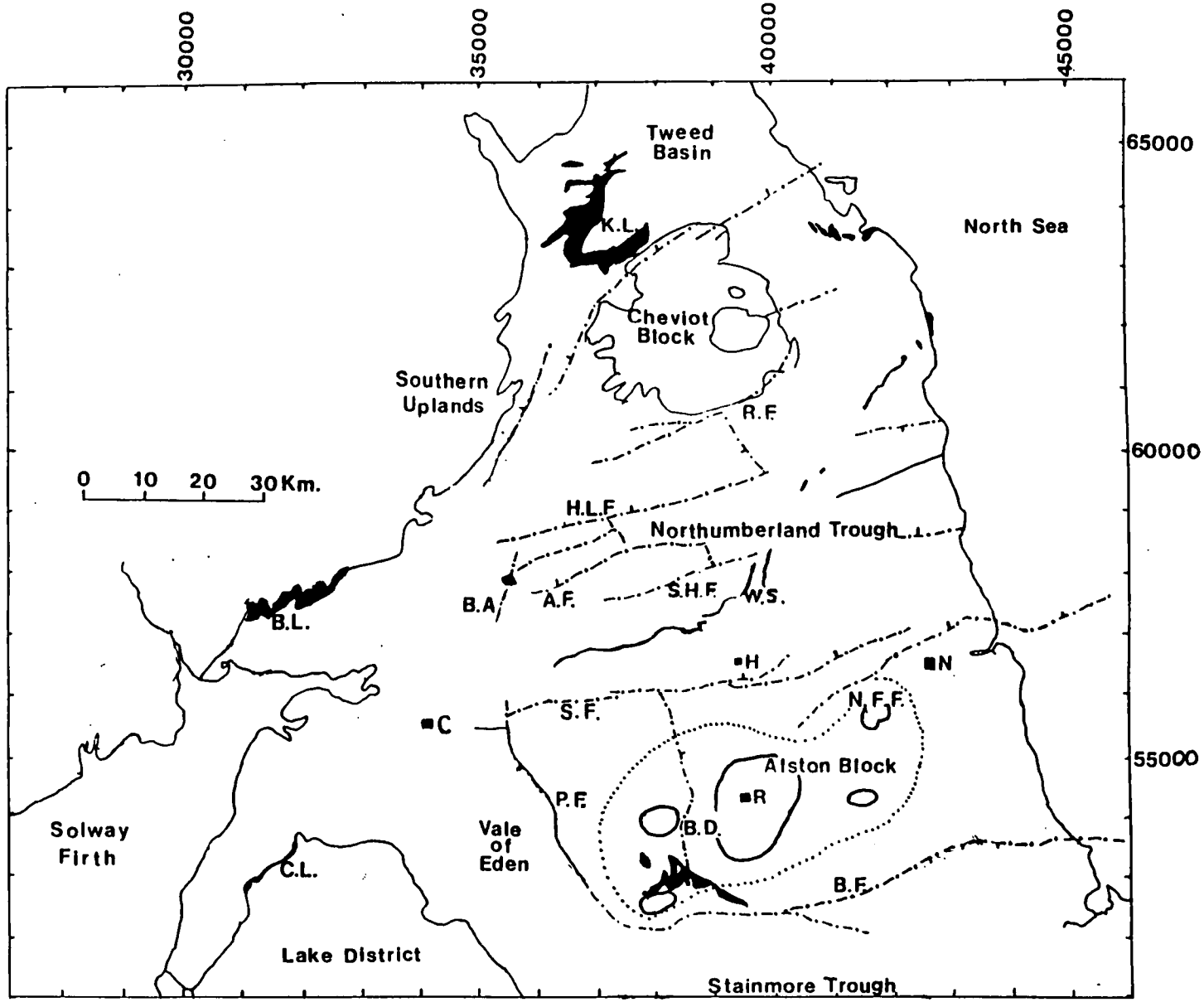
30000
35000
40000
45000
65000
60000
55000
Tweed Basin
K.L.
North Sea
Cheviot Block
Southern Uplands
R.F.
0 10 20 30Km.
H.L.F.
Northumberland Trough
B.A.
A.F.
S.H.F.
W.S.
B.L.
H
N
S.F.
N.F.F.
C
Alston Block
P.F.
R
B.D.
Solway Firth
Vale of Eden
C.L.
B.F.
Lake District
Stainmore Trough

Figure 7.9: The large negative gravity anomaly in the vicinity of the Alston Block (A.B.), caused by the intrusion of the Devonian age Weardale granite into a higher density basement (adapted from Evans *et al.* 1988). Within its presumed limits (dotted lines), the 5 subsidiary minima are associated with the cupolas (fig. 7.8). To the north and south of this block, there are longer wavelength anomalies caused by the sediment filled Northumberland Basin (N.B.) and Stainmore Trough (S.T.).

The location of the 'long' MT profile, which is the primary subject of this study is indicated by a thick line and some of the seismic profiles are marked by thinner lines (K; Kimbell *et al.* 1989, E3,E4,E5: Evans *et al.* 1988).

BOUGUER GRAVITY ANOMALY MAP
Bouguer anomalies at 1 mgal intervals (1 mgal = 10⁻⁵ m/s²)
Borehole
BGS 1986 seismic reflection lines (CDP traces)
MT profile
Approximate limits of Weardale granite
10 km
NB
K
A'
E5
E4
AE
E3
CT
870
860
850
840
830
820
810
370
380
390
400
410
420
430
440
450
460
470

feature (centred on Rowlands Gill, Cornsay, Scordale, Tynehead and Rookhope) are interpreted as interconnected cupolas (or bosses) on the upper surface of the batholith (fig. 7.8). Further to the north, the sediments within the Northumberland Basin also generate a broad negative gravity anomaly. Changes in this gravitational signature are usually attributed to the variations in the thickness of sediments across the basin. This basin is separated from the Alston Block by a hinge belt whose unexposed parts have been identified from its gravitational characteristics.

Quantitative modelling of the gravity anomalies has been undertaken in two and three dimensions during several previous investigations for both the depth to the top of the granite and the Lower Palaeozoic basement beneath the sedimentary rocks (Bott 1967, Yassi 1983, Evans *et al.* 1988, Kimbell *et al.* 1989). Like the models generated in the course of this study (fig. 8.11), the depth to the top of the granite cupolas has been found to be less than 1km. and increases outwards from the centre of the block to its fault bounded margins. Figure 7.10 gives a recent example of a detailed 2-D gravity model.

Magnetic surveys over this region (Bott and Masson-Smith 1957b, Cornwell and Evans 1986) have shown that the granite is less strongly magnetized than its surrounding rock. This phenomenon is also observed in the majority of other contemporary intrusions in the area (Allsop 1987). Similarly, the Northumberland sedimentary basin has little associated magnetic signature, except from the Devonian sandstones to the north. Superimposed on both the main structural units are many short wavelength features. These have been qualitatively interpreted as resulting from the presence of dykes (e.g. fig. 6.2), mineralized veins, the Whin Sill and the Stublick Fault. Quantitative interpretation of magnetic anomaly patterns is difficult because of the complex pattern which arises from induced and remnant magnetization. Nevertheless, Yassi (1983), has obtained broadly similar 2-D magnetic and gravity anomaly models across the region.

7.5.2. The Alston Block

The consolidated Weardale granite was very influential in the Post-Devonian geological history of the Alston Block (Dunham 1948, Bott and Johnson 1972, Robson 1980).

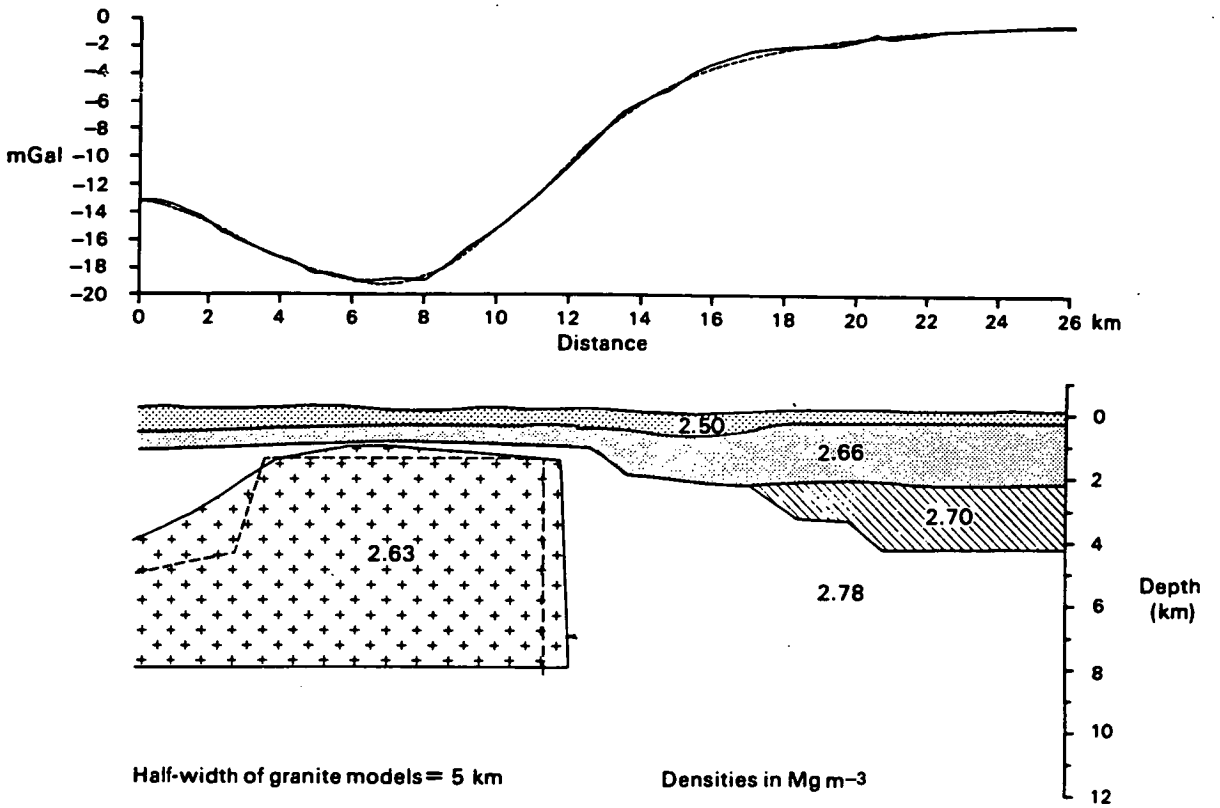

Figure 7.10: The 2-D gravity model proposed by Kimbell *et al.* (1989) for the coincident seismic reflection profile (K in fig. 7.9). The low density granite intruded into the higher density basement generates the large negative anomaly, whilst other more localized changes are attributed to variations in the thickness of the surficial sedimentary rock.

Firstly, the granite stabilized the Lower Palaeozoic basement rock around it into a single, distinct geological unit, which resisted the effects of later tectonic events. Consequently, there is little evidence of faulting in the overlying sub-horizontal Carboniferous rock such as that which affected other areas around the block.

Secondly, the low density granite provided buoyancy to the Alston Block, whilst other regions underlain by Lower Palaeozoic rock subsided during periods of crustal extension. In fact, whilst the sedimentary troughs were being formed, it is possible that the Alston Block rose in isostatic response to the erosion of the overlying Lower Palaeozoic rock. To this day, the block still remains a domed shaped area of relatively high topographic ground.

Thirdly, the slow upward isostatic adjustments to compensate for the granites gravitational deficiency were accommodated across hinge belts formed parallel to the sides of the intrusion. These fault systems now demarcate the limits of structural stability.

The current major fault systems around the Alston Block are the Lunedale - Butterknowle faults on the south side and the Stublick - 90 Fathom Faults to the north (fig. 7.8). These are the younger surface manifestations of the hinge belt fault systems. To the east, the margin is hidden beneath younger rocks, but it is thought to extend under the North Sea (e.g. Johnson 1984). An initial interpretation of a deep offshore seismic reflection line (the NEC line; Freeman *et al.* 1988) failed to detect its presence but upon reprocessing (Chadwick and Holliday 1991), these details emerged (fig. 8.17b).

The sediment depositional pattern suggests that the Alston Block and the Lake District massif behaved as one structural unit until the north-south trending Pennine Faults started to separate them during the Hercynian orogeny (Late Carboniferous). At approximately the same time, the north-south trending Burtreeford Disturbance (Dunham 1948) was formed. This monocline (fig. 7.11) throws eastwards and lies directly adjacent to the magnetotelluric traverse which is the subject of the current study.

Prior to Carboniferous sedimentary deposition on the Alston Block and over a period of 50 million years, severe erosion of the Lower Palaeozoic basement is thought to have exposed and weathered the granite cupolas. Compared

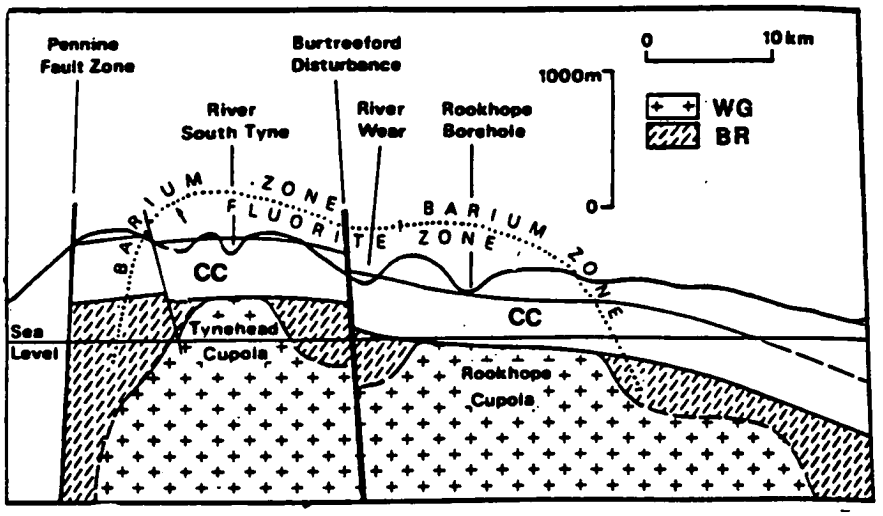

Figure 7.11: An east-west cross section through the Alston Block (from Robson 1980). The Weardale Granite (W.G.) cupolas at Rookhope and Tynehead are thought to directly subcrop the Carboniferous age Cover of sedimentary rock (C.C.). Elsewhere, the granite is concealed beneath a Lower Palaeozoic Basement Rock (B.R.), but its presence can be inferred from its gravitational anomaly (fig. 7.9) and zones of mineralization within the sedimentary rocks.

The Pennine Fault marks the western limit of the block, whilst the Burtreeford Disturbance displaces the sedimentary, metamorphic and igneous rocks down towards the east.

with the Northumberland Trough (section 7.5.4), only a thin and incomplete sequence (about 1 km.) of predominantly marine sediments were subsequently deposited as the sea transgressed towards the centre of the block.

7.5.3. The Stublick – 90 Fathom Fault System

This major system of faults has been observed to have a marked throw down towards the north. The presence of Whin Sill magma (section 7.8.1) in parts of the Stublick Fault complex shows that faulting occurred prior to the late Carboniferous. In fact these faults were probably active from at least the early Carboniferous until after the Permian. The 90 Fathom Faults are probably significantly younger (Post-Permian; Leeder *et al.* 1989).

The Stublick Fault complex controlled the early evolution (Courcyean to Asbian) of the Northumberland Trough by permitting differential subsidence between the block and basin. It has been proposed (e.g. Trotter and Hollingworth 1928, Dunham 1948, Robson 1980) that the Stublick Fault may be a re-activation of an ancient fracture in the basement rock, although little direct evidence exists to support this view (c.f. section 8.2.5).

Surface geological mapping has shown that the Stublick Fault appears to terminate on the Pennine Fault in the west and cannot be traced much further east than Hexham, close to the western most limit of the 90 Fathom Fault trace. Recently, the LANDSAT satellite image of east-west trending lineament (Bateson 1984) suggests that the Stublick Fault may extend further westwards, under the younger rocks in the Vale of Eden, to the Solway Firth.

7.5.4. The Northumberland Trough

Over a hundred years ago, geological mapping of rock exposures revealed that the Carboniferous age covering strata were thickened markedly in some areas of Northumberland. This is now recognized to be a manifestation of the large, asymmetrical Northumberland sedimentary basin which formed between the granite stabilized Alston and Cheviot Blocks (fig. 7.12).

Offshore seismic reflection data suggest that the Northumberland Trough extends eastwards into the North Sea (NEC line; reinterpreted by Chadwick and

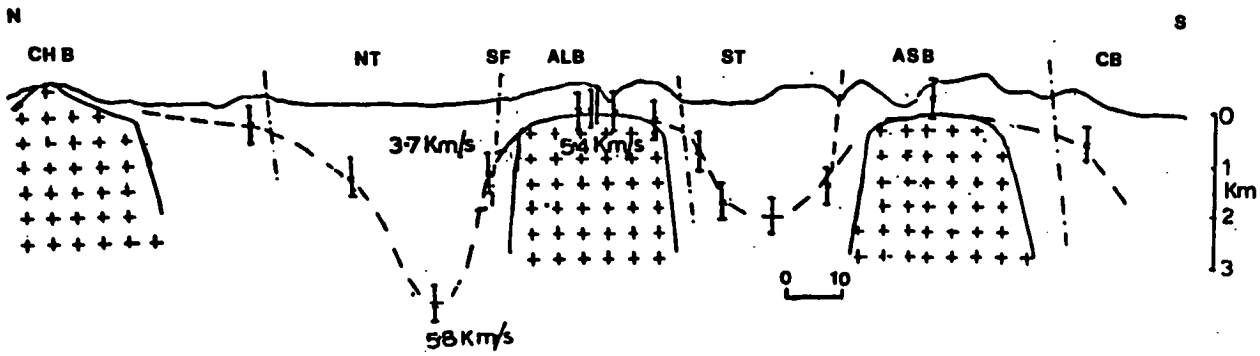

Figure 7.12: The cross section through the block and basin structure based on the results of the NERL seismic refraction survey (Swinburn 1975). The computed depth to basement shows that only a thin sequence of low velocity sedimentary rock exists above the granite supported blocks (i.e. the Cheviot (CHB), Alston (ALB) and Askrigg (ASB) Blocks). Between and beyond them, there is a significant increase in the sedimentary thickness in the basins (i.e. the Northumberland Trough (NT), Stainmore Trough (ST) and Craven Basin (CB)). The northward throwing Stublick Fault complex (SF) separates the Alston Block from the Northumberland Trough.

Holliday 1991), and westwards into the Solway Firth (the WINCH line; Hall *et al.* 1984, Beamish and Smythe 1986). On the NW side of the Northumberland Basin (fig. 7.1), the Carboniferous cover gives way to the older, Silo-Ordovician metamorphosed rocks (section 7.2.1), whilst in the NE these sedimentary rocks thin over the Cheviot-Alnwick ridge before thickening again within the Tweed Basin. The Alwinton-Ridless faults are considered to be part of the ill defined northern limit of the trough.

On geological evidence and from the presence of a gravitational anomaly, the Northumberland Trough is separated into 2 distinct basins. The Solway basin, to the west, is almost completely concealed beneath rocks of Permo-Triassic age except at the very margins of the basin. This is in marked contrast to the widespread exposure of the Northumberland Basin to the east. The 2 basins are separated by a complex of northward trending basement anticlines (Day 1970) at Bewcastle (also observed on the CSSP seismic line; fig. 7.4).

Almost all this region is covered by some, near horizontal sedimentary rocks of Dinantian and Early Namurian (Lower Carboniferous) age. At the southern margin of the Northumberland Basin, 2500m. of Lower Carboniferous sediments are thought to have been deposited, compared to only 300m. on the Alston Block. Upper Carboniferous (Late Namurian, Westphalian and Stephanian) rocks are thought to have been largely eroded, except in the SE and offshore. A more detailed discussion of the sedimentary rocks is given later.

7.6. INITIATION AND EVOLUTION OF THE NORTHUMBERLAND TROUGH

7.6.1. Initiation

The Northumberland Trough, like most Carboniferous age basins in the North of England is thought to have been initiated as the result of lithospheric thinning in response to north-south tensional stress (Leeder 1976,1982). Originally, mantle flow was thought to have been the source of this crustal tension (Bott 1967, Leeder 1976), but it is now recognised there are several alternative, tectonic explanations. Probably one of the most widely accepted is that during the Middle Devonian and Lower Carboniferous eras,

Northumberland formed part of a broad shelf on the Laurasian continental plate. The Mid-European oceanic crust attached to this plate was subducted below a Southern European continental margin, to the south of England (Leeder 1976, Bott *et al.* 1984, Bott 1987). Southward directed slab pull beneath the subduction zone, caused crustal extension in the back arc region from South Wales to the Midland Valley of Scotland. Tensional forces permitted the southward creep of the Laurasian continent until the collision which marked the Variscan orogeny (see fig. 7.13; Bott *et al.* 1984).

The presence of a crustal scale thrust or shear zone (section 7.2.3) has led to some speculation (e.g. Chadwick and Holliday 1991) that the Northumberland Trough was then formed by the subsidence of the hanging wall of the partially reactivated shear zone. This is considered again in the light of new observations from this study (section 8.2.5).

7.6.2. Basin Evolution

During the latter parts of the Devonian era, lithospheric stretching probably caused a partial melting of the upper mantle (at a depth of between 40 to 80 km.) and magma genesis (Johnson 1982, Leeder 1982) in areas of weak crust (fig. 7.14). The consequent increase in the rock volume caused an upwarp in the upper crustal rocks and an emergent land surface at the northern end of the Northumberland Trough (Leeder 1974,1982, Robson 1980, Johnson 1984).

Sub-aerial igneous activity (Leeder 1971, 1974, 1982, Collier 1989) also concentrated on the northern margin, started with the extrusion of the Birrenswark and Kelso alkali basalt lavas (fig. 7.8) at the start of the Carboniferous (360 Ma.). Further south, downwarping initiated the formation of the asymmetrical Northumberland Trough. Later, igneous rocks (Kershope lavas, Glencartholm Tuffs and numerous volcanic necks in the Visean age range 342-330 Ma.) all formed in an elongate NE-SW region along the pivotal line of maximum crustal flexure. These lava flows are thought to thin towards the south, into the centre of the basin (Leeder 1974). Limited volcanic activity also occurred on the south side of the Solway Basin during the Early Dinantian, with the extrusion of about 100m of olivine basalt lava at Cockermouth.

Upper crustal extension was accommodated by differential movement

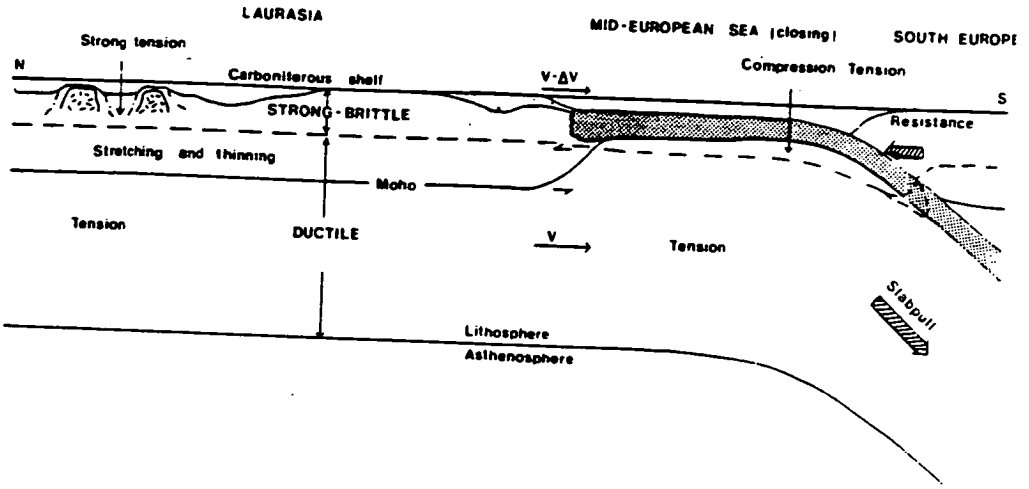

Figure 7.13: Southward directed subduction of oceanic crust beneath Southern Europe (from Bott *et al.* 1984). This probably occurred during the Late Devonian or Early Carboniferous eras. The resulting tensional forces at the subduction zone permitted southward creep of the Laurasian palaeo-continent (including Britain) and crustal extension over a wide region as far north as the Midland Valley of Scotland. Consequently, a chain of extensional basin were formed between the granite supported blocks of upper crust.

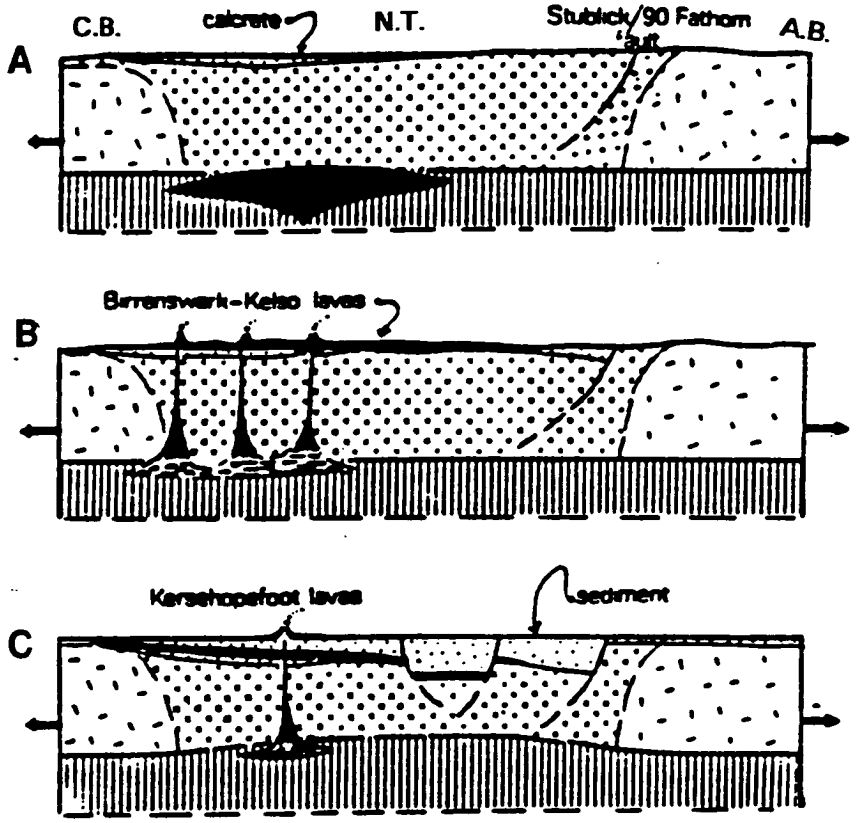

Figure 7.14: A possible scenario for the evolution of the Northumberland Trough (N.T.) between the granite stabilized Alston (A.B.) and Cheviot Blocks (C.B.) (adapted from Leeder 1982):

During the Devonian era (fig. 7.14a), there was a period of sedimentary deposition in the Scottish Borders. Partial melting of the upper mantle or lower crust generated an upwarp of the upper crustal rock. Lower Carboniferous extension (fig. 7.14b) was initially accommodated across the Stublick Fault hinge belt. On the downthrown (northern) side, the Northumberland Trough was formed. At approximately the same time lavas were extruded on the northern edge of the trough. Sediments rapidly accumulated within the basin which therefore further increased the rate of subsidence. Intra-basinal faulting developed (fig. 7.14c) in response to other periods of crustal extension. Finally more regional subsidence permitted sedimentary deposition to occur on block and basin alike.

between the Alston Block and the upper crust which now forms the base of the Northumberland Trough. The hinge belt separating them is thought to be close to the present day Stublick Fault system. The rift valley which formed on the downthrown side of this fault system rapidly filled with sediments, thereby increasing the rate of subsidence. Sediment deposition started earliest and continued more rapidly on the southern margin of the Northumberland Trough which is where the greatest thickness of sedimentary rocks is now found. Some later episodes of crustal extension were probably accommodated by the major intrabasinal faults (fig. 7.8) with ENE trends parallel to the Stublick Fault (e.g. Johnson 1984, Frost 1984).

Later in the Dinantian, sedimentation patterns show a distinct change to more regional deposition. This reflects a broader subsidence pattern no longer primarily controlled by the distribution of faults. The Alston Block ceased to be an island in the Asbian and by Namurian and Westphalian times (end Carboniferous), the blocks and basins from Southern Scotland to Lancashire were all subsiding at roughly the same rate, thereby acquiring similar thicknesses of sediments (Leeder 1982). This region was probably stabilized by the large volume of low density sediments which were deposited and which compensated for the buoyancy of the granites (Johnson 1982).

The evolution of the Northumberland Trough has been compared with the McKenzie (1978) model for sedimentary basin evolution (e.g. Leeder 1982,1987, Bott *et al.* 1984, Bott 1987, Barrett 1988). It explains the initial, rapid fault controlled subsidence in terms of the upper crustal response to uniform, short lived, lithospheric stretching, thinning and heating. A slower and more regional thermal and isostatic subsidence follows (the post rift or sag phase) as the lithosphere cools and thickens. This latter stage decays exponentially with time.

Fault restoration models, based upon incomplete seismic lines (Bott *et al.* 1984, Bott 1987, Kimbell *et al.* 1989), suggest that several modifications may be required to explain the evolution of the Northumberland Trough:

Firstly, differential lithospheric stretching may be required to explain an apparent discrepancy between upper crustal and whole lithospheric extension. This assumes that the brittle upper crust has moved more slowly than the

lower, more ductile parts of the lithosphere.

Secondly, the observed rate of post rift subsidence suggests that persistent (non-instantaneous) tension was the primary cause of the later subsidence phase rather than thermal subsidence. In fact, some recent models for the evolution of the Northumberland Trough have been proposed with several extensional and contractional phases throughout the Carboniferous (Collier 1989) with continued tectonic activity at least until the Silesian.

Towards the end of the Carboniferous, an east-west compressive event generated a number of folds and widespread faulting associated with the Hercynian orogeny (e.g. Haszeldine 1987, Robson 1980). These structures include the steep, west facing Lemmington, Holburn and Bewcastle anticlines and the Burtreeford Disturbance.

7.7. SEDIMENTARY STRATIGRAPHY OF NORTHUMBERLAND

This short review of the sedimentary stratigraphy is based upon several previous reviews including Dunham (1948), Day (1970), Frost and Holliday (1980), Gardiner (1983), Johnson (1984), Scott and Colter (1987) and Leeder *et al.* (1989). The published geological maps (e.g. B.G.S. 1966, 1975, 1980) provide very detailed surface geological information for certain areas.

During the Devonian and Carboniferous, Britain was probably located just to the south of the equator (e.g. Lovell 1977). The climate was very hot with mean summer temperatures around 40^{o}C. Johnson (1982) has suggested that the conditions that prevailed at that time were analogous to the present day Gulf Coast of the U.S.A.

The source of the clastic sediment is believed to have been derived predominantly from the Caledonian mountains of the Scottish Highlands to the north. The blocks, which were emergent islands during the early part of the Carboniferous, are not thought to have supplied much sediment. Deposition was predominantly in deltaic, lagoonal or marine environments. As the shoreline fluctuated, marine transgressions were followed by deltaic regressions. This has given rise to a characteristic pattern of sedimentation which repeats vertically in section about every 10m. These cyclotherms of

coal, limestone, shale, sandstone, siltstones and seatearth (Robson 1980) can be traced laterally throughout the Upper Carboniferous rocks of Northern Britain and also in parts of the United States of America. Tectonic movements or changes in sea level are thought to have caused this pattern of sedimentation (Leeder and Strudwick 1987).

The Devonian sequence of igneous rocks and sandstones (fig. 7.15) is thin or virtually absent over much of Northumberland. This era was characterized by uplift and severe erosion of the Lower Palaeozoic basement rock. Devonian age rocks are now only found on the flanks of the Cheviot Block. Further to the west, the base of the Carboniferous succession is taken to be the Birrenswark lavas (Robson 1980). The base of the Carboniferous is not seen in the south, but in the north deposition continued without interruptions from Upper Old Red sandstone times. The oldest commonly observed Carboniferous sediments are the Cementstones (Lower Border Group). These are layers of grey shales interbedded with thin sandstones and a few limestone bands. This band is typically 100-1000m. thick and the sediments were mainly deposited in a deltaic system thought to have been draining to the south. There is a change to massive cross bedded sandstones of the Fell Sandstone Group (300m thick). This gives way to a more cyclic form of sedimentation in the Scremerston Coal Group (Mid-Upper Border Group).

As more regional subsidence occurred, there was a change to widespread deposition of shallow water marine carbonates. The Limestone Group shows thicker and laterally more persistent limestones within the cycles of sedimentation. Palaeontological correlations are simpler because of the lengthy marine inundations and thicker limestones (e.g. the Great and Four Fathom limestones). Some 1000m. of sediments were then deposited. As more regional subsidence occurred, the margins of the blocks were submerged sooner and covered with conglomerates, sandstones, shales and limestones of the Orton Group. From the Asbian onwards, the rate of subsidence was approximately the same as the rate of sedimentation because deposition always took place at or near sea level (the water depth was never greater than 50m: Leeder and McMahon 1988). Persistent cycles can therefore be traced over considerable distances in Northern England, with the thickness of beds being less over the blocks than in the basins. The block continued to be buoyant throughout the Carboniferous causing drape folds in some Early

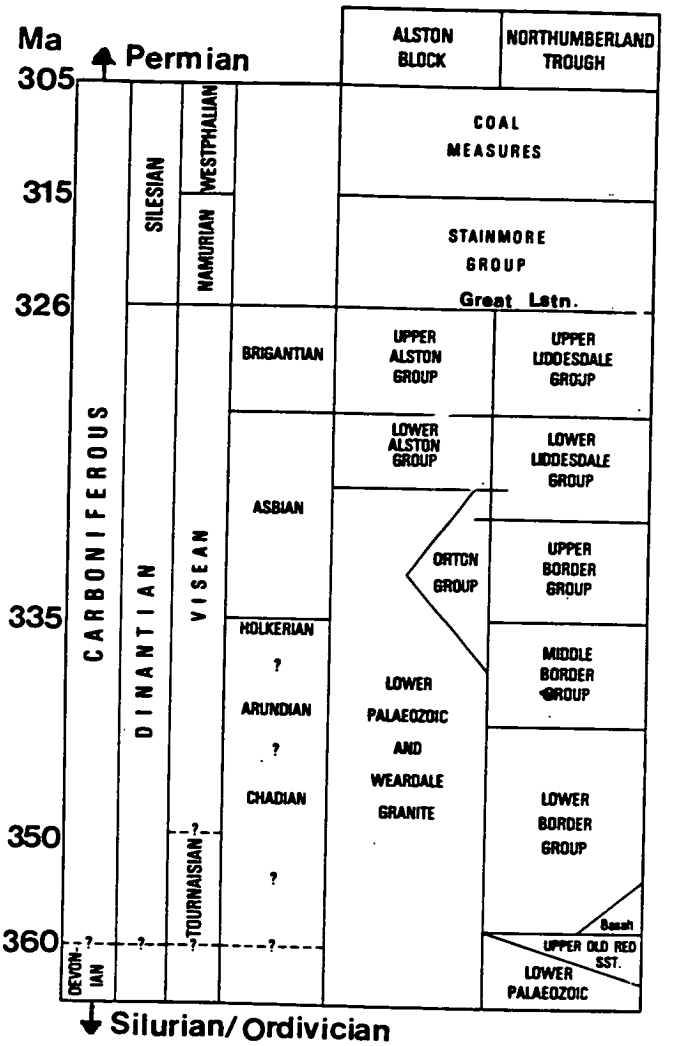

Figure 7.15: An approximate Carboniferous geological time scale for the rock groups which were deposited in the Northumberland Trough and on the Alston Block (based largely on Kimbell *et al.* 1989 and Collier 1989).

In the Northumberland Trough, Devonian sandstones and basalts gave way to rocks of the Border group. Meanwhile, the Weardale granite provided buoyancy to the surrounding Lower Palaeozoic rock and the Alston Block remained an island, until the Asbian. As differential subsidence waned, more regional subsidence allowed the margins of the block to be inundated by the sea. The Orton group of sedimentary rocks were deposited as a result. Finally, a more uniform sequence of sedimentary rocks covered both the block and basin alike (e.g. the Great Limestone). Westphalian and later Permian rocks, if deposited, have been largely eroded from the central area of interest to this study.

Permian sediments.

In most areas of Northumberland, economically important terringenous derived clastics and coals of Westphalian and Stephanian age were either never deposited or removed by erosion. The youngest deposits tend to be Permian aeolian sandstones found in the Vale of Eden, Solway Basin and in the North Sea.

7.8. RECENT GEOLOGICAL EVENTS

7.8.1. Late Carboniferous Intrusives

The Great Whin Sill (e.g. Ridd *et al.* 1970, Dunham *et al.* 1965, Robson 1980) is one of the most famous geological structures in the region. It runs, semi-continuously from Dunstanburgh and the Farne Islands, in the NE, along the line of Hadrians Wall near Hexham and then southwards down the line of the Pennine Faults (fig. 7.8). Because of its resistance to weathering, it has produced a pronounced topographic escarpment. The sill has been proved in a number of boreholes (e.g. Rookhope and Longhorsley (fig 8.20b)) and is thought to reside within a large area (about 5000 $km.^2$) of the sediments which cover the Northumberland Trough and the Alston Block.

The Great Whin sill has a maximum observed thickness of 100m. and is part of a suite of smaller quartz-dolerite sills which are concordant with the Carboniferous sedimentary sequence. These sills transgress stratigraphic levels over distances of several kilometeres.

The Whin sill complex was formed due to Hercynian compression and partial mantle melting during the late Carboniferous (dated to be 295 Ma. by Fitch and Miller 1967). During a number of distinct thermal pulses (Thorpe and MacDonald 1985), molten magma at $1150^{o}C$ (Randall 1985) was channelled through the Burtreeford Disturbance (Dunham 1948, Creaney 1980) and a number of north easterly trending dykes in other fault planes. Some of these are located close to the Stublick Fault system (fig. 6.2, Frost 1984). The sills subsequently developed within lower stratigraphic levels by gravity. The Great Whin Sill is often found close to the Great Limestone, which causes problems for the interpretation of both the seismic reflection (Kimbell *et al.* 1989) and electrical observations (section 8.4.6).

A final phase of intrusive activity is thought to have produced mineralization (Randall 1985), possibly in the Alston and the Lake District Blocks (Allsop 1987) at the same time.

7.8.2. Mineralization

The Alston Block has been economically important for a range of minerals for many centuries. Dunham (1948) details the distribution of fluorite, baryte, witherite, lead, zinc and iron ores found in veins within fault planes. Prior to drilling the Rookhope borehole, it had been believed that this mineralization was a direct consequence of the granitic intrusion *into the Carboniferous cover rocks*. Since it is now recognised that the mineralization continues into the Devonian granite, its presence is partially attributed to deep seated (upper mantle/lower crustal) saline fluids. A number of authors (Dunham *et al.* 1965, Fitch and Miller 1965, Bott 1967) have suggested that vertical tensional fractures within the granite may have provided an easier conduit, than the surrounding rock, for the upwards motion of low density mineralizing solution. In the near surface rocks, this solution has then been envisaged to spread out laterally along fissures until it reached cross-cutting fault planes. Owing to the significant thickness of the resulting mineralized veins Robson (1980) has suggested that considerable volumes of brine were involved.

Such mineralization was likely to have occurred during at least 2 episodes (at 295 and 225 Ma.) and possibly during other, later, less intense episodes.

In the presence of ferromagnetic material, the geophysical signature of igneous intrusives and some mineralized veins is readily detected from spatial magnetic anomaly patterns (Bott and Masson Smith 1957b, Cornwell and Evans 1986).

7.8.3. Regional Heat Flow

The late Carboniferous igneous intrusions (section 7.8.1) and mineralization (section 7.8.2) are both manifestations of the regional pattern of persistent high heat flow which has continued from the Weardale granite's emplacement to this day.

The vitrinite reflectance of the sedimentary rocks on the Alston Block

(Creaney 1980) has indicated a pre-Whin Sill heating which expelled free hydrocarbons and increased the coal volatile content (Bott 1967). The sedimentary diagenetic grade across the region (Wade and Robinson 1987) is also higher than would have been expected for the depth of burial of these rocks. Locally, the Whin sill intrusion has increased the maturity of organic material (Ridd *et al.* 1970).

The present heat flow regime across the Alston Block is still one of the highest in Great Britain (England *et al.* 1980, Downing and Gray 1986, B.G.S. 1988; fig. 7.16). The production of radiogenic heat from the granite elevates the observed heat flow from a background of about $50mWm^{-2}$ to $100mWm^{-2}$ at the Rowlands Gill cupola (Evans *et al.* 1988). The differences between the heat flow observed on the Askrigg and Alston Blocks has led England *et al.* (1980) to suggest that a thermal pulse gave rise to uranium enrichment of the latter locality, from a mid crustal source (10-16 km.). Precisely how many distinct thermal events have taken place is unclear from these studies but it is apparent by changes in the regional stress pattern, that the Weardale Granite has a long and probably intermittently rejuvenated thermal history.

The continued upward motion of hot fluids allows the heat generated to be transferred towards the surface and makes the Alston Block a likely candidate for the development of its geothermal potential (Evans *et al.* 1988).

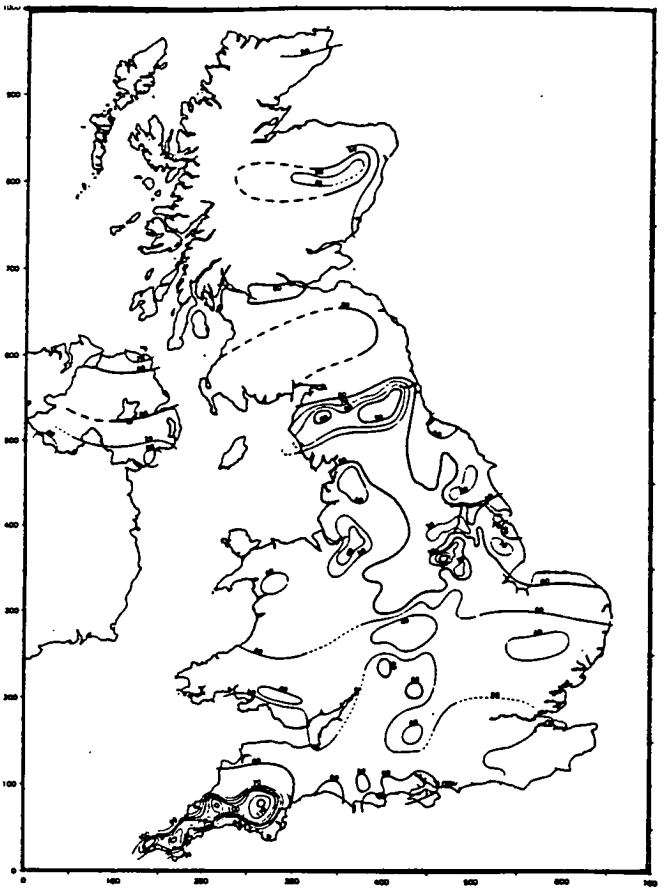

Figure 7.16: Heat flow (in $mW.m^{-2}$) across Britain (from B.G.S. 1988). The Lake District and Alston Blocks have considerably higher heat flows (up to 100 $mW.m^{-2}$), than the surrounding areas (about 50 $mW.m^{-2}$). In fact, the heat flow is thought to be the second highest in Britain, after Cornwall.

This enhanced level of heat flow in Northern England can be partly attributed to the presence of radiogenic heating from the granites, but there is some other evidence to suggest that the Alston Block may also have had a long and possibly rejuvenated thermal history.

CHAPTER 8

INTERPRETATION OF NORTHUMBRIAN GEOPHYSICAL MODELS

No man is an island, entire of itself,

every man is a piece of the continent,

a part of the main.

John Donne (1573-1631)

8.1. OVERVIEW

The methods used to generate geophysical models of the subsurface structure of Northern England and their preliminary interpretation were discussed in chapter 6. In the subsequent chapter, a review of some of the pertinent results from previous Earth science investigations of the area were then presented. In this chapter, the author's more detailed interpretation of the acquired MT, D.C. resistivity and gravitational models is given with regard to these investigations.

The deeply buried, lower crustal/upper mantle rocks are, in general, poorly resolved at most of the MT sites, but the models derived from the lower frequency soundings (< 0.01Hz.), suggest that upper mantle rocks demonstrate resistivities in the range from about 200-1000 Ω.m (c.f. Jones 1983c). Typical lower crustal rocks show comparable resistivities (100-1000+ Ω.m.) and are thus assumed to be a relatively 'dry' basement with little available pore space (section 2.9.1).

The author considers the location and nature of H.C.L.'s (High Conductivity Layers) within the mid/lower crust to be of particular interest and significance. The interpretation and implications of the electrical and possible correlation with deep seismic reflection results, are discussed in section 8.2.

The resistivity variation within the sub-sedimentary, basement rock is the subject of section 8.3. Since the depth to the top of the Lower Palaeozoic

basement and the Weardale granite can be determined from different types of geophysical observations, the results of an integrated interpretation are then presented and discussed.

The distribution and interpretation of the electrical resistivity variations within the sedimentary rock are the subject of section 8.4.

Finally, the results of some of the Earth science investigations are concatenated to provide a personal speculative model for the geological evolution of Northern England (section 8.5). As the inferences were usually drawn from an inadequate coverage of observations and over-simplified models, any conclusions must be treated with some caution.

8.2. HIGH CONDUCTIVITY LAYER (H.C.L)

8.2.1. The Geoelectric Interpretation

Numerous authors worldwide have identified highly conductive zones in the lower crust (c.f. Haak and Hutton 1986). In addition, several studies from Central and Southern Scotland and Northern England have also detected such a distinctive layer (Jain and Wilson 1967, Jones and Hutton 1979b, Novak 1981, Ingham and Hutton 1982, Sule 1985, Beamish 1986a,b, Beamish and Smythe 1986, Harinarayana 1987, S. Thatcher; person. commn., P. Jones; person. commn.) Rather than consider the results from these studies in virtual isolation, this author thought it was important to consolidate some of their separate observations in order that the extent of the conductive zone could be examined.

Many of the exploratory 1-D models (Appendix - C) derived for this study demonstrated the presence of a conductive zone (< 70 Ω.m.) in the mid and lower crust. Using spatial correlations and pseudo 2-D modelling techniques this feature could be identified at most of the intermediate and low frequency MT sites.

The depth to its upper surface was relatively well resolved and with a few exceptions, the overall emergent picture is consistent with there being a relatively smooth site-to-site transition of this parameter across most of the study region. The interpreted depths (in km.) at the individual sites from

within the study region are shown in fig. 8.1.

The top of the H.C.L. is at a depth of about 5 km. near to the Stublick Fault (e.g. RDY) but *apparently* dips down to the NNW, at an angle of 25^0 beneath the Northumberland Trough. It must be stressed that the precise orientation of this structure remains unclear because of the paucity of deep cross-line MT soundings. Within the study area, its upper surface reaches a maximum depth of about 30 km. under the southern portion of the Southern Uplands (e.g. BOR I). Only a few of the lower frequency soundings were properly able to resolve the base of the H.C.L. (e.g. LAM II in fig. 6.5) but their results showed that this layer was approximately 15 km. thick. These observations are most vividly demonstrated by the simplified pseudo 2-D model cross section (fig. 8.2a).

Underneath the Weardale granite (from HGN to HIL), the top of the H.C.L. also dips steeply to the south at an angle of about 65^0. It then flattens out at a depth of about 35-40 km. beneath ROO/HIL. This previously unrecognized structure apparently has comparable thicknesses and resistivities to its northward dipping counterpart. In fact, the high density of MT information now available near to the Stublick Fault suggests that the H.C.L. is one continuous structure across the entire length of the profile (over 90km. long).

The strictly 2-D MT model, derived for the southern part of the profile, supports many of the features observed in the pseudo 2-D model. For example, fig. 8.2b shows that the thickness of the H.C.L. is 15 km. beneath the Weardale granite and its layer resistivity is in the range from 35 to 55 Ω.m.. However, there are slight and potentially significant differences. In particular, the H.C.L. remains in the lower crust/upper mantle until the northern margin of the granite where it rises almost vertically towards the surface at DBK. Furthermore, the best fitting 2-D model could not resolve a more resistive layer underneath the H.C.L. for those sites to the north of DBK. At this time, the author prefers to avoid giving any special emphasis to either model (c.f. section 6.4.11) until more observations are collected and a more comprehensive 2-D model is elucidated.

The depth resolution of the MT method and the relatively high frequency range of the soundings precluded any firm assessment of whether the

Figure 8.1: The interpreted depth to the top of the H.C.L. (in km.) at each of the MT sites (c.f. fig. 3.5) in Northern England. The top of the H.C.L. is about 2km. from the surface near to the Stublick Fault and appears to dip down to the NNW to a depth of 30km. under the Southern Uplands. Many of the MT observations seem to suggest that it may also dip more steeply down to the south, beneath the Alston Block.

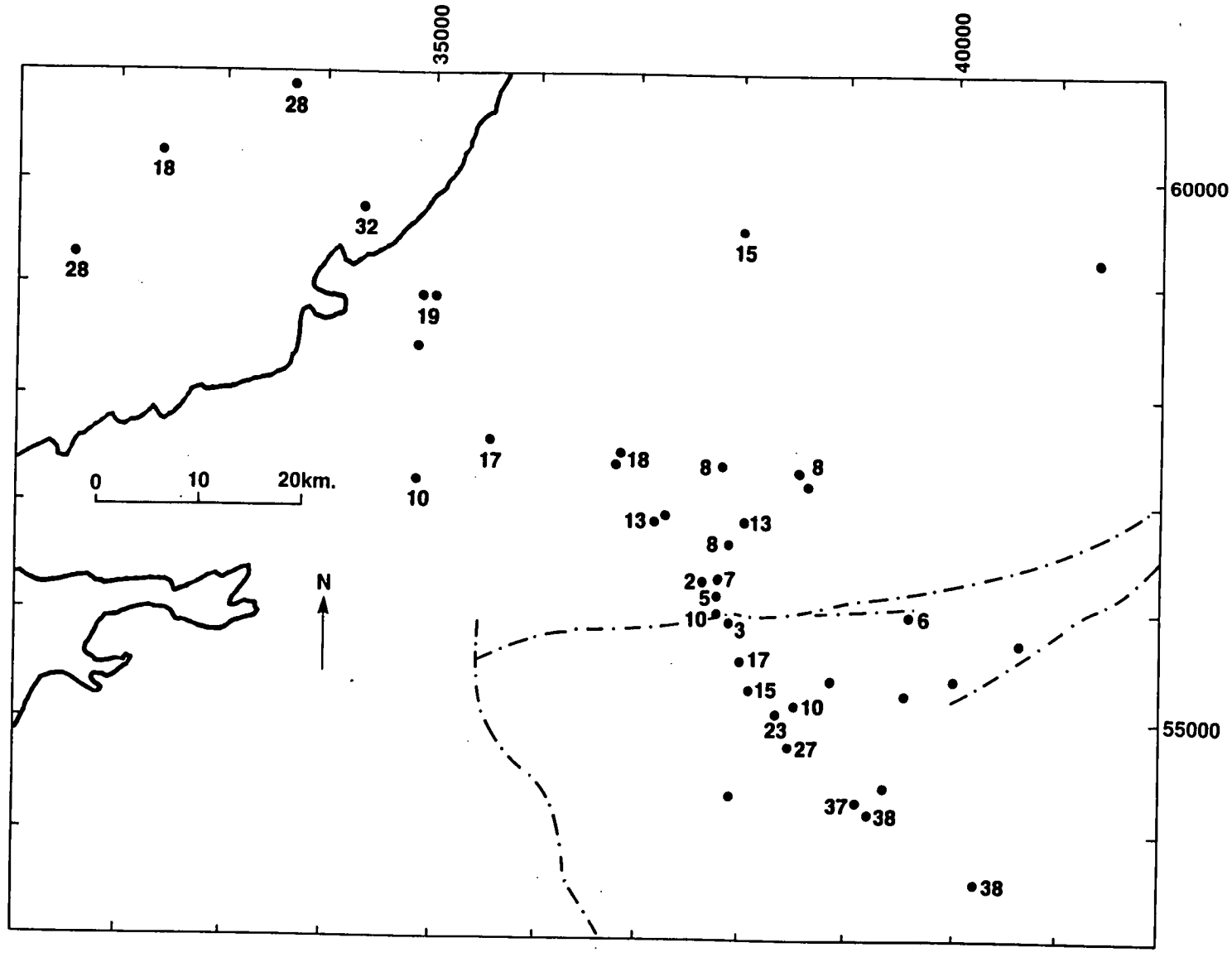
35000
40000
60000
55000
28
18
32
28
19
15
17
18
8
8
10
0
10
20km.
13
13
8
N
2
7
5
10
3
6
17
15
10
23
27
37
38
38

Figure 8.2: Simplified cross sections (c.f. figs. 8.9a,b) showing the interpreted resistivity with depth variation for the whole crust, along the 'long traverse' from the Alston Block in the south to the Southern Uplands in the north. These diagrams were derived from the results of pseudo 2-D modelling (fig. 8.2a) and strictly 2-D modelling (fig. 8.2b) applied to the response functions from the MT sites whose abbreviated codes are annotated along the top.

This figure shows that most of the crust is composed of resistive rock (> 70 Ω.m.). Two major and persistent conductive zones can be identified: the first surficial layer is the result of sedimentary rocks (fig. 8.19), whilst the second (the 'H.C.L.') dips to the north and south from the southern margin of the Northumberland Trough (DBK/WHI). The H.C.L. may extend up to intersect with the sedimentary rock layer, but the author interprets the data as showing that a thin more resistive basement separates them. This mid and lower crustal conductor is thought to be about 15km. thick, but as implied by the dashed boundaries, its lower margin was very poorly resolved by the MT observations.

The strictly 2-D model (fig. 8.2b) broadly supports the main conclusions based on the pseudo 2-D model except that it shows that the H.C.L. may remain in the mid and lower crust beneath the Alston Block as far north as the Stublick Fault.

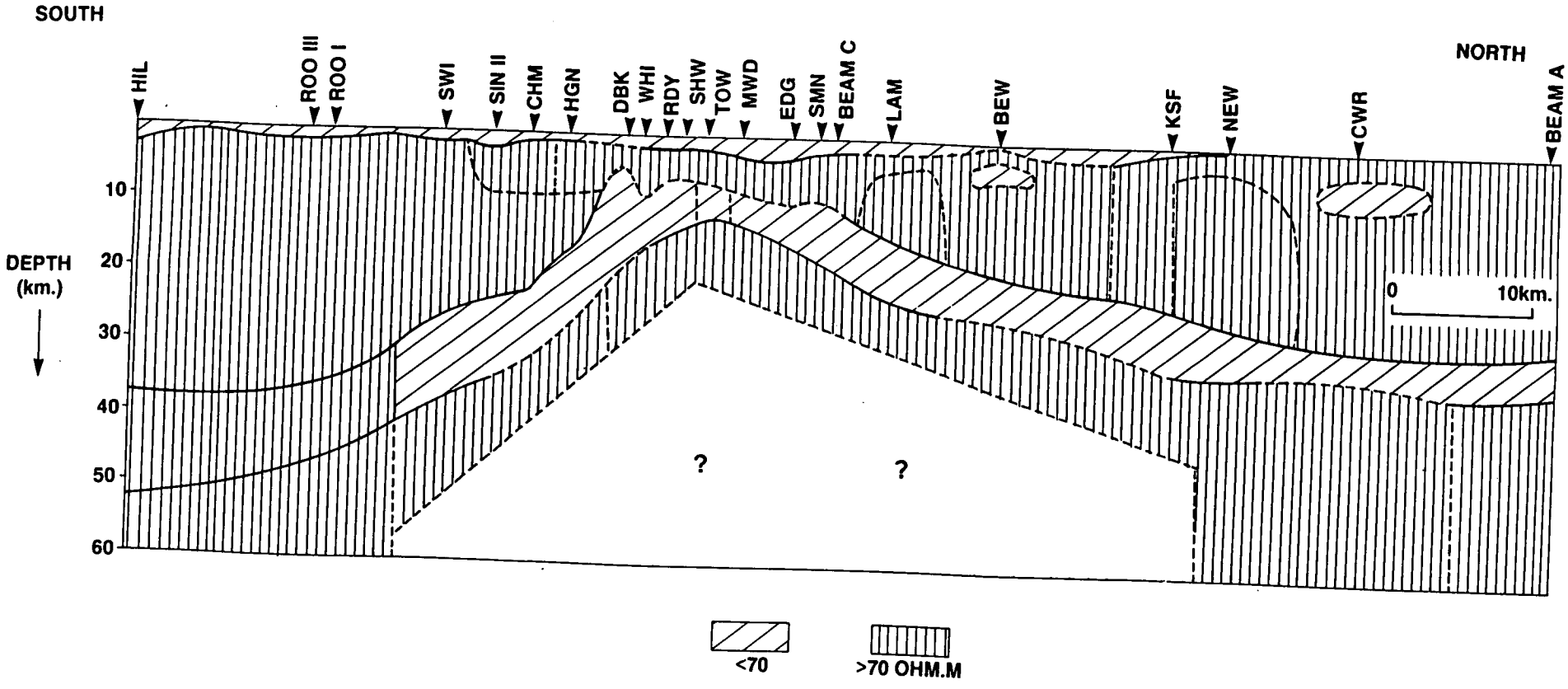
SOUTH
NORTH
HIL
ROO III
ROO I
SWI
SIN II
CHM
HGN
DBK
WHI
RDY
SHW
TOW
MWD
EDG
SMN
BEAM C
LAM
BEW
KSF
NEW
CWR
BEAM A
DEPTH (km.)
10
20
30
40
50
60
?
?
0
10km.
<70
>70 OHM.M

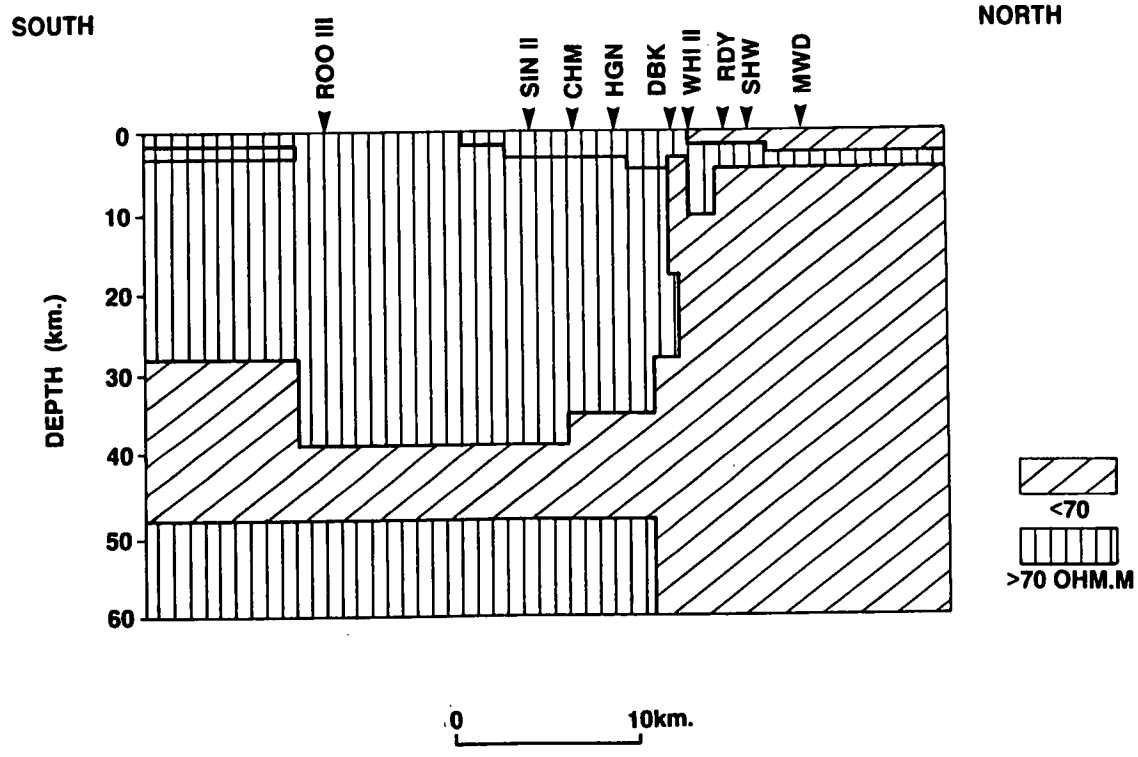
SOUTH
NORTH
ROO III
SIN II
CHM
HGN
DBK
WHI II
RDY
SHW
MWD
DEPTH (km.)
0
10
20
30
40
50
60
<70
>70 OHM.M
0
10km.

seismically determined Moho has any electrical significance (c.f. Jones 1983c). It is however suspicious that both the northward and southward dipping parts of the H.C.L. seem to sole out at, or just below, the Moho (30 km. deep here).

The pseudo and strictly 2-D models (figs. 8.2a,b) both show a narrow (1 km. wide) conductive zone which extends from the top of the H.C.L. and approaches the surface at DBK and WHI. Although it is possible that it may extend up to sub-crop the sedimentary rock, the author considers that a thin veneer (5 km. thick) of slightly more resistive basement rock separates them. Parameter resolution tests performed on the 2-D model also demonstrated that the size, shape and position of this conductive zone were relatively well constrained by the observations.

The location of this zone, directly adjacent to the Weardale granite is similar to a feature observed, along the strike of the Iapetus suture, next to the northern margin of the Leinster granite in Ireland (Whelan 1989; CZ in fig. 8.3).

Vertical magnetic variation observations (G.D.S.; chapter 1) have been used to identify the existence of an east-west trending anomaly at periods of 750s, on the northern edge of the Alston Block (Banks *et al.* 1983, Beamish and Banks 1983, Banks and Beamish 1984; fig. 8.4). The channelling of naturally induced electric currents through a conductive zone is thought to have caused such an attenuation of the magnetic fields. This zone is thought to reside either in the sedimentary layer (Banks and Beamish 1984) and/or within the more resistive basement, at a depth of about 5km. from the surface (Banks 1986). There is therefore a strong implication that the presence of the H.C.L. at shallow depths produces this anomaly. As a corollorary, the spatial extent of this geomagnetic anomaly implies that the shallow H.C.L. should persist across most of Northern England. However, on the basis of additional supporting seismic evidence (section 8.2.3), this zone may instead possess a more NE strike. In this author's opinion, it may prove instructive if, in the future, this geomagnetic anomaly were remodelled using the more detailed structural and resistivity control provided by this study (e.g. figs. 8.18 and 8.19).

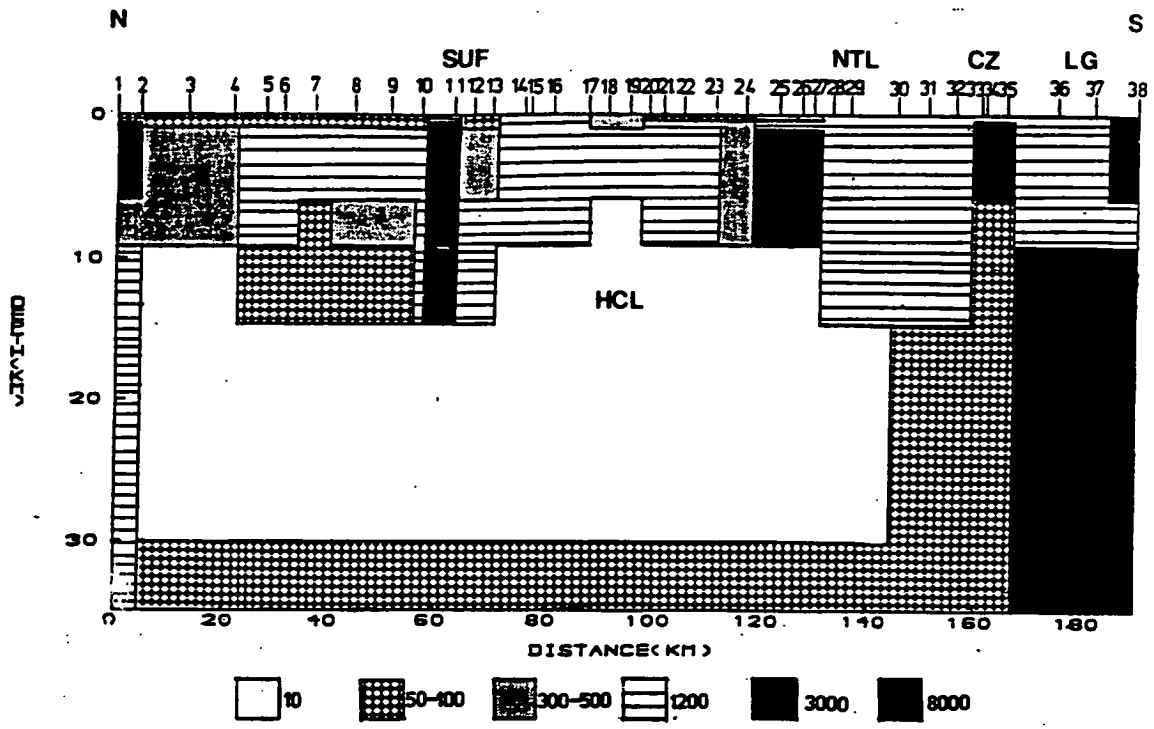

Figure 8.3: The results of a 2-D modelling study applied to the data acquired along the SIMP line in Ireland (from Whelan 1989). Like the Northern England results, a high conductivity layer (H.C.L; 10 Ω.m.) exists in the mid and lower crust across the length of the profile. At present most variations in the depth to the top of this layer cannot be readily correlated across the Irish Sea, but like the Alston Block, a conductive zone (C.Z.) approaches the surface on the northern margin of the Leinster granite (L.G.). The location of the Southern Uplands Fault (SUF) and the postulated extension of the Iapetus Suture (the Navan-Tipperary Line; NTL) are also shown.

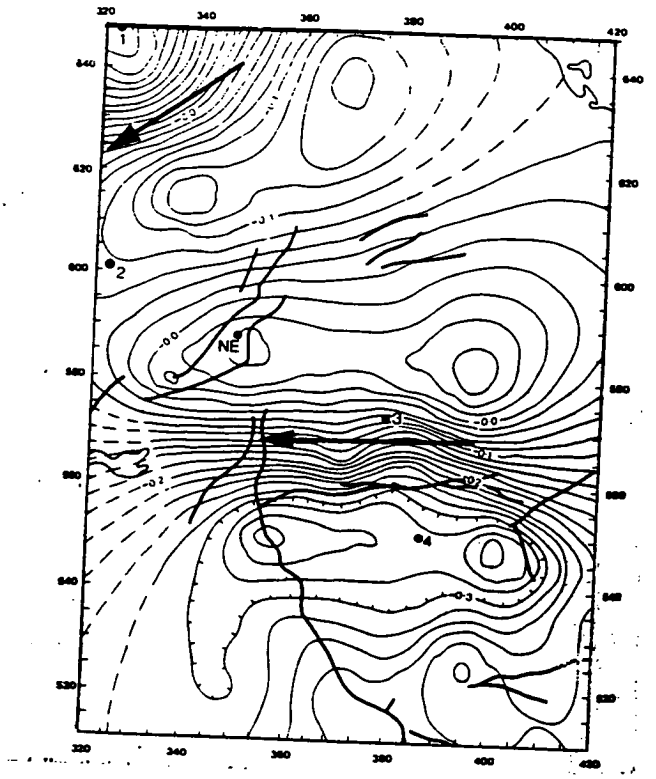

Figure 8.4: The vertical magnetic field anomaly pattern for Northern England and parts of Southern Scotland at periods of 750s, as determined by Banks (1986). The arrows show the direction of maximum current flow which is assumed to have been channelled through a more conductive layer.

The east-west trending anomaly on the southern margin of the Northumberland Trough may be attributable to either high conductivity sediments against the more resistive Alston Block or the mid-crustal H.C.L. (see fig. 8.2a,b at DBK/WHI). The results of other published studies also suggests that the Eskdalemuir anomaly (see also fig. 8.8c) in the NW portion of this map is caused by an intra-basement conductor at a depth of about 4km. (see CAP in fig. 8.8a)

8.2.2. Resistivity Variation of the H.C.L.

The models from the majority of the MT sites showed that the resistivity of the H.C.L. is relatively homogeneous and typically in the range from 20 to 70 Ω.m.. Slightly higher resistivities have been observed at HIL I (100 Ω.m.) at the deepest part of the H.C.L., and marginally lower resistivities were identified at SHW and TOW (about 10 Ω.m.), near to its shallowest location (see fig. 8.9, later for a more detailed geoelectric cross section). This variation could be attributed to observational noise or the equivalence principle (section 6.2.4), but it is worth noting that a lower resistivity (about 20 Ω.m.) was also required to produce a better fitting 2-D model for the response functions from RDY and SHW.

8.2.3. Integrated Interpretation of the H.C.L. and Deep Seismic Reflections

Several authors have tentatively correlated the depth of the northward dipping H.C.L. with a change in the acoustic properties of the rock (e.g. fig. 7.5). This author assumed that there exists a common cause for the coincidence of such boundaries (section 8.2.4), so that the depth to the top of the H.C.L. could be integrated with the depths to corresponding features from other studies in surrounding areas. This allowed a more regional and informed interpretation to be performed on these independent observations. In particular, the MT results obtained by Jones and Hutton (1979b), Ingham and Hutton (1982), Sule (1985), Harinarayana (1987), and P. Jones (person. commn.) were combined with information provided by the seismic reflection profiles presented by Brewer *et al.* (1983), Beamish and Smythe (1986), Klemperer and Matthews (1987), Evans *et al.* (1988) and Chadwick and Holliday (1991). In addition, if the H.C.L is related to the Iapetus suture, then the geoelectric results recently acquired by Whelan (1989) and Meju (1989) (the IMP and SIMP lines located in fig. 7.3) should also be considered.

In contrast to some previous studies (e.g. Chadwick and Holliday 1991), the author considered that a more geophysically realistic comparison would be drawn between the seismic reflection profiles and the depths to the H.C.L. as determined from *parametric* MT models (c.f. section 6.2.5). The deep seismic reflection sections show that a wide zone of reflective rocks exists beneath a relatively featureless middle crust (fig. 8.5). If the two-way-times are

Figure 8.5: The deep seismic reflections from portions of the WINCH 4 (fig. 8.5a), 2E (fig. 8.5b), 3 (fig. 8.5c) and NEC (fig. 8.5d) lines (redisplayed from Brewer *et al.* 1983 and Freeman *et al.* 1988).

Like fig. 7.5, the upper crust shows strong reflections from the sedimentary layer above a relatively unreflective middle crust. The depth to a wide band of reflective rock (interpreted boundary marked on each of the figures) can be correlated with the depth to the electrical H.C.L.. However, unlike the MT results, the reflective zone cannot be traced to depths shallower than 10km. from the surface.

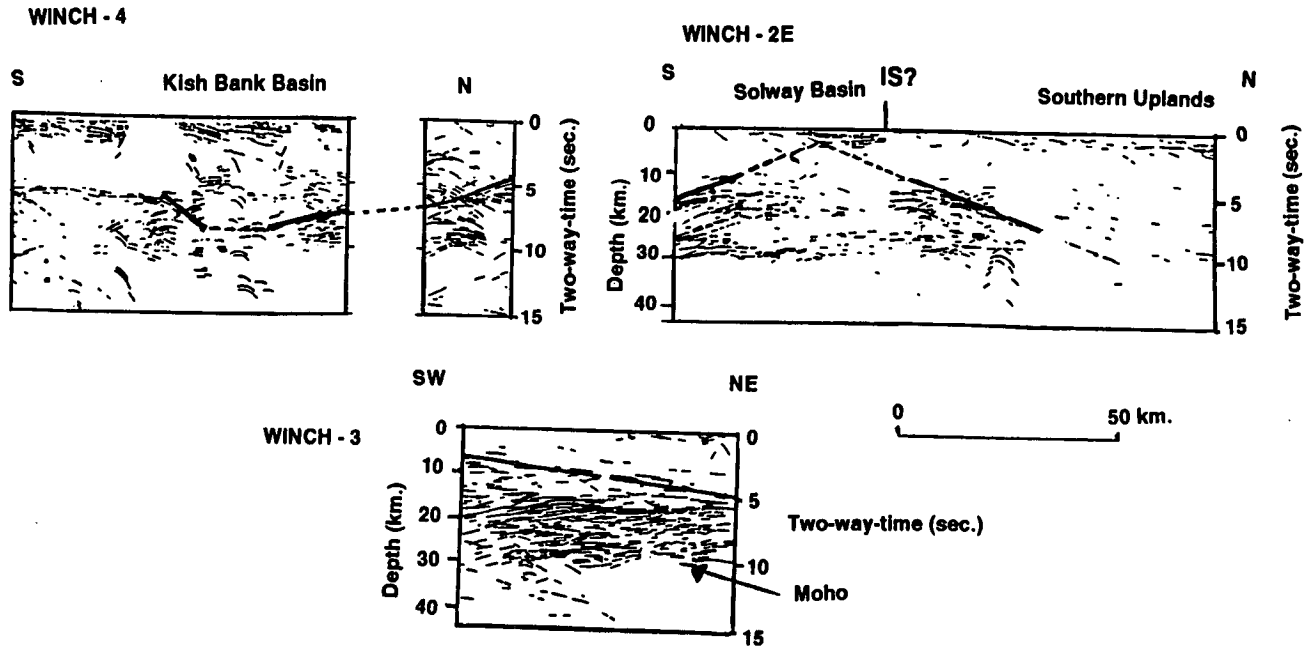
WINCH - 4
S
Kish Bank Basin
N
0
5
10
15
Two-way-time (sec.)
WINCH - 2E
S
Solway Basin
IS?
Southern Uplands
N
0
10
20
30
40
Depth (km.)
0
5
10
15
Two-way-time (sec.)
SW
NE
WINCH - 3
0
10
20
30
40
Depth (km.)
0
5
10
15
Two-way-time (sec.)
Moho
0
50 km.

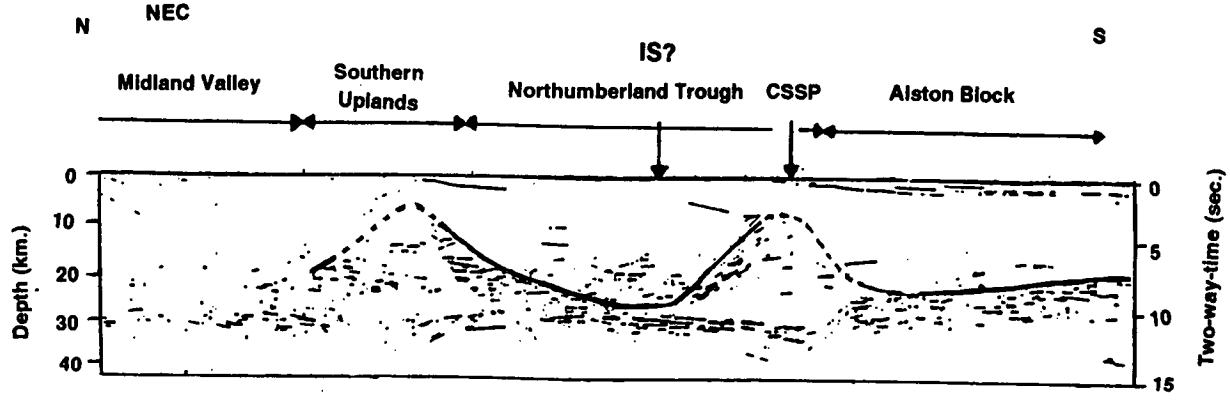
N
NEC
S
IS?
Midland Valley
Southern Uplands
Northumberland Trough
CSSP
Alston Block
0
10
20
30
40
Depth (km.)
0
5
10
15
Two-way-time (sec.)

converted to approximate depths (Brewer *et al.* 1983), the transition to this zone is at comparable depths (10-30 km.) to the H.C.L., for corresponding locations along the strike of the Iapetus suture. In general, the thickness of this reflecting packet of rocks is similar to that of the H.C.L., and neither feature extends substantially below the Moho.

Figure 8.6 shows the contoured compilation of the depths to the electrically and acoustically determined transition. These results support Klemperer and Matthews (1987) interpretation that there is a single NNW dipping structure at depths of between 10 and 30 km.. This extends at least from the NEC line in the North Sea (fig. 8.5d), through the region of interest to this study, the published commercial seismic data in the Solway Firth and towards the WINCH-2E line in the Irish Sea (fig. 8.5b). In general, this structure dips more steeply in the North Sea than in the Irish Sea and the MT results from this study suggest that there may be a localized change in dip, east of the Solway Firth.

The shallow depth to the H.C.L. which was observed in Northumberland (discussed in section 8.2.1) forms part of a "ridge" (fig 8.6) which extends right across the strike of the Iapetus suture and towards the Navan-Silvermines Fault in Ireland (located in fig. 7.2). In contrast to the MT results, the offshore seismic sections (fig. 8.5) failed to resolve a significant reflective zone at depths of less than 10 km.. This difference requires further consideration as it may signal that there is a major change in the acoustic properties or dip of this structure. It is recognized that the validity of the CSSP refraction results have been called into question (section 7.2.3), but it is worth noting that they did resolve an anomalously shallow depth to a "continental basement" (fig. 7.4; 4km.), close where the reflective/conductive zone is at its shallowest (e.g. fig. 8.5d).

Further south, a wide band of relatively flat seismic reflectors have been served onshore at depths of between 22 and 30km. (Evans *et al.* 1988; fig. 8.7). These also seem to coincide with the flatter portion of the H.C.L. beneath the Alston Block. On the northern margin of the Alston Block however, there is no seismic signature of the H.C.L.'s steeply southward dipping, or vertical interface with the base of the granite (section 8.2.1). This is perhaps not surprising in view of the inability of seismic reflection methods to image structures with

Figure 8.6: The contoured compilation of depths (in km.) to the top of the electrically conductive and seismically reflective layer. The interpreted minimum depths depths to this layer are signified by an "M".

A northward dipping structure can be traced from the NEC line in the North Sea (fig. 8.5d) in a WSW direction through Northumberland (fig. 8.2a), the WINCH lines (figs. 8.5a–c) and possibly extending towards the SIMP Irish MT profile (fig. 8.3). There is also some relatively substantial evidence for the presence of the southward dipping structure (fig. 8.2a) extending across the Irish Sea. A more complicated pattern is observed on the northern portion of this map.

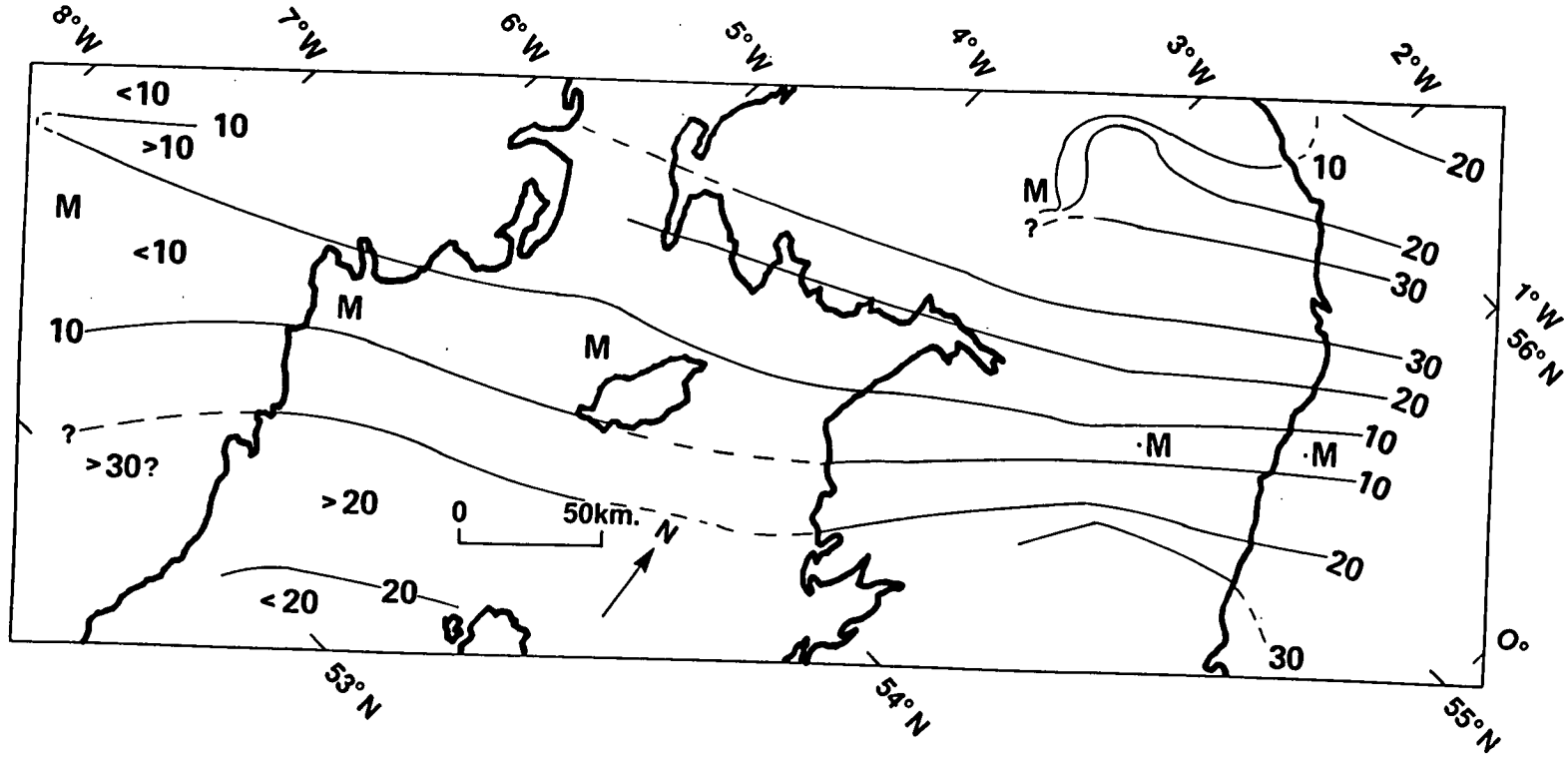
8°W
7°W
6°W
5°W
4°W
3°W
2°W
1°W
0°
56°N
55°N
54°N
53°N
<10
10
>10
M
<10
10
M
M
?
>30?
>20
0
50km.
N
<20
20
M
?
10
20
30
30
20
10
·M
·M
10
20
30

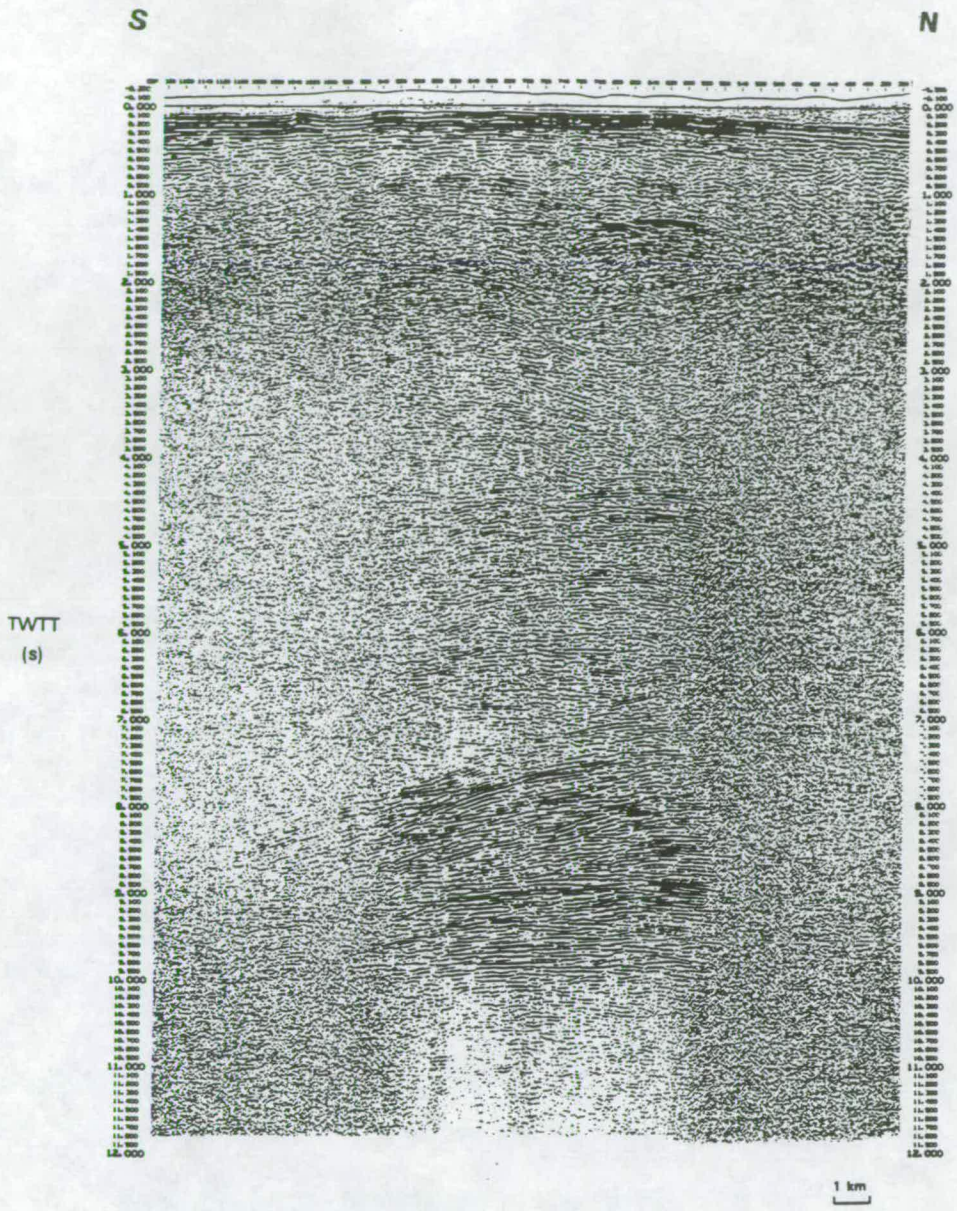

Figure 8.7: The deep onshore seismic reflections for a short profile across the Alston Block (published by Evans *et al.* 1988 and located in fig. 7.3). Note in particular the very strong band of reflectors in the lower crust (7.5 to 9.5s) which approximately coincides with the depth to the H.C.L. in this area (fig. 8.2b).

dips greater than about 40^{o} (Matthews 1986), unless accompanied by a displacement of strata.

The Irish MT results (e.g. fig. 8.4) show a H.C.L. comparable to that identified in Britain. Owing to the level of noise present in the response functions which have been acquired from several of the more crucial sites in the Whelan (1989) study, the correlation shown in fig. 8.6 between these studies remains weak. Reprocessing and remodelling of the original MT data may help to clarify the similarities.

The H.C.L. is entirely within the lower crust in Northern Northumberland, but approaches the surface again in Southern Scotland. The MT results from 3 sub-parallel profiles provide some useful comparisons. At the CAP (fig. 8.8a) and SAW (fig. 8.8b) MT sites, the H.C.L. lies at very shallow depths (< 5km.). These sites are located directly along the strike of the Eskdalemuir geomagnetic anomaly (Hutton *et al.* 1977, Banks *et al.* 1983; fig. 8.8c) so that it seemed likely that the currents concentrated within the shallow portion of the H.C.L. were responsible for this anomaly (c.f. section 8.2.1). However, the 2-D model results published by Ingham and Hutton (1982) from an intermediate traverse (fig. 8.8d) do not show any similar structures south of EAR. In order that the results from these studies can be reconciled, a more detailed consideration is required of the level of noise contamination and distortion effects upon these observations as well as the density of MT sites which are required to resolve what is probably only a narrow zone.

8.2.4. Source of the Correlation between Deep Conductive and Reflective Zones

In order that the depth to the top of the H.C.L. and the deep seismically reflective zone can be justifiably correlated, it is crucial that a common causal mechanism can be proposed.

There have been several explanations proposed for the source of lower crustal seismic reflectors in general (e.g. Matthews 1986, Hall 1986, McGeary *et al.* 1987, Hyndman and Shearer 1989) and for those in Northern England in particular (Beamish and Smythe 1986, Freeman *et al.* 1988, Chadwick and Holliday 1991). These include the presence of igneous intrusives, metamorphosed remnants of Iapetus ocean and fluids in the lower crust. It is widely accepted (e.g. Ibrahim and Keller 1981) that only a small volume of fluid

Figure 8.8: The results from previous EM investigations in and around the Southern Uplands of Scotland.

Figure 8.8a shows the 2-D model presented by Harinarayana (1987) which extends from Rookhope over the Weardale granite (W.G.) through the Northumberland sedimentary basin (N.B.) and to the Southern Uplands fault (S.U.F.). Many of these soundings have been reprocessed in the course of this study and will therefore not be discussed further. However, the shallow depth to a H.C.L. at CAP (fig. 8.8a) and SAW (fig. 8.8b; from Sule 1985) is of particular interest. They are both located along the strike of the Eskdalemuir geomagnetic anomaly (EA in fig 8.8c; from Hutton *et al.* 1977). The results from an intermediate MT traverse (fig. 8.8d; from Ingham and Hutton 1982) currently cast some doubt on the interpretation that the shallow H.C.L. directly caused this anomaly.

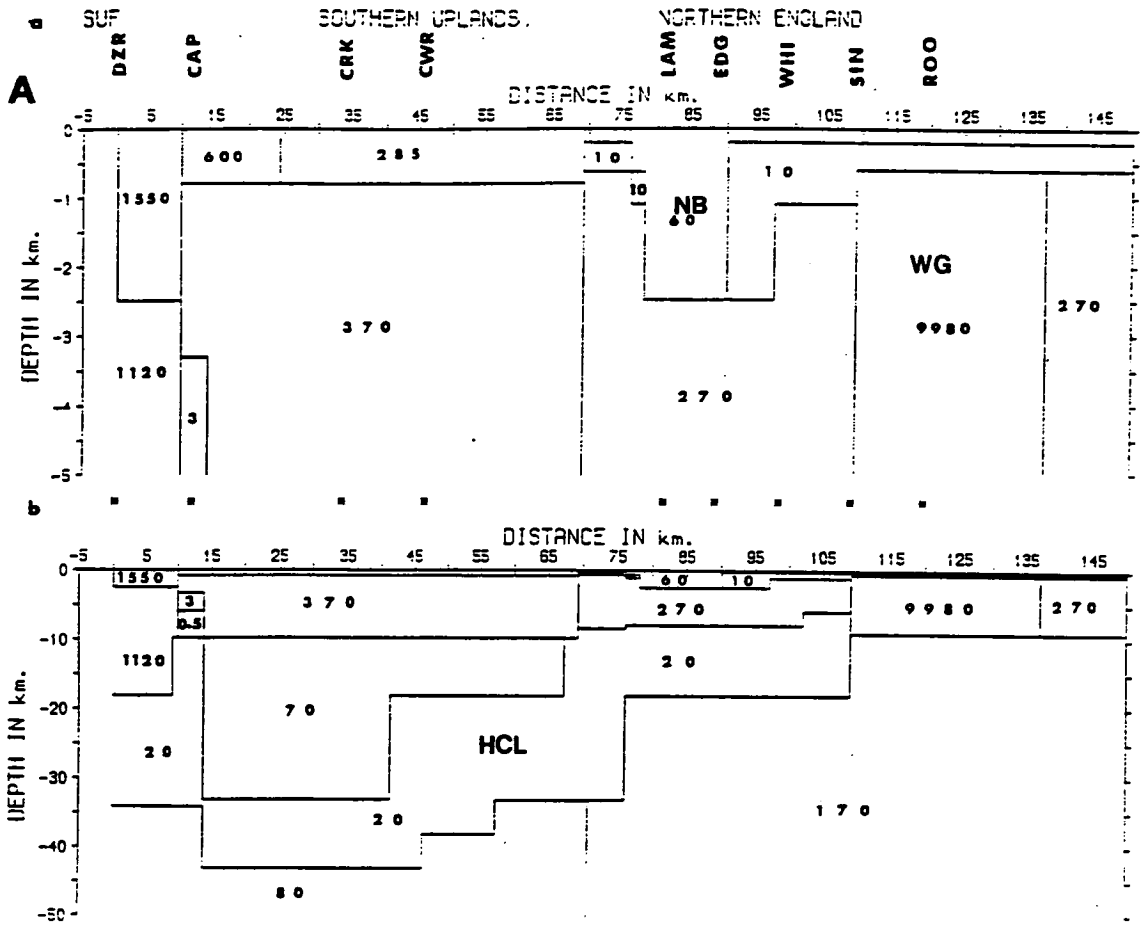
A
SUF
SOUTHERN UPLANDS.
NORTHERN ENGLAND
DZR
CAP
CRK
CWR
LAM
EDG
WHI
SIN
ROO
DISTANCE IN km.
DEPTH IN km.
600
285
10
1550
10
NB
10
WG
270
370
9980
1120
270
3
a
b
DISTANCE IN km.
DEPTH IN km.
1550
3
0.5
370
60
10
270
9980
270
1120
20
70
HCL
20
20
170
80

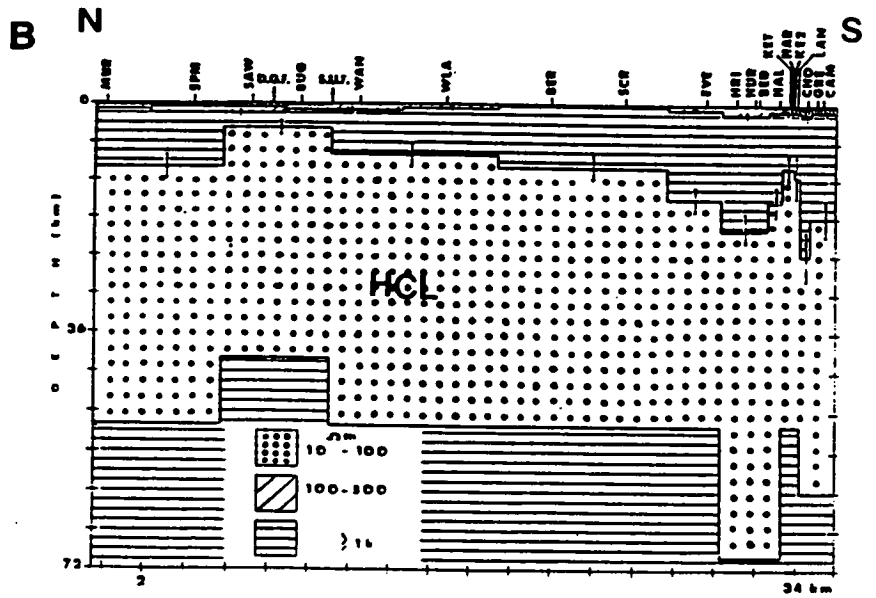
B
N
S
HCL
10 - 100
100-300
34 km

C

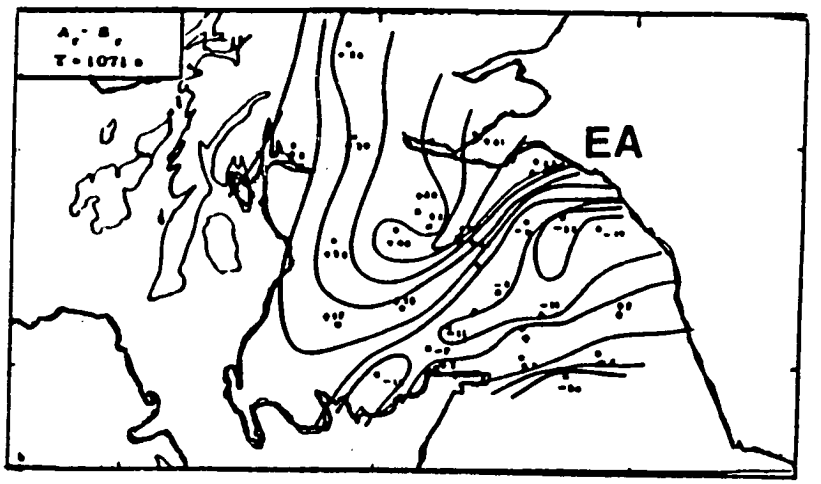
EA

D

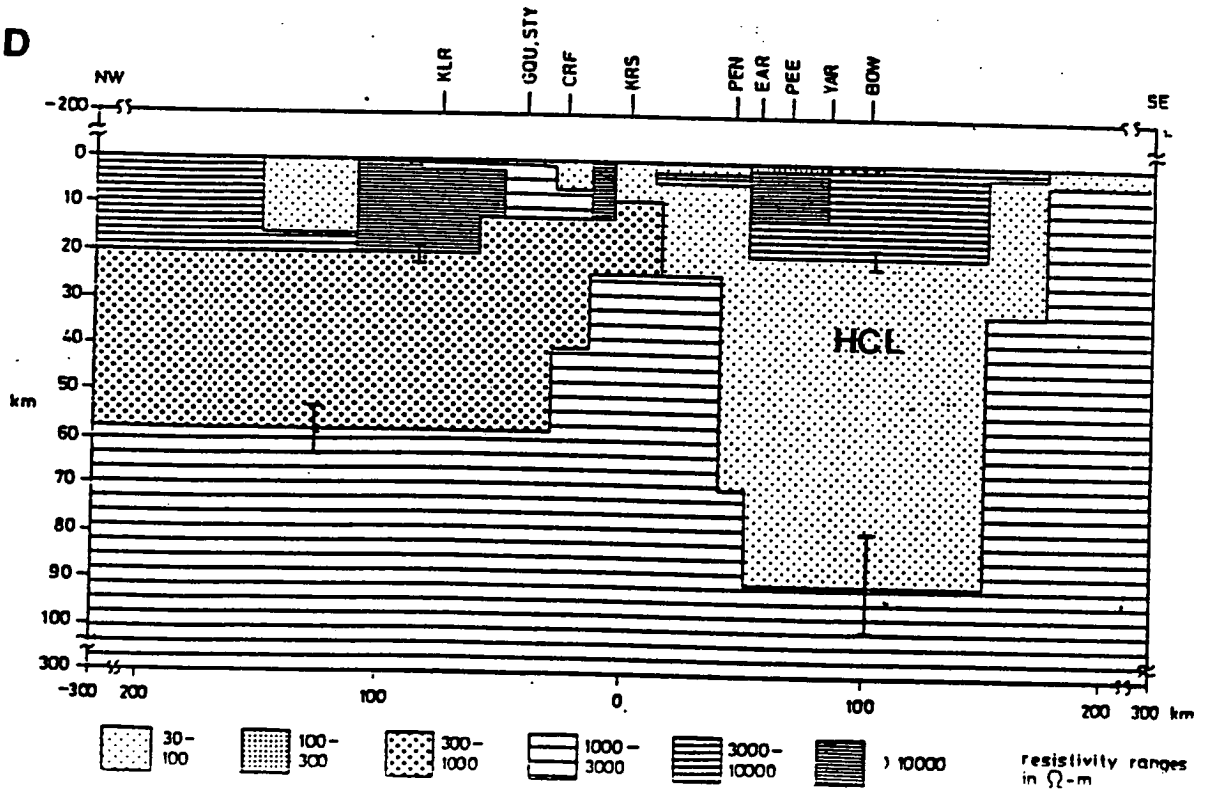
NW
SE
KLR
GOU,STY
CRF
KRS
PEN
EAR
PEE
YAR
BOW
HCL
km
-200
0
10
20
30
40
50
60
70
80
90
100
300
-300
200
100
0
100
200
300 km
30-100
100-300
300-1000
1000-3000
3000-10000
) 10000
resistivity ranges in Ω-m

filled pore space (< 0.5%) will have a dramatic effect on reducing the velocity of seismic waves (by about 10%). If the fluids have accumulated within horizons, then the resulting acoustic impedance contrast will mean that coherent reflectors may be detected on a seismic section. Similarly, as previously discussed (section 2.9.1), the presence of fluids within interconnected pore space significantly reduces the electrical resistivity of the rock.

This implies that the short seismic reflectors within the lower rock package may be due to the presence of fluid filled pores in discrete horizons, which cannot be individually resolved by MT but they collectively contribute to the high conductivity. Conversely, the absence of pore space leads to a largely resistive and unreflective middle crust.

On the assumption that fluid filled pores are responsible for the change in the geophysical characteristics of the rocks, it is interesting to speculate on the causes of porosity and the supply or containment of interstitial fluids.

8.2.5. Interpretation and Implications of the Fluid Filled Pores

The date of the formation of the joint conductive and reflective zone is critical to its interpretation. Unfortunately, the geophysical observations from this study provide little such concrete information. Nevertheless, its considerable lateral and vertical extent implies that it was formed during a period of major crustal change. There is little evidence that it extends out of the basement (i.e. it is Pre-Carboniferous), although as its shallowest location is directly beneath a major Carboniferous fault system, it probably exercised indirect control over subsequent sediment depositional patterns. Since its strike is parallel with that of the faunal Iapetus suture, the inescapable conclusion is that its formation is related to the closure of this ocean or the subsequent continental collision.

The unreflective/resistive and reflective/conductive zones could thus be interpreted as representing different terranes. In view of the geological history of the region (section 7.3) and the location and thickness of the northward dipping boundary, it is tempting to try and identify the latter zone with the remnants of the down going oceanic slab beneath Laurentia (fig. 8.21, later).

The direction of maximum dip (NNW; section 8.2.1) is also consistent with nearly orthogonal continental convergence along an ENE trending trench system (fig. 7.7). It clearly requires experimental confirmation, but it seems reasonable to expect that metamorphosed continental rock will be less porous (more resistive) and more homogeneous (less reflective) than the vesicular basalts which are formed in sub-sea ridge systems. Fluids or gases may have been encapsulated in the rock pores from its formation, or brine may have been trapped within the sedimentary sequence as the oceanic crust was subducted.

In the same fashion, the southward dipping component of this geophysically determined feature could be interpreted as being the remnant of southward directed subduction beneath Avalonia (section 7.3.1). The line of final closure of the Iapetus ocean should thus lie along the crest of this MT/seismic defined "ridge" denoted by the lines of "M"'s in fig. 8.6.

The author recognizes that there exist a few problems with this hypothesis:

1. Contemporary oceanic crust descends further into the mantle than the H.C.L. suggests.

2. Fluids probably cannot be contained within the lower crust for long periods of geological time owing to the effect of creep (Hall 1986) or metamorphism.

3. The crest of the shallow reflective/conductive "ridge" lies to the south of the Solway Line (section 7.2.3) in mainland Britain.

4. Some observations suggest that the top of the H.C.L. and seismic reflections extend up into the Lower Palaeozoic rock, which had presumably been overlying the continental plates and not been involved in subduction.

5. There is a discrepancy between the thickness of the seismic reflective zone and the H.C.L., at the southern margin of the Northumberland Trough. In particular, the onshore seismic reflectors observed by Chadwick and Holliday (1991) are at a depth of between 3 to 5 km. and were only seen to be 700 m. thick (fig. 7.6). Similarly, the H.C.L. at WHI II (fig. 8.2b) is also at a depth of 3km., but has an apparent thickness which is closer to 15km.

Some authors have therefore envisaged that a post-Iapetus shear zone developed close to the line of final closure of the palaeo-ocean (section 7.2.3).

It seems quite reasonable to expect that neither continental collision nor even Avalonian continental subduction would mark the end of tectonic activity. For example, the large scale strike-slip movements which marked the final continental 'docking' or the accretionary formation of other parts of Europe, could have set up compressional forces which caused shearing of the less homogeneous and more brittle rocks along the line of oceanic closure. The shear zone probably lies close to the boundary between the different terranes in the mid and lower crust and extends into the "infill" of Lower Palaeozoic rocks in the upper crust, which now forms the basement of the Northumberland Trough. The relative movement between the rock units is envisaged to have produced cracking and brecciation of the rocks. The resulting fine grained porous and possibly fluid filled rock is called a mylonite. This may be the source of the narrow band of quasi-continuous seismic reflectors observed on some seismic sections and the enhanced crack porosity will contribute to the high conductivity.

Some authors (e.g. Leeder 1982, Klemperer and Matthews 1987) have suggested that the formation of a long chain of Carboniferous age basins from the Northumberland Trough in Britain to the Limerick Basin in Ireland may have been initiated by a re-activation of the upper parts of this shear zone. Correspondingly, the shallowest part of the conductive/reflective zone (fig. 8.6) is found on the southern margin of the Northumberland Trough, south (up dip) of the faunal suture and the deep seismic reflective zone identified offshore. There has, as yet, been no concrete evidence to suggest that this zone actually sub-crops the Carboniferous sedimentary cover in Northumberland (c.f. Chadwick and Holliday 1991). In fact the MT results from this study (fig. 8.2b) imply the contrary.

Beamish and Smythe (1986) have also suggested that there is an apparent correlation between a bulge in the depth contours to the conductive/reflective zone and a thickened sedimentary sequence in the Solway Basin. In the absence of detailed depth to basement estimates, this author is unable to comment, but it remains an interesting possibility that increased crustal extension on the shear zone enhanced basin subsidence.

In order to explain the conductive zone flattening out close to the Moho, Freeman *et al.* (1988) have suggested that the crust and mantle were also in

relative motion. If such a model is valid, then the tectonic forces involved were being applied in a different direction from those encountered during earlier subduction.

It is relatively straightforward to explain the presence of fluids in such an environment. As the top of the postulated shear zone lies close to the surface, brine could percolate down from the overlying sedimentary rock and into the top of the shear zone. Alternatively the mantle may be a source of recharge water, as the dehydration of subducted oceanic crust or amphibole may occur at lower crustal temperatures (> 400 ^{o}C.). The porous rocks in the shear zone would probably focus fluids from the less porous rocks. The heated fluids would rise and then cool allowing any dissolved minerals to be precipitated. This could form an impermeable seal for later fluid migration and so both the high heat flow (section 7.8.3) and the H.C.L. would be limited to the basement rock.

8.2.6. Summary

The results of this and other separate studies sometimes unwittingly support the presence of a northward dipping conductive and seismically reflective zone in the mid and lower crust in Northern England, Southern Scotland and probably also in Ireland. In the Southern Uplands of Scotland there are several particularly interesting structures which require further clarification.

The author considers that there is fairly substantial evidence now to support a southward dipping feature beneath the Alston Block and in the Irish Sea. The results strongly suggest that the basement rock from the Midland Valley of Scotland to the Alston Block of England was affected by more than one tectonic event prior to the Carboniferous era.

To invoke explanations for the observations using only one continental collision would be too simplistic. However, with the exception of the area of particular interest to this study (section 8.5.1), it is still premature to speculate on the full implications of these models.

8.3. THE NATURE OF THE BASEMENT ROCK

The interpreted basement rock cannot be regarded as being a single homogeneous structure (section 6.4.5). It can be broadly divided into a moderately resistive layer (100 Ω.m.) underlying much of the Northumberland Trough and more resistive rock (> 1000 Ω.m.) within the Alston Block and the Southern Uplands. A more detailed picture of the nature of the basement rock emerges from the complete 2-D model resistivity sections (fig. 8.9a,b).

8.3.1. The Northumberland Trough

Beneath the Northumberland Trough, the electrical basement rock is relatively well resolved and typically demonstrates resistivities in the range from 70 to about 200 Ω.m.. The high resistivity with respect to the overlying sedimentary rocks and the depth of burial would imply either an igneous or metamorphic origin. The author would favour the latter explanation in view of the geological evolution of the region and the much higher resistivity of the granites (section 8.3.2)

At the northern edge of the trough, the resistivity of this layer seems to increase to about 500 Ω.m (fig. 8.9a). Unfortunately, the low density of MT sites along this part of the profile precludes any firm conclusions to be drawn. Nevertheless, some of the other MT models derived from sites off the long profile (e.g. BOR I and BEAM B in Appendix - C) also imply that there may be a regional resistivity transition here. Since this occurs close to the Solway Line, this could be interpreted as being a manifestation of the juxtaposition of rocks from the 2 palaeo-continents of Avalonia and Laurentia. This would not be entirely unexpected as these rock units are also known to demonstrate changes in other rock properties (section 7.2.2). Any future follow-up study should also consider the additional influence of resistive lavas at the base of the sedimentary sequence, in this area (section 7.6.2).

There appears to be evidence, albeit unsubstantiated, for other electrical structure in the basement rock. For example both LAM and NEW II demonstrate the presence of resistive rock apparently extending from the H.C.L. into the upper crust. These may be the result of experimental error with

Figure 8.9: The detailed crustal electrical profiles derived after the application of pseudo 2-D (fig. 8.9a) and strictly 2-D modelling (fig. 8.9b).

They show some lateral variations in the resistivity of the H.C.L. but much more significant changes in the resistivity of the overlying 'basement' rock. The resistive Weardale granite dominates the southern part of the profiles from HIL to HGN. Typical basement rock beneath the Northumberland Trough is more conductive but there is some evidence for a regional increase in the resistivity between BEW and KSF. Much of the smaller scale intra-basement structure is unsubstantiated and can only be observed at one site.

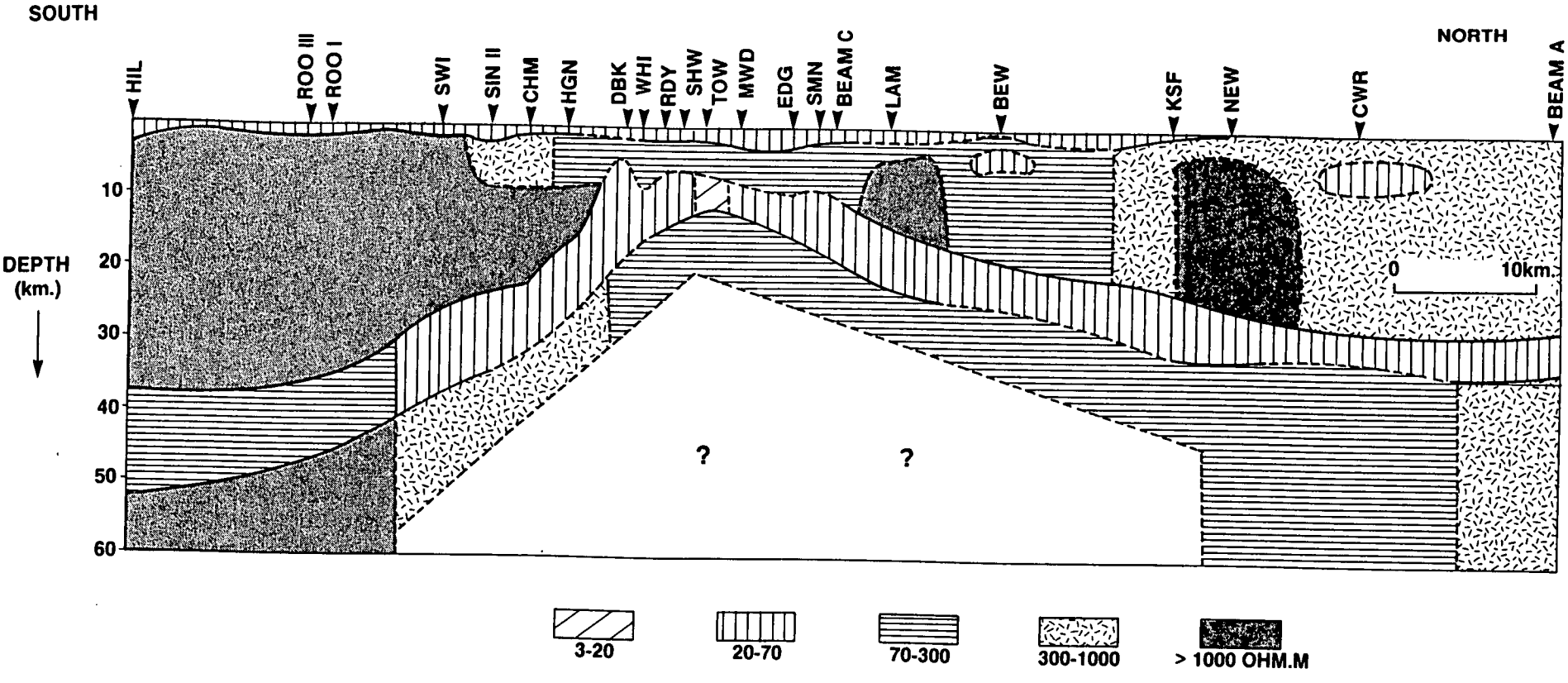
SOUTH
NORTH
HIL
ROO III
ROO I
SWI
SIN II
CHM
HGN
DBK
WHI
RDY
SHW
TOW
MWD
EDG
SMN
BEAM C
LAM
BEW
KSF
NEW
CWR
BEAM A
DEPTH (km.)
10
20
30
40
50
60
?
?
0
10km.
3-20
20-70
70-300
300-1000
> 1000 OHM.M

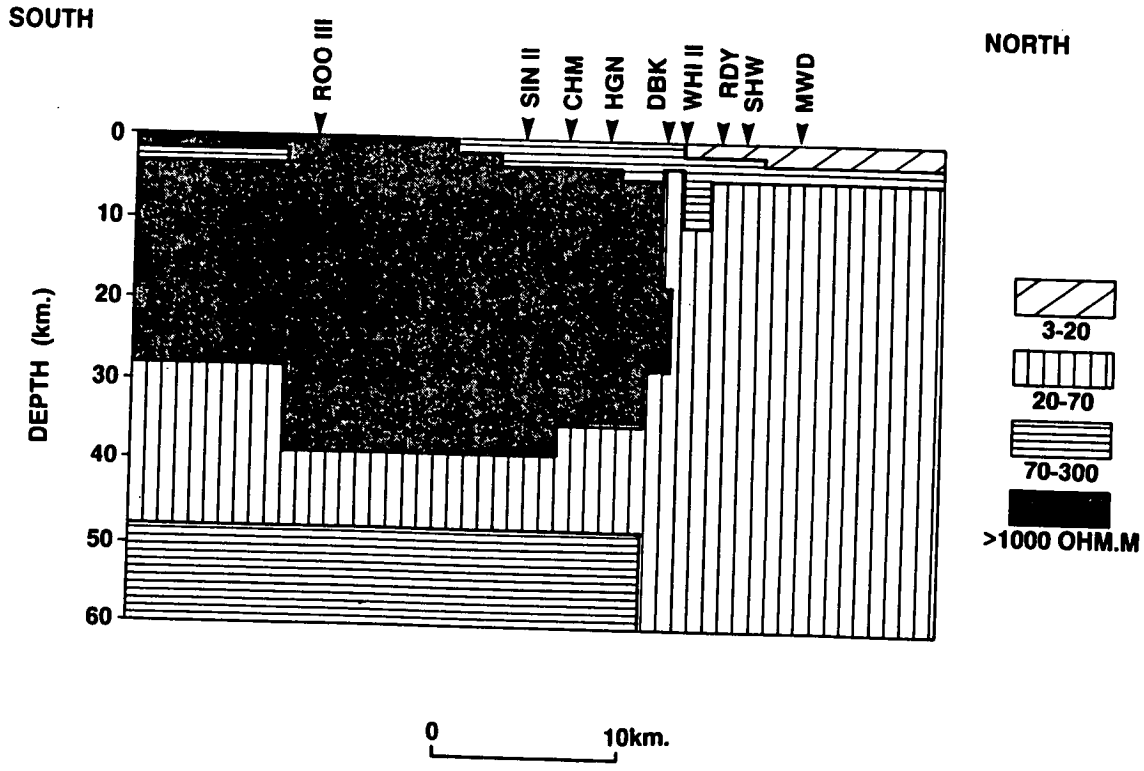
SOUTH
NORTH
ROO III
SIN II
CHM
HGN
DBK
WHI II
RDY
SHW
MWD
DEPTH (km.)
0
10
20
30
40
50
60
3-20
20-70
70-300
>1000 OHM.M
0
10km.

no geological implications. However, gravity models (Yassi 1983) have shown that there may be intra-basement granite intrusions in Northern Northumberland, particularly near the latter site. As most geophysical techniques have difficulty identifying and resolving such structures, this anomaly may be worthy of further MT investigation.

The conductor at a depth of 3 km. beneath BEW may, in some way, be related to the basement anticline, but again little information can be extracted from only one anomalous site. The MT response function from this site also demonstrated an unusually high degree of anisotropy (Appendix - C). Whereas the XY response function was typical of those observed elsewhere in Northumberland, the YX direction showed a virtually monotonic rise in apparent resistivity (to 1000 Ω.m.) with decreasing frequency. As a consequence, any 1-D model interpretation of the results from this site must be treated with caution.

Figure 8.10 shows that the lower frequency portions of the MT phase response functions become progressively flatter and closer to 45^{o}, when approaching sites SHW and MWD from both directions. Correspondingly, the resultant models demonstrate little appreciable resistivity contrast between the shallow H.C.L. (40 Ω.m.) and the thickened sedimentary layer (10-40 Ω.m.). In fact, the exploratory 1-D model for SHW (Appendix - C) did not resolve any high resistivity basement rock at all, but the 2-D model results (figs. 8.9a,b) implied that, like MWD, the basement was unusually thin at this location. The MT models were unable to resolve any layers which could indicate the presence of resistive lavas at the base of sedimentary layer, at the southern margin of the Northumberland Trough (c.f. Kimbell *et al.* 1989).

8.3.2. The Alston Block

The basement rock overlying the Weardale Granite (e.g. at SIN II in fig. 8.9a) appeared initially to have a higher resistivity than that observed further north. On the basis of subsequent 2-D modelling (fig. 8.9b), no lateral resistivity contrast was discernable. It would therefore now seem more likely that this anomaly resulted from the inappropriate application of 1-D modelling.

The electrical resistivity of the Weardale granite as determined in the

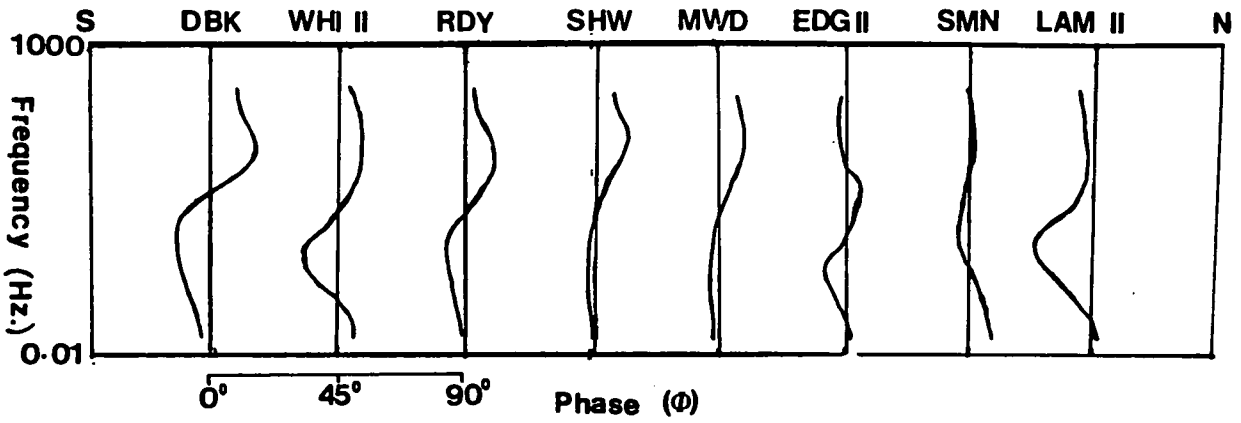

Figure 8.10: The effective invariant phase response functions from site DBK (on the northern edge of the Alston Block) to LAM II (in the middle of the Northumberland Trough). The low frequency portions of these response functions become progressively flatter and closer to 45^{O} towards MWD and SHW. This implies that the basement rock is more electrically homogeneous at these locations.

Rookhope borehole (1-2 k.Ω.m) was consistent with that of weathered igneous rock. Like other exposed granite intrusions (Beamish 1990), the resistivity has been significantly reduced owing to the presence of pores and fluid filled fractures. The layer identified from exploratory MT models, which was considered to be of igneous origin, had a wide range of resistivities which progressively increased towards the centre of the Alston Block (i.e. 500 Ω.m. at HGN to 7 kΩ.m. at ROO I). This variation has now been mainly attributed to the effect of 1-D models averaging resistivities across a major vertical contrast between the Weardale granite and Northumberland Trough sediments. Little significant lateral or vertical variation in the resistivity of the granite could be detected after pseudo 2-D or strictly 2-D modelling.

The depth to the top of the Weardale granite was well resolved beneath the conductive sedimentary rocks (e.g. at SIN I in Appendix - C), but more ambiguous where the igneous rock was concealed beneath the moderately resistive Lower Palaeozoic basement (e.g. CHM). Identification of the granite layer was aided by pseudo 2-D MT modelling (section 6.4.6), but because of the large density contrast between these igneous and metamorphic rocks, gravity models provided the most detailed and spatially extensive source of depth to granite information. The gravity models derived from this study (section 6.4.8; figs. 8.11a-d) show that the granite sub-crops the sedimentary layer for 3 out of 4 of these profiles (at 540N on line 380E, 535N and 545N on line 390E and from 535N to 550N on line 400E). These cupolas have very steep sides down to the main batholith which appears to reside at depths in excess of 6 km. (e.g. line 370E).

In order to acquire a more detailed estimate of the topography of the upper surface of the batholith the results from these gravity models were integrated with the comparable information provided by MT and the few published seismic lines which cross the Alston Block (Evans *et al.* 1988, Kimbell *et al.* 1989; fig. 8.12). The final collated and contoured depths to the top of the granite are shown in fig. 8.13.

Rock of igneous origin (high resistivity, low density) is thought to have been intruded into the Lower Palaeozoic basement as far north, but not beyond, the Stublick Fault. The models show that the northern limit of the batholith almost exactly coincides with the western end of the Stublick Fault

Figure 8.11: The simplified results of 2-D gravity modelling applied to 4 parallel north-south profiles (along National Grid coordinates 370E, 380E, 390E and 400E) from the Stainmore Trough across the Alston Block and into the Northumberland Trough (i.e. 500N to 600N). The upper parts of these diagrams show the observed and computed gravity anomalies above the corresponding model. The model comprises a sedimentary layer of variable thickness with a density contrast of about $-0.15 g.cm^{-3}$ with respect to basement. The model granite is assumed to extend upwards from a base at a depth of about 10km.. The cupolas on the upper surface of this low density intrusion (-011 to $-0.12 g.cm^{-3}$ with respect to basement) extend upwards to subcrop the sediments on 3 of the profiles (380E, 390E and 400E) and the resulting uncertain boundary is indicated by the dashed line.

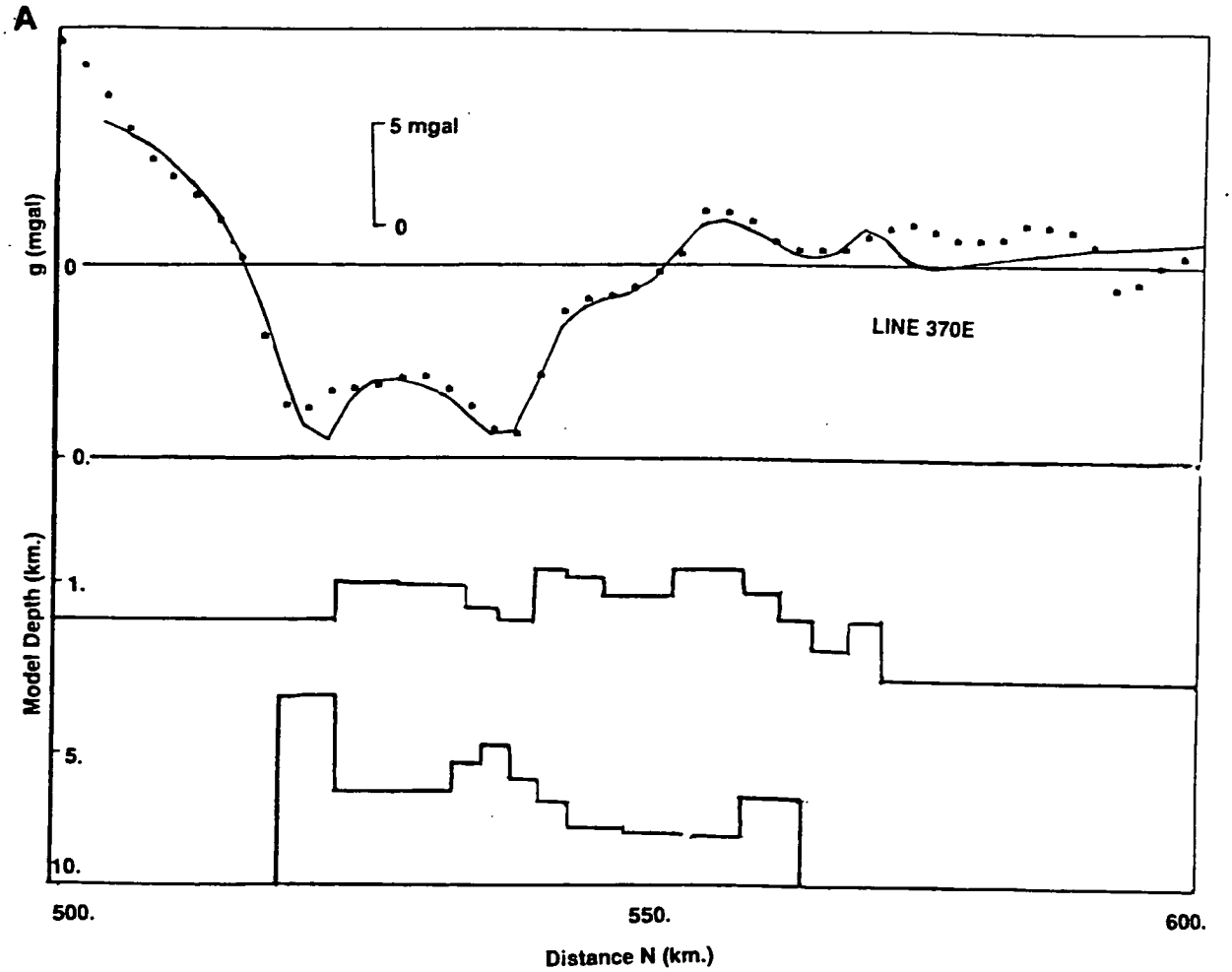
A
5 mgal
0
g (mgal)
0
0.
LINE 370E
Model Depth (km.)
1.
5.
10.
500.
550.
600.
Distance N (km.)

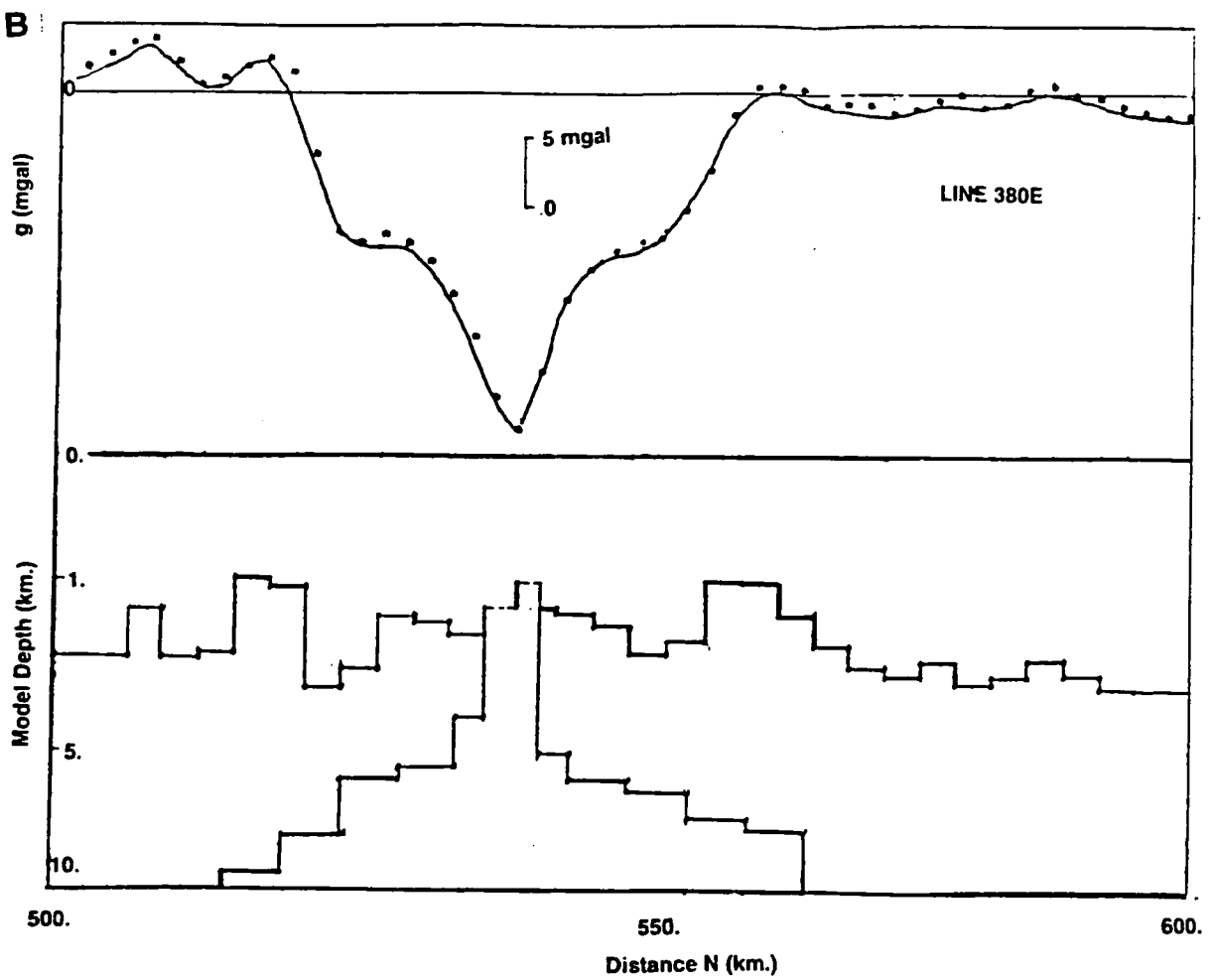
B
0
5 mgal
0
g (mgal)
LINE 380E
0.
Model Depth (km.)
1.
5.
10.
500.
550.
600.
Distance N (km.)

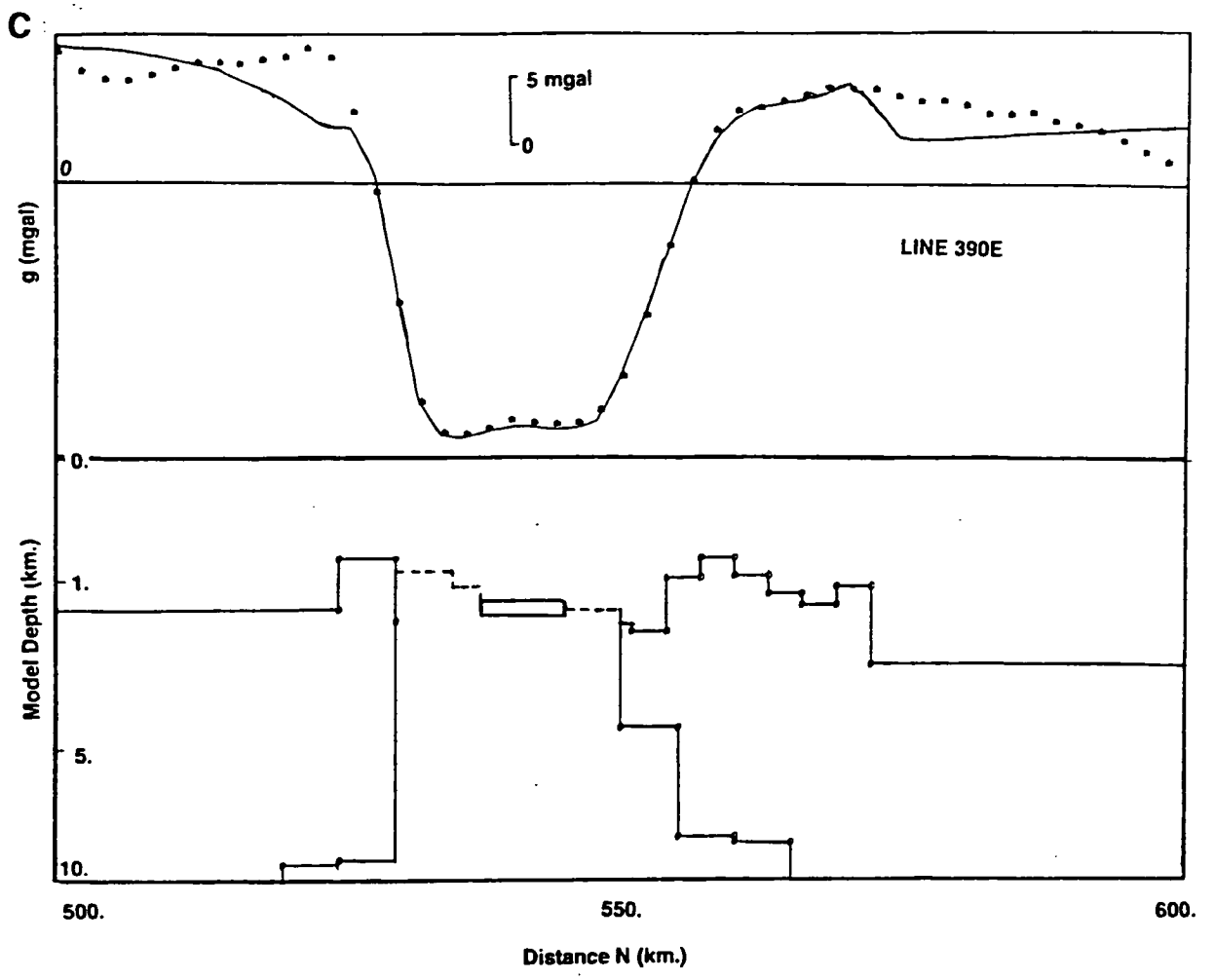
C
5 mgal
0
g (mgal)
0
LINE 390E
0.
Model Depth (km.)
1.
5.
10.
500.
550.
600.
Distance N (km.)

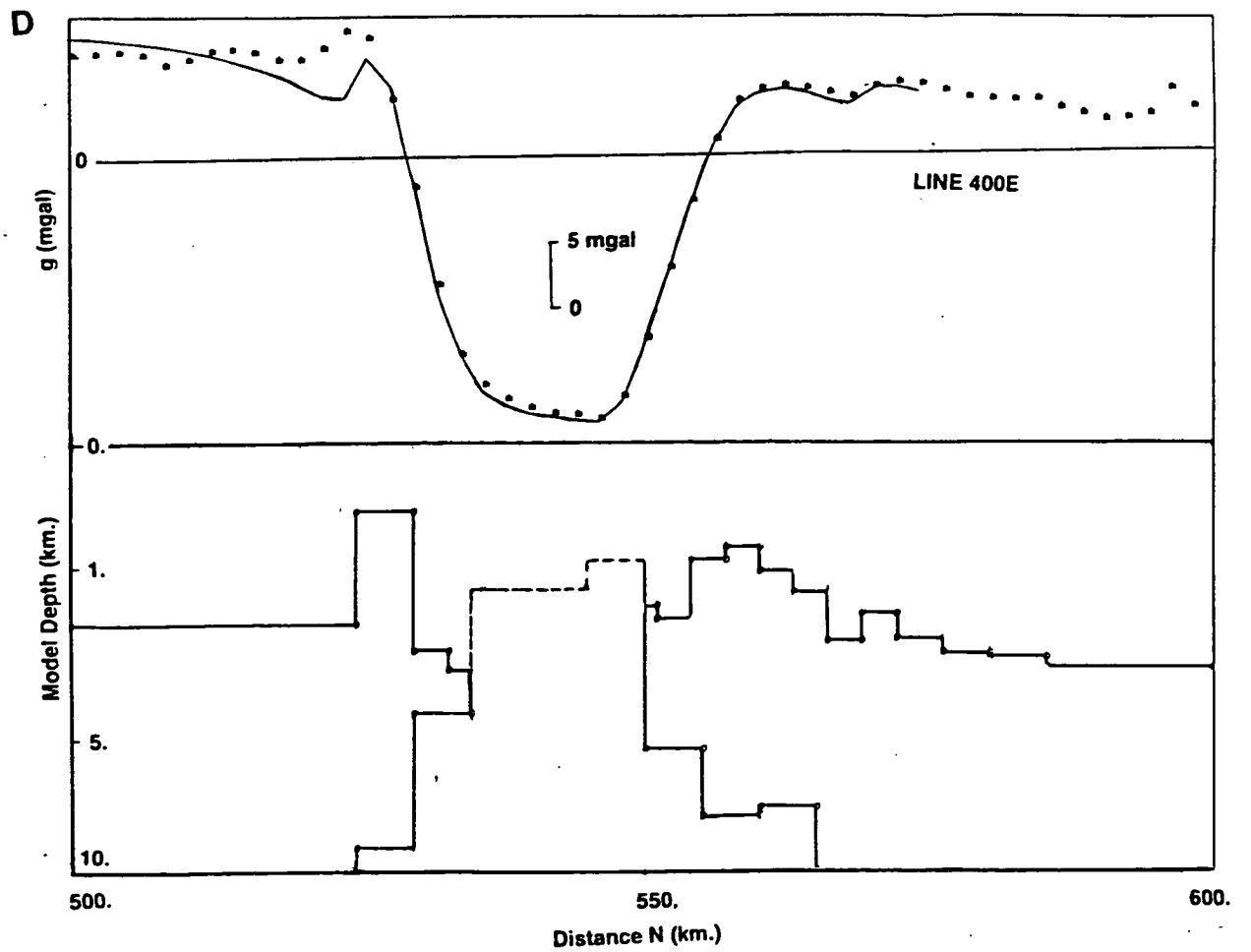
D
0
LINE 400E
5 mgal
0
g (mgal)
0.
Model Depth (km.)
1.
5.
10.
500.
550.
600.
Distance N (km.)

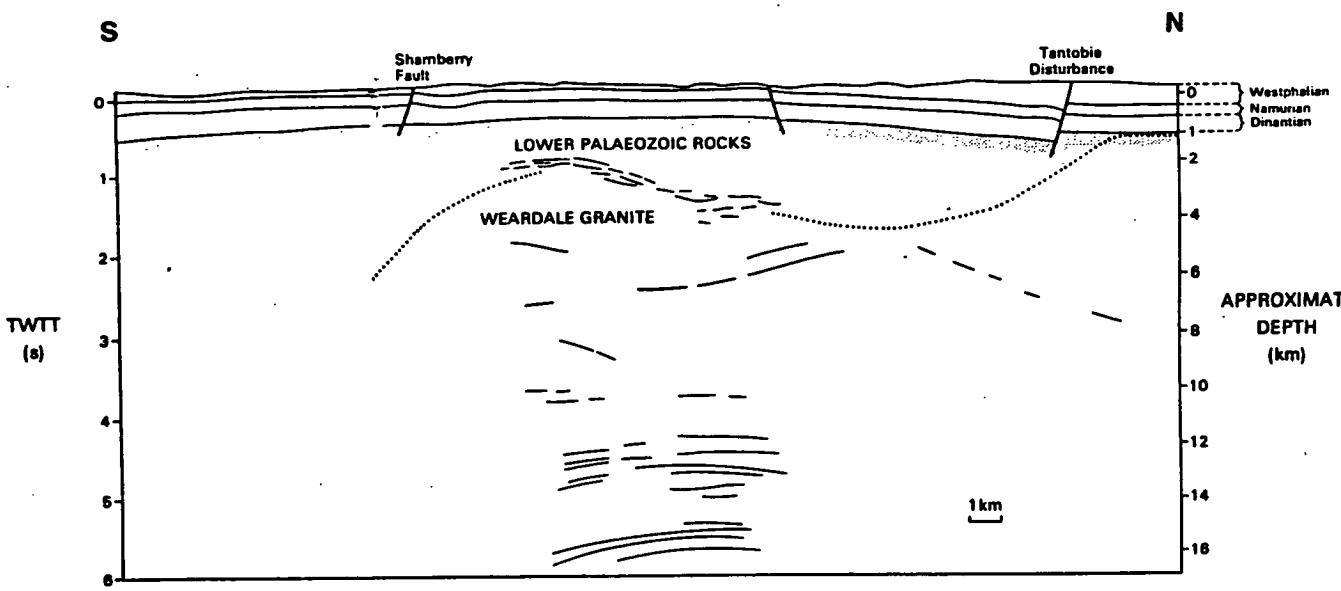

Figure 8.12: A line drawing (taken from Evans *et al.* 1988) showing the major fault boundaries identified from the E3 seismic reflection line (see fig. 7.9). The depth to both the granitic and non-granitic basement were used to help compile the contour map shown in figs. 8.13 and 8.18, respectively. The downthrown block south of the Tantobie Disturbance is thought to be related to the increase in sedimentary thickness noted in some of the electrical model from SIN II (fig. 8.16a). Reflections from the flanks of the granite are absent at some locations and so Evans *et al.* have inferred the boundary from gravity observations (dotted line).

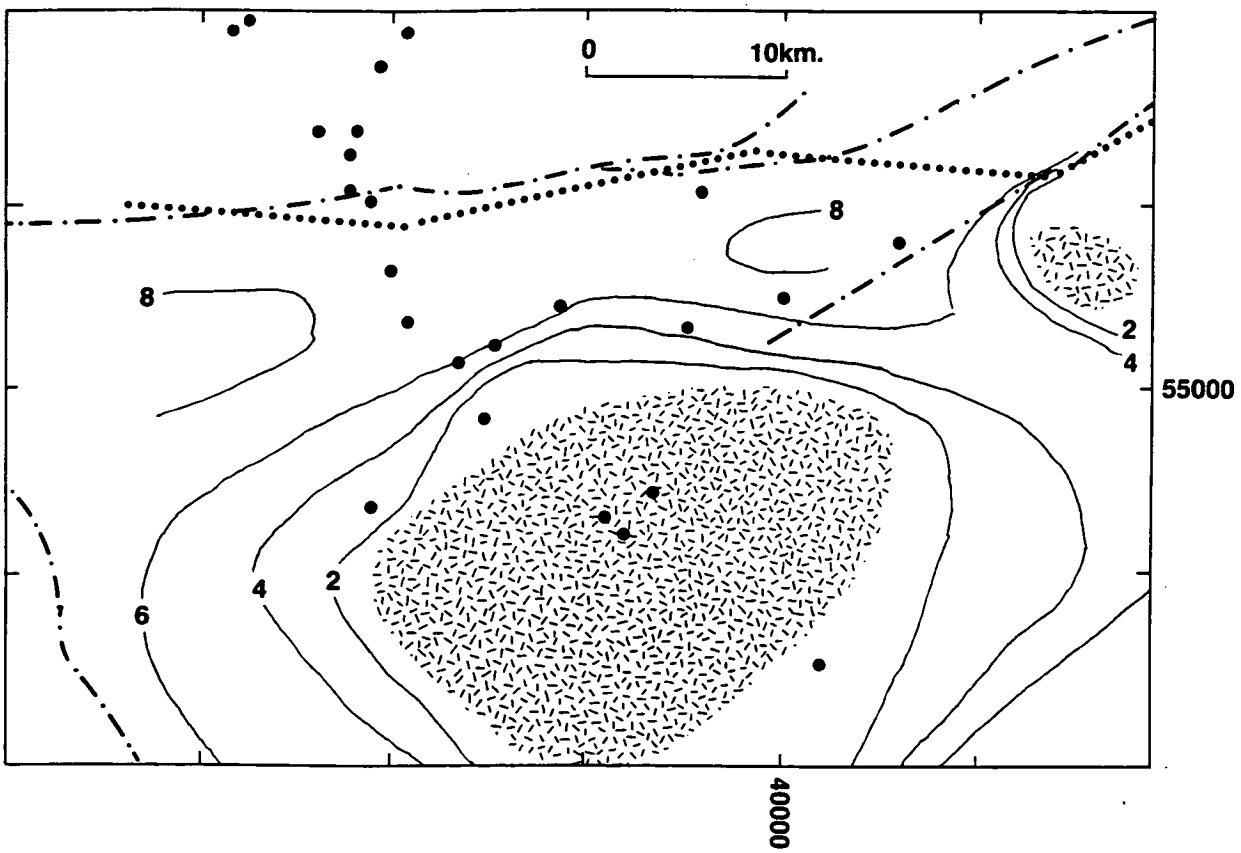

Figure 8.13: The final collation of the depths to the upper surface of the granite intrusion (2km. contour interval) from seismic reflection profiles, gravity and MT models (the MT sites are marked by large dots).

The parts of the cupolas which are thought to directly subcrop the sedimentary rocks have been shaded and the northern edge of the batholith marked by a line of small dots. This line approximately coincides with the Stublick Fault trace.

trace. At these locations the top of the granite is at about 10km. depth. The batholith rises steeply upwards towards the Rookhope cupola (39000E 54500N), where the granite rock is less than 2km. from the surface over a wide area. The depth to the granite in the vicinity of the Rookhope borehole was found to be between 400 and 600 m. from most of the different observations and is consistent with the known depth of about 400m. (section 7.4.1). In addition, the gravitational models also show that the sedimentary rocks lie directly above granitic rock at this cupola (e.g. fig. 8.11c). Figure 8.13 shows that the Early Carboniferous erosional surface was approximately concentric with the shape of the cupola.

A second cupola (Rowlands Gill: 415E 555N) is much smaller and interconnected with the first one at a depth of 5km. Its steep northern margin lies directly adjacent to the eastern end of the 90 Fathom Fault.

The results from a purely 3-D gravity modelling study (Evans *et al.* 1988) compare favourably with those from this study. Figure 8.14 shows the 2 main cupolas were at approximately the same depth as has been determined from this study. In contrast to fig. 8.13, Evans *et al.* have identified a third cupola, south of Rowlands Gill, and have modelled a more gently dipping northern flank to the batholith.

8.3.3. The Devonian Granites

Most gravitational studies have assigned a "base" to the model granite intrusion at depth of between 5 and 10km. The rocks also have a high electrical resistivity within the spatial extent of the gravitational anomaly, but this layer, and therefore presumably igneous rock, persists to much greater depths (i.e. to the H.C.L. at depths of up to 35 km.). The author would therefore suggest that the rocks are still of igneous origin down to this level, but they have no appreciable density contrast with the surrounding rock. From intermediate depths within the presumed granite (12 km.; 4.3s TWT: fig. 8.7), Evans *et al* (1988) have identified a band of horizontal reflectors. If possible causes of such seismic reflectors are considered (Matthews 1986) this author believes that they may mark sill like intrusions into the lower portion of the batholith.

On a more regional perspective, Leeder in 1976 noted that no granites

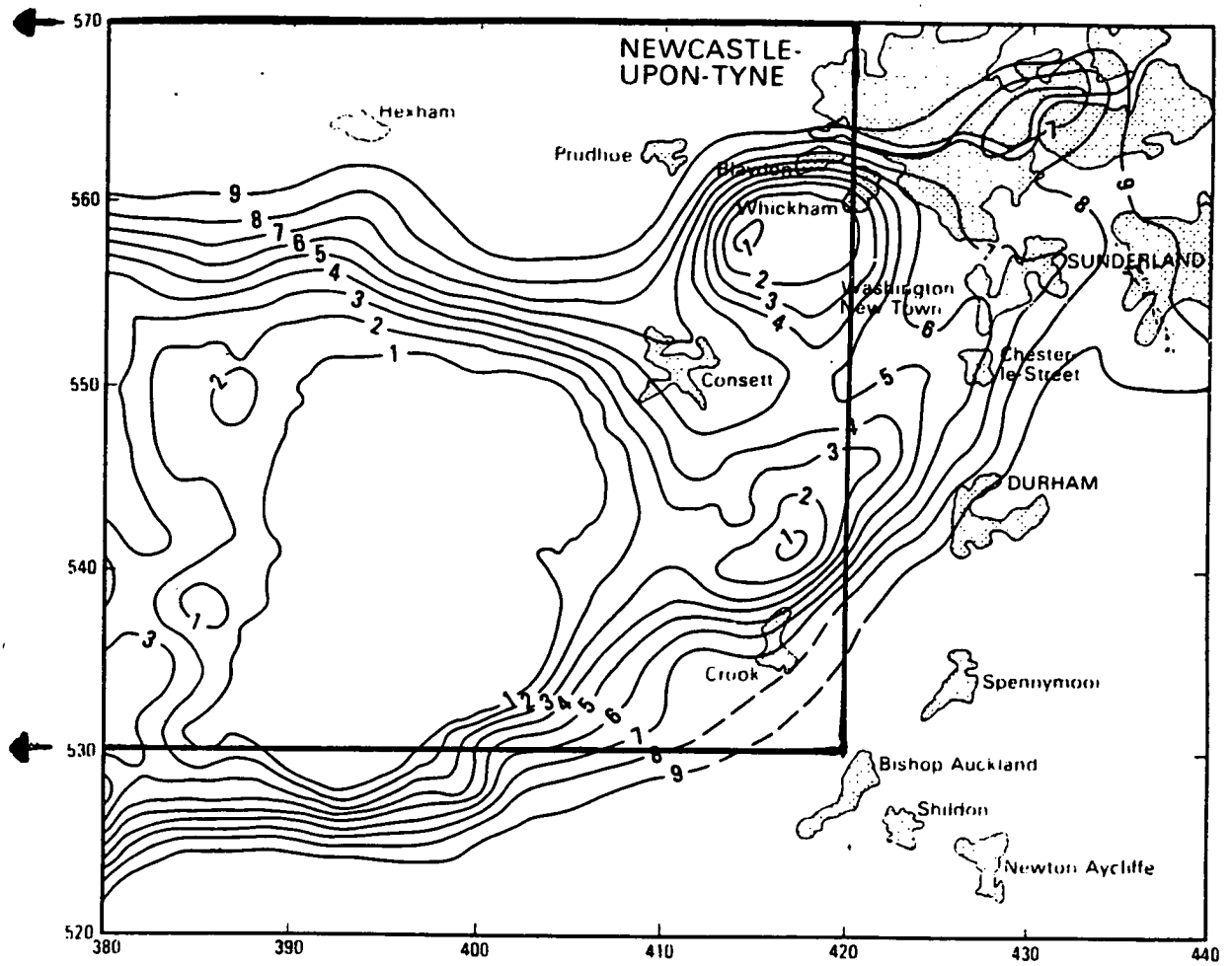

Figure 8.14: The results of a 3-D gravity modelling study undertaken by Evans *et al.* 1988 over the Alston Block. The area covered by fig. 8.13 is marked. The location and depth to the granite is relatively comparable between these 2 studies.

have been detected within the Northumberland Trough (c.f. section 8.3.1), even though they are very common elsewhere in Britain. Consideration of the MT results in fig. 8.9a suggests that this may be related to the relatively shallow depth to the H.C.L. and the postulated shear zone beneath the Northumberland Trough. Further investigations need to be undertaken, but the author proposes that the shear zone was responsible for partial melting and consequently the formation of Devonian age granite intrusions along lines of crustal weakness, on both sides of the Iapetus suture (e.g. the Weardale, Lake District and Leinster granites may all be located along the line of an Ordovician island arc).

The shear zone may also have been responsible for the presence of contemporary base metal deposits in Ireland (Phillips *et al.* 1976) and the long and rejuvenated thermal history of the Alston Block (section 7.8). The author envisages that H.C.L. derived fluids rise out of the lower crust via conduits within the granite, thereby enhancing the radiogenic derived heat flow. The 'thermal pulses' recognized from a number of different studies, would therefore reflect some movement along the shear zone. During at least one such episode, mineralizing fluids are known to have escaped into the upper crust (section 7.8.2).

This scenario has obvious implications for geothermal exploration since a fluid filled shear zone at comparatively shallow depths could provide a useful route for the migration of heated fluids from the lower crust. Further heat flow measurements are desirable in order to determine the correlation between the H.C.L., fluid migration and the elevated geothermal temperatures.

There clearly remain a number of questions to be answered. It is implicit in the foregoing argument, that the H.C.L. needs to be located in the lower crust for partial melting to have occurred. Figure 8.6 however predicts the H.C.L. to be at depths of less than 10km. beneath the Lake District and the western margins of the Alston Blocks (i.e. probably *within* the granite batholiths). In spite of the Irish MT study (Whelan 1989; fig. 8.4) not detecting a high conductivity zone beneath the Leinster granite, such a feature may become evident with the acquisition of new observations or a re-processing of the original Irish data set. Finally, the shallow depth to the H.C.L. in Southern Scotland (section 8.2.3; figs. 8.8a-d, 8.6) should also imply a high heat flow environment. This author is unaware of any such anomaly (c.f. fig.

7.16).

8.4. CARBONIFEROUS AGE SEDIMENTARY COVER

8.4.1. The Thickness of the Sedimentary Rocks: Geoelectric Results

In this study it was assumed that the thickness of the porous and water saturated sedimentary rock could be interpreted from a characteristic rise in the resistivity upon entering the metamorphic or igneous rock basement (section 6.4.5). It was recognized that this assumption was invalid if a) the response functions were excessively noisy (e.g. UPT), b) there was little appreciable contrast between the sedimentary and basement rocks (e.g. SHW) or c) the sedimentary rock had a significant number or thickness of more resistive interbeds. This latter problem can be demonstrated by comparing the resistivity profile from the LHR MT site, with that derived from an adjacent borehole (fig. 8.20b later). The transition to a higher resistivity rock at a depth of 1.2 km. was originally interpreted as being the base of the sedimentary sequence. Subsequently the smoothed borehole derived resistivity observations indicated that the corresponding transition was more likely to be the result of a variation within the sedimentary sequence itself.

Figures 8.15 and 8.16(a,b) summarize the interpreted thickness of the sedimentary rocks (or equivalently the depth to geoelectric basement) spatially and in cross section. The maximum observed thickness of the Carboniferous age rocks is about 3 km. (at MWD), but it rapidly thins across the Stublick Fault trace (at WHI) and is only 0.5–1.0 km. thick over the Alston Block. Further sediment thinning occurs over the Bewcastle anticline and to the NW, towards the Southern Uplands of Scotland. The MT results from the central parts of the Northumberland Trough were ambiguous because the sedimentary layer appears to be only 1 km. at LAM I whereas at LAM II it is considered to be nearer 3km. thick. In addition, the base of the conductive sequence at BEW could be taken to be 0.15 or 5.0 km.. At these locations, it was therefore necessary to make an informed interpretation on the basis of other geological and geophysical information.

Figure 8.15: The depth to basement (in km.) derived from the MT sites shown across the Alston Block and Northumberland Trough.

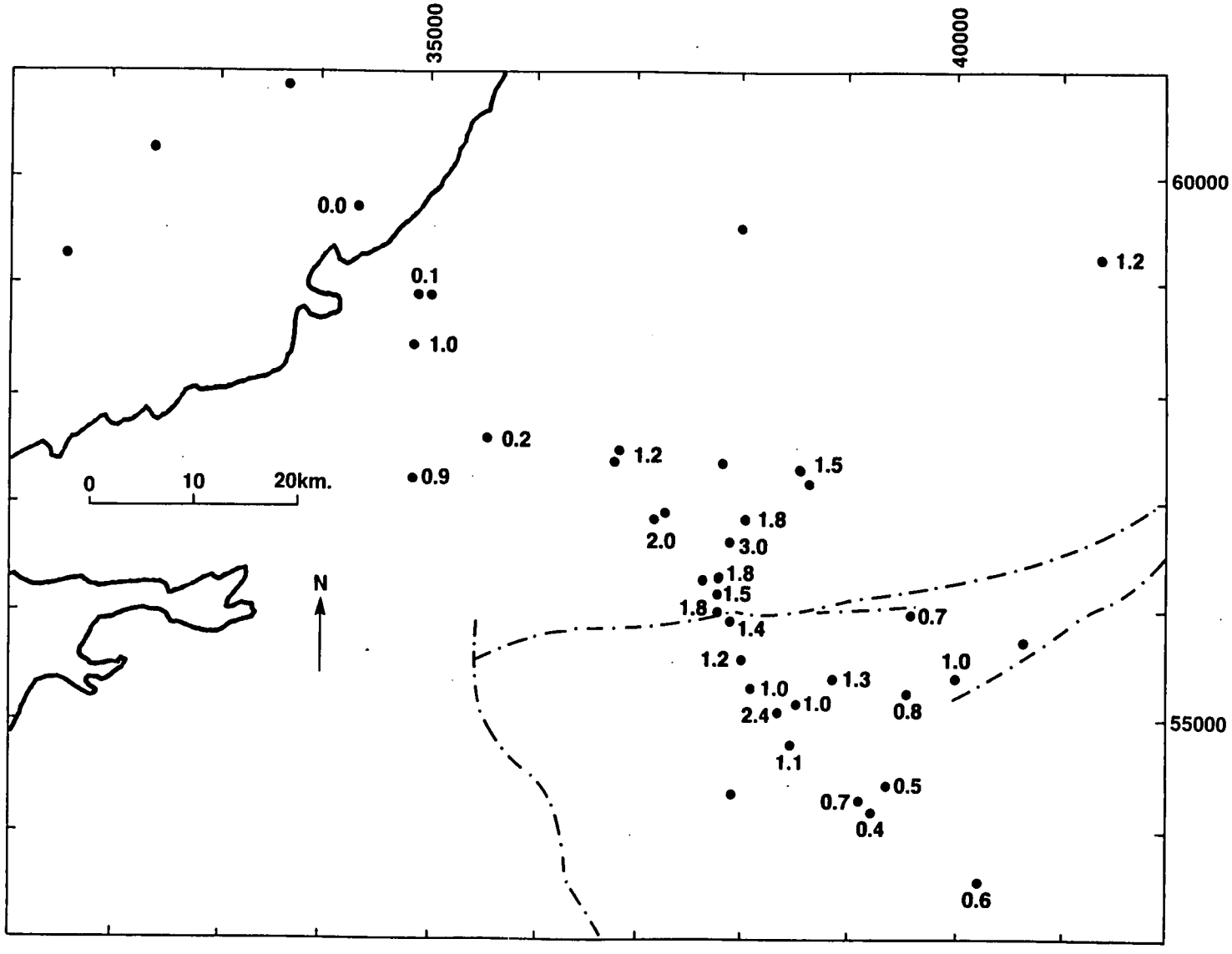
35000
40000
60000
55000
0.0
0.1
1.0
1.2
0.2
0.9
1.2
1.5
0
10
20km.
N
1.8
2.0
3.0
1.8
1.5
1.8
0.7
1.4
1.2
1.0
1.3
1.0
1.0
2.4
0.8
1.1
0.5
0.7
0.4
0.6

Figure 8.16: Simplified cross sections (c.f. fig. 8.19) of the upper crustal geoelectric structure derived from pseudo 2-D (fig. 8.16a) and strictly 2-D modelling (fig. 8.16b). In general the increase in resistivity at depths of between 1 and 3km. is attributable to the presence of metamorphic basement beneath more porous sedimentary rock. As a result, the depth to this electrical boundary may be used to estimate the variation in the thickness of the sedimentary layer across the block and basin.

The Rookhope cupola shows a very thin layer of conductive rock but there is an apparent increase in the depth to basement in the vicinity of SIN (section 8.4.5). There is also a large displacement in the basement on the north (down dip) side of the Stublick Fault. This has permitted 3km. of sediments to be later deposited. An antithetic fault may exist at EDG and the Bewcastle anticline (BEW) appears to have caused the greatly thinned sedimentary layer. No conductive rocks could be detected north of NEW.

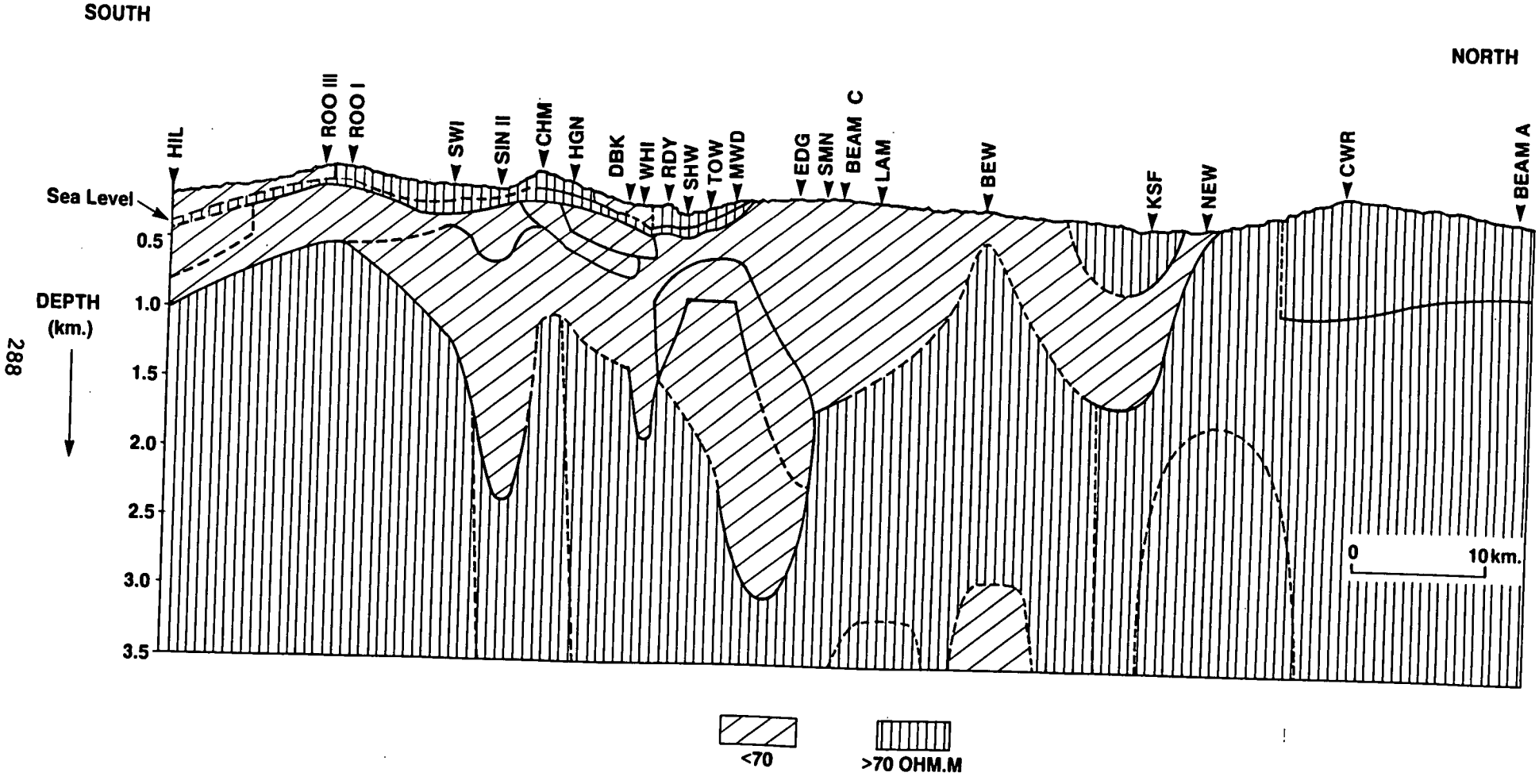
SOUTH
NORTH
HIL
ROO III
ROO I
SWI
SIN II
CHM
HGN
DBK
WHI
RDY
SHW
TOW
MWD
EDG
SMN
BEAM C
LAM
BEW
KSF
NEW
CWR
BEAM A
Sea Level
DEPTH (km.)
0.5
1.0
1.5
2.0
2.5
3.0
3.5
0
10 km.
<70
>70 OHM.M

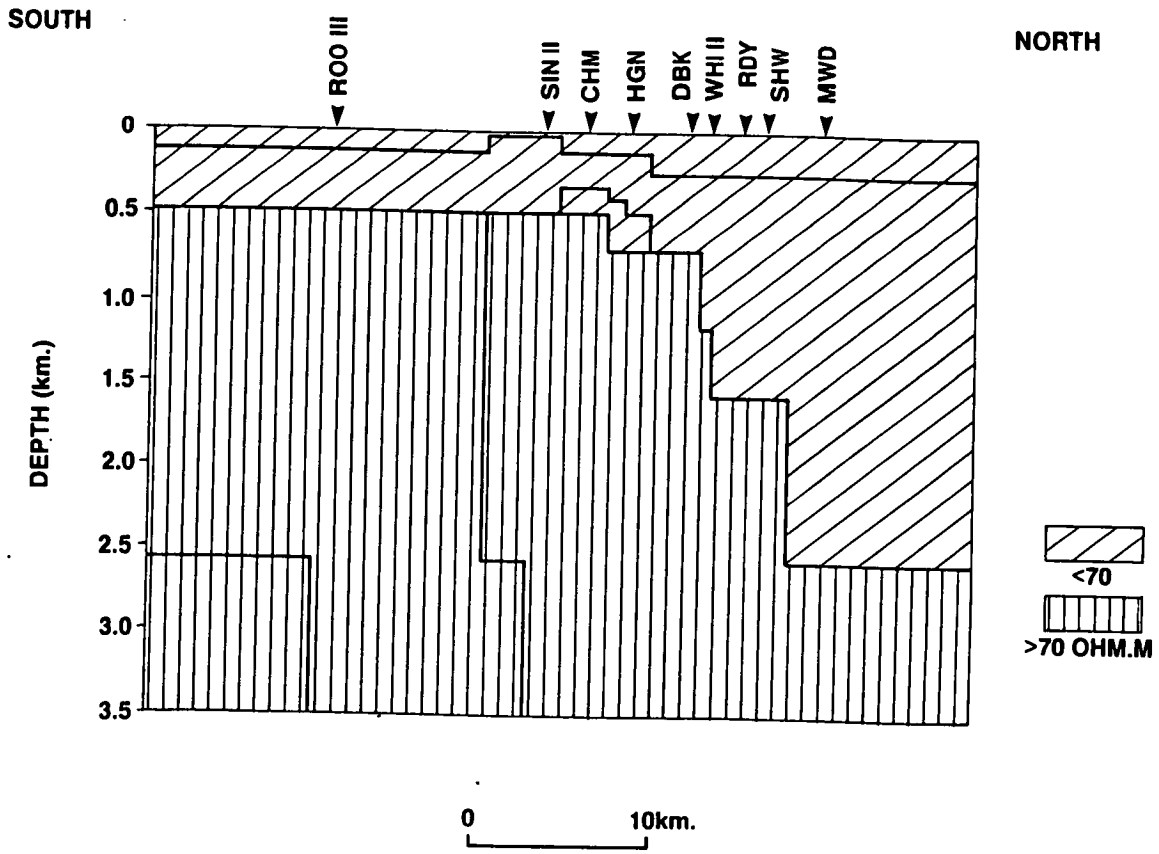
SOUTH
NORTH
ROO III
SIN II
CHM
HGN
DBK
WHI II
RDY
SHW
MWD
0
0.5
1.0
1.5
2.0
2.5
3.0
3.5
DEPTH (km.)
<70
>70 OHM.M
0
10km.

8.4.2. The Thickness of the Sedimentary Rocks: Integrated Results

The geological review which was presented in chapter 7 implied that the evolution of the basement and the Carboniferous age rocks was markedly different. The author therefore assumed that the unconformity which separates these 2 structural units will also show an appreciable change in a number of different geophysical properties (c.f. sections 6.4.9 and 6.4.10). In order to acquire a much more informative and extensive picture, a depth to basement map was constructed from the results of other geophysical studies in the region (some of them have already been introduced in section 7.4). In particular, the results of quarry blast measurements (Swinburn 1975, Banks and Gurbusz 1984), gravity modelling (Yassi 1983, Kimbell *et al.* 1989), seismic refraction (the NERL line; Swinburn 1975, CSSP line ; Bott *et al.* 1985) and reflection studies (the NEC line and onshore seismics; Chadwick and Holliday 1991 , Evans *et al.* 1988, Kimbell *et al.* 1989) were considered. Results from some of these studies have been reproduced in fig. 8.17.

At the majority of the MT site locations the presumed depth to basement integrated reasonably well with the estimates from the other studies. Any discrepancies were individually scrutinized and the models reassessed. Two particular problems were identified:

- The simple gravity models, computed by both Yassi (1983) and in the course of this study (section 6.4.8) seemed to underestimate the thickness of the sediments on the southern margin of the Northumberland Trough. This was considered to be due to the presence of higher density sediments at the base of the trough (Kimbell *et al.* 1989).

- The CSSP seismic refraction results were compatible with other studies onshore, but demonstrated a significant mis-tie with the NEC reflection line offshore (CSSP: 3.5km, NEC: 5km.). Such a mis-tie has also been detected with the WINCH line by Beamish and Smythe (1986) (c.f. section 7.2.3).

The final collated and contoured depth to basement map is given in fig. 8.18.

8.4.3. Northern and Western Northumberland

The depth to basement in the northern and western parts of the Northumberland Basin (typically 1.5-2 km.) is not as great as at the southern margin. The floor of the basin is relatively flat over a wide region extending from the Bewcastle anticline in the SW (35500E, 58000N), to the northern edge

Figure 8.17: Some previously published depth to basement results.

Quarry blast observations (Swinburn 1975) have permitted the depth to basement to be estimated over a very wide area from the Tweed Basin to the Stainmore trough (fig. 8.17a). Reprocessed seismic reflection data from the NEC line allowed Chadwick and Holliday (1991) to detect offshore extensions of the block and basin structure (fig. 8.17b). Yassi (1983) computed a number of north-south and east-west gravity models across the Northumberland Trough. The particular example shown here is taken along the National Grid line 380E (c.f. fig. 8.11b). Finally, detailed onshore seismic reflections profiles (fig. 8.17d) allowed Kimbell *et al.* (1989) to map the Carboniferous stratigraphy and identify the Stublick (S.F.) and Ninety Fathom Faults (N.F.F).:

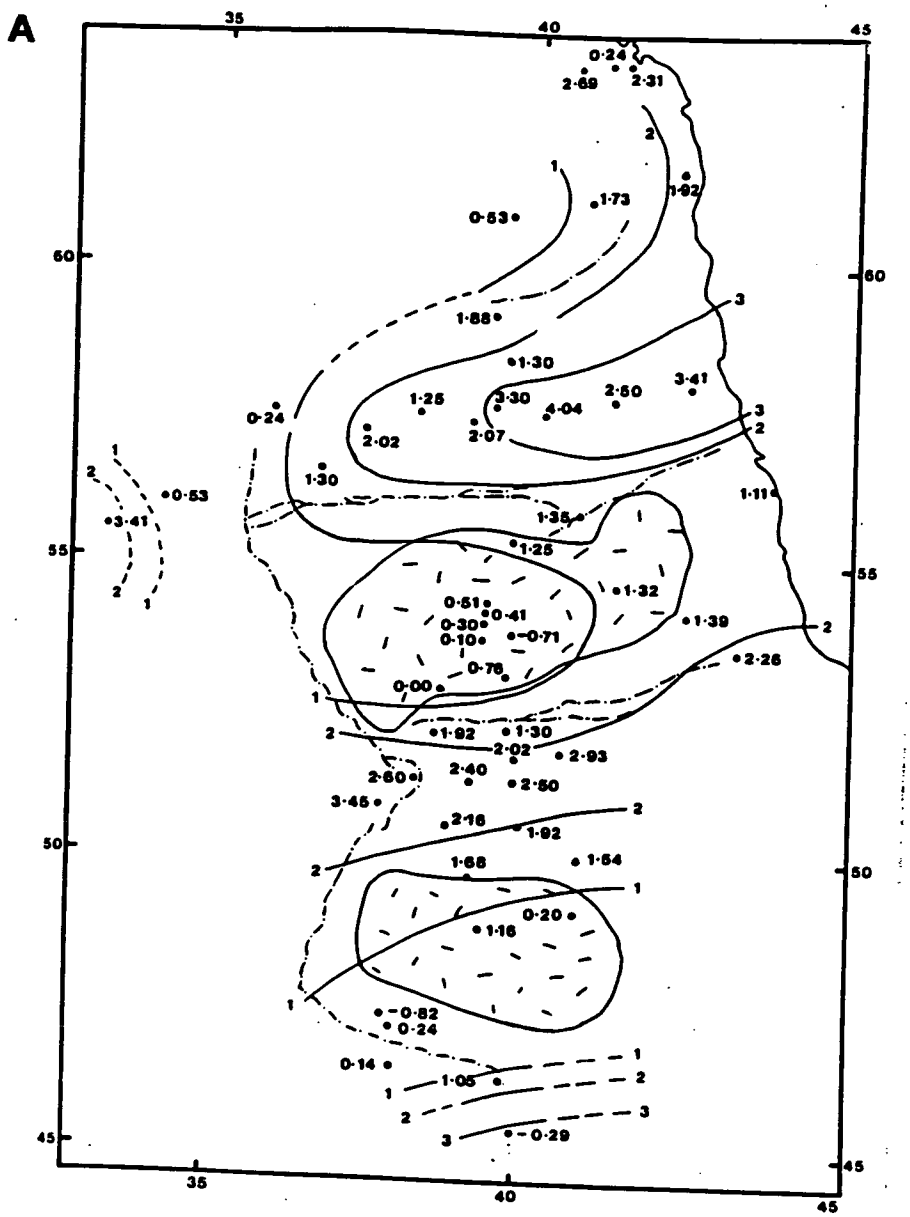
A
35
40
45
60
55
50
45
0·24
2·69
2·31
1·92
1·73
0·53
1·88
1·30
3·41
1·25
3·30
4·04
2·50
2·02
2·07
1·11
1·35
1·25
1·32
1·39
2·26
0·51
0·41
0·30
0·10
0·71
0·76
0·00
1·92
1·30
2·02
2·93
2·40
2·50
2·60
3·45
2·16
1·92
1·68
1·54
0·20
1·16
0·82
0·24
0·14
1·05
0·29

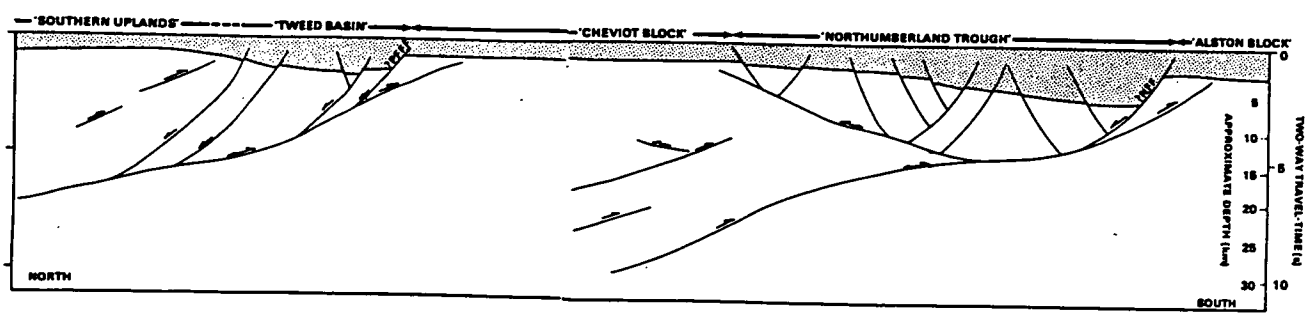
B
'SOUTHERN UPLANDS'
'TWEED BASIN'
'CHEVIOT BLOCK'
'NORTHUMBERLAND TROUGH'
'ALSTON BLOCK'
NORTH
SOUTH
APPROXIMATE DEPTH (km)
TWO-WAY TRAVEL-TIME (s)

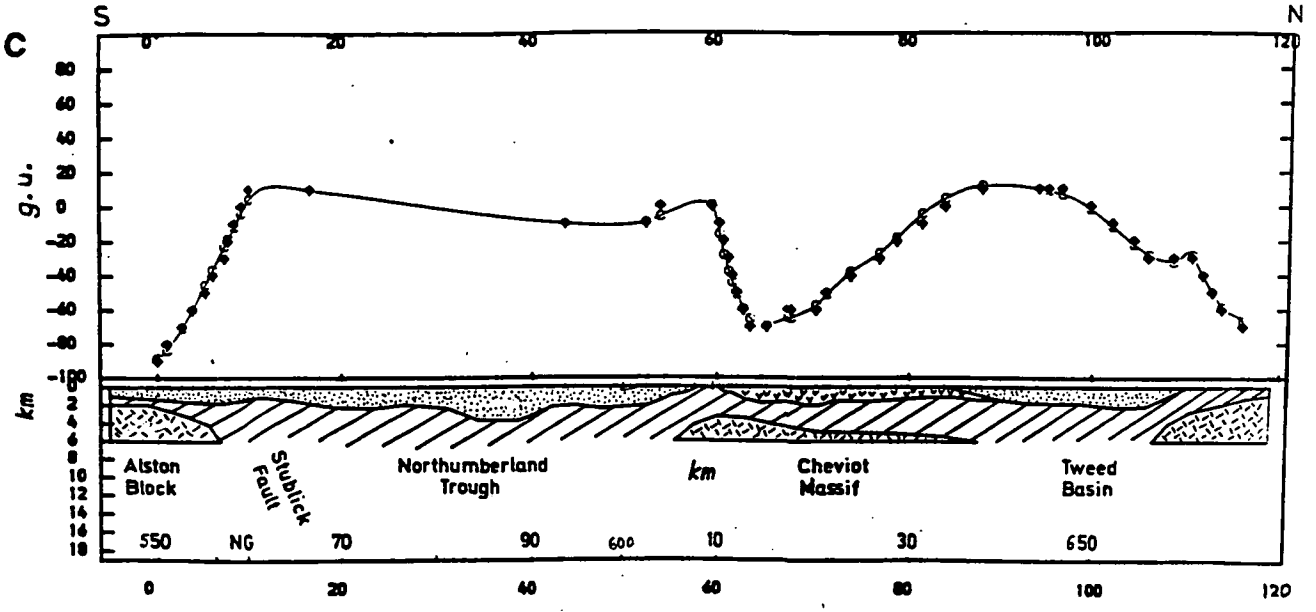
C
S
N
g.u.
km
Alston Block
Stublick Fault
Northumberland Trough
km
Cheviot Massif
Tweed Basin
550
NG
70
90
600
10
30
650

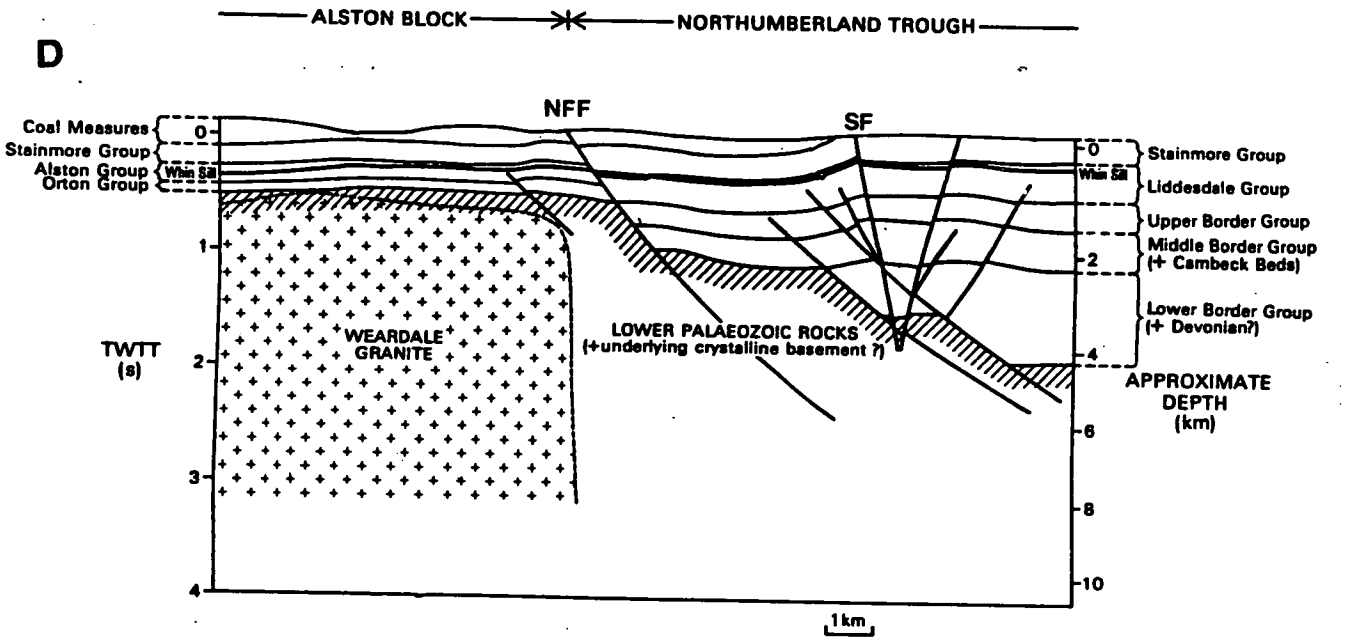
D
ALSTON BLOCK
NORTHUMBERLAND TROUGH
Coal Measures
Stainmore Group
Alston Group
Orton Group
Whin Sill
NFF
SF
WEARDALE GRANITE
LOWER PALAEOZOIC ROCKS
(+underlying crystalline basement ?)
TWTT
(s)
Stainmore Group
Liddesdale Group
Upper Border Group
Middle Border Group
(+ Cambeck Beds)
Lower Border Group
(+ Devonian?)
APPROXIMATE DEPTH
(km)
1km

Figure 8.18: A contour map showing the author's final collated and contoured depth to basement map (in km.) for the Northumberland Trough and Alston Block. The area in which information was available has been delineated by a dotted line.

The Northumberland Trough manifests itself as 2 main basement lows: the Solway Basin in the west (> 3km.) and the Northumberland Basin in the east (> 5km.) separated by the Bewcastle anticline (<500 m.). The narrow 'graben' like structure on the southern margin of the Northumberland Basin can be traced parallel to the Stublick fault from the MT profile in the west, to the NEC line in the North Sea. The sedimentary layer thins over the Cheviot and Alston Blocks. In the latter locality, some basement structure has been detected. The position of this structure is thought to have been dictated by variations in the depth to the granite intrusion.

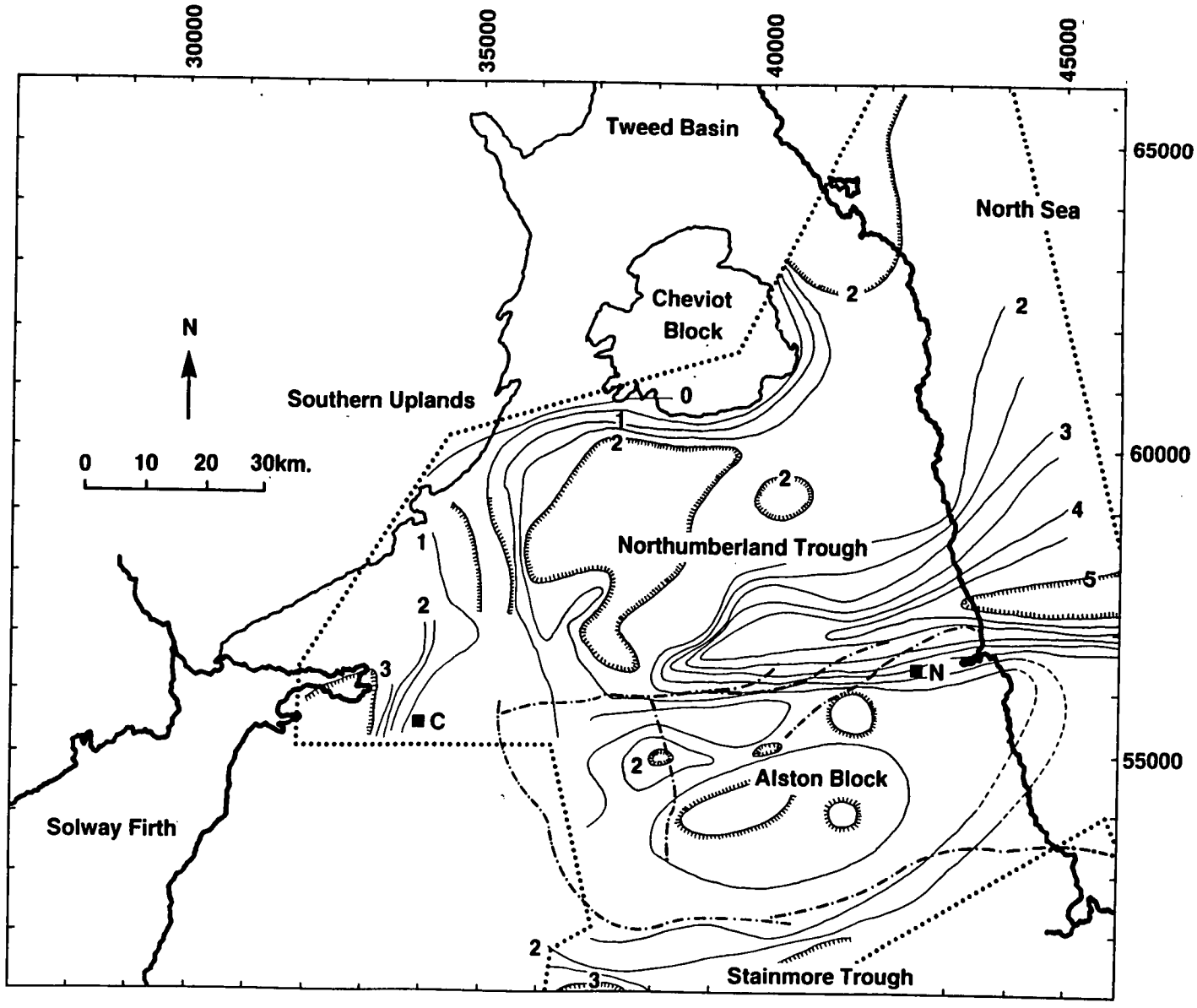
30000
35000
40000
45000
65000
60000
55000
Tweed Basin
North Sea
Cheviot
Block
Southern Uplands
N
0 10 20 30km.
Northumberland Trough
Alston Block
Solway Firth
Stainmore Trough
C
N

of the NEC line in the North Sea (44000E, 65000N). The major intra-basinal faults (fig. 7.8) did not have any discernable influence on the depth to basement but the sediments were found to thin rapidly over the Southern Uplands and the Cheviot Block. The limited information from further to the NE suggests that the sedimentary sequence thickens north of the Cheviot-Alnwick ridge, in the Tweed Basin.

There is a distinct northward trending basement high (35000E, 58000N), sub-parallel and almost coincident with the Bewcastle anticline complex extending from the Southern Uplands, possibly as far south as the Stublick Fault. Over its axis (e.g. the MT site BEW), the sedimentary sequence has been interpreted to be less than 200 m. thick. Further west, quarry blast, seismic refraction and the MT data from GIB shows that the sediment layer is considerably thickened (> 3km.) in the Solway Basin.

8.4.4. The Southern Margin of the Northumberland Basin

The integrated depth-to-basement contour map (fig. 8.18) shows that the 'long' MT profile crosses close to the western end of a major sediment filled basement depression (i.e. at site MWD; 37900E, 56700N). The collation of the MT data, together with offshore (fig. 8.17c) and onshore seismic results (fig. 8.17d) shows that the depression is approximately 3km deep at its western end and progressively increases to 5km in the North Sea. It is up to 50km. wide offshore, but narrows to less than 5km onshore before being truncated by a basement 'high' which trends in a NNE direction from close to the northern edge of the Burtreeford disturbance. From the shallow MT cross section (fig. 8.16a), the basement depression is like a fault bounded 'graben' within the main Northumberland Basin. Its limit is probably a concealed southward throwing antithetic fault located between EDG and SMN. It has a very steep southern margin with a distinct east-west trend which is coincident with the subsurface extension of the western portion of the Stublick Fault. However, the seismic and gravitational observations show that it cross-cuts the ENE trend of its eastern end and the 90 Fathom fault. These results seem to show that the original and most significant basinal faulting occurred along an almost straight line (with an east-west trend) close to the northern margin of the Weardale granite (fig. 8.13). This supports the hypothesis that it was

the buoyant granite which gave structural stability to the Lower Palaeozic rock in the vicinity of the Alston Block, but not the Northumberland Trough.

8.4.5. The Alston Block

There was a relatively high density of different depth-to-basement observations available across the central portion of the Alston Block. Virtually all of them showed a thinner sedimentary layer upon crossing the fault bounded margins of the block (< 1.5km.) and which further diminished towards the centre. The concentric depth contours over the centre of the block (fig. 8.18), seem to delineate the margins of the concealed batholith (c.f. the depth to the Great Limestone; Bott 1967). In fact, the position of 3 of the cupolas (at 41500E 55900N, 39500E 54500N and 41300E 54200N) are delineated by the 0.5 km. sediment contour. This reduced sequence of sediments suggest that the cupolas had been more resilient to erosion and thus remained as islands for some time after marine inundation of the rest of the Alston Block.

Both the Alston Block and the Northumberland Basin show a thicker sequence of sedimentary rocks offshore. It is therefore assumed that regional tilting occurred down towards the east, before younger rocks were deposited on the Carboniferous age base.

The Alston Block did not seem to resist the effects of faulting entirely, particularly in those areas which were not underpinned by the cupolas. The strictly 2-D MT model (fig. 8.16b) did not resolve any lateral variations across the cupola, but the pseudo 2-D (fig. 8.16a) and the 380E gravity model (fig. 8.11b) implied that the depth to metamorphic basement increases to about 2km. at SIN II (551 N). The depth of this structure is comparable to the depth to basement in the Northumberland Trough which suggests that faulting occurred on the Alston Block soon after the initiation of some of the main intra-basinal faults. This basement low is thought to be fault bounded, with its southern margin lying directly adjacent to the flanks of the Rookhope cupola (between SWI and ROO I). Its northern margin appears to be an upstanding block of metamorphic basement at CHM and HGN. There is little information concerning its western extension, but to the east, the author considers that this 'graben' may be associated with a down thrown block

observed to the south of the Tantobie Disturbance on the seismic interpretation shown in fig. 8.12.

The final compilation of results (fig. 8.18) suggest that this 'graben' persists from the 90 Fathom fault trace, to the north and west of the Rowlands Gill cupola, before turning more westwards in response to the Rookhope cupola. The relatively shallow depth to basement at SIN I does at present, seem to cast some doubt over the graben interpretation.

It is evident that the presence of the granite was very influential in inhibiting the effects of later faulting. The granite also dictated and controlled the positions of the major faults, yet it does not appear to show significant faulting itself. Later faulting across the Northumberland Basin and the Alston Block had a slightly more northerly component which appears to have been dictated by the cupolas on the upper surface of the batholith.

8.4.6. Regional Variation in the Resistivity

The gross geoelectric signature from much of the sedimentary sequence is comparatively uniform and featureless (e.g. LAM II in Appendix - C) with typical resistivities between 10 to 40 Ω.m. (fig. 8.19a,b). This is approximately consistent with the resistivity logs derived from the Rookhope (Dunham *et al.* 1964), Stonehaugh and Longhorsley boreholes (fig. 8.20a,b).

The thickest (1-3 km.) and most significant geoelectric horizon has an average resistivity of 40 Ω.m and it persists at the base of the sedimentary sequence across most of the profile (fig. 8.19a). The relatively high resistivity of this layer implies that it either contains more resistive interbeds (e.g. sandstones) or increased compaction has reduced the rocks porosity. The author loosely interprets this layer as representing the rocks of the Border Group (section 7.7) which are known to outcrop in Northern Northumberland. Like the MT results, seismic observations (Kimbell *et al.* 1989) have shown that this rock type resides beneath younger rock further south. A comparable layer is also seen covering the northern margin of the Alston Block overlying the Lower Palaeozoic rock. At SIN II in particular, the author believes that this horizon represents the Orton Group of sedimentary rocks (predominantly from the Upper Border Group) which were the first to overstep the margin of the block and fill the 'graben' described in section 8.4.5.

Figure 8.19: The detailed upper crustal resistivity structure derived from pseudo 2-D modelling on the 'long profile' (fig. 8.19a) and a strictly 2-D model computed from a subset of the response functions from around the Stublick Fault (fig. 8.19b).

The 2-D model mesh was not designed to give detailed information concerning the sedimentary rocks, but a broadly 2 layer (resistor-conductor) model emerges above the basement rock. A small highly conducting layer was detected in both models (from CHM to DBK). Figure 8.19a shows that it probably persists under a thin, very resistive layer which is thought to be the Whin Sill. At its northern end, the conductor may be terminated against the Stublick Fault plane, which also appears to have produced successively smaller displacements higher up in the sedimentary sequence.

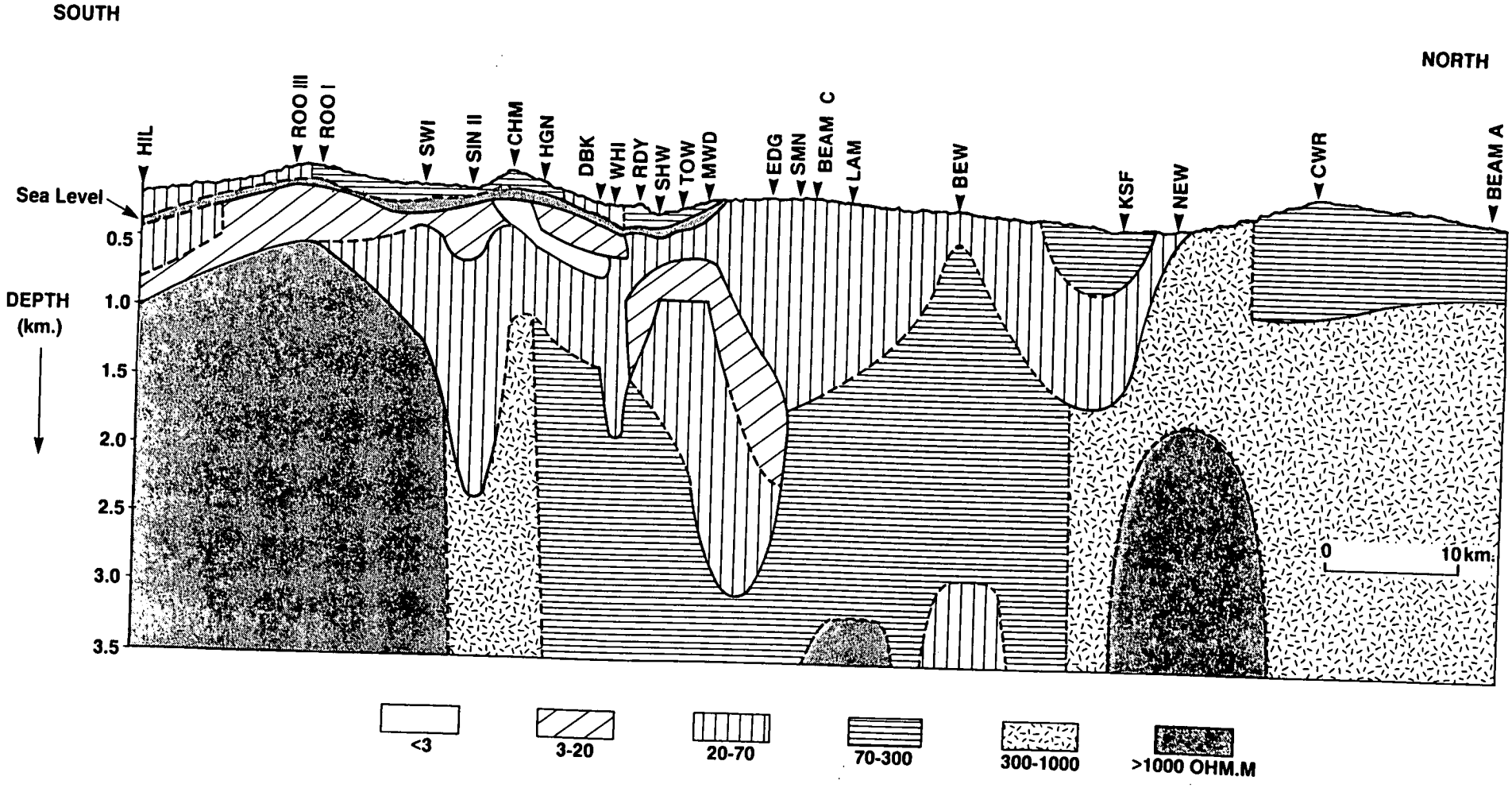
SOUTH
NORTH
HIL
ROO III
ROO I
SWI
SIN II
CHM
HGN
DBK
WHI
RDY
SHW
TOW
MWD
EDG
SMN
BEAM C
LAM
BEW
KSF
NEW
CWR
BEAM A
Sea Level
DEPTH (km.)
0.5
1.0
1.5
2.0
2.5
3.0
3.5
0
10 km.
<3
3-20
20-70
70-300
300-1000
>1000 OHM.M

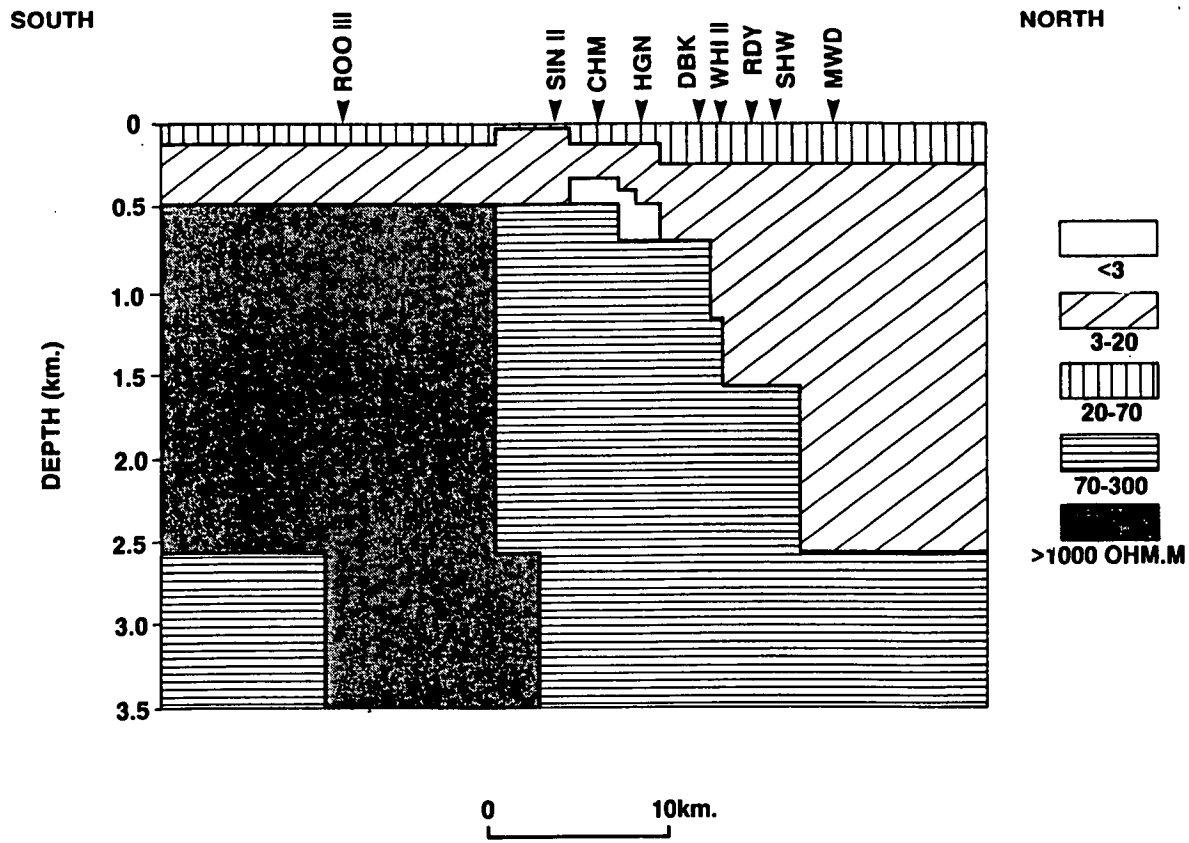
SOUTH
NORTH
ROO III
SIN II
CHM
HGN
DBK
WHI II
RDY
SHW
MWD
0
0.5
1.0
1.5
2.0
2.5
3.0
3.5
DEPTH (km.)
<3
3-20
20-70
70-300
>1000 OHM.M
0
10km.

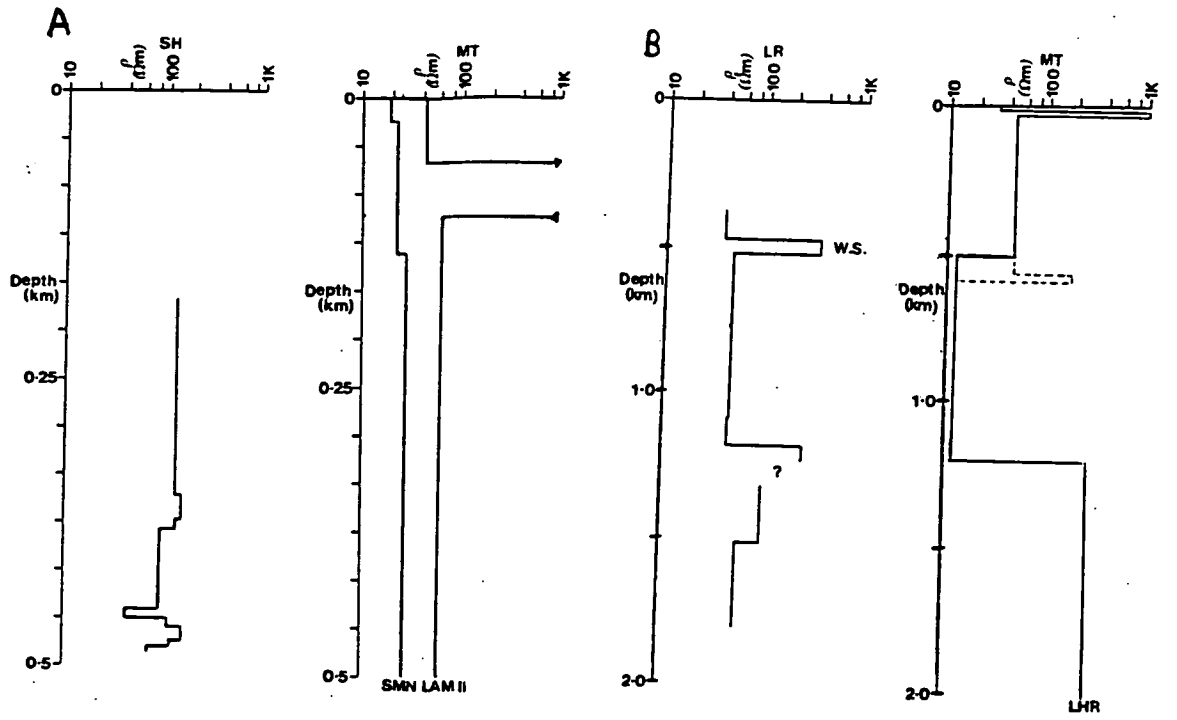

Figure 8.20: Resistivities derived from smoothing borehole observations (SH: Stonehaugh and LR: Longhorsley) and the results from nearby MT sites.

None of the MT sites were located directly adjacent to the Stonehaugh borehole (fig. 8.20a) but the resistivities from LAM II and SMN (approximately 5km. away) were consistent although slightly lower than those downhole. The Longhorsley borehole (fig. 8.20b) had a much greater depth of penetration and also showed typical resistivities in the range from 40 to 100 Ω.m. At the adjacent MT site (LHR) the model again appears to show a more conductive layer (between 0.5 and 1.2km. depth) than the earlier measurements had suggested. A number of the exploratory MT models surprisingly showed a thin layer of comparable resistivities and depths to the Whin Sill (W.S.).

The transition at a depth of 1.2km was originally interpreted as being the characteristic rise in resistivity at basement, but the borehole results imply that this was probably erroneous.

A more conductive layer is observed covering these older (40 Ω.m.) sediments and extending over the granite cupola at ROO III. At this site this layer typically has a thickness of 500 m., but becomes progressively thinner towards the northern edge of the Alston Block. It may also have a thicker northward extension in the Northumberland Trough (between RDY and EDG) at a lower level within the sedimentary sequence. The increased thickness of this layer may reflect the differential rates of subsidence which were known to occur between the block and basin. The author also proposes that subsequent movement on the Stublick fault hinge belt (between RDY and WHI) and possibly the concealed intra-basinal fault at SMN, caused the marked displacement of this layer. Since the Rookhope borehole proved the existence of late Asbian age sedimentary rocks lying above the granite, it is likely that most of this conductive zone corresponds to rocks from that era.

The Stublick Fault manifests itself by displacements in the depth to basement and truncations or disturbances in the overlying sedimentary sequence. It does not appear to be a single fault plane, but the hinge belt probably extends between the 2 large basement displacements from DBK to MWD. The most significant, and probably the earliest faulting occurred beneath SHW (throw 1.5 km.) before later migrating southwards towards the present day Stublick Fault trace (WHI; throw 0.5 km.). The uppermost sequences of later Carboniferous rocks do not seem to be strongly disturbed by the presence of the Stublick Fault. These observations are consistent with inferences based on parallel seismic reflection profiles (Chadwick and Holliday 1991 , Kimbell *et al.* 1989; figs. 7.6 and 8.17d).

On the southern margin of the Alston Block, 3 neighbouring MT sites (CHM, HGN and DBK; figs 6.4 and 8.19) identified a very conductive zone (1-3 Ω.m.) at or just below sea level. As it could not be detected at WHI (I or II), the author considered that this layer was truncated by the Stublick Fault plane. The 2-D MT model (fig. 8.19b) was found to be very sensitive to both the location and resistivity of this layer. Comparison between these 2 models shows that it persists further south in the latter.

The presence of a fluid filled or mineralized zone were considered to be 2 explanations for the electrical models. Either of these interpretations can be supported by other geophysical observations. For example, Bateson (1984)

identified lineaments from satellite images. One of them was parallel to the Stublick Fault (section 7.5.3) and the other crosses through this high conductivity region, in a NNE direction. Bateson interpreted these lineaments as basement conduits for transporting mineralizing solutions. The coincidence of the lineament and the Settlingstones mineral vein was cited as supporting evidence. Such a conduit would undoubtedly provide a low resistivity zone, but the MT results implied that this layer resides within the sedimentary rocks.

A major east-west trending magnetic anomaly was identified at Blanchland by Bott and Masson-Smith (1957b). It apparently terminates on the Burtreeford Disturbance, a few kilometres east of the conductive layer, but they have modelled it as a dyke like body whose upper surface is at depths of between 300 to 600 m. from the surface. This is strikingly similar to the depth to the MT determined anomaly. They proposed 3 possible interpretations for the magnetic anomaly: 1) an igneous intrusion, 2) volcanic lavas or most interestingly, 3) a mineralized vein.

No wholly satisfactory explanation can be proposed currently although the author suspects that the conductor represents a fluid filled fracture which is terminated to the north by the Stublick Fault and its dykes and to the east by the intrusion of lavas in the Burtreeford Disturbance. Short period geomagnetic depth sounding observations could help pinpoint this structure more carefully (e.g. Banks and Beamish 1984).

A relatively resistive rock layer (about 100 Ω.m.) exists at the very top of the sedimentary sequence, particularly in the southern half of the 'long profile' (fig. 8.19a). Some MT models (e.g. DBK in Appendix - C) and most D.C. resistivity models (e.g. MWD in fig. 6.5) show that a thin resistive layer is at least partly responsible. It remains to be proven, but the layer determined at individual sites was assumed to be part of a continuous feature across the Alston Block (fig. 8.19a). This could either be interpreted as a resistive intrusion (e.g. the Whin Sill) or a significant change in the lithology or porosity of the sedimentary sequence (e.g. the Great Limestone). The former explanation was preferred as, like the Whin Sill, this layer appeared to dip towards the south and could not be resolved further north than MWD.

A thin resistive layer does not seem to entirely explain the MT results. A

broader decrease in resistivity with increasing depth could be a particular characteristic of the lithology of this area (i.e. more resistive rocks are present in the upper part of the sedimentary sequence), but this phenomenon was also observed during an MT survey of the Permo-Triassic sedimentary basin at Worcester (fig. 6.6).

Two explanations should be considered. The elevated temperatures at the bottom of the basin may have increased fluid viscosity and therefore enhanced ion mobility. Alternatively, this change reflects variations in the concentrations of dissolved salts. Keller (1971) has suggested that salts and therefore mobile ions may have been leached out of near surface rocks.

8.5. SPECULATIVE REVIEW OF THE GEOLOGICAL EVOLUTION OF NORTHERN ENGLAND

The following discussion, based around figs. 8.21 and 8.22 aims to review the new and pre-existing observations from within and around Northumberland in the context of its geological evolution.

8.5.1. The Regional Model

The evidence for the presence of at least 2 separate palaeo-continental terranes (Avalonia and Laurentia) is clear and relatively unambiguous (section 7.2.2). During the Ordovician (fig. 8.21a) and Silurian (fig. 8.21b), northward subduction of the Iapetus oceanic crust allowed an accretionary prism to develop against the Laurentian margin (section 7.3.2). The remnants of the Iapetus oceanic crust are thought to comprise part of the reflective and conductive zone observed in the middle and lower crust. As the oceanic crust descended into the mantle, it heated and allowed molten igneous rock to rise into the upper crust. These formed some of the older granite plutons which are now found in the Scottish Highlands.

This study has provided the most substantial geophysical evidence, so far, for the southward subduction of oceanic crust beneath Avalonia. This is depicted schematically in fig. 8.21a. Correspondingly an accretionary prism developed along its continental margin and igneous activity was present south of the trench system.

Figure 8.21: Four cartoons summarizing the author's own personal model for the evolution of Northern England from the Ordovician until final continental docking in the Late Devonian.

Ordovician

A

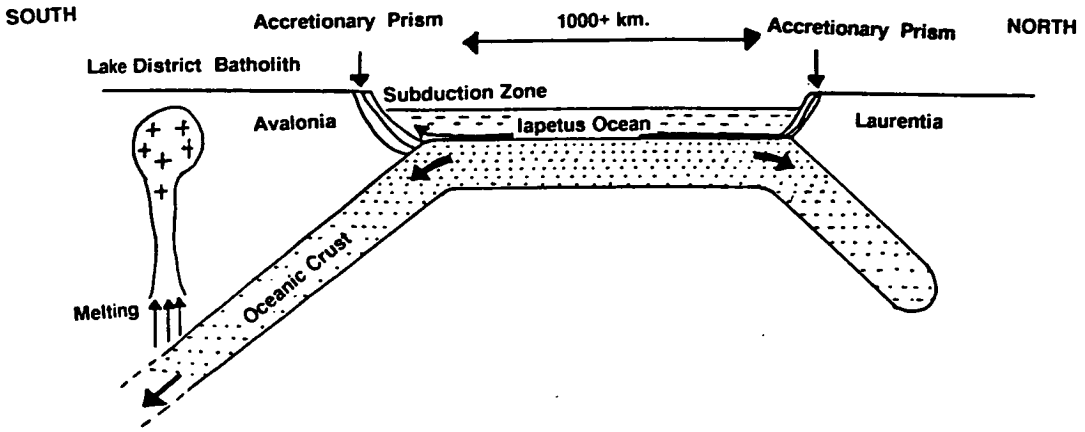

B SILURIAN

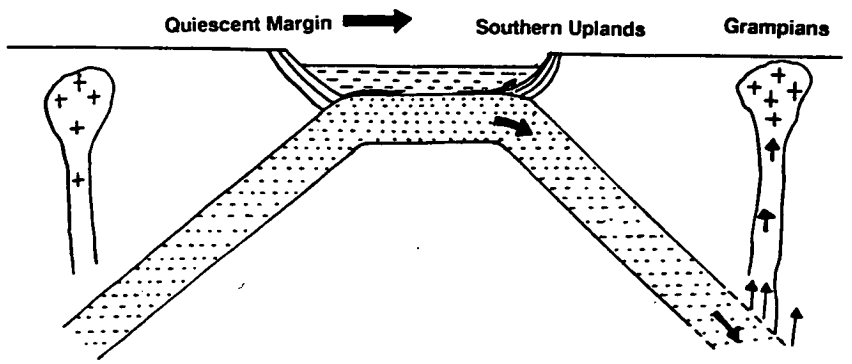

C END SILURIAN

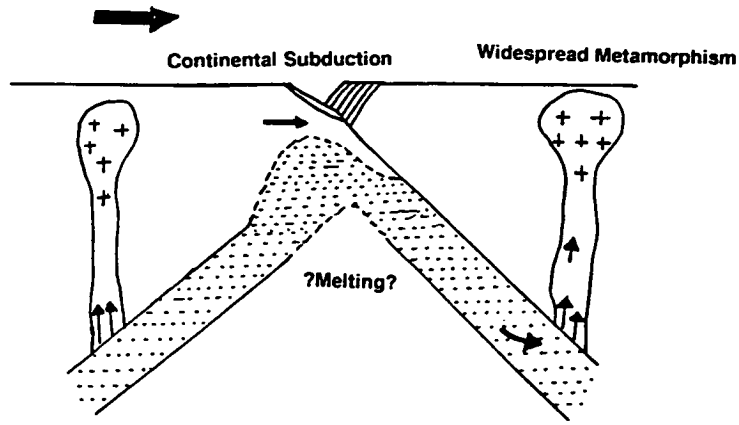

D EARLY DEVONIAN

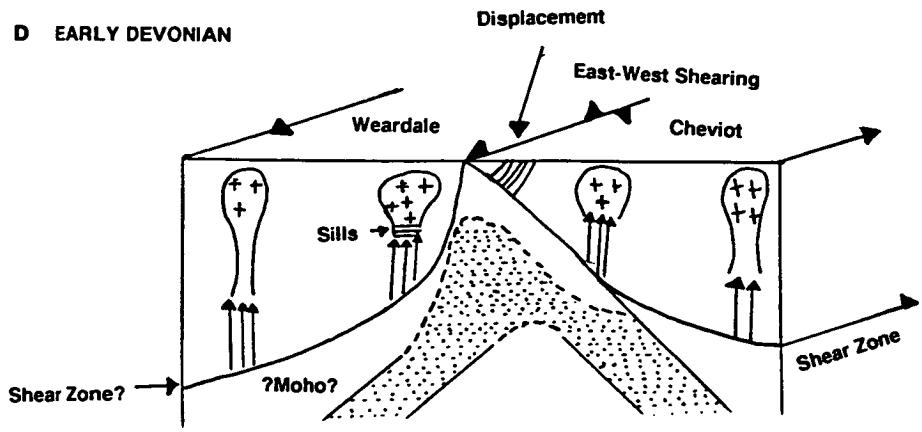

During the late Ordovician or early Silurian eras, southward directed subduction diminished and the Avalonian crust was pulled northwards as the Iapetus ocean closed by subduction beneath Laurentia (fig. 8.21b). As Iapetus ceased to be a barrier for the migration of marine animals, faunal mixing began to occur.

Continent-to-continent collision occurred towards the end of the Silurian (fig. 8.21c) and was marked by a period of widespread metamorphism in the overlying Lower Palaeozoic sedimentary rocks. Subduction did not immediately cease. In response to continued momentum from either the descending Iapetus oceanic crust pull, or forces pushing Avalonia northwards, the southern accretionary complex and continental margin were thrust beneath Laurentia (section 7.3.1). This would have undoubtedly been accompanied by a large rise in the geothermal gradient and possibly partial melting and re-working of the subducted oceanic crust and upper mantle. The author suggests the low density Avalonian igneous rocks (e.g. in the Lake District) would have been difficult to squeeze beneath Laurentia and therefore eventually hindered further continental subduction.

Oblique continental convergence (i.e. in a more east-west direction) or tectonic events occurring in surrounding areas, allowed a major northwards dipping shear zone to develop between the 2 different rock types marking the suture (fig. 8.21d). This probably displaced the uppermost Lower Palaeozoic metamorphic rocks, south of the Iapetus suture, down to, but not significantly within the upper mantle of Southern Scotland. A major phase of plutonism occurred either side of the suture as differential movement between the lower crust and upper mantle permitted the formation of igneous rocks. The bulk of these Early Devonian granites were formed before the Caledonian orogeny, but later spasmodic thermal pulses allowed continued underplating of the batholiths.

8.5.2. Evolution of the Northumberland Trough and Alston Block

The end of the Devonian era was marked by uplift and severe erosion which exposed the tops of the cupolas. Early Carboniferous extension was accomplished along the line of the former shear zone (fig. 8.22a). The Alston/Lake District Blocks remained buoyant and were relatively unaffected as

Figure 8.22: Four cartoons summarizing the author's personal model for the initiation and evolution of the Northumberland Trough and Alston Block from the Late Devonian until the end of the Carboniferous eras.

A LATE DEVONIAN

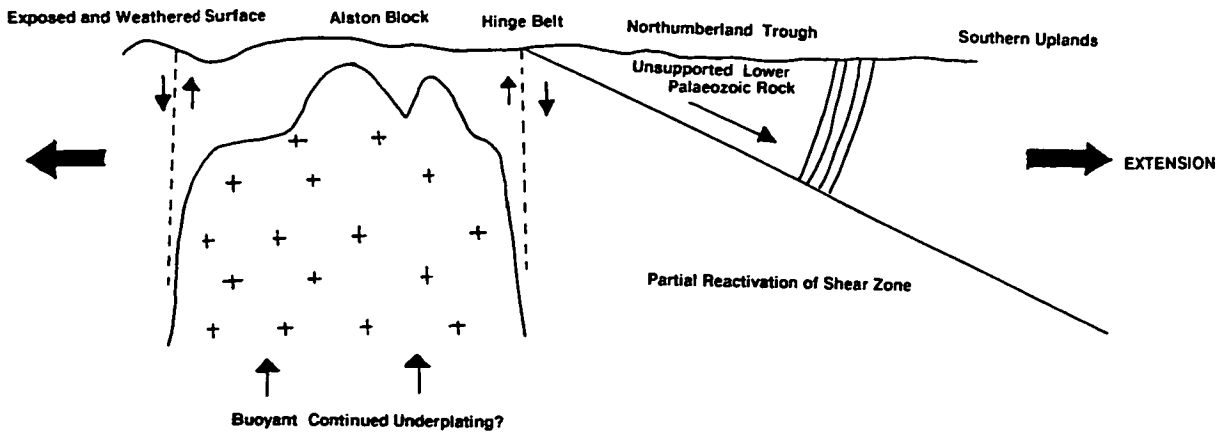

B EARLY CARBONIFEROUS

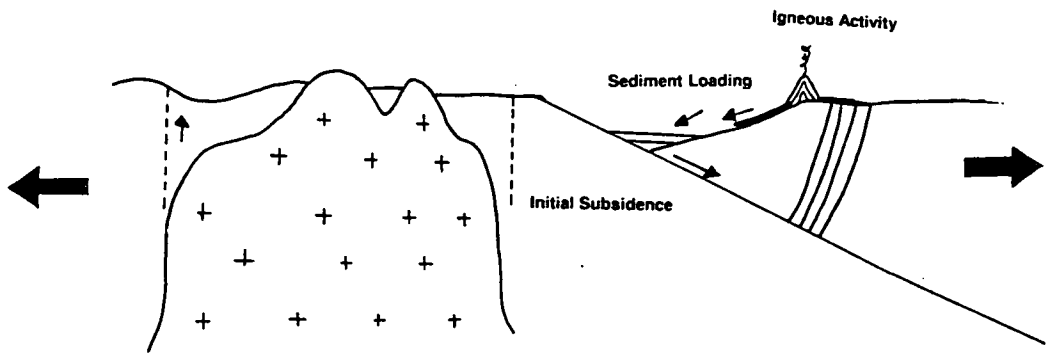

C MID CARBONIFEROUS

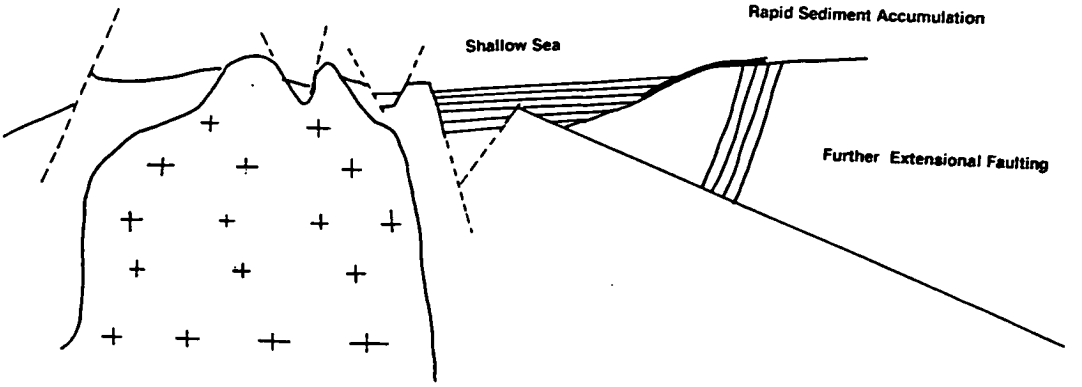

D END CARBONIFEROUS

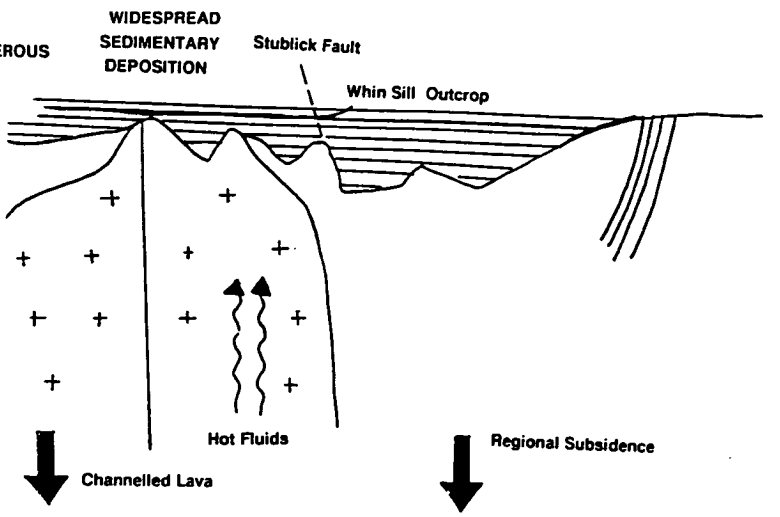

the unsupported rock sagged above the shear zone. The block and basin structure was thus initiated.

Frictional heating at the deeper part of the shear zone and fissuring of rocks along the northern pivotal line of the Northumberland Trough allowed sub-aerial igneous activity. The rate of subsidence within the Northumberland Trough increased due to sediment loading in a shallow marine environment (fig. 8.22b). These low density sediments were water saturated and initially very porous, although the later effects of compaction increased the resistivity of rocks at the base of the sequence.

Major fault zones developed parallel to the sides of the blocks to accommodate continued differential movement. The Stublick and 90 Fathom faults are now seen to be the surface expressions of a much more extensive fault system which developed close to the intra-basement shear zone. A deep graben structure evolved against the northern margin of the Alston Block. Other episodes of faulting affected the sedimentary rocks within the basin and also the less well supported Lower Palaeozic rock overlying the Weardale granite (fig. 8.22c).

Once the extensional forces had been removed, gravitational equilibrium was re-established by the low density sediment infill. Differential subsidence slowed to allow a thin and reduced sequence of sediments to cover the flanks of the block (fig. 8.22d). Eventually, both the block and basin were both subsiding at the same rate, possibly in response to cooling of the upper mantle. The granite cupolas were the last parts of the region to be inundated by marine sediments. Later tectonic movements, possibly related to the closure of the Hercynian ocean, allowed some further movement of the shear zone. This allowed the formation of a mineralized zone around the Weardale granite and the intrusion of the Whin Sill complex.

CHAPTER 9

CONCLUSIONS AND SUGGESTIONS FOR FURTHER WORK

Non Omnia Possumus Omnes

We can't all do everything!

Virgil 70-19 B.C.

In the course of this study, a number of processing and modelling procedures were developed. These new techniques reduced noise contamination and optimized the information contained within the MT observations. These were then applied to a large set of both newly acquired and pre-existing data. The resulting Earth models were used to gain a better understanding of the geological structure and evolution of Northern England.

This chapter summarizes some of the key conclusions before providing a few suggestions for future extensions to the work already undertaken.

9.1. CONCLUSIONS

9.1.1. Data Acquisition

Four component (2 electric and 2 magnetic) single site MT observations were collected in the frequency range from 200 to 0.01 Hz. at 9 sites in Northumberland, Northern England. These sites were located mainly in the vicinity of the Stublick Fault in order to supplement the results acquired during earlier studies by previous investigators.

Local (< 500m.) and remote reference (1-10km.) methods were developed around pre-existing MT data acquisition equipment and subsequently tested in the field. Post-field data processing demonstrated that both methods had a beneficial effect at reducing the level of noise induced bias which was present in the unreferenced apparent resistivity response functions. Remote referencing was theoretically the more desirable method and also appeared to give the best results in practice. In view of its complex and time consuming field logistics however, the author considers that further developmental work

on local reference could prove fruitful.

D.C. resistivity observations (half spread up to 1km.) were collected adjacent to 5 of the MT sites. This was undertaken at little extra field cost and without hindering the rate of MT data collection. The accuracy of the results was questionable, but after joint modelling the twin and independent sources of information allowed a more detailed examination of the shallow geoelectrical structure (the top 150 m.).

9.1.2. Magnetotelluric Data Processing

Parameter regression was fundamental to the research work carried out upon algorithms for processing and modelling MT data. Two chapters of this thesis have been concerned solely with reviewing the theory of the least squares method, its limitations, assumptions and its applications to a number of different MT problems. In this study, the most important of these applications was in the realm of MT impedance estimation.

Conventional single site computer programs were adapted to manipulate referenced MT observations. In view of the large volume of unreferenced MT data which had been collected in Northern England, much more emphasis was placed upon the development of the new methods for single site response function estimation. The concept of the electrical impedance was derived from basic EM wave theory and the sources of MT signals and noise were discussed prior to describing a number of the difficulties encountered in achieving good response functions.

The "constrained method", which was developed for this study, required that reasonable impedance estimates could be computed from Fourier transformed EM field observations. This was undertaken using a stabilized and statistically robust form of the Singular Value Decomposition (SVD) method. The resulting response function was then forced to conform to a number of characteristic features (i.e. that it was smoothly varying, self consistent and optionally, that it was compatible with the likely dimensionality of the geoelectric environment). Constrained parameter regression then used this "ideal response function" to inhibit the range of different impedance values that could be computed from the original set of observations.

The background, theory and the implementation of impedance estimation, response function smoothing and dispersion relation computation have been fully described. The capabilities of the constrained method were demonstrated on both synthetic and real data and also compared with the results which could have been attained by more conventional means. This method was thus found to be a useful tool for the acquisition of readily interpretable and, arguably more accurate, MT response functions. The constrained method was also routinely applied, and the results presented, for field data from a total of 21 sites which had been collected by this and an earlier investigator of the region. These algorithms, together with the integrated interpretation, were probably the most significant innovations in this study.

9.1.3. Magnetotelluric Data Modelling

The review of MT modelling implied that the frequency domain response functions could be transformed into models of the resistivity with depth variation, by a number of different routes. In this study a number of methods were developed from pre-existing programs or techniques. They were then applied not only to the processed response functions, but also to a further 21 which had been published following previous investigations.

The first of these methods utilized the approximate Bostick transformed apparent resistivity and phase information from each site. This information was collated and contoured for a profile of MT sites. The resulting section allowed a rapid appraisal of the gross geoelectric variations.

The second stage involved finding the 'optimum' parametric 1-D model by a new exploratory technique. This tested a number of random starting models using a linearized algorithm. The resulting model with the smallest difference between the observed and computed response functions was considered to be the best 1-D representation for that site. In addition, the range of final models which corresponded to slightly higher misfits were considered to determine the solutions' degree of non-uniqueness. The background and implementation of this method for MT and optionally for D.C. resistivity response functions has been described and demonstrated.

Exploratory models derived from the reprocessed observations have been compared with the original published results. The primary advantages of this

technique were found to be 1) the absence of user intervention and therefore bias, 2) determination of the optimum number of model parameters, 3) the identification of ill determined parameters. The display of the 'almost-equally-acceptable' models was also found to help prevent over-interpretation.

The results from the application of this method to a total of 42 MT sites, 7 of them jointly with D.C. resistivity data, have been presented.

The subsequent modelling stages were considered as interpretative tools which were based upon the results from the earlier non-interactive modelling. A computer program was developed to allow a constrained 1-D model (a "pseudo 2-D model") to be computed from response functions which showed consistency between adjacent MT sites. This was found to reduce inconsistencies between the separate models caused by the non-uniqueness of the results obtained by MT. It also provided a useful mechanism for testing 'structural layer' validity. This modelling technique was used to provide a shallow and deep geoelectric cross section along a 100km. line through Northern England.

The same linearized inversion algorithm used in stages 2 and 3 was also adapted to generate simple 2-D gravity models of the sedimentary layer and the Weardale granite intrusion, with respect to the higher density basement. In the same vein as the second stage, this was achieved automatically with a minimum of user intervention. Optionally, the model could be displayed and manually changed at any stage to permit additional information to be included or to prevent unphysical solutions being attained. This method was demonstrated on a set of gravity anomaly values from a 100km. long profile across the Alston Block and Northumberland Trough. The models from 3 parallel profiles were also computed. These provided more extensive estimates of the thickness of the sediments and the depth to the top of the granite.

The ultimate goal of both of these latter 2 stages was the development of a joint modelling program from both MT and gravity data. It was anticipated that constrained modelling of the depth to common boundaries would reduce the level of non-uniqueness and improve the resolution of each separate

model. In spite of the fact that the program never fully met the authors expectations, he remains confident that future research will prove this to be a valuable modelling and interpretational technique.

Finally, the author undertook strictly 2-D MT modelling to check the validity of parts of the pseudo 2-D model section, in the vicinity of the multi-dimensional Alston Block. This confirmed the presence of the major structures, but there were some significant differences for the lower crust in the final model. Tests performed on the resolution of some of the 2-D model parameters proved to be important in an uncertain region near the Stublick Fault.

No one stage of modelling provided the "best solution". Each had its own advantages and limitations in terms of computational load and complexity, apparent model resolution and interpretability. The exploratory and pseudo 2-D modelling methods did, however, provide the most useful interpretational information for this study.

9.1.4. The Northern England Study

The author has presented a wide ranging review of the geological and geophysical observations and models from Northern England. This attempted to provide a background to the MT observations considered and help support the authors interpretation of the results.

The geoelectric model results have been discussed in some detail for the lower crustal conductive zone, the metamorphic and igneous (granite) basement and the surficial sedimentary layer. The author frequently found that considerably more reliable information could be gleaned if the results from other geophysical studies were also considered, if not integrated, prior to final interpretation. D.C. resistivity observations allowed a more detailed examination of near surface resistive layers, seismic sections provided relatively consistent depth to basement estimates and gravity models also helped to determine the topography of the top of the granite batholith.

The results of this study have also supported and enhanced the correlation between a northward dipping deep seismically reflective zone and an electrically conductive layer beneath the Northumberland Trough. It remains

poorly imaged at most locations, but there is increasing evidence that it is a remnant of the Iapetus convergence zone and can be traced from Britain and into Ireland. As a result of the complex pattern in the depth to this layer, an evolutionary model invoking continental convergence solely by northward directed subduction must be too simplistic. The presence of a comparable southward dipping zone under the Alston Block may also suggest southward directed subduction, but the results from the Southern Uplands of Scotland imply that there has been a relatively complicated evolution.

There is also some evidence for a fluid filled shear zone near to the zone of the Iapetus continental collision and subduction. It appears to extend from a depth of 3 km. from the surface near the Stublick Fault, to a depth of about 30km at the northern edge of the Northumberland Trough. This shear zone may have played an important, if not controlling part in the initiation of the Northumberland Trough and possibly also the Devonian age granites.

Magnetotelluric and other geophysical observations have allowed the gross structure within and beneath the Northumberland sedimentary basin and Alston Block to be examined. As anticipated from earlier studies, the results show a much reduced sequence of sedimentary rocks over the granite supported Alston Block compared with the Northumberland Trough. Some subsurface manifestations of the Stublick Fault separating the block and basin, have been identified and discussed. Other intra-basinal structures have been detected and their implications for lithology, fluid content and mineralization noted.

9.2. SUGGESTIONS FOR FURTHER WORK

9.2.1. Data Acquisition Procedures

Magnetotelluric field procedures should aim to attain high quality EM observations, from the maximum number of different sites and within the minimum time and expenditure. The MT field equipment used in this study is flexible and can achieve high quality results in the presence of good signal to noise levels, but a number of modifications have been identified by this user. It is currently considered to be 1) too large and not portable enough to carry

to more remote sites, 2) not particularly robust and 3) too expensive. The author considers that a more effective exploration instrument would be a small, fully automated and self contained recording system designed for secure deployment as part of a large spatial array. Whilst the SPAM recorder could be radically simplified by limiting its flexibility, a major obstacle would be limiting the size of the sensors yet retaining the accuracy of the results. Future studies may clarify the level of instrumental accuracy required for a typical survey, in the presence of a typical level of noise contamination.

In order to give post-field data processing more flexibility, it would be desirable to record long uninterrupted data windows on high density disk packs. This would only be possible if the main SPAM computer was removed from its obligatory task of data analysis, possibly to play a more subserviant quality control function. The additional recording of real time markers would enormously simplify the type of remote reference used in this study.

9.2.2. Future Fieldwork

There is a relatively high density of MT soundings in Northern England, but there are still glaringly obvious regions in which there are few, if any observations (e.g. the east coast of England, the Cheviot and Lake District Blocks and SW Scotland).

The study of the lower crustal conductivity zone is still in its infancy. A relatively coarse density of sites (10–20 km. separation) is now required over a very wide region of Northern England and Southern Scotland. To substantiate the correlation drawn with the Irish H.C.L. (from the IMP and SIMP lines), MT measurements are also desirable in Northern Ireland. Simultaneously acquired G.D.S. data from these sites could help delineate the very interesting localities where the H.C.L. approaches the surface. A still more ambitious project would involve the acquisition of marine MT measurements in either the North or Irish Seas which would facilitate a more direct comparison with seismic reflection observations.

Interest in the Iapetus suture is still far from waning (e.g. Trench and Torsvick 1991, Blundell *et al.* 1991). The magnetotelluric methods unique capacity for probing the deep interior and the presence of electrical variations in the lower crust must mean that this technique has an important role to play

in future investigations.

There are a number of other basement structures that could benefit from more detailed investigations. These studies may involve: 1) testing the proposal that there is a resistivity increase between Avalonian and Laurentian crust, 2) examining the other ill-resolved high resistivity layers in Northern Northumberland, 3) mapping the crustal wide low resistivity zone near to the Stublick Fault and 4) its relationship with the Weardale granite. This batholith is worthy of much more detailed 2-D modelling.

The full role of the east-west trending Stublick Fault hinge belt may only become fully apparent if new MT data is collected along north-south profiles on both sides of the profile from this study (1-2km. site spacing and 10km. between profiles). The Newcastle conurbation will necessarily inhibit the role of MT to the east, but there are a number of areas westwards, towards and beyond the Pennine Faults, which should prove more suitable. Such a study may be able to provide evidence for a westward extension of the hinge belt into the basal sedimentary rocks in the Vale of Eden and possibly towards the northern edge of the Lake District Block. This study may also provide extra, and commercially useful, information concerning the 'graben' structure which seems to exist on the SW margin of the Northumberland Trough.

Other similar structural studies may prove informative on the northern edge of the Northumberland Trough (i.e. the Cheviot Block and Tweed Basin areas) and around the Bewcastle anticlinal structures.

On a purely local scale the very high conductive zone within the sedimentary sequence is a very interesting feature with possible implications for geothermal and mineral exploration. A high frequency (> 1Hz.) and high density (site spacing about 500m.) MT and D.C. resistivity study is required to confirm its presence and map its extent. This study would also enhance identification of the near surface resistive layer which was tentatively interpreted as being either the Whin Sill or the Great Limestone.

The MT data which the author has collected in and around the Worcester sedimentary basin has been used for illustrations on two occasions. Preliminary processing and modelling of the observation from 13 sites in the area has already been performed. Future investigations could be undertaken

to interpret these results with regard to the Permo-Triassic sedimentary rocks and the Pre-Cambrian basement and Malvern Axis. This may also provide a useful comparison with the results of this study from the Carboniferous Northumberland Trough.

9.2.3. Data Processing and Modelling

The author can see little value, at present, in major studies involving either re-processing or re-modelling the pre-existing Northern England data. Although there should now be a strong commitment to collecting new measurements, this data must not be forgotten during any reinterpretation. A data base should therefore be initiated to store the response functions and models for each locality. This could be undertaken jointly with, or along similar lines as, the resistivity data base recently proposed by Barker and Blunk (1991). The ease of access to MT response functions and models is important. This would be facilitated by the necessary, but painful, process of standardization of the presentation of such information as recently proposed by B. Hobbs (person. commn.).

The suite of processing and modelling programs is extensive, but many are not user friendly or fully tested. A considerable effort needs to be expended to consolidate these routines, possibly involving whole scale revision of some of the program code. It would then be necessary to test the methods using different types of real and artificial MT data. The 1-D synthetic data algorithm developed could be a potentially valuable method of assessing different impedance estimation methods and should therefore be expanded to allow 2 and 3-D models.

REFERENCES

Adam, A., Kaikkonen, P., Hjelt, S.E., Pajunpaa, K., Szarka, L., Vero, J., Wallner, A., 1982. Magnetotelluric and audiomagnetotelluric measurements in Finland, *Tectonophysics*, **90**, 77-90.

Adam, A. and Varga, G. 1990. Distortions of the electromagnetic field by shallow basins and by resistive outcrops, *Phys. Earth Planet Int.*, **60**, 80-88.

Allen, P.M., 1987. The Solway Line is not the Iapetus Suture, *Geol. Mag.*, **124**, 485-486.

Andrews, D.F., 1974. A robust method for multiple linear regression, *Technometrics*, **16**, 523-531.

Allsop, J. M., 1987. Patterns of late Caledonian intrusive activity from geophysics, radiometric dating and basement geology, *Procs. Yorks. Geol. Soc.*, **46**, 335-353.

Archie, G.E., 1942. The electrical resistivity log as an aid to determining some reservoir characteristics, *Trans. A.I.M.E*, **146**, 54-62.

Bahr, K., 1983. Joint interpretation of magnetotelluric and geomagnetic data and local distortion, *J. Geomag. Geoelectr.*, **35**, 555-566.

Bamford, D., Nunn, K., Prodehl, C. and Jacob, B. 1978. LISPB-IV: Crustal structure of Northern Britain, *Geophys. J. R. astr. Soc.*, **54**, 43-60.

Banks, R.J., 1986. The interpretation of the Northumberland Trough geomagnetic variation anomaly using two-dimensional current models, *Geophys. J. R. astr. Soc.*, **87**, 596-616.

Banks, R.J., Beamish, D. and Geake, M.J., 1983. Magnetic variation anomalies in northern England and southern Scotland, *Nature*, **303**, 516-518.

Banks, R.J. and Beamish, D, 1984. Local and regional induction in the British Isles, *Geophys. J. R. astr. Soc.*, **79**, 539-553.

Banks, R.J. and Gurbusz , C., 1984. An investigation of the crustal structure of North-West England using quarry blasts as seismic sources, *Proc. Yorks. Geol. Soc.*, **45**, 19-25.

Barker, R.D and Blunk, I, 1991. The national resistivity sounding database, *Geoscientist*, **1**, 6-7.

Barrett, P.A., 1988. Early Carboniferous of the Solway Basin: A tectnostratigraphic model and its bearing on hydrocarbon potential, *Marine and Petroleum Geology*, **5**, 271-281.

Barrodale, I. and Erickson, R.E., 1980. Algorithms for least squares linear prediction and maximum entropy spectral analysis-I: Theory, *Geophysics*, **45**, 420-432.

Bateson, J.H., 1984. The value of LANDSAT imagery in regional mineral reconnaissance exploration - the Northumberland Trough: a brief case history, *Rep. Br. Geol. Surv.*, **16/10**, 22-25.

Bateson, J.H. and Johnson, C.C., 1984 Whin sill in exploratory boreholes from Newbrough, Northumberland, *Procs. Yorks. Geol Soc.*, **45**, 1-10.

Beamish, D., 1986a. Deep crustal geoelectric structure beneath the Northumberland Basin, *Geophys. J. R. astr. Soc.*, **84**, 619-640.

Beamish, D., 1986b. Geoelectric structural dimensions from magnetotelluric data: Methods of estimation, old and new, *Geophysics*, **51**, 1298-1309.

Beamish, D., 1990. A deep geoelectric survey of the Carnmenellis granite, *Geophys. J. Int.*, **102**, 679-693.

Beamish, D. and Banks, R.J., 1983. Geomagnetic variation anomalies in Northern England: processing and presentation of data from a non-simultaneous array, *Geophys. J. R. astr. Soc.*, **75**, 513-539.

Beamish, D. and Smythe, D.K., 1986. Geophysical images of the deep crust: the Iapetus Suture, *J. Geol. Soc. Lond.*, **143**, 489-497.

Belsley, D.A., Kuh, E. and Welsch R.E., 1980. *Regression diagnostics: identifying influential data and sources of collinearity*, 292pp, Wiley, New York.

Berdichevsky, M.N. and Dimitriev, V.I., 1976. Basic principles of interpretation of magnetotelluric sounding curves, in *Geoelectric and geothermal studies*, pp 165-221, ed. Adam, A., KAPG Geophysical monograph, Budapest.

Berdichevsky, M.N., Vanyan, L.L., Kuznetsov, V.A., Levadny, V.T., Mandelbaum, M.M., Nechaeva, G.P., Okulessky, B.A., Shilovsky, P.D. and Shpak, I.P., 1980. Geoelectrical model of the Baikal region, *Phys. Earth Planet. Int.*, **22**, 1-11.

Berdichevsky, M.N., Vanyan, L.L and Dimitriev, V.I., 1989. Methods used in the USSR to reduce near surface inhomogeneity effects on deep magnetotelluric sounding, *Phys. Earth Planet. Int.*, **53**, 194-206.

Bhattacharya, P.K. and Patra, H.P., 1968. *Direct current geoelectric sounding*, 139pp, Elsevier, Amsterdam.

Biehler, S., Ferguson, J., Baldridge, W.S., Jiracek, G.R., Aldern, J.L., Martinez, M., Fernandez, R., Romo, J., Gilpin, B., Braile, L.W., Hersey, D.R., Luyendyk, B.P. and Aiken, C.L., 1991. A geophysical model of the Espanola Basin, Rio Grande rift, New Mexico, *Geophysics*, **56**, 340-353.

Bleil, D.F., 1964. *Natural electromagnetic phenomena below 30 kc/s*, Plenum Press, New York.

Blundell, D.J., Hobbs, R.W., Klemperer, S.L., Scott-Robinson, R., Long, R.E., West, T.E. and Duin, E., 1991. Crustal structure of the central and southern North Sea from BIRPS deep seismic reflection profiling, *J. Geol. Soc. Lond.*, **148**, 445-457.

Blohm, E.K., Worzyk, P. and Scriba, H., 1977. Geoelectrical deep soundings in Southern Africa using the Cabora Bassa power line, *J. Geophys.*, **43**, 665-679.

Bode, H.W., 1949. *Network analysis and feedback amplifier design*, 551pp, D. Van Nostrand, Toronto.

Boehl, J.E., Bostick Jr., F.X. and Smith, H.W., 1977. An application of the Hilbert transform to the magnetotelluric method, *Tech. Rep. Electrical geophysics Res. Lab.*, University of Texas at Austin.

Bott, M.H.P, 1967. Geophysical investigation of the Northern Pennine basement rocks, *Procs. Yorks. Geol. Soc*, **36**, 139-168.

Bott, M.H.P, 1978. Deep structure, in *The Geology of the Lake District*, pp24-40, ed. Moseley, F., Yorkshire Geological Society Publication.

Bott, M.H.P, 1987. Subsidence mechanisms of Carboniferous basins in Northern England, in *European Dinantian Environments*, pp21-32, eds. Miller, J., Adams, A.E. and Wright, V.P., J. Wiley and Sons, Chichester.

Bott, M.H.P, and Masson-Smith, D., 1957a. A geological interpretation of a gravity survey of the Alston Block and the Durham coalfield, *Q. J. Geol. Soc. Lond*, **113**, 93-117.

Bott, M.H.P, and Masson-Smith, D., 1957b. Interpretation of a vertical field magnetic survey of north-east England, *Q. J. Geol. Soc. Lond*, **113**, 119-129.

Bott, M.H.P. and Johnson, G.A.L., 1972. Structure of the Alston Block, in *Geology of Durham County*, ed. Hickling, G. *Trans. Nat. Hist. Soc. Northumberland*, **41**, pp152.

Bott, M.H.P, Swinburn, P.M. and Long, R.E., 1984. Deep structure and origin of the Northumberland and Stainmore Troughs, *Proc. Yorks. Geol. Soc*, **44**, 479-495.

Bott, M.H.P., Long, R.E., Green, A.S.P., Lewis, A.H.J., Sinha, M.C. and Stevenson, D.L., 1985. Crustal structure South of the Iapetus suture beneath Northern England, *Nature*, **314**, 724-727.

Branney, M.J. and Soper, N.J. 1988. Ordovician volcano-tectonics in the English Lake District, *J. Geol. Soc. Lond*, **145**, 367-376.

Brewitt-Taylor, C.R. and Weaver, J.T., 1976. On the finite difference solution of the two dimensional induction problem, *Geophys. J. R. astr. Soc*, **47**, 375-396.

Brewitt-Taylor, C.R., and Johns, P.B., 1980. Diakoptic solution of induction problems, *J. Geomag. Geoelectr*, **32, Suppl. I**, S173-S178.

Brewer, J.A., Matthews, D.H., Warner, M.R., Hall, J., Smythe, D.K. and

Whittington, R.J., 1983. BIRPS deep seismic reflection studies of the British Caledonides, *Nature*, **305**, 206-210.

British Geological Survey (BGS formerly IGS),1966. Geological survey of Great Britain: 1 : 50,000 series geological map: Sheet 9: Rothbury., H.M.S.O., London

British Geological Survey (BGS formerly IGS), 1975. Geological survey of Great Britain: 1:50,000 series geological map Sheet 19: Hexham, H.M.S.O., London.

British Geological Survey (BGS formerly IGS), 1976. I.G.S. boreholes 1975: Report No. 76/10, H.M.S.O. London.

British Geological Survey (BGS formerly IGS), 1980. Geological survey of Great Britain: 1:50,000 series geological map Sheet 13: Bellingham H.M.S.O., London.

British Geological Survey, 1988. *Geothermal energy in the United Kingdom*, Investigation of the geothermal potential of the UK series.

Brown, G.C., 1979. Geochemical and geophysical constraints on the origin and evolution of the Caledonian granites, *The Caledonides of the British Isles-Reviewed*, pp645-652, eds. Harris, A.L., Holland, C.H. and Leake, B.E., *Geol. Soc. Lond. Spec. Publn*, No. 8, Scottish Academic Press, Edinburgh.

Brown, G.C., Plant, J. and Lee, M.K., 1979. Geochemical and geophysical evidence on the geothermal potential of Caledonian granites in Britain, *Nature*, **280**, 129-131.

Businger, P.A. and Golub, G.H., 1969. Singular Value Decomposition of a complex matrix, *Comm. A. C. M.*, **12**, 564-565.

Cagniard, L., 1953. Basic theory of the magnetotelluric method of geophysical prospecting, *Geophysics*, **18**, 605-635.

Cantwell, T., 1960. Detection and analysis of low frequency magnetotelluric signals, *Ph. D. thesis*, M.I.T., Cambridge, Mass.

Chadwick, R.A. and Holliday, D.W., 1991. Deep crustal structure and

Carboniferous basin development within the Iapetus Convergence Zone, Northern England, *J. Geol. Soc.*, in press.

Chave, A.D., Von Herzen, R.P., Poehls, K.A. and Cox, C.S., 1981. Electromagnetic induction fields in the deep ocean North-East of Hawaii: implications for mantle conductivity and source fields, *Geophys. J. R. astr. Soc.*, **66**, 379-406.

Chave, A.D., Thomson, D.J., and Ander, M.E., 1987. On the robust estimation of power spectra, coherences and transfer functions, *J. Geophys. Res.*, **92**, 633-648.

Chave, A.D. and Booker, J.R., 1987. Electromagnetic induction studies, *Rev. Geophysics*, **25**, 989-1003.

Chave, A.D. and Thomson, D.J., 1989. Some comments on magnetotelluric response function estimation, *J. Geophys. Res.* **94**, 14215-14225.

Christopherson, K.R., 1991. Application of magnetotellurics to petroleum exploration in Papua New Guinea: A model for frontier areas, *Geophysics: The leading edge of exploration*, 21-27.

Chyba, J., 1983. On the interpretation of resistivity soundings by the least squares method, *Geophysical Prospecting*, **31**, 795-799.

Claerbout, J.F., 1976. *Fundamentals of geophysical data processing: with applications to petroleum prospecting*, McGraw - Hill, New York.

Clarke, J., Gamble, T.D., Goubau, W.M., Koch, R.H., and Miracky, R.F., 1983. Remote reference magnetotellurics: equipment and procedures, *Geophysical Prospecting*, **31**, 149-170.

Clay, C.S. and Hinich, M.J., 1981. Estimating the Earth's impedance function when there is noise in the electric and magnetic signals, in *Applied time series analysis II*, pp189-219, ed. Findley, D.F., Academic Press, New York.

Cocks, L.R.M. and Fortey, R.A., 1982. Faunal evidence for oceanic separations in the Palaeozoic of Britain, *J. Geol. Soc. Lond.*, **139**, 465-478.

Collier, R.E., 1989. Tectonic evolution of the Northumberland Basin; the

effects of renewed extension upon an inverted extensional basin, *J. Geol. Soc. Lond.*, **146**, 981–989.

Constable, C.G., 1988 Parameter estimation in non-Gaussian noise, *Geophysical Journal*, **94**, 131–142.

Constable, S.C., Parker, R.L. and Constable, C.G., 1987. Occams inversion: a practical algorithm for generating smooth models from electromagnetic sounding data, *Geophysics*, **52**, 289–300.

Cooley, J.W. and Tukey, J. 1965. An algorithm for the machine calculation of complex Fourier series, *Math. Comput.*, **19**, 297–301.

Cornwell, J.D. and Evans, A.D., 1986. Magnetic surveys and structures in the Whin Sill, Northern England, in *Geology in the real world - the Kingsley Dunham volume*, eds. Nesbitt, R.W. and Nichol, I., The institution of mining and metallurgy.

Creaney, S. 1980. Petrographic texture and vitrinite reflectance variation of the Alston Block, North-East England, *Procs. Yorks. Geol. Soc.*, **42**, 533–580.

Crossley, D.J. and Reid, A.B., 1982. Inversion of gamma-ray data for element abundances, *Geophysics*, **47**, 117–126.

Day, J.B.W., 1970. Geology of the country around Bewcastle, *Memoir of the Geological Survey of Great Britain: Sheet 13*, H.M.S.O., London.

Daniel, C. and Wood, F.S., 1971. *Fitting equations to data*, 342pp, Wiley, New York.

Devlin, T. 1984. A broadband electromagnetic induction study of the Travale geothermal field, Italy, *Ph. D thesis*, University of Edinburgh.

Dewey, J.F., 1982. Plate tectonics and the evolution of the British Isles, *J. Geol. Soc. Lond.*, **139**, 371–412.

Donato, J.A., Martindale, W. and Tully, M.C., 1983. Buried granites within the Mid North Sea High, *J. Geol. Soc. Lond.*, **140**, 825–837.

Dongarra, J.J., Moler, C.B., Buch, J.R. and Stewart, G.W., 1979. *LINPACK:*

users guide, Society for Industrial and Applied Mathematics, Philadelphia.

Dosso, H.W., Neinaber, W. and Hutton, V.R.S., 1980. An analogue model study of electromagnetic induction in the British Isles region, *Phys. Earth Planet Int.*, 22, 68-85.

Dosso, H.W., Nienaber, W. and Chen, J., 1989. Laboratory electromagnetic modelling of the subducting Juan de Fuca Plate, *Phys. Earth Planet. Int.*, 53, 221-227.

Downing, R.A. and Gray, D.A., 1986. Geothermal resources for the United Kingdom, *J. Geol. Soc. Lond.*, 143, 499-507.

Draper, N.R. and Smith, H., 1981. *Applied regression analysis*, 709pp, Wiley, New York.

Dunham, K.C., 1934. The genesis of the North Pennine ore deposits, *Q. J. Geol. Soc.*, 90, 689-720.

Dunham, K.C., 1948. Geology of the Northern Pennine Orefield: Vol I, Tyne to Stainmore, *Memoir of the Geological Survey of Great Britain*, H.M.S.O., London.

Dunham, K.C., Dunham, A.C., Hodge, B.L and Johnson, G.A.L., 1965. Granite beneath Visean sediments with mineralization at Rookhope, Northern Pennines, *Q. J. Geol. Soc. Lond.*, 121, 383-417.

Efron, B., 1982. *The Jackknife, the Bootstrap and other Resampling Plans*, Society for Industrial and Applied Mathematics, Philadelphia.

Egbert, G.D., 1990. Comments on 'Concerning dispersion relations for the magnetotelluric impedance tensor' by E. Yee and K.V. Paulson, *Geophys. J. Int.*, 102, 1-8.

Egbert, G.D. and Booker, J.R., 1986. Robust estimation of geomagnetic transfer functions, *Geophys. J. R. astr. Soc.*, 87, 173-194.

Egbert, G.D. and Booker, J.R., 1989. Multivariate analysis of geomagnetic array data I: The response space, *J. Geophys. Res.*, 94, 14227-14247.

Eliason, P.T., Donovan, T.J. and Chavez Jr., P.S., 1983. Integration of geologic, geochemical and geophysical data from the Cement oil field, Oklahoma, using spatial array processing, *Geophysics*, **48**, 1305–1317.

England, P.C., Oxburgh, E.R. and Richardson, S.W., 1980. Heat refraction and heat production in and around granite plutons in North-East England, *Geophys. J. R. astr. Soc.*, **62**, 439–455.

d'Erceville, I. and Kuntez, G., 1962. The effect of a fault on the Earth's natural electromagnetic field, *Geophysics*, **27**, 651–661.

Evans, C.J., Kimbell, G.S., and Rollin, K.E., 1988. Hot dry rock potential in urban areas, *Investigation of the geothermal potential of the United Kingdom* British Geological Survey Report.

Firman, R.J. and Lee, M.K., 1987. The English Lake District batholith – Ordovician Silurian, Devonian, .. or?, *Geol. Mag.*, **124**, 585–587.

Fischer, G., 1982. Magnetotelluric observational techniques on land, *Geophys. Surv.*, **4**, 373–393.

Fischer, G., 1985. Some remarks on the behaviour of the magnetotelluric phase, *Geophysical Prospecting*, **33**, 716–722.

Fischer, G., 1989. A strong topographic valley effect on AMT and VLF-R measurements, *Geophysical Journal*, **96**, 469–475.

Fischer, G. and Schnegg, P.- A., 1980, The dispersion relations of the magnetotelluric response and their incidence on the inversion problem, *Geophys. J. R. astr. Soc.*, **62**, 661–673.

Fischer, G., Schnegg, P.- A., Peguiron, M., Le Quang, B.V., 1981. An analytic one-dimensional magnetotelluric scheme, *Geophys. J. R. astr. Soc.*, **67**, 257–278.

Fischer, G. and Le Quang, B.V., 1982. Parameter trade-off in one dimensional magnetotelluric modelling, *J. Geophys.*, **51**, 206–215.

Fitch, F.J. and Miller, J.A., 1965. Age of the Weardale granite, *Nature*, **208**, 743–745.

Fitch, F.J. and Miller, J.A., 1967. The age of the Whin Sill, *Geological Journal*, 5, 233–250.

Fitton, J.G. and Hughes, D.J., 1970. Volcanism and plate tectonics in the British Ordovician, *Earth Planet Sci. Lett.*, 8, 223–228.

Fontes, S., 1988. Electromagnetic induction studies in the Italian Alps, *Ph. D. thesis*, University of Edinburgh, 351pp.

Fortey, R.A., Owens, R.M. and Rushton, A.W.A, 1989. The palaeogeographic position of the Lake District in the early Ordovician, *Geol. Mag.*, 126, 9–17.

Freeman, B., Klemperer, S.L. and Hobbs, R.W., 1988. The deep structure of Northern England and the Iapetus Suture Zone from BIRPS deep seismic reflection profiles, *J. Geol. Soc. Lond.*, 145, 727–740.

Freund, R.J. and Minton, P.D., 1979. *Regression methods: a tool for data analysis*, 261pp, Dekker, New York.

Frost, D.V., 1984. New information on the Dinantian stratigraphy and structure of Tynedale, Northumberland, *Procs. Yorks. Geol. Soc.*, 45, 45–49.

Frost, D.V. and Holliday, D.W., 1980. Geology of the country around Bellingham, *Memoir of the Geological Survey of Great Britain*, H.M.S.O., London.

Galanopolous, D., 1989. Magnetotelluric studies in geothermal areas of Greece and Kenya, *Ph. D. thesis*, University of Edinburgh, 340pp.

Gamble. T.D., Goubau, W.M., and Clarke, J., 1979a. Magnetotellurics with a remote reference, *Geophysics*, 44, 53–68.

Gamble. T.D., Goubau, W.M., and Clarke, J., 1979b. Error analysis for remote reference magnetotellurics, *Geophysics*, 44, 959–968.

Gardiner, A.R., 1983. Sedimentological studies of the Scremerston Coal and Lower Limestone Groups in the Northumberland Basin, *Ph. D. thesis*, University of Leeds.

Genc, T., 1989. Gravity and other geophysical studies of the crust in southern Britain, *Ph D. thesis*, University of Edinburgh.

Goldberg, S. and Rostein, Y., 1982. A simple form of presentation of magnetotelluric data using the Bostick transform, *Geophysical Prospecting*, **30**, 211-216.

Golub, G.H. 1969. Matrix decomposition and statistical calculations, in *Statistical computations*, eds. Milton, R.C. and Nelder, J.A., Academic Press.

Golub, G.H. and Saunders, M.A., 1970. Linear least squares and quadratic programming, in *Integer and Non-Linear Programming*, pp 229-256, ed. Abadie J., North Holland Publishers, Amsterdam.

Gomez-Trevino, E. and Edwards, R.N., 1983. Electromagnetic soundings in the sedimentary basin of southern Ontario- A case history, *Geophysics*, 311-320.

Goodall, C., 1983. M - estimators of location: An outline of the theory, in *Understanding Robust and Exploratory data analysis*, pp339-403, ed. Hoaglin, D.C., Mosteller, F. and Tukey, J.W., Wiley, New York.

Goubau, W.M., Gamble, T.D. and Clarke, J., 1978. Magnetotelluric data analysis: removal of bias, *Geophysics*, **43**, 1157-1166.

Goubau, W.M., Maxton, P.M., Koch, R.H. and Clarke J., 1984. Noise correlation lengths in remote reference magnetotellurics, *Geophysics*, **49**, 433-438.

Grant, I.S. and Phillips, W.R., 1980. *Electromagnetism*, 514pp, Wiley, Chichester.

Green, P.F., 1988. On the thermo-tectonic evolution of Northern England: evidence from fission track analysis, *Geol. Mag.*, **123**, 493-506.

Gubbins, D., Scollar, I. and Wisskirchen, P., 1971. Two dimensional digital filtering with HAAR and WALSH transforms, *Ann. Geophys.*, **27**, 85-104.

Gunst, R.F. and Mason, R.L., 1980. *Regression analysis and its applications: a data orientated approach*, 402pp, Dekker, New York.

Haak, V. and Hutton, R., 1986. Electrical resistivity in the continental lower crust. In *The nature of the lower continental crust*, pp35-49, eds. Dawson, J.B.,

Carswell, D.A., Hall, J. and Wedepohl, K.H.. Special publication of the Geological Society, 24.

Hall, J., 1986. Physical properties of the lower crust, in *The nature of the lower continental crust*, pp 51-62, eds. Dawson, J.B., Carswell, D.A., Hall, J. and Wedepohl, K.H., Special Publication of the Geological Society, 24.

Hall, J., Brewer, J.A., Matthews, D.H. and Warner, B.R., 1984. Crustal structure across the Caledonides from the "WINCH" seismic reflection profile: influences on the evolution of the Midland Valley of Scotland, *Trans. Roy. Soc. Edin. Earth Sci.*, 75, 97-109.

Hampel, F.R., Ronchetti, E.M., Rousseeuw, P.J. and Stahel, W.A. 1986. *Robust statistics: the approach based on influence functions*, Wiley, New York

Harinarayana, T., 1987. Lithospheric electrical conductivity structure across Southern Scotland and Northern England, *Ph D. thesis*, University of Edinburgh, 318pp.

Haszeldine, R.S., 1988. Crustal lineaments in the British Isles: their relationship to Carboniferous basins, in *Sedimentation in a synorgenic basin complex*, pp53-68, Blackie, Glasgow.

Hattingh, M., 1988. A new adaptive filtering program to remove noise from geophysical time or space series data, *Computers and Geosciences*, 14, 467-480.

Hatton, L, Worthington, M.H. and Makin, J., 1986. *Seismic data processing*, 177pp, Blackwell, Oxford.

Haworth, R.T., 1986. Some aspects of geophysical investigations in the Caledonides of the U.K., in *Synthesis of the Caledonian rocks of Britain*, pp281-301, eds. Fettes, D.J. and Harris, A.L., D Reidel, Dordecht.

Hermance, J.F., 1973. Processing of magnetotelluric data, *Phys. Earth Planet. Int.*, 7, 349-364.

Hermance, J.F., 1983. Electromagnetic induction studies, *Rev. Geophys. and Space Phys.*, 21, 652-665.

Hickling, G. (ed.), 1972. Geology of Durham County *Trans. Nat. Hist. Soc. Northumberland*, 41, pp152.

Hill, E.R.G., 1987. A magnetotelluric study in the Moine thrust region of northern Scotland, *Ph. D. thesis*, University of Edinburgh.

Hoaglin, D.C., Mosteller, F. and Tukey, J.W., 1983. *Understanding robust and exploratory data analysis*, 447pp, Wiley, New York.

Hobbs, B.A., 1982. Automatic model for finding the one-dimensional magnetotelluric problem, *Geophys. J. R. astr. Soc.*, 68, 253-264.

Hoerl A.E. and Kennard, R.W., 1970a. Ridge regression: Biased estimation for nonorthogonal problems, *Technometrics*, 12, 55-67.

Hoerl A.E. and Kennard, R.W., 1970b. Ridge regression: Applications to nonorthogonal problems, *Technometrics*, 12, 69-80.

Holland, J.G. and Lambert, R.J., 1972. Weardale granite, in *The geology of Durham County*, pp 103-108, ed. Hickling, G., *Trans. Nat. Hist. Soc. Northumberland*, 41.

Holland, C.H., Kelling, G., and Walton, E.K., 1979. O.T. Jones and after: a multitude of models, in *The Caledonides of the British Isles- Reviewed*, pp469-482, eds. Harris, A.L., Holland, C.H. and Leake, B.E., *Geol. Soc. Lond. Spec. Publn.*, No. 8, Scottish Academic Press, Edinburgh.

Hogg, R.V., 1979. An introduction to robust estimation, in *Robustness in statistics*, pp 1-17, ed. Launer, R.L., Academic Press, New York.

Hoover, D.B., Long, C.L. and Senterfit, R.M., 1978. Some results from audio magnetotelluric investigations in geothermal areas, *Geophysics*, 43, 1501-1514.

Hohmann, G.W., 1983. Three dimensional EM modelling, *Geophys. Surv.*, 6, 27-53.

Hoverstein, G.M., Dey, A. and Morrison, H.F., 1982. Comparison of five least squares inversion techniques in resistivity sounding, *Geophysical Prospecting*, 30, 688-715.

Huber, P.J., 1964. Robust estimation of a location parameter, *Am. Math. Statist. J.*, **35**, 73-101.

Huber, P.J. 1981. *Robust Statistics*, 308pp, Wiley, New York.

Hughes, L.J. and Carlson, N.R., 1987. Structure mapping at Trap Spring Oilfield, Nevada using controlled source magnetotellurics, *First Break*, **5**, 403-418.

Hutton, D.H.W, 1987. Strike-slip terranes and a model for the evolution of the British and Irish Caledonides, *Geol. Mag.*, **124**, 405-425.

Hutton, V.R.S., Sik, J.M. and Gough, D.I., 1977. Electrical conductivity and tectonics of Scotland, *Nature*, **266**, 617-620.

Hutton, V.R.S., Dawes, G.J.K., Devlin, T. and Roberts, R., 1984. A broadband tensorial magnetotelluric study in the Travale-Radicondoli geothermal field, 9pp, *EEC report series*.

Hyndman, R.D. and Shearer, P.M., 1989. Water in the lower continental crust: modelling magnetotelluric and seismic reflection results. *Geophys. J. Int.*, **98**, 343-365.

Ibrahim, A.W. and Keller, G.V., 1981. Seismic velocities and electrical resistivities of recent volcanics and their dependence on porosity, temperature and water saturation, *Geophysics*, **46**, 1415-1422.

Ilkisik, O.M. and Jones, A.G., 1984. Statistical evaluation of MT and AMT methods applied to a basalt-covered area in South-Eastern Anatolia, Turkey, *Geophysical Prospecting*, **32**, 706-724.

Ingham, M.R., 1988a. The use of invariant impedances in magnetotelluric interpretation, *Geophys. J.*, **92**, 165-169.

Ingham, M.R., 1988b. A magnetotelluric and magnetovariational traverse across the New Zealand subduction zone, *Geophys. J. R. astr. Soc.*, **92**, 495-504.

Ingham, M.R. and Hutton, V.R.S., 1982. Crustal and upper mantle electrical structure in Southern Scotland, *Geophys. J. R. astr. Soc.*, **69**, 579-594.

Inman, J.R., 1975. Resistivity inversion with ridge regression, *Geophysics*, 798-817.

Jackson, D.D., 1972. Interpretation of inaccurate, insufficient and inconsistent data, *Geophys. J. R. astr. Soc.*, **28**, 97-109

Jackson, D.D., 1976. Most Squares Inversion, *J. Geophys. Res.*, **81**, 1027-1030.

Jackson, D.D., 1979. The use of a-priori data to resolve non-uniqueness in linear inversion, *Geophys. J. R. astr. Soc.*, **57**, 137-157

Jady, R.J., Paterson, G.A. and Whaler, K.A., 1983. Inversion of the electromagnetic induction problem using Parker's algorithms with both precise and practical data, *Geophys. J. R. astr. Soc.*, **75**, 125-142.

Jain, S. and Wilson, C.D.V, 1967. Magneto-telluric investigations in the Irish Sea and Southern Scotland, *Geophys. J. R. astr. Soc.*, **12**, 165-180.

Johansen, H.K., 1977. A man/computer interpretation system for resistivity soundings over a horizontally stratified Earth, *Geophys. Prosp.*, **25**, 667-691.

Johnson, G.A.L., 1982. Geographical change in Britain during the Carboniferous period, *Proc. Yorks. Geol. Soc.*, **44**, 181-203.

Johnson, G.A.L., 1984. Subsidence and sedimentation in the Northumberland Trough, *Procs. Yorks. Geol. Soc.*, **45**, 71-83.

Johnson, M.R.W., Sanderson, D.J. and Soper, N.J., 1979. Deformation in the Caledonides of England, Ireland and Scotland, in *The Caledonides of the British Isles- Reviewed*, pp 165-186, eds. Harris, A.L., Holland, C.H. and Leake, B.E., *Geol. Soc. Lond. Spec. Publn.*, No. 8, Scottish Academic Press, Edinburgh.

Jones, A.G., 1980a. Geomagnetic induction studies in Scandanavia I, *J. Geophys.*, **48**, 181-194.

Jones, A.G., 1980b Report on the COPROD study (Comparative study of methods for deriving the conductivity profile within the Earth for 1-D magnetotelluric data), presented at the 5th workshop on electromagnetic induction in the Earth and Moon (Aug. 17-24, 1980, Istanbul)

Jones, A.G., 1982. On the electrical crust-mantle structure in Fennoscandia: no Moho, and the asthenosphere revealed?, *Geophys. J. R. astr. Soc.*, **68**, 371-388.

Jones, A.G., 1983a. The problem of "current channelling": a critical review, *Geophys. Surv.*, **6**, 119-122.

Jones, A.G., 1983b. On the equivalence of the "Niblett" and "Bostick" transformations in the magnetotelluric method, *J. Geophys.*, **53**, 72-73.

Jones, A.G., 1983c. The electrical structure of the lithosphere and asthenosphere beneath the Fennoscandian Shield, *J. Geomag. Geolectr.*, **35**, 811-827.

Jones, A.G., 1987. MT and seismic reflection: an essential combination, *Geophys. J. R. astr. Soc.*, **89**, 7-18.

Jones, A.G., 1988. Static shift of magnetotelluric data and its removal in a sedimentary basin environment, *Geophysics*, **53**, 967-978.

Jones, A.G., and Hutton, V.R.S., 1979a. A multi-station magnetotelluric study in Scotland - I. Fieldwork, data analysis and results, *Geophys. J. R. astr. Soc.*, **56**, 329-349.

Jones, A.G., and Hutton, V.R.S., 1979b. A multi-station magnetotelluric study in Scotland - II. Monte Carlo inversion of the data and its geophysical and tectonic implications, *Geophys. J. R. astr. Soc.*, **56**, 351-368.

Jones, A.G., Olafsdottir, B. and Tiikkainen, J., 1983. Geomagnetic induction studies in Scandanavia III, *J. Geophys.*, **54**, 35-50.

Jones, A.G. and Foster, J.H., 1986. An objective real-time data adaptive technique for efficient model resolution improvement in magnetotelluric studies, *Geophysics*, **51**, 90-97.

Jones, A.G., Chave, A.D., Egbert, G.D., Auld, D. and Bahr, K., 1989. A comparison of techniques for magnetotelluric response function estimation, *J. Geophys. Res.* **94**, 14201-14213.

Jones, A.G. and Craven, J.A., 1990. The North American Central Plains

conductivity anomaly and its correlation with gravity, magnetic, seismic and heat flow data in Saskatchewan, Canada, *Phys. Earth Planet. Ints*, **60**, 169–194.

Jupp, D.L.B., 1978. Estimation of the magnetotelluric impedance functions, *Phys. Earth Planet. Int*, **17**, 75–82.

Jupp, D.L.B. and Vozoff, K., 1975. Stable iterative methods for the inversion of geophysical data, *Geophys. J. R. astr. Soc*, **42**, 957–976.

Jupp, D.L.B. and Vozoff, K. 1977. Two dimensional magnetotelluric inversion, *Geophys. J. R. astr. Soc*, **50**, 333–352.

Kao, D.W. and Rankin, D., 1977. Enhancement of signal-to-noise ratio in magnetotelluric data, *Geophysics*, **42**, 103–110.

Kao, D.W., and Orr, D., 1982. Magnetotelluric studies in the Market Weighton area of eastern England, *Geophys. J. R. astr. Soc*, **70**, 323–327.

Kaufman, A.A., and Keller, G.V., 1981. *The magnetotelluric sounding method*, 595pp, Elsevier, Amsterdam.

Kay, R.W. and Kay, S.M., 1986. Petrology and geochemistry of the lower continental crust: an overview, in *The nature of the lower continental crust*, pp 147–159, eds. Dawson, J., Carswell, D.A., Hall, J. and Wedepohl, K.H., Spec. Publn. Geol. Soc. Lond., **24**.

Kanasewich, E.R., 1981. *Time sequence analysis in geophysics*, 480pp, University of Alberta Press, Edmonton.

Keller, G.V., 1971. Electrical characteristics of the Earths crust, in *Electromagnetic probing in geophysics* pp13–76, ed. Wait, J.R., Golem Press, Boulder.

Keller, G.V, 1987. Rock and mineral properties, in *Electromagnetic methods in applied geophysics – Theory, Vol. I*, ed. M.N. Nabighian, pp13–51, S.E.G., Tulsa.

Keller, G.V. and Frischknecht, F.C., 1970. *Electrical methods in geophysical prospecting*, 519pp, Pergamon Press, New York.

Kennan, P.J., Phillips, W.E.A. and Stragen, P., 1979. Pre-Caledonian basement to the paratectonic Caledonides in Ireland, in *The Caledonides of the British Isles- Reviewed*, pp 157-164, eds. Harris, A.L., Holland, C.H. and Leake, B.E., *Geol. Soc. Lond. Spec. Publn*, No. 8, Scottish Academic Press, Edinburgh.

Kimbell, G.S., Chadwick, R.A., Holliday, D.W. and Werngren, O.C., 1989. The structure and evolution of the Northumberland Trough from new seismic reflection data and its bearing on the modes of continental extension, *J. Geol. Soc. Lond.*, **146**, 775-787.

Kleiner, B., Martin, R.D. and Thomson, D.J., 1979. Robust estimation of power spectra, *J. R. Statist. Soc.*, **41**, 313-351.

Kleiner, B. and Graedel, T.E., 1980. Exploratory data analysis in the geophysical sciences, *Rev. Geophys. and Space Phys.*, **18**, 699-717.

Klemperer, S.L., 1989. Seismic evidence for the location of the Iapetus Suture West of Ireland, *J. Geol. Soc. Lond.*, **146**, 409-412.

Klemperer, S.L. and Matthews, D.H., 1987. Iapetus Suture located beneath the North Sea by BIRPS deep seismic profiling, *Geology*, **15**, 195-198.

Koefoed, O.E., 1980. Geosounding Principles: Vol. I, Elsevier, Amsterdam.

Kröger, P., Micheel, H.J. and Elsner, R. 1983. Comparison of errors in local and reference estimates of the magnetotelluric impedance tensor, *J. Geophys.*, **52**, 97-105.

Kunetz, G., 1972. Processing and interpretation of magnetotelluric soundings, *Geophysics*, **37**, 1005-1021.

Kurtz, R.D., De Laurier, J.M. and Gupta, J.C., 1986. A magnetotelluric sounding across Vancouver Island detects the subducting Juan de Fuca plate, *Nature*, **321**, 596-599.

Lanczos, C. 1961. *Linear Differential Operators*, 564pp, D. Van Nostrand, London.

Lanning, E.N. and Johnson, P.M., 1983. Automated identification of rock boundaries: An application of the Walsh transform to geophysical well log

analysis, *Geophysics*, **48**, 197–205.

Lanzerotti, L.J., Thomson, D.J., Meloni, A., Medford, L.V. and MacLennan, C.G., 1986. Electromagnetic study of the Atlantic continental margin using a section of transatlantic cable, *J. Geophys. Res.*, **91**, 7417–7427.

Larsen, J.C., 1975. Low frequency (0.1–6.0 c.p.d.) electromagnetic study of deep mantle electrical conductivity beneath the Hawaiian islands, *Geophys. J. R. astr. Soc.*, **43**, 17–46.

Larsen, J.C., 1977. Removal of local surface conductivity effects from low frequency mantle response curves, *Acta, Geodaet., Geophys. et Montanist. Acad Sci. Hung.*, **12**, 183–186.

Larsen, J.C., 1980. Electromagnetic response functions from interrupted and noisy data, *J. Geomag. Geoelect.*, **32**, Supp. I., 89–103.

Larsen, J.C., 1989. Transfer functions: smooth robust estimators by least squares and remote reference methods, *Geophys. J. Int.*, **99**, 645–664.

Lawson, C.L. and Hanson, R.J., 1974. *Solving Least Squares Problems*, Prentice-Hall, New Jersey.

Lee, M.K., 1986. A new gravity survey of the Lake District and three-dimensional model of the granite batholith, *J. Geol. Soc. Lond.*, **143**, 425–435.

Leeder, M.R., 1971. Initiation of the Northumberland Basin, *Geol. Mag.*, **108**, 511–516.

Leeder, M.R., 1974, Origin of the Northumberland Basin, *Scottish J. Geol.*, **10**, 283–296.

Leeder, M.R., 1976. Sedimentary facies and the origins of basin subsidence along the Northern margin of the supposed Hercynian ocean, *Tectnophysics*, **36**, 167–179.

Leeder, M.R., 1982. Upper Palaeozoic basins of the British Isles– Caledonide inheritance versus Hercynian plate margin processes, *J. Geol. Soc. Lond.*, *139*, 479–491.

Leeder, M.R., 1987. Tectonic and palaeogeographic models for Lower Carboniferous Europe, in *European Dinantian Environments*, pp1-20, eds. Miller, J., Adams, A.E. and Wright, V.P., J. Wiley and Sons, New York.

Leeder, M.R. and Strudwick, A.S., 1987. Delta-marine interactions: a discussion of sedimentary models for Yoredale-type cyclicity in the Dinantian of Northern England, in *European Dinantian Environments*, pp 115-130, eds. Miller, J., Adams, A.E. and Wright, V.P., J. Wiley and Sons, New York.

Leeder, M.R. and McMahon, A.H., 1988. Upper Carboniferous (Silesian) basin subsidence in Northern Britain, in *Sedimentation in a synorogenic basin complex*, pp 43-52, eds. Besly, B.M. and Kelling, G., Blackie, Glasgow.

Leeder, M.R., Fairhead, D., Lee, A., Stuart, G., Clemmey, A., El Haddahel, B. and Green, C., 1989. Sedimentary and tectonic evolution of the Northumberland basin, in *Role of tectonics In Devonian and Carboniferous sedimentation in the British Isles*, pp207-223, eds. Arthurton, R.S., Gutteridge, P. and Nolan, S.C., *Procs. Yorks. Geol. Soc. Occ. Publn.* 6.

Leggett, J.K., McKerrow, W.S. and Soper, N.J., 1983. A model for the crustal evolution of Southern Scotland, *Tectonics*, 2, 187-210.

Lennox, S.C. and Chadwick, M., 1977. *Mathematics for engineers and applied scientists*, 550pp, Heinemann, London.

Lienert, B.R., 1980. The effect of source field polarization on estimates of the magnetotelluric impedance tensor, *Geophysics*, 45, 1803-1812.

Lienert, B.R., Whitcomb, J.H., Philips, R.J., Reddy, I.K. and Taylor, R.A., 1980. Long term variations in magnetotelluric apparent resistivities observed near the San Andreas Fault in Southern California, *J. Geomag Geoelect.*, 32, 757-775.

Lines, L.R. and Treitel, S., 1984. Tutorial: A review of least squares inversion and its application to geophysical problems, *Geophysical Prospecting*, 32 159-186.

Lines, L.R., Schultz, A.K. and Treitel, S., 1988. Cooperative inversion of geophysical data, *Geophysics*, 53, 8-20.

Loewenthal, D., 1979. On the phase constraint of the MT impedance, *Geophysics*, **40**, 325-330.

Lovell, J.P.B, 1978. *The British Isles through geological time: A Northward drift*, 40pp, G. Allen and Unwin, London.

Madden, T.R., 1972. *Transmission systems and network analogies to geophysical forward and inverse problems*, Tech. Report, Dept. of Earth and Planetary Sciences, M.I.T.

Malergue, G., Aissa, J., Herisson, C. and Rainaud, J., 1986. Recent developments in the magnetotelluric prospecting method, *First Break*, **4**, 23-28.

Marquardt, D.W., 1963. An algorithm for least squares estimation of non-linear parameters, *J. Soc. Indust. Appl. Math.*, **11**, 431-438.

Marquardt, D.W., 1970. Generalized inverses, ridge regression, biased linear estimation and non-linear estimation, *Technometrics*, **12**, 591-612.

Matthews, D., 1986. Seismic reflections from the lower crust around Britain, in *The nature of the lower continental crust*, pp 11-22, eds. Dawson, J.B., Carswell, D.A., Hall, J. and Wedepohl, K.H.. Special publication of the Geological Society, **24**.

McGeary, S., Cheadle, M.J., Warner, M.R. and Blundell, D.J., 1987. Crustal structure of the continental shelf around Britain derived from BIRPS deep seismic profiling, in *Petroleum Geology of NW Europe*, pp 33-41, eds. Brooks, J. and Glennie, K., Graham and Trotman.

McKerrow, W.S., 1986. The tectonic setting of the Southern Uplands, in *Synthesis of the Caledonian rocks of Britain*, pp 207-220, eds. Fettes, D.J and Harris, A.L., Reidel, Dordecht.

McKerrow, W.S. and Cocks, L.R.M., 1986. Oceans, island arcs and olistostromes: the use of fossils in distinguishing sutures, terranes and environments around the Iapetus Ocean, *J. Geol. Soc. Lond.*, **143**, 185-191.

McKerrow, W.S. and Soper, N.J., 1989. The Iapetus Suture in the British Isles, *Geol. Mag.*, **126**, 1-8.

Meju, M. A., 1988. The deep electrical structure of the Great Glen Fault, Scotland, *Ph D. thesis*, University of Edinburgh.

Meju, M., 1989. The geoelectric structure across the northern Irish Caledonides, presented at *Deep geology and geophysics of Ireland and its continental margin*, University College, Galway, October 1989.

Menichetti, V. and Guillen, A., 1983. Simultaneous interactive magnetic and gravity inversion, *Geophys. Prosp.*, **31**, 929-944.

Menke, W., 1984. *Geophysical data analysis: Discrete inverse theory*, 266pp, Academic Press, Orlando.

Meyer, S.L., 1975. *Data analysis for scientists and engineers*, 513pp, Wiley, New York

Mosteller, F. and Tukey, J.W., 1977. *Data analysis and regression*, 588pp, Addison-Wesley, Reading, Mass.

Nichols, E.A., Morrison, H.F. and Clarke, J., 1988. Signals and noise in low-frequency geomagnetic fields, *J. Geophys. Res.*, **93**, 13743-13754.

Novak, M., 1981. A broadband magnetotelluric study in the North England high heat flow region, *Ph D. thesis*, University of Edinburgh, 162pp.

Oldenburg, D.W., 1988. Inversion of electromagnetic data: An overview of new techniques, presented at *IXth workshop on electromagnetic induction in the Earth and the Moon*, Sochi, USSR, October 1988.

O'Neill, D.J., 1975. Improved linear filter coefficients for application in apparent resistivity computations, *Bull. Aust. Soc. Explor. Geophys.*, **6**, 104-109.

Olhoeft, G.A., 1980. Electrical properties of rocks, in *Physical properties of rocks and minerals*, pp257-330, eds. Touloukian, Y.S., Judd, W.R. and Roy, R.F., McGraw-Hill, New York.

Olhoeft, G.A., 1981. Electrical properties of granite with implications for the lower crust, *J. Geophys. Res.*, **86**, 931-936.

Oristaglio, M.L. and Worthington, M.H., 1980. Inversion of surface and

borehole electromagnetic data for two dimensional electrical conductivity models, *Geophysical Prospecting*, 28, 633-657.

Orr, D., 1973. Magnetic pulsations within the magnetosphere - A review, *J. Atmos. Terr. Phys.*, 35, 1-50.

Palacky, G., 1987. Resistivity characteristics of geologic targets, in *Electromagnetic methods in applied geophysics - Theory, Vol. 1*, ed. M.N. Nabighian, pp52-130, S.E.G., Tulsa.

Parasnis D.S., 1982. *Principles of applied geophysics*, 275pp, Chapman and Hall, London.

Park, S.K., Orange, A.S. and Madden, T.R., 1983. Effects of three dimensional structure on magnetotelluric sounding curves, *Geophysics*, 48, 1402-1405.

Park, J. and Chave A.D., 1984. On the estimation of magnetotelluric response functions using the singular value decomposition, *Geophys. J. R. astr. Soc.*, 77, 683-709.

Parker, R.L., 1980. The inverse problem of electromagnetic induction: Existence and construction of solutions based on incomplete data, *J. Geophys. Res.*, 85, 4421-4428.

Parker, R.L., 1983. The magnetotelluric inverse problem, *Geophys. Surv.*, 6, 5-26.

Parker, R.L., and Whaler, K.A, 1981. Numerical methods for establishing solutions to the inverse problem of electromagnetic induction, *J. Geophys. Res.*, 86, 9574-9584.

Parkinson, W.D., 1983. *Introduction to Geomagnetism*, 433pp, Scottish Academic Press, Edinburgh.

Parkinson, W.D. and Hutton, V.R.S., 1989. The electrical conductivity of the Earth, in *Geomagnetism; Vol. 3*, pp 261-322, ed. Jacobs, J.A., Academic Press, London.

Patra, H.P. and Mallick, K., 1980. *Geosounding principles 2: Time varying geoelectric soundings*, Elsevier, Amsterdam.

Pedersen, L.B., 1977. Interpretation of potential field data: a generalized inverse approach, *Geophysical Prospecting*, **25**, 198–230.

Pedersen, L.B., 1979. Constrained inversion of potential field data, *Geophysical Prospecting*, **27**, 726–748.

Pedersen, L.B., 1982. The magnetotelluric impedance tensor – its random and bias errors, *Geophysical Prospecting*, **30**, 188–210.

Pedersen, L.B. and Svennekjaer, M., 1984. Extremal bias coupling in magnetotellurics, *Geophysics*, **49**, 1968–1978.

Petiau and Dupis 1980. Noise, temperature coefficient and long time stability of electrodes for telluric observations, *Geophysical Prospecting*, **28**, 792–804.

Petrick, W.R., Pelton, W.H. and Ward, S.H., 1977. Ridge regression inversion applied to crustal resistivity soundings from South Africa, *Geophysics*, **42**, 995–1005.

Philips, W.E.A., Stillman, C.J. and Murphy, T., 1976. A Caledonian plate tectonic model, *J. Geol. Soc. Lond.*, **132**, 579–609.

Poll, H.E., Weaver, J.T. and Jones, A.G., 1989. Calculations of voltages for magnetotelluric modelling of a region with near surface inhomogeneities, *Phys. Earth Planet Int.*, **53**, 287–297.

Porstendorfer, G., 1975. *Principles of magneto telluric prospecting*, Geoexplor. Monograph, Berlin.

Prieto, C., Perkins, C. and Berkman, E. 1985. Columbia River Basalts Plateau – An integrated approach to interpretation of basalt covered areas, *Geophysics*, **50**, 2709–2719.

Press, W.H., Flannery, B.P., Teukolsky, S.A. and Vetterling, W.T., 1986. *Numerical Recipes*, 818pp, Cambridge University Press, Cambridge.

Ranganayaki, R.P., 1984. The interpretive analysis of magnetotelluric data, *Geophysics*, **49**, 1730–1748.

Ridd, M.F., Walker, D.B. and Jones, J.M., 1970. A deep borehole at Harton on the margin of the Northumbrian Trough, *Procs. Yorks. Geol. Soc*, **38**, 75-103.

Raiche, A.P., Jupp, D.L.B., Rutter, H. and Vozoff, K., 1985. The joint use of coincident loop transient electromagnetic and Schlumberger sounding to resolve layered structures, *Geophysics*, **50**, 1618-1627.

Randall, B.A.O., 1985. Dolerite-pegmatites from the Whin Sill, near Barrasford, Northumberland, *Procs. Yorks. Geol. Soc*, **47**, 249-265.

Rankin, D., 1962. The magnetotelluric effect on a dyke, *Geophysics*, **27**, 606-676.

Rikitake, T., Sato, R. and Hagiwara, Y., 1987. *Applied mathematics for Earth scientists*, Terra Scientific Pulications, Tokyo.

Robson, D.A., (ed.), 1980. The geology of North East England, *Natural History Society of Northumbria Special Publication* 113pp.

Rokityansky, I.I., 1982. *Geoelectromagnetic investigations of the Earth's crust and mantle*, Springer Verlag, Berlin.

Rooney, D., 1976. Magnetotelluric measurements across the Kenyan Rift Valley, *Ph. D. thesis*, University of Edinburgh.

Rousseeuw, P.J., 1984. Least median of squares regression, *J. Am. Stat. Association*, **79**, 871-879.

Rousseeuw, P.J. and Leroy, A.M., 1987. *Robust regression and outlier detection*, Wiley, New York.

Roxis, N., 1984. The development of deep sounding technique using resistivity methods and an investigation of the associated interpretation problems, *Ph. D. thesis*, University of Leeds, 531pp.

Scott, J. and Colter, V.S., 1987. Geological aspects of current onshore Great Britain exploration plays, in *Petroleum Geology of NW Europe*, pp 95-107, eds. Brooks, J. and Glennie, K., Graham and Trotman.

Shankland, T.J. and Ander, M.C., 1983. Electrical conductivity, temperatures and fluids in the lower crust, *J. Geophys. Res.*, **88**, 9475-9484.

Silva, J.B.C. and Cutrim, A.O., 1989. A robust maximum likelihood method for gravity and magnetic interpretation, *Geoexploration*, **26**, 1-31.

Sims, W.E. Bostick Jr., F.X. and Smith, H.W., 1971. The estimation of magnetotelluric impedance tensor elements from measured data, *Geophysics*, **36**, 938-942.

Smith, J.T. and Booker, J.R., 1988. Magnetotelluric inversion for minimum structure, *Geophysics*, **53**, 1565-1576.

Soper, N.J., Webb, B.C. and Woodcock, N.H., 1987. Late Caledonian (Acadian) transpression in North-West England: timing, geometry and tectonic significance, *Procs. Yorks. Geol. Soc.*, **46**, 175-192.

Stanley, W.D., 1989. Comparison of geoelectrical-tectonic models for suture zones in the western U.S.A. and Eastern Europe: are black shales a possible source of high conductivities?, *Phys. Earth. Planet Int.*, **53**, 228-238.

Stillman, C.J., 1986. A comparison of Lower Palaeozoic volcanic rocks on either side of the Caledonian suture in the British Isles, in *Synthesis of the Caledonian rocks of the British Isles*, eds. D.J. Fettes and A.L. Harris, pp187-205, D. Reidel, Dordecht.

Stillman C.J. and Francis, E.H., 1979. Caledonide volcanism in Britain and Ireland, in *The Caledonides of the British Isles- Reviewed*, pp 557-578, eds. Harris, A.L., Holland, C.H. and Leake, B.E., *Geol. Soc. Lond. Spec. Publn.*, No. 8, Scottish Academic Press, Edinburgh.

Strangway, D.W., Redman, J.D. and Macklin, D., 1986. Shallow electrical sounding in the Precambrian crust of Canada and the United States, reprinted in *Magnetotelluric Methods*, ed. Vozoff, K., pp720-748, S.E.G., Tulsa.

Sule, P.O., 1985. A broadband magnetotelluric investigation in South East Scotland, *Ph. D thesis*, University of Edinburgh, 302pp.

Swift C.M. Jr.,1986. A magnetotelluric investigation of an electrical

conductivity anomaly in the South Western United States, in *Magnetotelluric Methods, Society of Exploration Geophysicists Reprint Series No. 5*, pp156-166, Ed. Vozoff, K., SEG, Tulsa.

Swinburn, P.M., 1975. The crustal structure of N. England, *Ph D. thesis*, University of Durham.

Talwani, M., Worzel, J.L. and Landisman, M., 1959. Rapid gravity computations for 2-D bodies with application to the Mendocino sub-marine fracture zone, *J. Geophys. Res.*, **64**, 49-59.

Tanner, J.G., 1967. An automated method of gravity interpretation, *Geophys. J. R. astr. Soc.*, **13**, 339-347.

Tarantola, A., 1987. *Inverse problem theory*, 613pp, Elsevier, Amsterdam.

Telford, W.M., Geldart, L.P., Sheriff, R.E. and Keys, D.A., 1976. *Applied Geophysics*, 860pp, Cambridge University Press, Cambridge.

Thayer, R.E., Bjornsson, A., Alvarez, L. and Hermance, J.F., 1981. Magma genesis and crustal spreading in the northern Neovolcanic zone of Iceland: Telluric - magnetotelluric constraints, *Geophys. J. R. astr. Soc.*, **65**, 423-442.

Thomson, D.J., 1977a. Spectrum estimation techniques for characterization and development of WT4 waveguide - I, *Bell. Tech. J.*, **56**, 1769-1813.

Thomson, D.J., 1977b. Spectrum estimation techniques for characterization and development of WT4 waveguide - II, *Bell. Tech. J.*, **56**, 1983-2005.

Thomson, D.J. and Chave, A.D., 1991. Jackknifed error estimates for spectra, coherences and transfer functions, (in press).

Thorpe, R.S. and MacDonald, R. 1985. Geochemical evidence for the emplacement of the Whin Sill complex of Northern England, *Geol. Mag.*, **4**, 389-396.

Tikhonov, A.N., 1986. On determining the electrical characteristics of the deep layers of the Earth's crust, reprinted in *Magnetotelluric Methods*, ed. Vozoff, K., pp2-3, S.E.G., Tulsa.

Travassos, J.M. and Beamish D., 1988. Magnetotelluric data processing- a case study, *Geophys. J.*, **93**, 377-391.

Trench, A. and Torsvick, T.H., 1991. A revised Palaeozoic apparent polar wander path for southern Britain (eastern Avalonia), *Geophys. J. Int.*, **104**, 227-233.

Tripp, A.C., Ward, S.H., Sill, W.R., Swift Jr., C.M. and Petrick, W.R., 1978. Electromagnetic and Schlumberger resistivity soundings in the Roosevelt Hot Springs KGRA, *Geophysics*, **43**, 1456-1469.

Trotter, F.M. and Hollingworth, S.E. 1928. The Alston Block, *Geological Magazine*, **65**, 433-448.

Twomey, S., 1977. *Introduction to the mathematics of inversion in remote sensing and indirect measurements, Developments in Geomathematics series No. 3*, 243pp, Elsevier, Amsterdam.

Tzanis, A. and Beamish D., 1989. A high-resolution spectral study of audiomagnetotelluric data and noise interactions. *Geophys. J.*, **97**, 557-572.

Van Hesswijk, M. and Fox, C.G., 1988. Iterative method and Fortran code for non-linear curve fitting, *Computers and Geosciences*, **14**, 489-503.

Vozoff, K., 1972. The magnetotelluric method in the exploration of sedimentary basins, *Geophysics*, **37**, 98-141.

Vozoff, K. (ed.), 1986. *Magnetotelluric Methods*, 763pp, S.E.G. publication, Tulsa.

Vozoff, K., and Jupp, D.L.B, 1975. Joint inversion of geophysical data, *Geophys. J. R. astr. Soc.*, **42**, 977-991.

Yassi, N.Y.D., 1983. Magnetic and gravity investigation in Northumberland Trough, N. E. England, *Ph D. thesis*, University of Newcastle - upon - Tyne.

Yee, E. and Paulson, K.V. 1988a. Concerning dispersion relations for the magnetotelluric impedance tensor, *Geophys. J.*, **95**, 549-559.

Yee, E. and Paulson, K.V., 1988b. Necessary and sufficient conditions for

the existence of a solution to the one-dimensional magnetotelluric inverse problem, *Geophys. J.*, **93**, 279-293.

Yee, E. and Paulson, K.V., 1989. The completion of the c-response function for utilization in exact inversion procedures, *Geophys. J.*, **97**, 41-50.

Yee, E. and Paulson, K.V., 1990. Reply to 'Comments on: Concerning dispersion relations for the magnetotelluric impedance tensor', by G.D. Egbert, *Geophys. J. Int.*, **102**, 9-13.

Wade, D.N. and Robinson, D. 1987. Diagenetic studies of Lower Carboniferous mudstones from the Alston Block and Northumberland Trough, Northern England, in *Petroleum Geology of North West Europe*, pp 245-250, eds. Brooks, J. and Glennie, K., Graham and Trotman, London.

Wait, J.R., 1971. *Electromagnetic probing in geophysics*, 391pp, Golem Press, Boulder, Colorado.

Wannamaker, P.E., Hohmann, G.W., and Ward, S.H., 1984. Magnetotelluric responses of three dimensional bodies in the layered Earth, *Geophysics*, **49**, 1517-1533.

Wannamaker, P.E., Stodt, J.A. and Rijo, L., 1985. *PW-2D - finite element program for the solution of two-dimensional resistivity structure: user documentation*, University of Utah Res. Inst. Rep., ESL-158.

Weidelt, P., 1972. The inverse problem of geomagnetic induction, *Z. Geophys.*, **38**, 257-289.

Weidelt, P., 1985. Construction of conductance bounds from magnetotelluric impedances, *J. Geophys.*, **57**, 191-206.

Weidelt, P., 1986. Inversion of two-dimensional conductivity structures, reprinted in *Magnetotelluric Methods*, pp430-439, ed. Vozoff, K., S.E.G., Tulsa.

Weisberg, S., 1980. *Applied linear regression*, 283pp, Wiley, New York.

Whelan, J., 1989 Electromagnetic induction studies in Ireland using the magnetotelluric method. *Ph. D. thesis*, University of Galway, Ireland.

Wiggins, R.A., 1972. The general linear inverse problem: implication of surface waves and free oscillations for Earth structure, *Rev. Geophys. Space Phys.*, **10**, 251–285.

Woolacott, D., 1923. On a boring at Roodymoor colliery, near Crook, Co. Durham, *Geological Magazine*, **60**, 50–62.

Zhang, P., Roberts, R.G. and Pedersen, L.B., 1987. Magnetotelluric strike rules, *Geophysics*, **52**, 267–278.

APPENDIX - A

CONSTRAINED ESTIMATION OF THE MAGNETOTELLURIC IMPEDANCE TENSOR

This paper was submitted to the Geophysical Journal International for publication in November 1989. The version presented here is now being re-submitted after revisions recommended by the referees.

CONSTRAINED ESTIMATION OF THE MAGNETOTELLURIC IMPEDANCE TENSOR

R.S. Parr and V.R.S. Hutton, *Department of Geology and Geophysics, University of Edinburgh, Mayfield Rd., Edinburgh, EH9 3JZ, UK.*

SUMMARY

Accurate frequency domain Earth response functions are essential for the correct interpretation of a magnetotelluric sounding, but noise contamination of the electromagnetic field observations can strongly influence the estimated electrical impedance. As a result, in recent years considerable attention has been paid to reducing these effects.

In this paper, we propose a practical method for the acquisition of a usable magnetotelluric response function even under conditions of severe noise contamination. The method uses the Fourier amplitudes of the observed electromagnetic field at a single site, to estimate the electrical impedance by least squares regression. A number of assumptions and constraining features are then imposed upon the overall form of the response function. The resulting enhanced 'idealized response function' is required to be smoothly varying with frequency, consistent with the dispersion relationships and also with any other assumptions concerning the dimensionality of the subsurface structure.

The effects of observational inadequacy due to noise contamination can then be reduced by using this response function to constrain a re-evaluation of the original impedance regression problem. The final impedance estimates are generally more accurate and less ambiguous if the underlying assumptions are valid. Thus the final response function is more readily interpretable. The proposed approach is demonstrated on both real and synthetic examples.

Finally a number of suggestions for the future adaptation of the basic technique by using other methods for the initial impedance estimation and suggestions for potential constraints are discussed.

Keywords: Magnetotelluric impedance, constrained robust least squares

1. INTRODUCTION

The aim of the magnetotelluric method is the measurement of accurate Earth response functions which will hopefully contain useful information concerning the sub-surface rock resistivity distribution. When certain source field assumptions are valid, one common Earth response function is determined by computing the Earth's electrical impedance as a function of the frequency of naturally occurring electromagnetic field variations. It is widely assumed that the Fourier transformed field observations of the electric (E(f)) and magnetic (H(f)) field, from two orthogonal directions (x: north, y: east), are linearly related through the rank 2 impedance tensor (Z(f)), by:

$$E(f) = H(f) \cdot Z(f) \qquad (1)$$

(e.g. Vozoff 1972, Hermance 1973)

In real situations, the impedance cannot be determined to arbitrarily high accuracy due to the presence of deficient (e.g. polarized) natural electromagnetic field variations, or because of the many different noise contaminants which are superimposed on them. The latter may not only be due to errors inherent in the data acquisition, but also from the presence of inhomogeneous electromagnetic fields. The overall noise structure is invariably a mixture of incoherent and coherent noise between the four different electromagnetic quantities which are recorded.

Although some errors are always present within the data collected, the signal to noise ratio can change substantially with frequency and time. It is therefore common practice to collect the field measurements over an extended time interval with the subsequent aim of identifying the "best" sections or 'events'. This may involve visual inspection and selection of each time series section, or by retaining those Fourier spectral amplitudes which give rise to the highest level of predicted coherence (e.g. Travassos and Beamish 1988). Both these data selection methods suffer drawbacks; the former can be time consuming and is often difficult and the latter can preferentially select sections of data which are contaminated by coherent noise.

The impedance is then usually estimated at each frequency by performing

least squares regression on the remainder of the frequency band and/or section averaged observational subset. As reviewed in the next section, several different techniques exist for estimating the impedance, all giving accurate results in the presence of specific types of noise. The aim of the constrained method, proposed in this paper, is the acquisition of a usable response function in the presence of a typical assortment of noise sources with variable levels of contamination over a broad frequency range. In principle this is achieved by using information extrapolated from the better defined regions of the response function, to improve the noisy impedance estimates. The basic method used in this study can be summarized as follows (see also fig. 1):

The first stage involves the calculation of a reasonably accurate initial estimate of the response function. For unreferenced magnetotelluric field data a robust hybrid of the singular value decomposition method is shown to produce impedance estimates that are sometimes less biased by noise than those obtained by more conventional least squares methods. However in many situations, both the apparent resistivity and phase curves, derived from amplitude and argument of the complex impedance, are distorted from the anticipated smoothly varying functions of frequency. The scatter is particularly obvious at those frequencies which are contaminated by noise coherent between the electric and magnetic fields.

The second stage involves calculation of an 'idealized response function' by imposing a number of physical constraints and assumptions upon the response function acquired from the first stage. In particular, the resulting response function is constrained to 1) be smoothly varying with frequency, 2) be consistent with the theoretically predicted dispersion relationships between the apparent resistivity and phase and, whenever applicable, 3) obey certain restrictions pertaining to the dimensionality of the geoelectric structure (section 3).

Finally, (section 4) the idealized response function is used as a source of quasi-independent impedance information to constrain a re-evaluation of the first stage impedance estimates. This re-evaluation does not appreciably change the well determined impedance estimates, but leads to significantly different results at those frequencies contaminated by noise or polarized

Figure 1: Summary flow diagram of the proposed method for the constrained estimation of the magnetotelluric impedance tensor.

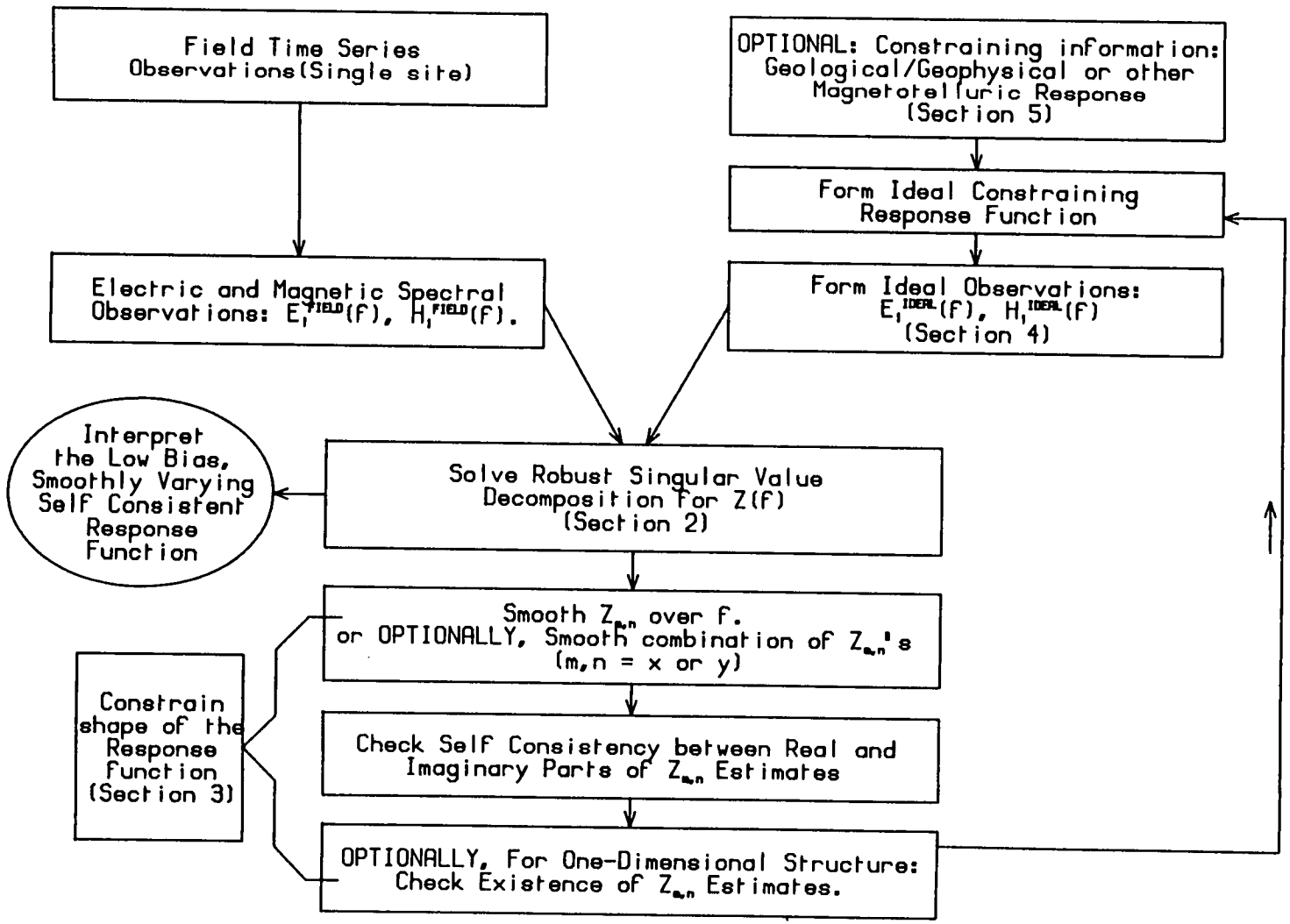
Field Time Series Observations(Single site)
OPTIONAL: Constraining information: Geological/Geophysical or other Magnetotelluric Response (Section 5)
Form Ideal Constraining Response Function
Electric and Magnetic Spectral Observations: $E_i^{FIELD}(f)$, $H_i^{FIELD}(f)$.
Form Ideal Observations: $E_i^{IDEAL}(f)$, $H_i^{IDEAL}(f)$ (Section 4)
Interpret the Low Bias, Smoothly Varying Self Consistent Response Function
Solve Robust Singular Value Decomposition for Z(f) (Section 2)
Smooth $Z_{m,n}$ over f. or OPTIONALLY, Smooth combination of $Z_{m,n}$'s (m,n = x or y)
Constrain shape of the Response Function (Section 3)
Check Self Consistency between Real and Imaginary Parts of $Z_{m,n}$ Estimates
OPTIONALLY, For One-Dimensional Structure: Check Existence of $Z_{m,n}$ Estimates.

signals.

The latter two stages are iteratively repeated until there is little change in the re-evaluated response function. The final response function is less influenced by noise, has smaller uncertainties, fewer ambiguities and consequently can be more readily inverted to Earth models.

Section 5 provides a discussion on the constraining method and a number of suggestions for possible modifications and extensions.

2. LEAST SQUARES ESTIMATION OF THE MAGNETOTELLURIC IMPEDANCE

On the assumption that the magnetic field is noise free and the errors in the electric field are random and drawn from a preferably Gaussian distribution with zero mean and uniform variance (e.g. Egbert and Booker 1986), then a typical least squares solution of eq. 1 for the impedance is given by:

$$Z(f) = (E(f).\ H(f)^H)\ .\ (\ H(f)\ .\ H(f)^H))^{-1} \qquad (2)$$

(e.g. Sims, Bostick and Smith 1971, Vozoff 1972)

where $H(f)^H$ is the Hermitian conjugate (complex conjugate transpose) of the Fourier transformed magnetic field observations.

The error assumptions are seldom completely valid.

For example, recent attention has been focused on the affects on parameter estimates of observational non-Gaussian random errors or 'outliers'. Many authors have described robust parameter estimation methods which are insensitive to a small number of these outliers (e.g. Huber 1981, Rousseeuw and Leroy 1987). Specifically, robust M-regression estimates have been applied to electromagnetic response estimation (Egbert and Booker 1986, Chave *et al.* 1987, Chave and Thomson 1989). This is a particularly easily implemented method which down-weights deviant observations prior to least squares regression.

In situations of severe noise contamination, or polarized signals, it may well be that there is insufficient *independent* information to resolve the 4 complex valued elements of the impedance tensor properly (c.f. Sims, Bostick and Smith 1971). Although a few thousand estimates of the Fourier amplitudes may have been collected, the least squares problem will remain underdetermined. In certain situations a linear combination of the impedance parameters may be resolvable, but to determine the values of the impedance tensor separately, more observations with less noise contamination must be collected. At certain locations and at specific frequencies, the signal to noise ratio may be so low that collecting and selecting these extra observations would be a time consuming and laborious task. As a result, the merits of undertaking constrained regression using the impedance estimated at less

contaminated frequencies, is more fully discussed later (section 4).

A final limitation of least squares is its inability to reduce noise contamination on the carrier observables (magnetic field observations in eq. 1). The resulting bias introduced into the apparent resistivity curve is well documented (e.g. Sims *et al.* 1971, Swift 1986, Pedersen 1982, Pedersen and Svenekjar 1984). In the case of eq. 2, it has been shown that generally the bias is downwards due to random magnetic field noise. Alternatively, eqn. 1 can be solved to obtain estimates which are biased upwards due to electric field noise.

A significant advance was proposed by Goubau, Gamble and Clarke (1978) and Gamble *et al* (1979a) who demonstrated that noise bias could often be removed by application of the remote reference technique. This requires simultaneous recording of electromagnetic time series data at two sites, sufficiently distant one from the other, that the noise sources affecting data at each site are uncorrelated (Goubau *et al* 1984). The remote reference observational procedure is now a relatively widely used method for which a robust data processing technique has recently been proposed (Chave and Thomson 1989).

The response functions estimated using a remote reference are invariably less biased, but the method suffers from a few drawbacks. It is more costly in field equipment and personnel and more inefficient because more observations are required to reduce the additional random error introduced by the reference observations. Above all, biasing may still occur if there is insufficient separation between the measuring and reference sites (Kröger *et al* 1983, Goubau *et al* 1984, Jones *et al.* 1989) or if there are influential outliers (leverage points) in the carrier observations (e.g. Rousseeuw and Leroy 1987, Chave and Thomson 1989).

A single site method for removing uncorrelated noise sources from all the observable quantities simultaneously was proposed by Jupp (1978). It utilizes a Singular Value Decomposition (S.V.D.) (e.g. Lanczos 1961, Lines and Treitel 1984) or factorization of the data matrix **A** =(Hx(f), Hy(f), Ex(f), Ey(f)) to determine a correlating signal matrix **B**, which minimizes the Euclidean norm of $||\ \mathbf{A}-\mathbf{B}\ ||$ and a residual error matrix **E** . The impedance at a frequency f, can

then be estimated from the 'noiseless' matrix B. Alternatively, these estimates can be calculated directly from the equations giving the linear dependencies between the columns of A, corresponding to the null eigenvalues (Park and Chave 1984).

The S.V.D. method has been used during earlier studies with mixed success. Although Chave *et al.* (1981) have found that the impedance estimates often lie between the more usual least squares up and downwards biased results, Lienert (1980) and Lienert *et al.* (1980) have suggested that the apparent resistivity response function can still be strongly biased. In this paper, a modified form of this S.V.D. method (described in the appendix) is used to gain reasonably accurate initial estimates of the impedance. These provide a starting point for the subsequently applied constraints.

SYNTHETIC RESPONSE FUNCTION EXAMPLE

A synthetic example of the application of two different least squares impedance estimation procedures is shown in fig. 2. Here synthetic observations are generated from the response functions of a two layer model, over the frequency range from 0.01 to 200Hz. (the continuous line). A set of electric field observations are then computed from real magnetic Fourier spectral observations by using equation 1 (c.f. Goubau *et al.* 1978).

All four components of the electromagnetic observations are perturbed by contaminants drawn from a complex noise model. Random errors are added over the complete frequency spectrum of interest. These are drawn primarily from a Gaussian distribution but also with a fraction of gross outliers present. In addition, over certain narrow frequency bands (indicated by 'C' in fig. 2), coherent noise is simulated between either the two magnetic or the electric and magnetic components.

The overall signal to noise ratio is variable with frequency but fairly low, especially for frequencies less than 2 Hz. The resulting spectrum corresponds to that of typical observations from a noisy site in the United Kingdom.

The response function shown in fig. 2a is obtained by adapting a robust remote reference impedance estimation program (RRRMT; Chave and Thomson

Figure 2: The magnetotelluric response of a one dimensional, two layer synthetic model (the continuous line) for the frequency range 0.01 to 200 Hz. All the electromagnetic observations derived from this model have been perturbed primarily by random incoherent noise, but over narrow frequency bands (indicated by "C"), coherent noise has additionally been simulated. The resulting spectrum corresponds to typical observations for a noisy site in the United Kingdom. Displayed are the apparent resistivity (top) and phase (bottom) estimates from the 2 orthogonal, unrotated directions resulting from: (a) the modified Chave and Thomson (1989) method of single site, robust le· squares, shown by up and down pointing triangles for the respective b. estimates, (b) the robust singular value decomposition method describeo this paper.

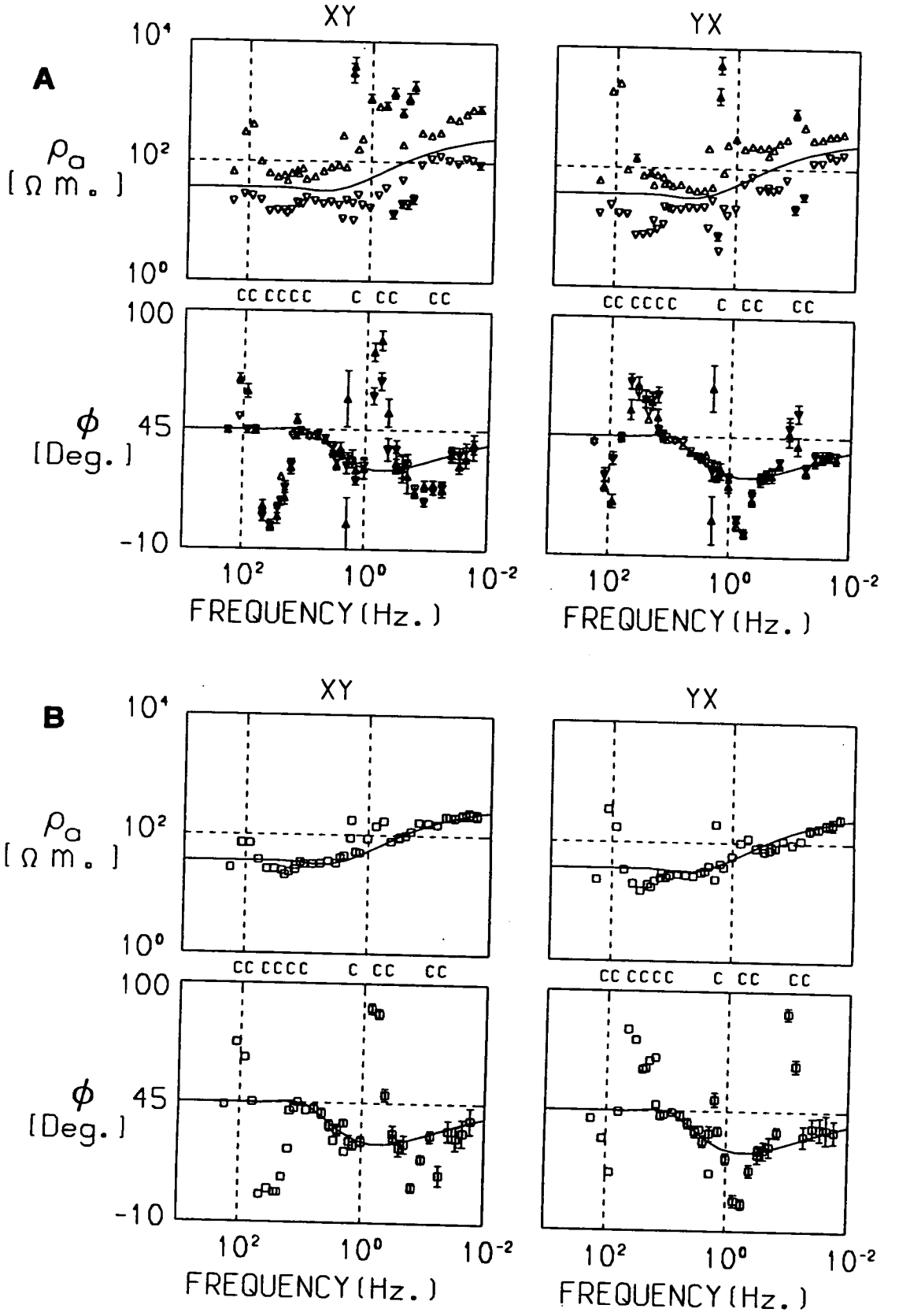
A
XY
YX
10^4
10^2
10^0
ρ_a
[Ω m.]
CC CCCC C CC CC
100
45
-10
ϕ
[Deg.]
10^2
10^0
10^{-2}
FREQUENCY (Hz.)
B
XY
YX
10^4
10^2
10^0
ρ_a
[Ω m.]
CC CCCC C CC CC
100
45
-10
ϕ
[Deg.]
10^2
10^0
10^{-2}
FREQUENCY (Hz.)

1989) for use with these single site measurements. The upwards and downwards biased estimates are displayed (up and down pointing triangles) in the two orthogonal, unrotated directions. The apparent resistivity response function is shown to be strongly biased due to the presence of incoherent noise on the magnetic field observations and the coherent noise between the electric and magnetic field. This overall level of bias is approximately the amount predicted by Swift (1986) for a one dimensional model with random incoherent noise. As expected the phase is largely unaffected by biasing except where coherent noise is present (Boehl, Bostick and Smith 1977, Clay and Hinich 1981).

Remotely referenced observations could have reduced the major part of the bias due to incoherent noise and possibly also the remaining coherent noise bias. In spite of this, small jacknife error estimates (Chave and Thomson 1989) reflect the very low random error which resulted from the large number of observations used.

The application of the robust singular value decomposition method to the same data set is shown in fig. 2b. This gives a resistivity response function which is in relatively good agreement with that computed for the Earth model considered. There is little significant biasing of the apparent resistivity estimates at any but the frequencies contaminated by coherent noise, whilst the phase has been as well determined as by use of the robust least squares method.

As far as this study is concerned, the most significant feature is that the second method more accurately determines the apparent resistivity and in general, without excessive bias. This is particularly important for the constraints applied to the response function. These are discussed in the next section.

3. MAGNETOTELLURIC CONSTRAINTS

Based on the initial estimates of the impedance acquired over a range of frequencies, a number of desirable and physically realistic constraints can now be applied to form the "idealized response function".

SMOOTHNESS

As a result of the filtering effect of the electrically conducting Earth upon the electromagnetic field variations, the magnetotelluric method is unable to resolve fine structures. Consequently, an ideal response function should be a smoothly varying function of frequency. The presence of any random scatter is likely to be the result of noise contamination.

The first constraint therefore involves minimizing the difference between adjacent frequency domain impedance estimates. Around each impedance estimate in turn, the coefficients are sought for a low order polynomial which approximately reproduces the impedance observed at a small number of surrounding frequencies. At the central frequency, the coefficients are then used to calculate an interpolated estimate of the impedance, independent of that which is actually observed. After the entire process is repeated for all of the frequencies of interest, the first stage ideal response function can be constructed from the individual interpolated impedances. This effectively low pass filters the response function, removes isolated biased impedance estimates and smoothes out any broader band inconsistencies.

This particular form of 'local smoothing' was developed to overcome a few of the difficulties which had been encountered by other authors (Larsen 1975,1980, Fischer and Schnegg 1980, Hobbs 1982) who had attempted to find the most appropriate order of polynomial which would reproduce the entire non-polynomial response function (Parker 1983, Yee and Paulson 1989). Such methods consequently lost the important fine structure within the response function. This is not considered to be a serious problem in this study, as the particular polynomial fitting and smoothing method used only interpolates across a short segment of the response function at any one time. In order to retain the three dimensional information the smoothing procedure is, under normal levels of noise contamination, repeated for all 4 components of the

impedance tensor separately.

DIMENSIONALITY

Although the real Earth is three dimensional, interpretation of the magnetotelluric data is frequently performed upon one or two dimensional models which approximately reproduce the response function. Therefore in simple geoelectric environments theoretical inter-relationships between the elements of the impedance tensor can be utilized. This constitutes the second constraint.

If, for example, the geoelectric structure is assumed to be two-dimensional, the diagonal elements of the impedance tensor should take the value Zxx(f) = -Zyy(f), regardless of the orientation of the measuring axes (Vozoff 1972). Thus if a smoothing polynomial is fitted to both Zxx(f) and (-Zyy(f)) simultaneously, the data redundancy which is present in the impedance tensor can be exploited. Since twice as much information is then used to find the most appropriate values for these two tensor elements jointly, the resultant may be less strongly affected by noise bias than the individual from which it was formed. If however, an approximately one-dimensional structure is present, the idealized response function may be less distorted if one of the average impedances (e.g. Berdichevsky *et al.* 1980, Ranganayaki 1984, Ingham 1988) is smoothed and used to represent the off-diagonal tensor elements (Zxy(f),Zyx(f)), whilst both of the diagonal elements (Zxx(f), Zyy(f)) are set to zero.

DISPERSION RELATIONS

The real and imaginary parts of the impedance, or equivalently, the apparent resistivity and phase are not independent, but linked through integral relationships known as dispersion relations, or Hilbert transforms (Weidelt 1972, Boehl *et al.* 1977, Jones 1980,1982, Rokityansky 1982, Fischer *et al.* 1981). These dispersion relations were therefore used to provide a consistency check between the smoothed, idealized apparent resistivity and phase responses. The particular method used here for evaluating these equations, follows that described by Fischer and Schnegg (1980) for one dimensional or two dimensional structures rotated to their major and minor axes (see Appendix for details). Yee and Paulson (1988a) have suggested that the approach for three

dimensional dispersion relations is not significantly different.

On the assumption that the true noiseless response function is most likely to lie between the limiting cases suggested by the phase and the apparent resistivity curves separately, a compromise between them is taken to represent the idealized response. Firstly, at each frequency in turn, phase estimates are computed from the derivative of the apparent resistivity. Secondly, the mean of the phase estimates (i.e. the observed and computed) is taken to be the best representation of the response function. The difference between these 2 estimates of the phase are considered to reflect the uncertainty inherent in the idealized response function. Finally, it is possible to calculate a consistent estimate for the apparent resistivity from the compromise phase value. In practice, this step was seldom undertaken since it was found that the resulting apparent resistivity estimates were grossly in error unless the phase had been accurately determined over the whole frequency spectrum. The apparent resistivity used to form the idealized response function was therefore a smoothed version of the one which had been observed.

EXISTENCE

Under the assumption of a truly one dimensional data set, a final constraint can be imposed. A number of authors have described the conditions upon the response function for the existence of an appropriate conductivity-depth profile (Parker 1980, Parker and Whaler 1981, Yee and Paulson 1988b). In particular Parker (1983) has shown that the construction of a D^+ model is a necessary and sufficient condition. In this study, response functions assumed to be one dimensional are fitted by a D^+ modelling routine. If the resulting model has a χ^2 misfit less than a tolerable threshold (Parker 1983, Jady, Paterson and Whaler 1983) then all the estimates are acceptable for the idealized response. However, if the misfit is above the threshold the few impedance estimates which contributed most to the excess misfit are rejected on the assumption that they have higher dimensional characteristics resulting from noise contamination. The D^+ routine is then applied again and the whole procedure iteratively repeated until the misfit reached the threshold.

A SYNTHETIC EXAMPLE OF THE APPLICATION OF THE CONSTRAINTS

The application of the constraining procedures can be visualised by consideration of the synthetic example which was described earlier. In fig. 3a the rotationally invariant 'effective' impedance has been smoothed. On average, the apparent resistivity and phase estimates are both closer to the input model than the initial responses shown in fig. 2b. The robust nature of the smoothing scheme has ensured that any sudden variations from the smooth profile are largely rejected. There are some residual effects due to the high concentration of noise around 1Hz. and more significantly, the coherent noise above 10Hz. These are both partially alleviated at a later stage.

Figure 3b, shows the response function obtained after it has been checked using the dispersion relations (Fischer and Schnegg 1980) and the existence criteria (Parker 1983). Although the apparent resistivity curves are slightly smoother than those shown in fig. 3a, the adopted dispersion relation has left their values otherwise unchanged. In contrast, the phase response function now represents a compromise between the smoothed phase curve shown in fig. 3a and that which has been predicted by the apparent resistivity. The estimated errors reflect the size of the difference between these two extremes. The response function (fig. 3b) has been checked by applying the D^+ modelling routine and the impedance estimates at two frequencies (0.42 and 0.56 Hz.) rejected before the response function could be properly reproduced. These impedance estimates corresponded to frequencies which had demonstrated a large deviation from the input model and small calculated error.

Although this idealized response (fig. 3b) can be more readily interpreted than the original function (fig. 2b), the former may be strongly influenced by a few exceptionally noisy impedance estimates. Furthermore, it does not necessarily contain any new or extra information which was not already contained in the original function. Thus the authors prefer to use the idealized response as a quasi-independent source of impedance estimates to constrain a re-evaluation of the initial regression problem. A simple method of achieving this is described in the next section.

Figure 3: The magnetotelluric response after the application of constraining features on the initial, robust singular value decomposition estimate (Figure 2b) by: (a) smoothing the rotationally invariant impedance and (b) the subsequent application of the dispersion relation consistency check. Finally, on the basis of the conditions for the existence of a one-dimensional profile, the impedance at each of two frequencies has been rejected.

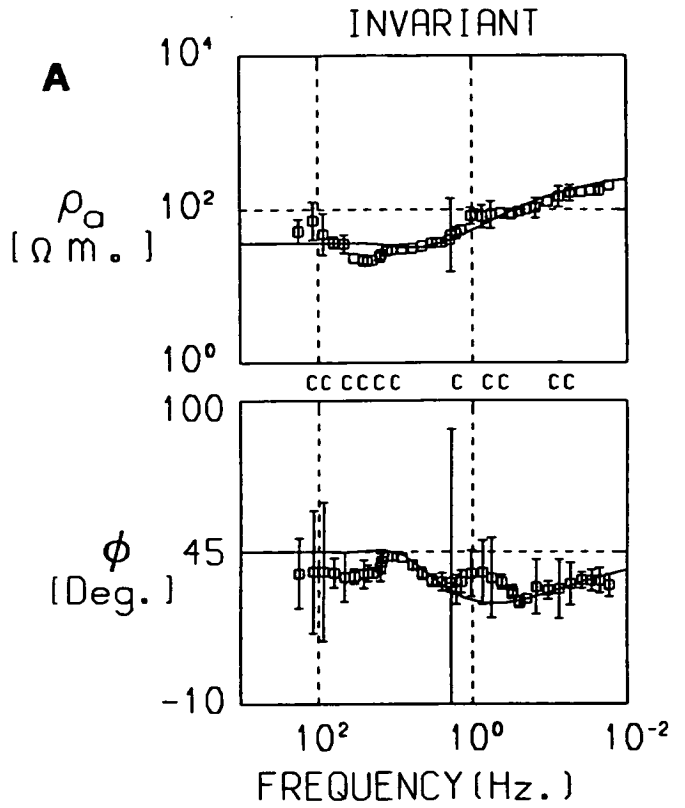
INVARIANT
A
10^4
ρ_a
[Ω m.]
10^2
10^0
cc cccc c cc cc
100
ϕ
[Deg.]
45
-10
10^2
10^0
10^{-2}
FREQUENCY (Hz.)

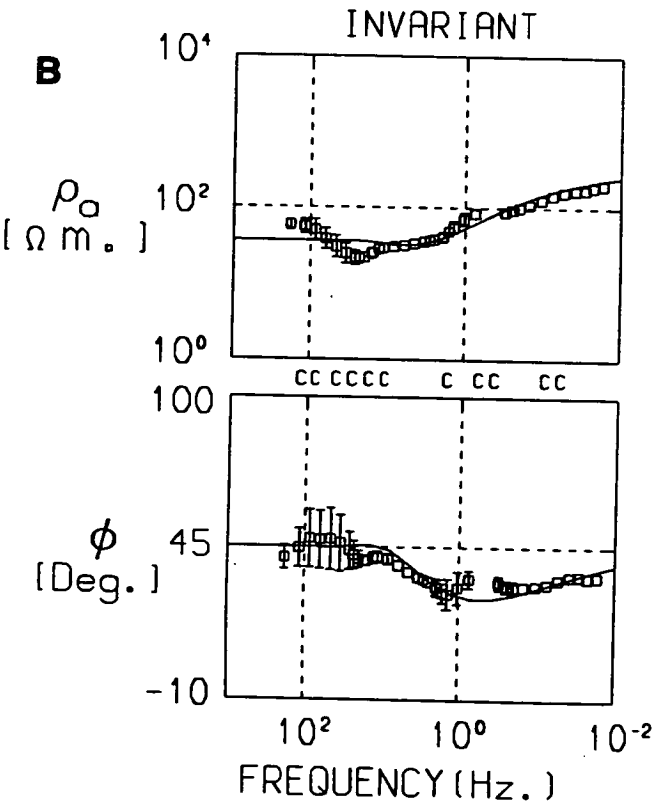
INVARIANT
B
10^4
ρ_a
[Ω m.]
10^2
10^0
cc cccc c cc cc
100
ϕ
[Deg.]
45
-10
10^2
10^0
10^{-2}
FREQUENCY (Hz.)

4. CONSTRAINED REGRESSION

Constrained parameter regression is becoming increasingly common in different branches of geophysics. In many parameter estimation situations, some 'a priori' information about the data set or likely parameter values can be incorporated to improve the overall accuracy and reduce the range of possible solutions. Geological and/or geophysical evidence often supports a certain range of parameter values more strongly than all other possible values which could fit the observations. Examples of this method are often found when a variety of geophysical observations are inverted to real Earth parameters (e.g. Claerbout 1976, Pedersen 1979, Chyba 1983, Meju 1988).

Since each of the impedance estimates in the idealized response function is primarily determined from the impedance observed at surrounding frequencies, this is considered to be a quasi-independent source of information. As such it is then used to constrain a re-evaluation of the initial impedance estimates.

Constrained regression is implemented by applying a set of weak constraints (Menke 1984) to the standard magnetotelluric impedance estimation procedure. These weak constraints can be considered to be synthetic 'ideal observations' computed from the product of the idealized response function and the real magnetic field observations ($H(f)^{IDEAL} = H(f)^{FIELD}$). Coherent source field effects between the 2 orthogonal components of the magnetic field are removed by the addition of some random variations to $Hx(f)^{IDEAL}$ and $Hy(f)^{IDEAL}$ independently. To prevent the estimated impedance being constrained to be identical to that given by the idealized response function, impedance error information is also factored in. This is achieved by perturbing the idealized impedance tensor elements by random numbers drawn from a Gaussian distribution with mean zero and standard deviation equal to the estimated error. The ideal electric field observations ($E(f)^{IDEAL}$) are then calculated from $H(f)^{IDEAL}$ and the perturbed impedance estimates by using eq. 1.

In order to bias the re-evaluation of the impedance, these ideal observations are augmented directly onto to the real data matrix and the joint least squares problem solved:

$$\begin{vmatrix} E(f)^{FIELD} \\ \hline \beta.E(f)^{IDEAL} \end{vmatrix} = \begin{vmatrix} H(f)^{FIELD} \\ \hline \beta.H(f)^{IDEAL} \end{vmatrix} . Z(f) \qquad (3)$$

where β is a scaling factor for the relative importance of the true observations and the set of ideal observations. This is usually set at a value around 1.

Depending upon which combination of constraints was applied to the idealized response function, the addition of these extra 'observations', could result in some of the following improvements:

1. Stabilisation of the robust singular value decomposition method by increasing the eigenvalue separation.
2. More accurate initial parameter estimates and therefore a more rapid elimination of true outliers.
3. Higher parameter resolution, particularly at frequencies with insufficient independent observations.
4. Reduction of parameter uncertainties.
5. Suppression of higher dimensional characteristics.
6. Reduction of coherent noise biasing.
7. Resistance to a greater degree of noise contamination.

Consider the effect of constrained regression upon the synthetic example presented in figs. 2 and 3. Figure 4 shows that the resultant apparent resistivity and phase response functions derived from a re-evaluation of the impedance estimates constrained by the extra 'ideal observations' is significantly more accurate than its initial and unconstrained counterpart shown in fig. 2. The increased consistency in the constrained response function should also aid its later modelling and interpretation.

In principle, the whole procedure can be repeated a number of times (fig. 1). The constrained response function can itself be further constrained by the methods described in section 3. This then allows a further re-application of the constrained regression technique with an increased scaling factor β (eq.

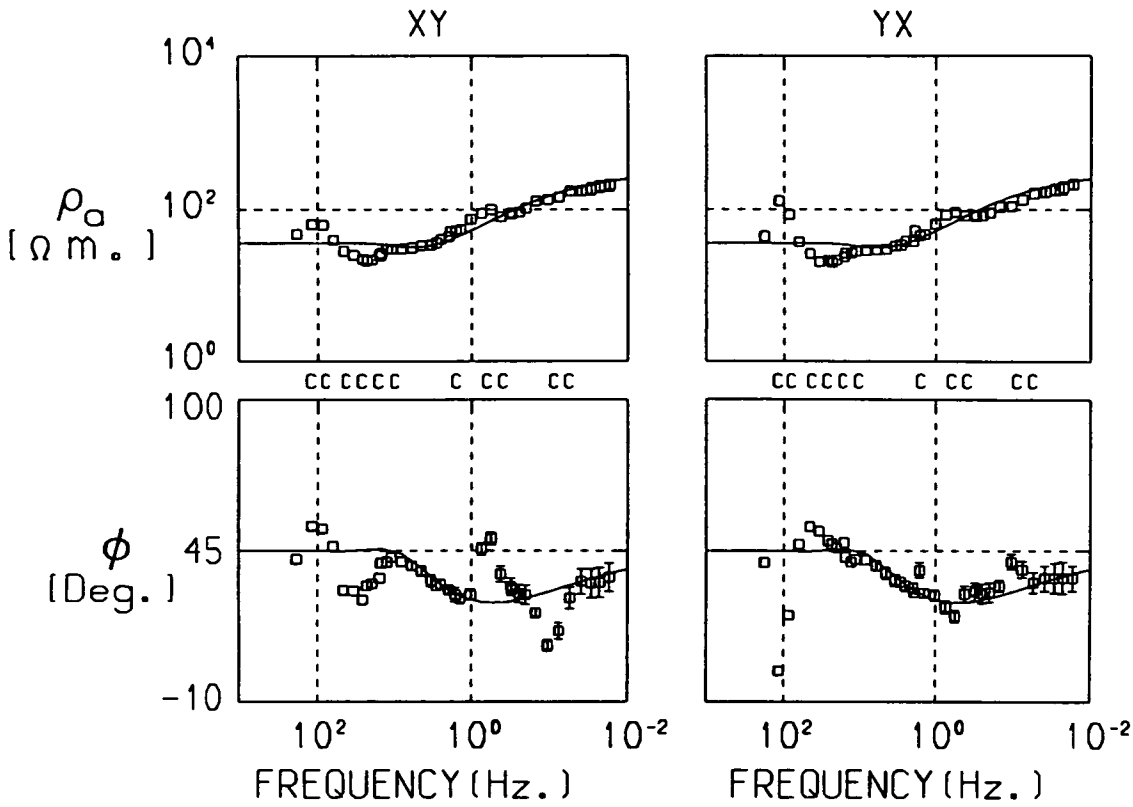

Figure 4 The magnetotelluric response after a re-evaluation of the initial regression problem, but constrained by the idealized response function (Figure 3b).

4) reflecting the increased confidence in the constrained compared to the original response.

REAL EXAMPLE OF CONSTRAINED IMPEDANCE ESTIMATION

A second example of the proposed methods is taken from a real sounding at a particularly noisy site in Northumberland, Northern England (National Grid coordinates NY801554). Figure 5a exhibits the upwards and downwards biased impedance estimates derived from the single site, robust least squares program used earlier. Apart from a narrow frequency band around 30Hz., the response is very strongly biased, particularly in the XY direction. Although preliminary digital notch filtering of the electromagnetic time series observations had been performed, there remains evidence of coherent noise contamination at the mains power line frequency and its harmonics (greater than 50Hz.). The phase estimates appear to be consistent in both directions in the middle of the frequency range (0.4–40Hz.). Normally careful observational screening would be required to produce a usable response function from these observations.

The robust S.V.D. method described in this paper provided the response function shown in fig. 5b. Although there is some slight scatter in the individual estimates, the gross features of the apparent resistivity curves are immediately evident. The phase estimated by this method is very similar to that obtained by the more conventional method (shown in fig. 5a). As might be expected, both of the methods give identical apparent resistivity and phase response functions at those frequencies where high quality magnetotelluric observations have been collected (around 30 Hz.).

In this instance, the constraints applied to the S.V.D. estimated response function are evaluated for the slightly more general situation in which the smoothness and dispersion constraints are carried out independently on the major and minor axes of the rotated impedance tensor. In order that noise present in the diagonal elements of the tensor could be suppressed, the magnitude of the corresponding values in the idealized response function are suppressed. The idealized response function for this example is shown in fig. 5c.

Figure 5 The magnetotelluric response estimated from a real set of very noisy observations by: (a) the modified Chave and Thomson (1989) method, (b) the robust singular value decomposition method, (c) the application of constraining features to the response function shown in Figure 5b, (d) a re-evaluation of (5b) constrained by the response in (5c).

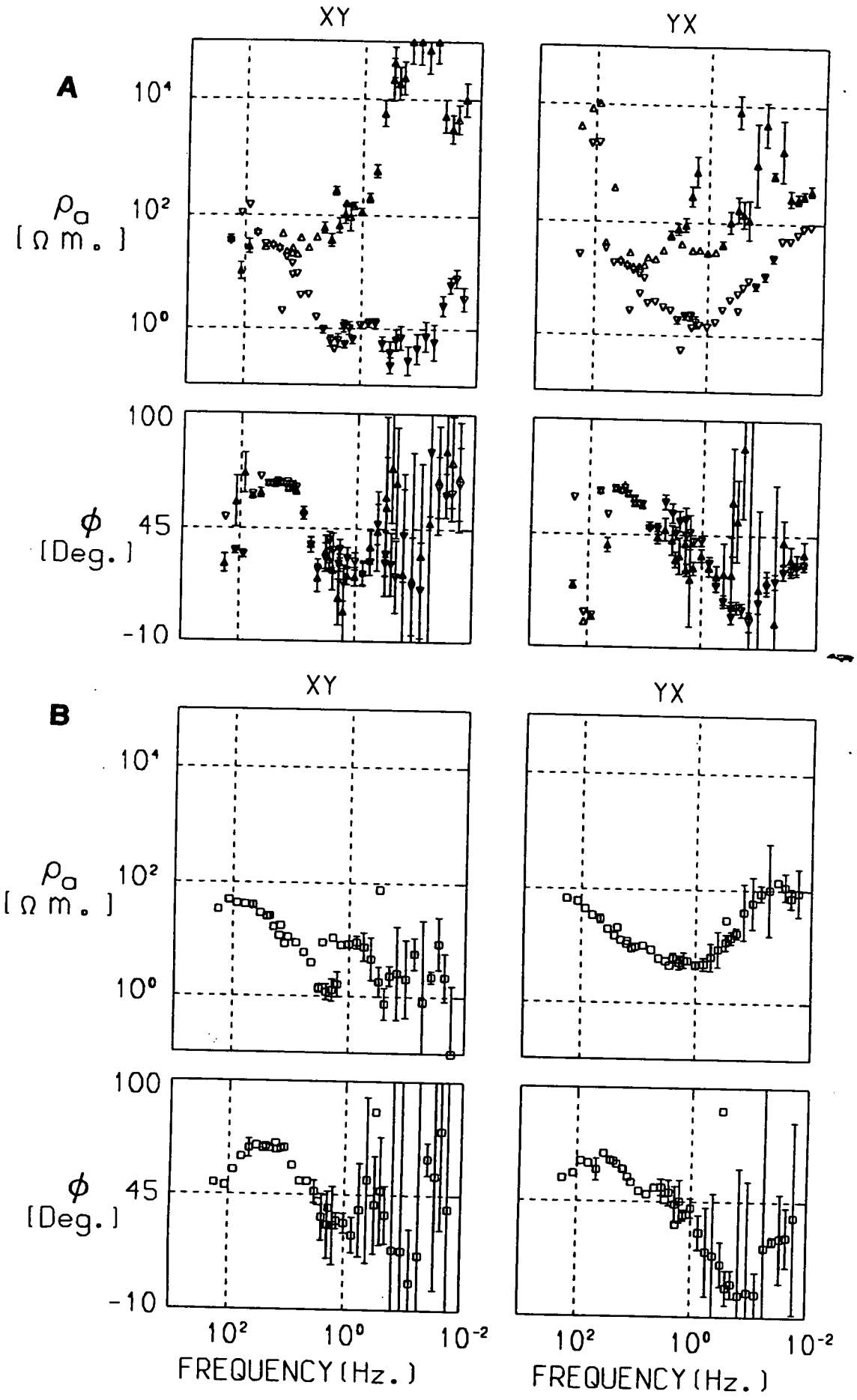
XY
YX
A
10^4
10^2
10^0
ρ_a
[Ω m.]
100
45
-10
ϕ
[Deg.]
B
XY
YX
10^4
10^2
10^0
ρ_a
[Ω m.]
100
45
-10
ϕ
[Deg.]
10^2
10^0
10^{-2}
FREQUENCY (Hz.)
10^2
10^0
10^{-2}
FREQUENCY (Hz.)

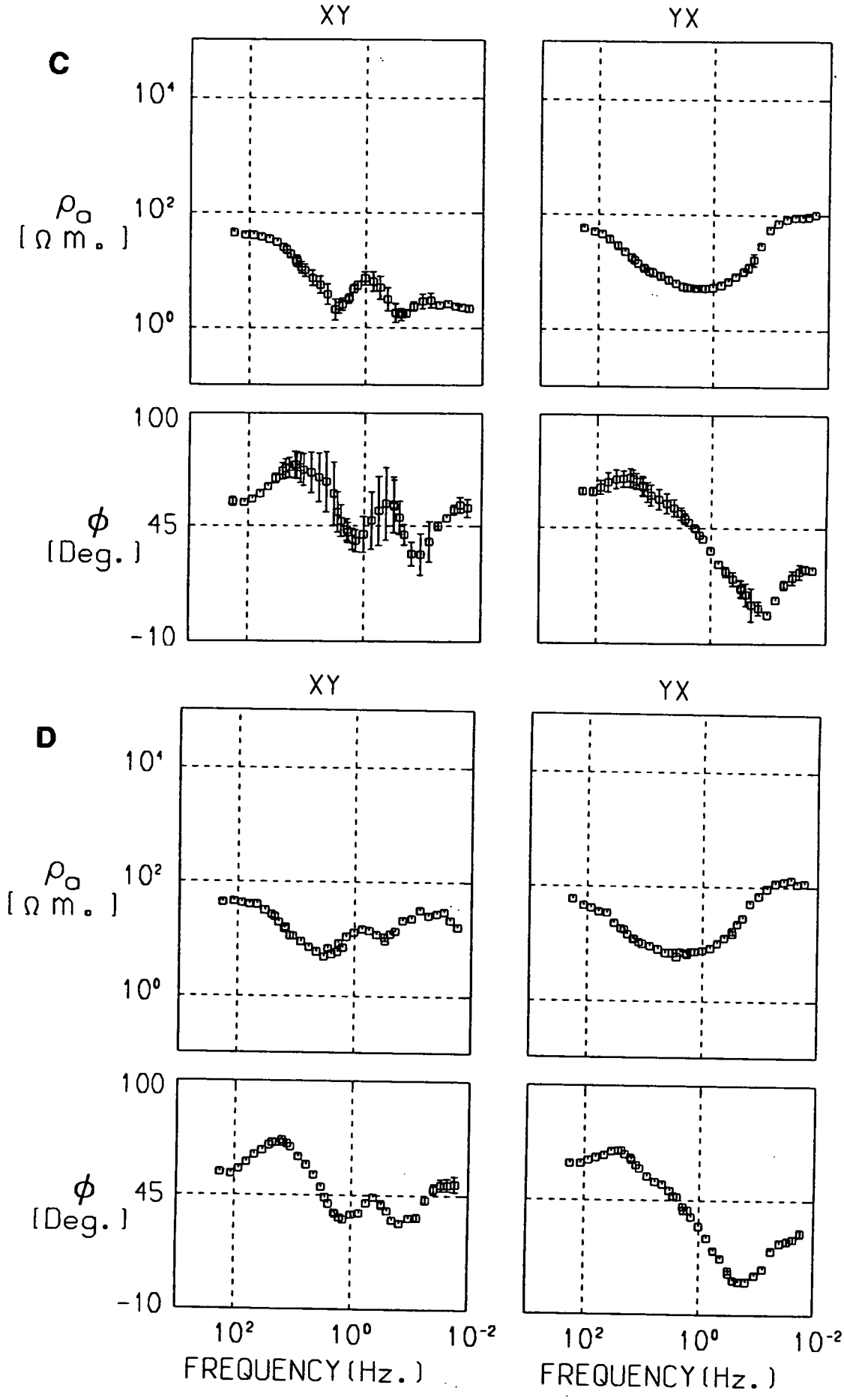
C
XY
YX
10^1
10^2
10^0
ρ_a
[Ω m.]
100
45
-10
ϕ
[Deg.]
D
XY
YX
10^1
10^2
10^0
ρ_a
[Ω m.]
100
45
-10
ϕ
[Deg.]
10^2
10^0
10^{-2}
FREQUENCY (Hz.)
10^2
10^0
10^{-2}
FREQUENCY (Hz.)

The constrained regression procedures described earlier has been repeated three times to derive the final constrained response function shown in fig. 5d. This contains the well resolved features of the original functions (figs. 5a and 5b) but demonstrates considerably more self consistency at the frequencies contaminated by more noise. This response also shows some differences from the idealized response function (fig. 5c) at the lowest frequencies in the XY direction and around 5 Hz. in the YX direction. This emphasises the need to use the idealized response function to constrain a re-evaluation of the impedance estimates, rather than be used as the final result in itself. The constrained method seemed to be ineffective at those frequencies where there was very strong input coherent noise (100 Hz.).

Confidence in the accuracy of the final constrained response function can be obtained by comparing it with that estimated by robust single site least squares from a considerably less noisy neighbouring site (Parr 1991). Figure 6 shows that the gross shape of the response functions from this second site are closer to the constrained response than any of the intermediate steps.

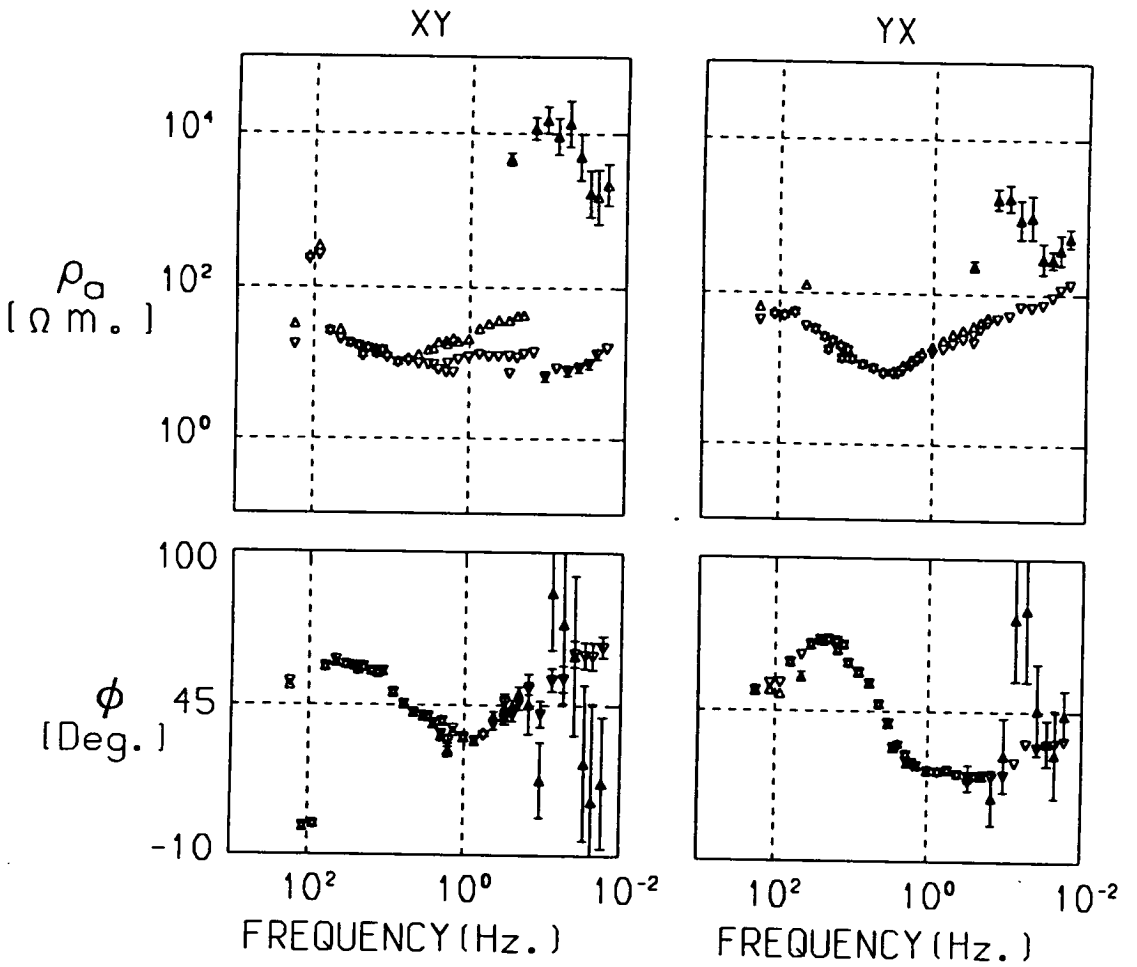

Figure 6 The magnetotelluric response at a much quieter site, adjacent to that associated with the response of Figure 5. This response has been evaluated by the modified robust least squares method of Chave and Thomson (1989) for single site up and down biased impedance estimates. At frequencies less than 0.3 Hz. there is evidence of noise contamination of the electric field, but over much of the frequency range there is very little appreciable bias. These response functions are significantly closer to that shown in fig. 5d, than any other functions shown.

5. DISCUSSION AND SUGGESTIONS FOR FUTURE MODIFICATIONS

In many developed regions of the world, MT field measurements contain noisy observations which can strongly affect the resulting response functions. In the presence of considerable random, incoherent electromagnetic noise the robust singular value decomposition impedance estimation method has usually been found to give satisfactory results. However, no impedance estimation method can guarantee an accurate and unbiased response function, particularly if there is a significant contribution from coherent noise. There is therefore justification for looking at methods to further constrain the observations and/or parameters values.

The particular method which has been discussed in this paper was mainly concerned with the imposition of constraints upon the form of the response function. These included smoothness, consistency and, where applicable, dimensionality and one-dimensional model constraints. These can have a beneficial effect on the reliability and interpretability of the resulting idealized response function.

Using a 1-D synthetic model, it has been demonstrated that the idealized response can be closer to the true response than the original set of impedance estimates which were used as its basis. The results of the application of this method to real data also implies that it may hold for 2-D structures. Sometimes, the idealized response function may be adequate for interpretation purposes. However, the methods used in its construction are largely cosmetic and can do little to reduce any noise contamination or deficiency in the data.

In general, the idealized response function should only be used as source of quasi-independent impedance information to facilitate a constrained re-evaluation of the initial impedance estimation. This will reduce ambiguities and deficiencies in the original observations at the noisier frequencies by extrapolation from better defined regions of the response function. To facilitate this a simple constrained regression method has been described. The resulting response function is overall, less influenced by all types of noise contamination and is clearly more readily interpretable than the unconstrained original from which it was derived.

Several possible alterations and extensions to the methods described in this paper have been identified by the authors.

Firstly, as magnetotelluric observations are now frequently made with additional remote reference information, the authors recognize that the method described here may have some value in the reprocessing of single site measurements which had previously been deemed to be too noisy for accurate interpretation. Alternatively, the method could be modified to allow constrained impedance estimation from remotely referenced observations.

Secondly, although the primary goal of the methods described has been the enhancement of the acquired impedance values, future studies may consider addressing the estimation of other Earth response functions (e.g. tippers) and errors more fully.

Thirdly, a more restricted idealized response function would result from smoothing the impedance estimates by using a physically admissable function (Parker 1983, Yee and Paulson 1989) rather than polynomials.

Fourthly, as discussed in section 3, Yee and Paulson (1988a) have derived dispersion relations in the more general three dimensional situation. Consideration of real data situations (e.g. fig. 5d), suggests that this constraint upon the diagonal elements of the impedance tensor is more desirable and may help to remove some of the remaining variability within the idealized response.

Fifthly, additional constraints can be derived from other geological/ geophysical observations. Within an assumed simple geoelectrical environment, such as a sedimentary basin, some 'a-priori' information is often available for example, the depth to basement, surface D.C. or electromagnetic (E.M.) resistivity observations or potentially most valuable of all, borehole resistivity log information. Any such information could be transformed into an idealized response function by forward modelling. Such constraints upon the likely form of the response function can then be incorporated into an initial constrained regression. This may help select preferentially those observations which give parameters closer to the expected response, whilst the robust down-weighting would reduce the influence of those truly outlying.

This last suggestion may be more generally applicable if the idealized response is derived from a neighbouring site. It has sometimes been found that a noisy site can be located close to a much quieter one (e.g. fig. 6). Thus assuming little lateral variation in the geoelectric response between sites in a high density survey, a low noise response function from one site could, in principle, be used to constrain the response at a neighbouring site. Final interpretation of an individual site's response function may be improved by the enhancement of common features between adjacent sites. In practice, a major problem is then the selection of the appropriate scaling factor β, in eq. 4, for the relative importance of the field observations and the constraining ideal observations drawn from the idealized response function.

ACKNOWLEDGEMENTS

The authors gratefully acknowledge the help and encouragement from Dr. A. Reid of Robertson Research International and financial support in the form of a Research Studentship to one of us (RSP) by NERC. Comments from both of the referees and the editor helped to constrain and enhance the content of an earlier draft of this paper.

6. REFERENCES

Berdichevsky, M.N., Vanyan, L.L., Kuznetsov, V.A., Levadny, V.T., Mandelbaum, M.M., Nechaeva, G.P., Okulessky, B.A., Shilovsky, P.D. and Shpak, I.P., 1980. Geoelectrical model of the Baikal region, *Phys. Earth planet. Int.*, **22**, 1-11.

Belsley, D.A., Kuh, E. and Welsch, R.E. 1980. *Regression Diagnostics*, Wiley, New York.

Boehl, J.E., Bostick Jr., F.X. and Smith, H.W., 1977. An application of the Hilbert transform to the magnetotelluric method, *Tech. Rep. Electrical geophysics Res. Lab.*, University of Texas at Austin.

Businger, P.A. and Golub, G.H., 1969. Singular Value Decomposition of a complex matrix, *Comm. A. C. M.*, **12**, 564-565.

Chave, A.D., Von Herzen, R.P., Poehls, K.A. and Cox, C.S., 1981. Electromagnetic induction fields in the deep ocean North-East of Hawaii: implications for mantle conductivity and source fields, *Geophys. J. R. astr. Soc.*, **66**, 379-406.

Chave, A.D., Thomson, D.J., and Ander, M.E., 1987. On the robust estimation of power spectra, coherences and transfer functions, *J. Geophys. Res.*, **92**, 633-648.

Chave, A.D. and Thomson, D.J., 1989. Some comments on magnetotelluric response function estimation, *J. Geophys. Res.*, **94**, 14215-14225.

Chyba, J., 1983. On the interpretation of resistivity soundings by the least squares method, *Geophysical Prospecting*, **31**, 795-799.

Claerbout, J.F., 1976. *Fundamentals of geophysical data processing: with applications to petroleum prospecting*, McGraw - Hill, New York.

Clay, C.S. and Hinich, M.J., 1981. Estimating the Earth's impedance function when there is noise in the electric and magnetic signals, in *Applied time series analysis II*, pp189-219, ed. Findley, D.F., Academic Press, New York.

Egbert, G.D. and Booker, J.R., 1986. Robust estimation of geomagnetic

transfer functions, *Geophys. J. R. astr. Soc.*, **87**, 173-194.

Egbert, G.D. and Booker, J.R., 1989. Multivariate analysis of geomagnetic array data I: The response space, *J. Geophys. Res.*, **94**, 14227-14247.

Fischer, G. and Schnegg, P.- A., 1980, The dispersion relations of the magnetotelluric response and their incidence on the inversion problem, *Geophys. J. R. astr. Soc.*, **62**, 661-673.

Fischer, G., Schnegg, P.- A., Peguiron, M., Le Quang, B.V., 1981. An analytic one-dimensional magnetotelluric scheme, *Geophys. J. R. astr. Soc.*, **67**, 257-278.

Gamble. T.D., Goubau, W.M., and Clarke, J., 1979a. Magnetotellurics with a remote reference, *Geophysics*, **44**, 53-68.

Gamble. T.D., Goubau, W.M., and Clarke, J., 1979b. Error analysis for remote reference magnetotellurics, *Geophysics*, **44**, 959-968.

Golub, G.H. and Saunders, M.A., 1970. Linear least squares and quadratic programming, in *Integer and Non-Linear Programming*, pp229-256, ed. Abadie J., North Holland Publishers, Amsterdam.

Goubau, W.M., Gamble, T.D. and Clarke, J., 1978. Magnetotelluric data analysis: removal of bias, *Geophysics*, **43**, 1157-1166.

Goubau, W.M., Maxton, P.M., Koch, R.H. and Clarke J., 1984. Noise correlation lengths in remote reference magnetotellurics, *Geophysics*, **49**, 433-438.

Hermance, J.F., 1973. Processing of magnetotelluric data, *Phys. Earth planet. Int.*, **7**, 349-364.

Hobbs, B.A., 1982. Automatic model for finding the one-dimensional magnetotelluric problem, *Geophys. J. R. astr. Soc.*, **68**, 253-264.

Huber, P.J. 1981. *Robust Statistics*, Wiley, New York.

Ingham, M.R., 1988. The use of invariant impedances in magnetotelluric interpretation, *Geophys. J.*, **92**, 165-169.

Jackson, D.D., 1972. Interpretation of inaccurate, insufficient and inconsistent data, *Geophys. J. R. astr. Soc.*, **28**, 97–109

Jady, R.J., Paterson, G.A. and Whaler, K.A., 1983. Inversion of the electromagnetic induction problem using Parker's algorithms with both precise and practical data, *Geophys. J. R. astr. Soc.*, **75**, 125–142.

Jones, A.G., 1980. Geomagnetic induction studies in Scandanavia I, *J. Geophys.*, **48**, 181–194.

Jones, A.G., 1982. On the electrical crust–mantle structure in Fennoscandia: no Moho, and the asthenosphere revealed?, *Geophys. J. R. astr. Soc.*, **68**, 371–388.

Jones, A.G., Chave, A.D., Egbert, G.D., Auld, D. and Bahr, K., 1989. A comparison of techniques for magnetotelluric response function estimation, *J. Geophys. Res.*, **94**, 14201–14213.

Jupp, D.L.P., 1978. Estimation of the magnetotelluric impedance functions, *Phys. Earth planet. Int.* **17**, 75–82.

Jupp, D.L.P. and Vozoff, K., 1975. Stable iterative methods for the inversion of geophysical data, *Geophys. J. R. astr. Soc.*, **42**, 957–976.

Kröger, P., Micheel, H.J. and Elsner, R. 1983. Comparison of errors in local and reference estimates of the magnetotelluric impedance tensor, *J. Geophys.*, **52**, 97–105.

Lanczos, C. 1961. *Linear Differential Operators*, D. Van Nostrand, London.

Larsen, J.C., 1975. Low frequency (0.1–6.0 c.p.d.)electromagnetic study of deep mantle electrical conductivity beneath the Hawaiian islands, *Geophys. J. R. astr. Soc.*, **43**, 17–46.

Larsen, J.C., 1980. Electromagnetic response functions from interrupted and noisy data, *J. Geomag. Geoelect.*, **32**, Supp. I., 89–103.

Lawson, C.L. and Hanson, R.J., 1974. *Solving Least Squares Problems*, Prentice–Hall, New Jersey.

Lienert, B.R., 1980. The effect of source field polarization on estimates of the magnetotelluric impedance tensor, *Geophysics*, **45**, 1803-1812.

Lienert, B.R., Whitcomb, J.H., Philips, R.J., Reddy, I.K. and Taylor, R.A., 1980. Long term variations in magnetotelluric apparent resistivities observed near the San Andreas Fault in Southern California, *J. Geomag Geoelect*, **32**, 757-775.

Lines, L.R. and Treitel, S., 1984. Tutorial: A review of least squares inversion and its application to geophysical problems, *Geophysical Prospecting*, **32** 159-186.

Meju, M. A., 1988. The deep electrical structure of the Great Glen Fault, Scotland, *Ph D. thesis*, University of Edinburgh.

Menke, W., 1984. *Geophysical data analysis: Discrete inverse theory*, Academic Press, Orlando.

Park, J. and Chave A.D., 1984. On the estimation of magnetotelluric response functions using the singular value decomposition, *Geophys. J. R. astr. Soc.*, **77**, 683-709

Parker, R.L., 1980. The inverse problem of electromagnetic induction: Existence and construction of solutions based on incomplete data, *J. Geophys. Res.*, **85**, 4421-4428.

Parker, R.L., 1983. The magnetotelluric inverse problem, *Geophys. Surv.*, **6**, 5-25.

Parker, R.L., and Whaler, K.A, 1981. Numerical methods for establishing solutions to the inverse problem of electromagnetic induction, *J. Geophys. Res.*, **86**, 9574-9584.

Parr, R.S. 1991. Development of magnetotelluric processing and modelling procedures- application to Northern England, *Ph. D thesis*, (submitted), University of Edinburgh.

Pedersen, L.B., 1979. Constrained inversion of potential field data, *Geophysical Prospecting*, **27**, 726-748.

Pedersen, L.B., 1982. The magnetotelluric impedance tensor - its random and bias errors, *Geophysical Prospecting*, **30**, 188-210.

Pedersen, L.B. and Svennekjaer, M., 1984. Extremal bias coupling in magnetotellurics, *Geophysics*, **49**, 1968-1978.

Ranganayaki, R.P., 1984. The interpretive analysis of magnetotelluric data, *Geophysics*, **49**, 1730-1748.

Rokityansky, I.I., 1982. *Geoelectromagnetic investigations of the Earth's crust and mantle*, Springer Verlag, Berlin.

Rousseeuw, P.J. and Leroy, A.M., 1987. *Robust regression and outlier detection*, Wiley, New York.

Sims, W.E. Bostick Jr., F.X. and Smith, H.W., 1971. The estimation of magnetotelluric impedance tensor elements from measured data, *Geophysics*, **36**, 938-942.

Swift C.M. Jr.,1986. A magnetotelluric investigation of an electrical conductivity anomaly in the South Western United States, in *Magnetotelluric Methods, Society of Exploration Geophysicists Reprint Series No. 5*, pp156-166, Ed. Vozoff, K., SEG, Tulsa.

Travassos, J.M. and Beamish D., 1988. Magnetotelluric data processing- a case study, *Geophys. J.*, **93**, 377-391.

Twomey, S., 1977. *Introduction to the mathematics of inversion in remote sensing and indirect measurements, Developments in Geomathematics series No. 3*, Elsiever.

Vozoff, K., 1972. The magnetotelluric method in the exploration of sedimentary basins, *Geophysics*, **37**, 98-141.

Yee, E. and Paulson, K.V. 1988a. Concerning dispersion relations for the magnetotelluric impedance tensor, *Geophys. J.*, **95**, 549-559.

Yee, E. and Paulson, K.V., 1988b. Necessary and sufficient conditions for the existence of a solution to the one-dimensional magnetotelluric inverse problem, *Geophys. J.*, **93**, 279-293.

Yee, E. and Paulson, K.V., 1989. The completion of the c - response function for utilization in exact inversion procedures, *Geophys. J.*, **97**, 41-50.

Weidelt, P., 1972. The inverse problem of geomagnetic induction, *Z. Geophys.*, **38**, 257-289.

APPENDIX

This appendix summarizes some of the underlying procedures used for a) calculating the robust S.V.D. impedance estimates, b) smoothing the response function and c) computing the dispersion relations. Further details of the theoretical background and associated computer programs are given by Parr (1991).

IMPLEMENTATION OF THE ROBUST SINGULAR VALUE DECOMPOSITION (S.V.D.) METHOD

The S.V.D. method of impedance estimation requires that a large number (N) of reasonably accurate measurements of the 4 electromagnetic field components has been acquired around a central frequency f. These N observations are stacked in a complex valued matrix **A**:

$$\mathbf{A} = (Hx(f), Hy(f), Ex(f), Ey(f)) = (a^{O}_{i,j}): \qquad i=1,Nj=1,4 \quad (A1)$$

Under ideal circumstances, two linear relations exist between the columns of **A** of the form (c.f. eqn. 1):

$$\begin{aligned} Ex(f) &= Hx(f) \,.\, Zxx(f) + Hy(f) \,.\, Zxy(f) \\ Ey(f) &= Hx(f) \,.\, Zyx(f) + Hy(f) \,.\, Zyy(f) \end{aligned} \qquad (A2)$$

The impedance parameters can be readily estimated after a complex valued S.V.D. (Businger and Golub 1969) is performed on eq. A1. This involves a factorization into 3 matrices:

$$\mathbf{A} = \mathbf{U} \,.\, \mathbf{\Lambda} \,.\, \mathbf{V}^{H} \qquad (A3)$$

where **U** and **V** are orthonormal matrices of dimension (N by 4) and (4 by 4) respectively and $\mathbf{\Lambda}$ is a diagonal matrix of eigenvalues with $\lambda_1 >= \lambda_2 >= \lambda_3 >= \lambda_4 >= o$.

If the two linear relations (eq. A3) exist in the four component observations, the expected rank of **A** is 2 (e.g. Lanczos 1961, Jupp 1978) and $\lambda_3 = \lambda_4 = 0$ (Jupp and Vozoff 1975). However, the true rank of **A** may not be 2 (Jupp 1978, Park and Chave 1984, Twomey 1977) as a result of the existence of interdependencies between the observable quantities arising from

observational outlying errors or polarized signals. Robust re-weighting (described later) and constrained regression (section 4) can usually help to improve the separation between the two zero and the two non-zero eigenvalues.

The Eckhart-Young theorem (e.g. Golub and Saunders 1970, Lawson and Hanson 1974) can be used to construct a 'signal' matrix (**B**) from the 2 non-zero eigenvalues which minimises the Euclidean norm $||\ \mathbf{A} - \mathbf{B}\ ||$. **B** can then be used to obtain the normal least squares impedance estimates (eq. 2) with the uncorrelated noise sources removed.

Alternatively, Park and Chave (1984) obtained impedance estimates from $\mathbf{V}_0$, the part of the **V** matrix corresponding to the zero eigenvalues by using the relation:

$$\mathbf{A} \cdot v_j = 0, \qquad \text{for } \lambda_j = 0 \qquad j=3,4 \quad \text{(A4)}$$

(e.g. Lanczos 1961, Lawson and Hanson 1974, Belsley, Kuh and Welsch 1980).

Simultaneous solution of the two linear equations comprising equation A4 allows the tensor impedance to be evaluated. In fact, since only elements of the **V** matrix are required for this calculation, the impedance can be more conveniently estimated from:

$$\mathbf{A}^H \cdot \mathbf{A} = \mathbf{V} \cdot \Lambda^2 \cdot \mathbf{V}^H \qquad \text{(A5)}$$

(e.g. Egbert and Booker 1989).

Although the formation of $\mathbf{A}^H.\mathbf{A}$ may involve numerical inaccuracies (Lines and Treitel 1984), the increase in computational efficiency is very significant. For example, on a NAS EX/30 computer, a complex singular value decomposition of **A** takes 0.185 c.p.u. seconds (when N = 78, M = 4). On the much larger data matrix (N= 1170, M = 4), the formation of $\mathbf{A}^H.\mathbf{A}$ and the subsequent acquisition of the **V** matrix takes only 0.079 c.p.u. seconds.

Both these singular value decomposition methods require the assumption that the elements of the residual error matrix **E**, are drawn from a Gaussian distribution with zero mean and uniform variance (isotropic errors). The impedance estimates can be strongly in error unless suitable pre-conditioning of **A** is performed.

In this paper, two different types of weighting have been found to improve the reliability of the impedance estimates.

Firstly, column scaling (post multiplication of A by a 4 by 4 diagonal matrix) was performed to equalize the relative magnitudes of the four electromagnetic components (Jupp 1978, Park and Chave 1984):

$$a''_{i,j} = a'_{i,j}/S_j \qquad i=1,N\ j=1,4 \quad (A6)$$

Where S_j is a scale estimate for the jth electromagnetic component.

Initial impedance estimates were then obtained by solution of equation A5.

Robust iterative re-weighting (pre-multiplication of A by a general N by N matrix) was undertaken to reduce the strong influence of a few non-Gaussian outlying observational errors. The outliers were identified and the corresponding observations weighted according to the size of the residual error between the observed and predicted electric field data:

$$R_{i,j} = a^{O}_{i,j} - a_{i,j}^{PRED.} \qquad j=3,4 \quad (A7)$$

where, e.g. $a_{i,3}^{PRED.} = Hx_i(f)\ .\ Zxx(f) + Hy_i(f)\ .\ Zxy(f)$ is the predicted electric field based on the current impedance estimates.

Since robust M parameter estimates are not scale invariant (Rousseeuw and Leroy 1987), the residuals ($R_{i,j}$) must be pre-scaled. Egbert and Booker (1986) and Chave *et al.* (1987) detail scaling procedures ($R_{i,j}/\sigma_j$) , which are based on estimates of the spread of the residuals σ_j.

Weights are usually computed for each set of electromagnetic field observations by using a Huber type weighting function:

$$\begin{aligned} W_{i,j} &= 1. && |R_{i,j}/\sigma_j| < 1.5 \\ W_{i,j} &= 1.5/|R_{i,j}/\sigma_j| && |R_{i,j}/\sigma_j| > 1.5 \end{aligned} \qquad i=1,N\ \ j=1,4 \quad (A8)$$

This gives smaller weights to those observations which have outlying errors identified by a large residual. In this study, these weights were applied to the data matrix A of this study by forming 'modified electric field observations' (Egbert and Booker 1986):

$$a^{O}_{i,j} = a_{i,j}^{PRED.} + W_{i,j}\ .\ R_{i,j} \qquad i=1,Nj=3,4 \quad (A9)$$

Equation A9 alters the electric field observations and pulls those values towards their predicted from the current impedance estimates. The entire process of scaling and re-weighting can be iteratively repeated until there is little change in the impedance estimated from the modified observations.

Finally, in this study, the estimated standard impedance errors were evaluated from the fully iterated data matrix **A**, by the methods described in Park and Chave (1984). It was found to be necessary to compensate for the loss of observational degrees of freedom during robust re-weighting. The resulting errors were then propagated into the apparent resistivity and phase estimates (see e.g. Gamble *et al.* 1979b).

'LOCAL SMOOTHING' OF THE RESPONSE FUNCTION

Local smoothing of the estimated response function (section 3) was undertaken by fitting a polynomial approximation to a segment of the response function at successive frequencies. Weighted least squares was used to compute the coefficients of the best fitting polynomial function from the complex valued impedance at frequencies surrounding the current one of interest. This was deemed to be a compromise between the need to acquire an accurate interpolated impedance and the recognition that a low order polynomial approximation may no longer be valid if impedance estimates far removed from the central frequency of interest were used. In practice, the smoothing was applied to the logarithm of the frequency, rather than the frequency itself. This helped to correct for the equal sampling in the log frequency domain. Furthermore, preliminary removal of the frequency dependence (e.g. $Zxy(f)/\sqrt{f}$) seemed to give a better least squares fitted reproduction to the apparent resistivity and phase curves.

The smoothing routine also incorporated a facility to reduce the order of the fitted polynomial when the variance of the calculated polynomial parameters was deemed to be large (c.f. Jackson 1972). Robust re-weighting was then performed to curb the influence of any outlying impedance estimates which did not reflect the smooth transitions which should exist in the response function. In this instance, robust methods were not always effective as only a small number of impedance estimates were being fitted. Finally the error was estimated from the difference between the observed and

interpolated impedance values at each frequency.

EVALUATION OF THE INTEGRAL DISPERSION RELATIONS

The phase ($\phi = \pi/4 - \arg(Z)$) can be computed at a frequency f_O from the derivative of the apparent resistivity response curve $P(f) = \rho_a/\rho_1$, by using equation 12 in Fischer and Schnegg (1980):

$$\phi(f_O) = -1/\pi \cdot P \int_{-\infty}^{\infty} \delta[\ln f] \cdot \ln \left| \frac{f + f_O}{f - f_O} \right| \cdot \frac{\delta[\ln P(f)]}{\delta[\ln f]} \qquad \text{(A10)}$$

Equation A10 strictly requires integration over the whole logarithmic frequency range, but in practice only those frequencies in the immediate vicinity of f_O contribute significantly (Weidelt 1972). This integration can therefore be performed over only the principal (denoted by P) part of the frequency spectrum. However, to compute the phase near the observed frequency limits, it is necessary to extrapolate the response function by between 1 and 2 decades. This was most readily achieved by finding a two layer, one dimensional model which approximately fitted the last 3 apparent resistivity and phase estimates. Then by forward modelling, the likely response at frequencies beyond this point was calculated. This procedure was repeated for both the high and low frequency limits of the response functions.

Performing this type of extrapolation also allowed the near surface resistivity (ρ_1) to be estimated. This parameter was required to scale the apparent resistivity curve, as the phase can only be used to determine changes in the apparent resistivity curve from this 'baseline'.

The authors found that equation A10 could be solved numerically. Firstly the response functions had to be interpolated to approximately 3 times the number of frequencies present. Next, the derivative of the scaled apparent resistivity curve was computed from the coefficients of a low order polynomial fitted to it. Thirdly, the integrand was evaluated using Simpsons rule.

Some care was required when calculating the function $\ln|f + f_O / f - f_O|$ near to $f = f_O$. A second integration was performed, with a finer spacing, to gain an approximate solution.

APPENDIX - B

SUMMARY OF MAGNETOTELLURIC PROCESSING PROGRAMS

B.I INTRODUCTION

In this appendix both the modified and the alternative programs written by this author, are described. These programs are concerned with the computation and subsequent modelling of the Earth response functions which are shown in Appendix - C. It is anticipated that the following detailed description of the programs will help interested readers to understand the pre-existing coding. This appendix may also help clarify some of the more important processing sequences which could be incorporated into new programs. The sequence of steps and programs which were used for the estimation of the MT response functions are summarized by fig. B.1.

Remotely referenced time series observations, recorded by 2 independent SPAM systems (section 3.2.4), require preliminary selection and the joining of appropriate data files by the program **RRMERGE**. All the single site and referenced field observations are then transformed into the frequency domain using **ROBANAL**. The impedance can either be determined from the auto and cross spectral powers using **RRPROG**, or after ordering the Fourier amplitudes (in **AMTOCHAVE**), the impedance can be estimated using **CHAVE2** or **ROBEST**. The latter program, which was entirely written by this author, permits the optional automatic selection of the "best" observations and the imposition of a model to constrain and enhance the consistency between the resulting impedance estimates. This model is generated by either an 'a priori' 1-D block model (**MTSTRAINT**), an adjacent MT site response, or more often, as a result of imposition of a number of constraining features upon initial, quasi-independent estimates of the impedance (Appendix -A). The suite of programs **ZFIT**, **FISCHZ** and **DPLUS** facilitates this procedure. Final MT response functions, obtained by any of these methods, are plotted prior to subsequent modelling (e.g. by **MAXMUL**) and interpretation.

The following sections describe each of these programs. The program subroutines are each discussed in turn and extra program notes are also

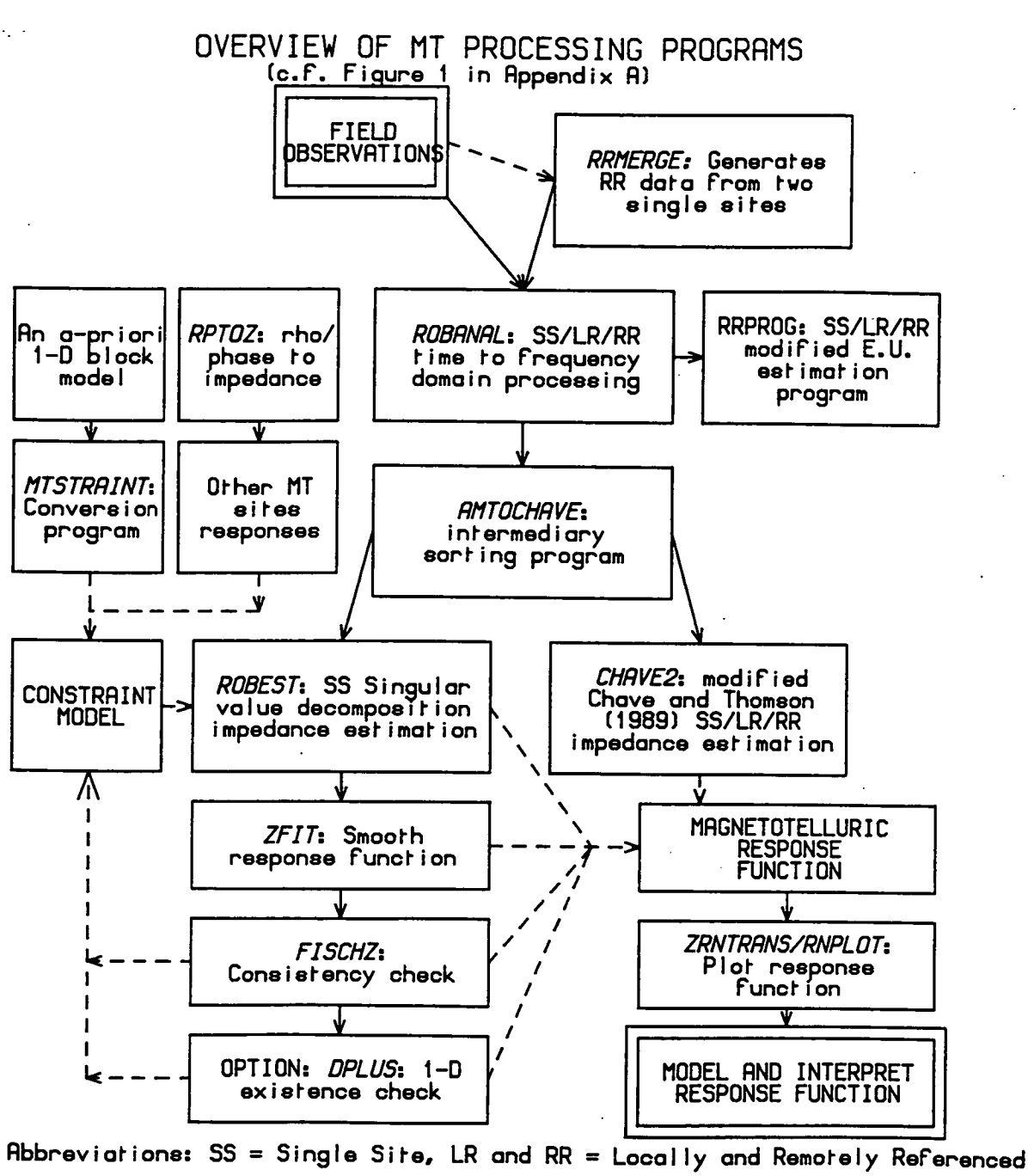

Figure B.1: A flow diagram showing the possible sequence of processing steps involved in the estimation of the MT response function from either single site (SS), locally referenced (LR) or remotely referenced (RR) time series observations. Each of the computer programs, denoted by capital letters, are described in detail in the following sections.

provided to illuminate some of the functions currently situated within the main program listings.

B.II . Program - RRMERGE

This program enables the post-field formation of remotely referenced observations by combining EM time series sections (windows) from 2 SPAM MT sites. If, as commonly occurs, the data collected at both sites consists of 4 component EM field measurements then either [Hx,Hy] or [Ex,Ey] can be selected for use as the reference. Corrupt or non-simultaneous time series sections from either or both sites are manually rejected prior to writing out the data in a format compatible with the input to **ROBANAL** (i.e. a pseudo SPAM output file).

B.III . Program - ROBANAL

This program (fig. B.2) processes the MT field time series windows from NCMPT (usually 4 [Hx,Hy,Ex,Ey] components or referenced 6 [Hx,Hy,Ex,Ey,Rx,Ry]) simultaneously acquired measurements. A number of compulsory and optional time domain data enhancement techniques are utilized prior to transformation into the frequency domain by Fast Fourier Transform (FFT). A quantitative assessment of the data quality, from each window and over the frequency range, is facilitated by averaging the spectral estimates over a frequency sub-band. Finally, the Fourier amplitudes and the quality statistics are usually passed via **AMTOCHAVE** for impedance estimation using **ROBEST**.

The original data analysis program ("**AMANAL**") of the University of Edinburgh MT group was written by Rooney (1976) and has been altered numerous times by this and other users. Consequently, the new version developed here, by this author, is as yet, long and unnecessarily complicated. The main aim of fig. B.2 is thus to provide an outline of the major and novel steps. A number of explanatory program notes and a description of the subroutines is given below.

Note 1: **ROBANAL** processes all the EM data at a specified MT site from each of the SPAM 's 4 recording frequency bands (section 3.2.2), in turn.

Figure B.2: A flow diagram outlining the processing steps within the program called **ROBANAL**. This transforms EM time series windows (i.e. from the SPAM) into the frequency domain. A number of optional and obligatory data enhancement features are also incorporated in both domains. The resulting spectral amplitudes or powers are then passed to the impedance estimation programs (**RRPROG**, **CHAVE2** or **ROBEST**).

The program notes and a more detailed description of each of the subroutines is given in the main text.

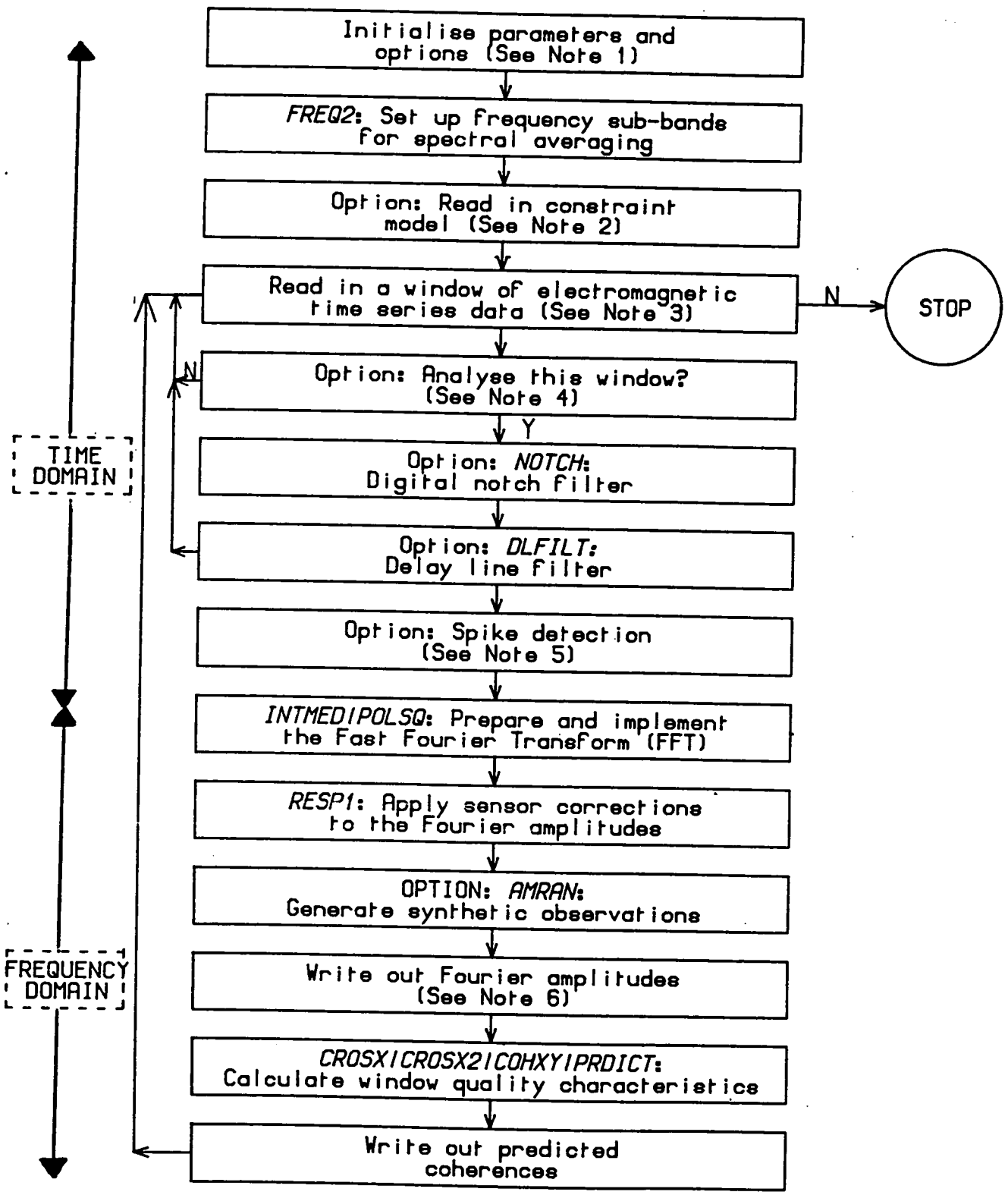
ROBANAL
Initialise parameters and options (See Note 1)
FREQ2: Set up frequency sub-bands for spectral averaging
Option: Read in constraint model (See Note 2)
Read in a window of electromagnetic time series data (See Note 3)
N
STOP
N
Option: Analyse this window? (See Note 4)
Y
Option: NOTCH: Digital notch filter
Option: DLFILT: Delay line filter
Option: Spike detection (See Note 5)
INTMEDIPOLSQ: Prepare and implement the Fast Fourier Transform (FFT)
RESP1: Apply sensor corrections to the Fourier amplitudes
OPTION: AMRAN: Generate synthetic observations
Write out Fourier amplitudes (See Note 6)
CROSXICROSX2ICOHXYIPRDICT: Calculate window quality characteristics
Write out predicted coherences
TIME DOMAIN
FREQUENCY DOMAIN

FREQ2: To permit the maximum resolution of the response function, the impedance should ideally be estimated at each of the (128) FFT frequencies (i.e. maximize the number of independent impedance estimates to minimize the effects of random errors). In this subroutine, NBS frequency spectral averaging sub-bands are constructed according to the limitations of the measuring sensors filters in each SPAM recording band. Each of these has a constant bandwidth (on a log scale) with 8 to 10 sub-bands generated in each frequency decade. To achieve this, it is necessary for each sub-band to be associated with a different number of spectral estimates from its neighbour. Furthermore, to improve consistency between the resulting impedance parameters in the low 'fold' region (at the lowest frequencies), a slight overlap between sub-bands is incorporated. Any spectral estimates sampled close to the mains power line frequency (or its harmonics) are discarded.

Note 2: The optional model to constrain the impedance estimation in **ROBANAL** comprises an acquired a priori impedance tensor and its errors which are sampled at discrete points over the entire frequency range of interest. The subroutine **ZNEAR** interpolates this function at any required intervening frequency (see also **AUGIN** and **AUGMNT** in **ROBEST**).

Note 3: For each of the NCMPT observables, a window consists of 254 time ordered samples of the EM field amplitude (plus 2 samples containing sensor amplification information). These measurements are corrected for amplifier gain, telluric line length etc., prior to processing.

Note 4: If corrupt windows have been identified in the field or by visual inspection, **ROBANAL** includes a function which permits their manual deletion.

NOTCH: This subroutine is used to remove digitally narrow frequency band noise which is contaminating a time series window. This is particularly useful for the removal of the mains power line frequency (and its associated harmonics), which constitutes a strong coherent noise source (section 4.7.2). Details of the implementation of this filter are given by Kaneswich (1981), Meju (1988) and Fontes (1988).

DLFILT: This delay line (comb) filter which, like the notch filter, is particularly useful for removing data at frequencies contaminated by artificial coherent noise (Fischer 1982). Fontes (1988) found that the delay line filter

was more effective than the notch filter in the presence of non-sinusoidal noise. This technique however produces a shorter window length and padding by zeros (see **POLSQ**) becomes necessary.

Note 5: Time series spike detection (section 5.2.1). The application of robust univariate statistics allows this function within **ROBANAL** to automatically identify and remove short duration and anomalously high power sections of the time series data. While manual editing into shorter uncontaminated window lengths (e.g. 128 samples) can remove more obvious spikes in a laborious manner, the frequency resolution is degraded (Malergue *et al.* 1986). Consequently, an automatic approach, which retains all the samples, has been developed.

From each of the NCMPT EM field observables in turn:

1. A robust estimate of the scale of the EM variations encountered in each window is calculated (eqn. 5.6.1).

2. If the average amplitude of 3 consecutive samples is greater than a scale estimate multiplied by a user specified tuning constant (usually around 4), then the central observation is deemed to be an outlier.

3. The value of the outlier is replaced by a zero (c.f. **POLSQ**).

4. If greater than 15% of the samples are rejected in this manner, the whole window is discarded owing to the excessive spike noise content.

This technique is particularly useful for the identification of electric fence noise as shown in fig. B.3. Such impulsive noise often totally corrupts measurements in the dead band (section 2.7), at frequencies around 1Hz. However, its routine adoption is questionable since it cannot discriminate between large amplitude signals and impulsive noise. It could therefore degrade otherwise good quality results. Two possible future extensions to this method have been identified:

1. Acquisition of a scale estimate across a number of data windows would improve the detection of the less obviously anomalous sections and spikes.

2. A maximum entropy extension (Barrodale and Erickson 1980, Fontes 1988) across the position of the former spike to remove the need for padding by zeros.

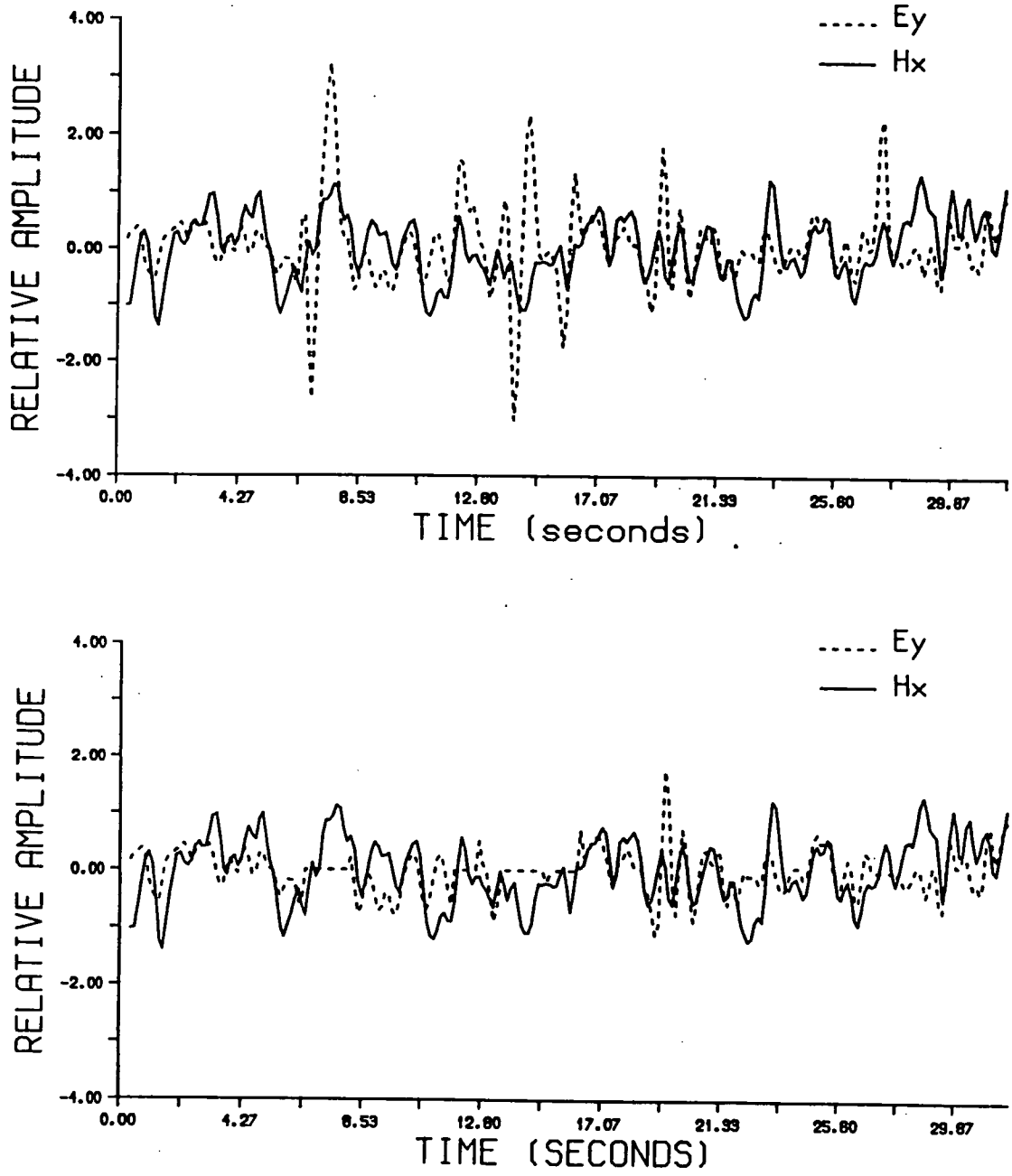

Figure B.3: The automatic spike detection and removal approach which is a built in function of **ROBANAL**. The top figure (fig. B.3a) shows that this particular EM time series 'window' contains a significant content of short duration 'spike' noise in the electric (dashed line) and magnetic (continuous line) field amplitudes. This was probably caused by electric fences discharging currents into the ground close to the MT site (MWD; fig. 3.5).

Application of the robust spike detection method (fig. B.3b) has identified the worst of the contamination and replaced the amplitudes value by zero. In this example, relatively little damage has been inflicted on the segments of uncontaminated data between the impulses.

INTMED/POLSQ: Prior to transformation from time to frequency domain, a few preparatory computations are performed on each of the NCMP time series in each window (e.g. Kaneswich 1981, Whelan 1989), as now described:

1. A linear trend is removed by least squares to reduce the possibility of low frequency spectral leakage.

2. A cosine taper is applied to 10% of the samples at each end of the window to remove spectral distortion due to the finite window length.

3. Zeros are added to pad the window out to the full 256 samples ($=2^M$, M = integer as required for FFT).

4. The FFT, performed by **RHARM** (written by Cooley and Tukey 1965) is then applied to calculate the complex Fourier spectral amplitudes.

RESP1: This subroutine applies sensor calibration factors to the electric and magnetic spectra in the frequency domain.

AMRAN: This subroutine, developed by this author, optionally substitutes all the real electric field observations with a synthetic set based on a user specified 1-D geoelectric model and the genuine magnetic field spectra. Three types of noise (Kröger *et al.* 1983) are then added to these 'observations':

I) Random, incoherent noise, drawn from a number of Gaussian and non-Gaussian distributions with different characteristics is generated at all frequencies and then independently added to each of the NCMPT observables. A random selection of grossly erroneous observations are also included to simulate the presence of outliers.

II) Over specified narrow frequency bands, input coherent noise (high COH(**Hx**,**Hy**); eqn. 2.5.6) is simulated by using the real **Hx** observations as the basis of both the synthetic **Hx** and **Hy**. To avoid complete duplication, some random variation is added separately to these 2 field components.

III) Finally, (multiple) coherent noise (e.g. high COH(**Hy**,**Ex**)) is simulated by evaluating the electric field noise contribution from the product of the magnetic field spectra and an interference impedance tensor (which is often significantly different from the true geoelectric impedance). Like type (II)

noise, this is most realistically applied over certain discrete frequency bands.

At all frequencies, the applied signal to noise ratio for each of the electromagnetic field observables is calculated. An example of the type of response function estimated from this type of noisy synthetic data is displayed in Figure 2 of Appendix – A.

This author believes that further development of such synthetic noise algorithms should concentrate on reproducing real noise distributions more closely.

NOTE 6: The Fourier amplitudes for each window and all the NCMPT observables are stored for later impedance estimation.

CROSX: This subroutine can be used to assess the data quality in each window and frequency sub-band by computing the up, down and average of the ordinary biased apparent resistivities (section 4.7.2) by least squares. Optionally, a user specified model can be used to constrain the parameter values. This process can help indicate if constrained impedance estimation on the full data set would be beneficial (see **FUZZWK** in **ROBEST**).

CROSX2/COHXY/PRDICT: For each frequency sub-band, these subroutines compute:

1. Auto and cross spectral power estimates (e.g. $Hx^{H}.HX$, $Hx^{H}.Ex$). If required these are written to a data file for later impedance calculations using the program **RRPROG**.

2. The "input" coherence COH(Hx,Hy). The author found that this gave a useful estimate of the degree of random variation between these 2 field observables. Highly coherent magnetic fields are detrimental to impedance estimation (section 4.7.2).

3. The coherences between the observed electromagnetic fields and those predicted by the estimated impedance: $COH(Ex,Ex^{PRED.})$ and $COH(Ey,Ey^{PRED.})$ give a measure of the random noise content.

An example of the type of output information generated by the program **ROBANAL** is given in fig. B.4.

Figure B.4: An annotated example of some of the tests performed on EM field data by **ROBANAL**. This particular window of EM time series data has been Fourier transformed and the 110 useable spectral amplitudes binned into 10 frequency sub-bands between 1 and 25 Hz.. In each of the sub-bands, **CROSX** has been used to compute the impedance tensor and the resulting up, down and average of the 2 biased estimates of the apparent resistivity, for the 2 principal directions (XY and YX; eqn. 2.5.3) are shown. The relatively small range of values implies that there is a low level of random observational noise present. This is further supported by the reasonably high predicted coherences computed from the impedance tensor in the subroutine **PRDICT** (eqn. 2.5.6). The high coherence between the magnetic fields, around 5 Hz., may however, indicate the presence of 'input' coherent noise (section 4.7.2).

WINDOW: 1

FREQ2 OUTPUT:

Frequency sub-band number	Spectral estimate bounds lower	upper	Central Frequency
1	6	9	1.600542
2	7	11	1.968141
3	9	13	2.474691
4	12	17	3.347718
5	16	22	4.471997
6	21	29	5.965012
7	28	40	8.196515
8	39	53	11.19781
9	52	72	15.17426
10	71	116	22.88321

CROSX OUTPUT: (NBS=10, NDEC=10)

Frequency	RHO XY (Ω.m)			RHO YX (Ω.m)		
(Hz.)	down	average	up	down	average	up
1.601	19.	19.	23.	15.	15.	16.
1.968	14.	14.	18.	12.	12.	12.
2.475	14.	14.	4.	13.	13.	14.
3.348	9.	9.	12.	10.	10.	12.
4.472	12.	12.	13.	10.	10.	10.
5.965	13.	13.	12.	10.	11.	12.
8.197	10.	10.	11.	12.	12.	12.
11.198	13.	13.	14.	15.	15.	15.
15.174	16.	16.	18.	14.	14.	14.
22.883	13.	13.	13.	19.	19.	19.

PRDICT OUTPUT:

Frequency (Hz.)	COH(Ex,$EX^{PRED.}$)	COH(Ey,$Ey^{PRED.}$)	COH(Hx,Hy)
1.601	0.93	0.98	0.25
1.968	0.95	0.97	0.29
2.475	0.90	0.98	0.44
3.348	0.85	0.96	0.52
4.472	0.87	1.00	0.64
5.965	0.90	0.99	0.60
8.197	0.99	0.99	0.30
11.198	0.98	0.99	0.20
15.174	0.92	0.99	0.26
22.883	0.96	0.99	0.28

WINDOW: 2
WINDOW: 3
etc.

B.IV. AMTOCHAVE

This transitional program rearranges the coherences and spectral measurements in a more convenient form for the impedance estimation programs **ROBEST** and **CHAVE2**. For ease of access, all the windowed spectral measurements for each frequency sub-band are deposited together in one part of the output data file.

B.V. RRPROG

This program is a variant of the traditional Edinburgh University impedance estimation method, adapted by the author to perform single site and/or referenced (local or remote) MT impedance estimation. The program usually relies heavily upon preliminary screening to detect and reject observations with a low coherence, low power or anomalous sign of the impedance tensor elements. The impedance is estimated by the standard least squares equations (eqn. 4.7.5) but a novel form of impedance averaging then follows.

B.VI. ROBEST

This program robustly estimates the MT impedance and errors from a given set of spectral amplitudes, across all the windows and within each frequency sub-band. The impedance estimates are determined by use of the singular value decomposition (SVD) method discussed in section 5.4.3. Optionally, weak constraints are placed upon the estimated values by specifying an 'a priori' response function model. If required, two preliminary data screening techniques can also be used to enhance selectively the data sample.

Possible future extensions to this program include:

1. Analysis of the vertical magnetic field data **Hz** and estimation of the tippers (eqn. 2.5.2).
2. Incorporation of remote reference data [**Rx,Ry**].
3. Optional application of fixed (strong) constraints (section 5.7.4) to the parameter values

The program sequence is summarized in fig. B.5. A summary of the

subroutines is given below.

ROBEST - SUMMARY OF SUBROUTINES

AUGIN: This subroutine is optionally used to read in the model which is used to constrain the impedance estimation, later in the program. The model consists of an impedance tensor (ZA) and its standard errors (EZA) specified over the entire frequency range.

IPSP: This subroutine uses the output file from **AMTOCHAVE** to input the following information, for each frequency sub-band in turn:

1. The central frequency (FREQ).
2. Number of observations (N) = Number of observations in each sub-band (NBAND) x Number of windows (NWIN). The estimated impedance from these N observations is assumed to be representative of the central frequency of the sub-band.
3. N, complex valued estimates of the 4 (= NCMPTS) observed components of the EM field [**Hx, Hy, Ex, Ey**].
4. NWIN estimates of the predicted coherence (COH) in both directions [$COH(Ex,Ex^{PRED.})$ and $COH(Ey,Ey^{PRED.})$].

CHECKSP: For each of the NCMPT observables, this is used to identify and remove any of the N observations which have an extreme (high or low) spectral auto-power. For each of the NCMPT components, N autopowers are computed and then ordered using a rapid sorting algorithm (see **HEAPSORT**; Press *et al.* 1986). The subsequent rejection of the autopowers with the highest values was found to be useful in this study if spike noise contamination was present, whilst the low power test was able to identify those observations which had been acquired during times of low natural signal or broken field sensor connections.

REJCOH: This subroutine rejects any of the remaining observations which are assumed to have a high level of random noise owing to their low predicted COH. This is performed either by rejecting a fixed percentage of the N observations, or by preselecting a minimum acceptable coherence threshold.

ASSIGN: The N by 4 data matrix **X = [Hx, Hy, Ex, Ey]** is formed.

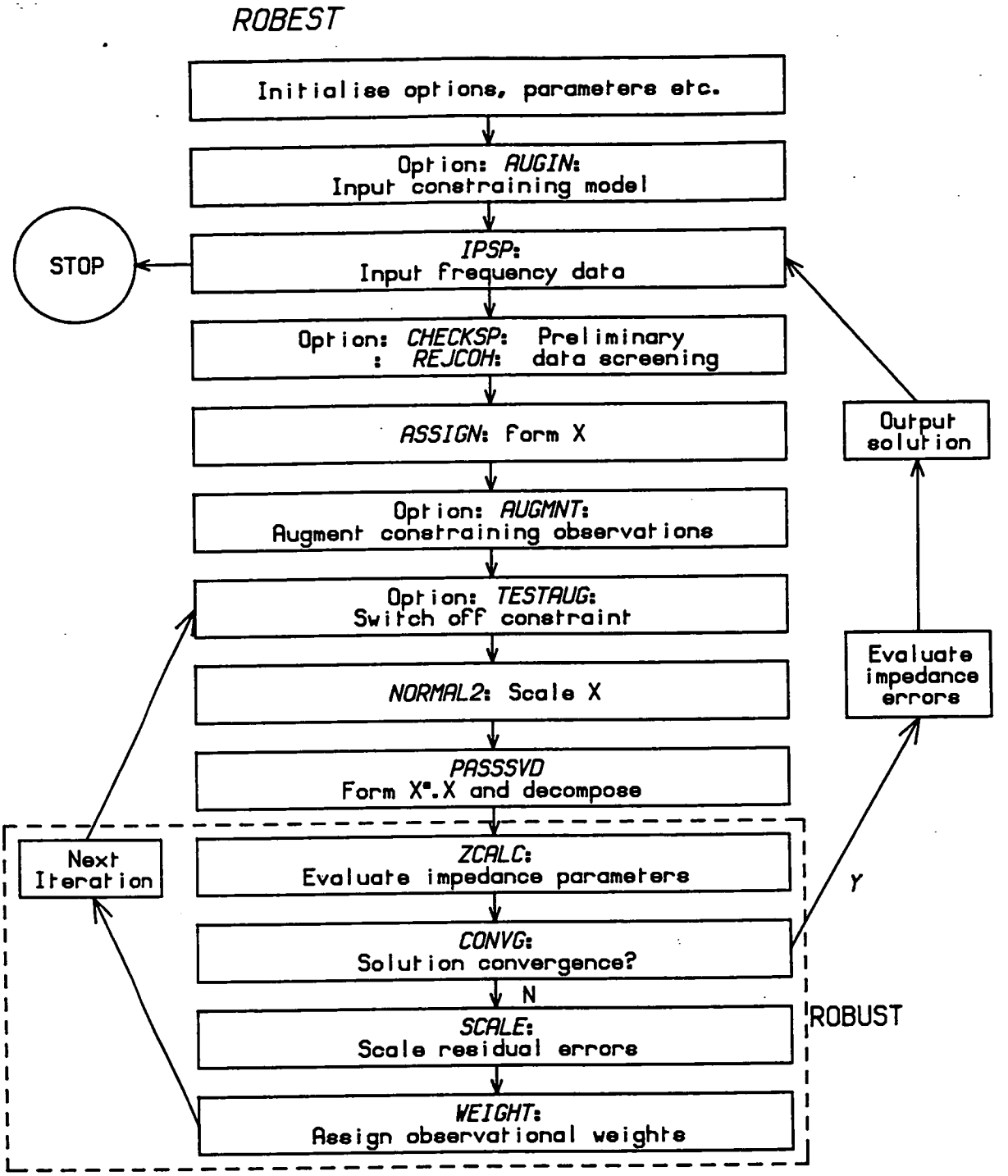

Figure B.5: A flow diagram summarizing the subroutines which are pertinent to the robust and constrained SVD impedance program **ROBEST**. The subroutines within the dotted line constitutes a typical robust M – parameter estimation algorithm.

AUGMNT: Constraining observations are simulated and augmented onto the data matrix **X** by the following steps:

1. The constraining impedance (ZAUG, EZAUG) is computed at the current frequency (FREQ) of interest by interpolation of ZA and EZA using a subroutine called **ZNEAR**.

2. The NAUG (<=N) **Hx** and **Hy** spectral amplitudes are selected. These subsequently form the constraining observations.

3. The magnetic field coherence, COH(**Hx**,**Hy**) is computed for these observations.

4. Since the estimated impedance can be strongly in error when COH(**Hx**,**Hy**) is large (section 4.7.2), it is sometimes necessary to add a random variation independently to **Hx** and **Hy**, to reduce their level of correlation. To avoid significantly changing the relative weighting of the constraining observations, this subroutine attempts to limit the overall change in the magnitude of **Hx** and **Hy**.

5. A subroutine known as **FUZZWK** is used to form NAUG, **Ex** and **Ey** synthetic observations corresponding to the selected **Hx** and **Hy** from the impedance ZAUG perturbed by a Gaussian distribution of random errors with mean zero and variance of EZAUG. These random errors are computed from a NAG Fortran library routine (number G05DDF).

6. A weighting factor is applied for these 'ideal' constraining observations relative to the true observations.

7. These constraining observations are augmented onto the data matrix **X** : i.e. N = N + NAUG.

TESTAUG: If required, this subroutine removes the constraining observations at a predetermined iteration: i.e. N = N - NAUG.

NORMAL2: To produce a more homogeneous error variance (c.f. section 5.5), the magnitude of the elements in each column of **X** are equalized (Jupp 1978, Park and Chave 1984, Appendix-A). For all the NCMPT observables, each of the N observations is divided by a factor ANORM, so that the summed power of each column in **X** is 1.

PASSSVD: This subroutine transports the data to and from the SVD routine by:

1. Forming the matrix product $\mathbf{X}^H.\mathbf{X}$.

2. Decomposing $X^H.X$ into the matrix products $V.\Lambda^2.V^H$ (section 5.4.2, eqn. A5 in Appendix - A) by a complex singular value decomposition subroutine (**CSVD**: Businger and Golub 1969).

3. Evaluating the condition number (section 5.4.3). Low values (less than about 3) suggest that the corresponding eigenvectors are ill determined possibly as a result of a high level of random noise. On the other hand, very high values (> 100) suggest that there is an abnormally good separation between the 'null' and 'non-null' eigenvectors. This may signal the presence of coherent noise. The condition number usually increases as robust down-weighting is applied.

ZCALC: This subroutine estimates the impedance from the **V** matrix by the following procedure. It:

1. denormalizes (c.f. **NORMAL2**) the **V** matrix (i.e. the column elements of **V** are divided by their corresponding ANORM).

2. uses eqn. 5.4.8, to evaluate the impedance tensor the central frequency of the current sub band.

3. denormalizes the **X** matrix (i.e. each of the column elements of **X** are multiplied by ANORM).

4. calculates the N predicted observation values for **Ex** and **Ey** (i.e. **Hx**, **Hy** and the estimated **Z** are used to determine $E^{PRED.}$ using eqn. 2.5.7) and

5. finally, finds the residual errors from the difference between $E^{PRED.}$ and E (eqn. A7 in Appendix - A).

ROBUST: Although particular details may vary (e.g. the exact method of parameter estimation), the following subroutines broadly encompass the steps required for M- robust regression (section 5.6.6) by iterative re-weighting. To avoid needless repetition, these are referred to later and as a whole.

CONVG: Tests for solution convergence as follows:

1. The invariant impedance (eqn. 6.2.3) **ZINV** is computed from all 4 elements of the impedance tensor.

2. If there is only a small change (< 1%) in the real and imaginary parts of **ZINV** from the previous iteration, the program assumes solution convergence and ceases further robust iterations.

SCALE: Estimates the residuals scale (or spread) for both **Ex** and **Ey**

directions (eqn. 5.6.1).

WEIGHT: Calculates the observational weights based on the scaled residual errors and then applies them:

1. The weights are evaluated for each of the N observations in both the Ex and Ey directions, from the scaled residuals by a) the Huber function (eqn. 5.6.8 or eqn. A8 in Appendix - A) if far from convergence, or b) the Thomson function (eqn. 5.6.9) otherwise.

2. Modifies all N Ex and Ey observations by these weights (eqn. A9 in Appendix - A).

Two annotated examples, taken during the execution of **ROBEST** are presented in fig. B.6.

B.VII . ZFIT

The aim of this program is to find a smooth response function which fits the majority of the individual impedance estimates, whilst ignoring those which are obviously outlying. The resulting response function could be used directly for interpretational purposes, but more often the author preferred to use it, after consistency checking (**FISCHZ**), as a source of quasi-independent constraints. These were then imposed to constrain a re-evaluation of the initial impedance estimates by **ROBEST**.

In order to obtain a smoothly varying and independent estimate of the impedance at each frequency, a Chebychev polynomial function is robustly fitted to sets of 6-8 neighbouring impedance estimates. The resulting coefficients are then used to interpolate the response function to the central frequency currently of interest. Mathematical details of this method have already been given in section 5.2.3 and the computer program is summarized by fig. B.7.

ZFIT PROGRAM NOTES

Note 1: It has been found that the reliability of the fitted function is increased if:

- The frequencies are first transformed onto a log (base 10) scale.

Figure B.6: An annotated copy of the computer terminal display, generated by the execution of the impedance estimation program **ROBEST**. The upper figure shows the results of unconstrained impedance estimation on EM spectral observations centered around 1.02Hz. The subroutine **CHECKSP** rejects a total of about 50% of the observations from the 2 magnetic and electric field components on the basis of extreme power. A second data screening procedure rejects 50% of the remainder, owing to their low level of predicted coherence (< 0.9), as estimated in **ROBANAL**.

In this example, 3 robust iterations are performed on the data:

1. Huber weights are applied to each set of observations following non-robust SVD impedance estimation.

2. the impedance is re-evaluated and since the "effective" combination of the impedance tensor elements (eqn. 6.2.3) only demonstrates a modest change of 1% (to give an apparent resistivity of 19 Ω.m), then

3. a final set of Thomson observational weights are computed and are applied to allow the fully iterated parameter values to be calculated.

The lower figure shows the results of constrained impedance estimation applied to the same data set shown above. The constraining model used has resistivities of 16 and 17 Ω.m. in the principal directions. All of the real observations (100%) are then used as the basis of the synthetic constraining observations. The input coherence of these observations was deemed to be slightly too high (0.22) and so a small random variation was applied to Hx and Hy independently. This reduced the coherence to 0.17, but resulted in a 25-32% average change in their power. As before, 3 robust iterations were required on the augmented observational data set, prior to convergence.

This procedure is repeated for the data all all other frequencies in each selected sub-band.

```
**********************************************************
READING IN FREQUENCY        1.0246 Hz.

\\\\\\\\\\\\\\ SPECTRAL REJECTION \\\\\\\\\\\\\\\\\\
\\\ Hx: NO. OBSRVNS. PRESENT: 2470 OF WHICH  463 ARE RJTD.
\\\ Hy: NO. OBSRVNS. PRESENT: 2007 OF WHICH  403 ARE RJTD.
\\\ Ex: NO. OBSRVNS. PRESENT: 1600 OF WHICH  260 ARE RJTD.
\\\ Ey: NO. OBSRVNS. PRESENT: 1340 OF WHICH  197 ARE RJTD.

\\\\\\\\\\\\ COHERENCE REJECTION \\\\\\\\\\\\\\\\\\\\
\\\      NO. OBSRVNS. PRESENT: 1143 OF WHICH  569 ARE RJTD.
\\\      50.4% REJECTION: MINIMUM COHERENCE 0.90

(iteration 1: display the percentage weights applied for Ex and Ey)
! ITRN   1: % WEIGHT APPLIED Ex :   95.9   Ey :   96.7
(iteration 2: display: 1) the current invariant apparent resistivity
                       2) the percentage change in the invariant impedance
                       3) the data matrix condition number
                       4) the new weights)
FREQ.   1.02 APP. RESIS.   19 , AV. % IMPED. CHANGE   1.0 CONDN.      6
! ITRN   2: % WEIGHT APPLIED Ex :   96.3   Ey :   97.4
(final iteration: convergence achieved, change to Thomson weight)
FREQ.   1.02 APP. RESIS.   18 , AV. % IMPED. CHANGE   0.5 CONDN.      7
! ITRN   0: % WEIGHT APPLIED Ex :   99.9   Ey :   99.9

..... Read in and process the next frequency sub-band data ....>



**********************************************************
READING IN FREQUENCY        1.0246 Hz.

\\\\\\\\\\\\\\\ NO SPECTRAL REJECTION \\\\\\\\\\\\\\\\\\
\\\\\\\\\\\\\\\ NO COHERENCE REJECTION \\\\\\\\\\\\\\\\\\

==========================================================
=== CONSTRAINING MODEL AT  1.025 Hz. HAS: ρxy=   17. ρyx=    16.Ω.m =====
100.0% TRUE OBSERVATIONS USED FOR CONSTRAINT ONES
RELATIVE SCALING FACTOR: 1.0
!!!! I/P DATA HIGH COH(Hx,Hy) (=0.22): ADJUSTED TO 0.17 =>
     OBSERVATIONAL POWER CHANGE: Hx  25%, Hy 32% !!!!!!!!!!!!!
==========================================================

! ITRN   1: % WEIGHT APPLIED Ex :   97.3   Ey :   97.3
FREQ.   1.02 APP. RESIS.   18 , AV. % IMPED. CHANGE   2.0 CONDN.      11
! ITRN   2: % WEIGHT APPLIED Ex :   98.7   Ey :   98.7
FREQ.   1.02 APP. RESIS.   18 , AV. % IMPED. CHANGE   0.2 CONDN.      12
! ITRN   0: % WEIGHT APPLIED Ex :   99.9   Ey :   99.9

..... Read in and process the next frequency sub-band data ....>
```

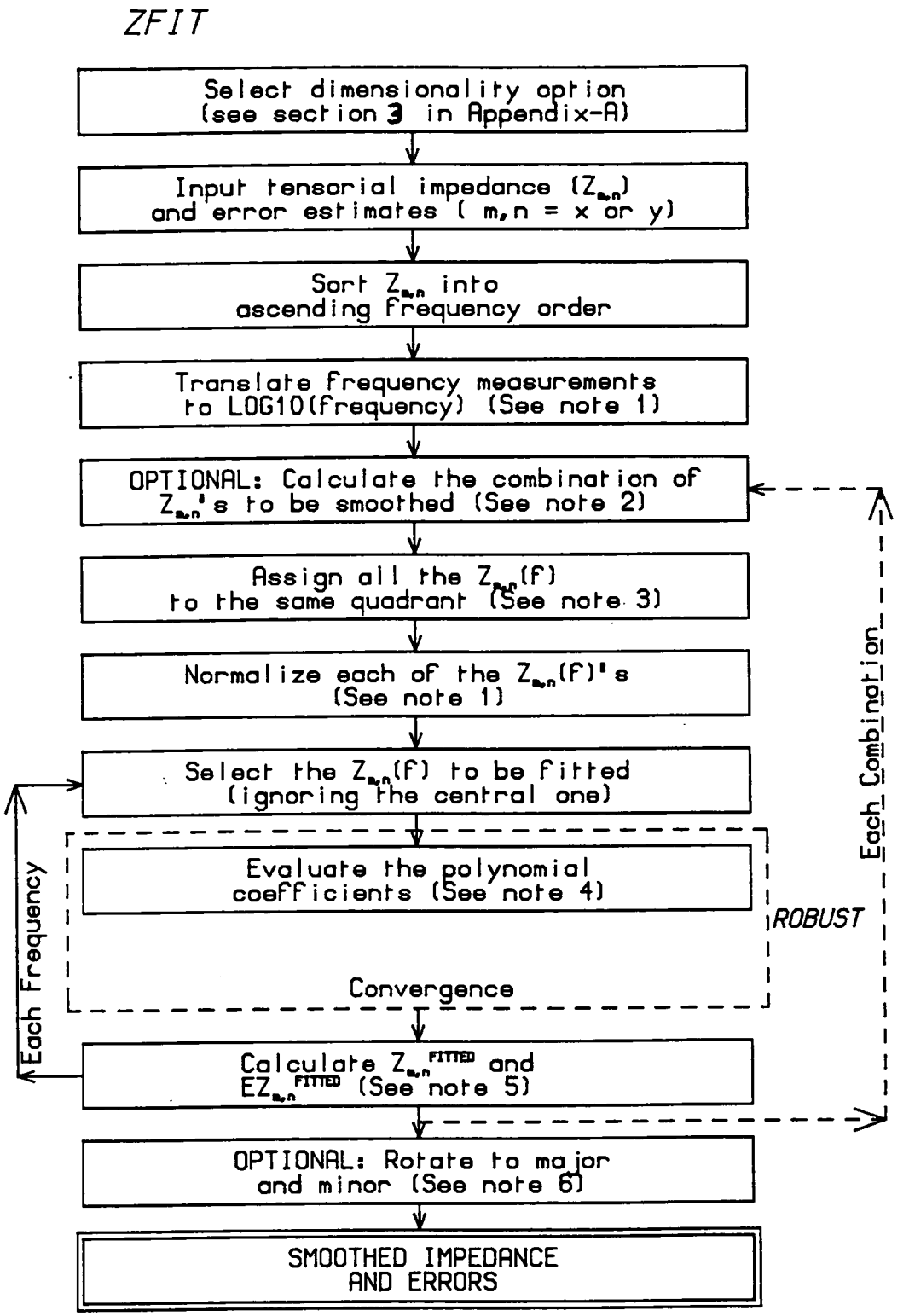

Figure B.7: The steps involved in the program **ZFIT**, which smoothes and interpolates estimates of the MT impedance over a specified frequency range.

- The dependent observables (impedance) are pre-normalized by √(0.2/FREQ) to remove their frequency dependence.

Note 2: The choice of dimensionality option determines which combination of the impedance tensor elements are to be smoothed. In general, all 4 tensor elements are smoothed independently, although in the 1-D situation, only a rotationally invariant combination (e.g. eqn. 6.2.3) of impedance elements requires processing.

Note 3: Sometimes as a result of noisy observations, a number of isolated impedance estimates have a different sign, in the real and/or imaginary parts, from those at neighbouring frequencies. The resulting fitted impedance is strongly in error unless these ambiguities are removed at an early stage. Since the apparent resistivity and phase are ultimately of most interest, this process can be justified by considering that their respective definitions are both independent of the sign of the impedance (c.f. eqn. 2.3.7 and section 2.3.2). The correct signs are subsequently re-assigned to the impedance tensor elements after polynomial fitting in order to obtain the correct azimuthal estimates.

The author recognizes that this is not an entirely satisfactory technique. In fact, any future work should consider outright rejection of those impedance estimates with anomalous signs, if it can be judged that they were caused by noise.

Note 4: **ZFIT** performs a weighted least squares (section 5.5) fit to the selected impedances at frequencies around the one of current interest and the polynomial coefficients are obtained by the Lanczos method (section 5.7.2) after the application of complex valued SVD. If the variance of the calculated coefficients is deemed to be too great owing to the presence of small singular values, the order of the polynomial is reduced and the coefficients re-computed. The residual misfit between the observed and predicted impedances is further minimized by a **ROBUST** outlier down-weighting scheme (see **ROBEST**). The final polynomial coefficients largely ignore any isolated extreme impedance values (fig. B.8).

Note 5: In this study, the estimated impedance errors (c.f. eqn. 4.3.5) were

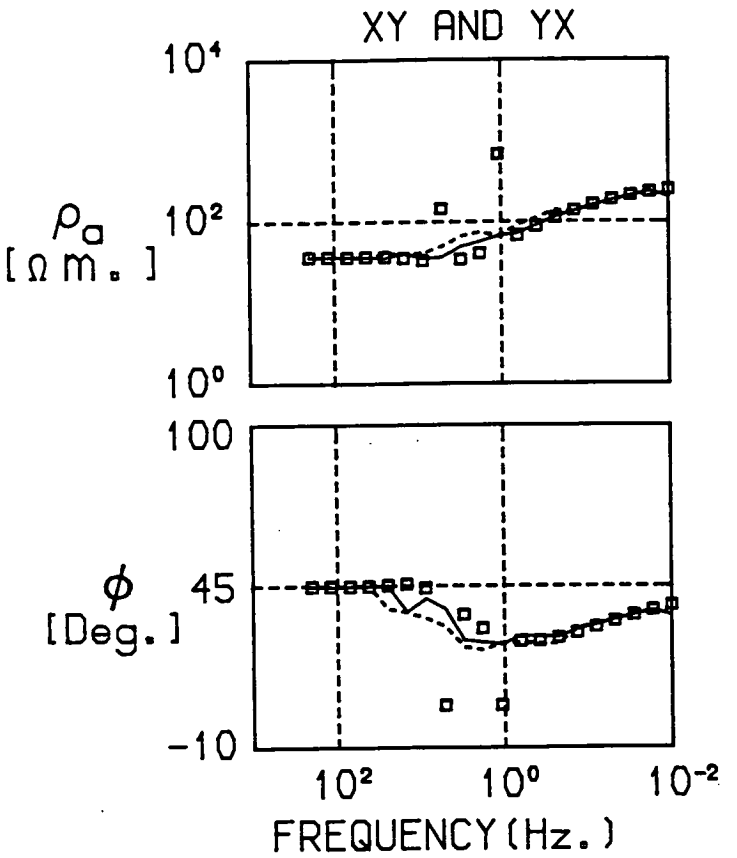

Figure B.8: Application of ZFIT to a synthetic response function based on a 2 layer, 1-D model. Most of the "observed" impedance estimates are smoothly varying with respect to frequency (represented by squares), but 2 extreme outliers affect both the apparent resistivity (ρ_a) and phase (ϕ) curves at frequencies of 1 and 7 Hz.. Non-robust interpolation using ZFIT (the dashed line) can generate a good reproduction of the response function at the extremes of the frequency spectrum, but it is excessively influenced by outliers at the centre. The application of iterative robust M-regression sucessively downweights these observations and helps to improve the fit (solid line). Some of the remaining misfit is removed in a later stage of processing (fig. B.11).

often found to show little resemblance to the scatter in the response function. This was probably due to the small number of impedances and high proportion of outliers, to which polynomials were fitted. However in this program, the impedance computed at each distinct frequency is virtually independent of that observed (c.f. **FREQ2** in **ROBANAL**). Thus a more reasonable estimate of the error can be calculated from the difference between them.

Note 6: Rotating to the major and minor impedances (section 2.5.2) is necessary for the correct application of the dispersion relations (**FISCHCZ**) to 2-D geoelectric situations.

B.VIII FISCHZ

This program was written to check the consistency between the NFREQ estimates of the apparent resistivity (RHO) and phase (PH) of a 1-D (e.g. the invariant) or rotated 2-D (major and minor directions) MT response function.

By the application of one of the dispersion relations (eqn. A10 in Appendix - A; also section 2.6), an estimate of the phase ($PH^{CALC.}$) is calculated from the observed, but interpolated, apparent resistivity ($RHO^{INTRP.}$) response function (**STEP A**). Secondly, the observed phase is also interpolated ($PH^{INTRP.}$) to the same NFREQ2 equally spaced, intervening frequencies (**STEP B**). Thirdly, the average of $PH^{CALC.}$ and $PH^{INTRP.}$ is taken to be a compromise output phase value ($PH^{O/P}$) and the error ($EPH^{O/P}$) estimated from their difference (**STEP C**). Alternatively, $PH^{O/P}$ and $EPH^{O/P}$ can be computed after fitting a polynomial to $PH^{CALC.}$ and $PH^{INTRP.}$ (**STEP C'**). Finally, the output apparent resistivity ($RHO^{O/P}$) is usually taken to be identically $RHO^{INTRP.}$ (**STEP D**), although this program alternatively permits the estimation of a $RHO^{O/P}$ which is consistent with $PH^{O/P}$ (**STEP D'**) by application of the second dispersion relation (eqn. A11 in Appendix - A). All four of these steps are repeated with the minor response data if the 2-D option has been selected.

Finally, the output impedance, ZOUT and associated errors EZOUT, are computed from $RHO^{O/P}$, $PH^{O/P}$ and $EPH^{O/P}$ (c.f. **RPTOZ**). Figures B.9(a,b) provide further details concerning **FISCHZ**.

Figure B.9: The steps involved in the computation of a self consistent response function by application of the dispersion relationships (section 2.6). Figure B.9a outlines the main parts of the program **FISCHZ**, whilst fig. B.9b gives the details of the optional and mandatory steps (A to D) for the computation and application of the dispersion relations.

- Step A: Compute the phase ($PH^{CALC.}$) from the observed apparent resistivity response function.
- Step B: Interpolate the observed phase ($PH^{INTP.}$).
- Step C: Calculate the average of the phases and its difference ($PH^{OP.}$, $EPH^{OP.}$), or
- Step C': Compute $PH^{OP.}$ by fitting a polynomial to $PH^{CALC.}$ and $PH^{INTP.}$.
- Step D: Assume the output apparent resistivity ($RHO^{OP.}$) is identical to the observed, or
- Step D': Compute a consistent $RHO^{OP.}$ from $PH^{OP.}$.

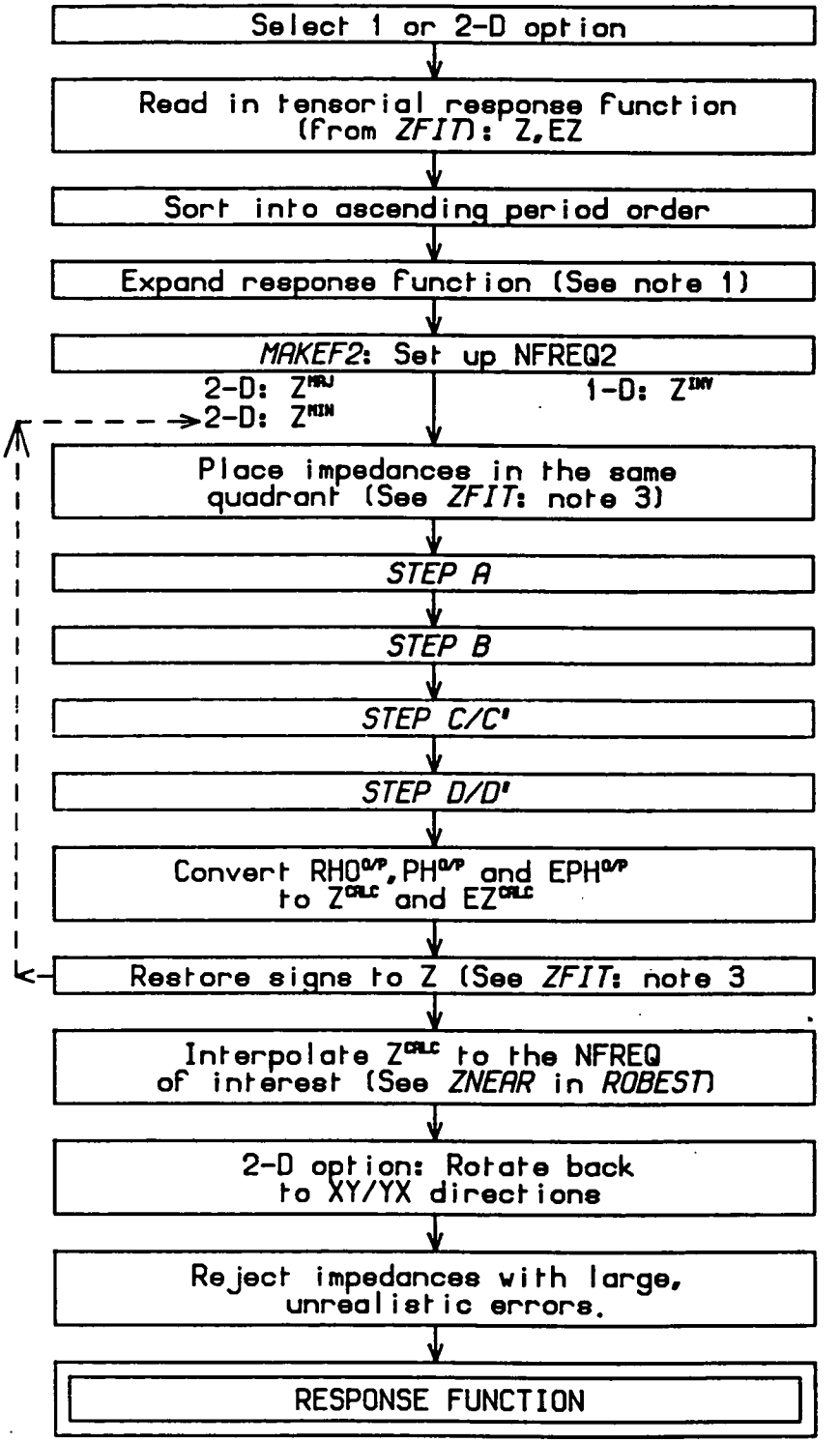
Select 1 or 2-D option
Read in tensorial response function (from ZFIT): Z,EZ
Sort into ascending period order
Expand response function (See note 1)
MAKEF2: Set up NFREQ2
2-D: Z^MAJ
1-D: Z^INV
2-D: Z^MIN
Place impedances in the same quadrant (See ZFIT: note 3)
STEP A
STEP B
STEP C/C'
STEP D/D'
Convert RHO^O/P, PH^O/P and EPH^O/P to Z^CALC and EZ^CALC
Restore signs to Z (See ZFIT: note 3
Interpolate Z^CALC to the NFREQ of interest (See ZNEAR in ROBEST)
2-D option: Rotate back to XY/YX directions
Reject impedances with large, unrealistic errors.
RESPONSE FUNCTION

B

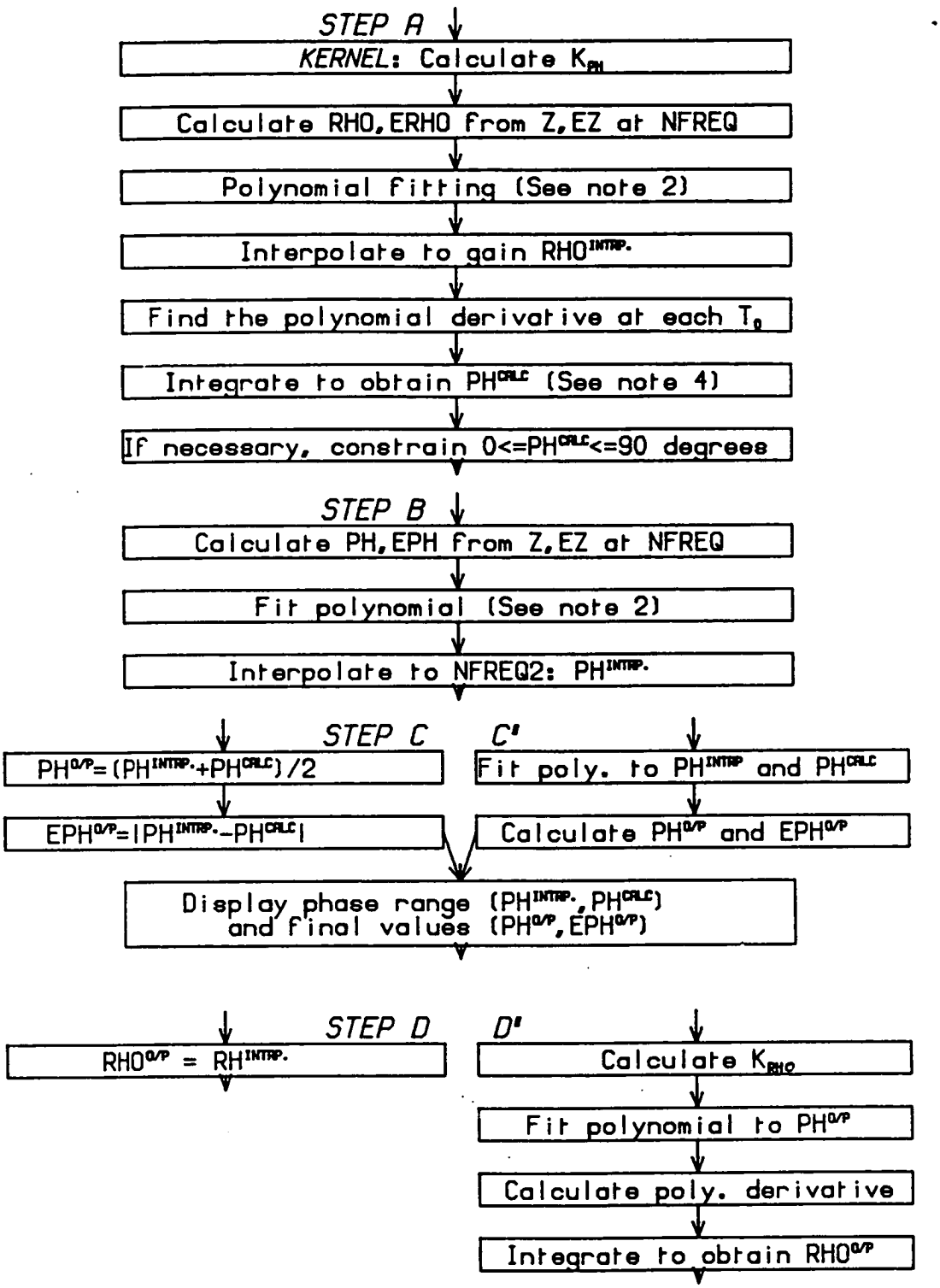
STEP A
KERNEL: Calculate K_{PH}
Calculate RHO, ERHO from Z, EZ at NFREQ
Polynomial fitting (See note 2)
Interpolate to gain $RHO^{INTRP.}$
Find the polynomial derivative at each T_0
Integrate to obtain PH^{CALC} (See note 4)
If necessary, constrain $0<=PH^{CALC}<=90$ degrees
STEP B
Calculate PH, EPH from Z, EZ at NFREQ
Fit polynomial (See note 2)
Interpolate to NFREQ2: $PH^{INTRP.}$
STEP C
$PH^{O/P}=(PH^{INTRP.}+PH^{CALC})/2$
$EPH^{O/P}=|PH^{INTRP.}-PH^{CALC}|$
C'
Fit poly. to PH^{INTRP} and PH^{CALC}
Calculate $PH^{O/P}$ and $EPH^{O/P}$
Display phase range ($PH^{INTRP.}$, PH^{CALC}) and final values ($PH^{O/P}$, $EPH^{O/P}$)
STEP D
$RHO^{O/P} = RH^{INTRP.}$
D'
Calculate K_{RHO}
Fit polynomial to $PH^{O/P}$
Calculate poly. derivative
Integrate to obtain $RHO^{O/P}$

NOTE 1: Solution of either of the two dispersion relations at a period T_0, strictly requires that the integral be evaluated over the entire period range from 0->T->∞. While this is clearly impossible in practice, the results of equation A10 in Appendix - A has been found to be scarcely influenced by the impedances at either extreme end of the spectrum (see **KERNEL**). An adequate practical solution is therefore deemed to be the termination of both the long and short period limits by a 2 layer, 1-D model, whose parameters are obtained by trial-and-error forward modelling of the last three extreme periods (Fischer and Schnegg 1980). These models are then used to project the response function beyond the limit of the acquired observations until it asymptotically approaches that of a uniform half-space (by at least 1 to 2 frequency decades). This has been found to be particularly important for the correct evaluation of the second dispersion relation as the derivative in eqn. A11 in Appendix - A results in a significant contribution from the shorter periods, to the computed apparent resistivity.

MAKEF2: This subroutine sets up the NFREQ2 (approx. 3-5 times NFREQ) intervening periods which are equally spaced (separation of Δ) on a log scale which are used for later numerical interpolation, differentiation and integration.

NOTE 2: A similar type of Chebychev polynomial fitting is performed by (non-robust) weighted least squares as that discussed earlier (**ZFIT**). In this application all the impedance estimates, including the central one, are used to calculate the coefficients.

KERNEL: To determine $RHO^{CALC.}$ or $PH^{CALC.}$ at a period T_0, the kernels (in equations A10 and A11 in Appendix - A) weight the contribution from the derivative of $PH^{INTRP.}$ and $RHO^{INTRP.}$ and integrate over all T. Since the NFREQ2 periods are equally spaced on a log scale, the kernel only needs to be evaluated once for RHO to PH (K_{PH}) and PH to RHO (K_{RHO}) over the entire range of 2.NFREQ2 possible $LOG10(T/T_0)$ values using:

$$K_{PH} = LN \left| \frac{T + T_0}{T - T_0} \right| \quad \text{and} \quad K_{RHO} = LN \left| \frac{T^2}{T_0^2 - T^2} \right| \qquad (B.1)$$

Figure B.10 shows a graph of these 2 functions over at the central part of the period range. As K_{PH} approaches a delta function (c.f. eqn. 2.6.6), then the

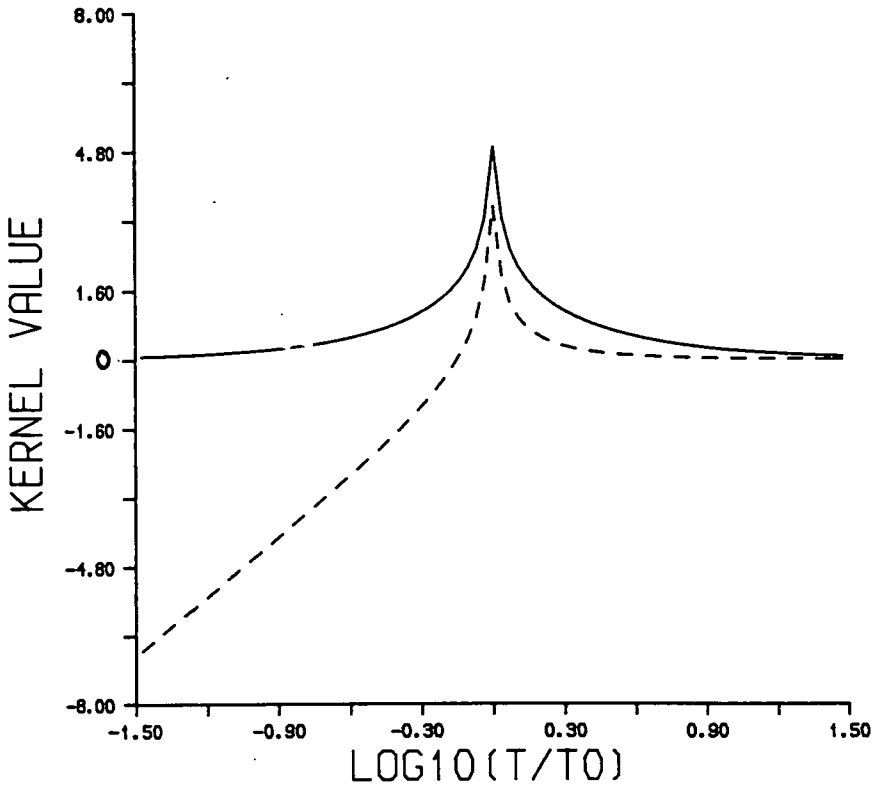

Figure B.10: The change in the value of K^{PH} and K^{RHO}, computed from eqn. B.1, over a range of T/T_0 values. The solid line shows that K^{PH} has a negligible value for periods (T), which are far removed from the one at which the dispersion relation is being computed (T_0). The phase dispersion relation is therefore mainly determined from apparent resistivity estimates which are within 1 decade of T_0 (c.f. eqn. 2.6.6). This limits the effects of noise contamination.

K^{RHO} (dotted line) also shares this property, for periods greater than T^0 (i.e. low frequency contributions are band limited), but it allows all the phase estimates to contribute from $T < T_0$. Noise contamination of the phase response function at the highest frequencies can therefore result in erroneous apparent resistivities computed for *all* lower frequencies (see fig. B.11).

contribution to the integral A10 is negligible for apparent resistivity estimates at periods either 1 decade less or greater than T_0. However, as K_{RHO} does not share the same properties for periods less than T_0, then any errors in the phase estimates can contaminate the calculated apparent resistivity (c.f. Note 1).

Since the value of both K_{PH} and K_{RHO} are indeterminate at precisely $T = T_0$, Fischer and Schnegg (1980) have suggested that an analytic solution can be found. Alternatively in **FISCHZ**, an approximate solution is found by performing a second numerical integration, with fine spacing, between $LN(T_0)-\Delta/2$ and $LN(T_0)+\Delta/2$.

Note 3: Strictly it is the function $P(T_0)^{INTRP.}$ $[=RHO(T_0)^{INTRP.}/\rho_1]$ which is interpolated. The parameter ρ_1 is the resistivity of the model's uppermost layer and its value is estimated from the preliminary trial-and-error modelling discussed in Note 1.

Note 4: After evaluating the coefficients of the best fitting polynomial (eqn. 5.2.1), the derivatives of the function are computed at each of the NFREQ2 periods. Simpson's method (e.g. Lennox and Chadwick 1977) is used to integrate numerically the product of these values with their appropriate weighting factor (K_{PH}) over the range of T. This gives $PH^{CALC.}$ over the extended period (T_0) range.

An example of the type of results obtained is given in fig. B.11. Taking the smoothed data resulting from the application of **ZFIT** and shown in fig. B.8 (marked by squares with their associated errors), the first dispersion relation is used to compute $PH^{CALC.}$ (STEP A only). In fig. B.11 this response function is shown by a dashed line in the lower (phase) graph. There is clearly a difference between the smoothed and computed phase response functions at those frequencies where outlying impedance estimates had been simulated earlier (around 0.5 Hz.). Routinely, the program **FISCHZ** takes a compromise between these two limits to represent the output phase response function (STEP C). However, the remaining error in the phase response means that, after the application of the second dispersion relation (STEP D' only), the calculated apparent resistivity is seriously in error. This is demonstrated in the upper graph of fig. B.11 which shows $RHO^{CALC.}$ (dashed line) is divergent at

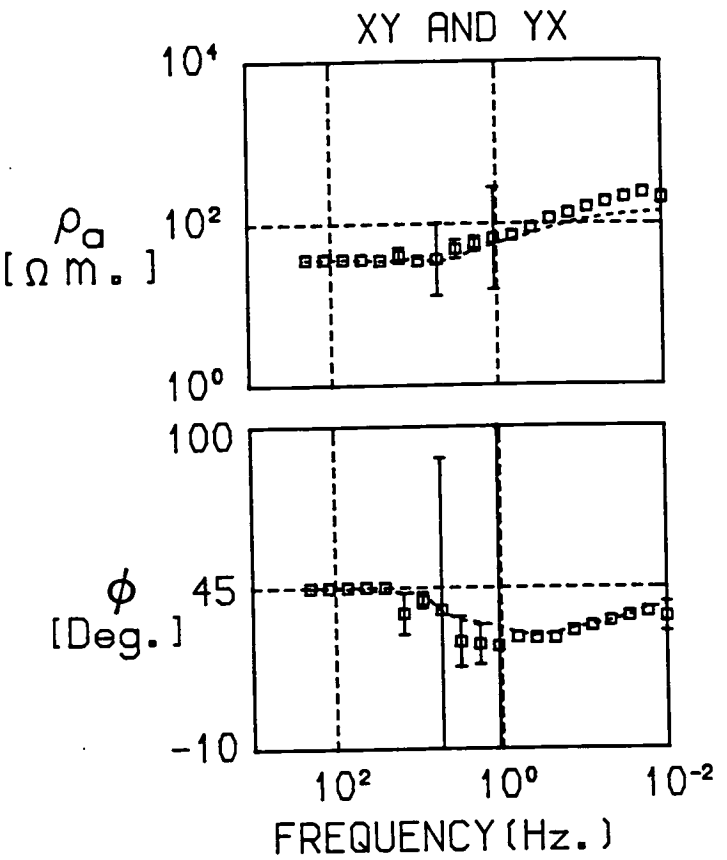

Figure B.11: The application of **FISCHZ** to the smoothed synthetic response function which was shown earlier (in fig. B.8) and has been reproduced here with its computed error bounds.

The computed phase (dashed line in the lower panel of this diagram) from this apparent resistivity response function (Step A only in fig. B.9b) appears to have sucessfully corrected the remaining post-smoothing bias. The computed apparent resistivity curve (dashed line in the upper panel) from the smoothed phase response (Step D' only in fig. B.9b) is also marginaly closer to the true input model response (i.e. the apparent resistivity is slightly lower around 1Hz.). However, the presence of even a slight error in the phase estimates has resulted in a bias for all computed apparent resistivities below 1 Hz. (c.f. fig. B.10).

all frequencies below those which were contaminated by noise. This is a direct result of the unconstrained form of the K_{RHO} weighting function.

The author now recognizes that very little extra programming effort is required to adapt this program to apply the dispersion relations in the more general 3-D situation (Yee and Paulson 1988). However, preliminary attempts did not show substantial changes in the constrained regression results. Therefore, this author suggests that future work on this method should concentrate on improving the efficiency and coding of the 2 computer programs ZFIT and FISCHZ. This may involve combining some of their current individual functions.

B.IX. DPLUS

If a D^+ model (section 6.2.5) fits an MT response function, then there exists a valid 1-D model for it (Parker 1983). A recent unaltered version of this program is used to identify those impedance estimates which demonstrate a large residual misfit. These are then rejected from the ideal response function on the basis that either they are too noisy or derived from a geoelectric structure with higher dimensional characteristics.

B.X. RPTOZ

Using a re-arrangement of equations like 2.5.3, this program converts the frequency, apparent resistivity, phase and phase error information into MT impedance tensor elements. It is a particularly useful method of transforming published response functions into crude, but usable, impedance estimates (section 3.5.2). These are then used either to remodel and interpret the acquired data by means of the new programs or to constrain the impedance estimation procedure on data from another site.

B.XI. MTSTRAINT

This program was written to find the most likely MT response function given a range of 1-D block models. It is used both to obtain a set of weak or strong impedance constraints (section 5.7.5, Appendix - A), and also, at an exploratory pre-data acquisition stage, to ensure there is sufficient frequency

bandwidth to resolve the target structure.

This program requires the user to specify an assumed 1-D, NR layer resistivity/depth model together with the upper and lower limits on these parameter values. It then takes all possible combinations of the 3x(2xNR-1) parameter values in turn and computes a forward model for each to determine the range of response functions. At each frequency, the median value of all these apparent resistivity and phase estimates is converted into the impedance, whilst a robust estimate of their scale provided an impedance error estimate.

An example of an input three layer, resistor-conductor-resistor model is shown on the right hand side of fig. B.12. The model is specified in terms of its estimated most likely parameter values (solid lines) and some upper and lower bounds (dotted lines). **MTSTRAINT** then calculates the median apparent resistivity and phase response functions (solid lines on left hand side graphs) and their uncertainties (dotted lines). As might be expected, the uncertainty accumulates at lower frequencies.

B.XII. CHAVE2

This computer program was originally developed for the robust least squares estimation of the MT impedance from a referenced set of time series observations and is fully described by Chave *et al.* (1987) and Chave and Thomson (1989).

Two major changes have been made to the program code by this author:

1. The removal of the time series to frequency domain transformation.
2. The optional inclusion of single site impedance estimation.

These two adaptations permitted a fuller comparison between **CHAVE2** and **ROBEST** by facilitating the processing of identical, synthetic and real spectral data. Figure 2 (in Appendix A) and fig. 5.9 show that it would probably be desirable if, in the future, some manual or automated preliminary data selection criteria (e.g. the coherence) were incorporated in this program to reduce the influence of strong noise in the independent observations.

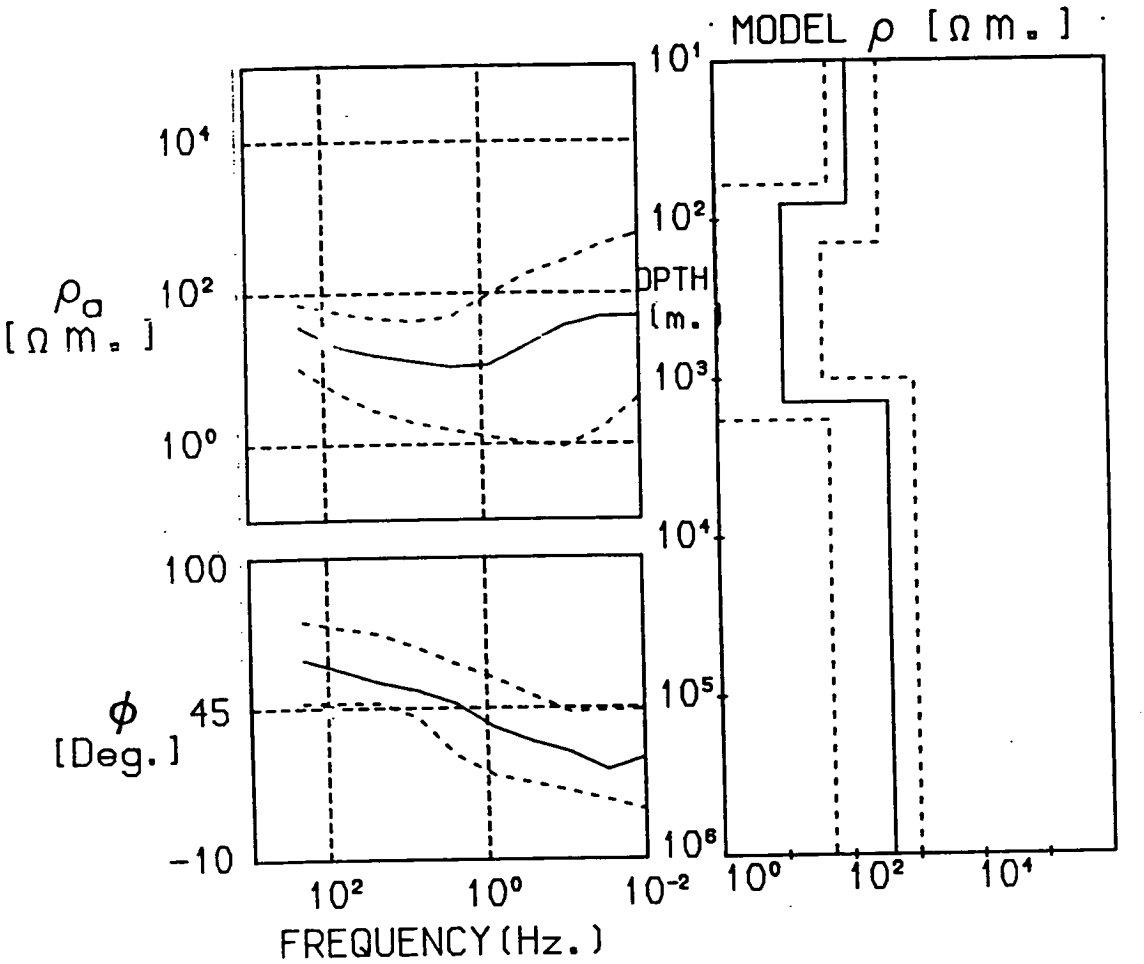

Figure B.12: The MT model to response function program **MTSTRAINT**. If an 'a priori' 3 layer resistor-conductor-resistor 1-D model is specified (right hand panel: solid line) together with some upper and lower bounds (dashed line), then this program will compute a forward model and response function for all combinations of the model parameters. The output is given in terms of its most likely apparent resistivity and phase response (solid line in left hand panel) and estimated 'error' bounds (dashed lines)

B.XIII. ZRNTRANS

This program converts elements of the unrotated or rotated impedance tensor and their errors, over a range of frequencies, into the corresponding apparent resistivity and phase. These are written out for modelling/interpretational purposes or translated into a format appropriate for the plotting routine **RNPLOT**.

B.XIV. RNPLOT

This computer file contains all the instructions for plotting the Earth response functions and a 1-D model by **EASYGRAPH**, an Edinburgh (Multi Access System) graphics package. A second graphics file containing graph labels (generated by a computer package called **NOTICE**), is superimposed on the first, prior to display and generation of a hardcopy.

B.XV Programs for Modelling Geophysical Response Functions

The following 2 basic adaptations were made to the MT response function modelling program (**MTINV**) originally developed by Meju (1988):

1. The determination of a global minimum misfit, 1-D MT and/or D.C. resistivity model and an exploration of its degree of uniqueness (section 6.4.3).

2. The inversion of a number of adjacent M.T./D.C. soundings and/or a traverse of gravity anomaly values. This adaptation also incorporated optional interactive modelling using a model/response visual display, manual model intervention and robust down-weighting of outliers (sections 6.4.6 to 6.4.10).

These adaptations share a common solution to their respective non-linear inverse problem. This involves a model linearization around some starting values followed by iterative refinement by computing parameter correction values using ridge regression (section 5.7.3). **MTINV** has been fully discussed by Meju (1988) and he has also demonstrated the methods' capabilities for recovering a synthetic, 1-D MT model. A simplified summary of the subprogram, **RDGSOLVE**, which is relevant to this study, is given by fig. B.13.

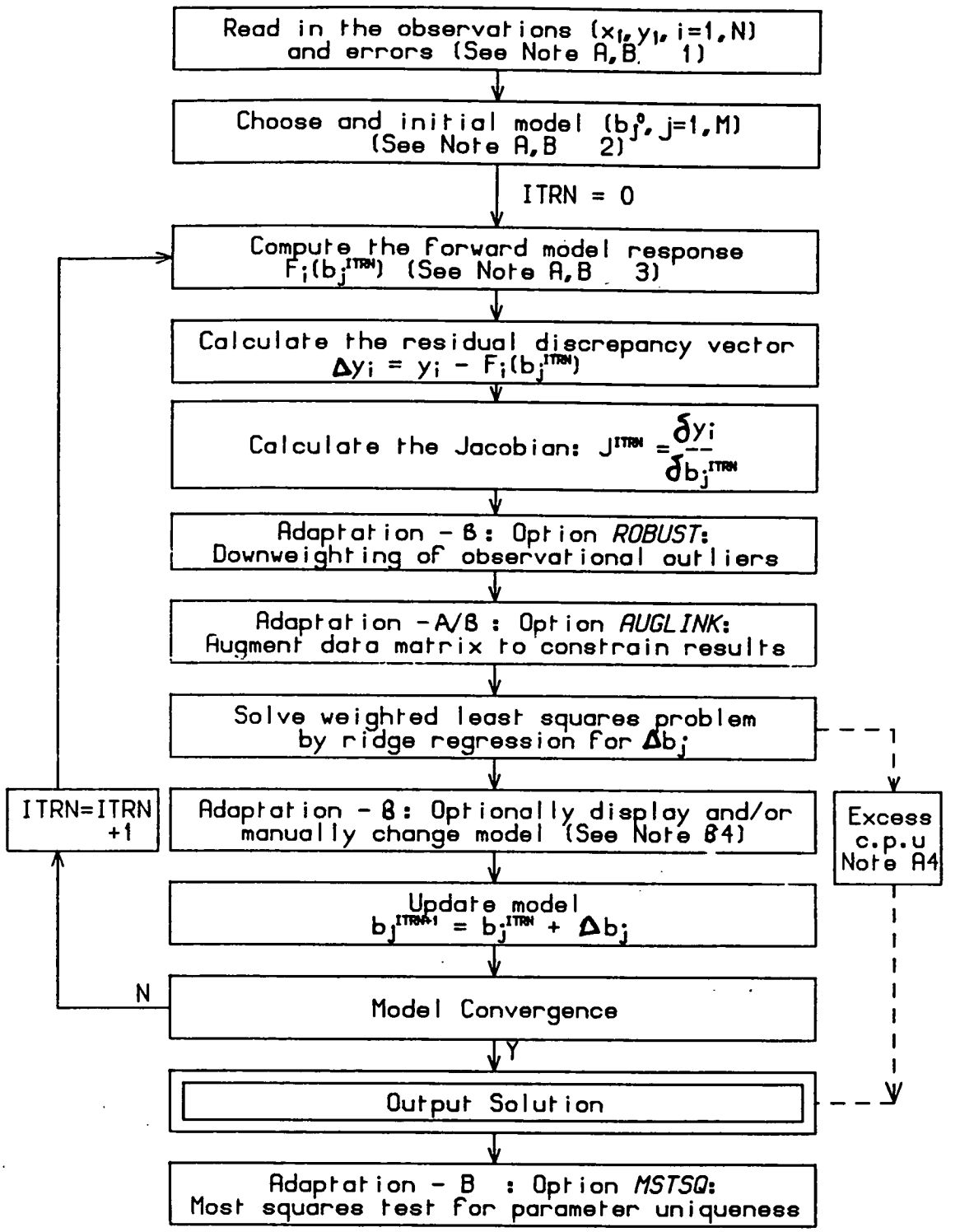

Figure B.13: The steps involved in the program **RDGSOLVE**, which performs linearized model inversion for exploratory 1-D and pseudo 2-D modelling.

B.XVI. Exploratory Modelling; MAXMUL

This suite of programs was used to compute an exploratory (section 6.4.3) 1-D block model from MT, and when appropriate, jointly from D.C. resistivity observations. The five stage procedure commences by the generation of a number of random and therefore relatively unbiased parametric starting models (c.f. Monte-Carlo method: section 6.2.3) which are then tested and their parameter values enhanced by **MTINV**. From the set of resulting refined models, the one with the smallest misfit is taken to be the optimum solution, whilst a number of models with misfits close to the minimum are used to explore the degree of individual parameter resolution. Ideally, those models which have misfits (section 4.6.1) which are within some confidence limits (e.g. 95%; section 4.3.4) are retained. In practice the estimated impedance error was not well enough determined to undertake this and consequently this author only used the misfit as a relative indicator of model acceptability.

The steps involved in **MAXMUL** are as follows:

1. **MAXCRT**: a) takes an arbitrary NR layered model (usually of constant resistivity equal to the average apparent resistivity at equally spaced LOG10(depths)), b) generates all the instructions for approximately 20 runs of **MTINV** and then c) randomizes the layer resistivities for each of these input models. Depth randomization was unnecessary because **MTINV** finds the most appropriate depth parameter values at the same time as optimizing the resistivity structure.

2. **MAXCRT** is then re-run for other values of NR.

3. Executes the instruction file which initiates **RDGSOLVE**.

Note A1: The input MT observations are apparent resistivity and/or phase estimates over a frequency range. The D.C. resistivity observations consist of a number of measurements of the apparent resistivity over increasing half-spread distance (AB/2) using a Schlumberger array (section 3.3). Ideally, these are equally spaced on a log scale, but the forward modelling routine used is, if necessary, able to interpolate the acquired measurements to the required constant spacing. In order that neither data set dominates the results, the MT impedances are scaled by their calculated errors (c.f. section 5.5) and the D.C. resistivity measurements by an estimate of their observational error.

Note A2: The model is an NR layered resistivity/depth section generated by **MAXCRT**. The D.C. resistivity forward modelling routine could however only compute the response of the top 5 of these layers.

As an alternative to a discontinuous parameterization, a smoothly varying 'Occam' type model (section 6.2.5) can be defined. In this, the layer depths are constants and the resistivities are automatically set up from either the results of a preliminary Bostick transform (MT; section 6.2.2) and/or derived from the local average of the D.C. apparent resistivities. Since, this is an underdetermined problem in which the large number of parameters cannot be properly resolved using either or both sets of observations, a subroutine (**AUGLINK**; see also **MAXMAY**) was used to augment constraining 'observations' (section 5.7.4) onto the data matrices.

Since the model resistivities and depths vary over several orders of magnitude (c.f. section 6.2.4), all the 2.(NR-1)+1 parameters were transformed onto the more natural LOG (base 10) scale by **RDGSOLVE**. Furthermore, this constrains their values to be strictly positive and avoided unphysical solutions.

Note A3: The **FORWD** MT forward modelling routine calculates the theoretical 1-D MT response for the given model (eqn. 2.3.10). D.C resistivity forward modelling is performed using an adapted program (**RESINV88**) whose background is described by O'Neill (1975).

Note A4: Computational efficiency is increased by limiting the number of options used in **MTINV** and imposing a liberal maximum c.p.u. time limit for each trial model.

MTOPLOT2: Collates all the acceptable model solutions and determines the best fitting solution and its nearest 6-10 neighbours.

RNPLOT: Plots the selected models and their response functions.

Figure B.14 shows an example of 6 random input models generated by **MAXCRT** and 2 resulting models which achieved a small misfit. All of the 1-D models given in Appendix - C were the result of the application of **MAXMUL** on real data.

Moderate over-parameterization can be readily identified by considering

Figure B.14: Demonstration of the effectiveness of the exploratory MT modelling program **MAXMUL** on the observed response function from SHW. In this example, 6 random input models were generated (left hand side of fig. B.14a) and compared with the observed (right hand side of fig. B.14a). Applying linearized inversion to each of these in turn, and retaining those with the smallest misfit gives the results shown in fig. B.14b.

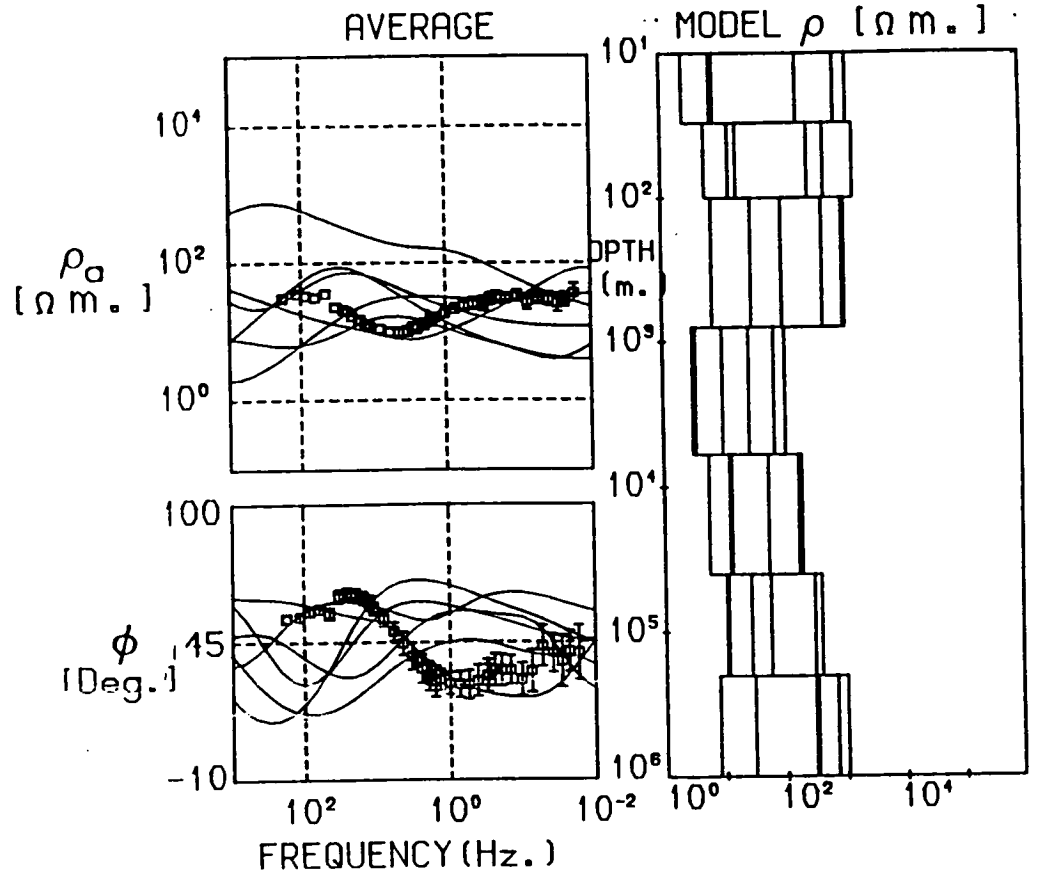
AVERAGE
MODEL ρ [Ω m.]
ρa [Ω m.]
φ [Deg.]
DPTH (m.)
FREQUENCY (Hz.)

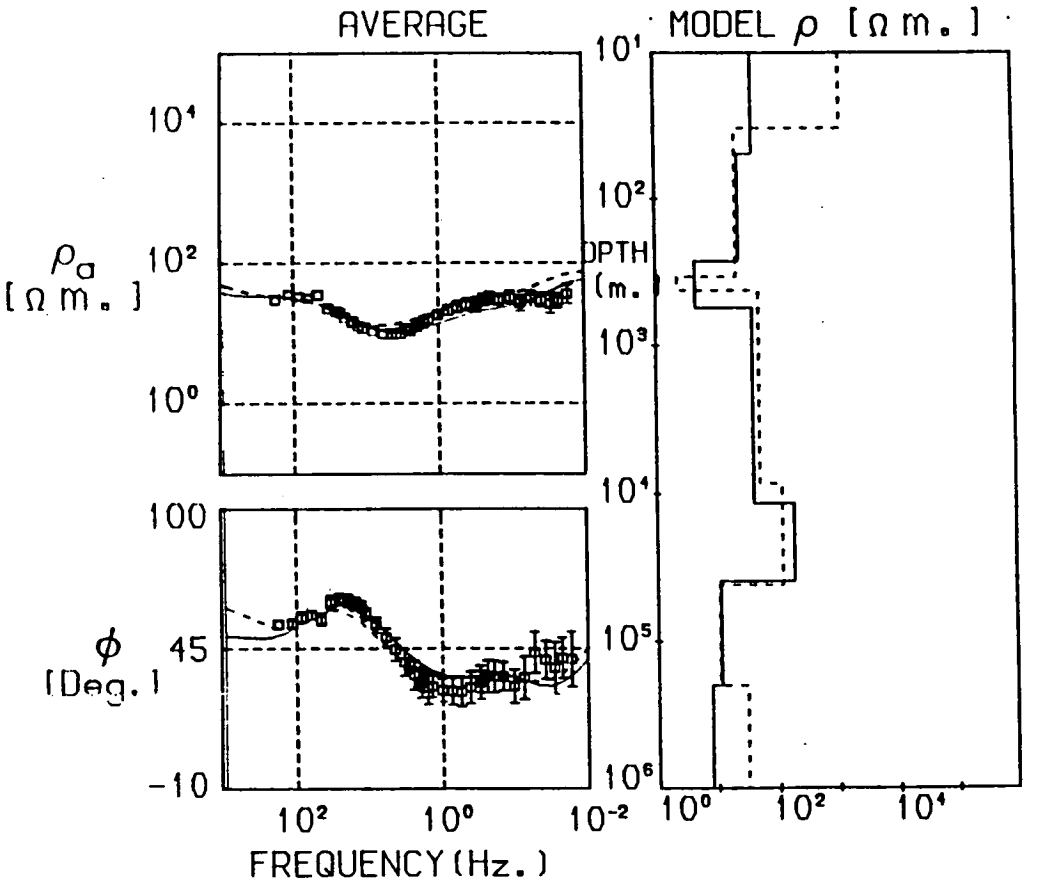
AVERAGE
MODEL ρ [Ω m.]
ρa [Ω m.]
φ [Deg.]
DPTH (m.)
FREQUENCY (Hz.)

the range of resulting models which fit the measurements at particular depths. If the starting model is severely over-parameterized, **MTINV** does not converge to a realizable model, so that models with an excess number of layers do not necessarily produce the global minimum misfit.

Needless to state, the computational cost of **MAXMUL** is greater than any single application of **MTINV** and the range of initial models explored is inevitably finite. In the examples given in Appendix-C, the 1-D response function from each site considered in this study, was typically fitted with 60 trial, 5 to 8 layered models. At a total cost of about 300 c.p.u. seconds, a reasonably extensive range of models could be explored at only moderate effort.

B.XVII. Pseudo 2-D MT / Gravity Modelling: MAXMAY

The aims of this program are the determination of a) a pseudo 2-D geoelectric model which is site-to-site consistent (section 6.4.6), b) a simple 2-D gravity model (section 6.4.8) and c) whenever applicable a joint and constrained inversion of common parameters between (a) and (b) (section 6.4.10). As implementation of these 3 aims is not trivial, **MAXMAY** can currently only be regarded as a crude and cumbersome preliminary attempt to achieve them. Consequently fig. B.13 tries to summarize only the author's major adaptations to **RDGSOLVE** relevant to the aims of **MAXMAY**.

Note B1: Often only a representative sample of the observations is modelled owing to the heavy computational load which would otherwise result.

- M.T./D.C.: same as Note A1, except that the response functions from up to 5 sites along a traverse are simultaneously modelled. Consecutive application of the method on sets of 5 adjacent response functions allows a composite model to be obtained for the longer traverse.

- Gravity: Bouger anomaly values (in mgals) along a linear traverse.

If, as in this study, the gravity observational errors are unavailable, it is necessary to make an accurate estimate of them in order that a successful joint weighted regression with MT and D.C. resistivity observations can be performed. If for example, the gravity errors are under-estimated, the final joint model will not reflect the EM response functions at all.

Note B2: A considerable reduction in the computational load is achieved by first obtaining the best fitting models for each individual geoelectric site and each geophysical data set, prior to joint modelling.

- M.T./D.C.: same as Note A2, except separate models are specified for up to 5 sites along a traverse.

- Gravity: A 3 layer, 2-D model which comprises:

  * a) A surface layer of variable thickness and lateral extent. This is approximated by NSHALL adjacent blocks whose thicknesses could be altered by parameter regression. All of the blocks in this layer have a uniform density contrast $\Delta\rho_{ab}$ with respect to (b).

  * b) An underlying basement.

  * c) A deep layer of fixed maximum depth, but consisting of NDEEP adjacent blocks, each of variable thickness. Again, this layer has a uniform density contrast $\Delta\rho_{cb}$, with respect to (b).

  Both $\Delta\rho_{ab}$ and $\Delta\rho_{cb}$ are also parameters whose values are automatically fine tuned by regression.

Both these models can be more clearly visualized by inspection of fig. 6.9a.

Since no unique depth information can be gleaned, a gravity model is more ambiguous than its M.T./D.C. resistivity counterparts. The accuracy of the gravity starting model therefore tends to be more critical when calculating parameter correction values. In this study, this starting point is obtained by visual trial-and-error fitting prior to iterative refinement by **RDGSOLVE**. This is facilitated by the modelling package developed by Genc (1989). The blocked model is then passed on to the parameter optimization scheme based on **RDGSOLVE**.

Note B3: MT/D.C. resistivity forward modelling is performed by the method described in note A3. Genc's (1989) interactive gravity modelling program includes a forward modelling subroutine (**TAL**) based on the Talwani *et al.* (1959) method for computing the response of a polygonal shaped body.

Note B4: The author found that interactive modelling was beneficial for constrained modelling of geoelectric data and essential for the gravity data. In the former case, common electrical layers from separate sites could be more readily identified and in the latter case it was found to be much simpler to

visually construct a gravity model. Furthermore, the ability to halt the **RDGSOLVE** iterations temporarily, inspect the models and perform some manual model adjustments allowed unrealistic or mis-specified model parameters to be identified and removed.

Near to convergence, joint or individual M.T./D.C. resistivity or gravity modelling was found to benefit from the optional down-weighting of outlying observations using a **ROBUST** (see **ROBEST**) type of scheme. This ensured that the model obtained fitted the observations more closely. If initiated too early, the final model did not seem to reflect any fine geophysical structure but was instead strongly biased towards the starting model.

AUGLINK: This subroutine places constraints on the values that selected parameters can take during the automatic modelling procedure. When 'linking' is performed, the values of the 2 selected parameters are initially set to be the same and equal to their average. They are then allowed to vary during the inversion iterations subject to the constraint 'observations' augmented onto the base of the Jacobian matrix (eqn. 5.7.12). These force the difference between the linked parameter values to be as small as possible.

APPENDIX - C

DETAILED RESULTS OF NORTHERN ENGLAND

FIELD STUDIES

This appendix presents the detailed results obtained from magnetotelluric and where applicable, D.C. resistivity measurements in Northern England. The following table (fig. C.1) gives the site locations, processing codes and source of the data for each MT site. The detailed response functions and 1-D models for each of the sites are then presented.

The results are displayed in 3 formats.

Firstly, the time series EM field variations [data from Harinarayana (1987) and Parr (this study)] were fully processed by the methods described in Appendix - A to give constrained estimates of the:

- Unrotated apparent resistivity (ρ_a) and phase (ϕ) response functions with frequency in the 2 principal orthogonal directions (XY and YX).
- The effective invariant (INVAR.) apparent resistivity and phase computed using eqn. 6.2.3.
- Number (N) of estimates used to calculate the impedance over each frequency sub-band.
- Coherence (COH) between the predicted and observed electric fields (eqn. 2.5.6) in the 2 orthogonal directions prior to robust re-weighting.
- Skew (SKW) (eqn. 2.5.5) computed from all 4 elements of the impedance tensor to give an assessment of the geoelectric structural dimensions.
- Azimuth (AZ; section 2.5.2) angle, around which the impedance tensor was rotated to obtain its major and minor values.
- Set of 1-D geoelectric models (MODEL ρ_a) which have been found to fit the invariant response function using the **MAXMUL** program described in Appendix - B. The solid line represents the best fitting model (minimum χ^2 value), whilst the dashed lines give the range of models with misfit close to this minimum. The computed response function for each model is overlain upon the invariant observations.

Figure C.1: The location, frequency range, altitude and source of the observations for each MT site used in this study. This table consists of the following columns of information:

- Processing code number.
- Abbreviated site name.
- Full site name.
- National Grid coordinates (eastings and northings)
- The frequency range of the observations (to the LOG 10 scale)
- Altitude above sea level, in metres.
- Source of the information.

The MT observations from 2 of the sites (EDG II and ROO III) were collected during 2 different field seasons but were processed together.

PROC. CODE NO.	ABBRVD. NAME	SITE NAME	NAT. GRID EAST	COORDS. NORTH	FREQ. RANGE (log10)	ALT. (m.)	SOURCE
004	BEAM A	SITE "A"	33650	60890	-1→-4	230	B
608	ESK	ESKDALEMUIR	32360	60260	2→-2	300	H
502	CWR	CAREWOODRIG	34355	59760	2→-2	340	H
005	BEAM B	SITE "B"	38040	59510	-1→-4	340	B
009	BOR I	BORELAND	31515	59290	-1→-3	230	J
861	LHR	LONGHORSELY	41444	59255	-2→-1	100	P
501	NEW II	NEWCASTLETON	34840	58925	2→-2	120	H
008	NEW I	NEWCASTLETON	34980	58925	-1→-3	120	J
605	KSF	KERSHOPEFOOT	34830	58450	2→ 0	150	H
505	BEW	BEWCASTLE	35510	57630	2→-2	180	H
506	LAM II	LAMPERT	36850	57455	2→-2	250	H
117	LAM I	LAMPERT	36810	57440	3→1,-1→-3	240	N
006	BEAM C	SITE "C"	37850	57360	-1→-4	300	B
509	GIB	GIBSTOWN	34830	57240	2→ 0	100	H
757	SMN	SIMONBURN	38560	57300	2→-2	200	P
161	UPT	UPPERTOWN	38660	57220	3→ 1	230	N
507/606	EDG II	EDGES GREEN	37250	56910	2→-2	230	H
120	EDG I	EDGES GREEN	37233	56867	3→1,-1→-3	210	N
756	GDN	GRINDON MILL	38020	56875	2→-2	240	P
755	MWD	MORWOOD	37875	56690	2→-2	250	P
007	TOW	TOWHOUSE	37640	56370	-1→-3	100	J
754	SHW	SHAWS	37835	56330	2→-2	160	P
753	RDY	RIDLEY COMMON	37785	56230	2→-2	250	P
508	WHI II	WHITFIELD	37785	56062	2→-2	240	H
119	WHI I	WHITFIELD	37788	56049	3→1,-1→-3	240	N
160	LLW	LINNEL WOOD	39540	56015	3→ 0	130	N
751	DBK	DODD BANK	37915	55945	2→-2	240	P
003	BEAM 3	SITE "3"	40590	55800	-1→-4	110	B
750	HGN	HOLLINGREEN	38010	55545	2→-2	360	P
162	HXC	HEXHAMSHIRE COM.	38850	55390	3→ 0	330	N
159	DWT	DERWENT	39945	55412	3→ 0	310	N
752	CHM	CHIMNEYS	38080	55315	2→-2	470	P
163	BLD	BLANCHLAND	39500	55280	2→ 0	390	N
116	SIN I	SINDERHOPE	38500	55200	3→1,-1→-3	330	N
604	SIN II	SINDERHOPE	38300	55130	2→-2	320	H
113	SWI I	SWINHOPE	38440	54800	3→1,-1→-3	370	N
002	BEAM 2	SITE "2"	37850	54360	-1→-4	470	B
115	ROO II	ROOKHOPE	39295	54410	3→ 0	450	N
112	ROO I	ROOKHOPE	39025	54240	3→1,-1→-3	450	N
511/603	ROO III	ROOKHOPE	39175	54200	2→-2	450	H
512	HIL II	HILLEND	40110	53560	2→-2	240	H
118	HIL I	HILLEND	40120	53548	3→1,-1→-3	240	N

Abbreviations: H = Harinarayana (1987), J = Jones and Hutton (1979b), N = Novak (1981), B = Beamish (1986), P = Parr (previously unpublished).

Secondly, for all other published data sets, the 'manually transcribed' apparent resistivity and phase response functions (section 3.5.2) are shown for the rotated major and minor directions. The computed average of these values approximates to the invariant in simple geoelectric environments (c.f. eqn. 6.2.2) and has thus been used for modelling purposes.

Thirdly, for those MT sites which were adjacent to D.C. resistivity soundings, an additional diagram is presented which can be used to compare the 1-D model derived solely from MT data (left hand side) with that jointly determined from the MT and D.C. resistivity response functions (right hand side). The observed and computed D.C. resistivity response functions are shown at the bottom of each of the diagram and plotted as functions of the half spread length (AB/2; c.f. fig. 2.3).

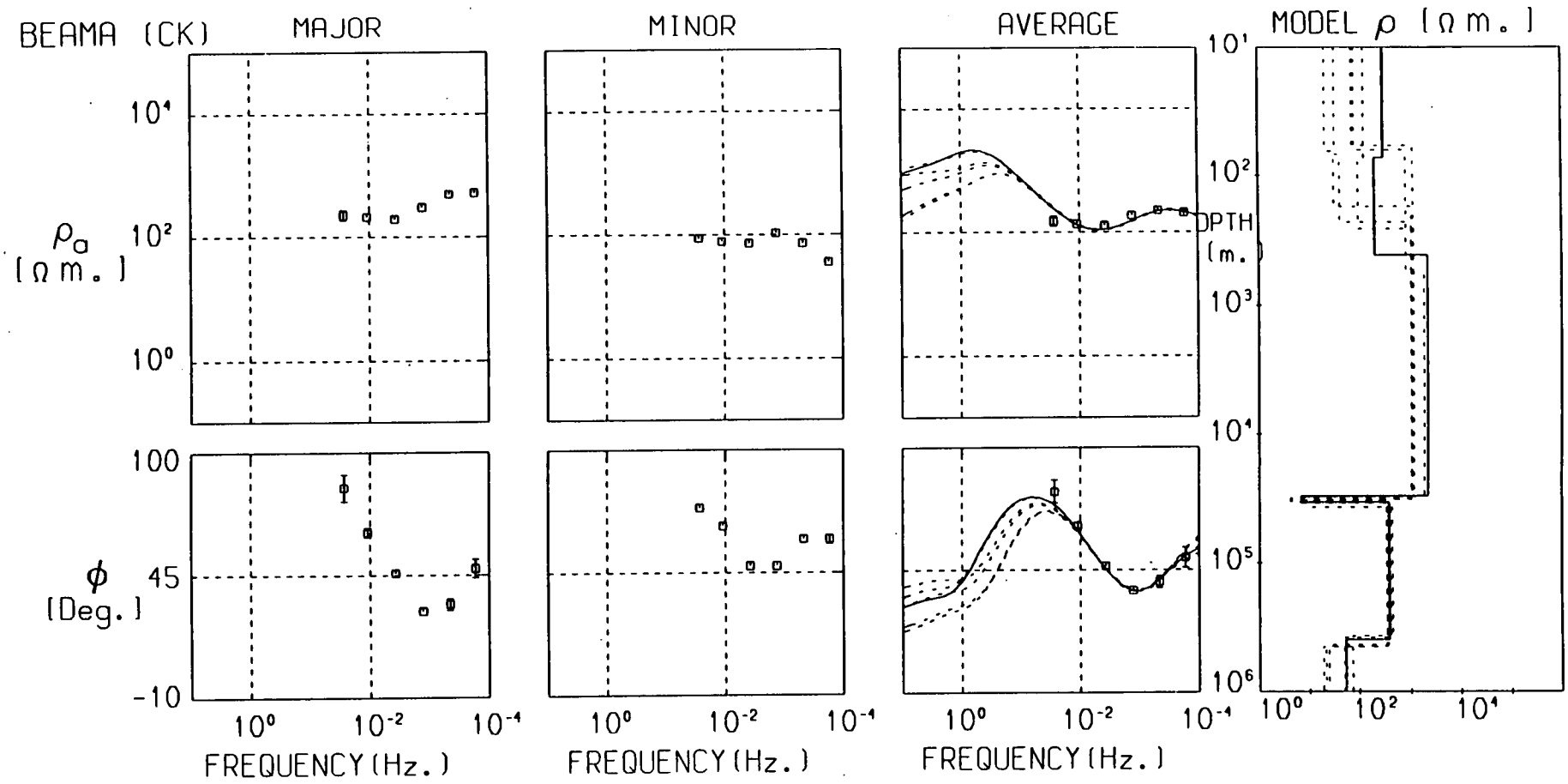
BEAMA (CK)
MAJOR
MINOR
AVERAGE
MODEL ρ [Ω m.]
ρ_a [Ω m.]
10^4
10^2
10^0
ϕ [Deg.]
100
45
-10
10^0
10^{-2}
10^{-4}
FREQUENCY (Hz.)
10^1
10^2
10^3
10^4
10^5
10^6
DEPTH (m.)

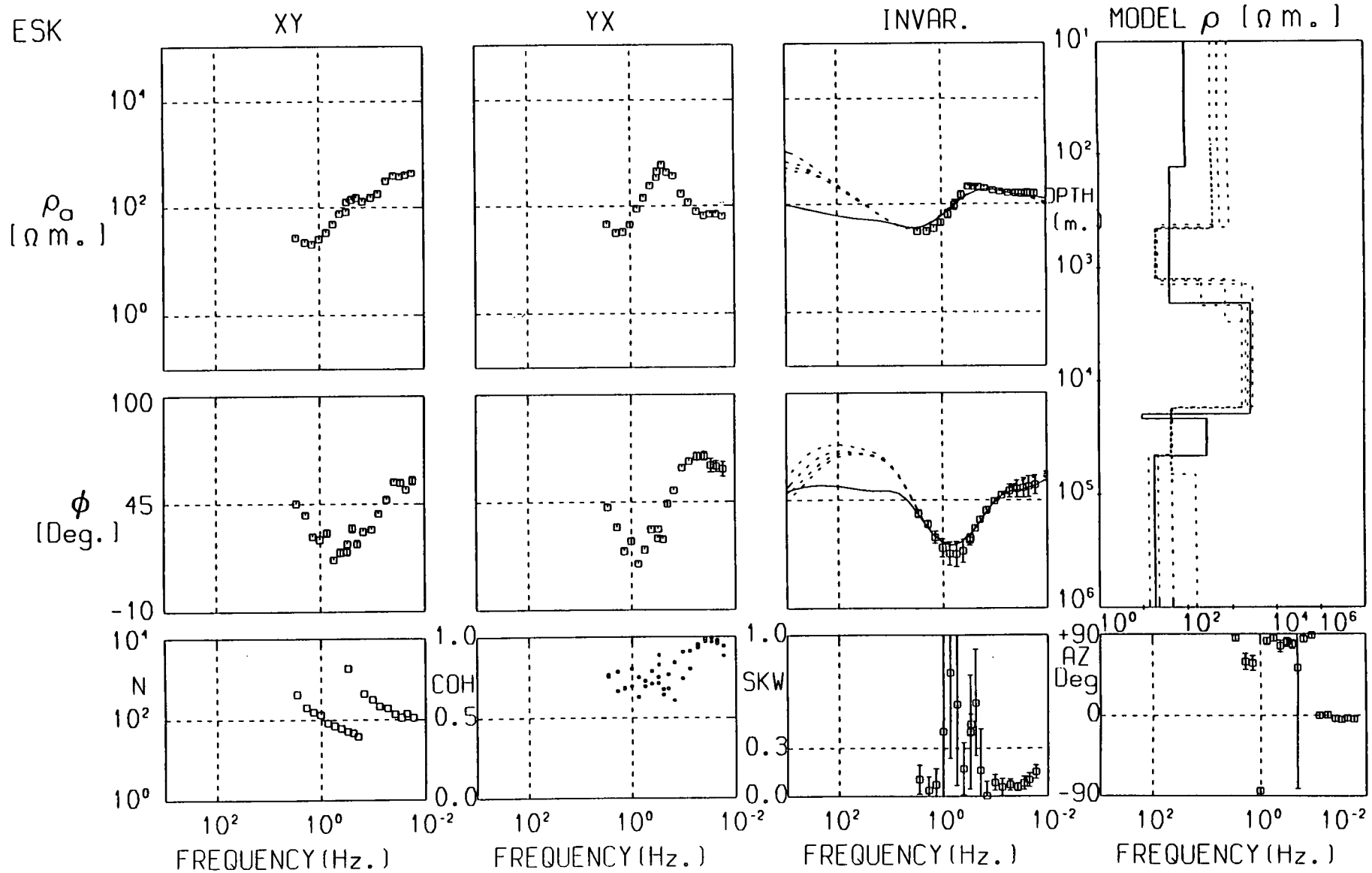
ESK
XY
YX
INVAR.
MODEL ρ [Ω m.]
ρa [Ω m.]
φ [Deg.]
N
COH
SKW
DPTH (m.)
AZ Deg
FREQUENCY (Hz.)
FREQUENCY (Hz.)
FREQUENCY (Hz.)
FREQUENCY (Hz.)

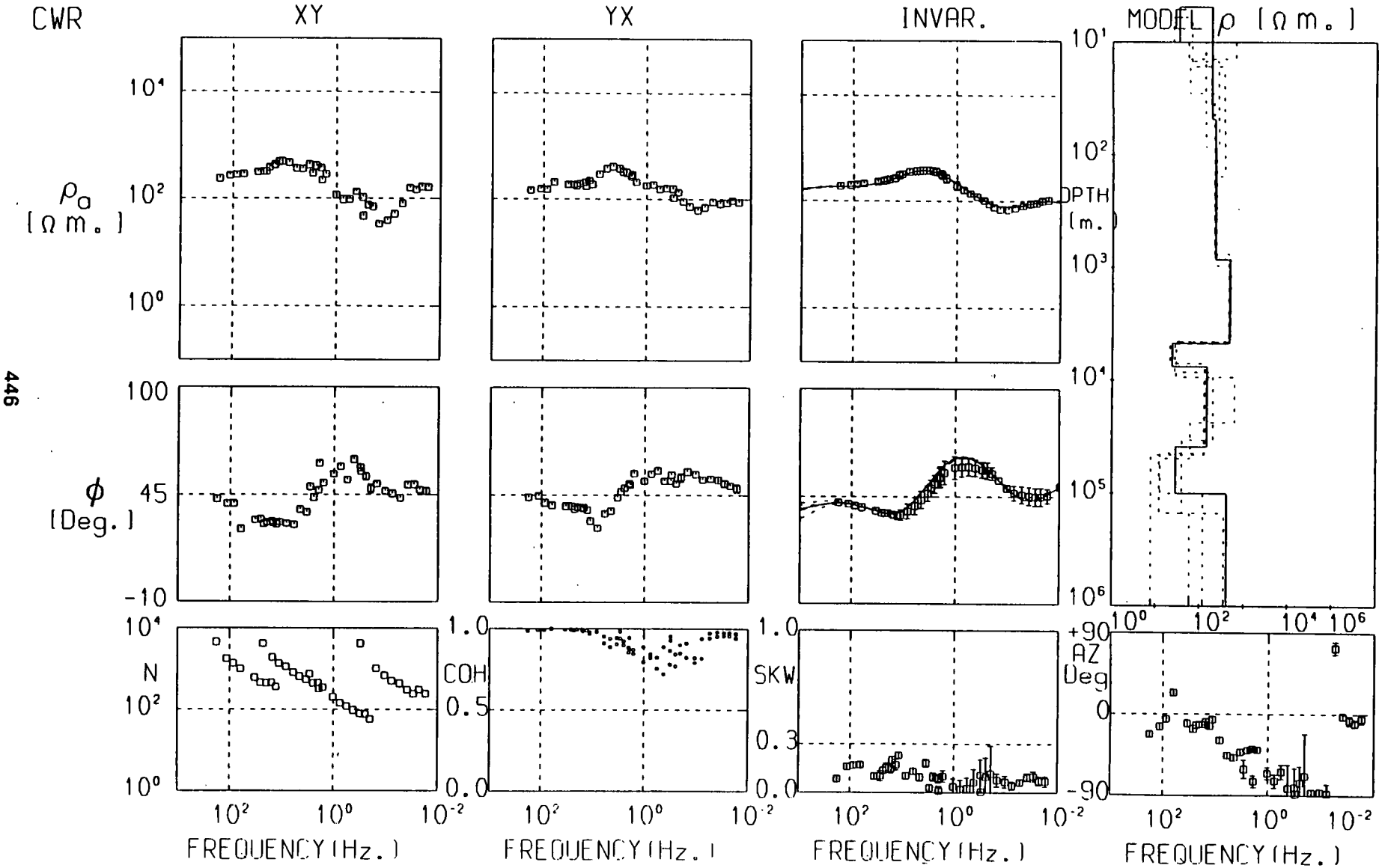
CWR
XY
YX
INVAR.
MODEL ρ [Ω m.]
ρ_a [Ω m.]
10^4
10^2
10^0
ϕ [Deg.]
100
45
-10
N
COH
SKW
1.0
0.5
0.0
0.3
DPTH [m.]
10^1
10^2
10^3
10^4
10^5
10^6
+90
AZ Deg
0
-90
10^2 10^0 10^{-2}
FREQUENCY(Hz.)

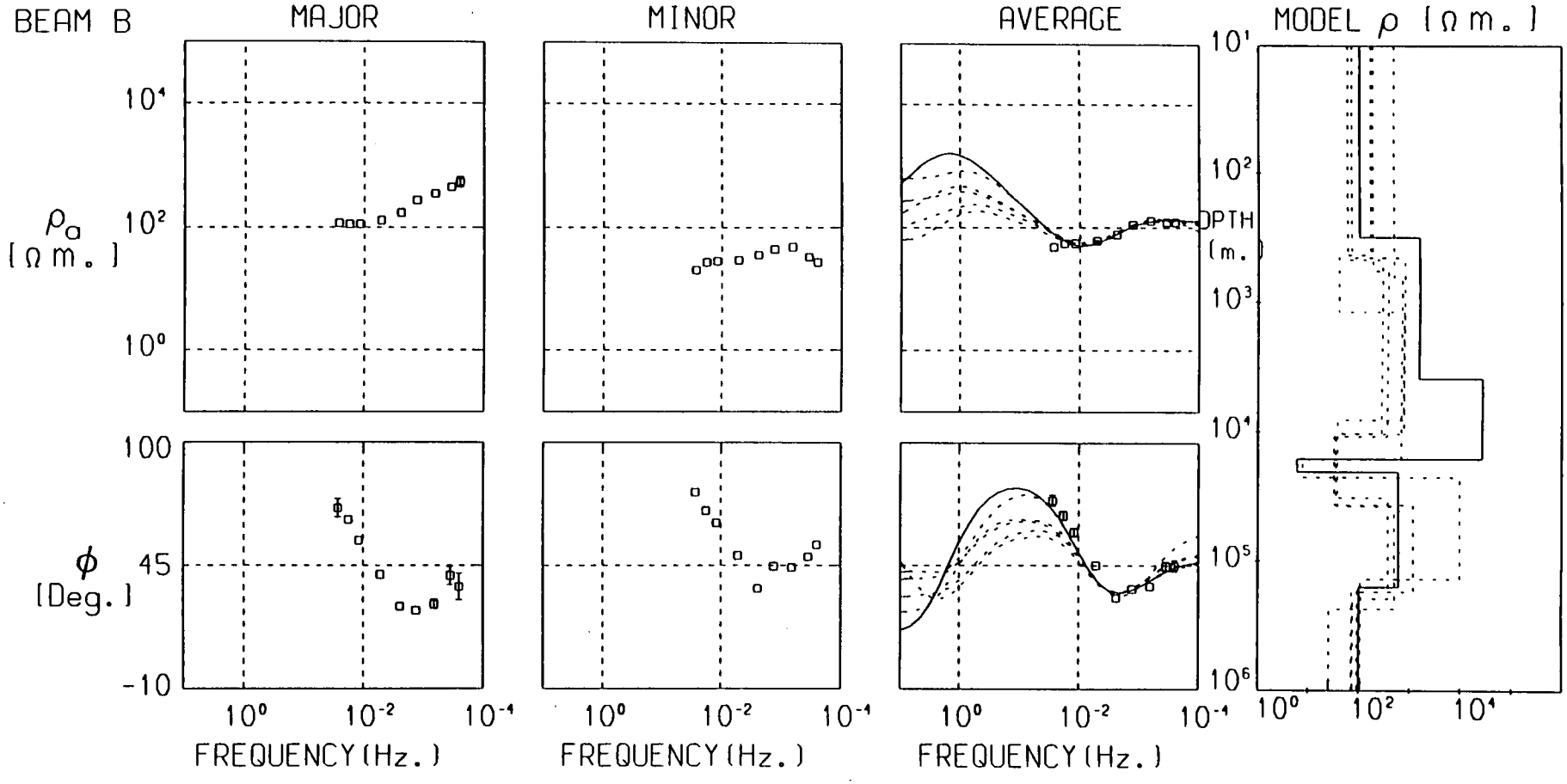
BEAM B
MAJOR
MINOR
AVERAGE
MODEL ρ [Ω m.]
ρ_a [Ω m.]
ϕ [Deg.]
10^4
10^2
10^0
100
45
-10
10^0
10^{-2}
10^{-4}
FREQUENCY(Hz.)
10^1
10^2
10^3
10^4
10^5
10^6
DEPTH (m.)

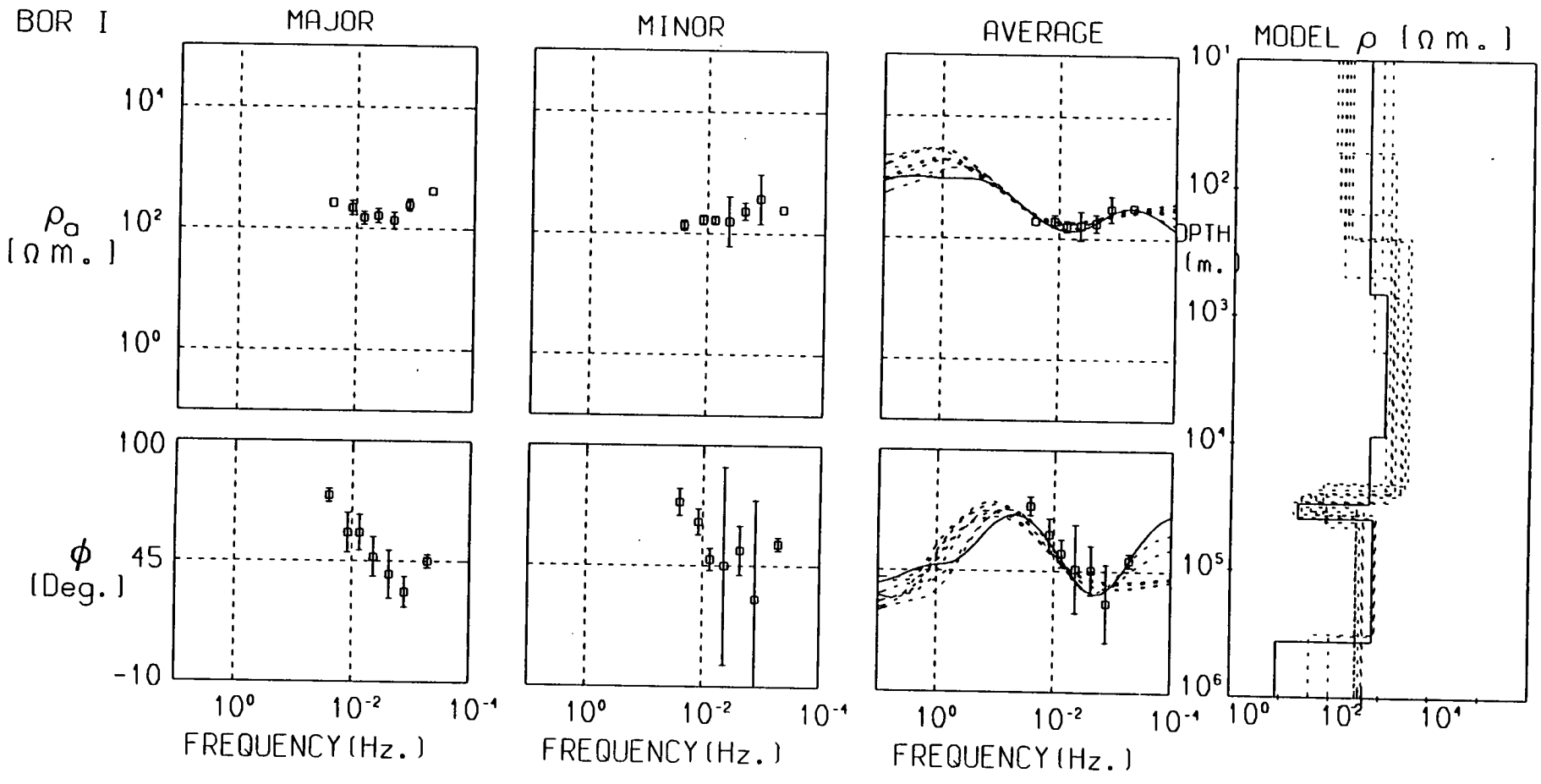
BOR I
MAJOR
MINOR
AVERAGE
MODEL ρ [Ω m.]
ρa [Ω m.]
10⁴
10²
10⁰
100
φ [Deg.]
45
-10
10⁰
10⁻²
10⁻⁴
FREQUENCY (Hz.)
10¹
10²
10³
10⁴
10⁵
10⁶
DEPTH (m.)

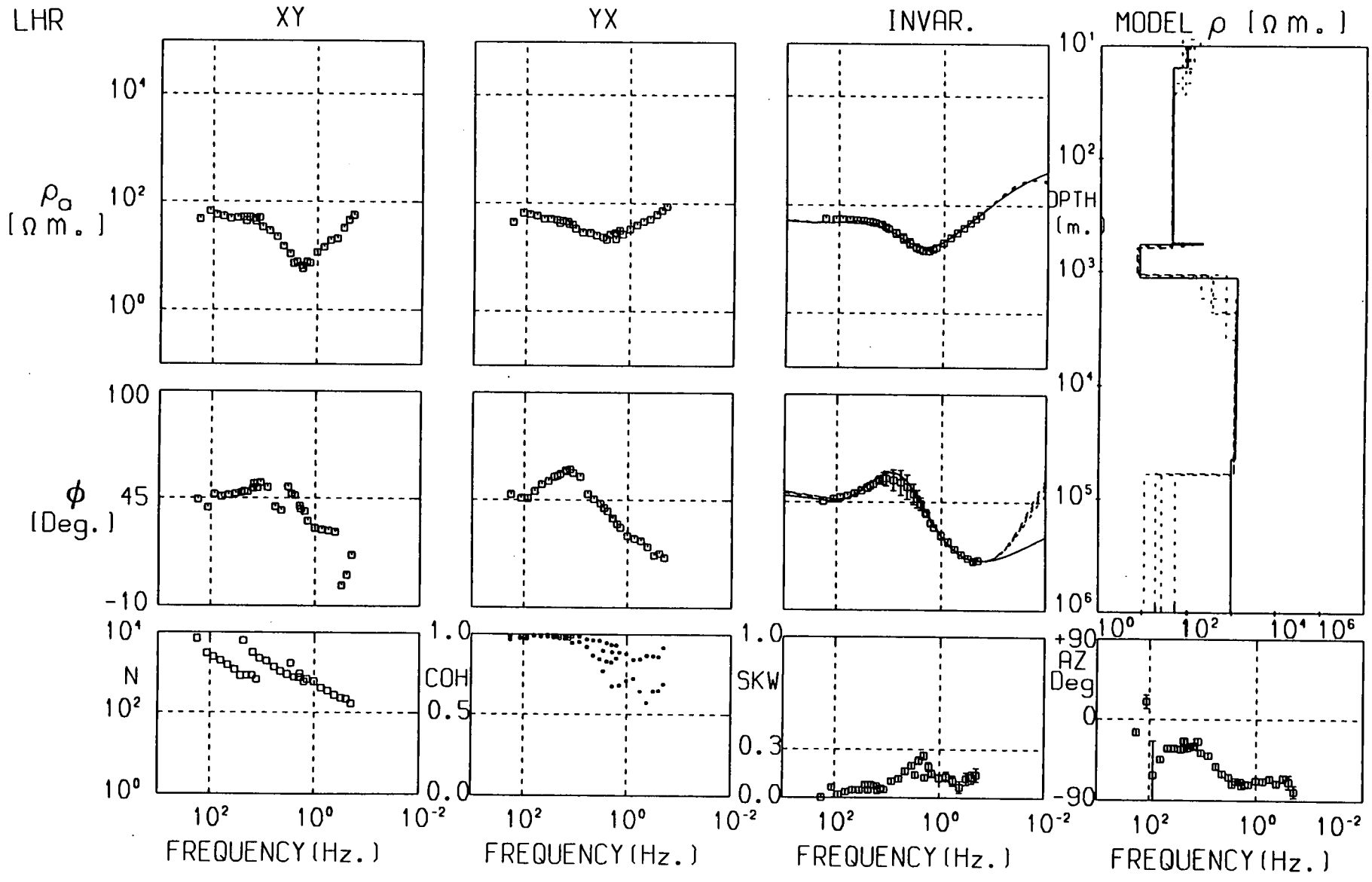
LHR
XY
YX
INVAR.
MODEL ρ [Ω m.]
ρa [Ω m.]
φ [Deg.]
N
COH
SKW
AZ Deg
DPTH (m.)
FREQUENCY (Hz.)
FREQUENCY (Hz.)
FREQUENCY (Hz.)
FREQUENCY (Hz.)

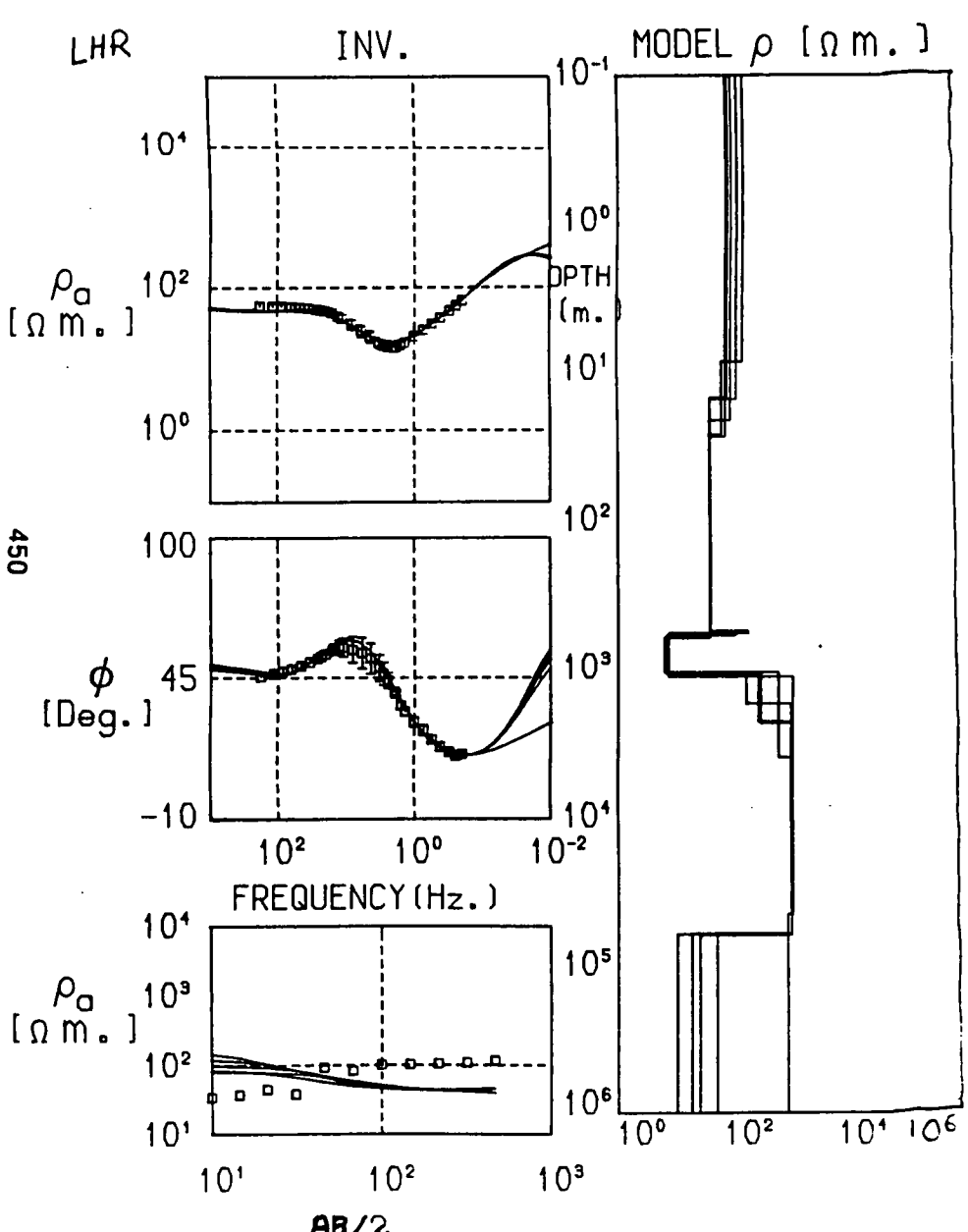
LHR
INV.
MODEL ρ [Ω m.]
ρa [Ω m.]
φ [Deg.]
DPTH (m.)
FREQUENCY (Hz.)
AB/2

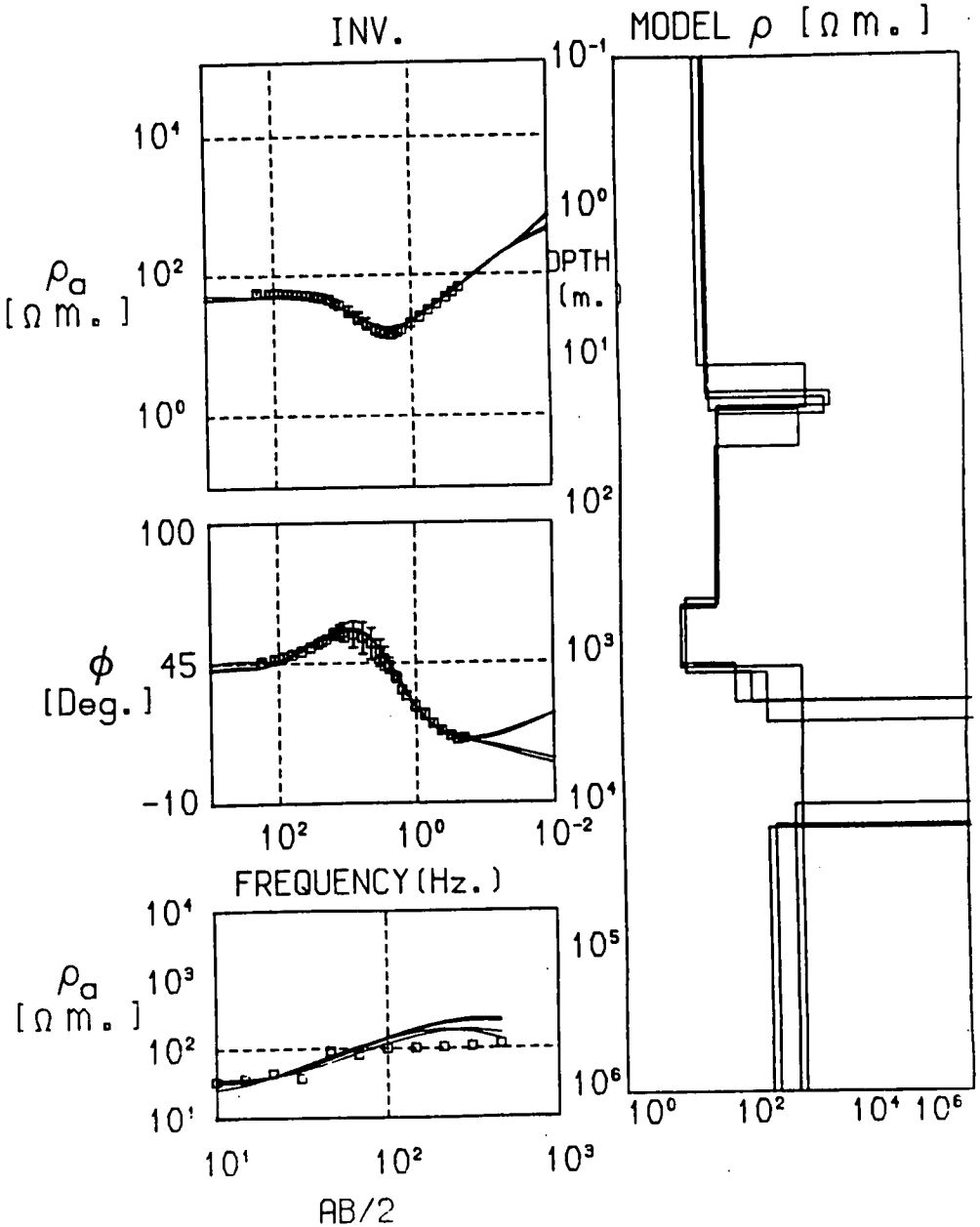
INV.
MODEL ρ [Ω m.]
ρa [Ω m.]
φ [Deg.]
DPTH (m.)
FREQUENCY (Hz.)
AB/2

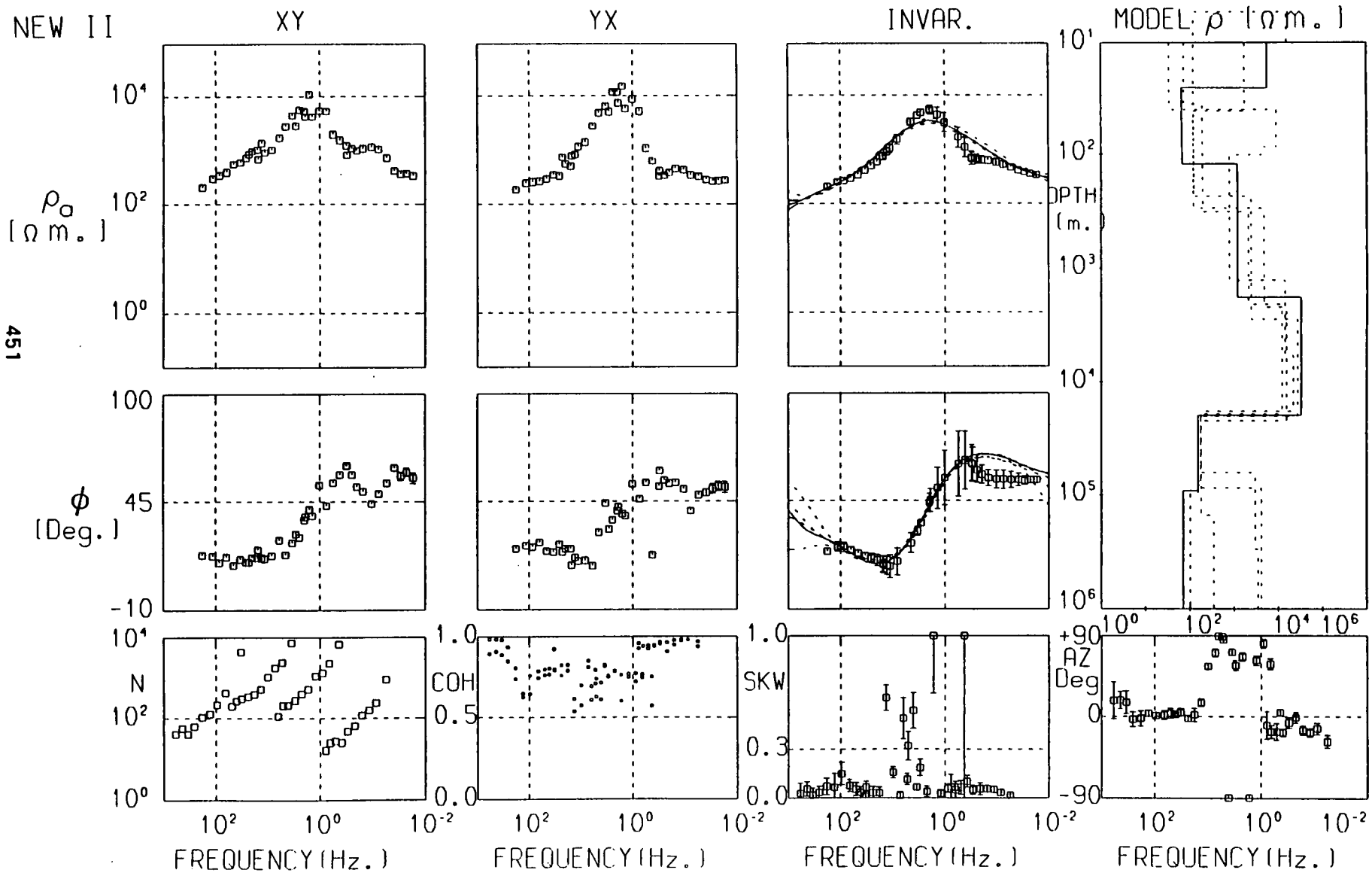
NEW II
XY
YX
INVAR.
MODEL ρ (Ω m.)
ρa (Ω m.)
φ (Deg.)
N
COH
SKW
DPTH (m.)
AZ Deg
FREQUENCY (Hz.)
FREQUENCY (Hz.)
FREQUENCY (Hz.)
FREQUENCY (Hz.)

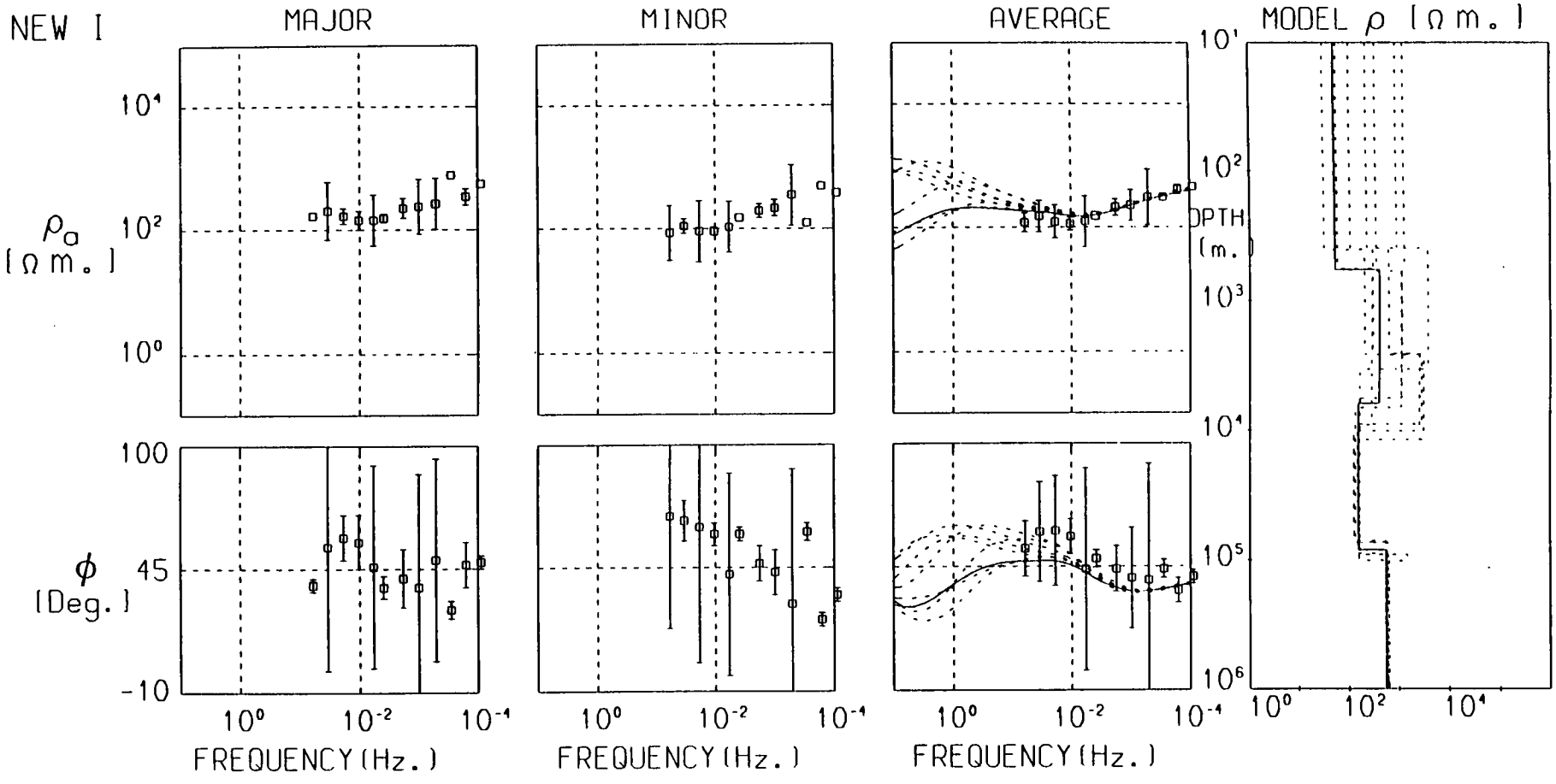
NEW I
MAJOR
MINOR
AVERAGE
MODEL ρ [Ω m.]
ρa [Ω m.]
10⁴
10²
10⁰
100
φ [Deg.]
45
-10
10⁰
10⁻²
10⁻⁴
FREQUENCY(Hz.)
10¹
10²
DPTH (m.)
10³
10⁴
10⁵
10⁶
10⁰
10²
10⁴

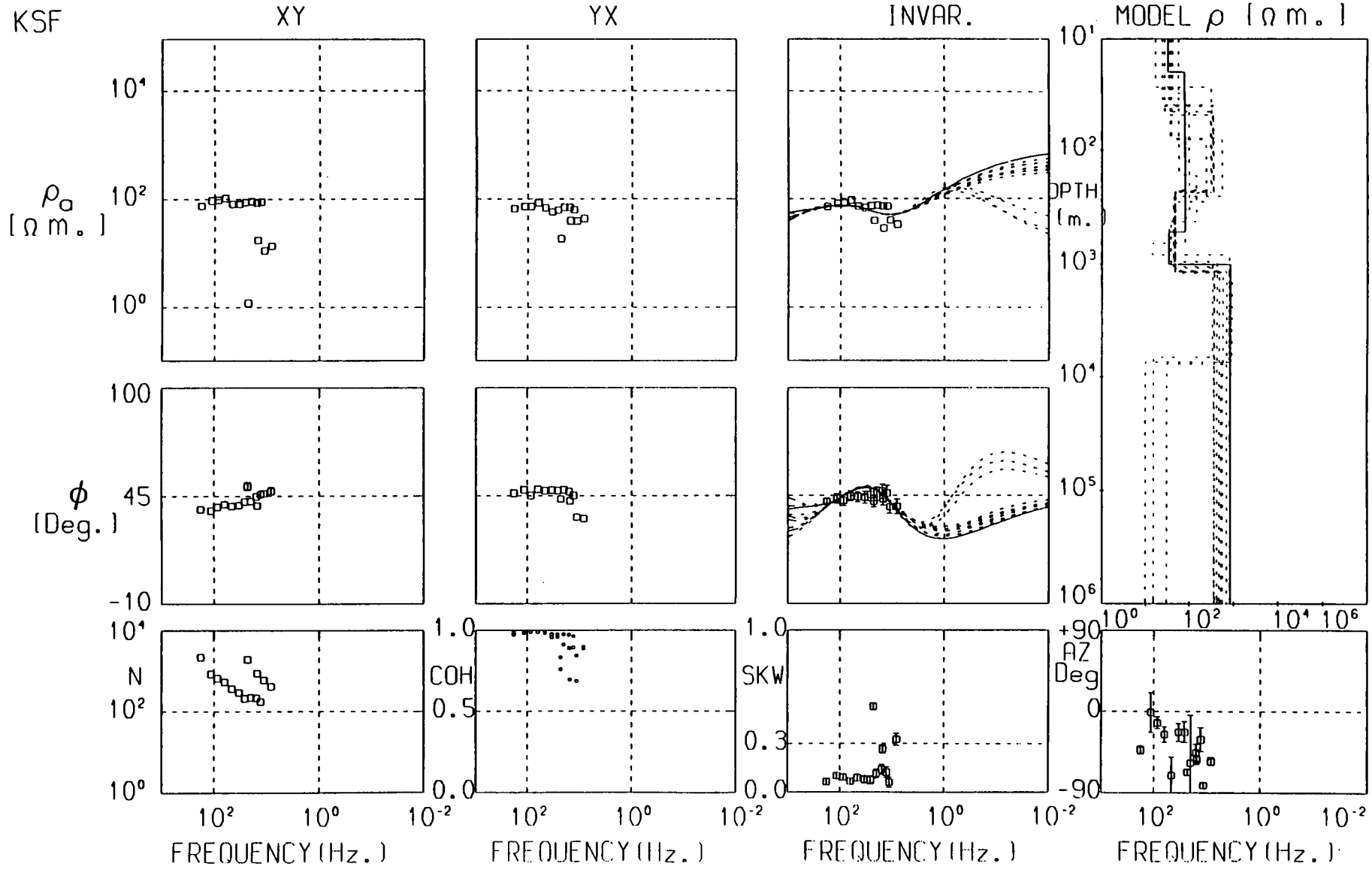
KSF
XY
YX
INVAR.
MODEL ρ [Ω m.]
ρa [Ω m.]
φ [Deg.]
N
COH
SKW
AZ Deg
DPTH (m.)
FREQUENCY (Hz.)
FREQUENCY (Hz.)
FREQUENCY (Hz.)
FREQUENCY (Hz.)

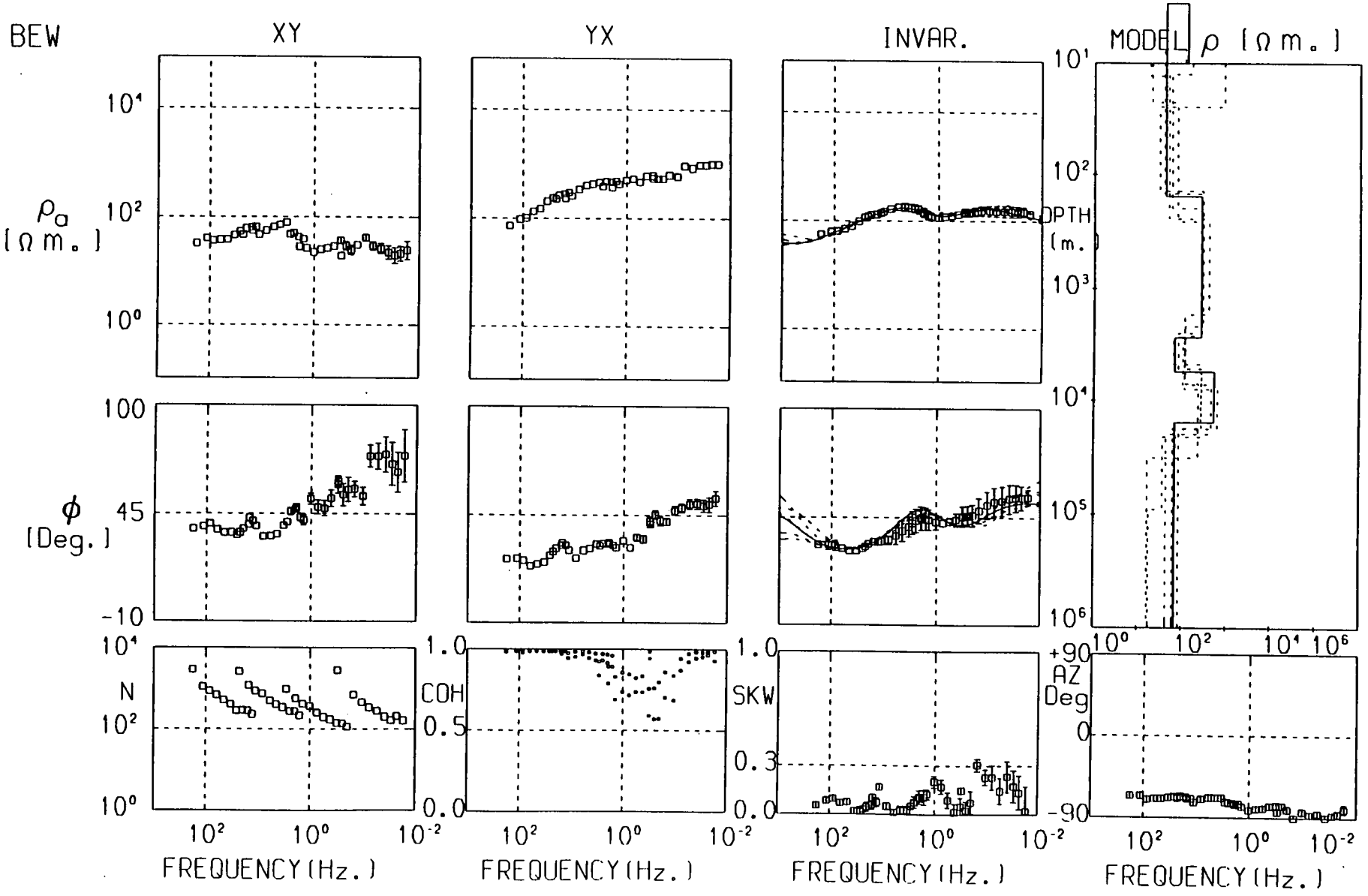
BEW
XY
YX
INVAR.
MODEL ρ (Ω m.)
ρa (Ω m.)
10⁴
10²
10⁰
100
φ (Deg.)
45
-10
N
COH
SKW
1.0
0.5
0.3
0.0
DPTH (m.)
10¹
10²
10³
10⁴
10⁵
10⁶
+90
AZ Deg
0
-90
10² 10⁰ 10⁻²
FREQUENCY (Hz.)

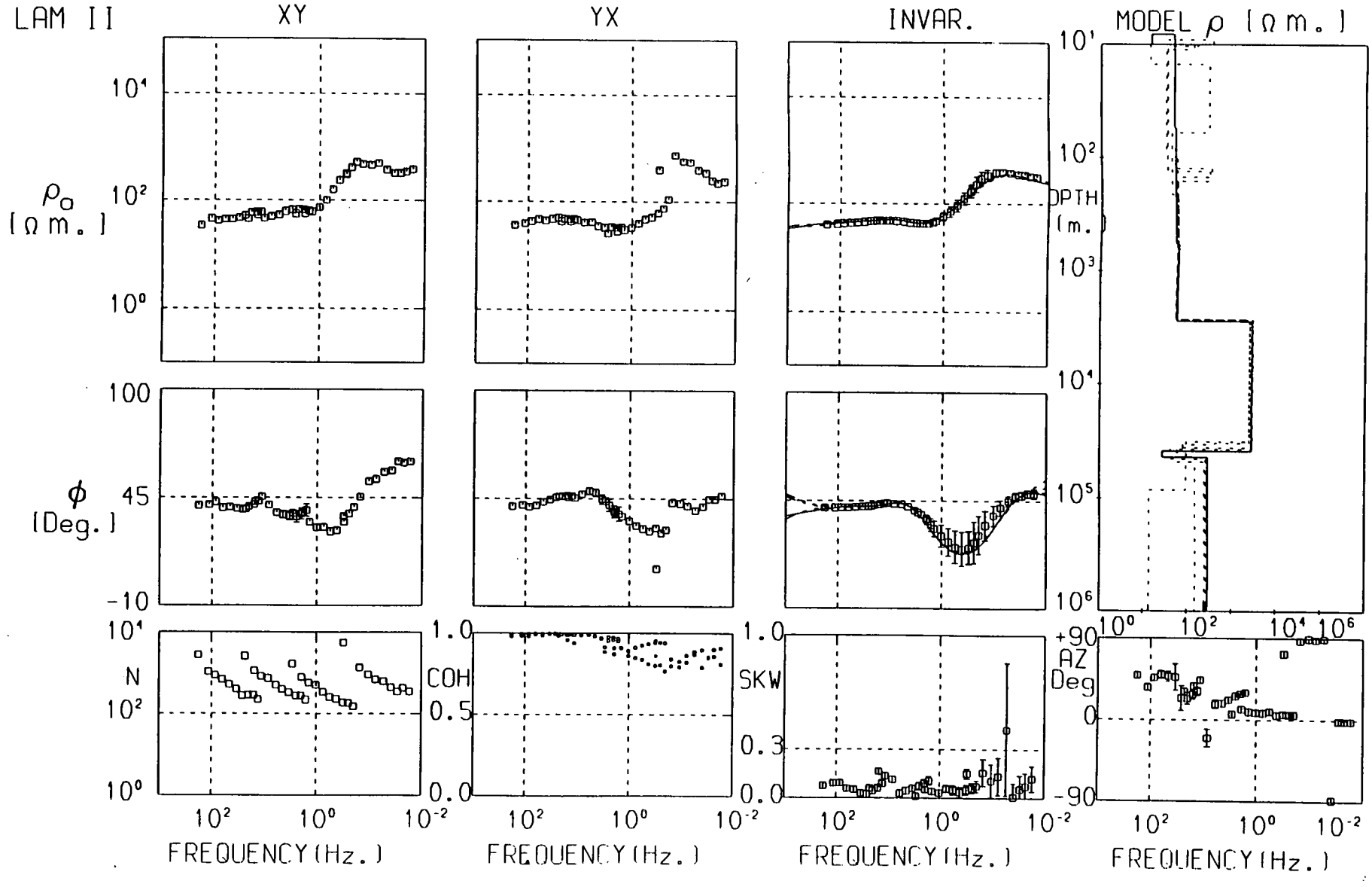
LAM II
XY
YX
INVAR.
MODEL ρ (Ω m.)
ρa (Ω m.)
φ (Deg.)
N
COH
SKW
AZ Deg
DPTH (m.)
FREQUENCY(Hz.)
FREQUENCY(Hz.)
FREQUENCY(Hz.)
FREQUENCY(Hz.)

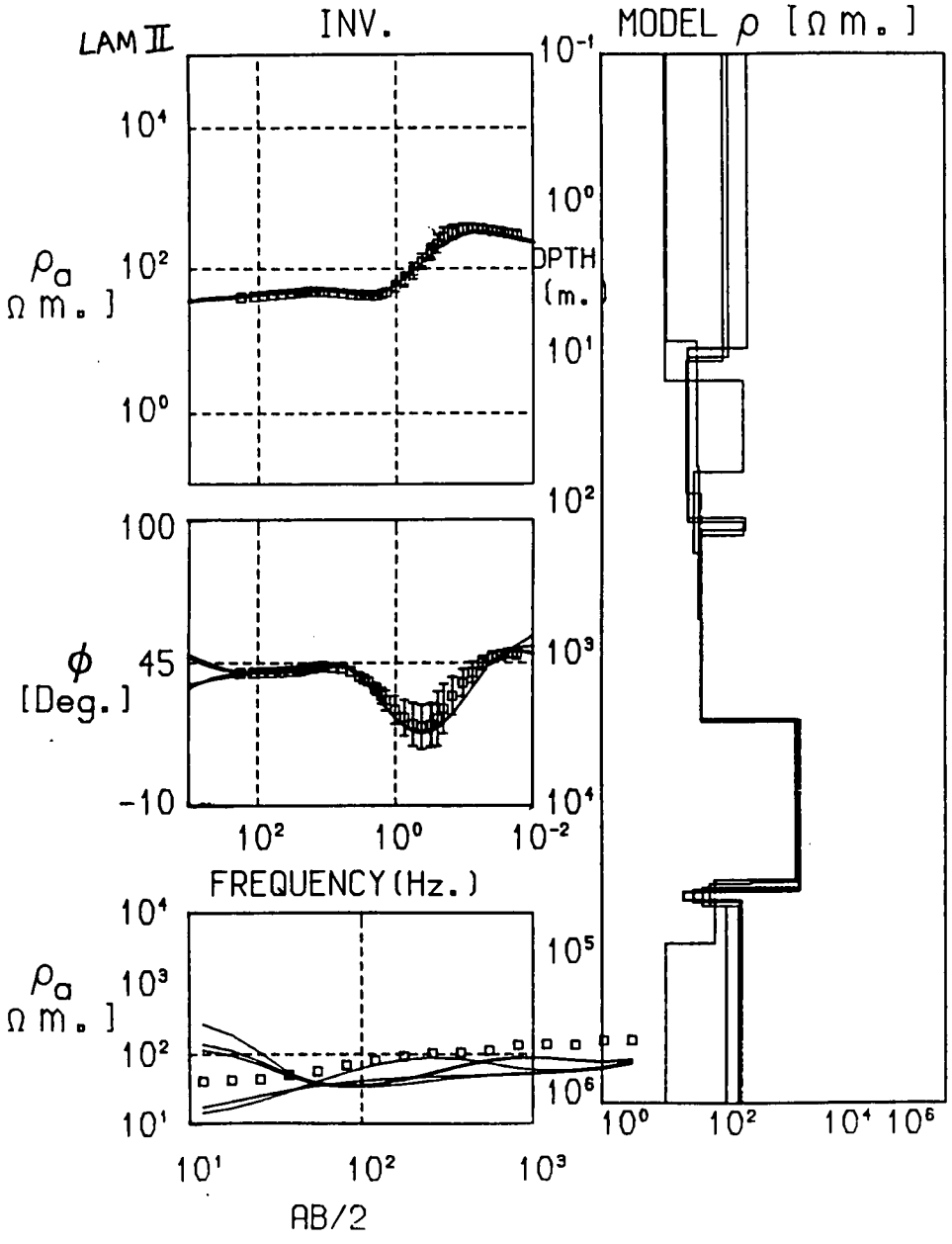
LAM Ⅱ
INV.
MODEL ρ [Ω m.]
ρ_a Ω m.
ϕ [Deg.]
FREQUENCY (Hz.)
AB/2
DPTH (m.)

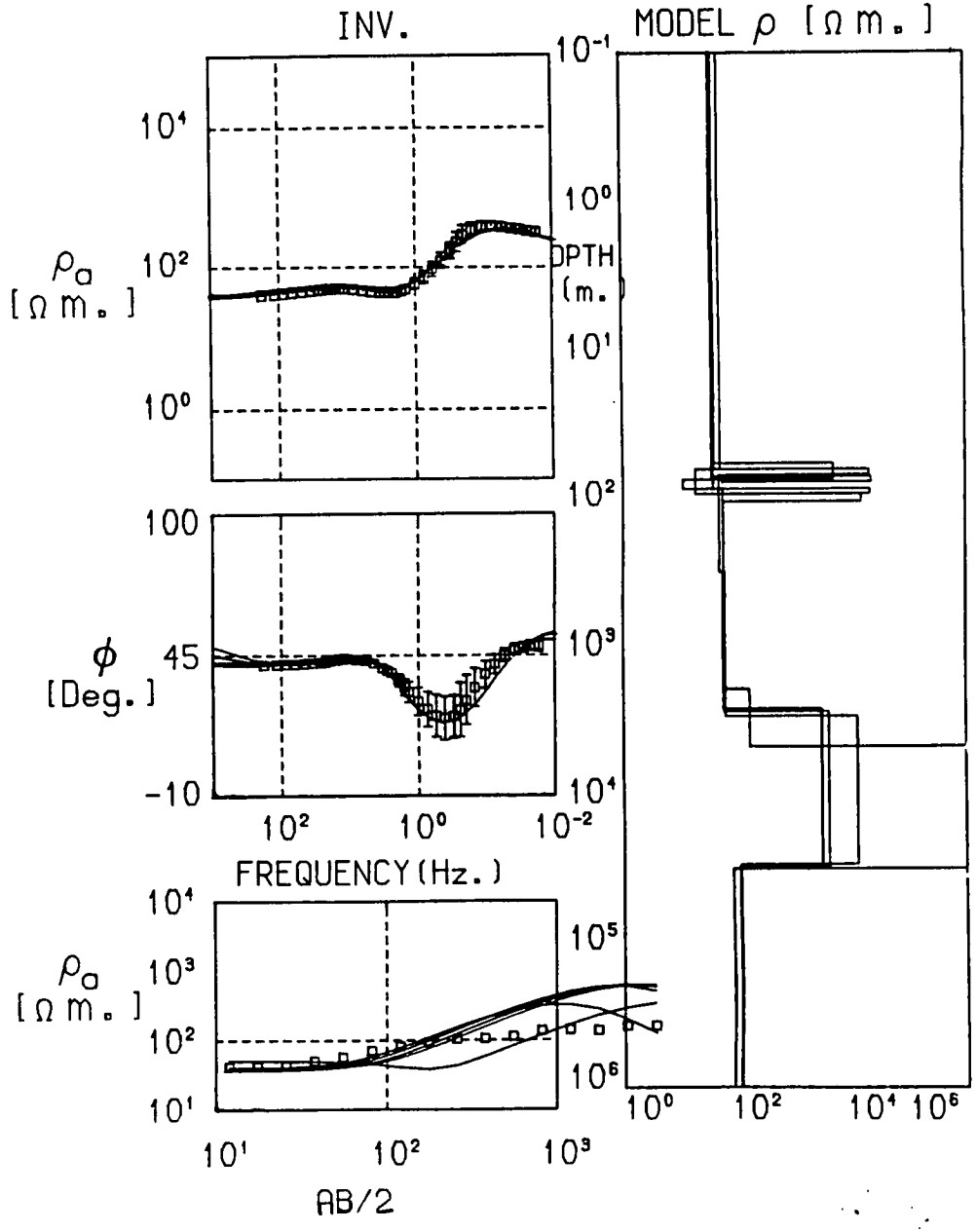
INV.
MODEL ρ [Ω m.]
ρ_a [Ω m.]
ϕ [Deg.]
FREQUENCY (Hz.)
AB/2
DPTH (m.)

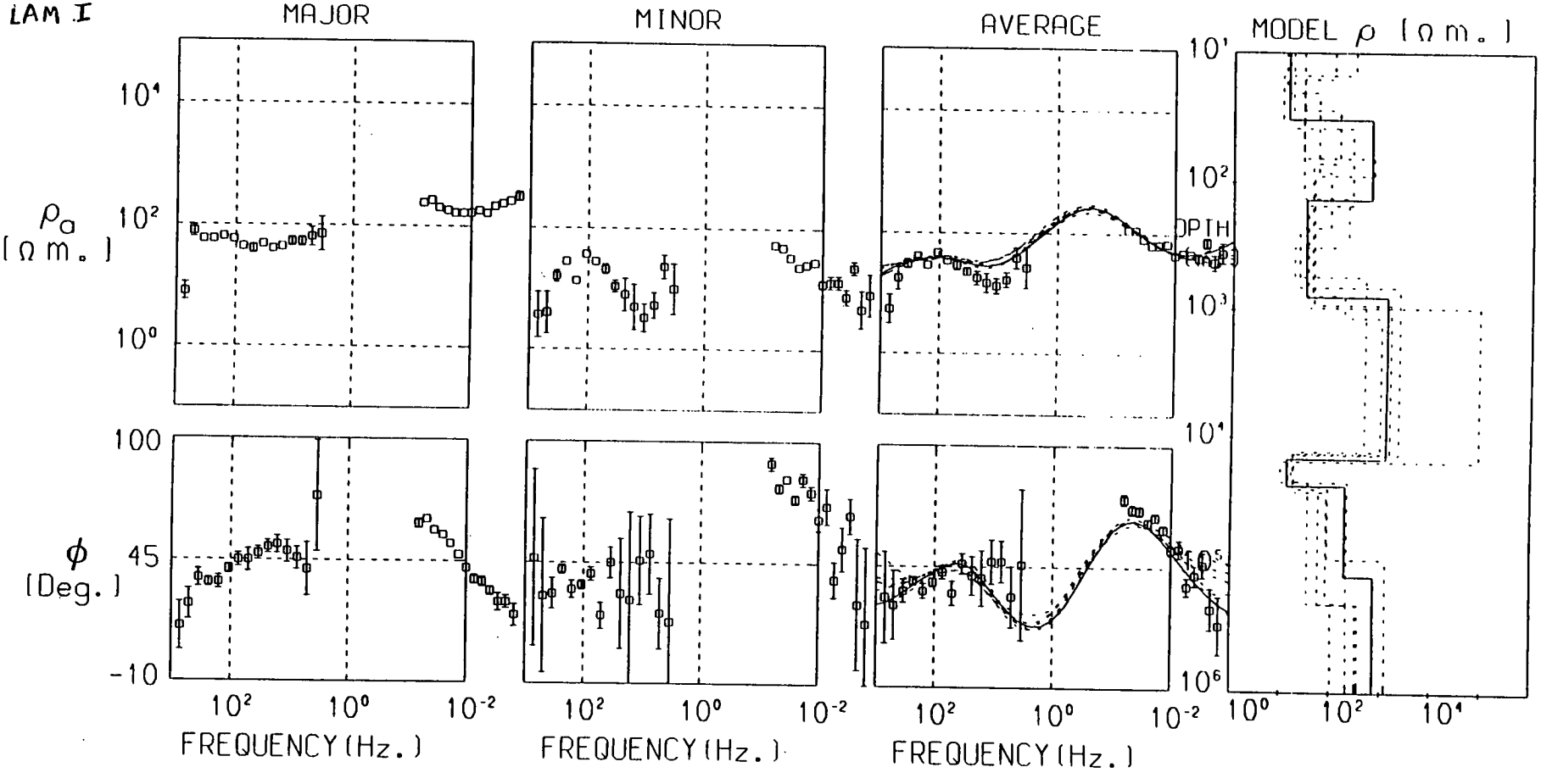
LAM I
MAJOR
MINOR
AVERAGE
MODEL ρ [Ω m.]
ρ_a [Ω m.]
ϕ [Deg.]
FREQUENCY (Hz.)
FREQUENCY (Hz.)
FREQUENCY (Hz.)
DEPTH

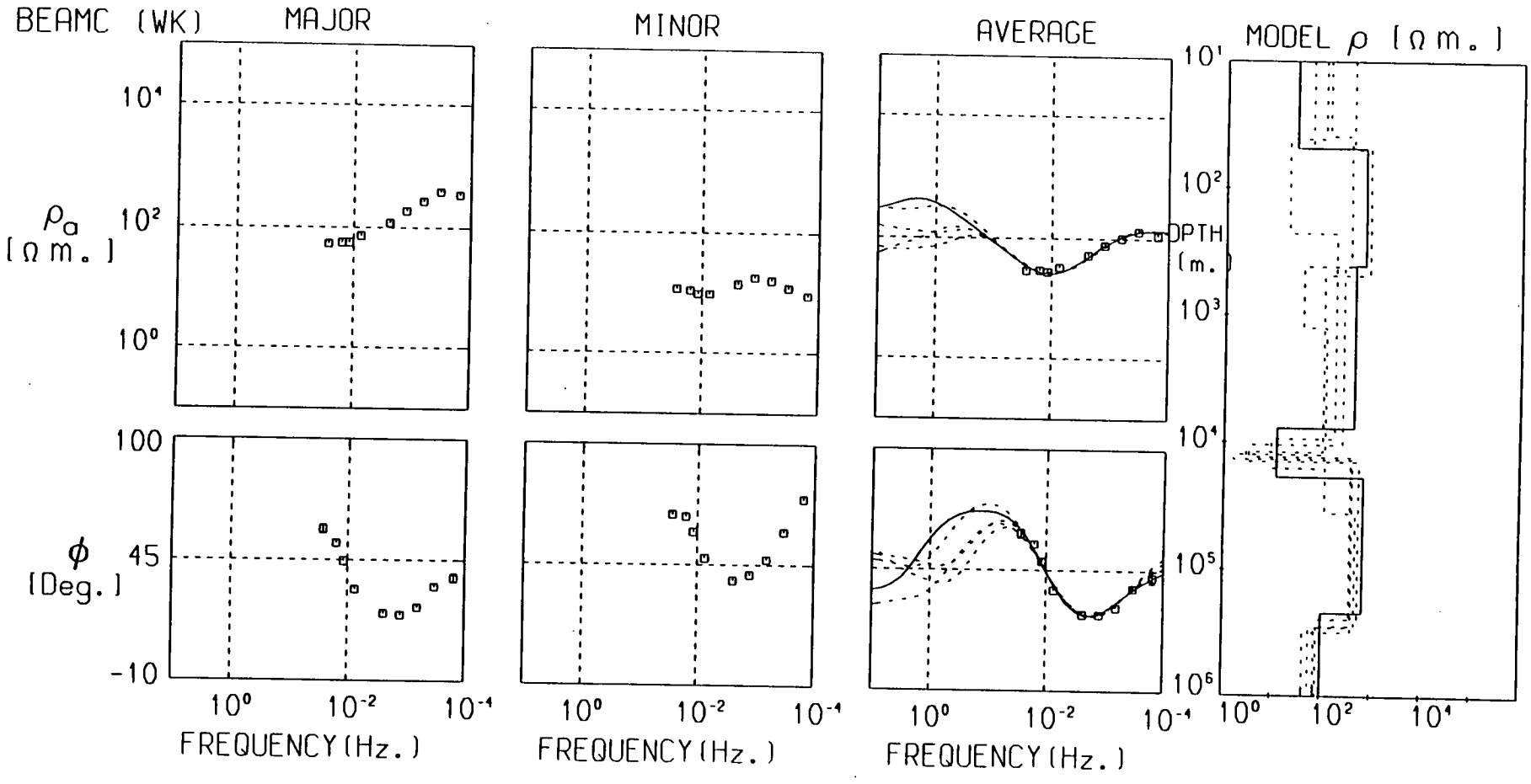
BEAMC (WK)
MAJOR
MINOR
AVERAGE
MODEL ρ [Ω m.]
ρa [Ω m.]
10¹
10²
10⁰
100
φ [Deg.]
45
-10
10⁰
10⁻²
10⁻⁴
FREQUENCY (Hz.)
DEPTH (m.)
10¹
10²
10³
10⁴
10⁵
10⁶

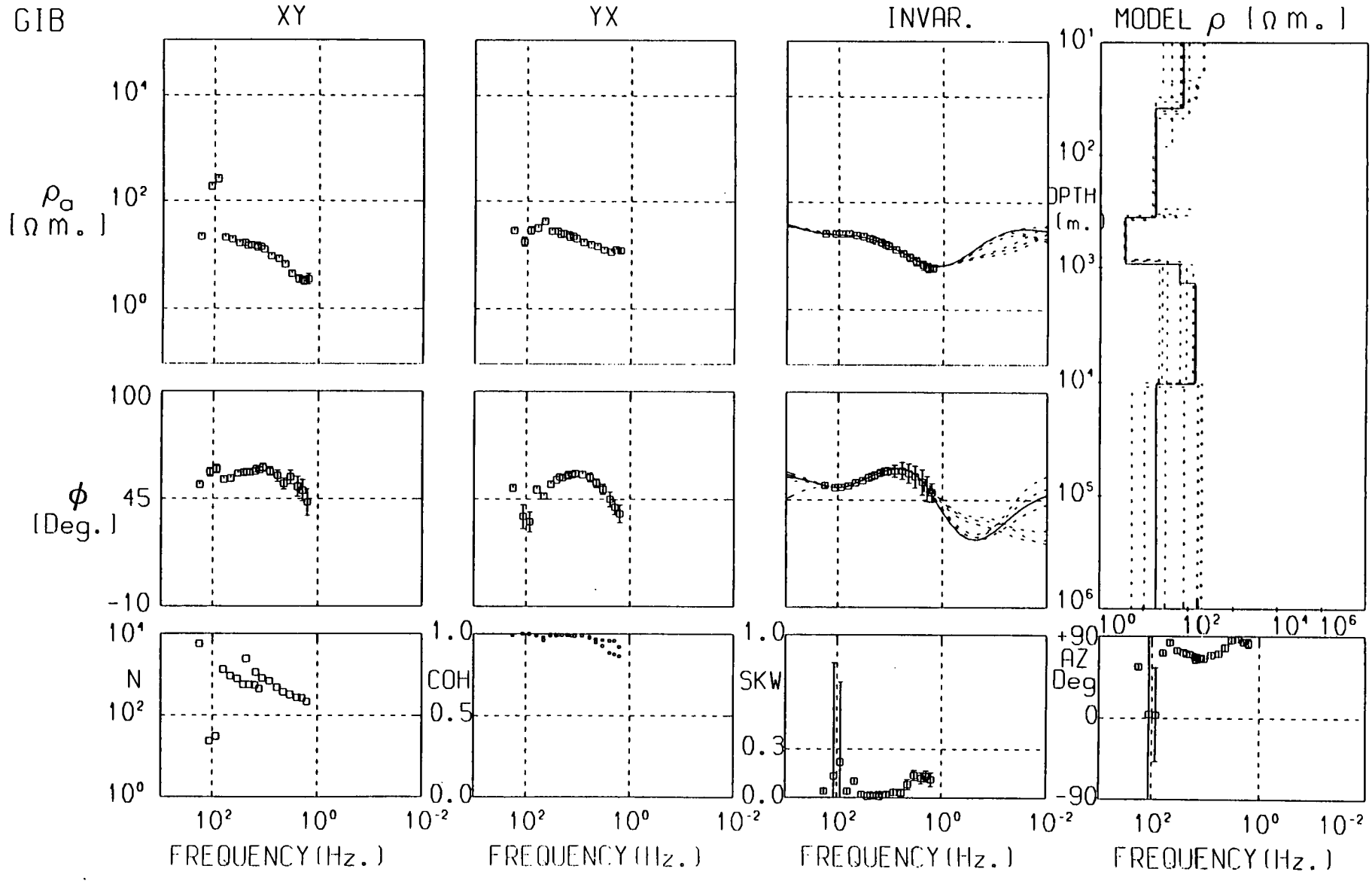
GIB
XY
YX
INVAR.
MODEL ρ [Ω m.]
ρa [Ω m.]
10⁴
10²
10⁰
DPTH (m.)
10¹
10²
10³
10⁴
10⁵
10⁶
φ [Deg.]
100
45
-10
N
COH
SKW
1.0
0.5
0.3
0.0
+90
AZ Deg
0
-90
10⁰
10²
10⁴
10⁶
10⁻²
FREQUENCY (Hz.)

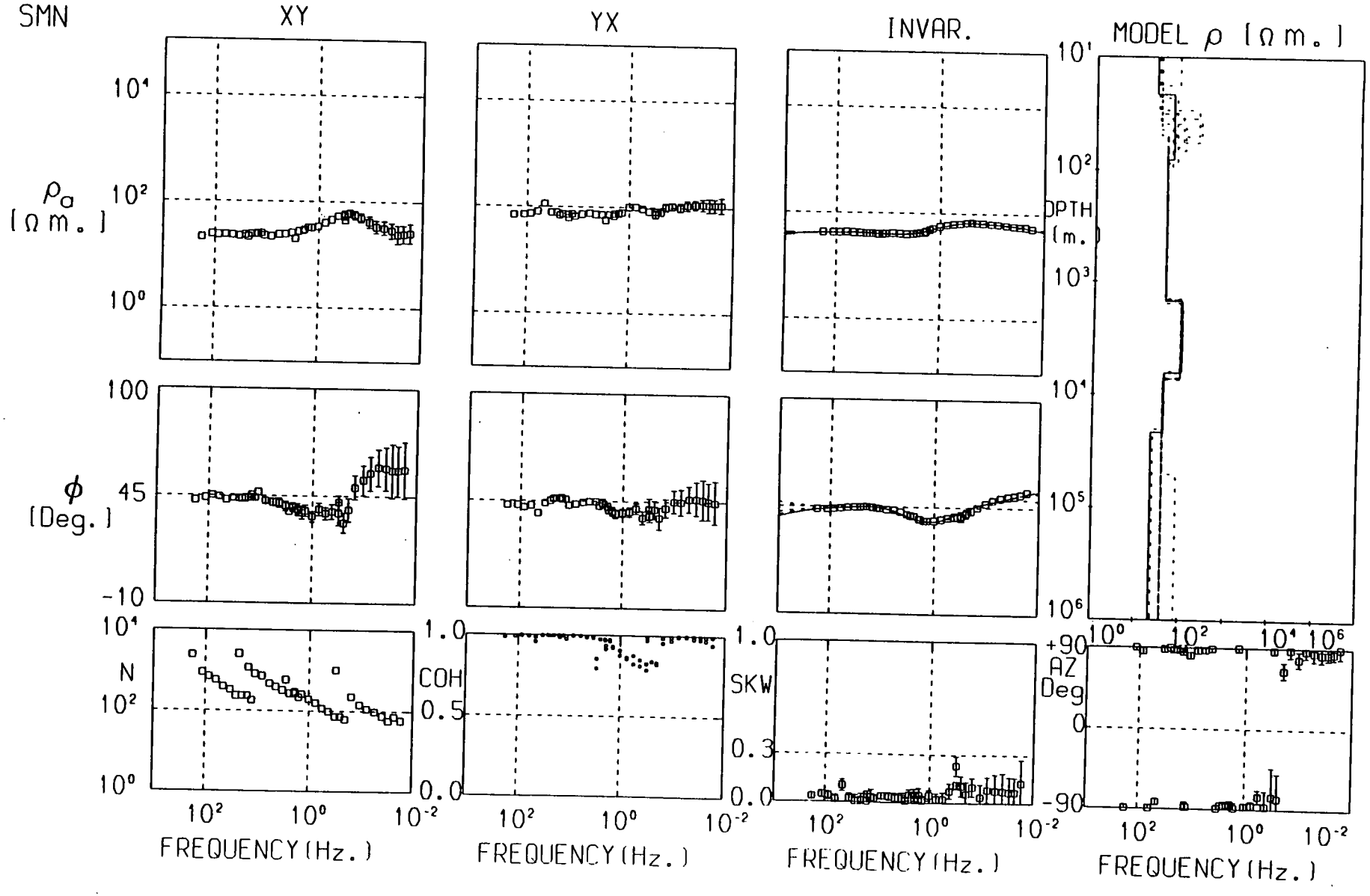
SMN
XY
YX
INVAR.
MODEL ρ [Ω m.]
ρa [Ω m.]
10¹
10²
10⁰
100
45
-10
φ [Deg.]
N
COH
SKW
1.0
0.5
0.3
0.0
DPTH (m.
10³
10⁴
10⁵
10⁶
+90
AZ Deg
0
-90
10²
10⁰
10⁻²
FREQUENCY (Hz.)

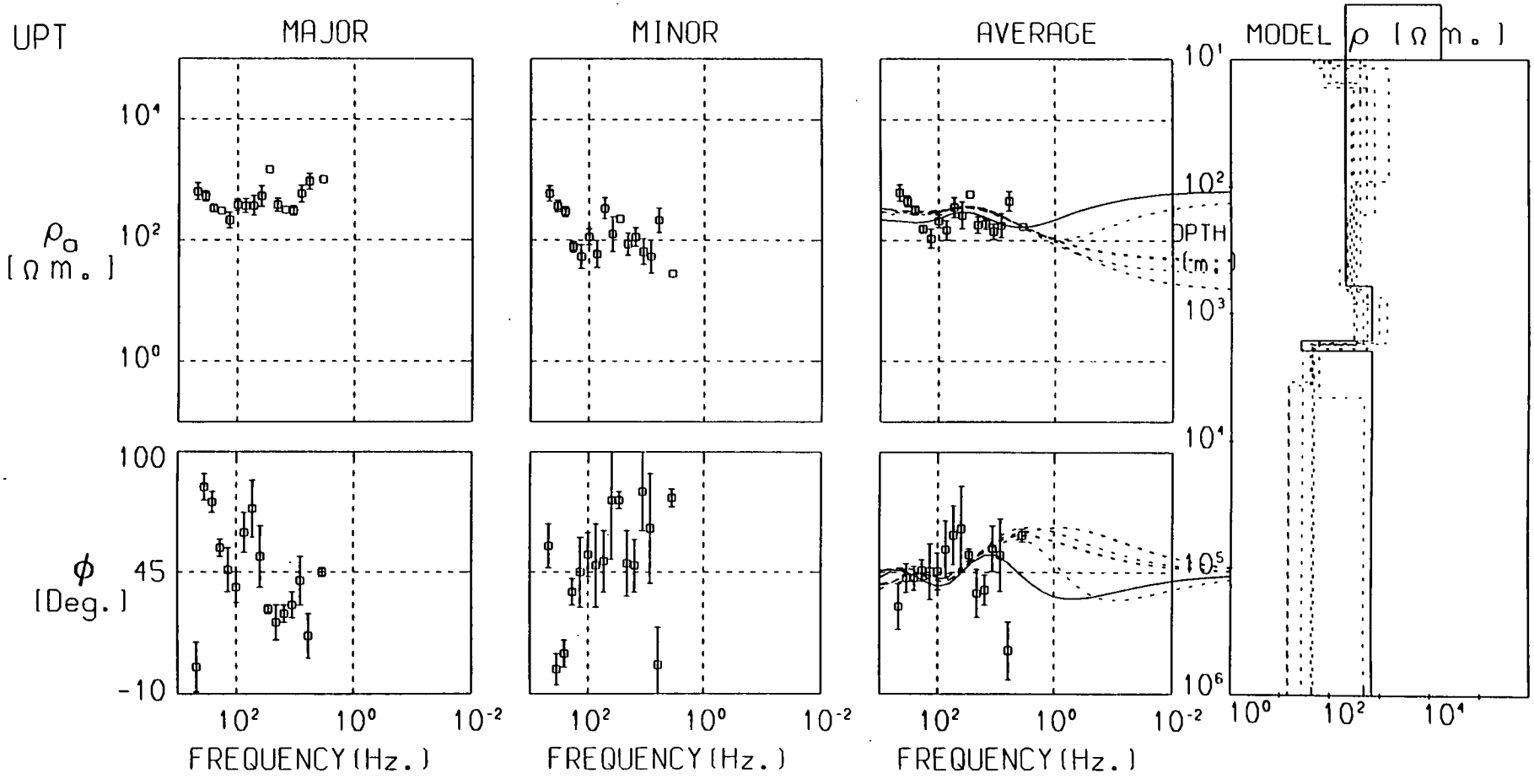
UPT
MAJOR
MINOR
AVERAGE
MODEL ρ [Ω m.]
ρ□ [Ω m.]
φ [Deg.]
10⁴
10²
10⁰
100
45
-10
10²
10⁰
10⁻²
FREQUENCY(Hz.)
10¹
10²
10³
10⁴
10⁵
10⁶
DEPTH (m.)

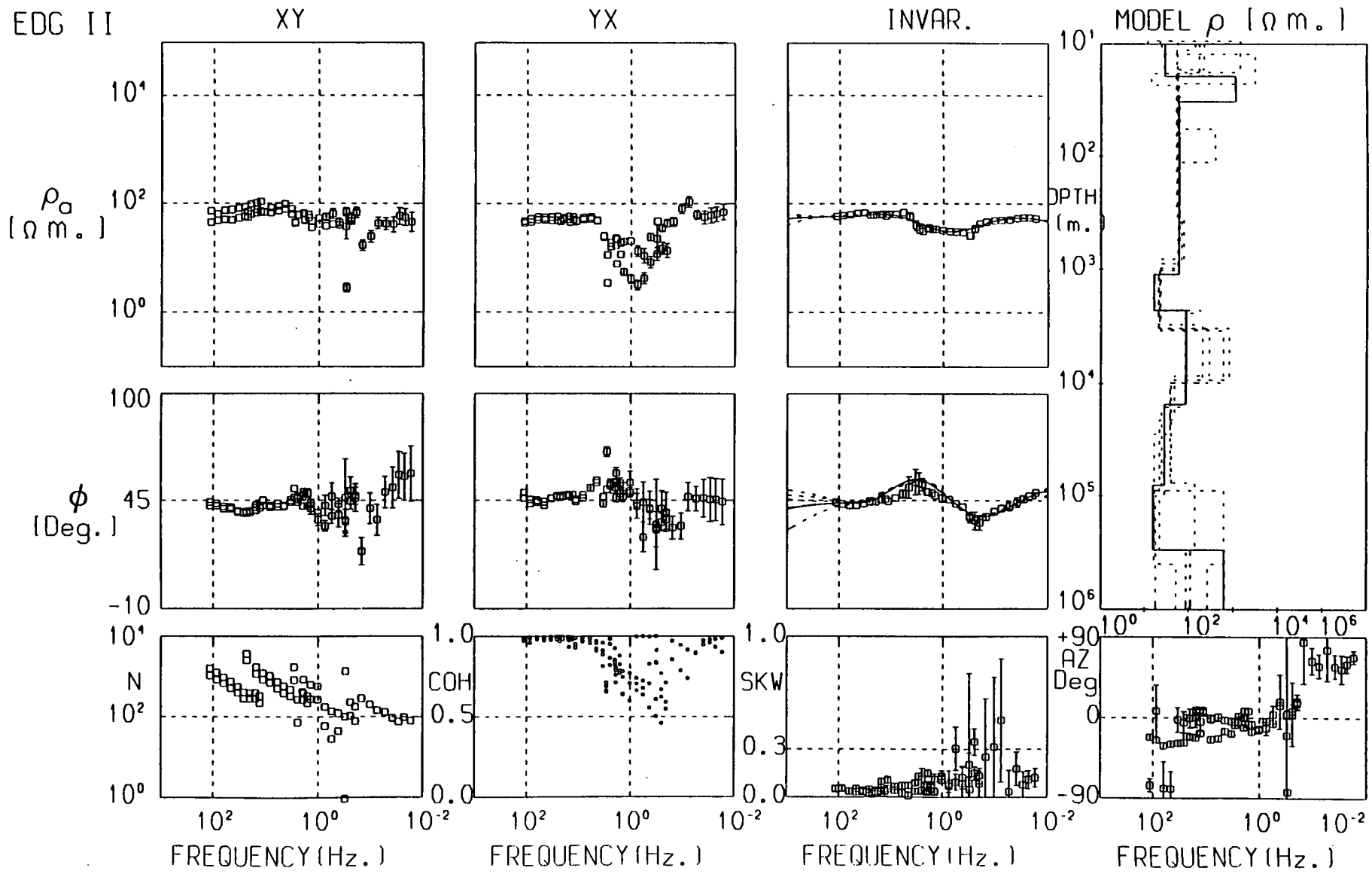
EDG II
XY
YX
INVAR.
MODEL ρ (Ω m.)
ρa (Ω m.)
10⁴
10²
10⁰
100
φ (Deg.)
45
-10
DPTH (m.)
10¹
10²
10³
10⁴
10⁵
10⁶
N
B
COH
1.0
0.5
0.0
SKW
0.3
0.0
+90
AZ Deg
0
-90
10⁰
10²
10⁴
10⁶
10⁻²
FREQUENCY (Hz.)

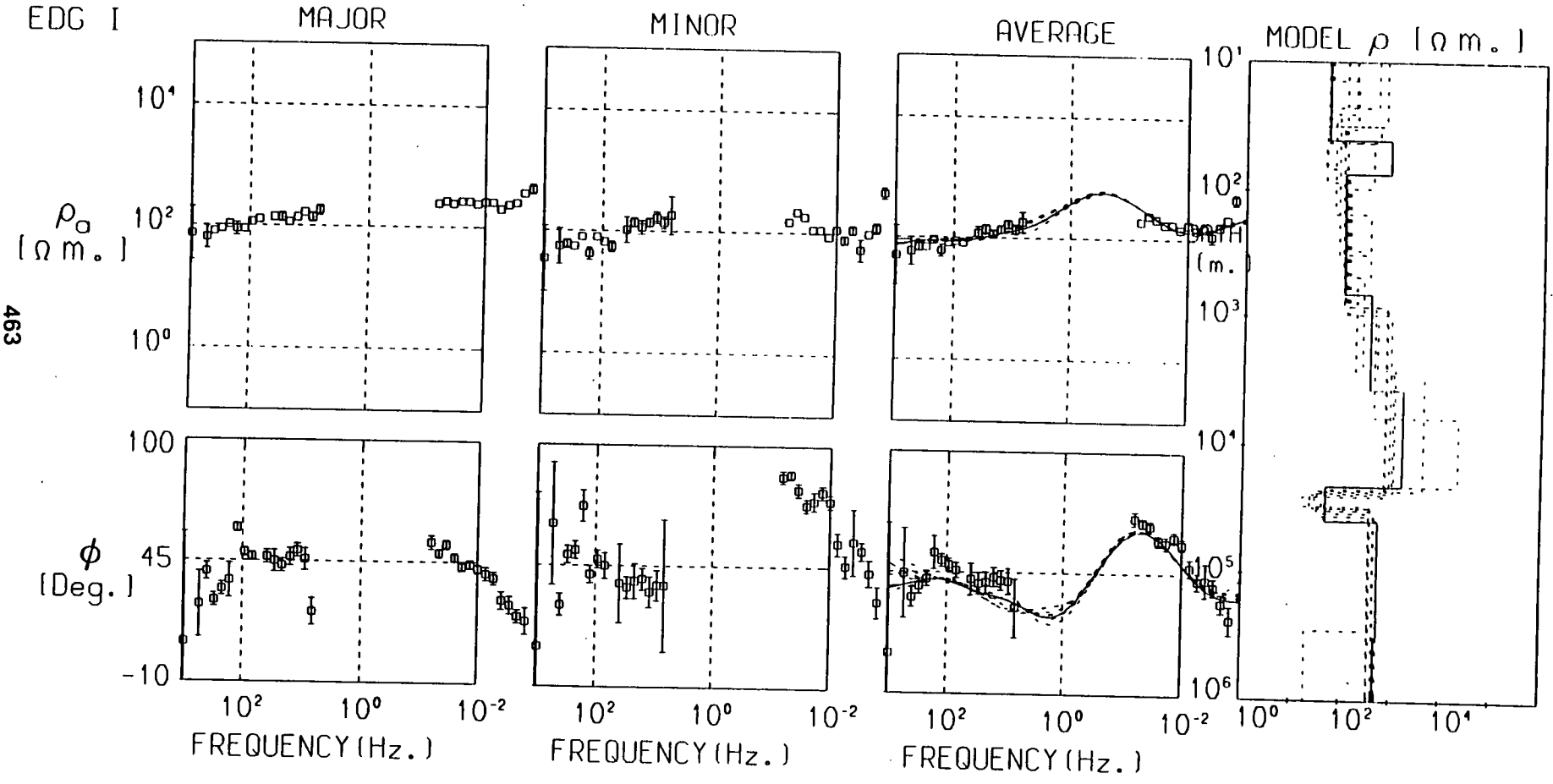
EDG I
MAJOR
MINOR
AVERAGE
MODEL ρ (Ω m.)
ρa (Ω m.)
φ (Deg.)
10⁴
10²
10⁰
100
45
-10
10¹
10²
10³
10⁴
10⁵
10⁶
10²
10⁰
10⁻²
FREQUENCY (Hz.)
DEPTH (m.)

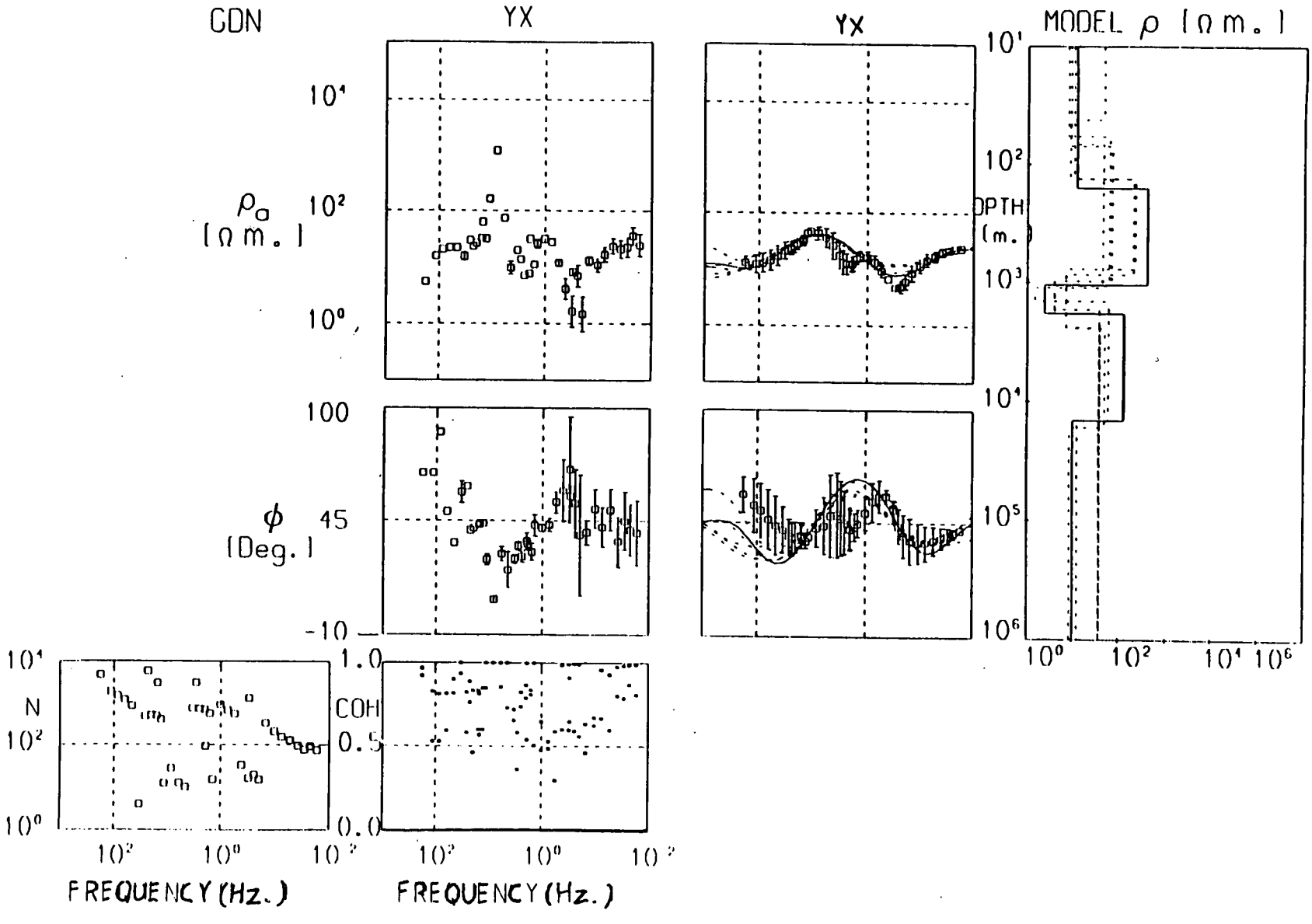
CDN
YX
YX
MODEL ρ (Ω m.)
ρ_a (Ω m.)
10^4
10^2
10^0
100
ϕ 45
(Deg.)
-10
10^1
10^2
DPTH (m.
10^3
10^4
10^5
10^6
10^0 10^2 10^4 10^6
N
10^4
10^2
10^0
COH
1.0
0.5
0.0
10^2 10^0 10^{-2}
10^2 10^0 10^{-2}
FREQUENCY (Hz.)
FREQUENCY (Hz.)

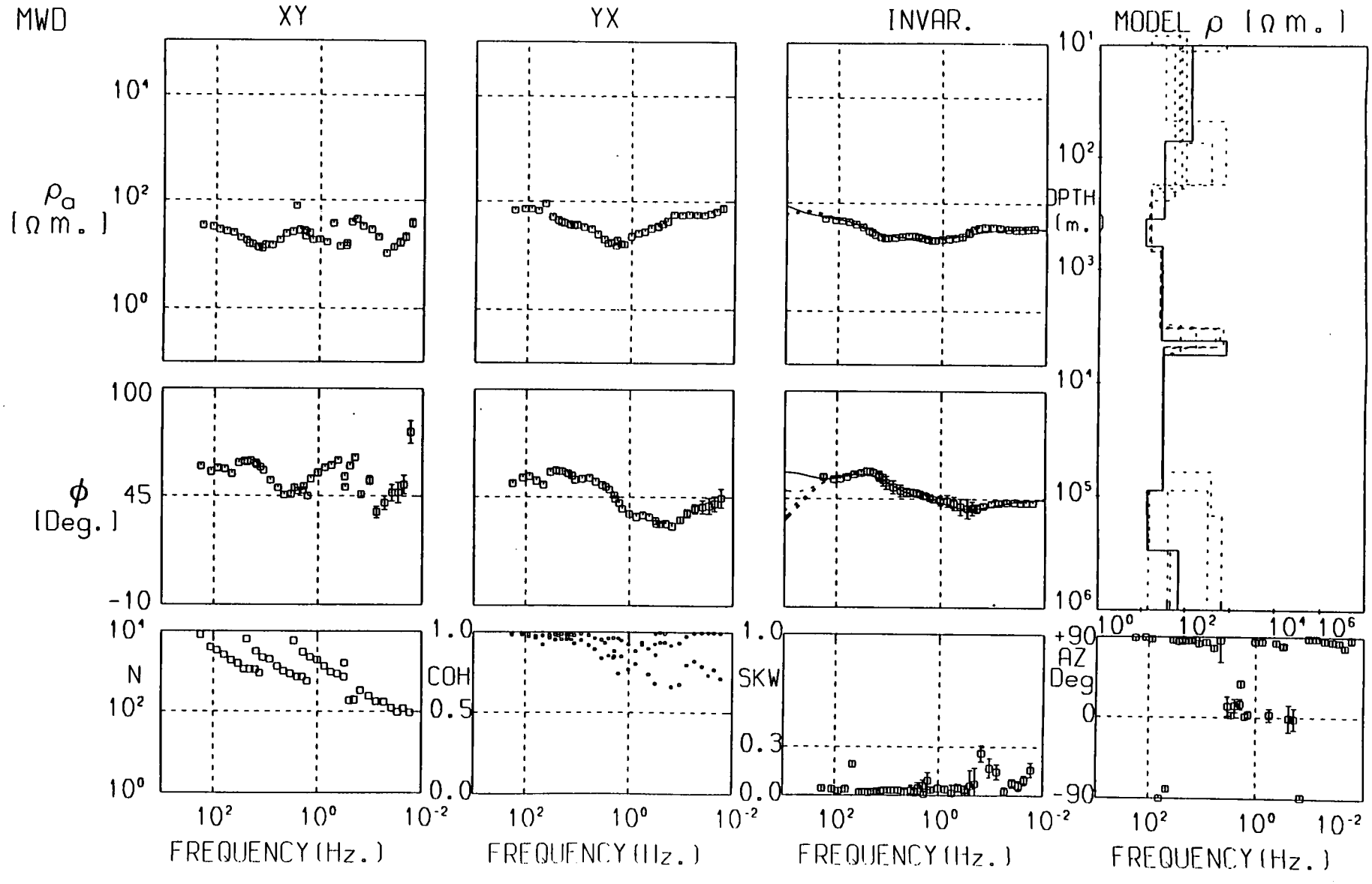
MWD
XY
YX
INVAR.
MODEL ρ (Ω m.)
ρa (Ω m.)
φ (Deg.)
N
COH
SKW
AZ Deg
DPTH (m.)
FREQUENCY (Hz.)
FREQUENCY (Hz.)
FREQUENCY (Hz.)
FREQUENCY (Hz.)

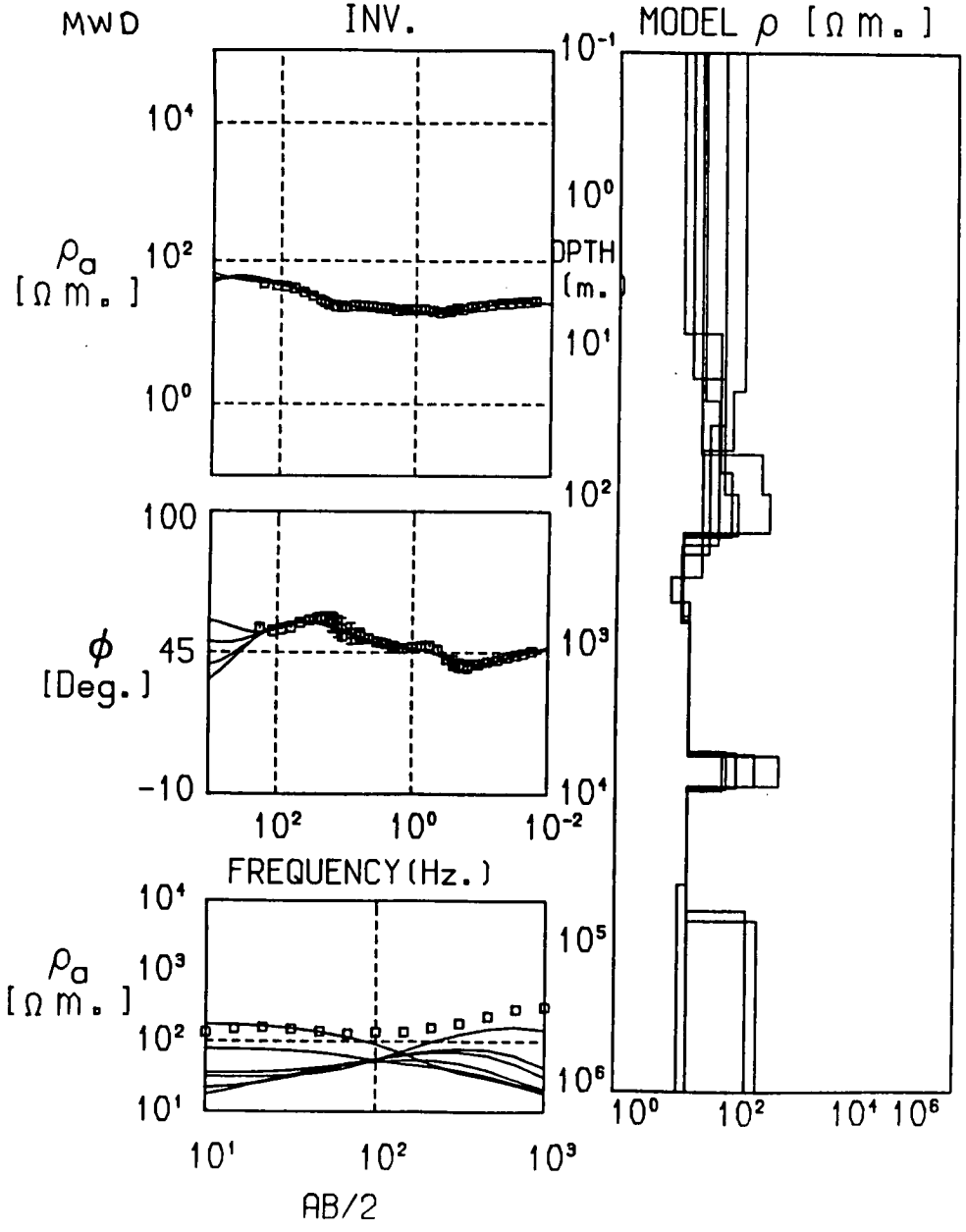
MWD
INV.
MODEL ρ [Ω m.]
ρa [Ω m.]
φ [Deg.]
DPTH (m.
FREQUENCY (Hz.)
AB/2

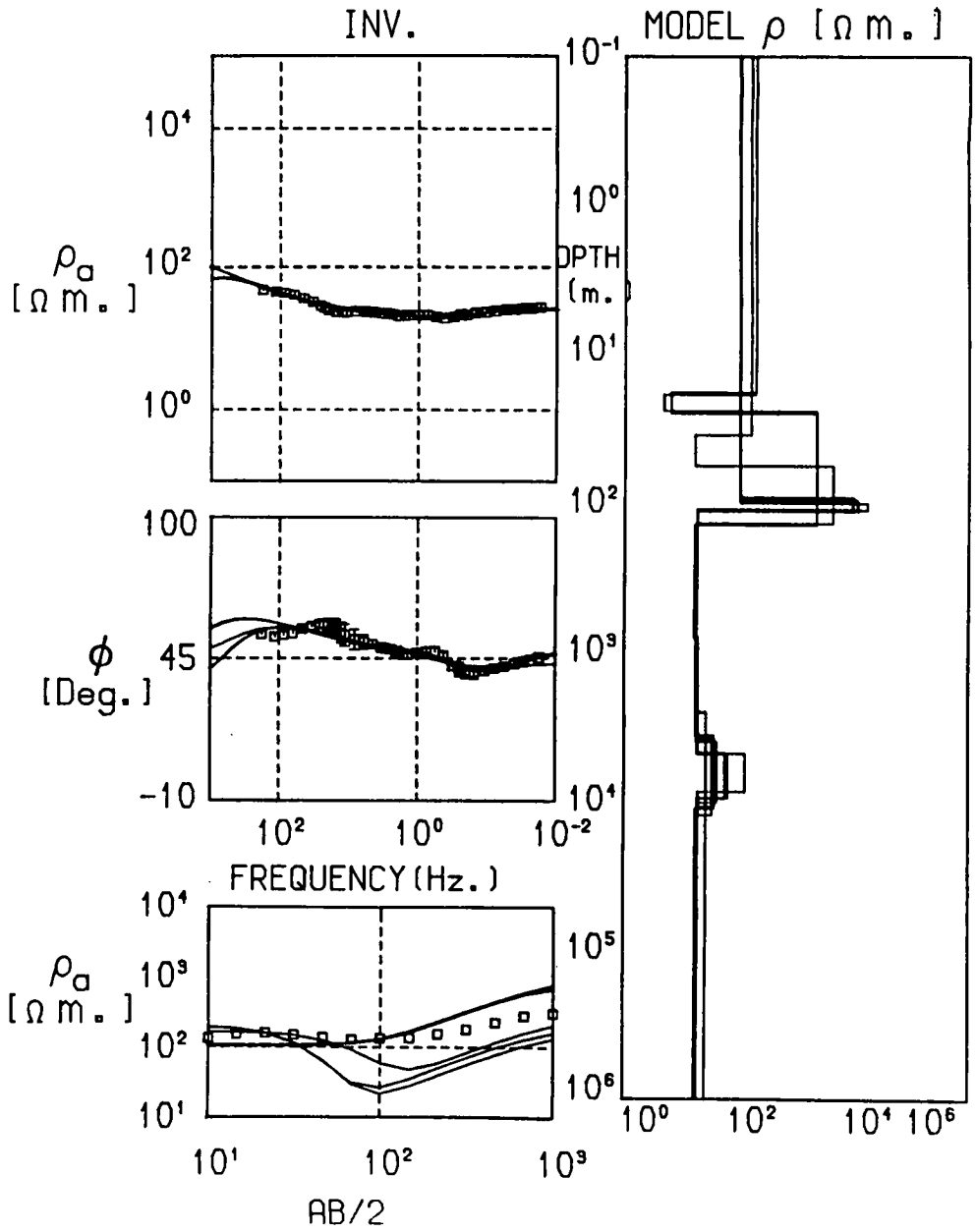
INV.
MODEL ρ [Ω m.]
ρa [Ω m.]
φ [Deg.]
DPTH (m.
FREQUENCY (Hz.)
AB/2

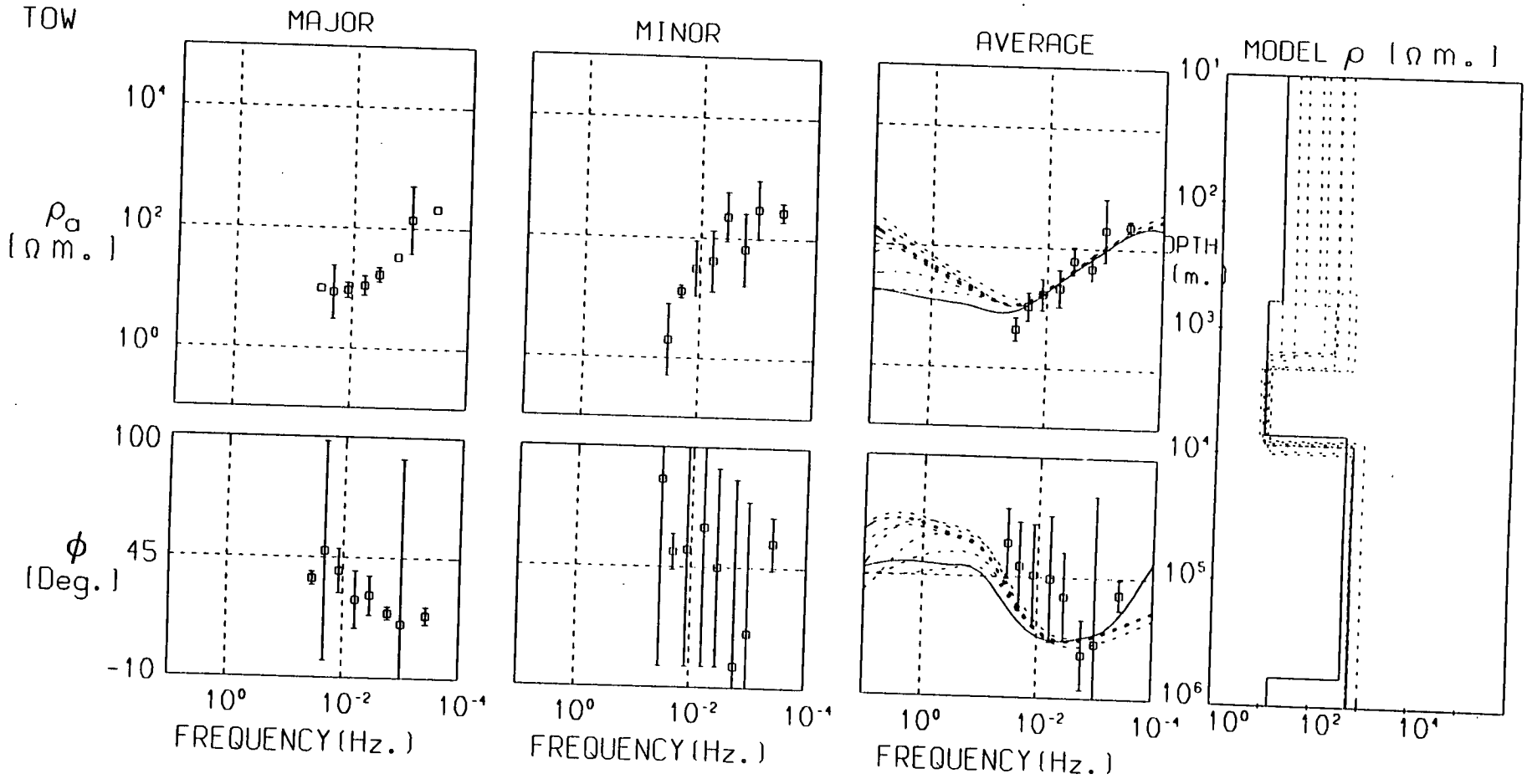
TOW
MAJOR
MINOR
AVERAGE
MODEL ρ (Ω m.)
ρa (Ω m.)
φ (Deg.)
10⁴
10²
10⁰
100
45
-10
10⁰
10⁻²
10⁻⁴
FREQUENCY (Hz.)
DEPTH (m.)
10¹
10²
10³
10⁴
10⁵
10⁶

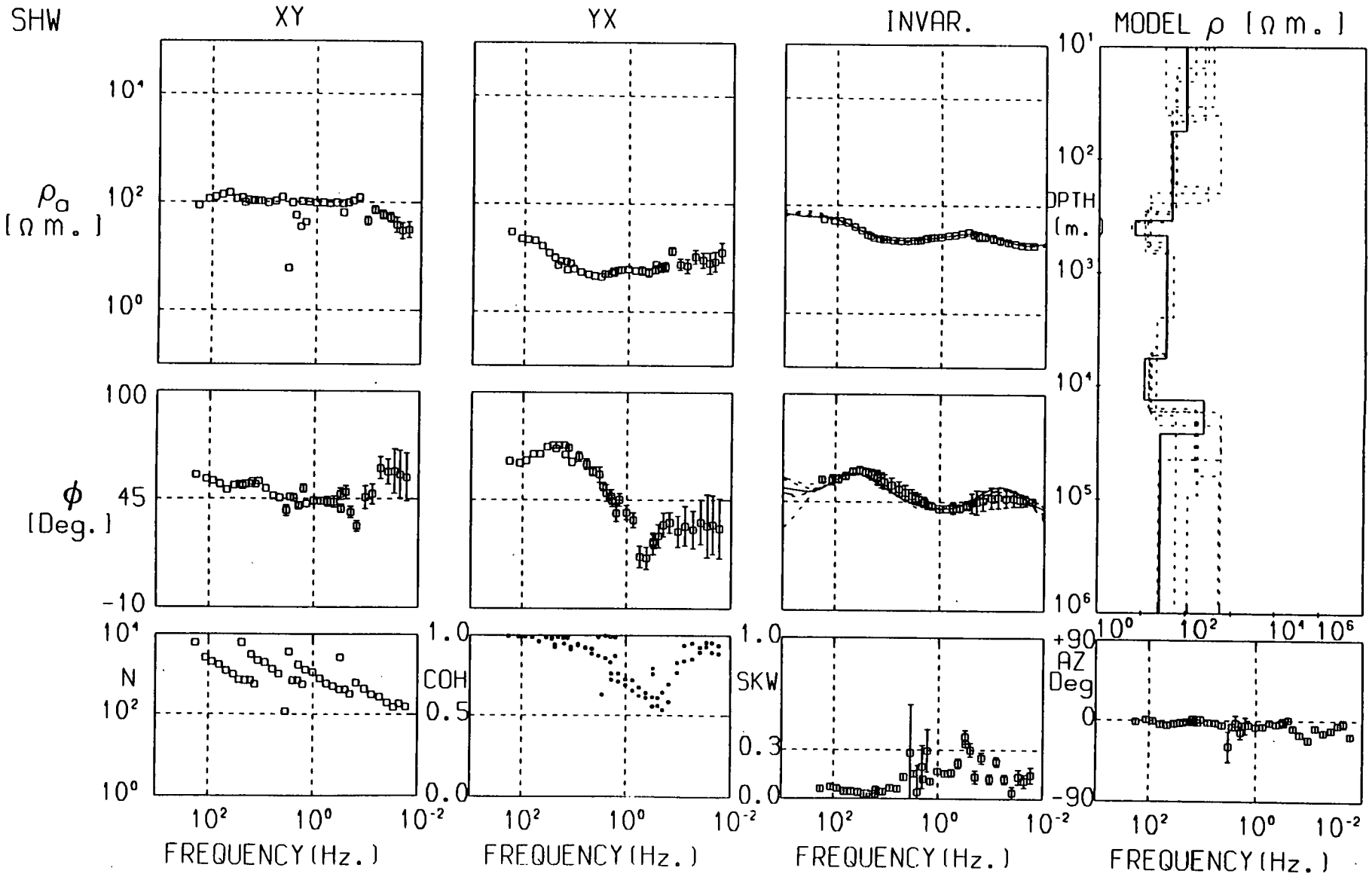
SHW
XY
YX
INVAR.
MODEL ρ [Ω m.]
ρa [Ω m.]
φ [Deg.]
N
COH
SKW
AZ Deg
DPTH (m.)
FREQUENCY (Hz.)
FREQUENCY (Hz.)
FREQUENCY (Hz.)
FREQUENCY (Hz.)

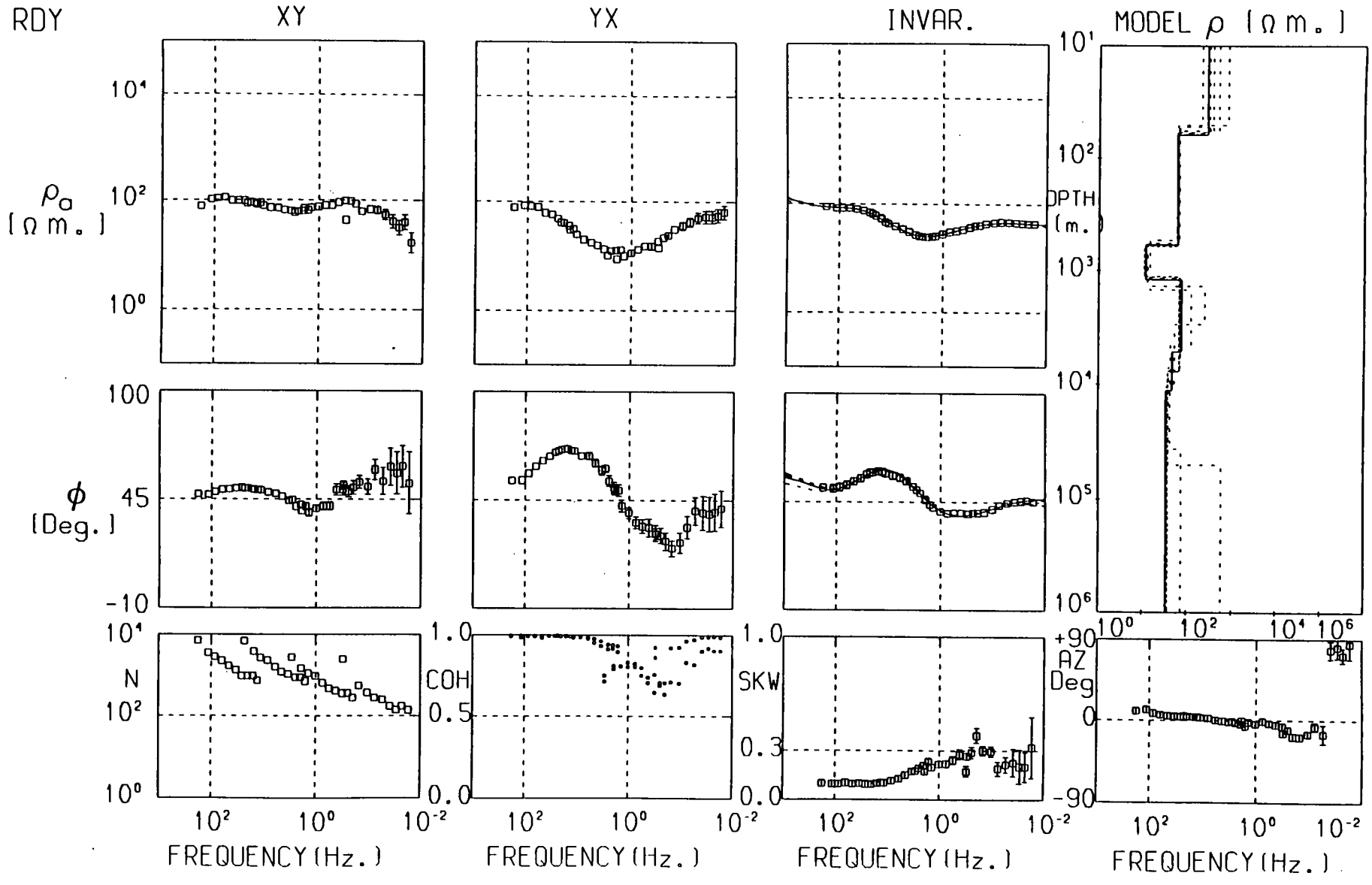
RDY
XY
YX
INVAR.
MODEL ρ (Ω m.)
ρa (Ω m.)
φ (Deg.)
N
COH
SKW
AZ Deg
DPTH (m.)
FREQUENCY (Hz.)
FREQUENCY (Hz.)
FREQUENCY (Hz.)
FREQUENCY (Hz.)

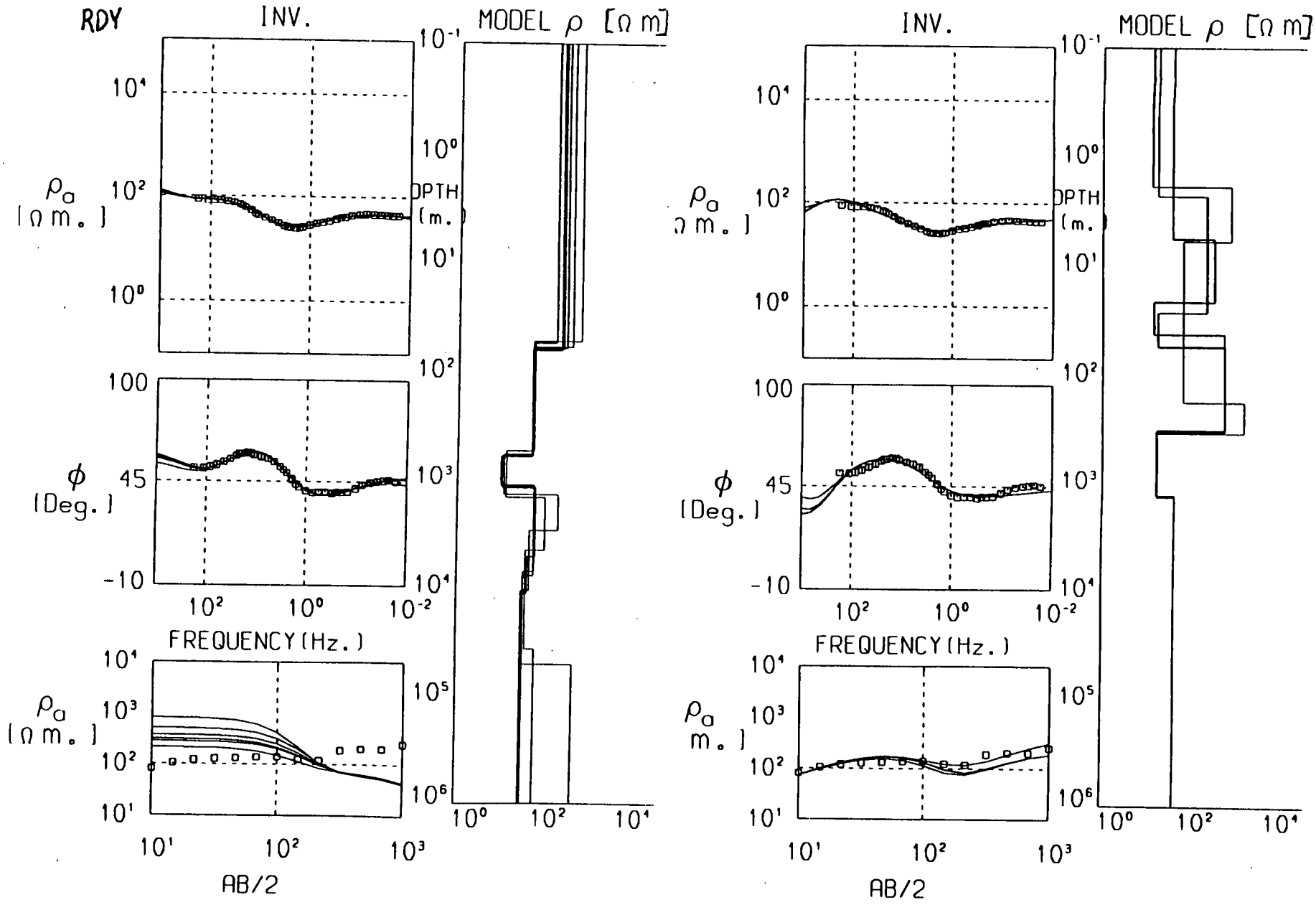
RDY
INV.
MODEL ρ [Ω m]
ρa [Ω m.]
φ [Deg.]
DPTH (m.)
FREQUENCY (Hz.)
AB/2
INV.
MODEL ρ [Ω m]
ρa Ω m.]
φ [Deg.]
DPTH (m.)
FREQUENCY (Hz.)
ρa m.]
AB/2

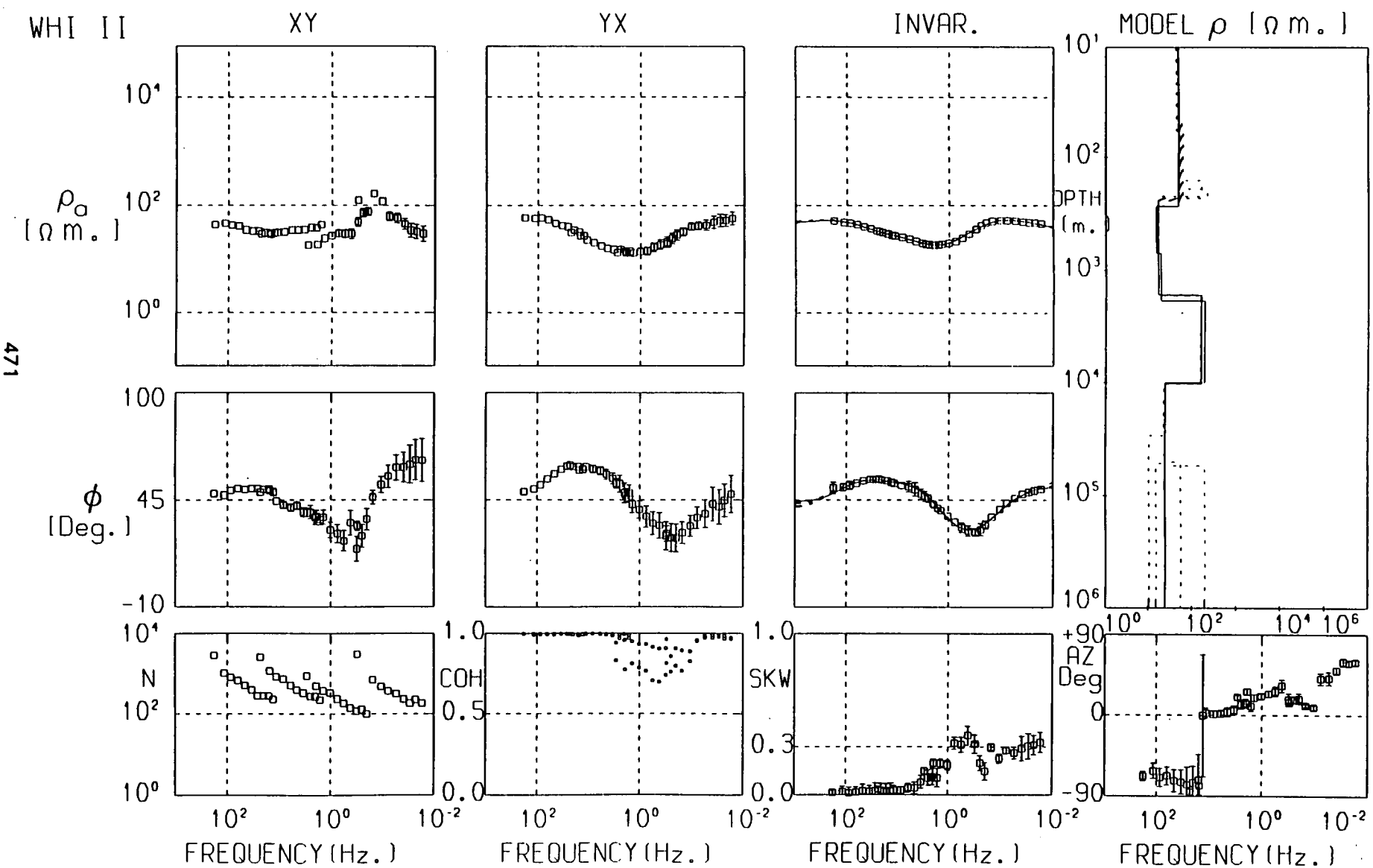
WHI II
XY
YX
INVAR.
MODEL ρ [Ω m.]
ρa [Ω m.]
φ [Deg.]
N
COH
SKW
AZ Deg
DPTH (m.)
FREQUENCY (Hz.)
FREQUENCY (Hz.)
FREQUENCY (Hz.)
FREQUENCY (Hz.)

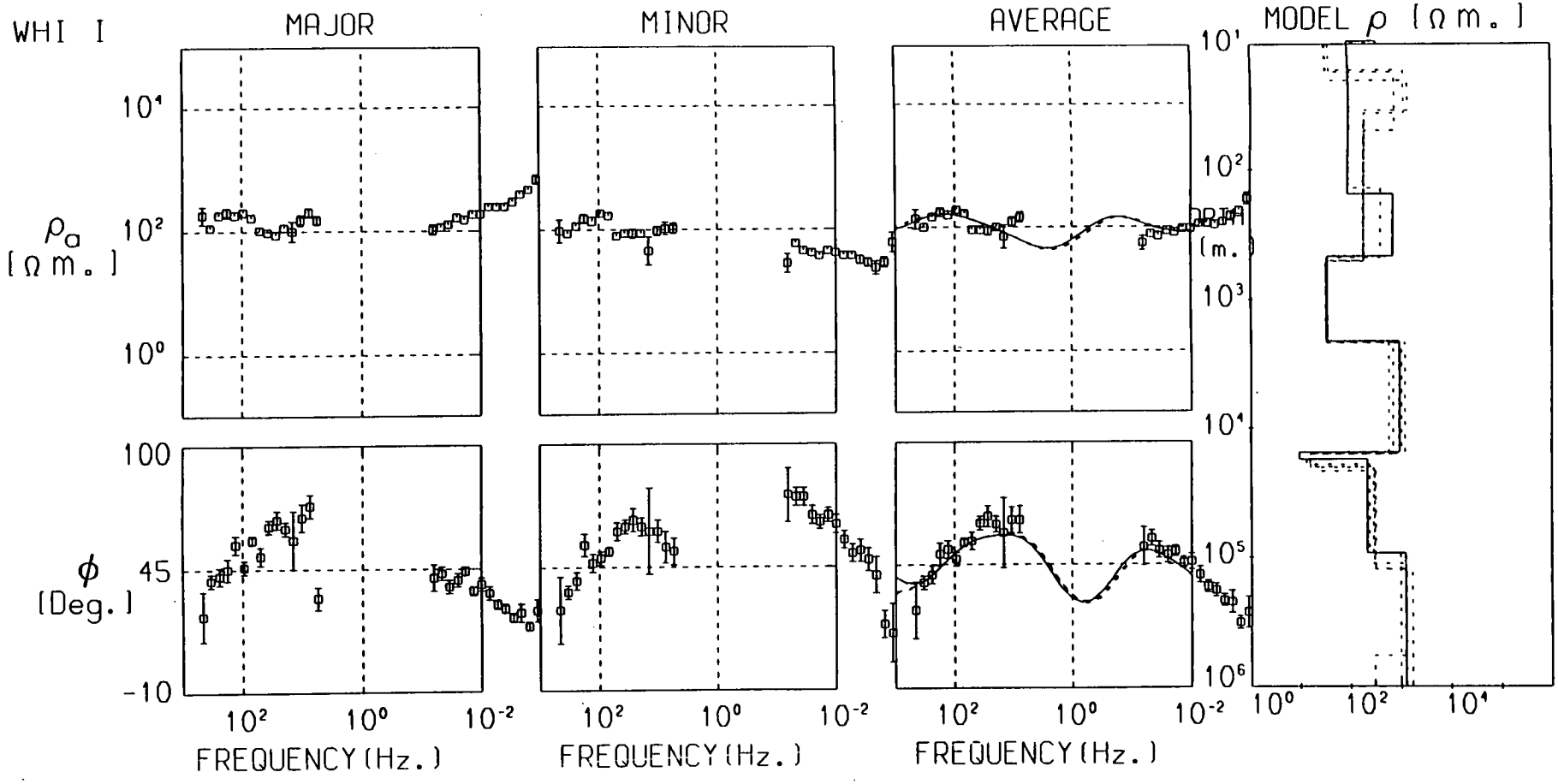
WHI I
MAJOR
MINOR
AVERAGE
MODEL ρ [Ω m.]
ρa [Ω m.]
φ [Deg.]
FREQUENCY (Hz.)
FREQUENCY (Hz.)
FREQUENCY (Hz.)
DEPTH (m.)

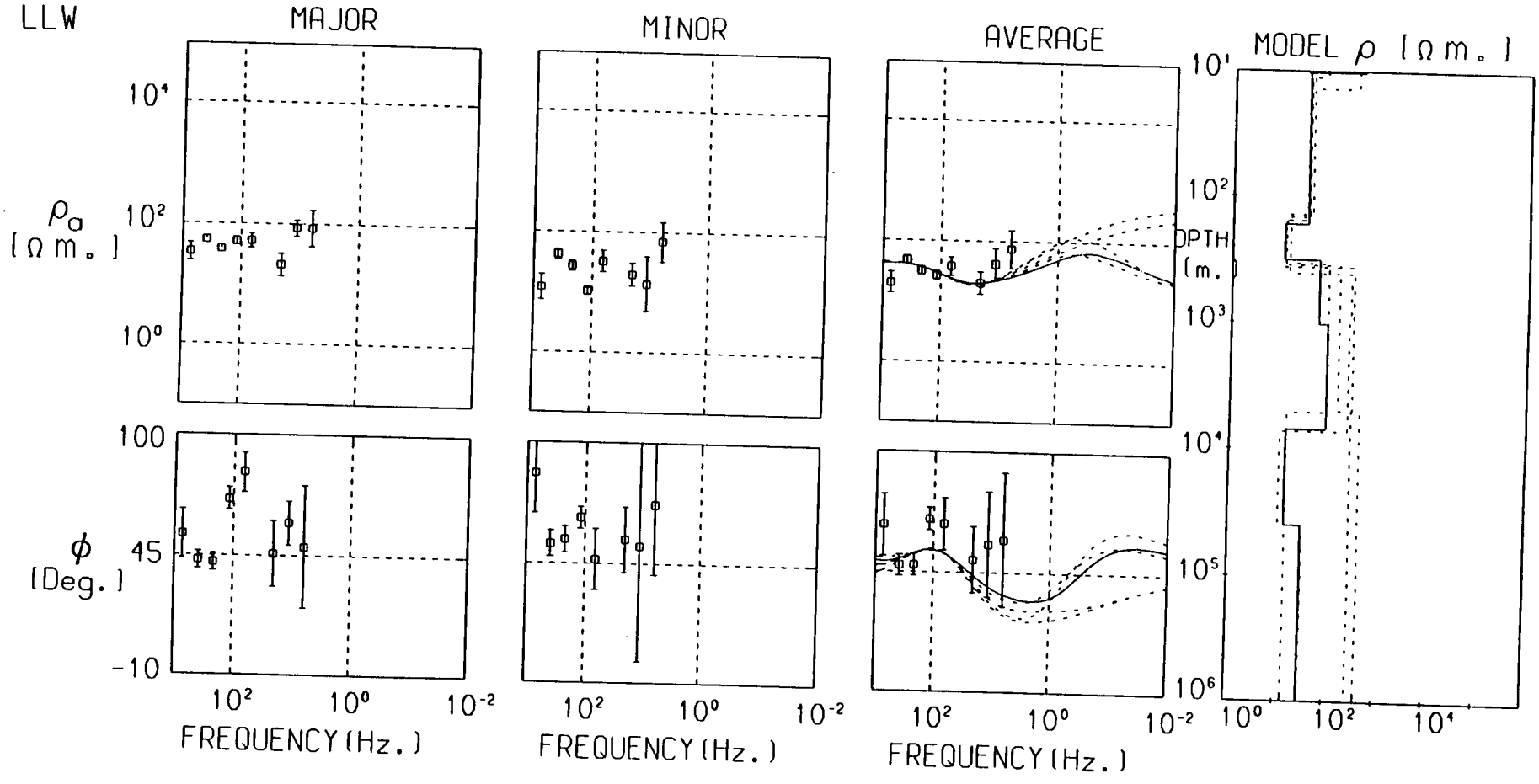
LLW
MAJOR
MINOR
AVERAGE
MODEL ρ (Ω m.)
ρa (Ω m.)
φ (Deg.)
10¹
10²
10⁰
100
45
-10
10²
10⁰
10⁻²
FREQUENCY (Hz.)
DEPTH (m.)
10¹
10²
10³
10⁴
10⁵
10⁶
10⁰
10²
10⁴

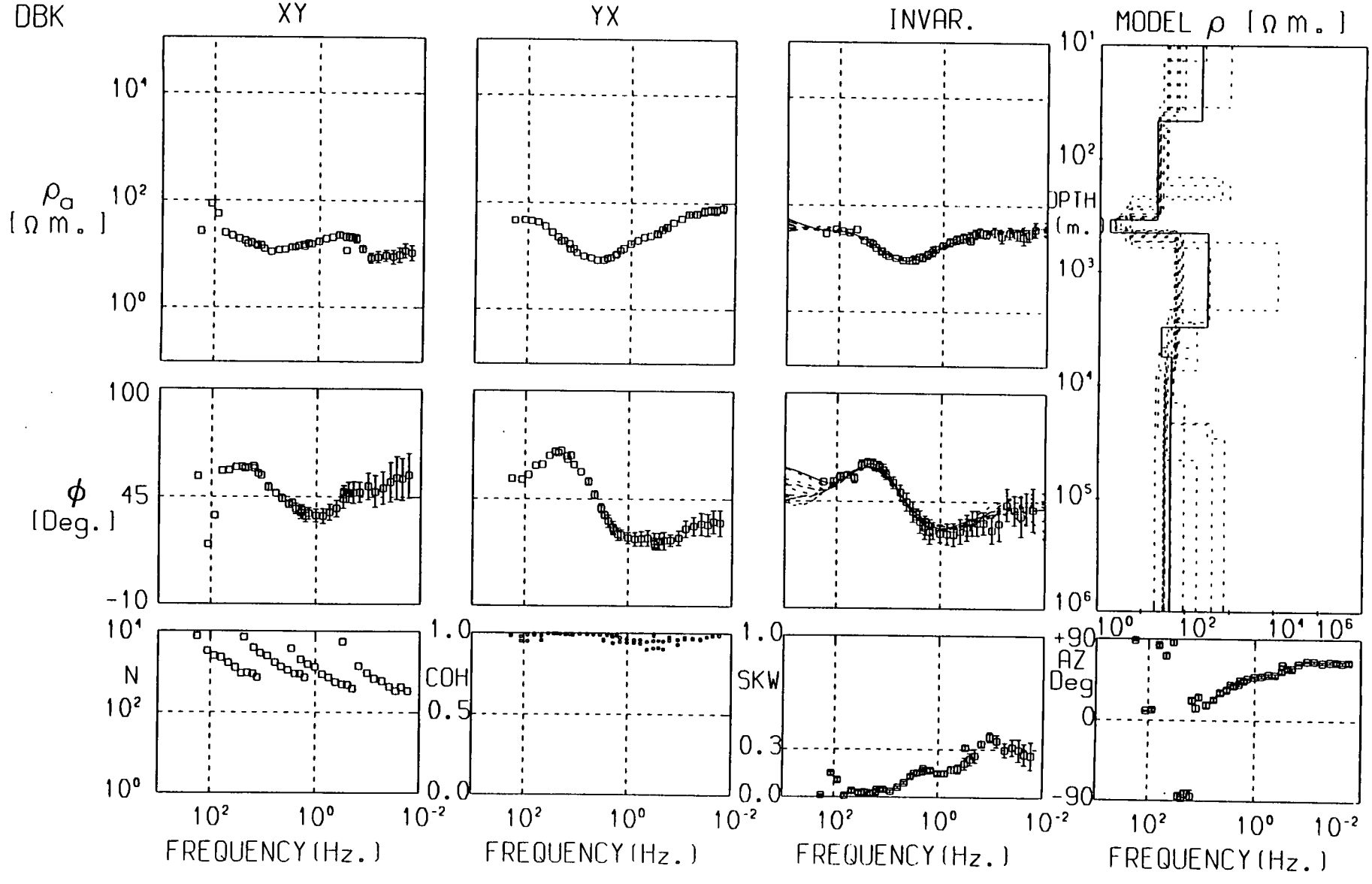
DBK
XY
YX
INVAR.
MODEL ρ [Ω m.]
ρa [Ω m.]
10¹
10²
10⁰
100
φ [Deg.]
45
-10
N
COH
1.0
0.5
0.0
SKW
0.3
DPTH (m.)
10³
10⁴
10⁵
10⁶
+90
AZ Deg
0
-90
10²
10⁰
10⁻²
FREQUENCY(Hz.)

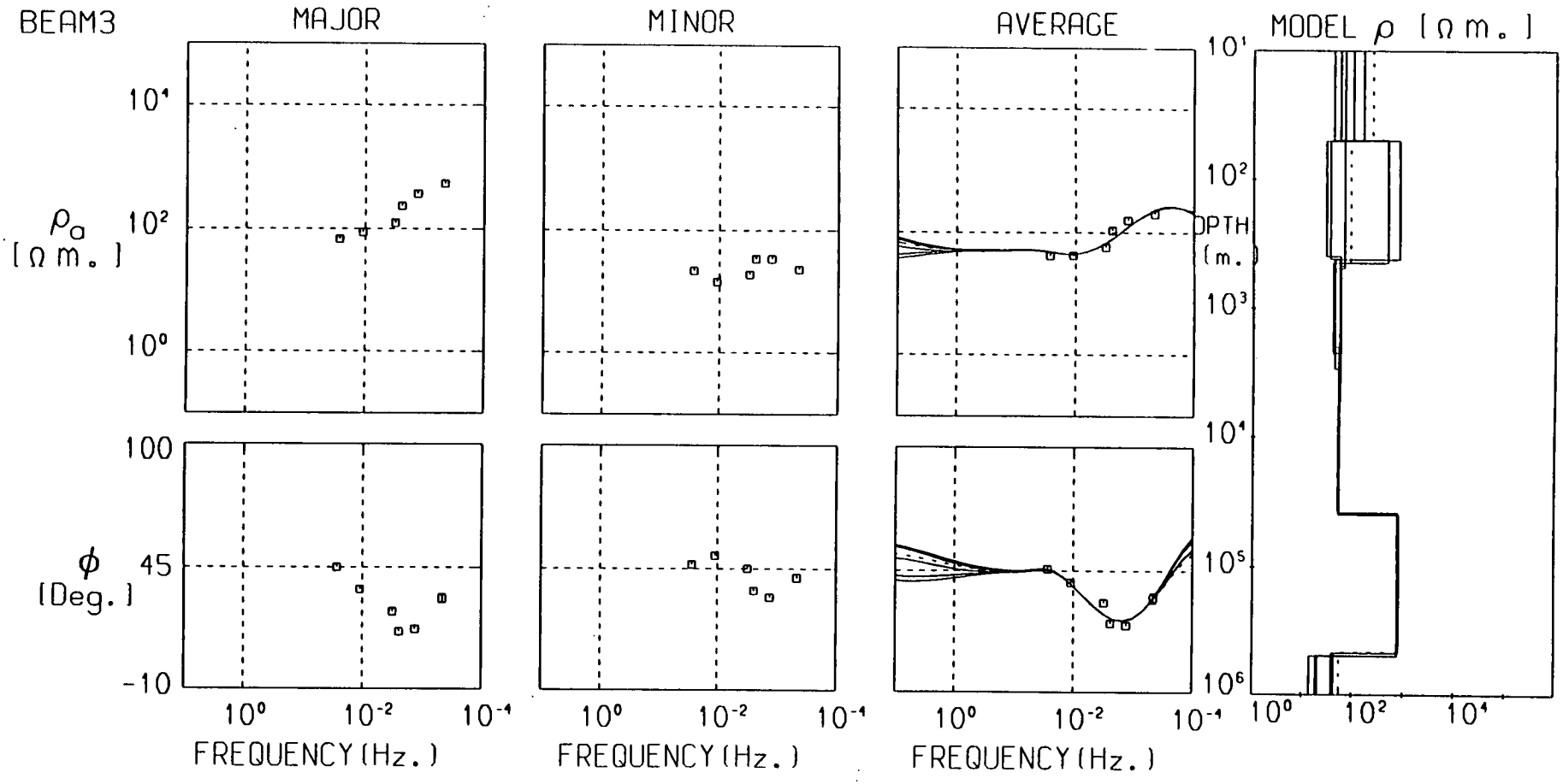
BEAM3
MAJOR
MINOR
AVERAGE
MODEL ρ [Ω m.]
ρa [Ω m.]
φ [Deg.]
FREQUENCY (Hz.)
FREQUENCY (Hz.)
FREQUENCY (Hz.)
DEPTH (m.)

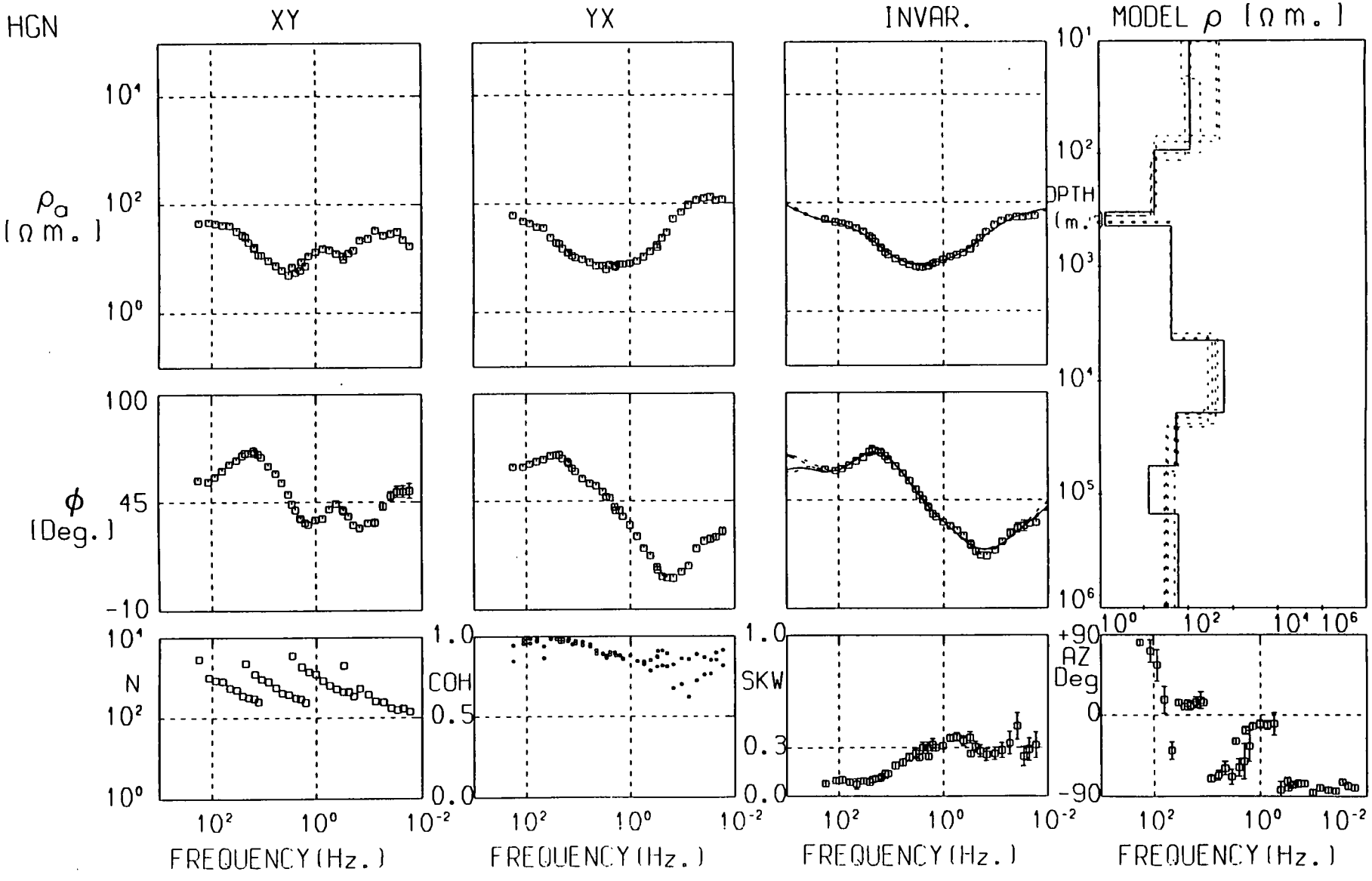
HGN
XY
YX
INVAR.
MODEL ρ (Ω m.)
ρa (Ω m.)
10⁴
10²
10⁰
DPTH (m.)
10¹
10³
10⁵
10⁶
φ (Deg.)
100
45
-10
N
COH
SKW
1.0
0.5
0.3
0.0
+90
AZ Deg
0
-90
10²
10⁰
10⁻²
10⁴
10⁶
FREQUENCY (Hz.)

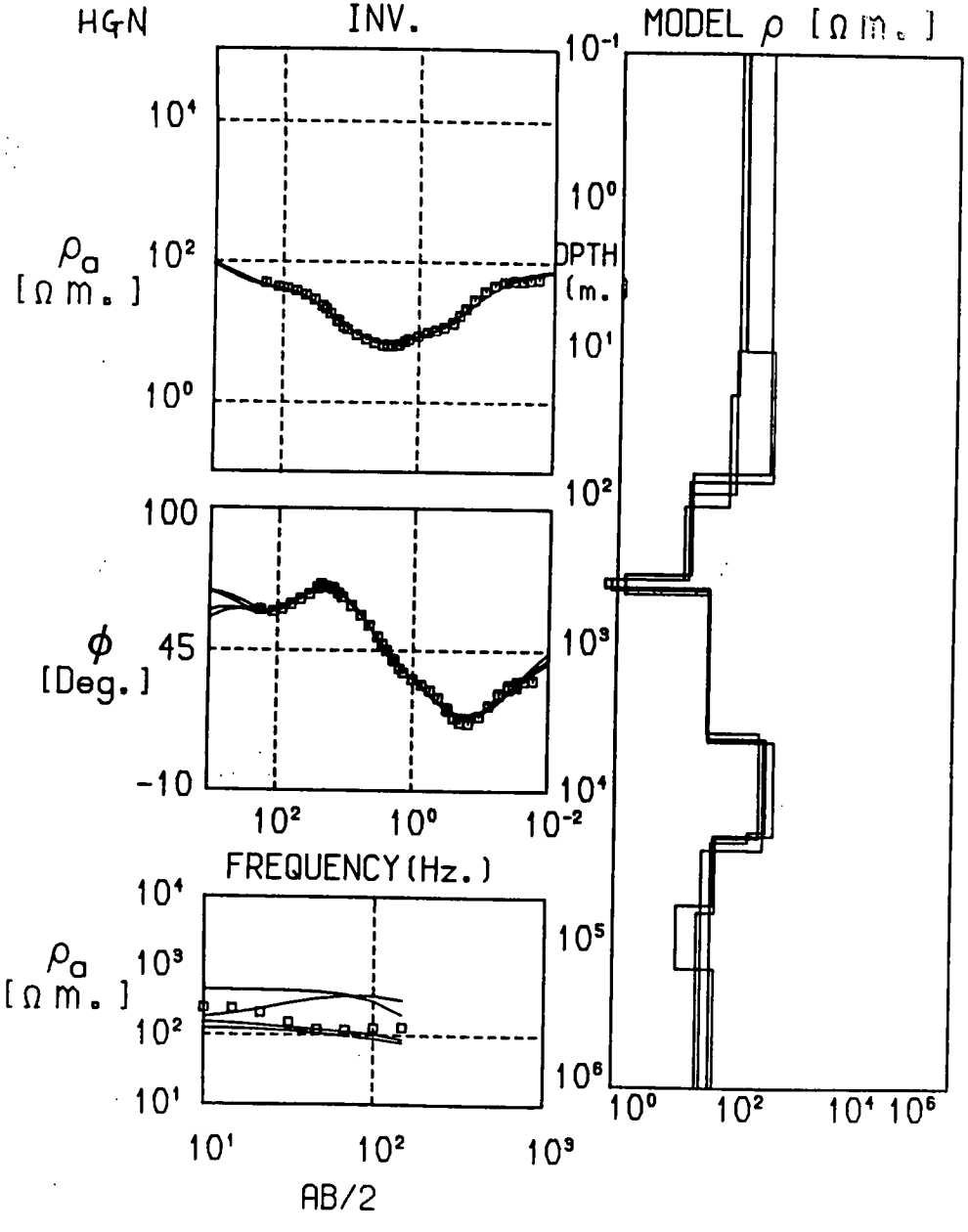
HGN
INV.
MODEL ρ [Ω m.]
ρa [Ω m.]
DPTH (m.
φ [Deg.]
FREQUENCY (Hz.)
AB/2

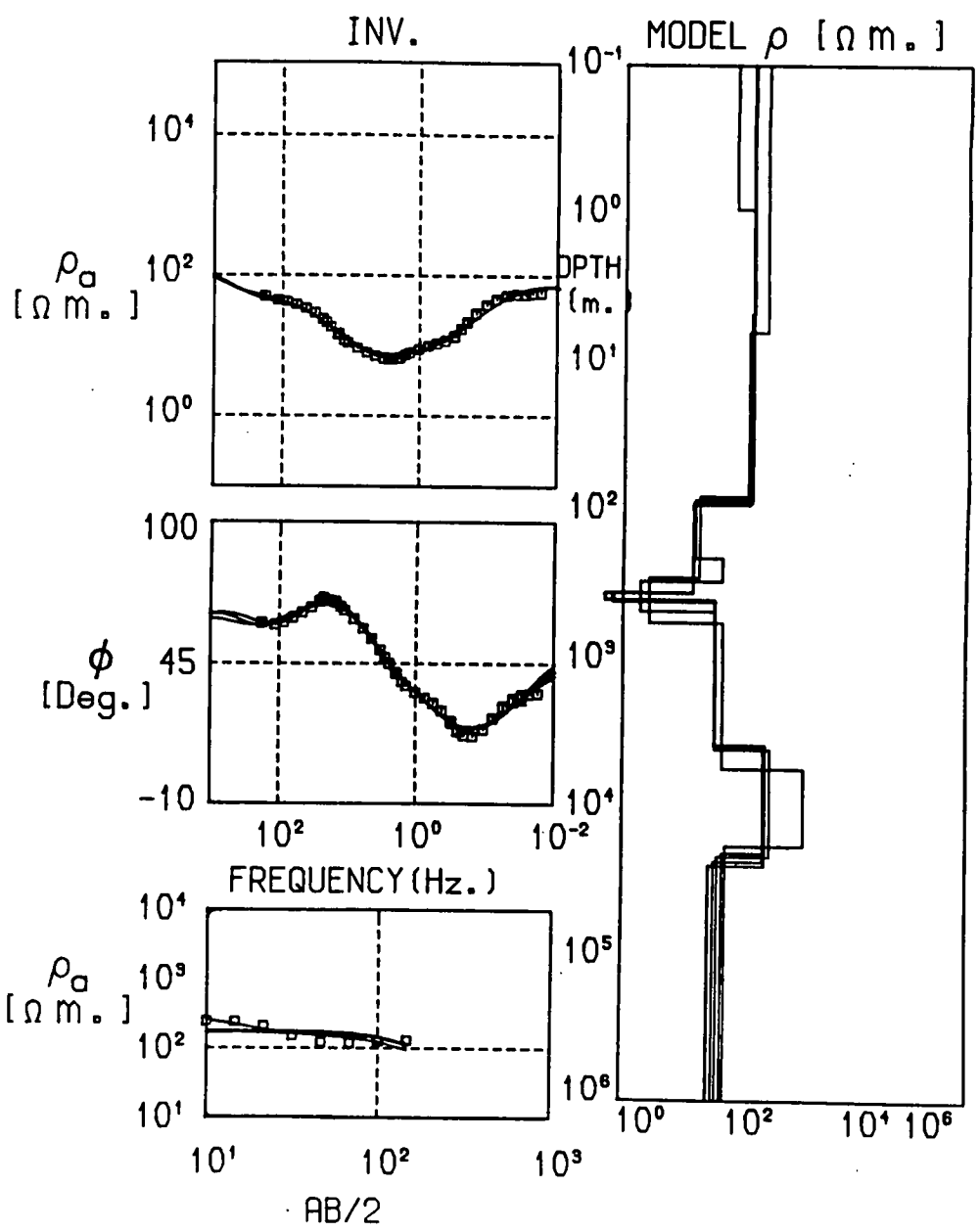
INV.
MODEL ρ [Ω m.]
ρa [Ω m.]
DPTH (m.
φ [Deg.]
FREQUENCY (Hz.)
AB/2

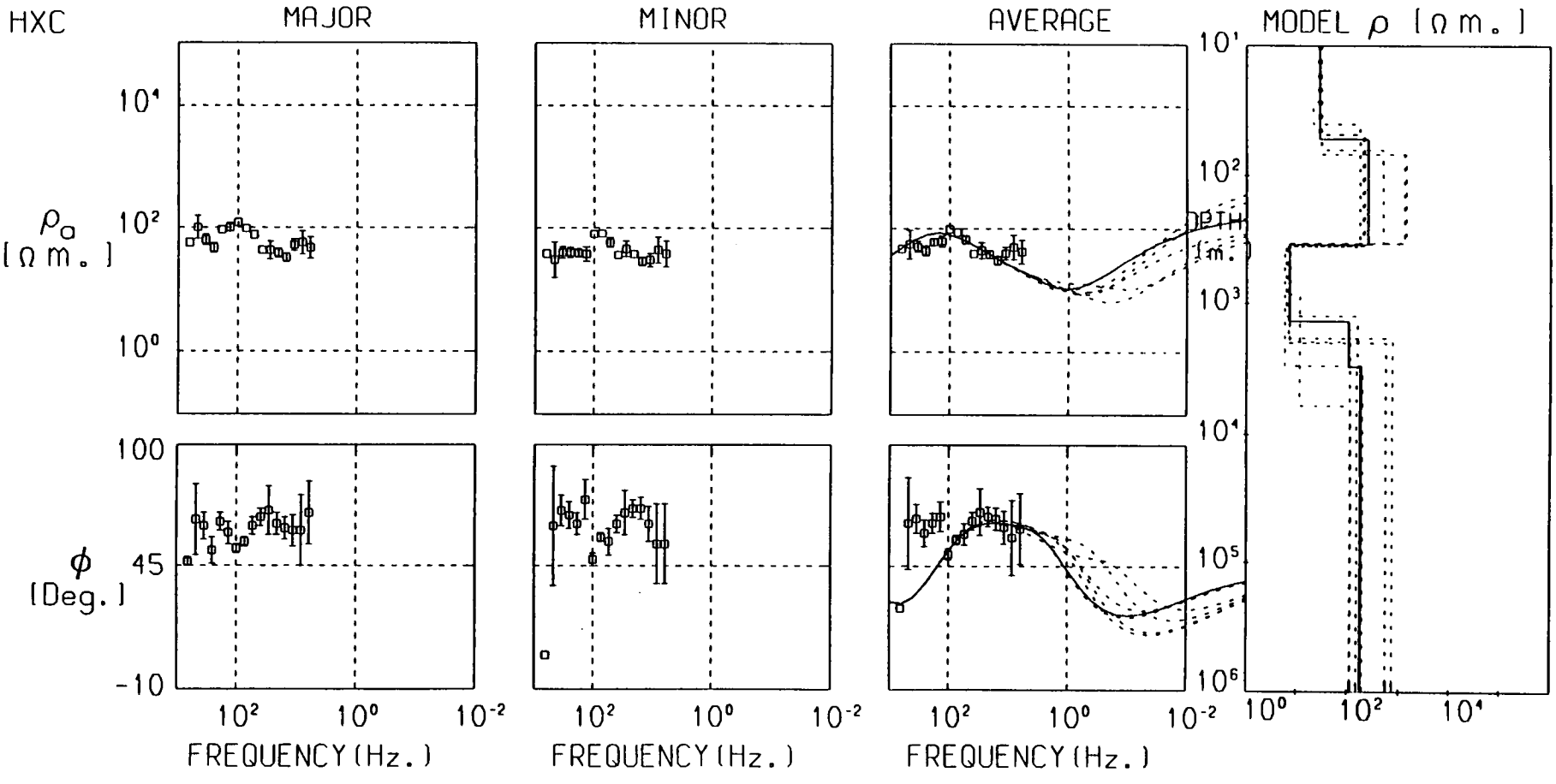
HXC
MAJOR
MINOR
AVERAGE
MODEL ρ [Ω m.]
ρa [Ω m.]
φ [Deg.]
10⁴
10²
10⁰
100
45
-10
10²
10⁰
10⁻²
FREQUENCY (Hz.)
10¹
10²
10³
10⁴
10⁵
10⁶
DEPTH (m.)

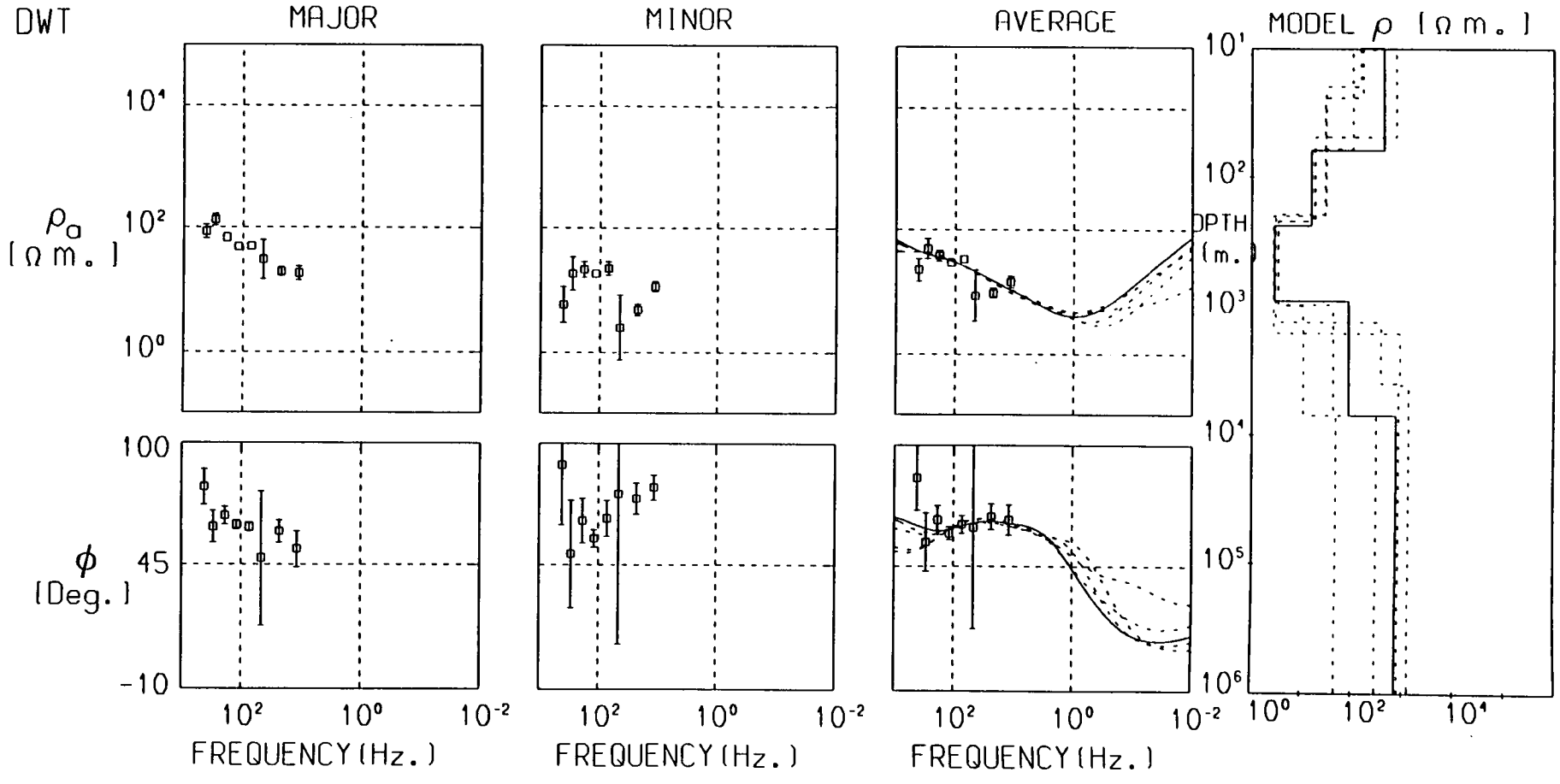
DWT
MAJOR
MINOR
AVERAGE
MODEL ρ [Ω m.]
ρa [Ω m.]
10⁴
10²
10⁰
100
φ [Deg.]
45
-10
10²
10⁰
10⁻²
FREQUENCY(Hz.)
DPTH (m.
10¹
10²
10³
10⁴
10⁵
10⁶

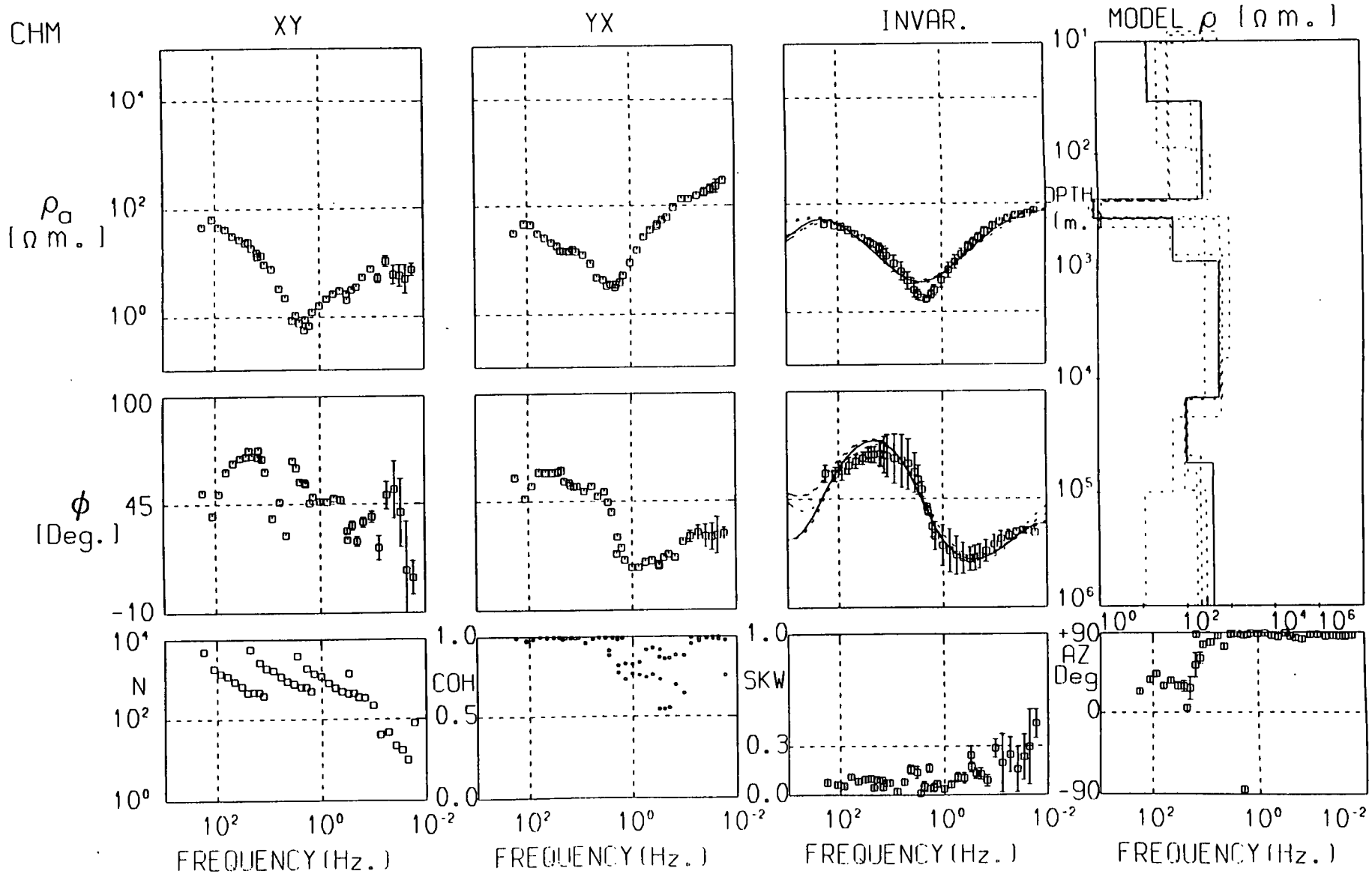
CHM
XY
YX
INVAR.
MODEL ρ [Ω m.]
ρa [Ω m.]
φ [Deg.]
N
COH
SKW
DPTH (m.)
AZ Deg
FREQUENCY(Hz.)
FREQUENCY(Hz.)
FREQUENCY(Hz.)
FREQUENCY(Hz.)

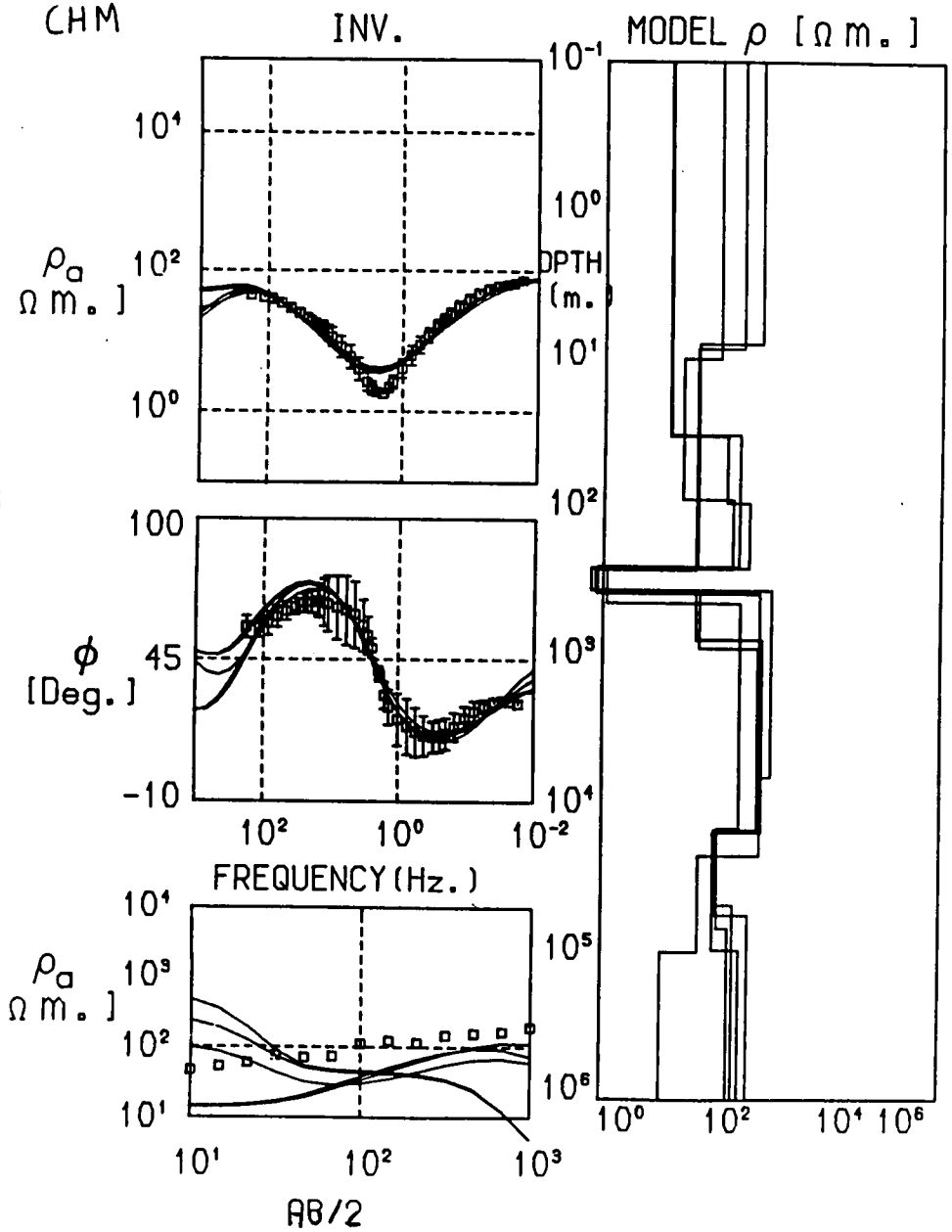
CHM
INV.
MODEL ρ [Ω m.]
ρa [Ω m.]
φ [Deg.]
DPTH (m.)
FREQUENCY (Hz.)
AB/2

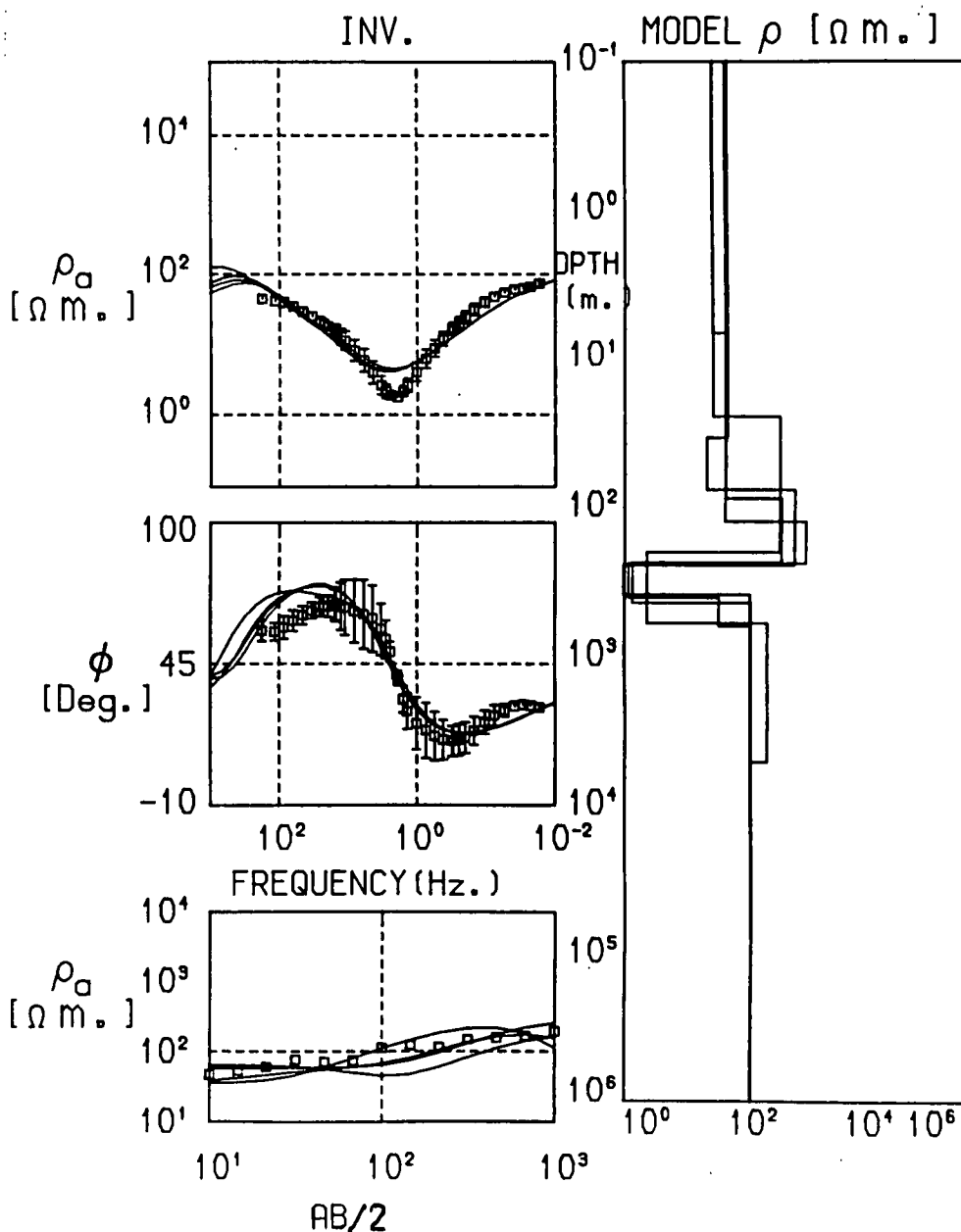
INV.
MODEL ρ [Ω m.]
ρa [Ω m.]
φ [Deg.]
DPTH (m.)
FREQUENCY (Hz.)
AB/2

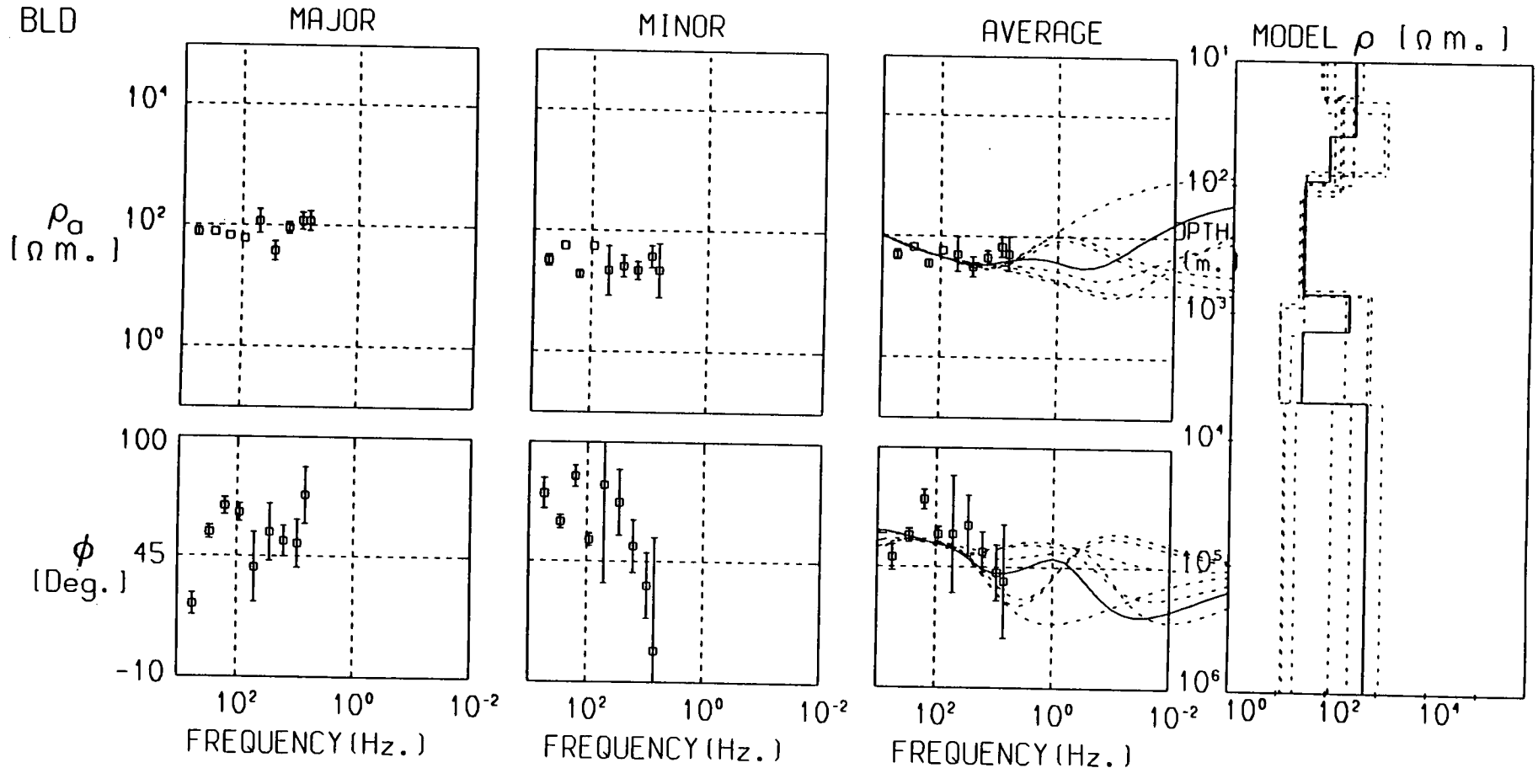
BLD
MAJOR
MINOR
AVERAGE
MODEL ρ [Ω m.]
ρa [Ω m.]
10⁴
10²
10⁰
100
45
-10
ϕ [Deg.]
10²
10⁰
10⁻²
FREQUENCY (Hz.)
DPTH (m.)
10¹
10²
10³
10⁴
10⁵
10⁶

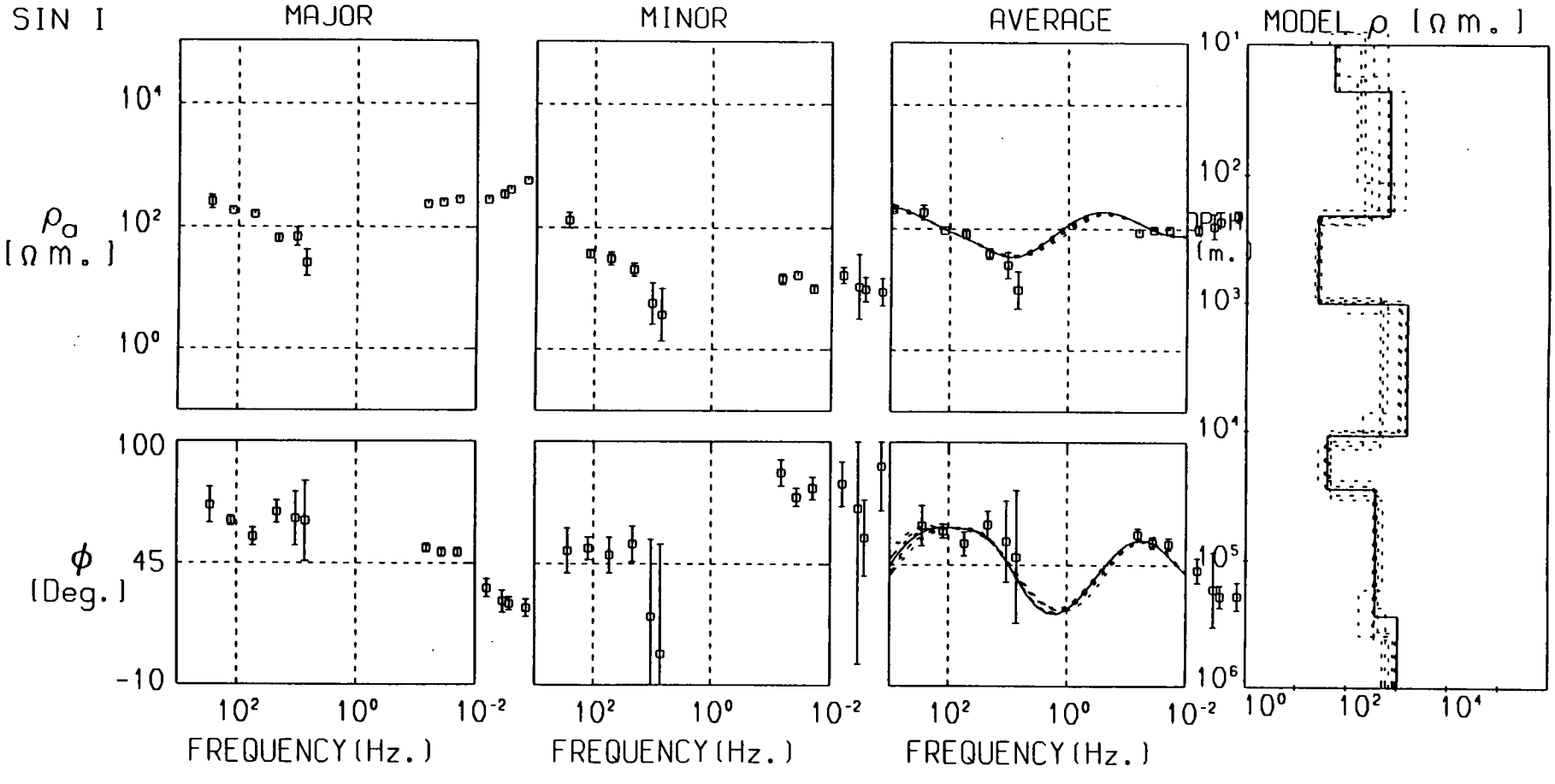
SIN I
MAJOR
MINOR
AVERAGE
MODEL ρ [Ω m.]
ρa [Ω m.]
φ [Deg.]
10⁴
10²
10⁰
100
45
-10
10²
10⁰
10⁻²
FREQUENCY (Hz.)
10¹
10²
10³
10⁴
10⁵
10⁶
(m.)

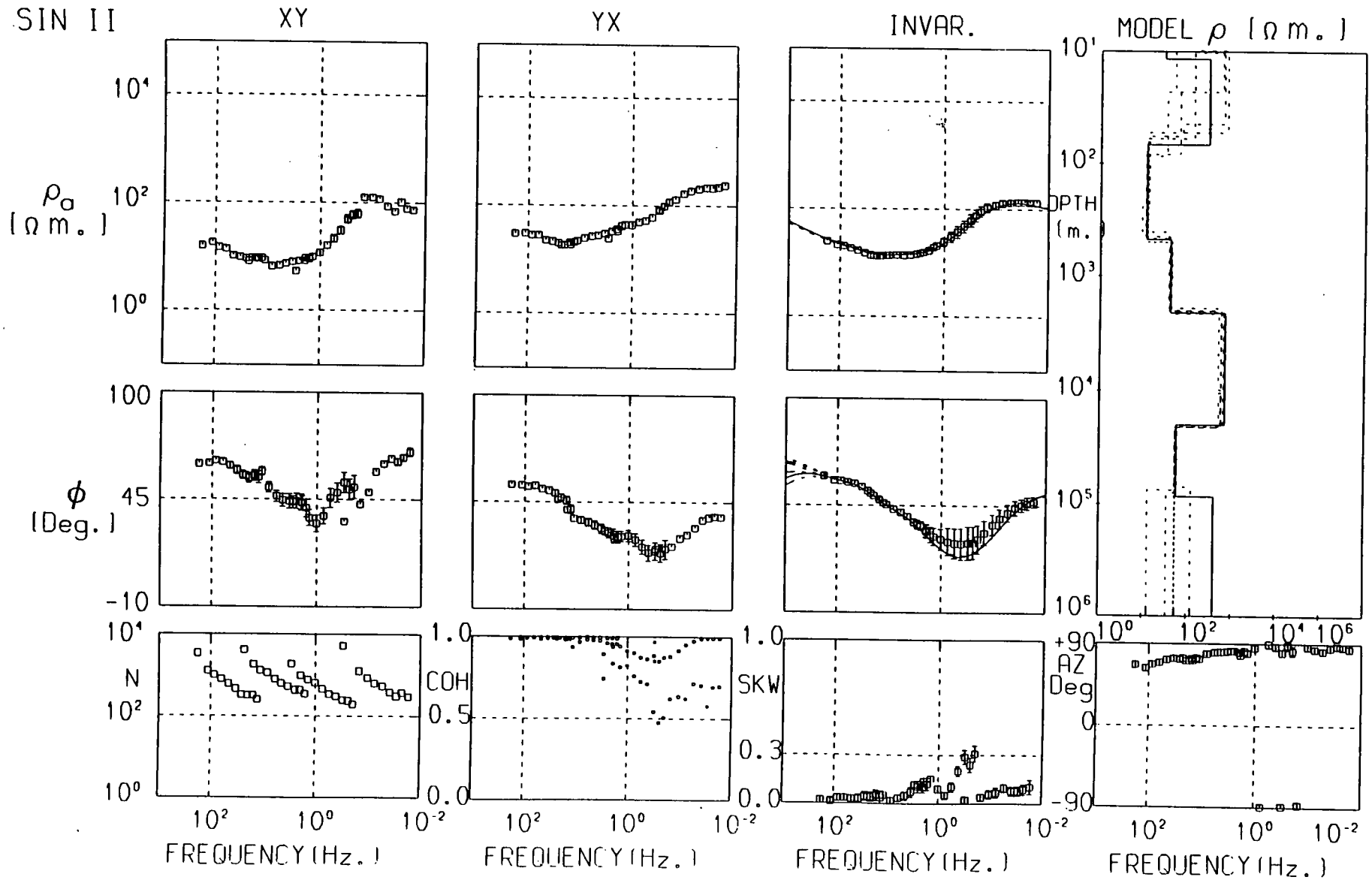
SIN II
XY
YX
INVAR.
MODEL ρ [Ω m.]
ρa [Ω m.]
10⁴
10²
10⁰
10¹
10³
10⁵
10⁶
DPTH [m.]
φ [Deg.]
100
45
-10
N
COH
SKW
1.0
0.5
0.3
0.0
+90
AZ Deg
0
-90
10²
10⁰
10⁻²
10⁴
FREQUENCY(Hz.)

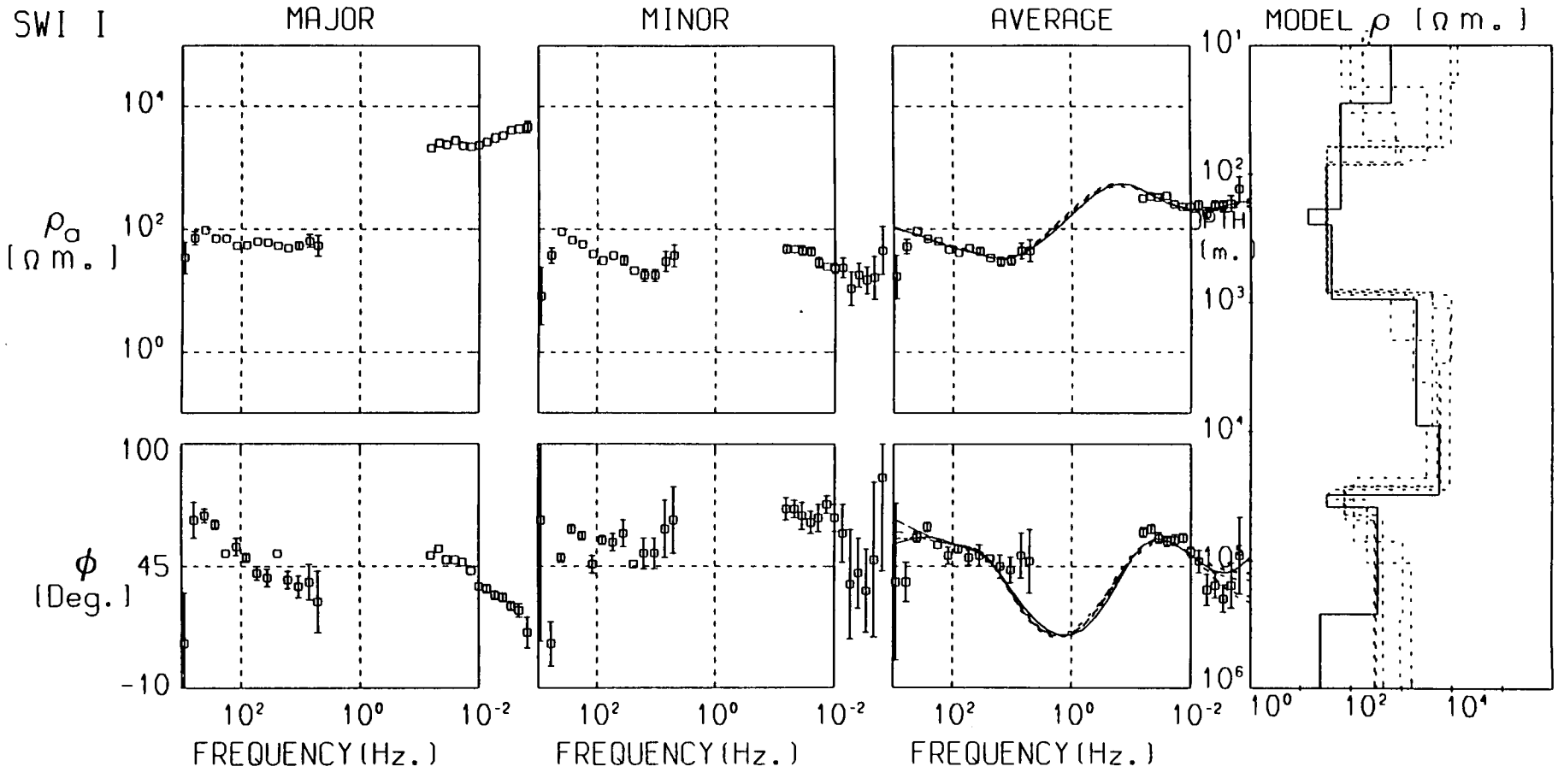
SWI I
MAJOR
MINOR
AVERAGE
MODEL ρ [Ω m.]
ρa [Ω m.]
φ [Deg.]
DEPTH [m.]
FREQUENCY [Hz.]
FREQUENCY [Hz.]
FREQUENCY [Hz.]

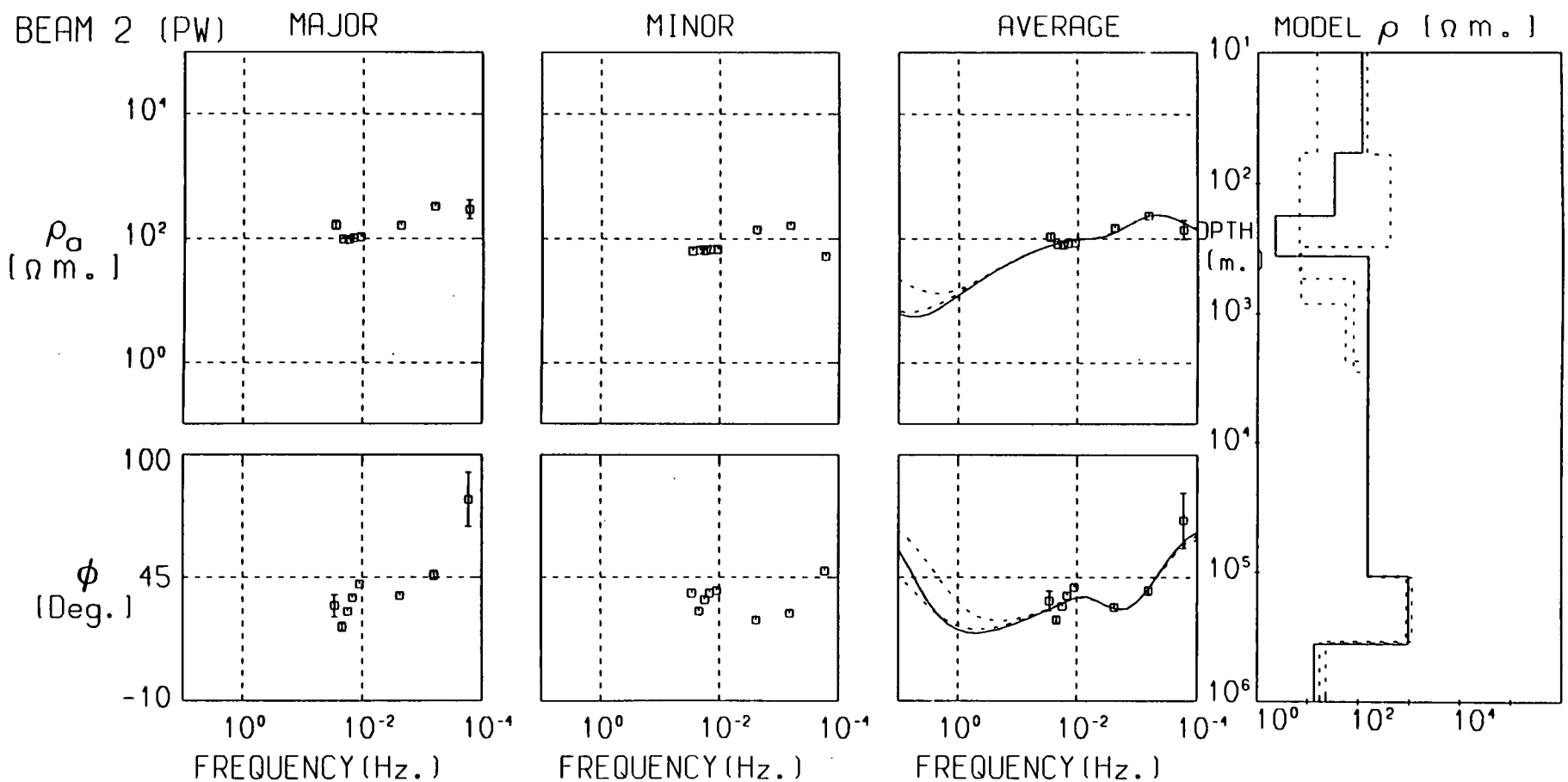
BEAM 2 (PW)
MAJOR
MINOR
AVERAGE
MODEL ρ (Ω m.)
ρa (Ω m.)
φ (Deg.)
FREQUENCY (Hz.)
DEPTH (m.)

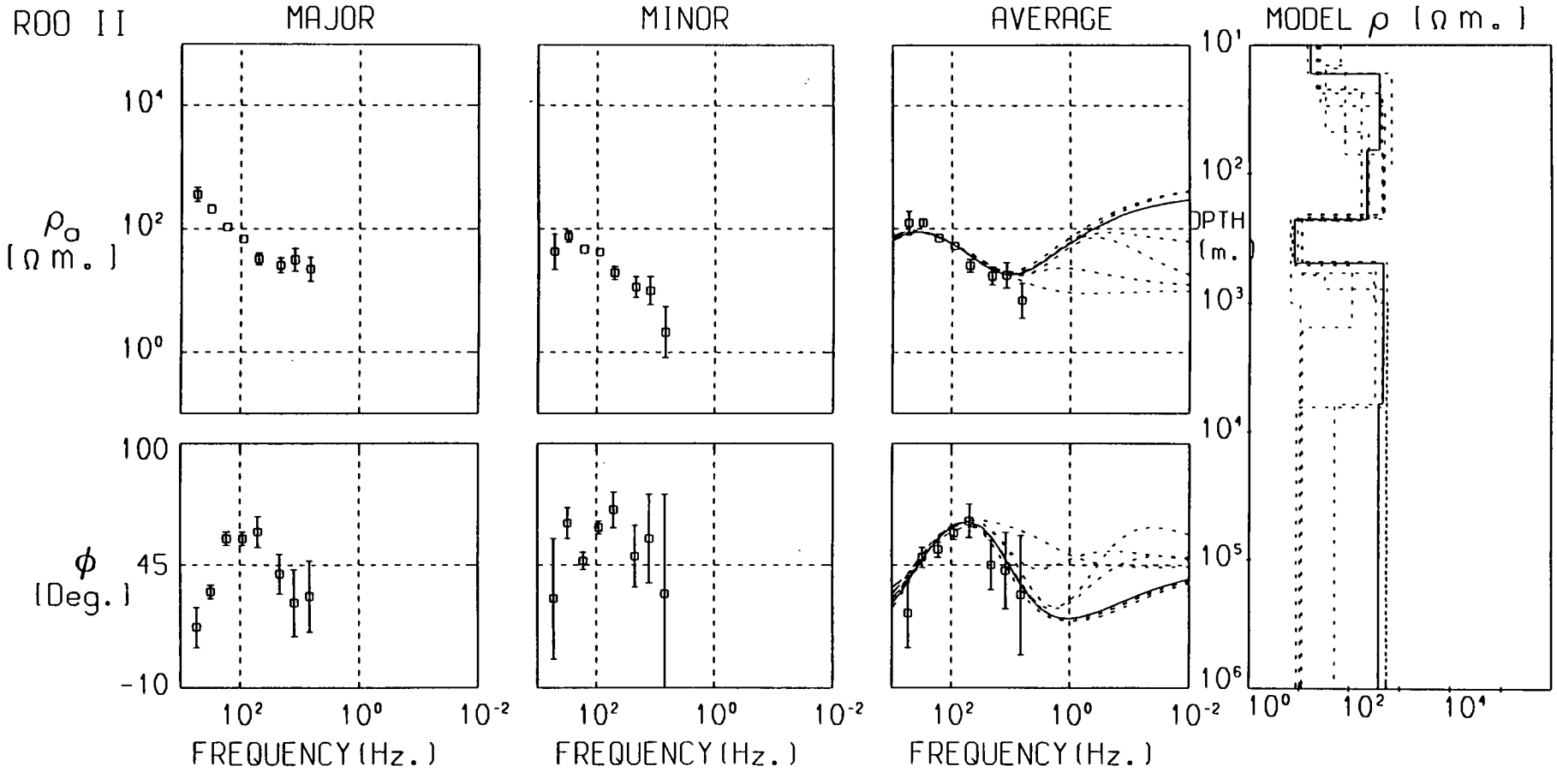
ROO II
MAJOR
MINOR
AVERAGE
MODEL ρ [Ω m.]
ρ_a [Ω m.]
10^4
10^2
10^0
10^1
10^3
10^5
10^6
DPTH (m.)
100
ϕ [Deg.]
45
-10
10^2
10^0
10^{-2}
10^4
FREQUENCY (Hz.)

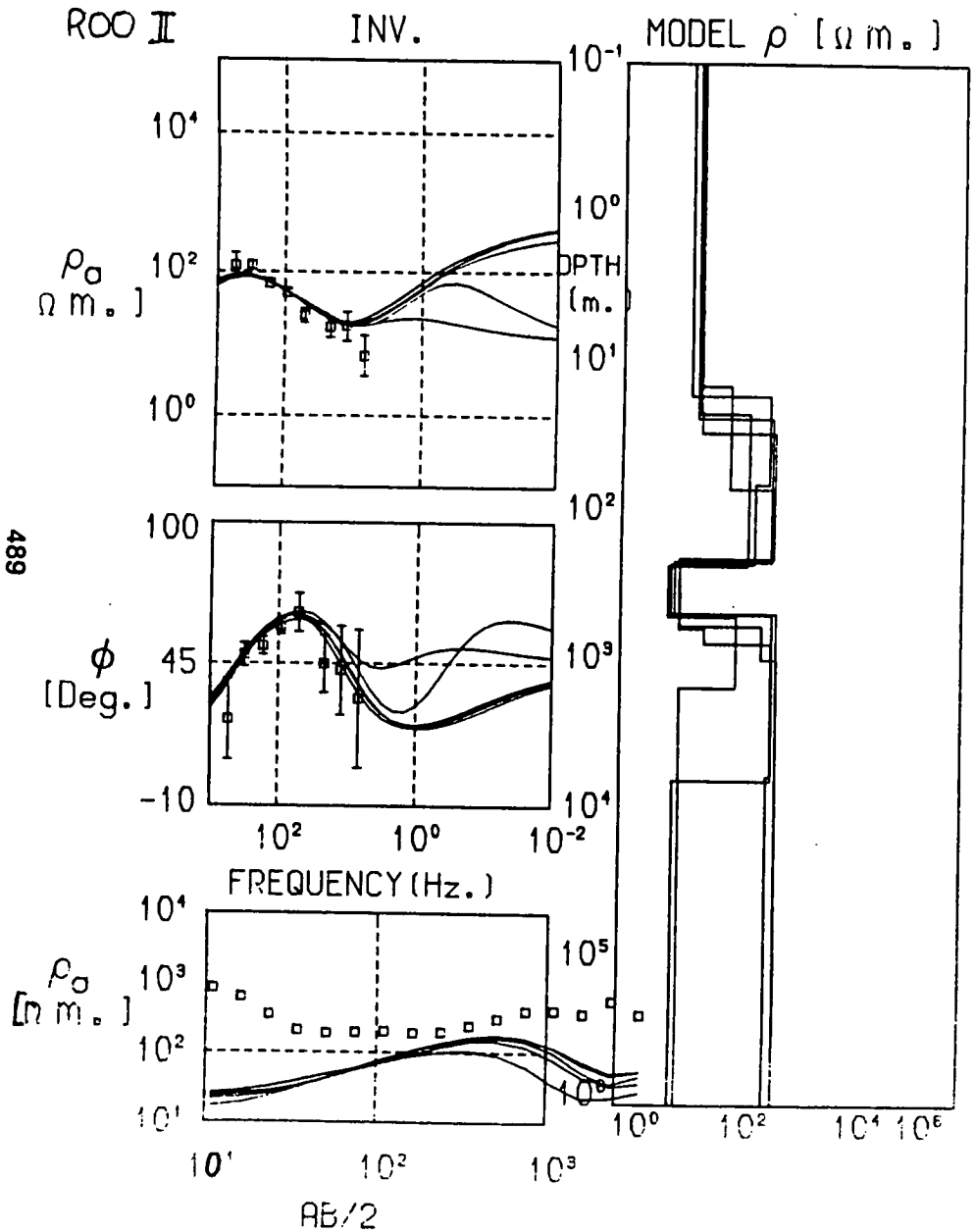
ROO Ⅱ
INV.
MODEL ρ [Ω m.]
ρa [Ω m.]
φ [Deg.]
DPTH (m.)
FREQUENCY (Hz.)
AB/2

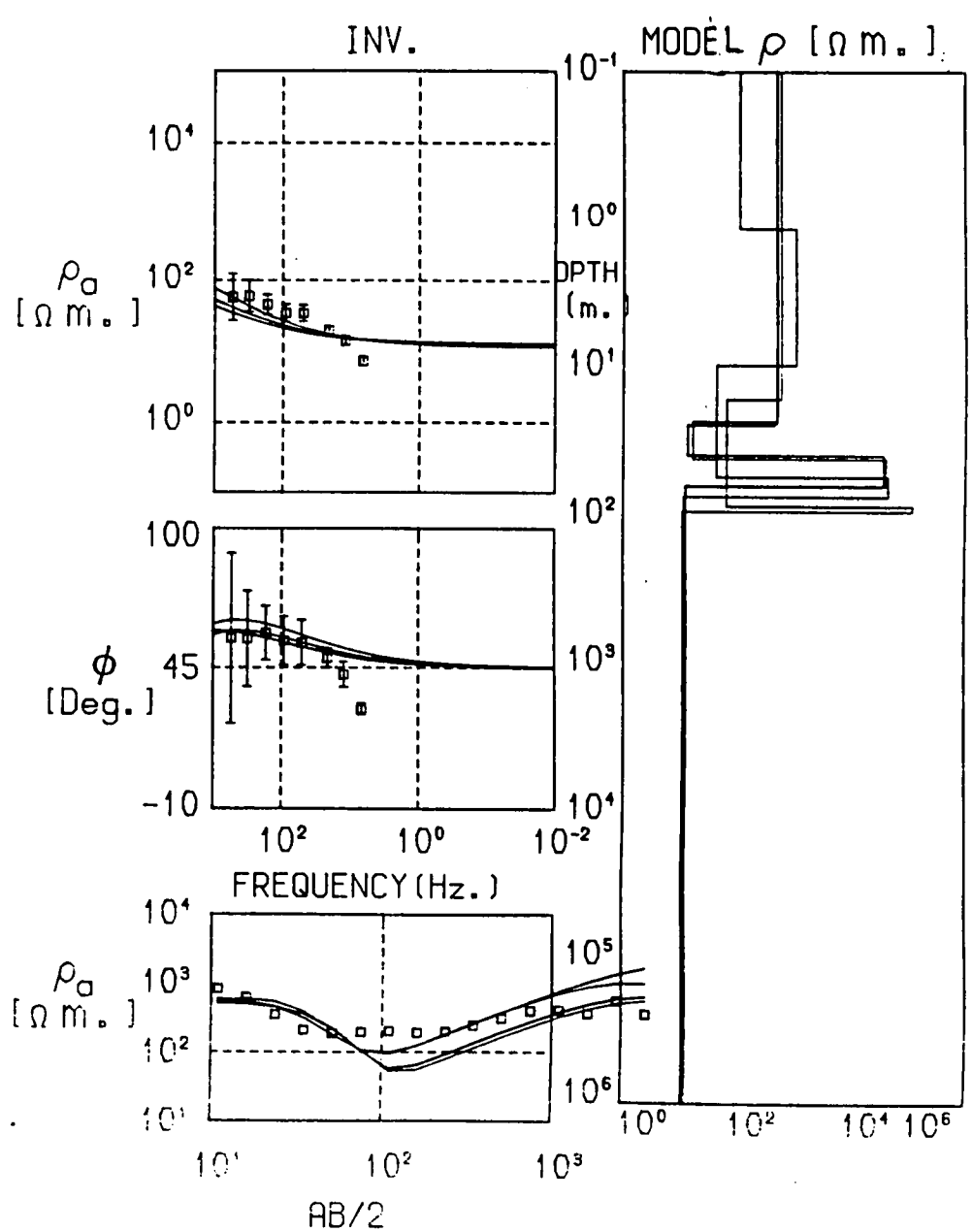
INV.
MODEL ρ [Ω m.]
ρa [Ω m.]
φ [Deg.]
DPTH (m.)
FREQUENCY (Hz.)
AB/2

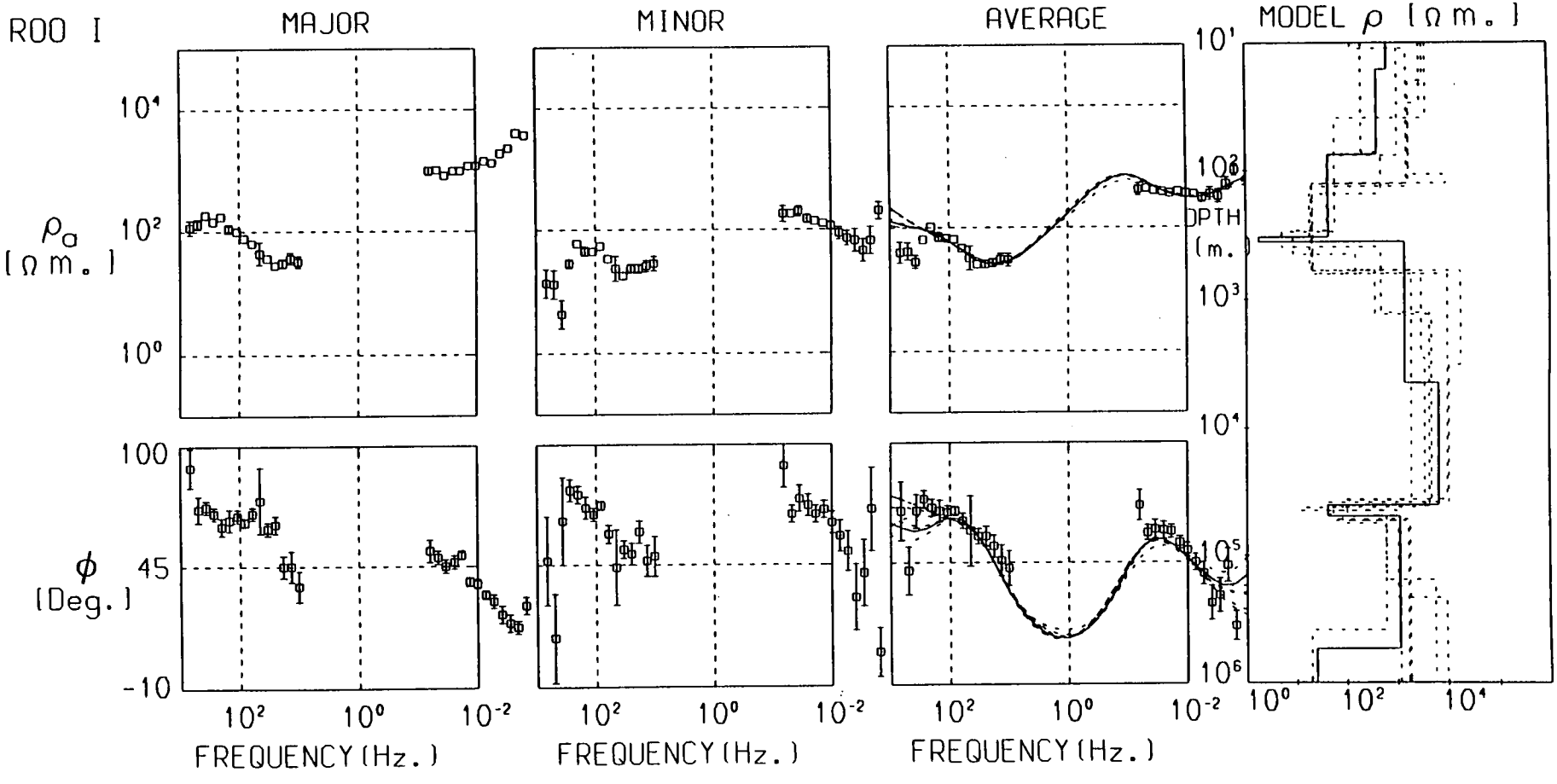
ROO I
MAJOR
MINOR
AVERAGE
MODEL ρ [Ω m.]
ρa [Ω m.]
10⁴
10²
10⁰
100
45
-10
φ [Deg.]
10²
10⁰
10⁻²
FREQUENCY (Hz.)
10¹
10²
DPTH (m.
10³
10⁴
10⁵
10⁶

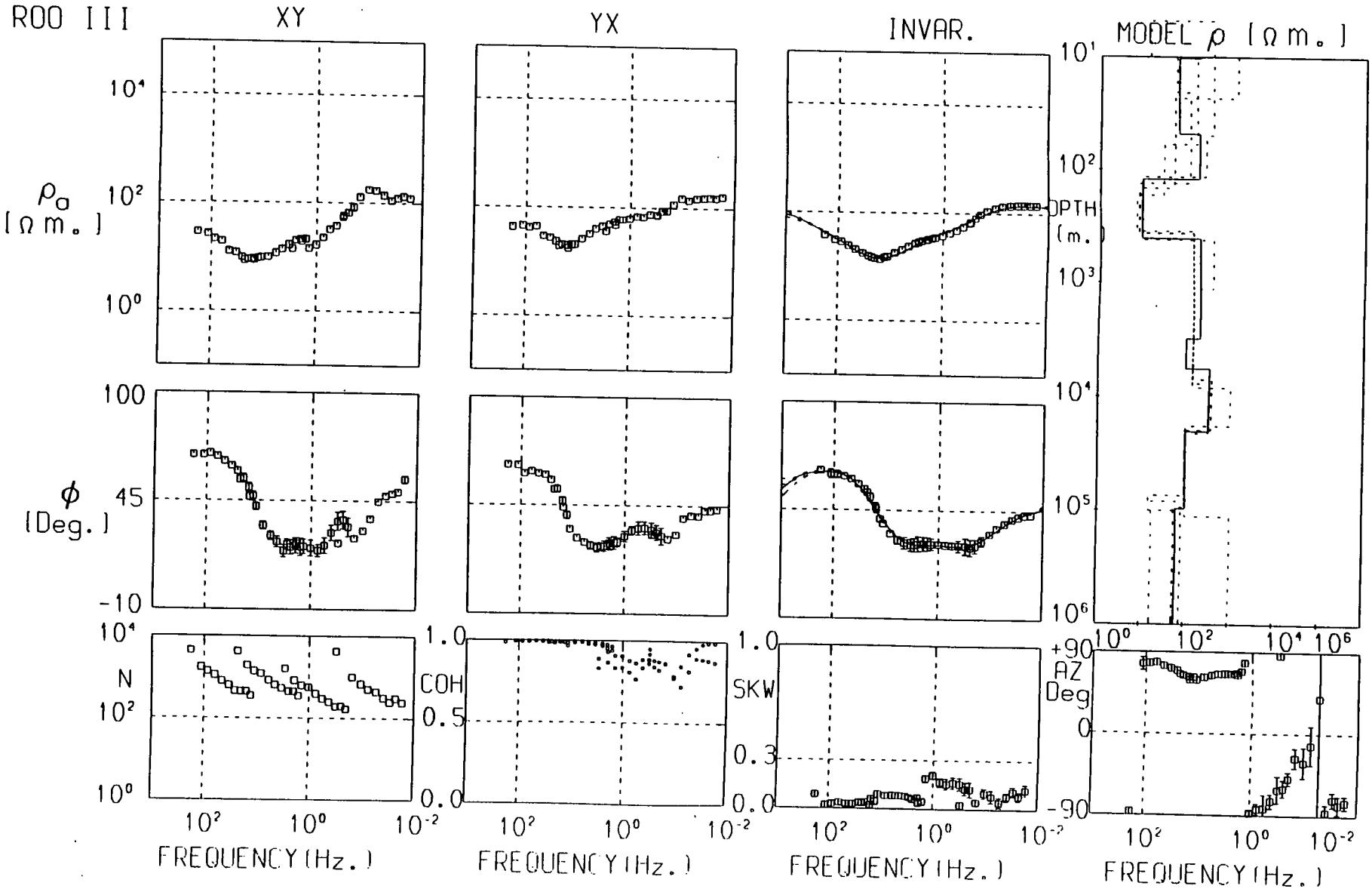
ROO III
XY
YX
INVAR.
MODEL ρ (Ω m.)
ρa (Ω m.)
φ (Deg.)
N
COH
SKW
AZ Deg
DPTH (m.)
FREQUENCY(Hz.)
FREQUENCY(Hz.)
FREQUENCY(Hz.)
FREQUENCY(Hz.)

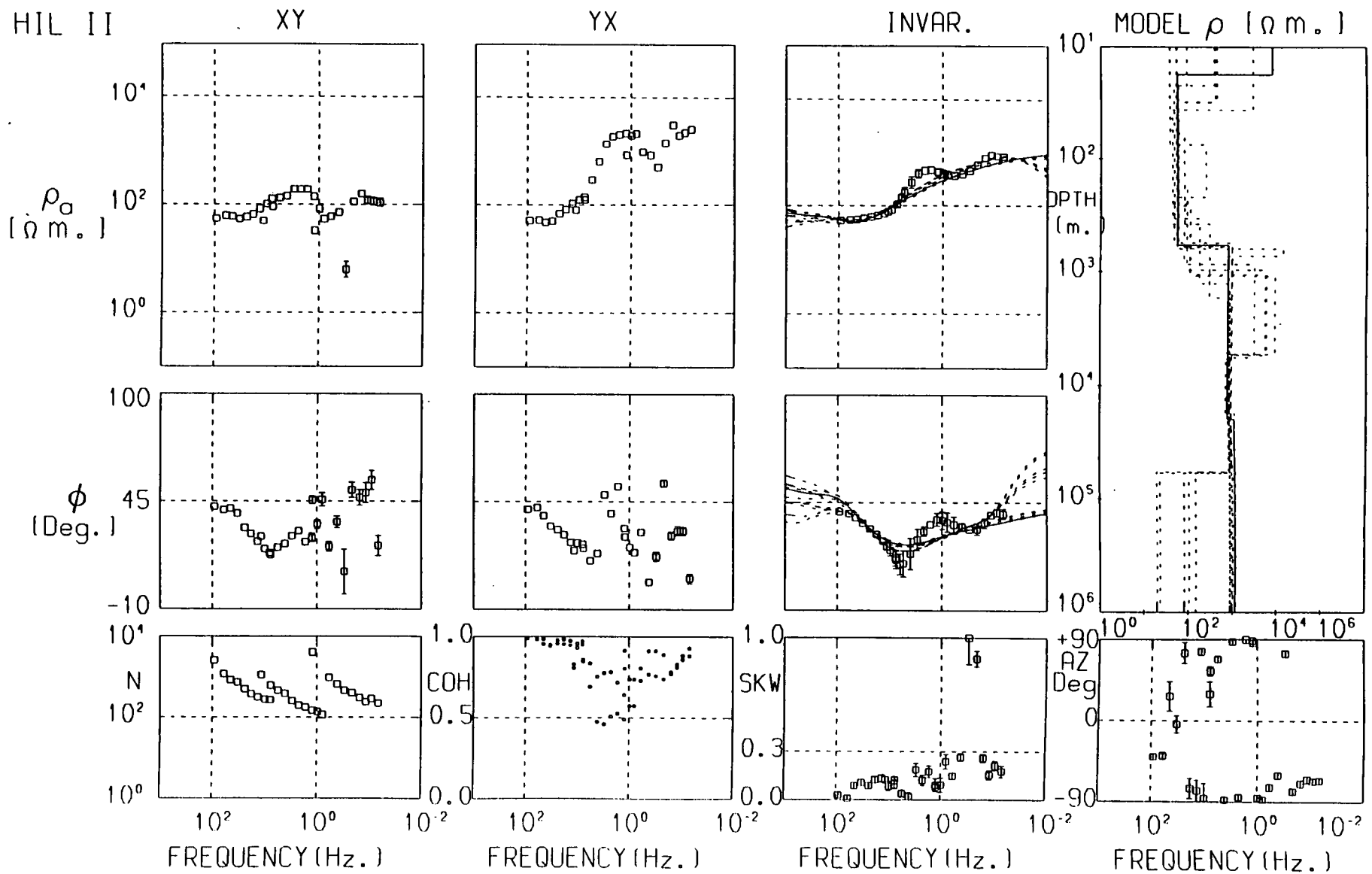
HIL II
XY
YX
INVAR.
MODEL ρ [Ω m.]
ρa [Ω m.]
10¹
10²
10⁰
100
φ [Deg.]
45
-10
N
COH
0.5
0.0
SKW
1.0
0.3
DPTH (m.)
10³
10⁴
10⁵
10⁶
+90
AZ Deg
0
-90
10⁻²
FREQUENCY (Hz.)

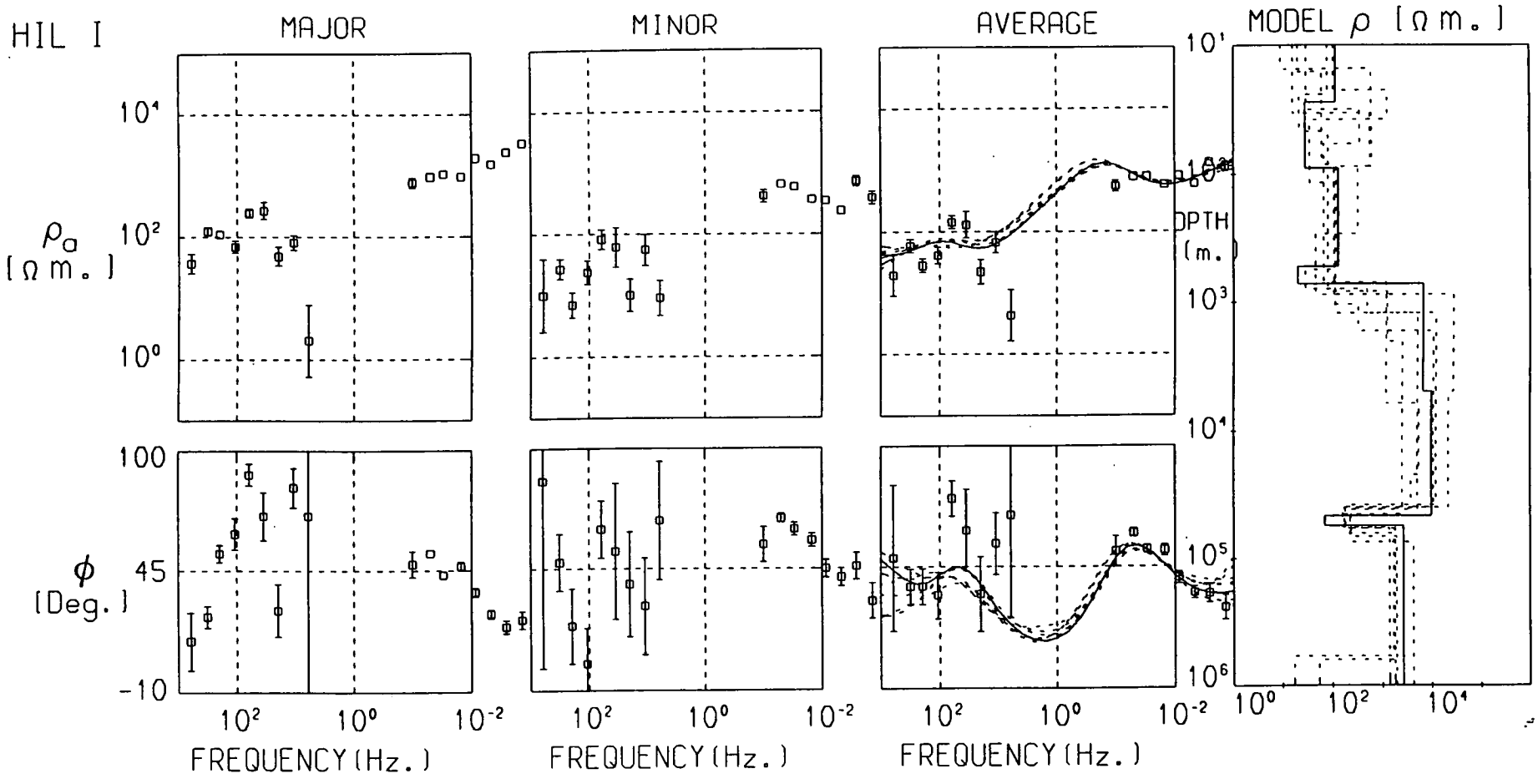
HIL I
MAJOR
MINOR
AVERAGE
MODEL ρ [Ω m.]
ρa [Ω m.]
φ [Deg.]
FREQUENCY (Hz.)
FREQUENCY (Hz.)
FREQUENCY (Hz.)
DEPTH (m.)